

The Machinability of a Gamma Titanium Aluminide Intermetallic

by

Richard Hood

A thesis submitted to
The University of Birmingham
for the degree of
DOCTOR OF PHILOSOPHY

School of Mechanical Engineering
The University of Birmingham
June 2010

UNIVERSITY OF
BIRMINGHAM

University of Birmingham Research Archive

e-theses repository

This unpublished thesis/dissertation is copyright of the author and/or third parties. The intellectual property rights of the author or third parties in respect of this work are as defined by The Copyright Designs and Patents Act 1988 or as modified by any successor legislation.

Any use made of information contained in this thesis/dissertation must be in accordance with that legislation and must be properly acknowledged. Further distribution or reproduction in any format is prohibited without the permission of the copyright holder.

SYNOPSIS

The work reported details the machinability of the latest generation gamma titanium aluminide intermetallic (γ -TiAl) alloy Ti-45Al-8Nb-0.2C which is able to operate at temperatures of up to 800°C. This high temperature capability allows this alloy to be considered for replacement of nickel alloys, as the material of choice for selected aeroengine components including turbine and compressor blades. Weight saving is the main driver as γ -TiAl alloy density is typically around 50% that of nickel based superalloys. Despite extensive alloy and manufacturing process development, no commercial aeroengine manufacturer currently operates with γ -TiAl alloys. A contributory factor in this is the difficulty in producing components of acceptable integrity, due mainly to the alloy's extremely low room temperature ductility of <2%. Additionally, machining data is also presented for a burn resistant titanium alloy, Ti-25V-15Cr-2Al-0.2C (%wt) (BuRTi).

Following a literature review (Objective 1) on relevant alloy development, cutting and abrasive processes, surface integrity, the machinability of γ -TiAl, burn resistant and orthorhombic titanium alloys and experimental design, the thesis details the results from two phases of experimental work. The first focused on high speed milling trials using coated tungsten carbide ball nose end mills whilst the second phase provided an assessment of intermittent dress creep feed grinding, using both conventional (SiC) and superabrasive (diamond and CBN) wheels with free jet nozzles used to supply grinding fluid. Full and fractional factorial (Taguchi) experimental designs were employed to identify the effect of key operating factors and levels on output measures (tool life/wheel wear, forces, power, and workpiece surface roughness). In addition, benchmarking the new alloy against the previously investigated γ -TiAl alloy Ti-45Al-2Mn-2Nb +0.8%vol. TiB₂, BuRTi and Ti-6Al-4V was undertaken. Main effect plots are detailed, together with Analysis of Variance (ANOVA) data and percentage contribution ratio (PCR) values. In addition, workpiece surface integrity evaluation including assessment of microstructure and microhardness is also presented.

In Phase 1A and 1B high speed ball nose end milling trials (Objective 2) tool life was generally excellent with a distance machined in excess of 800m, even at a cutting speed of 160m/min. When using high operating parameters including feed rates of 0.12 to 0.15mm/tooth and axial and radial depth of cuts of 0.5 to 1mm, tool life (in terms of distance cut) was, in some cases extremely short (<10m). Benchmarking trials (Objective 3) of Ti-45Al-8Nb-0.2C against the previously investigated γ -TiAl alloy, Ti-45Al-2Mn-2Nb +0.8%vol. TiB₂ established that the new alloy showed a ~25% increase in tool life for a

maximum flank wear criteria of 300 μ m. At a cutting speed of 160m/min, the distance machined for both γ -TiAl alloys was greater than 500m and was a considerable improvement over previously performed work as a consequence of the finer grade (0.3 μ m) WC substrate and an AlTiN coating. In benchmarking tests (Objective 4), Ti-45Al-8Nb-0.2C outperformed the burn resistant titanium (BuRTi) alloy by a factor of 10 times. Assessment of γ -TiAl surface/subsurfaces (Objective 2) showed fracture/pullout that was in general restricted to <50 μ m, with this damage appearing to be marginally larger in terms of size, depth and incidence with Ti-45Al-8Nb-0.2C than Ti-45Al-2Mn-2Nb+0.8% vol. TiB₂. Plastic deformation was visible on γ -TiAl surfaces in the form of bending of the lamellae which at lower operating parameters was restricted to <10 μ m from the workpiece surface.

In Phase 2A creep feed grinding trials (Objective 5), a G-ratio of ~30 was achieved using high grit content/low porosity SiC grit wheels at a low wheel speed of 15m/s, a depth of cut of 1.25mm and a feed rate of 150mm/min. Assessment of surfaces produced using these operating parameters showed the presence of a hardened layer with only a moderate increase in hardness of up to 520HK_{0.025} and damage consisting of intermittent deformation/bending of the lamellae to a depth of ~4 μ m with no visible cracking. Increasing the wheel speed and/or depth of cut and feed rate caused an increase in workpiece surface burn and cracking along with an increase in a hardened layer of up to ~150 HK_{0.025} higher than bulk and increased levels of bending of the lamellae up to ~20 μ m. Tests using more open SiC wheels showed lower forces and power levels along with a reduction in surface burn and cracking, however, G-ratios were reduced to <5.

G-ratios using superabrasive grinding wheels (Objective 6) were typically ~1000% higher than for SiC abrasive wheels using similar operating parameters as consequence of the increased grit hardness and thermal conductivity. These properties allowed surfaces to be produced using superabrasives at wheel speeds of up to 50m/s, which were comparable in terms of microhardness and surface/subsurface damage to SiC surfaces produced at low wheel speeds.

Benchmarking of Ti-45Al-8Nb-0.2C against BuRTi (Objective 7) showed that the γ -TiAl alloy was considerably easier to grind with a 10x higher G-ratio when using SiC abrasives and 4x higher when using superabrasives. In benchmarking trials (Objective 8), the G-ratio for Ti-45Al-8Nb-0.2C was ~9 times higher when using conventional abrasives and ~71 times higher when using superabrasives than those measured when grinding Ti-6Al-4V

ACKNOWLEDGEMENTS

The author would like to thank the following people and organisations for their help and assistance during this project.

Mr. David Aspinwall, Reader in Advanced Manufacturing Technology in the School of Mechanical Engineering and Head of Machining Research for his guidance, encouragement and supervision.

The Engineering and Physical Sciences Research Council for financial assistance and the loan of the FLIR Thermacam SC3000 for temperature measurement trials.

The industrial project partners including Dr. Wayne Voice, Mr. Colin Sage and Dr. Andrew Mantle of Rolls-Royce, Mr. John McTernan, Mr. Chris Waterhouse, Mr. David Martin and Mr. Bill McKaskill of Hardinge-Bridgeport, Mr. Paul Dando, Mr. Chris Davis and Mr. Steve Woods from Saint-Gobain Abrasives, Mr. Mike Jones, Mr. Michael Roach and Dr. Moshe Goldberg of Iscar Tools, Mr. Karl Tuffy and Mr. Neels Pretorius of Element Six and Mr. Dave Alexander and Mr. Lee Bott of Pumps and Equipment (Warwick).

Mr. Frederik Lechner, Mr Colin Johnson and Mr. Mathieu Lanette for assistance and cooperation in performing the high speed ball nose end milling and creep feed grinding trials benchmarking the performance of γ -TiAl alloy against the BuRTi alloy.

Mrs. Elaine Aspinwall, Senior Lecturer in the School of Mechanical Engineering for assistance in the design of experiments and statistical analysis.

Dr. Leung Soo, Lecturer in the School of Mechanical Engineering for his advice.

Prof. Paul Bowen, Professor of Mechanical Metallurgy in the School of Engineering (Metallurgy and Materials/Research Centre in Structural Materials).

Technical staff within the School of Mechanical Engineering and in particular Mr. Richard Fasham, Mr. Andy Loat, Mr. Alan Sewell and Mr. Peter Thornton for their assistance and advice.

Members of the Machining Research Group, School of Mechanical Engineering for support and advice during the duration of the project.

TABLE OF CONTENTS

LIST OF FIGURES	vii
LIST OF TABLES	xvi
LIST OF NOMENCLATURE	xix
1. INTRODUCTION	1.1
1.1 Background to the project	1.1
1.2 Aims and objectives of the project	1.4
1.3 Industrial collaborators and funding	1.6
2. LITERATURE REVIEW	2.1
2.1 Gamma titanium aluminide intermetallic alloys	2.1
2.1.1 Properties	2.1
2.1.2 Industrial applications	2.1
2.1.3 Alloy development and microstructure	2.2
2.2 Burn resistant titanium alloy (BuRTi)	2.6
2.3 Machinability	2.6
2.4 Economics of machining/grinding	2.7
2.5 Mechanics of milling/grinding	2.10
2.5.1 Mechanics of milling	2.10
2.5.2 Mechanics of grinding – undefined cutting geometry	2.12
2.6 Tool/grinding wheel wear	2.16
2.6.1 Tool wear mechanisms	2.16
2.6.2 Visible forms of tool wear	2.19
2.6.3 Grinding wheel wear	2.22
2.7 Grinding fluid application	2.24
2.8 Workpiece surface integrity	2.32
2.9 Machinability of gamma titanium aluminide intermetallic alloys	2.34
2.9.1 Introduction	2.34
2.9.2 Milling processes	2.35
2.9.3 Abrasive processes	2.43
2.9.4 Turning	2.55
2.9.5 Drilling, tapping and boring	2.60
2.9.6 Non-conventional machining processes	2.61
2.10 Machinability of burn resistant titanium alloys	2.63
2.11 Machinability of orthorhombic TiAl alloys	2.64
2.12 Experimental design	2.66
3. EXPERIMENTAL WORK	3.1
3.1 Workpiece materials	3.1
3.2 Machine tools, fixturing and equipment	3.3
3.2.1 Phase 1, high speed ball nose end milling	3.3
3.2.2 Phase 2, creep feed grinding	3.5
3.3 Cutting tools	3.7
3.4 Creep feed grinding wheels	3.8
3.5 Analysis equipment	3.9
3.6 Experimental programmes	3.13

3.6.1	Phase 1, high speed ball nose end milling	3.15
3.6.1.1	Phase 1A: Assessment of significant operating parameters	3.15
3.6.1.2	Phase 1B: Comparison of the machinability of Ti-45Al-8Nb-0.2C and Ti-45Al-2Mn-2Nb +0.8%vol. TiB ₂	3.18
3.6.1.3	Phase 1C: High speed ball nose end milling of burn resistant titanium alloy (BuRTi)	3.20
3.6.2	Phase 2, creep feed grinding	3.21
3.6.2.1	Phase 2A: Assessment of significant operating parameters when creep feed grinding Ti-45Al-8Nb-0.2C using conventional abrasive wheels	3.21
3.6.2.2	Phase 2B: Assessment of significant operating parameters when creep feed grinding Ti-45Al-8Nb-0.2C using superabrasive wheels	3.28
3.6.2.3	Phase 2C: Benchmarking of Ti-45Al-8Nb-0.2C against Ti-6Al-4V	3.31
4.	RESULTS AND DISCUSSION: PHASE 1, HIGH SPEED BALL NOSE END MILLING	4.1
4.1	Phase 1A: Assessment of significant operating parameters	4.1
4.2	Phase 1B: Comparison of the machinability of Ti-45Al-8Nb-0.2C and Ti-45Al-2Mn-2Nb +0.8%vol. TiB ₂	4.25
4.3	Phase 1C: High speed ball nose end milling of burn resistant titanium alloy (BuRTi)	4.40
5.	RESULTS AND DISCUSSION: PHASE 2, CREEP FEED GRINDING	5.1
5.1	Phase 2A: Assessment of significant operating parameters when creep feed grinding Ti-45Al-8Nb-0.2C using conventional abrasive wheels	5.1
5.1.1	Phase 2Ai: Initial assessment and benchmarking against BuRTi	5.1
5.1.2	Phase 2Aii: Further assessment	5.18
5.1.3	Phase 2Aiii: Comparison of the performance of different wheel specifications	5.24
5.1.4	Phase 2Aiv: Production of a demonstrator component blade root	5.28
5.2	Phase 2B: Assessment of significant operating parameters when creep feed grinding Ti-45Al-8Nb-0.2C using superabrasive wheels	5.29
5.2.1	Phase 2Bi: Preliminary testing of Ti-45Al-8Nb-0.2C using superabrasive wheels	5.29
5.2.2	Phase 2Bii: Further assessment and benchmarking against BuRTi	5.37
5.2.3	Phase 2Biii: Comparison of the performance of different wheel specifications	5.47
5.3	Phase 2C: Benchmarking of Ti-45Al-8Nb-0.2C against Ti-6Al-4V	5.49
6.	CONCLUSIONS	6.1
7.	SUGGESTIONS FOR FUTURE WORK	7.1

8. REFERENCES	8.1
APPENDICES	
Appendix A: Workpiece surface integrity	A1
Appendix B: Milling modes	B1
Appendix C: Additional experimental results	C1
C1 Phase 1, high speed ball nose end milling	C1
C2 Phase 2, creep feed grinding	C35
Appendix D: List of publications	D1

LIST OF FIGURES

Figure 1.1:	Material utilisation in a Rolls-Royce Trent 800 aero engine (Courtesy of Rolls-Royce Plc)	1.1
Figure 1.2:	Requirements for future gas turbine aero engines [3]	1.2
Figure 1.3:	Comparison of burn resistance between different titanium alloys using 1x25x50mm coupons at 300°C, 695kPag air pressure and 150m/s air velocity [4]	1.3
Figure 1.4:	Rolls-Royce Manufacturing Capability Readiness Level Definitions (Courtesy of Rolls-Royce Plc)	1.4
Figure 2.1:	Sample components made out of γ -TiAl (alloys), (a) cast (HP) compressor blades [14], (b) investment cast combustion chamber diffuser [11], (c) turbine wheel of automotive turbocharger [13], (d) Cast γ -TiAl automotive valves [15]	2.2
Figure 2.2:	Titanium-aluminium phase diagram [17]	2.3
Figure 2.3:	Microstructure of gamma TiAl alloys [20]	2.4
Figure 2.4:	Microstructures of a γ -TiAl base alloy of the composition Ti-47Al-3.7(Nb,Cr,Mn,Si)-0.5 B (at. %), [14]	2.5
Figure 2.5:	Variation of cost and time per component with cutting speed [33]	2.9
Figure 2.6:	Chip formation schematics (a) Orthogonal cutting (2d cutting process), (b) Oblique cutting (Top view showing inclination angle) [29]	2.11
Figure 2.7:	Schematic of the grinding process [29]	2.12
Figure 2.8:	Schematic showing force orientations [41]	2.13
Figure 2.9:	Systematic overview of measures for influencing technical grinding result [45]	2.16
Figure 2.10:	Basic wear mechanisms in metal cutting, (a) abrasive wear, (b) diffusive wear, (c) oxidation wear, (d) fatigue wear, (e) adhesive/attritious wear [31]	2.17
Figure 2.11:	Tool damage mechanisms and cutting temperature [47]	2.18
Figure 2.12:	Visible forms of milling tool wear [54]	2.21
Figure 2.13:	Boundary layer effects (a) cutting fluid backing up, (b) layers of air and fluid passing beneath the grinding wheel [59]	2.25
Figure 2.14:	Major different types of fluid application methods [72]	2.27
Figure 2.15:	Nozzles (a) free jet, (b) conventional [61]	2.29
Figure 2.16:	Main effects plot - means for tool life when high speed end milling [100]	2.36
Figure 2.17:	Taylor tool life curve when high speed end milling [100]	2.37
Figure 2.18:	Maximum cutting forces when high speed ball nose end milling [104]	2.38
Figure 2.19:	Cutting force when ball nose end milling Ti-45Al-2Mn-2Nb +0.8%vol. TiB ₂ (a) schematic of the cutting process and force directions, (b) cutting force and flank wear with increasing distance cut [104]	2.38

Figure 2.20:	Cross sections of machined surface ($v=70\text{m/min}$, $d=0.2\text{mm}$, $a=0.2\text{mm}$, $f=0.06\text{mm/tooth}$, dry, flank wear $=300\mu\text{m}$, 0°) when ball nose end milling [106]	2.40
Figure 2.21:	Cross sections of the machined workpiece surface, $v=70\text{m/min}$, $d=(a) 0.1\text{mm}$, $(b) 0.2\text{mm}$, $f=0.06\text{mm/tooth}$, dry, flank wear $=300\mu\text{m}$, 45° when ball nose end milling [106]	2.40
Figure 2.22:	Microhardness profiles for ball nose end milling, $v=70\text{m/min}$, $d=0.2\text{mm}$, $a=0.2\text{mm}$, $f=0.06\text{mm/tooth}$, dry, flank wear $=300\mu\text{m}$, (a) 0° , (b) 45° [106]	2.40
Figure 2.23:	Main Effects Plot - means for residual stress when ball nose end milling [106]	2.41
Figure 2.24:	SN curves for machined surfaces [108, 109]	2.41
Figure 2.25:	Tool life results after face milling Ti-47Al-2Nb-2Mn +0.8%vol TiB ₂ (MG=micrograin, CG=coarse grain) [110]	2.42
Figure 2.26:	Results of face milling Ti-47Al-2Nb-2Mn +0.8%Vol TiB ₂ (a) surface roughness Ra, (b) microhardness [110]	2.43
Figure 2.27:	Comparison in surface finish and G-ratio when grinding (a) Ti-6Al-4V and (b) Ti-45Al-2Mn-2Nb [108, 112]	2.44
Figure 2.28:	Surface grinding results (a) forces, (b) surface roughness Ra [114]	2.45
Figure 2.29:	Surface grinding results (a) microhardness, (b) residual stress [114]	2.46
Figure 2.30:	Further surface grinding results (a) main effects plot – means for maximum normal force, (b) microhardness [114]	2.47
Figure 2.31:	Microhardness depth profiles for conventional abrasive CFG [108]	2.50
Figure 2.32:	Microhardness depth profiles for superabrasive abrasive CFG [108]	2.50
Figure 2.33:	Force against dresser infeed rate when creep feed grinding using conventional abrasive wheels (a) normal, (b) tangential [108]	2.52
Figure 2.34:	Residual stress against dresser infeed rate when creep feed grinding using conventional abrasive grinding wheels [108]	2.52
Figure 2.35:	Tool wear and specific grinding energy for speed stroke grinding [120]	2.53
Figure 2.36:	Analysis of the workpiece surface layer for speed stroke grinding [120]	2.54
Figure 2.37:	Residual stress and crack formation for speed stroke grinding [120]	2.54
Figure 2.38:	Taylor tool life curve for the turning of two different γ -TiAl alloys [126-128]	2.56
Figure 2.39:	Transverse cross-sections of a turned γ -TiAl [130]	2.57
Figure 2.40:	Tool life when turning Ti-45Al-2Mn-2Nb +0.8%vol. TiB ₂ using various cutting tool types and fluid application methods [136]	2.58
Figure 2.41:	Entry and exit fracture when twist drilling [142]	2.60
Figure 2.42:	Images showing entry and exit of ultrasonically machined holes [143]	2.61
Figure 2.43:	Sample EDWM'd surface showing cracks and HAZ [144]	2.62
Figure 2.44:	Tool wear in high speed ball nose end milling trials [150]	2.64

Figure 2.45:	SEM images of workpiece surface damage and cross sections after HSM [150]	2.64
Figure 2.46:	v-T curves when high speed end milling orthorhombic TiAl and Ti-45Al-2Mn-2Nb +0.8%vol. TiB ₂ [152]	2.65
Figure 3.1:	Ti-45Al-8Nb-0.2C workpiece microstructure	3.1
Figure 3.2:	Ti-45Al-2Mn-2Nb +0.8% vol. TiB ₂ workpiece microstructure	3.2
Figure 3.3:	(a) BuRTi blade in the received state, (b) BuRTi blade machined to create section for tests and (c) bulk microstructure	3.3
Figure 3.4:	Machining centres used for Phase 1, high speed ball nose end milling tests	3.3
Figure 3.5:	γ -TiAl workpiece, nozzle and cutting tool holder setup	3.4
Figure 3.6:	BuRTi workpiece and fixture at an angle of (a) 0°, (b) 45°	3.4
Figure 3.7:	Bridgeport FGC1000 (a) machine, (b) spindle power/torque curve	3.5
Figure 3.8:	Grinding arrangements (a) γ -TiAl and Ti-6Al-4V (b) BuRTi workpieces	3.6
Figure 3.9:	Nozzles (a) free jet, (b) low pressure spark suppression	3.6
Figure 3.10:	Dressing equipment (a) hydraulic diamond roller dresser and plain profile hand set sintered diamond roll, (b) hand set sintered diamond roll, (c) “lobe” type diamond roller dresser	3.7
Figure 3.11:	IC900 cutting tool (a) micrograph of substrate, (b) cross-section [159]	3.8
Figure 3.12:	Images showing the orientation used for milling tests, (a) Isometric view, (b) Left side view (Cutting tool feed direction: out of paper), (c) Right side view (Cutting tool feed direction: into the paper)	3.10
Figure 3.13:	FLIR Thermacam SC3000 and mounting bracket	3.11
Figure 3.14:	Schematic showing location and nomenclature of samples used for high speed milled workpiece surface integrity assessment	3.12
Figure 3.15:	Schematic showing location and nomenclature of samples used for creep feed ground workpiece surface integrity assessment	3.12
Figure 3.16:	Phases of work chart	3.14
Figure 3.17:	Grinding wheel and nozzle arrangement	3.24
Figure 3.18:	Nozzle disposition schematic	3.25
Figure 4.1:	Maximum flank wear against distance machined for all tests (Phase 1A)	4.1
Figure 4.2:	Distance machined against material removal rate (Phase 1A)	4.2
Figure 4.3:	Maximum flank wear against distance machined for Test 10	4.3
Figure 4.4:	Test 10 wear scar photographs	4.4
Figure 4.5:	View of ball nose end mill showing four cutting edges	4.5
Figure 4.6:	Side view of the cutters (Tooth 1 and 3 (odd))	4.5
Figure 4.7:	Side view of the cutting tool (Tooth 2 and 4 (even))	4.6
Figure 4.8:	SEM images of cutting tools from Test 9	4.7
Figure 4.9:	EDX analysis of worn tools used in Test 9. From Figure 4.8 (a) and (c): (a) Region 1, (b) Region 2, (c) Region 3	4.7
Figure 4.10:	Main Effects Plot - means for distance machined	4.9

Figure 4.11:	Maximum flank wear against distance machined for Test 8	4.12
Figure 4.12:	Main Effects Plot - means for forces	4.13
Figure 4.13:	Main Effects Plot - means for workpiece surface roughness (Phase 1A)	4.15
Figure 4.14:	Workpiece surface after the initial preparation stage	4.17
Figure 4.15:	Machined workpiece surfaces	4.17
Figure 4.16:	Machined workpiece surface and surface damage from Test 2	4.18
Figure 4.17:	Machined workpiece surface and surface damage from Test 4	4.18
Figure 4.18:	SEM views showing machined workpiece surface from Test 2	4.19
Figure 4.19:	SEM views showing the machined workpiece surface from Test 4	4.19
Figure 4.20:	Microhardness depth profiles (Phase 1A)	4.21
Figure 4.21:	Surface/subsurface micrographs of electrical discharge wire machined surfaces	4.22
Figure 4.22:	Cross sectional micrographs of the workpiece surface/subsurface from Test 2	4.23
Figure 4.23:	Cross sectional micrographs of the workpiece surface/subsurface from Test 4	4.23
Figure 4.24:	Cross sectional micrographs of the workpiece surface/subsurface in a direction parallel to the feed direction	4.24
Figure 4.25:	Cross sectional micrograph of the workpiece surface/subsurface from Test 15	4.24
Figure 4.26:	Cross sectional micrographs of the workpiece surface/subsurface from Test 16	4.25
Figure 4.27:	Maximum flank wear against distance machined (Phase 1B)	4.26
Figure 4.28:	Taylor tool life (vT) curve	4.27
Figure 4.29:	Digital image of the cutting tool when machining Test 3	4.29
Figure 4.30:	Images showing the cutting temperatures	4.30
Figure 4.31:	A bar chart showing cutting temperature	4.30
Figure 4.32:	Main Effects Plot - means for maximum cutting temperature	4.31
Figure 4.33:	Cutting forces and maximum flank wear against distance machined for Test 1: v=160m/min	4.32
Figure 4.34:	Workpiece surface roughness Ra (Phase 1B)	4.34
Figure 4.35:	Main Effects Plot - means for workpiece surface roughness Ra (Phase 1B)	4.34
Figure 4.36:	Images of machined workpiece surface (Phase 1B)	4.36
Figure 4.37:	Microhardness depth profiles for Tests 1 to 3 (Ti-45Al-8Nb-0.2C)	4.37
Figure 4.38:	Microhardness depth profiles for Tests 4 to 6 (Ti-45Al-2Mn-2Nb +0.8%vol. TiB ₂)	4.38
Figure 4.39:	Workpiece surface/subsurface cross-sectional images (Phase 1B) (1)	4.39
Figure 4.40:	Workpiece surface/subsurface cross-sectional images (Phase 1B) (2)	4.40
Figure 4.41:	Maximum flank wear against distance machined (Phase 1C)	4.41

Figure 4.42:	Main Effects Plot - means for tool life	4.42
Figure 4.43:	Wear scar photographs showing adhered material (Phase 1C)	4.42
Figure 4.44:	Wear scar photographs show wear location (Phase 1C)	4.43
Figure 4.45:	Maximum flank wear against distance machined or material removed	4.44
Figure 4.46:	Main Effects Plot - means for resultant force	4.45
Figure 4.47:	Force against maximum flank wear for Tests 5 and 9	4.46
Figure 4.48:	Main Effects Plot - means for workpiece surface roughness Ra (Phase 1C)	4.47
Figure 4.49:	Images of the machined workpiece surface (Phase 1C)	4.49
Figure 4.50:	Microhardness depth profiles (Phase 1C)	4.50
Figure 4.51:	Images of the machined workpiece surface/subsurface (Phase 1C)	4.51
Figure 5.1:	G-ratio against volume of workpiece material removed (Phase 2Ai, γ -TiAl)	5.1
Figure 5.2:	Wheel profile wear	5.2
Figure 5.3:	Main Effects Plot - means for G-ratio (Phase 2Ai)	5.4
Figure 5.4:	Main Effects Plot - means for normal force (Phase 2Ai)	5.5
Figure 5.5:	Main Effects Plot - means for tangential force (Phase 2Ai)	5.5
Figure 5.6:	Main Effects Plot - means for power (Phase 2Ai)	5.6
Figure 5.7:	Main Effects Plot - means for specific energy (Phase 2Ai)	5.7
Figure 5.8:	Main Effects Plot - means for surface roughness Ra (Phase 2Ai)	5.7
Figure 5.9:	Selected γ -TiAl workpiece surface images (Phase 2Ai, γ -TiAl)	5.10
Figure 5.10:	Selected BuRTi workpiece surface images (Phase 2Ai, BuRTi)	5.12
Figure 5.11:	Higher magnification images of the ground surface (Phase 2Ai, γ -TiAl)	5.13
Figure 5.12:	Higher magnification images of the ground surface (Phase 2Ai, BuRTi)	5.13
Figure 5.13:	Microhardness depth profiles (Phase 2Ai, γ -TiAl)	5.14
Figure 5.14:	Microhardness depth profiles (Phase 2Ai, BuRTi)	5.16
Figure 5.15:	Surface/subsurface cross-sectional micrographs (Phase 2Ai, γ -TiAl)	5.17
Figure 5.16:	Surface/subsurface cross-sectional micrographs (Phase 2Ai, BuRTi)	5.18
Figure 5.17:	G-ratio and workpiece surface roughness Ra (Phase 2Aii)	5.19
Figure 5.18:	Normal and tangential force (Phase 2Aii)	5.20
Figure 5.19:	Power and specific energy (Phase 2Aii)	5.21
Figure 5.20:	Workpiece surface images (Phase 2Aii)	5.22
Figure 5.21:	High magnification workpiece surface images (Phase 2Aii)	5.23
Figure 5.22:	Microhardness depth profiles (Phase 2Aii)	5.23
Figure 5.23:	Workpiece surface/subsurface cross-sectional images (Phase 2Aii)	5.24
Figure 5.24:	G-ratio and surface roughness (Phase 2Aiii)	5.25
Figure 5.25:	Forces and power (Phase 2Aiii)	5.25

Figure 5.26:	Workpiece surface images (Phase 2Aiii)	5.27
Figure 5.27:	Demonstrator blade root	5.28
Figure 5.28:	G-ratio against volume of workpiece material removed (Phase 2Bi)	5.29
Figure 5.29:	Forces and power against volume of material removed (Phase 2Bi)	5.31
Figure 5.30:	Workpiece surface roughness Ra (Phase 2Bi)	5.32
Figure 5.31:	Workpiece surface images (Phase 2Bi)	5.33
Figure 5.32:	Higher magnification images of the machined workpiece surface (Phase 2Bi)	5.34
Figure 5.33:	Microhardness depth profiles (Phase 2Bi)	5.35
Figure 5.34:	Workpiece surface/subsurface cross-sectional images (Phase 2Bi)	5.36
Figure 5.35:	G-ratio against volume of workpiece material removed (Phase 2Bii)	5.38
Figure 5.36:	Main Effects Plot - means for G-ratio (Phase 2Bii)	5.39
Figure 5.37:	Main Effects Plot - means for normal force (Phase 2Bii)	5.40
Figure 5.38:	Main Effects Plot - means for tangential force (Phase 2Bii)	5.40
Figure 5.39:	Main Effects Plot - means for power (Phase 2Bii)	5.40
Figure 5.40:	Main Effects Plot - means for specific energy (Phase 2Bii)	5.41
Figure 5.41:	Main Effects Plot - means for workpiece surface roughness Ra (Phase 2Bii)	5.41
Figure 5.42:	Workpiece surface images (Phase 2Bii, γ -TiAl)	5.43
Figure 5.43:	Workpiece surface images (Phase 2Bii, BuRTi)	5.44
Figure 5.44:	Higher magnification image of the surface produced using Test 7 parameters	5.45
Figure 5.45:	Higher magnification images of the machined workpiece surface (Phase 2Bii)	5.45
Figure 5.46:	Microhardness depth profiles (Phase 2Bii)	5.46
Figure 5.47:	Workpiece surface/subsurface cross-sectional images (Phase 2Bii)	5.47
Figure 5.48:	G-ratio against volume of workpiece material removed (Phase 2Biii)	5.48
Figure 5.49:	Workpiece surface images (Phase 2Biii)	5.49
Figure 5.50:	Bar chart showing G-ratio against material removed for γ -TiAl and Ti-6Al-4V	5.50
Figure 5.51:	Force profiles for Test 5 (a) and Test 6 (b)	5.50
Figure 5.52:	Workpiece surface images and talysurf plot	5.50
Figure B1:	Schematic showing up milling in a horizontal downwards direction using a ball nose end milling and a workpiece tilt angle of 45°	B1
Figure B2:	Schematic showing down milling in a horizontal downwards direction using a ball nose end milling and a workpiece tilt angle of 45°	B3
Figure B3:	Schematic of up milling in a horizontal downwards direction	B4
Figure B4:	Schematic of down milling in a horizontal downwards direction	B5
Phase C1:	Maximum flank wear against machining time (Phase 1A)	C1
Phase C2:	Maximum flank wear against volume of workpiece material	C2

	removed (Phase 1A)	
Phase C3:	Machining time against material removal rate	C3
Phase C4:	Workpiece material removed against material removal rate	C3
Phase C5:	Maximum flank wear against distance machined for Test 1	C4
Phase C6:	Maximum flank wear against distance machined for Test 2	C4
Phase C7:	Maximum flank wear against distance machined for Test 3	C5
Phase C8:	Maximum flank wear against distance machined for Test 4	C5
Phase C9:	Maximum flank wear against distance machined for Test 6	C6
Phase C10:	Maximum flank wear against distance machined for Test 9	C6
Phase C11:	Maximum flank wear against distance machined for Test 13	C7
Phase C12:	Maximum flank wear against distance machined for Test 15	C7
Phase C13:	Maximum flank wear against distance machined for Test 16	C8
Phase C14:	Test 1 wear scar photographs (Phase 1A)	C8
Phase C15:	Test 2 wear scar photographs (Phase 1A)	C9
Phase C16:	Test 3 wear scar photographs(Phase 1A)	C9
Phase C17:	Test 4 wear scar photographs (Phase 1A)	C10
Phase C18:	Test 6 wear scar photographs (Phase 1A)	C10
Phase C19:	Test 9 wear scar photographs (Phase 1A)	C11
Phase C20:	Test 13 wear scar photographs (Phase 1A)	C11
Phase C21:	Test 15 wear scar photographs (Phase 1A)	C12
Phase C22:	Test 16 wear scar photographs (Phase 1A)	C12
Phase C23:	SEM analysis of worn tooling from Test 1	C13
Phase C24:	SEM analysis of worn tooling used in Test 3	C13
Phase C25:	SEM analysis of worn tooling used in Test 10	C14
Phase C26:	SEM analysis of worn tooling used in Test 13	C14
Phase C27:	SEM analysis of worn tooling used in Test 16	C15
Phase C28:	Main effects plot - means for machining time and volume of workpiece material removed	C15
Phase C29:	Interactions plot for distance machined	C17
Phase C30:	Maximum flank wear against distance machined for Test 3 (replication)	C18
Phase C31:	Maximum flank wear against distance machined for Test 4 (replication)	C18
Phase C32:	Maximum flank wear against distance machined for Test 9 (replication)	C19
Phase C33:	Maximum flank wear against distance machined for Test 13 (replication)	C19
Phase C34:	Workpiece surface roughness bar chart (Phase 1A)	C20
Phase C35:	Individual microhardness profiles for Tests 1 to 8 (Phase 1A)	C21
Phase C36:	Individual microhardness profiles for Tests 9 to 16 (Phase 1A)	C22
Phase C37:	Maximum flank wear against machining time (Phase 1B)	C23
Phase C38:	Maximum flank wear against volume of workpiece material	C23

	removed (Phase 1B)	
Phase C39:	Test 1 wear scar photographs (Phase 1B)	C24
Phase C40:	Test 2 wear scar photographs (Phase 1B)	C24
Phase C41:	Test 3 wear scar photographs (Phase 1B)	C25
Phase C42:	Test 4 wear scar photographs (Phase 1B)	C25
Phase C43:	Test 5 wear scar photographs (Phase 1B)	C26
Phase C44:	Test 6 wear scar photographs (Phase 1B)	C26
Phase C45:	Graph showing cutting forces and maximum flank wear against distance machined for Test 2	C27
Phase C46:	Graph showing cutting forces and maximum flank wear against distance machined for Test 3	C28
Phase C47:	Individual microhardness profiles for Tests 1 and 2 (Phase 1B)	C29
Phase C48:	Individual microhardness profiles for Tests 2 and 3 (Phase 1B)	C30
Phase C49:	Individual microhardness profiles for Tests 4 and 5 (Phase 1B)	C31
Phase C50:	Individual microhardness profiles for Tests 5 and 6 (Phase 1B)	C32
Phase C51:	Normal force against volume of workpiece material removed (Phase 2Ai, γ -TiAl)	C35
Phase C52:	Tangential force against volume of workpiece material removed (Phase 2Ai, γ -TiAl)	C35
Phase C53:	Power against volume of workpiece material removed (Phase 2Ai, γ -TiAl)	C36
Phase C54:	Specific energy against volume of workpiece material removed (Phase 2Ai, γ -TiAl)	C36
Phase C55:	Surface roughness Ra results for γ -TiAl (Phase 2Ai, γ -TiAl)	C37
Phase C56:	G-ratio against volume of workpiece material removed (Phase 2Ai, BuRTi)	C37
Phase C57:	Normal force against volume of workpiece material removed (Phase 2Ai, BuRTi)	C38
Phase C58:	Tangential force against volume of workpiece material removed (Phase 2Ai, BuRTi)	C38
Phase C59:	Power against volume of workpiece material removed (Phase 2Ai, BuRTi)	C39
Phase C60:	Specific energy against volume of workpiece material removed (Phase 2Ai, BuRTi)	C39
Phase C61:	Surface roughness Ra results for BuRTi (Phase 2Ai, BuRTi)	C40
Phase C62:	Interactions plot for G-ratio (Phase 2Ai, γ -TiAl)	C43
Phase C63:	Individual microhardness depth profiles for Tests 1 and 2 (Phase 2Ai)	C43
Phase C64:	Individual microhardness depth profiles for Tests 3 to 9 (Phase 2Ai)	C44
Phase C65:	Individual microhardness depth profiles (Phase 2Aii)	C45
Phase C66:	Individual microhardness depth profiles (Phase 2Bi)	C46
Phase C67:	Normal force against volume of workpiece material removed (Phase 2Bii, γ -TiAl)	C47

Phase C68:	Tangential force against volume of workpiece material removed (Phase 2Bii, γ -TiAl)	C47
Phase C69:	Power against volume of workpiece material removed (Phase 2Bii, γ -TiAl)	C48
Phase C70:	Specific energy against volume of workpiece material removed (Phase 2Bii, γ -TiAl)	C48
Phase C71:	Surface roughness Ra results for γ -TiAl (Phase 2Bii, γ -TiAl)	C49
Phase C72:	G-ratio against volume of workpiece material removed (Phase 2Bii, BuRTi)	C49
Phase C73:	Normal force against volume of workpiece material removed (Phase 2Bii, BuRTi)	C50
Phase C74:	Tangential force against volume of workpiece material removed (Phase 2Bii, BuRTi)	C50
Phase C75:	Power against volume of workpiece material removed (Phase 2Bii, BuRTi)	C51
Phase C76:	Specific energy against volume of workpiece material removed (Phase 2Bii, BuRTi)	C51
Phase C77:	Surface roughness Ra results for BuRTi (Phase 2Bii, BuRTi)	C52
Phase C78:	Individual microhardness depth profiles (Phase 2Bii)	C56
Phase C79:	Tangential force against volume of workpiece material removed (Phase 2Biii)	C57
Phase C80:	Tangential force against volume of workpiece material removed (Phase 2Biii)	C57
Phase C81:	Tangential force against volume of workpiece material removed (Phase 2Biii)	C58
Phase C82:	Tangential force against volume of workpiece material removed (Phase 2Biii)	C58

LIST OF TABLES

Table 2.1:	Table 2.1: Properties for a range of materials [1, 4, 6-10]	2.1
Table 2.2	Grinding fluid characteristics [62]	2.25
Table 2.3:	Description of workpiece surface integrity data sets [89]	2.33
Table 2.4:	Operating parameters for surface integrity assessment when high [106, 107]	2.39
Table 2.5:	Cutting conditions for face milling Ti-47Al-2Nb-2Mn +0.8%vol. TiB ₂ [110]	2.42
Table 2.6:	Operating parameters for grinding Ti6Al4V and Ti-45Al-2Mn-2Nb [108, 112]	2.44
Table 2.7:	Operating parameters for surface grinding Ti-45Al-2Mn-2Nb +0.8%vol. TiB ₂ [104, 114]	2.45
Table 2.8:	Parameters used for surface ground fatigue test specimens [108, 109]	2.48
Table 2.9:	Operating parameters used for creep feed grinding trails using conventional and superabrasive grinding wheels [108, 118]	2.49
Table 2.10:	Operating parameters used for creep feed grinding trials using superabrasive grinding wheels [108]	2.51
Table 2.11:	Operating parameters used for creep feed grinding trails using conventional abrasive grinding wheels [108, 119]	2.51
Table 2.12:	Operating parameters used for speed stroke grinding [120, 121]	2.53
Table 3.1:	Conventional abrasive and superabrasive grinding wheel specifications	3.9
Table 3.2:	Grinding, polishing and etching regime for γ -TiAl alloys	3.12
Table 3.3:	Grinding, polishing and etching regime for BuRTi alloy	3.13
Table 3.4:	List of possible factors and levels for Phase 1, high speed ball nose end milling [163]	3.15
Table 3.5:	Phase 1A test details	3.17
Table 3.6:	Phase 1B test details	3.19
Table 3.7:	Phase 1C test details	3.21
Table 3.8:	List of possible factors and levels for Phase 2, creep feed grinding [108]	3.22
Table 3.9:	Phase 2Ai test details	3.23
Table 3.10:	Phase 2Aii test details	3.26
Table 3.11:	Phase 2Aiii test details	3.27
Table 3.12:	Phase 2Bi test details	3.28
Table 3.13:	Phase 2Bii test details	3.30
Table 3.14:	Phase 2Biii test details	3.31
Table 3.15:	Phase 2C test details	3.31
Table 4.1:	ANOVA table for distance machined (Phase 1A)	4.11
Table 4.2:	ANOVA table for F _x	4.14
Table 4.3:	ANOVA table for F _y	4.14

Table 4.4:	ANOVA table for Fz	4.14
Table 4.5:	ANOVA table for workpiece surface roughness (Phase 1A)	4.16
Table 4.6:	Modified ANOVA table for machining time	4.28
Table 4.7:	Modified ANOVA table for cutting temperature	4.32
Table 4.8:	Modified ANOVA table for workpiece surface roughness Ra	4.35
Table 4.9:	ANOVA table for distance machined (Phase 1C)	4.45
Table 4.10:	ANOVA table for surface roughness Ra perpendicular to the feed direction	4.48
Table 5.1:	ANOVA table for G-ratio (Phase 2Aii)	5.9
Table 5.2:	ANOVA table for G-ratio (Phase 2Aiii)	5.42
Table 6.1:	Fixed operating parameters and levels (γ -TiAl)	6.3
Table 6.2:	List of preferred operating parameters for each output measure (γ -TiAl)	6.3
Table 6.3:	Fixed operating parameters and levels (BuRTi)	6.4
Table 6.4:	List of preferred operating parameters for each output measure (BuRTi)	6.4
Table 6.5:	Fixed operating parameters and levels (γ -TiAl and BuRTi)	6.5
Table 6.6:	List of preferred operating parameters for each output measure (γ -TiAl and BuRTi, SiC wheels)	6.5
Table 6.7:	List of preferred operating parameters for each output measure (γ -TiAl and BuRTi, superabrasive wheels)	6.7
Table A1:	The techniques used to detect and locate surface inhomogeneity in metals [87]	A1
Table C1:	ANOVA table for machining time (Phase 1A)	C16
Table C2:	ANOVA table for workpiece material removed (Phase 1A)	C16
Table C3:	ANOVA table machining time (Phase 1B)	C27
Table C4:	ANOVA table for cutting temperature (Phase 1B)	C27
Table C5:	ANOVA table for workpiece surface roughness Ra (Phase 1B)	C28
Table C6:	ANOVA table for material removed (Phase 1C)	C33
Table C7:	ANOVA table for machining time (Phase 1C)	C33
Table C8:	ANOVA table for maximum resultant force with a new tool (Phase 1C)	C33
Table C9:	ANOVA table for maximum resultant force with a worn tool (VBmax=300 μ m) (Phase 1C)	C34
Table C10:	ANOVA table for surface roughness Ra parallel to the feed direction (Phase 1C)	C34
Table C11:	ANOVA table for normal force (Phase 2Ai, γ -TiAl)	C40
Table C12:	ANOVA table for tangential force (Phase 2Ai, γ -TiAl)	C40
Table C13:	ANOVA table for power for (Phase 2Ai, γ -TiAl)	C41
Table C14:	ANOVA table for specific energy (Phase 2Ai, γ -TiAl)	C41
Table C15:	ANOVA table for workpiece surface roughness Ra (Phase 2Ai, γ -TiAl)	C41
Table C16:	ANOVA table for G-ratio (Phase 2Ai, BuRTi)	C41

Table C17:	ANOVA table for normal force (Phase 2Ai, BuRTi)	C41
Table C18:	ANOVA table for tangential force (Phase 2Ai, BuRTi)	C42
Table C19:	ANOVA table for power (Phase 2Ai, BuRTi)	C42
Table C20:	ANOVA table for specific energy (Phase 2Ai, BuRTi)	C42
Table C21:	ANOVA table for workpiece surface roughness Ra (Phase 2Ai, BuRTi)	C42
Table C22:	ANOVA table for normal force (Phase 2Bii, γ -TiAl)	C52
Table C23:	ANOVA table for tangential force (Phase 2Bii, γ -TiAl)	C52
Table C24:	ANOVA table for power (Phase 2Bii, γ -TiAl)	C53
Table C25:	ANOVA table for specific energy (Phase 2Bii, γ -TiAl)	C53
Table C26:	ANOVA table for workpiece surface roughness (Phase 2Bii, γ -TiAl)	C53
Table C27:	ANOVA table for G-ratio (Phase 2Bii, BuRTi)	C53
Table C28:	ANOVA table for normal force (Phase 2Bii, BuRTi)	C54
Table C29:	ANOVA table for tangential (Phase 2Bii, BuRTi)	C54
Table C30:	ANOVA table for power (Phase 2Bii, BuRTi)	C54
Table C31:	ANOVA table for specific energy (Phase 2Bii, BuRTi)	C54
Table C32:	ANOVA table for workpiece surface roughness Ra (Phase 2Bii, BuRTi)	C55

LIST OF NOMENCLATURE

ANOVA	Analysis of Variance
%at.	Atomic percentage (%)
%vol.	Volume percentage (%)
a	Axial depth of cut (mm)
Al ₂ O ₃	Aluminum oxide
BCC	Body centred cubic
BUE	Built up edge
BUL	Built up layer
BuRTi	Burn resistant titanium
C	Machining cost per component
C ₁	Non-productive cost per component
C ₂	Cost of machining time
C ₃	Tool changing cost
C ₄	Tool cost per component
C ₅	Material costs
CBN	Cubic boron nitride
CVD	Chemical Vapour Deposition
d	Depth of cut (grinding) (mm)
D	Grinding wheel diameter (mm)
d	Radial depth of cut (milling)(mm)
DOF	Degrees of freedom
ECM	Electro-chemical machining
EDWM	Electrical discharge wire machining
EDX	Energy Dispersive Spectrometry
f	Feed rate (mm/min)
F _h	Horizontal force component
F _n	Normal force component (N)
F _t	Tangential force component (N)
F _v	Vertical force component (N)
F _x , F _y , F _z	Force (x, y or z direction) (N)
G-ratio	Grinding ratio
HAZ	Heat affected zone
HCF	High cycle fatigue
HIP	Hot Isostatically Pressed
HK _{0.025}	Knoop hardness (25gram load)
HSM	High speed machining
ISO	International Standards Organisation
l	Contract length (mm)
LCF	Low cycle fatigue

MSS	Mean sum of squares
PCD	Polycrystalline diamond
PCR%	Percentage contribution ratio (%)
PVD	Physical vapour deposition
Ra	Arithmetical mean roughness of a surface (μm)
SEM	Scanning electron microscopy
SiC	Silicon carbide
SS	Sum of squares
t	Undeformed chip thickness (mm)
T _C	Machining time per component
T _L	Non-productive time per component
T _T	Production time per component
T _X	Tool changing time per component
u	Specific energy (J/mm^3)
UAC	Ultrasonic assisted cutting
v	Cutting (m/min) /wheel (m/s) speed
Vol _{chip}	Chip volume (mm^3)
WC	Tungsten carbide
wt%	Weight percentage (%)
γ -TiAl	Gamma titanium aluminide
θ x	Arc of contact ($^\circ$)

1. INTRODUCTION

1.1 Background to the project

Conventional titanium alloys such as Ti-6Al-4V, which account for between 50–60% of total titanium alloy production, are characterised by high tensile strength $\sim 1100\text{MPa}$ at 20°C combined with low density ($\sim 4\text{g/cm}^3$) and good corrosion resistance. Such qualities explain why titanium accounts for around 33% of engine weight in current commercial aircraft [1]. Figure 1.1 details the material utilisation in a Rolls-Royce Trent 800 aero engine and highlights the usage of titanium in the cooler parts of the engine (fan and compressor) and nickel based superalloys in the hotter parts of the engine (combustor and turbine).

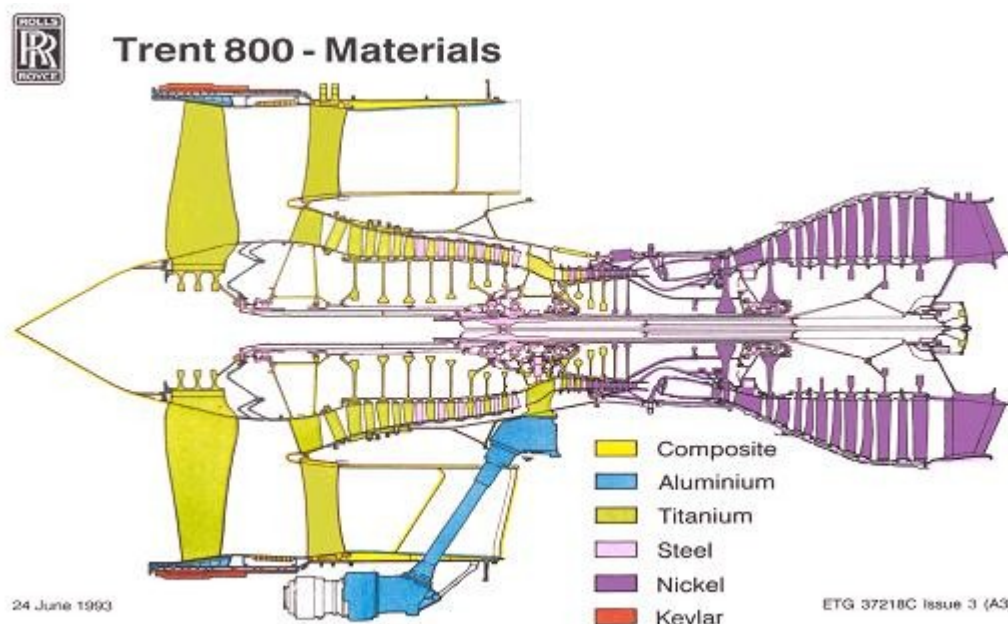


Figure 1.1: Material utilisation in a Rolls-Royce Trent 800 aero engine
(Courtesy of Rolls-Royce Plc)

Two main problems however, restrict the use of titanium in this area, namely the ability to operate at temperatures significantly above $\sim 350^\circ\text{C}$ and alloy burn resistance, see Figure 1.2. Consequently, heavier but far more durable and thermally stable nickel based superalloys are the preferred choice for the hotter parts of the gas turbine. As a guide, temperatures in the high pressure (HP) compressor are typically up to 600°C and nickel based alloys such as Inconel 718 are used to accommodate these and even higher gas flow temperatures.

Gamma titanium aluminide intermetallic ($\gamma\text{-TiAl}$) alloys are a series of intermetallic compounds composed of titanium and 45-47% (at.%) aluminium with additional alloying elements such as niobium or manganese to improve mechanical properties. The latest

generation of thermomechanically produced duplex γ -TiAl alloys such as Ti-45Al-8Nb-0.2C at.%, which has a tensile strength above 900MPa, is able to operate at temperatures of up to 800°C [2]. This higher temperature capability allows these alloys to be considered for replacement of nickel alloys as the material of choice for selected aeroengine components including intermediate (IP) and high (HP) pressure compressor blades and stators as well as low pressure (LP) turbine blades [2]. Weight saving is the main driver as γ -TiAl alloy density is typically around 50% that of nickel based superalloys.

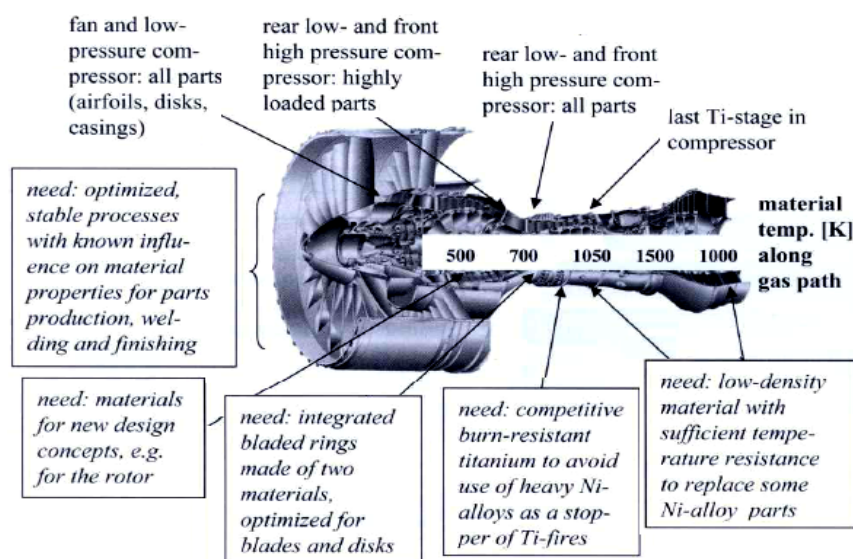


Figure 1.2: Requirements for future gas turbine aero engines [3]

Figure 1.2 also shows a requirement for competitive burn resistant titanium alloys to avoid the use of nickel based superalloys. In the intermediate pressure (IP) compressor, friction rub causes thin sections of titanium alloy such as blades, to have a propensity to ignite and burn. As with high temperature capability, titanium alloys have to be replaced with heavier nickel based superalloys. Figure 1.3 details a comparison of burn resistance between three different titanium alloys when subjected to similar conditions to those found in the intermediate compressor. It shows γ -TiAl's (Ti-45Al-2Nb-2Mn-0.8%vol. TiB₂) superior burn resistance when compared to the standard titanium alloy Ti-6Al-4V and demonstrates why γ -TiAl alloys could be the material of choice to fulfil this need [4]. An alternative to γ -TiAl alloys is burn resistant titanium (BuRTi), Ti-25V-15Cr-2Al-0.2C (%wt), which is a proprietary titanium alloy developed in association with Rolls Royce plc [4]. The burn resistant characteristic of BuRTi is due to the addition of significant amounts of vanadium (V) and chromium (Cr) to the alloy makeup. Figure 1.3 places the burn resistance of BuRTi somewhere between that of

γ -TiAl and Ti-6Al-4V however BuRTi does not have the same low room temperature ductility problems that γ -TiAl alloys suffer [4].



Figure 1.3: Comparison of burn resistance between different titanium alloys using 1x25x50mm coupons at 300°C, 695kPag air pressure and 150m/s air velocity [4]

Despite extensive alloy and manufacturing process development, no commercial aeroengine manufacturer currently operates with γ -TiAl alloys. A contributory factor in this is the difficulty in producing components of acceptable integrity, due mainly to the alloy's extremely low room temperature ductility of <2%. This low value means that the workpiece surface is prone to the formation of cracks which may act as fatigue crack initiation sites and lead to part failure. In a safety critical aerospace application such as blades in the IP compressor or low pressure turbine, the presence of cracks or other types of damage in the workpiece surface is not acceptable and often objectives such a minimum machining time, minimum part cost and maximum profit rate may be sacrificed in order to achieve a component with the desired integrity [5]. In spite of the wide range of γ compositions/formulations available, the machinability of γ -TiAl alloys is in general considered much more difficult than that of conventional titanium alloys, particularly with respect to workpiece integrity [6].

A number of investigations have been performed into the machinability of γ -TiAl alloys, encompassing processes such as turning, drilling, face milling, end milling, surface grinding, creep feed grinding (CFG), electrical discharge machining (EDM), ultrasonic machining and electro chemical machining (ECM). Key processes include creep feed grinding and high speed milling for the production of blades and stators for aeroengines. Most of this work has been performed on 3rd generation alloys such as Ti-45Al-2Mn-2Nb +0.8%vol. TiB₂, rather than the more recently developed and thermomechanically processed alloys such as Ti-45Al-8Nb-0.2C (TNB) hence the requirement for the current work to asses the machinability

performance of the new alloy. In contrast, very few publications exist detailing the machinability of the BuRTi alloy, therefore the requirement for the current study arose.

1.2 Aims and objectives of the project

The aim of the project was to provide machinability evaluation of gamma titanium aluminide intermetallic alloy Ti-45Al-8Nb-0.2C involving high speed ball nose end milling and creep feed grinding.

Figure 1.4 shows a chart of the Roll-Royce Manufacturing Capability Readiness Level Definitions. The project conformed with Phase 1 requirements ‘Technology assessment and proving’, levels 1-3. As a consequence and due to limited supplies of workpiece material (Ti-45Al-8Nb-0.2C, Ti-45Al-2Mn-2Nb +0.8%vol.TiB₂ and BuRTi), experimentation was to be undertaken to identify ‘preferred’ operating parameters as apposed to optimised values which would have required a greater number of tests.

Programme phase	MCRL	State of development
Phase 3 Production implementation	9	Fully production capable process qualified on full range of parts over extended period (all Business Case metrics achieved)
	8	Fully production capable (FAIR Stage 2) process qualified on full range of parts over significant run lengths
	7	Capability and rate confirmed (FAIR Stage 1 without concessions) via economic run lengths on production parts
Phase 2 Pre-production	6	Process optimised for capability and rate using production equipment
	5	Basic capability demonstrated using production equipment
Phase 1 Technology assessment and proving	4	Process validated in laboratory using representative development equipment
	3	Experimental proof of concept completed
	2	Applicability and validity of concept described and vetted, or demonstrated
	1	Process concept proposed with scientific foundation

Figure 1.4: Rolls-Royce Manufacturing Capability Readiness Level Definitions
(Courtesy of Rolls-Royce Plc)

The following objectives were identified in order to meet the aim of the project.

1. Perform a literature review to determine the current status of information on the machinability of advanced titanium alloys such as gamma titanium aluminide intermetallic, burn resistant and orthorhombic titanium alloys.
2. Determine preferred tooling, operating parameters and conditions when high speed ball nose end milling Ti-45Al-8Nb-0.2C for assessment criteria tool life: workpiece surface roughness and workpiece surface integrity.
3. Benchmark Ti-45Al-8Nb-0.2C against the previously investigated γ -TiAl alloy Ti-45Al-2Mn-2Nb +0.8%vol. TiB₂ when high speed ball nose end milling for assessment criteria: tool life, workpiece surface roughness and workpiece surface integrity.
4. Benchmark Ti-45Al-8Nb-0.2C against BuRTi when high speed ball nose end milling for assessment criteria: tool life, workpiece surface roughness and workpiece surface integrity.
5. Determine the preferred grinding wheel specification, operating parameters and conditions when creep feed grinding Ti-45Al-8Nb-0.2C using conventional abrasive (SiC) grinding wheels for assessment criteria: wheel life, workpiece surface roughness and workpiece surface integrity.
6. Determine the preferred grinding wheel specification, operating parameters and conditions when creep feed grinding Ti-45Al-8Nb-0.2C using superabrasive grinding wheels for assessment criteria: wheel life, workpiece surface roughness and workpiece surface integrity.
7. Benchmark Ti-45Al-8Nb-0.2C against burn resistant titanium alloy (BuRTi) when creep feed grinding for assessment criteria: wheel life, workpiece surface roughness and workpiece surface integrity.
8. Benchmark Ti-45Al-8Nb-0.2C against the conventional titanium alloy Ti-6Al-4V when creep feed grinding for assessment criteria: wheel life.

During the course of the work up to the date of thesis submission no industrial standard had been produced for acceptable tool life, workpiece surface roughness or surface integrity when machining components from γ -TiAl alloys. As a consequence 'preferred' parameters were selected based on the longest tool life, the lowest workpiece surface roughness and the 'best' workpiece surface integrity which included the lowest levels of surface damage in relation to cracks, fracture/pullout, smeared material, adhered material and heat effect zone. Additional

assessment criteria such as cutting/grinding forces, power and specific energy were also included however testing was not undertaken to determine the preferred levels.

The thesis is organised into 7 Chapters. The first of these introduces the project including the background to the work, it establishes the aims and objectives and details the industrial collaborators and funding. Chapter 2 provides a detailed literature review on workpiece materials, cutting and grinding processes, workpiece surface integrity and the machinability of gamma titanium aluminide, burn resistant titanium and orthorhombic TiAl alloys in order to fulfil the criteria to meet Objective 1. Chapter 3 details the design of experiments process including the workpiece materials, machine tools, fixturing and equipment, cutting tools and creep feed grinding wheels, analysis equipment and the experimental programmes performed to achieve the required objectives. Results and discussion is divided into two sections, the first, Chapter 4 focuses on Phase 1, high speed ball nose end milling and relates to Objectives 2 to 4 whilst Chapter 5 focuses on Phase 2, creep feed grinding and Objectives 5 to 8. Chapter 6 details the conclusions from the work including tables giving preferred operating conditions and parameters. Finally Chapter 7 provides suggestions for future work.

1.3 Industrial collaborators and funding

The project involved six collaborating companies:

- Rolls-Royce supplied γ -TiAl and BuRTi workpiece materials and financial support of £45,000.
- Hardinge-Bridgeport provided a Bridgeport Flexible Grinding Centre (loan agreement).
- Iscar Cutting Tools Ltd supplied ball nose end mills and financial support of £4,000.
- Saint-Gobain Abrasives Plc supplied both conventional (SiC) and superabrasive (diamond and CBN) grinding wheels in addition to financial support of £6,000.
- Element Six Ltd supplied diamond and CBN grit material to Saint-Gobain to produce the grinding wheels in addition to financial support of £6,000.
- Pumps and Equipment (Warwick) Ltd supplied fluid and mist extraction systems.
- The Engineering and Physical Sciences Research Council provided financial support of around £37,500 and the loan of the FLIR Thermacam SC3000.

In addition, all companies provided specialist technical knowledge in their relevant fields. The following is a list of the nominated representatives of each sponsoring company.

Dr. Wayne Voice, Mr. Colin Sage and
Dr. Andrew Mantle
Manufacturing technology.
Rolls-Royce plc.
PO Box 31.Derby
DE24 8BJ, UK.

Mr. Mike Jones
ISCAR Tools Ltd.
Woodgate Business Park,
Bartley Green, Birmingham.
B32 3DE, UK.

Mr. Paul Dando
Saint-Gobain Abrasives Ltd
Unit 25 Anson Business Park
Cheltenham Road East.
Staverton. Gloucestershire.
GL2 9QU, UK.

Mr. Lee Bott and Mr. Dave Alexander
Pumps and Equipment (Warwick) ltd
6 Collins Road
Heathcote Industrial Estate
Warwick
CV34 6TF, UK.

Mr. John McTernan, Mr. Chris Waterhouse,
Mr. Bill McCaskill and Mr. David Martin
Hardinge Machine Tools Ltd.
Whiteacres, Cambridge Road
Whetstone, Leicester
LE8 6BD, UK.

Mr. Karl Tuffy
Element Six ltd.
Shannon Airport
Shannon, Co Clare,
Ireland

Mr. Steve Woods
Saint-Gobain Abrasives Ltd
Doxey Road
Stafford
ST16 1EA, UK.

2. LITERATURE REVIEW

2.1 Gamma titanium aluminide intermetallic alloys

2.1.1 Properties

Gamma titanium aluminide intermetallic alloys (γ -TiAl) alloys have high stiffness ($E=175\text{GPa}$ at 20°C to 150GPa at 700°C), a density normalised strength similar to cast nickel based superalloys and a low thermal conductivity of 22W/m.K . When compared to steels and aluminium alloys their thermal conductivity is much lower but it is, nevertheless, double that of nickel based superalloys and titanium alloys [3]. Table 2.1 provides further data comparing the properties of γ -TiAl alloys with other materials.

	Unit	Steels	Aluminium	Nickel alloys	Ti-6Al-4V	γ -TiAl	BuRTi
Density	g/cm^3	7.87	2.70	8.30	4.43	3.80	5.1
Young's modulus	GPa	195-200	69-79	180-214	110	150-175	113-126
Room temperature ductility	%	65	45	3-10	~ 20	2	15.4-22.6
Operating temperature ductility	%	-	-	10-20	high	5-12	
Tensile strength	N/mm^2	415-1750	90-600	345-1450	895-1035	450-800	957-1125
Yield strength	N/mm^2	205-1725	35-500	105-1200	825-965	400-650	895-1108
Melting point	$^\circ\text{C}$	1536	660	1455	1600	1460	
Thermal conductivity	W/mK	~ 50	230	11.3	7,3	22	10

Table 2.1: Properties for a range of materials [1, 4, 6-10]

2.1.2 Industrial applications

The aerospace industry is the main driver for γ -TiAl alloys with typical target applications including blades and stators in the (HP) compressor; (LP) turbine blades, exhaust components, combustor chambers and casings [3, 11, 12]. In addition, the automotive industry also utilises γ -TiAl alloys, with the production of exhaust valves, turbocharger rotors and connecting rods for high performance engines having been reported [13, 14]. As the component safety requirement for automotive applications is lower than that of an aerospace component, the uptake of γ -TiAl alloys has generally been faster however high manufacturing costs have limited its use to high performance engines such as those used in Formula 1 cars [15]. Figure 2.1 shows various components produced using γ -TiAl alloys.

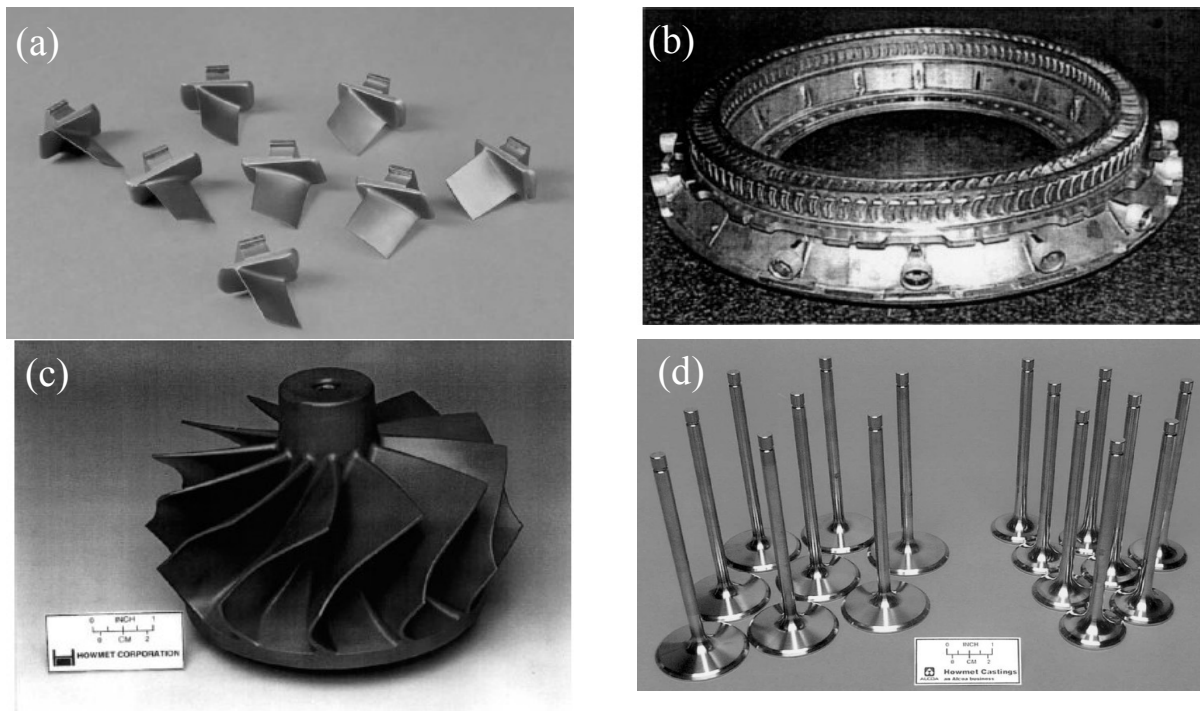


Figure 2.1: Sample components made out of γ -TiAl (alloys), (a) cast (HP) compressor blades [14], (b) investment cast combustion chamber diffuser [11], (c) turbine wheel of automotive turbocharger [13], (d) Cast γ -TiAl automotive valves [15]

2.1.3 Alloy development and microstructure

Intermetallic alloys such as γ -TiAl consist of two or more elements that have a strong affinity for each other and form long range ordered structures in which each element has a preferred position in the crystal lattice. As they have long range atomic ordering and strong intermetallic bonding, intermetallic alloys typically have strength at high temperatures, good resistance to oxidation and corrosion as well as low density. As a group of alloys however, their major drawback is that they tend to have low ductility and fracture toughness. In the case of γ -TiAl alloys, their room temperature ductility generally ranges from 0.1–2% with a fracture toughness of $12\text{MPam}^{1/2}$ at room temperature and $25\text{MPam}^{1/2}$ at 500°C and a high fatigue crack growth rate which leads to poor damage tolerance [3, 14]. These properties mean that producing components from γ -TiAl with the required component integrity is challenging. Despite extensive research programmes implemented during the mid 1950's through to the present day, the uptake of γ -TiAl's within the aerospace sector has been extremely slow. Indeed, no commercial aeroengine manufacture operates commercially with an engine that uses components made from γ -TiAl alloys, however General Electric has reported that its GENxTM aeroengine will operate with γ -TiAl (LP) turbine blades [16].

The partial titanium-aluminium phase diagram, shown in Figure 2.2, shows three solid phases. Titanium aluminide alloys can be subdivided into two categories, single phase (γ) and

two phase ($\gamma + \alpha_2$) alloys. The ($\alpha_2 + \gamma$) / γ phase boundary at $\sim 1100^\circ\text{C}$, occurs at an aluminium content of $\sim 49\%$, depending on the type and level of the additional alloying elements. Single phase γ alloys generally contain a third alloying element such as niobium or tantalum to promote strengthening and enhancement of oxidation resistance [17].

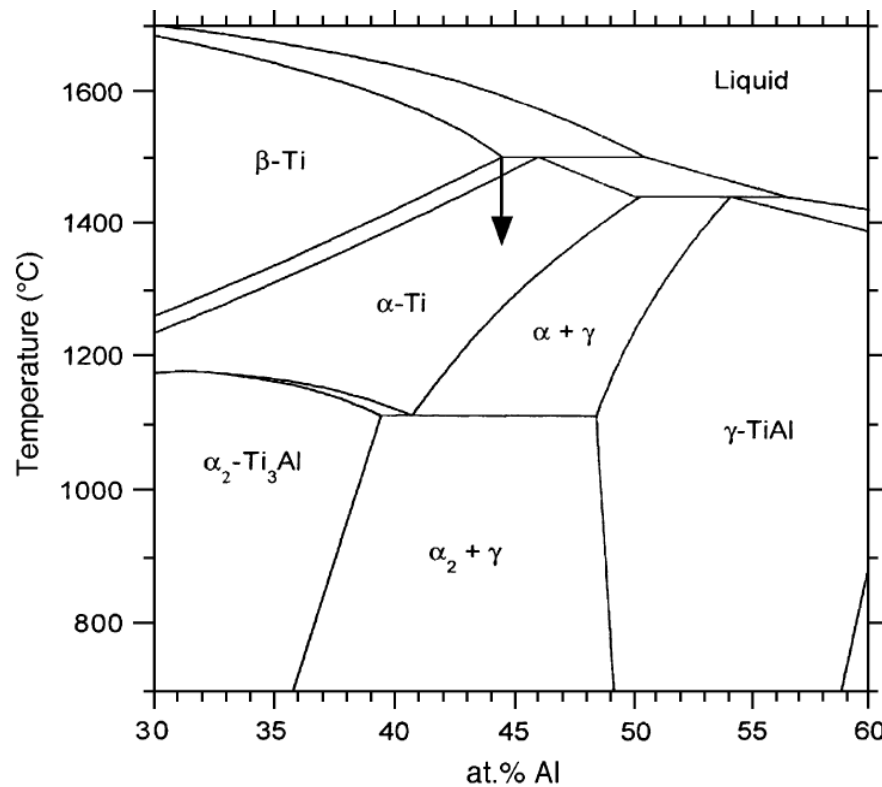


Figure 2.2: Titanium-aluminium phase diagram [17]

The room temperature ductility of a γ -TiAl alloy is limited to $<2\%$ because this is an inherent property of the TiAl phase which is the major constituent of the two phase compound. Gamma TiAl alloys undergo a thermally activated brittle to ductile transition (BDT) which makes stress relaxation through plastic deformation more preferable than through failure. The thermally activated relaxation process occurs both in the grain boundaries and in the grain interior; however the relaxation process in the grain boundaries may take place at a lower temperature to that in the grain interior. Ductility above the transformation temperature increases rapidly due to increased twinning and slip system activity [18].

The major phases of these alloys are γ -TiAl with the tetragonal $L1_0$ structure and the α_2 - Ti₃Al with a hexagonal DO_{19} structure. A broad range of microstructures can be obtained by a variety of heat treatments. Figure 2.3 shows a schematic of the microstructures that can be generated: fully lamellar, nearly lamellar, duplex and near gamma structure. Appropriate thermo- mechanical processing of the morphology of the phases can be adjusted

to produce either lamellar or equiaxed morphologies or a mixture (duplex structure) of the two. The lamellar structure can lead to refinement of the microstructure with improved ductility and a decreased microstructure scale by recrystallisation of the fine γ grains. Control of the microstructure in single phase γ alloys requires optimisation of grain size and morphology. Grain morphology varies considerably depending on composition, solution treatment, temperature and time, cooling rate and stabilization temperature and time. Grain size decreases with reduced aluminium content and with the addition of vanadium, manganese and chromium [17, 19].

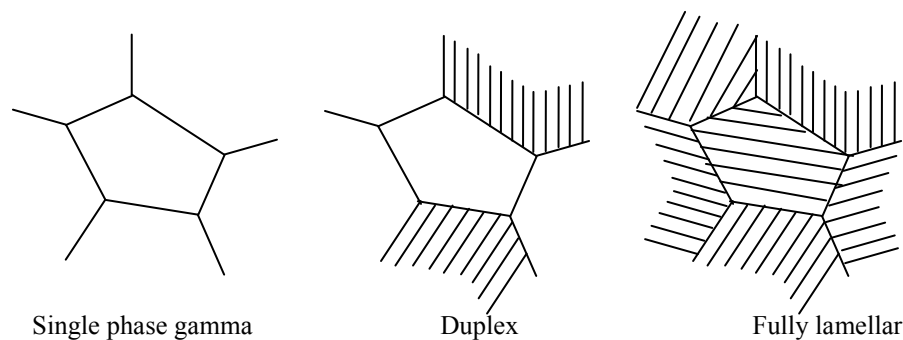
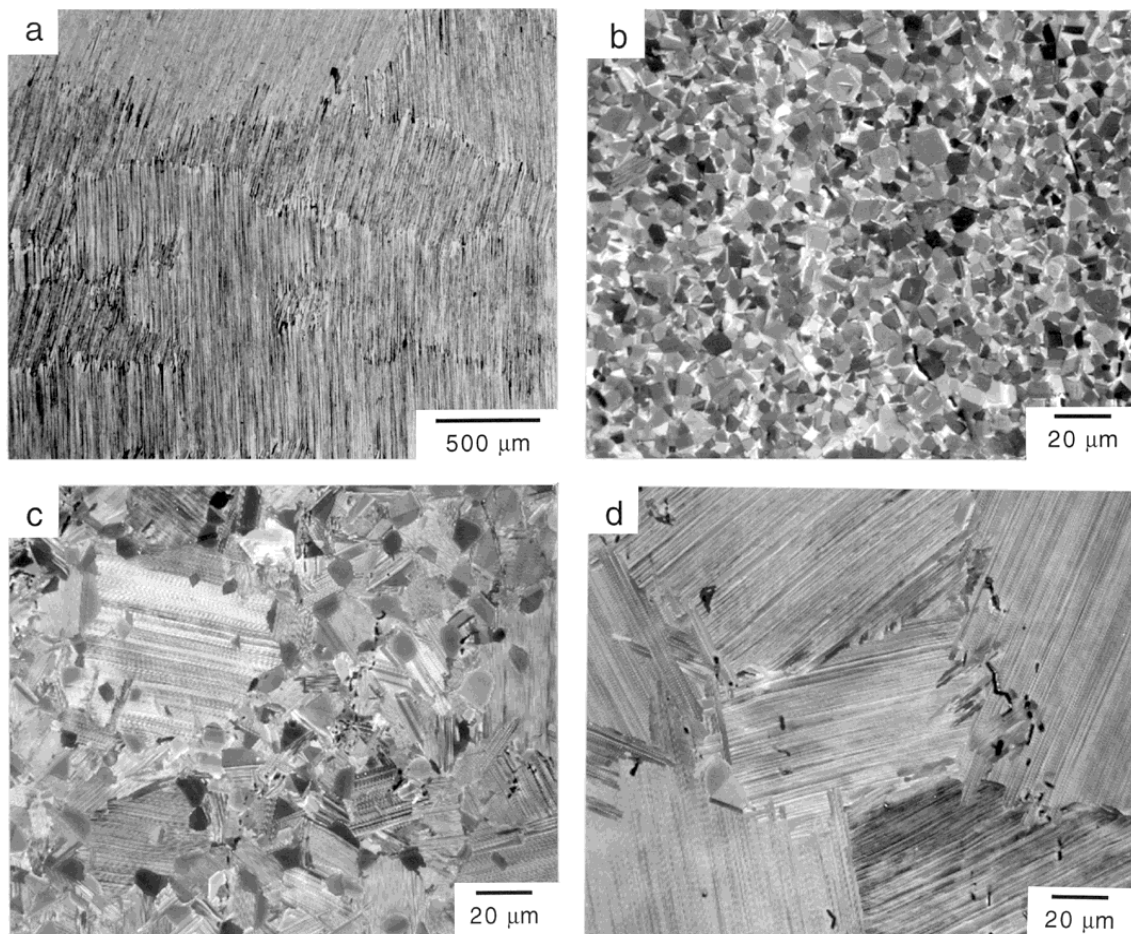


Figure 2.3: Microstructure of gamma TiAl alloys [20]

Figure 2.4 shows examples of γ -TiAl alloys with these microstructures. The different microstructures are often characterized in terms of the volume fraction of the lamellar colonies and equiaxed γ grains [15]. Alloys containing less than 49% Al (at) can be heat treated in the single phase α field to produce a fully lamellar structure which consists of thin parallel α (Ti_3Al) and γ platelets. Duplex grains consist of gamma grains and colonies of lamellae whilst single phase gamma is comprised solely of gamma grains. Cooling rate also has an effect, with a relatively slow cooling rate giving coarse lamellae and a high cooling rate producing refined lamellae [16].

Cast alloys can have a very large grain size of up to 2mm which results in anisotropic properties (properties that differ according to the direction of measurement). Grain refined alloys can be produced with isotropic properties, higher tensile strength and ductility, however with some loss of creep strength [21]. In order to improve properties 3rd generation cast alloys use the XDTM (exothermic dispersion) process developed by Martin Marietta for grain refinement. An exothermic reaction is promoted by adding Al-TiB₂ powders to the molten base alloy. Grain growth is prevented by the fine dispersion of TiB₂ particles acting to pin the grain boundaries [22].



(a) Coarse, nearly lamellar microstructure of the ingot material (optical microscopy), (b–d) backscattered electron SEM micrographs of microstructures established by extrusion and subsequent forging, followed by heat treatments at different temperatures T , (b) equiaxed microstructure, $T = 1,300^{\circ}\text{C}$, (c) duplex microstructure, $T = 1,340^{\circ}\text{C}$, (d) nearly-lamellar microstructure, $T = 1,360^{\circ}\text{C}$

Figure 2.4: Microstructures of a γ -TiAl base alloy of the composition Ti-47Al-3.7(Nb,Cr,Mn,Si)-0.5 B (at. %), [14]

Lamellar microstructures usually have a lower tensile strength and ductility when compared to duplex microstructures because of their large grain sizes, lack of slip/twinning activity and a tendency for lamellae platelet separation and low cleavage strength. Increases in tensile strength and ductility have been found with reduced grain size. The fracture toughness of γ -TiAl alloys has been shown to be primarily a function of microstructure [14]. In lamellar alloys fracture occurs by lamellae interface delamination and colony boundary failure whilst in duplex and single phase alloys it occurs by cleavage and grain boundary failure. These result in lamellar microstructures having approximately double the fracture toughness of duplex microstructures ($20\text{--}35\text{MPam}^{1/2}$ compared to $10\text{--}16\text{MPam}^{1/2}$) [23].

2.2 Burn resistant titanium alloy (BuRTi)

Development of a Ti-V-Cr system was originally pioneered in the USA, where Pratt and Whitney's Alloy C, Ti-35V-15Cr is used [24]. An alternative to this is burn resistant titanium (BuRTi), Ti-25V-15Cr-2Al-0.2C (%wt), which is a proprietary titanium alloy recently developed by the University of Birmingham and Rolls Royce Plc [25]. The burn resistant characteristic of BuRTi is due to the addition of significant amounts of vanadium (V) and chromium (Cr) in the alloy makeup. The tendency for both elements to form oxides under burning conditions helps to extinguish flames. A higher thermal conductivity is also achieved, aiding the burn resistance. Aluminium is used both as a master alloy to V and Cr to limit the amount and cost of the raw materials (by nearly a factor of 10) and to aid in the melting during production [26]. In initial attempts to produce BuRTi from the master alloy, the material produced was found to be brittle as a result of oxygen residue from the aluminothermic residual [26]. By adding a relatively high level of carbon (0.2%), the oxygen is scoured from the alloy matrix and tied to carbide precipitates which also constrain grain size during processing [27].

2.3 Machinability

Trent and Wright [28] state that the machinability of an alloy is similar to the palatability of wine - easily appreciated but not readily measured in quantitative terms. In fact machinability has no unique or unambiguous meaning. "To the active practitioner however, engaged in a particular set of operations, the meaning of the term is clear and the machinability of a work material can often be measured in terms of the numbers of components produced per hour, the cost of machining the component or the quality of the finish on a critical surface" [28].

Machinability may be assessed by one or more of the criteria below [28-31]. These machinability assessment criteria are also the type of information required by industry

- Tool life - The amount or rate of material removed by a tool, under standard conditions until either the performance of the tool becomes unacceptable or the tool flank wear has reached a standard amount.
- Cutting forces or power - Forces acting on the tool measured using a dynamometer under specified conditions or the power consumption.
- Surface finish, integrity and component accuracy - Surface finish produced under specified cutting conditions.

- Chip shape - The chip shape as it influences the clearance of the chips from around the tool, under standardized conditions.

Materials exhibiting good machinability have long tool life, low cutting force and power requirements and good surface finish [31]. There are many ways in which the cutting tool may be worn (flank wear, crater wear, etc) with a number of possible parameters (maximum, average, etc) which could be used to describe each type of wear [32]. There are also many different types of cutting tool and the conditions under which they may be used to machine material are infinitely variable. Machinability is therefore not a function of any one or two basic properties of the material although the mechanical/physical properties, microstructure and metallurgy may be used to provide a rough guide. Machinability specified empirically for a particular set of conditions does not necessarily enable predictions to be made of the behaviour of the material when the conditions are changed. Experimental work has shown that whilst there may be a relationship between machinability observed in one type of test and that obtained in another test or that measured under other conditions, such relationships remain entirely empirical. The rank order of the machinability of a number of materials may change in different tests and under different conditions within the same test [28, 32]. The determination of the machinability of a material for a particular practical machining operation may have to be conducted under the specific conditions of that operation if a meaningful 'value' of the machinability is to be obtained. In addition, the form of the workpiece material has to be considered with possible differences in machinability between bar and cast/forged blades where 'bulk' material properties are different. Although machinability tests of many types have been conducted for a variety of material removal operations, not all machinability features will be common to more than one process, given the same tool and workpiece materials. Thus it is likely that the short term savings of using 'equivalent' data and not carrying out machinability tests for the process under consideration will be more than offset by the high cost penalty which could result from the use of inappropriate cutting conditions [32]. This is one of the main reasons why machinability data is required by industry and is especially important for the aerospace industry where safety and components being fit for purpose is of paramount concern.

2.4 Economics of machining/grinding

Shaw [30] states that some of the most important problems in the workshop involve the choice of cutting speeds and feeds, tool geometry, tool and work materials, cutting fluids and

the machine tools themselves. It is suggested that there are only three basic considerations associated with all these decisions. Firstly, the chosen conditions must be capable of producing parts that meet the required component specification in relation to size, shape, finish and integrity. Secondly that the required production schedules must be met, and thirdly that parts should be produced at the lowest possible cost [30]. In addition, the manufacturing situation is usually a complex one and a single machining operation is seldom the only operation carried out on a component by the manufacturer. Establishing conditions to give a certain production rate at one stage of the manufacture will influence the production at other stages and will influence storage costs for other components. The situation is further complicated by the fact that in general, most manufacturing machine tools are used for more than one type of component and these give different economic returns. The manufacturing company is interested in the overall profit in a given time interval and this is concerned with the product mix and the production rate at each manufacturing stage. This will give the company the greatest return on the overhead investment and the lowest running costs including the both the raw material cost and machine operating cost. Armarego and Brown [33] suggest that a full optimization of the different values of operation at different production rates and possible variation in anticipated sales may be approached using dynamic programming, however the solution is complex and seldom attempted.

Assuming that the desired level of workpiece surface integrity is achieved, several criteria can be used for the successful operation of a machine tool. The three most common are (a) minimum cost criterion, (b) maximum production rate (minimum machining time) or (c) maximum profit rate [33]. It is easy to confuse the effects of each criterion as there could be a considerable difference between cutting conditions for minimum cost and maximum production but in reality these two criteria are often very similar [33]. In general, the minimum cost criterion will give a lower production rate whereas the maximum production rate criterion will have a higher cost per component with the overall optimum usually between the two. Factors including high cost of component storage or employment related aspects may push the conditions for overall optimisation outside of the limits. A maximum profit criterion involving maximising the return on the operation per unit time will depend on both the production rate and the cost of production.

The machining cost per component (C) is made up of a number of different costs including the non-productive cost per component (C_1), the cost of machining time (C_2), the tool-changing time cost (C_3), the tool cost per component (C_4) and the material costs (C_5). Reducing the non-productive time, the machining time and the tool changing time would lead

to a decrease in the cost per component. Improved tool materials and tool geometry which give longer tool-life values would reduce the number of tool replacements, thus lowering the cost per component. Work materials giving lower tool wear rates would also reduce the cost providing that the workpiece cost does not increase. The cost per component can also be lowered by decreasing the machining time, increasing the cutting speed or feed generally reduces the machining time but also reduces the tool life and has an opposing effect on the cost per component. Thus an optimum cost occurs due to the increasing tool costs [33], see Figure 2.5 (a) for further details.

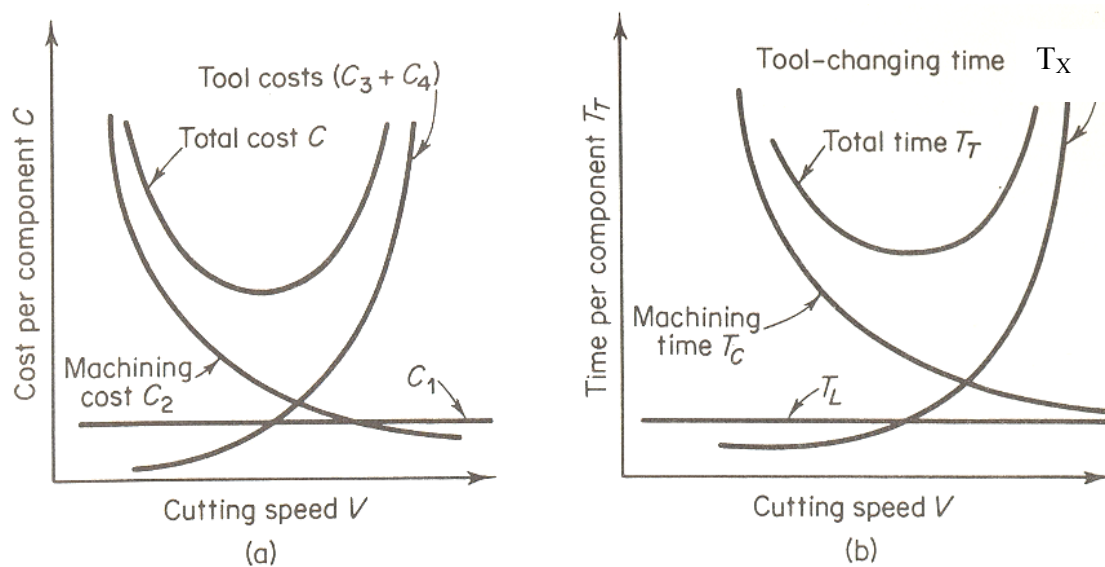


Figure 2.5: Variation of cost and time per component with cutting speed [33]

The maximum production rate is inversely proportional to the production time per component (T_T) and is obtained by summing the non-productive time per component (T_L), machining time per component (T_C) and the tool changing time per component (T_X). For the minimum cost case, decreasing all three factors will increase the production rate. As with the minimum cost case, if the cutting speed or feed rate is increased, the machining time will reduce however the tool changing time per part will increase. Thus a minimum time per component will exist [33], see Figure 2.5 (b).

The profit rate is determined by subtracting the cost per component from the income per component and then dividing by the time per component. Thus the variables that reduce the cost per component and increase the production rate will increase the profit rate. In view of the fact that variations in cutting speed or feed rate will give optimum values of cost per component and production rate, a maximum profit rate will also occur [33].

Machinability information including the effect of operating parameters such as cutting speed, feed rate, depth of cut and cutting conditions on output measures such as tool/wheel life, forces, power and workpiece surface integrity can then be used along with the (a) minimum cost criterion, (b) maximum production rate (minimum machining time) or (c) maximum profit rate to determine the optimum conditions for machining. For example, a component can be produced with acceptable workpiece surface integrity using a cutting tool operating at a cutting speed of 100m/min up to a maximum flank wear criteria of 300 μ m. Operating at a cutting speed of 300m/min, the same tool and conditions may only be capable of achieving acceptable workpiece surface integrity when the maximum flank wear level is less than 100 μ m. The selection of the cutting speed will effect the tool wear rate and subsequently the number of tools and tool changes required leading to differences in the machining cost, the production rate and the profit rate for either method. The manufacturing engineer then has to select which cutting speed to use to achieve the required objectives such as the minimum cost of a component. This would be impossible to achieve without first determining machinability information.

2.5 Mechanics of milling/grinding

2.5.1 Mechanics of milling

Chip formation, in a simplified model is described as the shearing of work material along a plane which is at an angle ϕ° to the workpiece surface. The shear angle influences chip thickness, cutting forces, cutting temperatures and power consumption. In reality shearing takes place in a zone around the shear plane while the actual chip formation mechanism varies depending of the material being cut, the process employed and the operating parameters used. Figure 2.6 (a) shows that the tool has a rake angle of α which can be positive or negative and a relief or clearance angle. The workpiece is undeformed below the shear plane linear transition through the shear plane/zone provides a chip which moves up the rake face. The relative velocity causes friction between the rake face and the chip. The vast majority of cutting operations are 3 dimensional or oblique. One of the main differences between 2D and 3D models is that the cutting edge is at an angle called the inclination angle (i), see Figure 2.6 (b) [29]. The chip flows up the rake face of the tool at the chip flow angle (α_f), measured in the plane of the tool face. The normal rake angle (α_n) is the angle between the workpiece surface normal and the line on the tool face [29, 30]. The chip produced has two surfaces, one in contact with the tool rake face and the other from the original workpiece

surface. As the tool side of the chip climbs up the tool it rubs against the rake face causing the surface to be shiny or burnished in appearance. The other side of the chip has a jagged or step like appearance which is caused by a shearing mechanism [29].

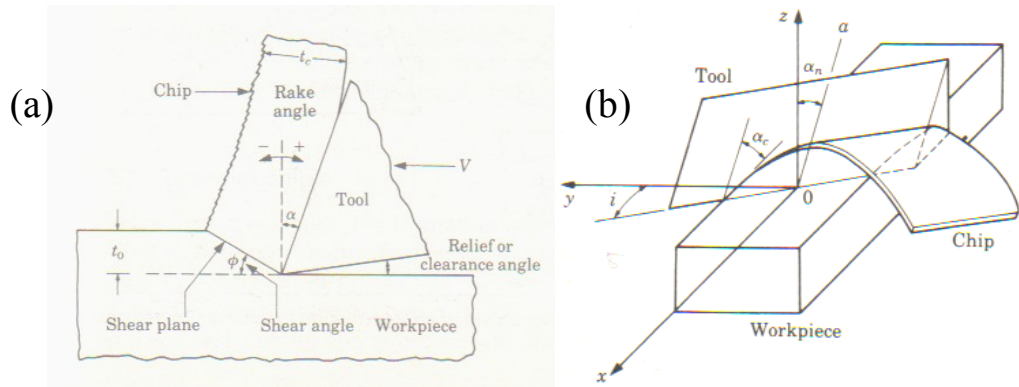


Figure 2.6: Chip formation schematics (a) Orthogonal cutting (2d cutting process), (b) Oblique cutting (Top view showing inclination angle) [29]

The forces acting in orthogonal cutting are the cutting force (F) which acts in the direction of the cutting speed, V and the thrust force (F_t) which acts in the direction normal to the cutting velocity and is perpendicular to the workpiece [29]. In oblique cutting, the axial force (F_a) acting along the cutting edge is also added. Lee and Altintas [34] present the mechanics of cutting with helical ball-end mills and suggest that the ball-end mill is modeled analytically with the flute expressed in a parametric form and divided into small oblique cutting edges. The geometry of each elemental oblique cutting edge is then related to the conventional practical machining coefficients from orthogonal cutting data via the use of mathematical relationships. Using the geometry and kinematics of the ball nose end milling process, the tangential, radial and axial force components can be calculated. These are compatible with the cutting, thrust and axial force in oblique cutting. The elemental forces are then summed along each cutting edge to yield the final cutting forces.

Knowledge of the forces and power involved in cutting operations is important as it allows the determination of a machine tool with adequate rigidity and suitable spindle power capacity [29]. Cutting forces are affected by the mechanical and physical properties of the workpiece material as well as the operating parameters. For example, it has been reported that an increase in cutting speed reduces cutting forces however an increase in tool wear, feed rate and depth of cut have all been shown to increase cutting forces [28].

A number of studies [35-38] have been conducted to provide an analytical prediction of surface roughness after ball nose end milling with flat and inclined workpiece surfaces.

Such modeling approaches are useful to gain an understanding of the process and provide predictive data in order to optimize workpiece topography, assist in maximizing tool life and minimizing cost. In all cases, the analytical models have been verified and proven to show good agreement with experimental results. In some cases the models have even been integrated into CAM software [34-35].

2.5.2 Mechanics of grinding – undefined cutting geometry

In grinding, an individual abrasive grain replaces the cutting tool to provide a method of chip removal. The major factors that differentiate the action of a single point grain from a single point tool are [29]:

- Irregular grain geometry with spacing randomly distributed around wheel periphery.
- Grains have a highly negative ($< -60^\circ$) rake angle resulting in very low shear angles.
- There is a variance in the grains radial position.
- Grinding wheel cutting speeds are very high.

In analysing the mechanics of grinding it is advisable to start with a surface grinding operation where a grinding wheel of diameter D is removing a layer of workpiece material (also known as the depth of cut) d . An individual grain on the periphery of the wheel is moving in a tangential velocity v and the workpiece is moving at a feed velocity of f . The abrasive grain is removing a chip whose undeformed thickness (grain depth of cut) is t with an undeformed length of l . Figure 2.7 shows these variables on a schematic. Shaw [39] states that it is well known that in fine grinding the mean undeformed chip thickness plays an important role relative to grinding forces, surface finish, surface temperatures and wheel wear, more so than does the wheel depth of cut. Figure 2.7 shows down grinding, with the wheel moving downwards through the arc of cut as opposed to up grinding where the wheel moves upwards. Down grinding is the more commonly used mode as grinding fluid which must be aimed in the direction the wheel is rotating is directed at the point of maximum metal removal rate [40].

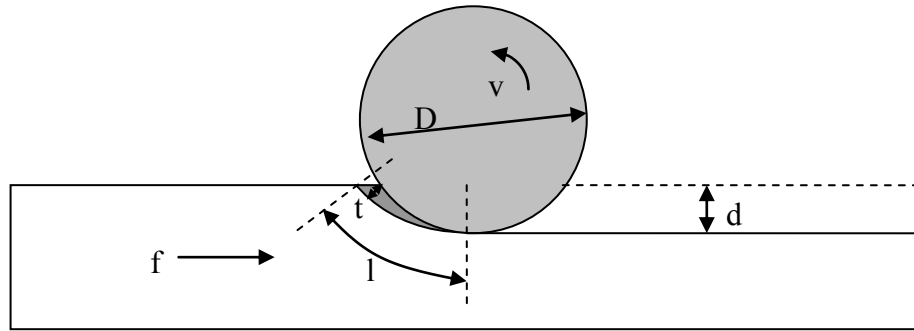


Figure 2.7: Schematic of the grinding process [29]

For $f \ll v$, the contact length (l) mm is also known as the chip contact length:

$$l \cong \sqrt{Dd} \quad (1) [29]$$

Where D (mm) is the wheel diameter and d is the depth of cut (mm). In order to derive the relationship between t and the other process variables the number of cutting points per unit area of the wheel surface C has to be defined. For simplicity, the width of the workpiece is set to unity and therefore the number of chips generated per unit time is vC and the volume of material removed is fd . If r is the ratio of chip width (w) to average the chip thickness, the volume of a chip with a rectangular cross-sectional area and constant width is:

$$Vol_{chip} = \frac{vtl}{2} = \frac{rt^2l}{4} \quad (2) [29]$$

The volume of the material removed per unit time is therefore the product of the number of chips produced per unit time and the volume of each chip or:

$$vC \frac{rt^2l}{4} = fd \quad (3) [29]$$

Substituting Equation 1 into Equation 3 the undeformed chip thickness, t is given by:

$$t = \sqrt{\frac{4f}{vCr}} \sqrt{\frac{d}{D}} \quad (4) [29]$$

Experimental observations for C indicate it to be in the order of 0.1-10 per square mm, with a finer grain size wheel producing a larger value. The magnitude of r is between 10 and 20 for most grinding applications. If these are substituted into Equation 4 a typical value for t will be in the range of ~ 0.3 - $0.4 \mu\text{m}$ [29].

a) Forces

As with machining operations, information concerning the forces in grinding is necessary for grinding machine design, workpiece tolerances as well as the design and use of workholding devices. Figure 2.8 shows the force orientations in grinding.

F_h =horizontal force component
 F_v =vertical force component
 F_t =tangential force component
 F_n =normal force component

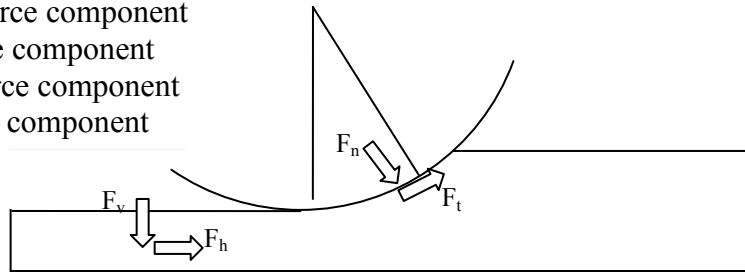


Figure 2.8: Schematic showing force orientations [41]

Besse [41] states that in shallow grinding, the tangential force (F_t) component can be assumed to be the horizontal force (F_h) component, however in creep feed grinding using a higher depth of cut this assumption is not realistic and that the forces must be resolved. Equations 2.5 and 2.6 provide formulas for calculating the normal and tangential force components. The term X in the Equations is the angle at which it is assumed that the forces act, it is recommended that this is either 0.67 [29] or the point where the line of action of the total resultant force intersects the grinding zone [42].

$$F_N = \tau_v \cos(X\theta) - \tau_h \sin(X\theta) \quad (5) [41]$$

$$F_T = \tau_v \sin(X\theta) + \tau_h \cos(X\theta) \quad (6) [41]$$

Where θ is the arc of contact.

$$\theta = 2\sqrt{\frac{d}{D}} \text{ (Theta in radians)} \quad (7) [41]$$

If the force on the grain is assumed to be proportional to the undeformed chip it can be shown that the relative grain force is [29]:

$$\text{Relative grain force} \propto \frac{v}{v_c} \sqrt{\frac{d}{D}} \quad (8) [29]$$

b) Power

Grinding power, Equation 9 is defined as the product of the tangential force and the wheel velocity [42].

$$\text{Grinding power} = \text{Tangential force} \times \text{Wheel velocity} \quad (9) [42]$$

c) Specific energy

The specific energy in a grinding process is defined as the grinding power per unit volume of material removed, see Equation 10 [42].

$$\text{Specific energy} = \frac{\text{Power}}{\text{Material removal rate}} \quad (10) [42]$$

Specific energy consists of three components, see Equation 11. The specific energy required for chip formation by plastic deformation is u_{chip} , the specific energy required for ploughing, which is plastic deformation without chip removal is $u_{\text{ploughing}}$ and the specific energy for sliding U_{sliding} , is caused by friction when the wear flat of the abrasive grit slides along the workpiece. As the wear flat increases due to attritious wear, grinding forces, power and specific energy increase [29].

$$u = u_{\text{chip}} + u_{\text{ploughing}} + u_{\text{sliding}} \quad (11) [42]$$

Typical specific energies in grinding are considerably higher than for cutting processes with geometrically defined edges. This can be generally attributed to three factors: 1) The size of a grinding chip being roughly two orders of magnitude lower than for a chip in other processes. Grinding involves higher specific energies than for cutting, as smaller pieces of metal have greater strength, thus extremely high dislocation densities occur in the shear zone during chip formation which influences the grinding energies involved. 2) As a wear flat requires frictional energy for sliding, this energy can contribute considerably to the total energy consumed. The size of the wear flat in grinding is much larger than the grinding chip. 3) The average rake angle of the grain is highly negative, consequently the shear strains are very large indicating that the energy required for plastic deformation to produce a grinding chip is higher than for any other cutting process. Ploughing also consumes energy without contributing to chip formation [42].

The specific energy decreases exponentially as the specific material removal rate increases providing the wheel speed and coolant supply are kept at a fairly constant state. Smaller chip thicknesses which correspond to low material removal rates, tend to have fairly high specific energy values. This is reported to be possibly due to the larger effective rake angles near the tips of the abrasive grits. Instead of pure cutting, a large proportion of the grinding energy is consumed when the grits plough and slide on the workpiece surface [43].

Figure 2.9 provides details on the effect of the workpiece, machine tool setting parameters and the grinding wheel on grinding results (cutting forces, G-ratio, surface roughness and cutting temperature). In general, increasing the material removal rate by increasing the depth of cut and feed rate provides an increased undeformed chip thickness and as a result the forces and wheel wear increase. As the wheel speed is increased the undeformed chip thickness reduces therefore the cutting forces should decrease and as a consequence reduced wheel wear should be observed. The use of faster wheel speeds also results in an increase in the sliding length per unit volume of material removed which may

cause more attritious wear and dulling of the abrasive grains. It has been reported that this is the case in high speed grinding of silicon nitride with electroplated diamond wheels. Here, enhanced grinding performance was achieved by reducing the wheel depth of cut and increasing the feed rate so to decrease the sliding length. The authors suggest that the sliding length is a critical factor and should be considered when selecting operating parameters [44].

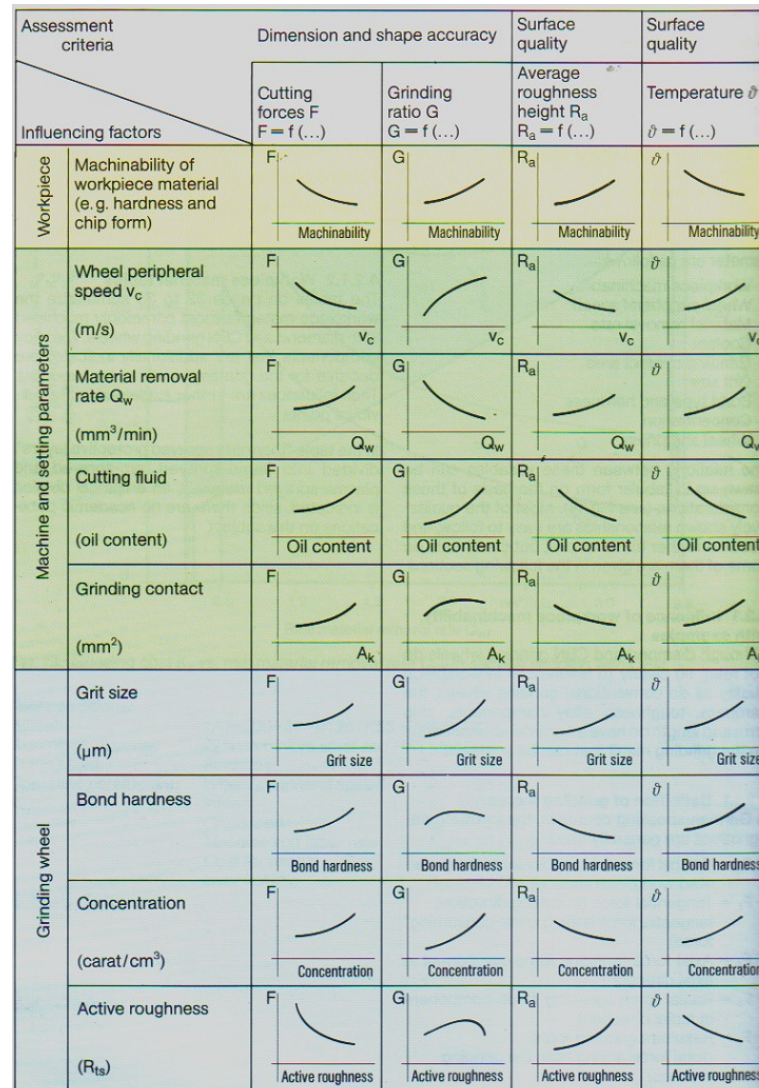


Figure 2.9: Systematic overview of measures for influencing technical grinding result [45]

2.6 Tool/grinding wheel wear

2.6.1 Tool wear mechanisms

Tool wear is defined as being “the change in shape of the cutting part of a tool from its original shape, resulting from the gradual loss of tool material during cutting” [46]. Tool wear is one of the most important and complex aspects of any machining operation and depends on the physical, chemical and mechanical properties of the tool and the workpiece as well as the

tool geometry, cutting fluid properties and various other operating parameters with the type of wear depending on the relative roles of these variables [29]. Considerable difficulty is presented by studying tool wear analytically therefore knowledge of tool wear is based largely on experimental data [28-29]. Relevant literature [28-31, 47-49] has suggested that there are several main tool wear mechanisms which are detailed below:

a) Abrasive wear

Abrasive wear involves the loss of material by the formation of chips as in abrasive machining and is typically caused by sliding hard particles against the cutting tool. The hard particles can come from either the workpiece material or parts of the cutting edge that have broken away [47]. A simplified schematic of this mechanism is shown in Figure 2.10 (a).

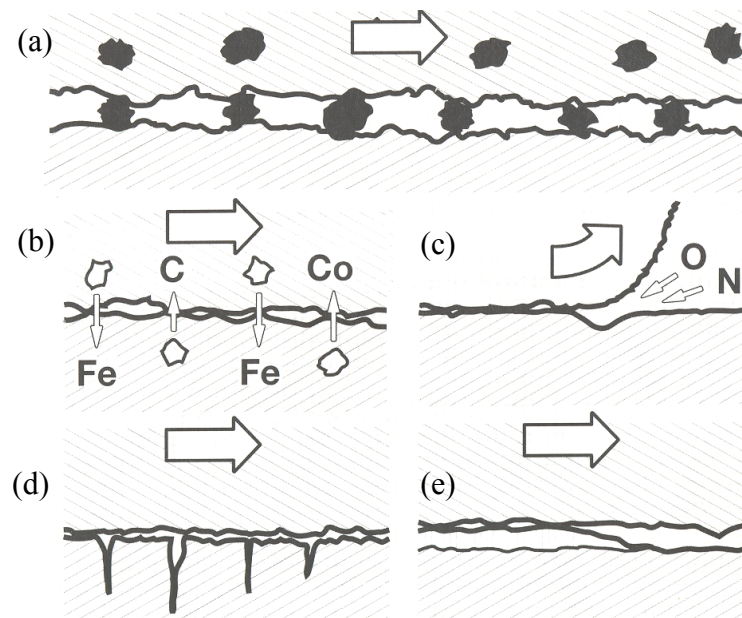


Figure 2.10: Basic wear mechanisms in metal cutting, (a) abrasive wear, (b) diffusive wear, (c) oxidation wear, (d) fatigue wear, (e) adhesive/attritious wear [31]

For this wear mechanism to occur, it is a requirement that one pair of the sliding surfaces be harder than the other member of the sliding pair. Alternatively hard particles can be formed by chemical reaction of the wear debris. Wear can be minimised by making the hardness of the sliding surfaces as high as possible, choosing a mating pair of surfaces that are compatible, reducing the surface roughness of the mating surfaces, ensuring that the surfaces are well lubricated and minimising the load on the sliding surfaces [30]. Figure 2.11 shows that the abrasion wear mechanism lies in the mechanical damage group where an increase in cutting speed and hence temperature does not cause an increase in this domain.

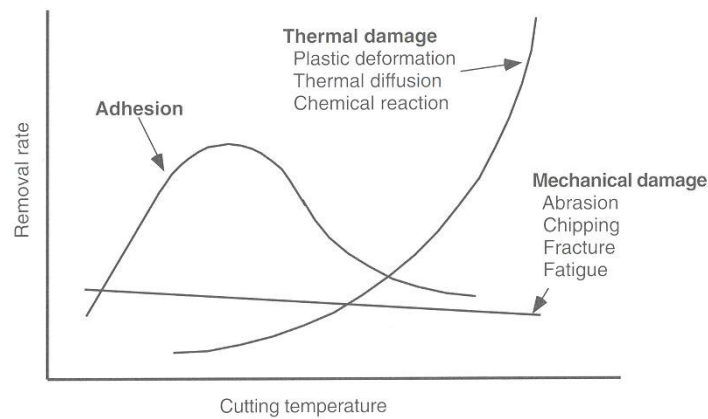


Figure 2.11: Tool damage mechanisms and cutting temperature [47]

b) Adhesive/attritious wear

When a mating pair of surfaces comes close together a particle may transfer from one surface to the other if the bonds that are formed between the surfaces are stronger than the local strength of the material [30]. This type of wear mechanism is called adhesive or attritious wear, as illustrated in Figure 2.10 (e) and occurs at lower cutting speeds, when temperatures are low and wear based on plastic deformation or diffusion does not occur. The most common indication of this type of wear is the formation of a built up edge (BUE) at relatively low rates of material removal. This type of wear mechanism is not accelerated by temperature as shown in Figure 2.11 and tends to disappear at higher cutting speeds [47]. Several authors [50, 51] report tool wear when high speed milling Inconel 718 occurring by adhesion and attrition with the formation of a BUE seen on the tool due to the high pressure and high chemical affinity of the workpiece to the tool material.

c) Diffusive wear

Diffusive wear occurs when atoms of the cutting tool material, diffuse into the underside of the chip or atoms of the workpiece material may diffuse into and react with surface layers of the tool to alter its microstructure and hence strength. Figure 2.10 (b) illustrates this wear mechanism with the C and Co atoms diffusing into the workpiece whilst the Fe atoms from a steel workpiece diffuse into the cutting tool. The rate of diffusive wear depends on tool-workpiece material combination, their solubility, temperature, pressure and time [30]. Increasing the hardness of the tool material alone without changing the tool-workpiece material combination will not affect the wear rate as diffusion wear rates are very dependant on the metallurgical relationship between the tool and work materials. This is especially important when machining materials such as titanium alloys. Diffusion is also very temperature dependant, and occurs more rapidly at the higher temperatures caused by higher

cutting speeds, however, this is often masked by plastic deformation [28]. Zoya and Krishnamurthy [52] suggested that when turning titanium using CBN tools, diffusive wear was the predominate wear mechanism due to reactions between the tool material, nitrogen and atmospheric oxygen. Arrazola et al. [53] also suggest diffusion taking place at the tool -chip interface when turning Ti-6Al-4V using WC tools as carbon was found in material adhered to the cutting tool.

d) Fatigue wear

Fatigue wear is caused by either cyclic mechanical or thermal loads on the tool and is especially important in interrupted cutting operations such as milling where the load and temperature acting on the cutting edge are varied during the rotation of the tool. Thermal fatigue is often identified when numerous short cracks, running at right angles to the cutting edge are observed. These cracks as illustrated in Figure 2.10 (d), are caused by alternating expansion and contraction of the surface layers of the tool as they are repeatedly heated during cutting, then cooled by conduction into the body of tool. The initiation site for the cracks is usually at the hottest position on the rake face, some distance from the cutting edge then spreading across the edge and down the flank. High depths of cut, high feed rates and hard workpiece materials accelerate fatigue wear by increasing the cutting force on the cutting edge. The use of coolant can also accelerate thermal wear by promoting thermal cycling [29, 30].

e) Plastic deformation

Plastic deformation, which is not strictly a wear process as no material is removed from the tool, occurs due to high temperatures and stresses occurring on the cutting edge. Deformation usually starts at the tool nose leading to rounding of the cutting edge which in turn, causes higher temperatures and stresses. Figure 2.11 shows that plastic deformation is a common wear mechanism at high cutting speeds and high feed rates giving rise to high cutting temperatures or when machining hard materials. As a consequence, to withstand plastic deformation a cutting tool with a high hot hardness is required [28].

2.6.2 Visible forms of tool wear

ISO 8688: 1989: Tool Life Testing in Milling [54] describes six main tool deterioration phenomena occurring in characteristic positions on a milling tool depending on the tool/workpiece combination and the cutting conditions used. A brief discussion of the types and the main wear mechanisms causing them follows.

a) Flank wear (VB)

Flank wear is the loss of tool material from the tool side or flank leading to the development of a flank wear land [56], see Figure 2.12. ISO8688: 1989: Tool Life Testing in Milling [54] further breaks this visible form of wear down into uniform (VB 1), non-uniform (VB 2) and localised flank wear (VB 3). Flank wear is considered the most common wear form and the easiest to measure and is generally attributed to sliding of the tool material along the machined surface causing adhesive wear and/or abrasive wear, depending on the materials involved [29, 49]. At higher cutting speeds, it has been suggested that diffusion is the main mechanism causing flank wear because it depends upon high temperatures and the rapid flow of material to transport away atoms of the tool material [28]. Flank wear follows a general trend with an initial period of rapid wear which then levels off and a period of steady state wear follows. Once the wear scar reaches a critical size, the tool undergoes heavy wear or catastrophic failure. In practice, this region of wear should be avoided [55]. When heavy flank wear is observed, it has been suggested that the cutting speed is too high and either should be reduced or a more wear resistant tool grade selected. The only exception is when machining heat resistant material with ceramic tools where an increase in cutting speed is generally recommended [31].

b) Face wear (KT)

Face wear is the gradual loss of tool material from the tool face during cutting [54]. The factors that effect flank wear also influence face wear including abrasive and diffusion wear mechanisms. A crater is formed by the hard particle grinding action or at the hottest part of the chip face through diffusive action between the tool and chip material. Tool hardness, hot hardness and minimum chemical affinity between materials minimises the tendency for crater wear [31]. The presence of crater wear on the rake face can lead to weakening of the cutting edge causing it to fail catastrophically [29].

c) Chipping (CH)

Chipping is deterioration of the cutting edge where parts of the edge break away [54]. These pieces may be very small or relatively large fragments of the tool. Chipping is a phenomenon that results in sudden loss of the tool material unlike wear which is a more gradual process and may occur in a region of the tool where a defect or crack already exists. The two main causes of chipping are mechanical shock and thermal fatigue [29].

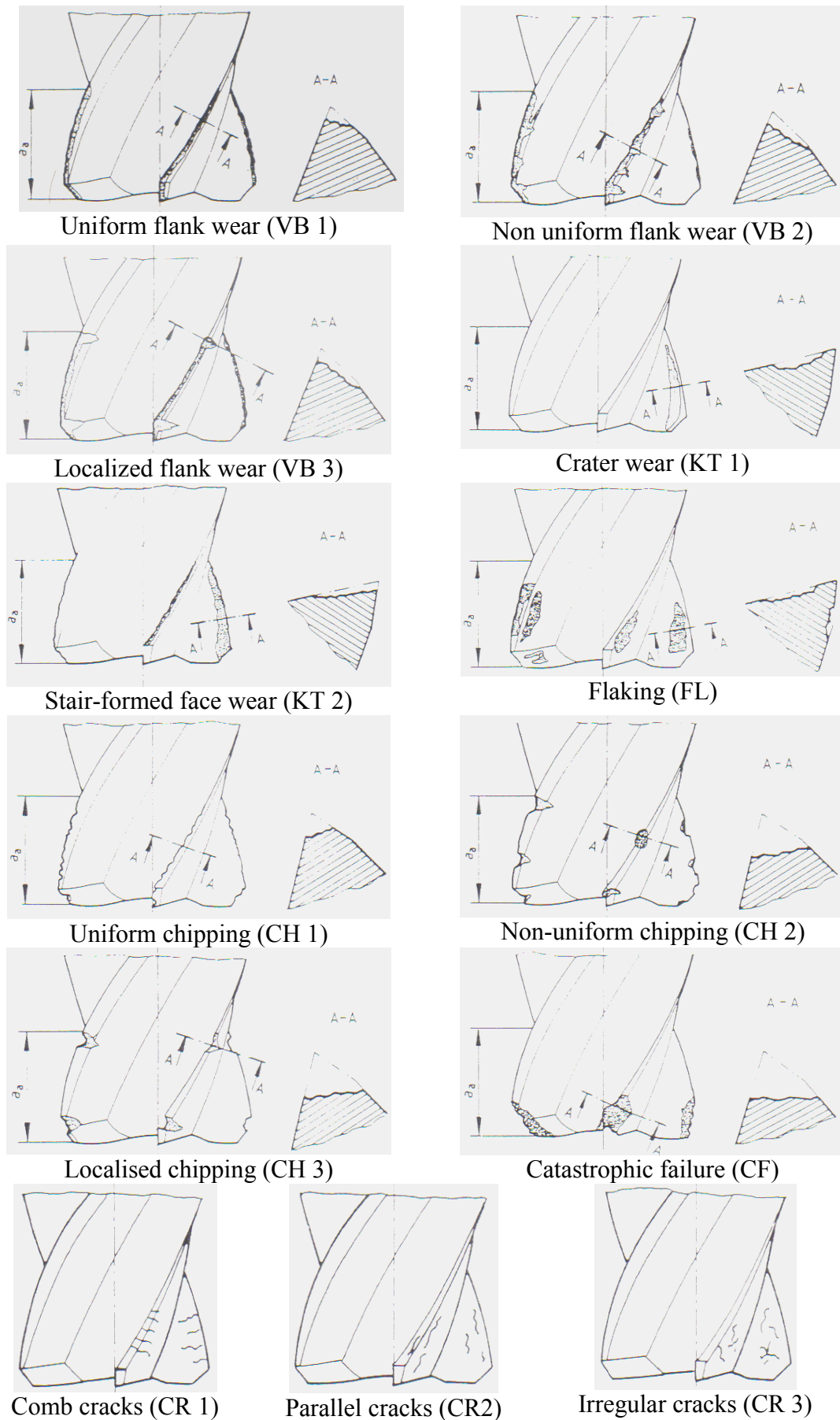


Figure 2.12: Visible forms of milling tool wear [54]

d) Cracks (CR)

Cracks are fractures in the cutting tool that do not immediately lead to loss of material [54]. Thermal cracks are mainly caused by the thermal cycling of the tool in interrupted cutting processes such as milling and generally occur perpendicular to the cutting edge [28]. Mechanical cracking is due to continual variation in load where the load is not large enough to cause fracture. These cracks generally occur parallel to the cutting edge.

e) Flaking (FL)

Flaking is the loss of tool fragments in the form of flakes and is most frequently observed when coated tools are used however may be observed with other tool materials [56]. When turning Ti-6Al-4V using uncoated WC inserts, flaking at the outer edge of crater wear has been reported [57]. This occurred in all trials using wet or cryogenic cooling with the flaking being absent under dry machining and was probably caused by thermal shock.

f) Catastrophic failure (CF)

Catastrophic failure is rapid deterioration or complete failure of the cutting part of the tool [56]. This is the most harmful of all visible wear types and should be avoided as far as possible. It is often the end of the line for the other wear types with the change in geometry, weakening of the edge and rise of temperatures and forces leading to edge failure [31].

2.6.3 Grinding wheel wear

The three main types of wheel wear mechanism are attritious wear, grain fracture and bond fracture. Radial grinding wheel wear typically consists of an initial transient regime at a progressively decreasing rate to a steady state wear regime where parity is reached between the generation of wear flats and new cutting edges [58]. If this parity is broken and there is an increase in grain flat generation, then the wheel should in the case of vitrified bonded wheels be dressed or the grit replaced in the case of electroplated wheels.

a) Attritious wear

Here the cutting edges of the sharp grain become dull by attrition and develop a wear flat which is similar to flank wear in cutting tools. Complex reactions between the grain and the workpiece material lead to the development of the wear. These reactions include diffusion, chemical degradation or decomposition of the grain, fracture at a microscopic scale, plastic deformation and melting. In general, the selection of an abrasive for low attritious wear is based on the reactivity of the grain and the workpiece and their general mechanical properties

such as hardness and toughness. Grinding fluid and the environment can also have an influence on grit-workpiece interaction [59].

If the wear flat caused by attritious wear is excessive then the grain becomes dull and grinding becomes inefficient which results in an increase in temperature. In order to combat this, the grain should fracture at a moderate rate to develop new, sharp cutting edges during the grinding operation. Dressing may be required when attritious wear becomes excessive and hence dulls the grinding wheel or when the wheel becomes loaded with chips. Loading generally occurs when grinding soft materials with inappropriate selection of the grinding wheel or process parameters. Loaded wheels usually cut very inefficiently and generate excessive frictional heat which can cause surface damage [60].

b) Grain fracture

This involves removal of abrasive fragments by fracture within the grain [60]. A grain should fracture at a moderate rate so that new sharp cutting edges are produced continuously during grinding.

c) Bond fracture

Bond fracture involves dislodging abrasives from the binder [60]. The strength of the bond is a very significant parameter in grinding operations. In general, softer bonds are recommended for the hard materials to reduce residual stresses and thermal damage of the workpiece, with stronger bonds used for softer materials and for higher material removal rates [29]. If the bond is too weak then the grains are dislodged easily and the wear rate of the wheel is excessive leading to difficulties maintaining component dimensional accuracy.

d) Wear measures

Grinding wheel wear is generally correlated with the amount of material being ground by a parameter called the grinding ratio (G-ratio) which is defined as:

$$G - ratio = \frac{\text{Volume of workpiece material removed}}{\text{Volume of wheel material removed}} \quad (12) [29]$$

It should be noted that attempting to achieve as high a G-ratio as possible isn't necessarily desirable in practice, as high ratios may indicate grain dulling and possible surface damage. A lower G-ratio may be acceptable if an overall economic analysis provides justification [29].

2.7 Grinding fluid application

Application of fluid in grinding is critical to the life of the grinding wheel and the quality of the machined workpiece surface. In creep feed grinding, this statement is especially true where the arc of contact is long, the specific energy is high resulting in high thermal input and the chips produced and abrasive lost from the grinding wheel need to be flushed away [61]. The benefits of effective grinding fluid application include [61]:

- Reduced dressing frequency owing to less workpiece loading and more effective use of the extreme pressure additives.
- Reduced thermal damage to the workpiece therefore allowing higher removal rates.
- An increase in the useful coolant flowrate, such that the overall applied flowrate can be reduced.
- Reduction in foaming, misting and vapour problems.
- Reduced disturbance of the jet from the air barrier surrounding the wheel.
- A robust wheel/workpiece setup is possible with generic nozzles used for profiled wheels.
- No need to reduce wheel speed to alleviate burn.

Irani et al [62] suggest that the application of cutting fluid in the grinding process reduces the amount of friction due to its lubricating properties and also reduces heat by conducting energy into the fluid instead of the workpiece, thus the colder the fluid the more effective the heat transfer. Applying fluid also removes chips and abrasive particles that could clog up the grinding wheel and so avoid the rubbing and ploughing leading to an increase in forces, energy and heat input to the workpiece [62].

a) Fluid type

These mainly fit into four main categories based on their compositions, synthetics semi-synthetics, soluble oil and straight oil. Table 2.2 gives a ranking of their characteristics. Neat oils are often used in grinding applications as they allow better surface finish, however, environmental concerns have meant that these are being phased out. In addition, there is a fire risk associated with neat oils, especially when grinding titanium alloys as the industry moves towards higher wheel speeds and higher fluid pressures [63].

	Synthetics	Semi-synthetics	Soluble oil	Straight oil
Heat removal	4	3	2	1
Lubricity	1	2	3	4
Maintenance	3	2	1	4
Filterability	4	3	2	1
Environmental	4	3	2	1
Cost	4	3	2	1
Wheel life	1	2	3	4

Table 2.2: Grinding fluid characteristics [62]

The use of water based fluids in a demanding process such as creep feed grinding can cause severe workpiece integrity problems as well as wheel life problems because the viscosity of the water based fluid is much lower than that of the oil. This results in a lower Reynolds number which promotes a dispersed jet when using a conventional nozzle design and requires the nozzle to be placed as close to the grinding arc to minimize the overspray [63]. Wang and Kou [64] determined the cooling effectiveness for water and oil using the finite difference method. They established that water had the better cooling effect and that in creep feed grinding the cooling effectiveness of the grinding fluid should be as high as possible. They suggest that most of the heat entering the workpiece will be carried away with the grinding fluid and that as a consequence in order to ensure the cooling effect, the fluid should be adequately injected into the grinding zone. Minke [65] investigated the grinding of M2 and M3 steels and suggest that with regard to grinding forces and heat impact on the workpiece, there is an advantage in using neat oils. Also in trials with water based emulsion they found that improved cooling performance led to higher process forces that ultimately resulted in relatively high thermal effects on the workpiece surface. Ye and Pearce [66] suggest that neat oil gave less wear than water based fluid for the grinding of a nickel based superalloy, however oil is not recommended for creep-feed grinding, due to its inferior ability to remove heat from the grinding zone. Use of oil resulted in workpiece surface burn being observed at lower material removal rates than when grinding with a water based fluid. In work by Chattopadhyay and Hinetermann [67], loading of the grinding wheel was observed in dry grinding of soft steel shortly after grinding commenced. These loaded particles unfavorably changed the topography of the grinding wheel and in turn increased the tangential force because of rubbing with the workpiece surface. Addition of a water based grinding fluid caused an immediate reduction in the amount of loading observed and as a result the forces were lower.

Methods of cooling and lubricating the grinding zone are not only restricted to liquid coolants in flood form. Graphite can be used as a lubricating medium to reduce the heat generated in the grinding zone. Work by Shaji and Radhakrishnan [68] reported the use of a paste containing fine graphite powder mixed with water soluble oil and a small quantity of grease. In comparative tests with a more conventional flood coolant method the tangential force and workpiece surface roughness were lowered by $\sim 27\%$ and $\sim 13\%$ respectively using the graphite/grease approach however normal force was $\sim 16\%$ higher for the graphite method over flood cooling.

b) Useful fluid application

The effective or useful coolant flowrate is determined by the amount of fluid that enters the grinding contact zone. The term useful is often used since a large proportion of the flowrate may bypass the grinding contact and is therefore regarded as non-useful. The effective flowrate is dependent on the wheel properties, jet quality, jet position, wheel speed and the geometry of the grinding arrangement. In published literature it generally ranges from 0.4% to 50% depending on the above parameters [69]. It has been estimated through experiments and CFD analysis, achievable useful flow can be $\sim 50\%$ of the surface pore space of the grinding wheel. Higher porosity wheels therefore allow a higher percentage of useful flow when compared to lower porosity wheels [70].

An air barrier or boundary layer forms around the periphery of the grinding wheel when the grinding wheel rotates at high speed. This air barrier can prevent fluid flowing into the contact zone resulting in a loss of useful coolant flowrate [59]. The depth of the air barrier depends on the grit size and porosity of the wheel and is difficult to estimate [61]. Figure 2.13 (a) shows how the boundary layer can lead to a reduction in useful coolant flowrate. The grinding wheel is rotating at 33.5m/s and is 80 μm above the workpiece surface. The picture clearly shows no fluid passing underneath the grinding wheel because a significant portion of the air boundary layer reverses as it approaches the gap and has enough momentum to hold the fluid back. Figure 2.13 (b) shows that when the gap between the grinding wheel and the workpiece is increased above the minimum gap size of 80 μm , fluid passes under the wheel because much more of the air boundary layer passes beneath the wheel rather than being reversed [59].

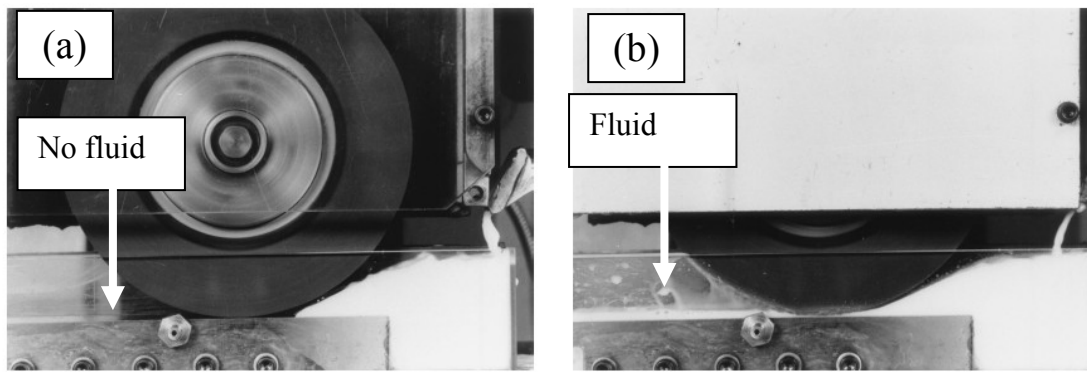


Figure 2.13: Boundary layer effects (a) cutting fluid backing up, (b) layers of air and fluid passing beneath the grinding wheel [59]

Conventional methods of delivering cutting fluid either via a shoe or jet nozzle tangential to the wheel are not believed to enable full penetration of the boundary layer [59]. Under high speed grinding conditions, the energy of the fluid is not sufficient to penetrate the air barrier [59]. Hydrodynamic lift or hydroplaning can be experienced by low porosity wheels because the cutting fluid becomes compressed in the gap between the workpiece and grinding wheel. During grinding, swarf may fill the gap and increase the pressure. If the stiffness of the machine is too low then the wheel can actually lift away from the workpiece [71].

c) Nozzle design

A variety of nozzles using different supply strategies have been developed for grinding applications, see Figure 2.14. The most common types are the shoe nozzle and the free jet nozzle, both belonging to the group of flooding nozzles [72]. The shoe nozzle is a low-pressure method of applying cutting fluid and works by fluid entering a manifold which is then propelled to the wheel speed in the shoe and carried into the cutting zone. One of the reasons why shoe nozzles are very effective is that they are able to maximize the amount of cutting fluid passing through the grinding zone however they have to be in very close proximity to the grinding wheel periphery. Adjustment of the position of the shoe is therefore required as the wheel wears or is dressed. This is described as being difficult, especially with continuous dressing [61] although it can be achieved using a mechanical servo with such a design called an active nozzle [73]. This in turn adds complexity to the system and exposes mechanisms to a harsh environment [72]. Another method of solving the adjustment problem is to use a replaceable tip that is ground by the grinding wheel [74].

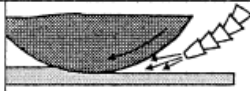
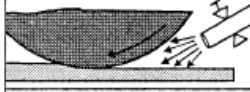





flooding nozzles		conventional flooding nozzles a: flexible segmented hose b: tube c: free jet nozzle	$Q_{CL} \uparrow \uparrow$
			
			
		shoe nozzle	$Q_{CL} \uparrow$
		spot jet nozzle	$Q_{CL} \uparrow$ or $Q_{CL} \downarrow$
		spray nozzle	$Q_{CL} \downarrow \downarrow$
		internal supply	$Q_{CL} \uparrow$ or $Q_{CL} \downarrow$
$\uparrow \uparrow$ very high, \uparrow high, \downarrow low, $\downarrow \downarrow$ very low			

Figure 2.14: Major different types of fluid application methods [72]

Ramesh et al. [75] have developed a coolant shoe which covers nearly 60° of the grinding wheel in order to reduce the effect of the air barrier. The upper portion of the shoe was built with a constantly loaded block and was used for scrapping the air curtain. The shoe also had three orifices to remove the remaining air curtain and supply coolant into the grinding zone at a flowrate of 20 l/min. In grinding deep slots in a SCM15, hypodermic needle the coolant shoe method reduced grinding forces by 40-60%, surface roughness R_a by 10-20% and allowed an increase in the material removal rate before the onset of surface burn, when compared to grinding without the coolant shoe. In addition, the shoe method, increased penetration of the fluid in the sliding region and reduced the temperatures to the extent that lower levels of material adhering to the CBN wheel were observed.

Free jet nozzles offer improved jet coherency, allow a reduction in air entrainment in the grinding fluid, more accurate matching of the fluid velocity to the wheel velocity and more accurate focusing into the cutting zone. These nozzles are often designed to produce a coherent jet that allows them to be placed at a convenient distance from the grinding arc [76]. Webster and his co researchers [61, 77] have been the leading proponents of this method of grinding fluid application and have brought coherent nozzle designs to the forefront of research. Figure 2.15 compares the cross section of a free jet coherent nozzle against a more traditional nozzle and shows the key design features of smooth, concave surface (to prevent boundary layer growth) with sharp exit edges and a high contraction ratio (inlet to exit/outlet

diameter). A contraction ratio of at least 2:1 is recommended [61]. In addition, it is suggested that elbows and changes in the plumbing diameter should be avoided to minimize turbulence. If the pumping ability of the grinding wheel exceeds the flowrate of applied coolant then this starvation will cause the hydrodynamic pressure to develop and the squeezing effect will not occur. The squeezing effect can be exploited when using individual round jets to cover a wide profile. The diameter of the nozzles that cover areas prone to thermal damage such as sidewalls are greater than on flatter surfaces that are less prone to thermal damage. If only nozzles with a single diameter are available, then several nozzles should be focused on these areas. Webster [61] suggests that nozzles do not have to match perfectly with the profile being ground. The internal profile of such nozzles is far from ideal and can force breakup of the jet coherency.

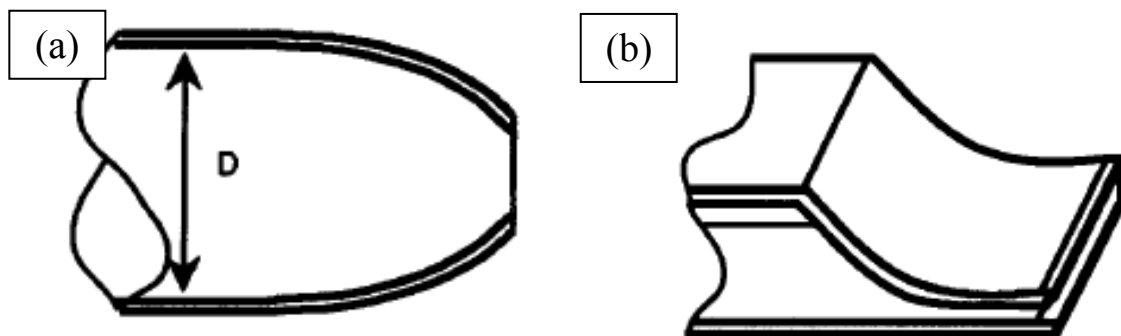


Figure 2.15: Nozzles (a) free jet, (b) conventional [61]

d) Jet nozzle placement

In general, the consensus view [61, 63, 69, 70, 72] is that cooling performance has only a limited sensitivity to nozzle angle as long as the flow is directed into the grinding zone however placement of the jet, onto the wheel ahead of the grinding zone can help remove the air barrier [61]. The nozzle should be able to be adjusted to compensate for a change in grinding wheel size as the wheel either is dressed or wears. A flow guide or dummy workpiece can be fitted to the workholding fixture to improve coolant flow into the grinding zone [40]. Hydrodynamic pressure will force a jet that is placed at the centre of the wheel out towards the edge of the wheel. A second nozzle providing a flow of nominally low pressure is recommended to prevent burn on the back edge of the workpiece. Ebrell et al. [59] showed that nozzle position had an effect on the volume of cutting fluid passing beneath the grinding wheel. They suggest that increased flow beneath the wheel could be achieved by raising the nozzle above the area of reversed flow.

The air barrier can be overcome or reduced by using a rigid scraper fitted close to the wheel surface. This would have to be adjusted every time the grinding wheel is dressed and is therefore more suitable for single layer electroplated superabrasive wheels where no dressing is required. In addition, deposits of swarf generated during the grinding process and carried around by the grinding wheel can clog up the scraper [61]. High pressure cleaning jets can also be aimed at the periphery of the grinding wheel in order to remove the air barrier and clean the grinding wheel. The closer this high pressure jet is to the grinding zone the less time there is for the air barrier to be reestablished [61]. Gift Jr. et al. [78] proposed a layout of scrubber nozzles on both sides of the grinding wheel at different locations. It is suggested that using this layout, there would be a reduction in the amount of material adhering to the grinding wheel [78]. The Very Impressive Performance Extreme Removal (VIPER) process uses an indexable nozzle to force coolant at 50-70bar into the wheel structure ahead of its entry point into the grinding zone. Centrifugal force then causes the fluid to be expelled just at the point of grinding. This method of applying grinding fluid arose because of the requirement to grind the surfaces of aerospace components using one clamping where the wheel had to index to several positions [79]. Hitchiner [80] states that injecting coolant ahead of the grinding zone has been common practice since the 1980's, however, the novelty of the VIPER process was the precise angling of the nozzle to direct coolant.

e) Jet velocity

The pressure of the jet controls the velocity of the fluid whilst the flowrate and temperature control the rate of heat transfer into the fluid. Many researchers [61, 69, 70, 72] agree that in order to maximize useful coolant flowrate, the nozzle jet velocity should be matched to the wheel speed in order to match spindle power and fluid delivery power. At these conditions, the useful coolant flowrate should be maximized [69]. Morgan et al. [70] suggest that jet flowrate should be 4 times larger than the achievable useful flowrate with a jet speed ~80-100% of the wheel speed. Kovacevic and Mohan [81] experimented with higher jet velocities of up to 365m/s in order to overcome the air barrier effect. They suggest that when grinding using an Al_2O_3 grinding wheel rotating at 35m/s, the higher the fluid velocity the better, with up to 25% lower forces and surface roughness R_a reduced by 50% when compared to conventional fluid supply.

f) Radial coolant jets

Instead of providing coolant externally through the use of a nozzle, another option is to apply grinding fluid through the grinding wheel so that the coolant is in direct contact with the grinding zone and can be used more effectively. A radial cooling mechanism is presented in [82] using a perforated electroplated CBN wheel with radial jets. The fluid is forced through coolant holes at high pressure and is thought to break the boundary layer. It is reported that the workpiece surface in the grinding zone was kept below the film boiling temperature of 140°C for water based coolants even at high flux levels. The Diati 50 process developed by Raysun Design Ltd. [83] uses a similar principle where fluid is initially fed into labyrinths within the wheel and then exits through holes in the wheel circumference. External fluid at a pressure of up to ~80 bar is also directed on to the wheel for flushing and cooling. The use of a grooved wheel where grinding fluid can be held and stirred can also cause the heat transfer coefficient to rise. This method can potentially improve the efficiency when grinding using superabrasive wheels with little or no porosity [84].

g) Dual fluid supplies

A simultaneous application of oil and water based fluids is presented by M and K Yokogawa [85]. Oil is added radially to the wheel, just in front of the contact zone in order to reduce friction whereas water based fluid is used for cooling of the workpiece surface. It is reported that surface roughness and material removal rates comparable to those of emulsion can be achieved. The main disadvantage of this type of system is that an additional process is required to separate the oil and water. Irani et al. [86] developed a new cutting fluid delivery system for creep feed grinding involving the application of a single cutting fluid type however at two different concentrations. High concentration synthetic cutting fluid was provided using a high speed free jet nozzle with a velocity of 136m/s (6times the speed of the grinding wheel) and a flowrate of 6.4l/min to the grinding zone to lubricate the system. Low concentration fluid was delivered to the side of the workpiece via a coherent jet (pressure of 7bar and flowrate of 9.5l/min) to remove the heat generated through convection and prevent corrosion. The flows were kept separate using baffles and air scrapers. Trials of the new system against a single coherent jet when grinding hardened steel using Al₂O₃ wheels, showed that an increase in material removal rate of 83% could be achieved before the threshold limit was reached [86].

2.8 Workpiece surface integrity

Workpiece surface integrity is defined as “the inherent or enhanced condition produced in a machining or other surface generation operation” [87] and involves the study and control of surface texture and surface metallurgy. Surface texture encompasses surface roughness and is essentially a measure of surface topography. Surface metallurgy is a study of the nature of the surface layer produced by the machining processes and includes surface alterations. This surface layer has, depending on the workpiece material and machining conditions, been found to have a strong influence on component mechanical properties and subsequent performance [87]. The types of surface alterations associated with both conventional and non-conventional material removal processes are [88]:

- Plastic deformation as a result of hot or cold work.
- Tears, laps and crevice like defects associated with the “built up edge” produced in machining.
- Recrystallisation.
- Change in hardness of the surface layer.
- Phase transformations.
- Intergranular attack and preferential solution of microconstituents.
- Micro cracking and macro cracking.
- Residual stress distribution of the surface layer.
- Embrittlement by chemical absorption of elements such as hydrogen or halogens.
- Spattered coating or remelted metal deposited on the surface during electrical discharge, electron beam or laser machining.

The main causes of these surface alterations are high temperatures or high temperature gradients developed in the machining process, plastic deformation or chemical reactions and subsequent absorption into the workpiece surface [87]. Khales and Field [89] developed a procedure for approaching surface integrity evaluation which specifies three integrity data sets that should be performed depending on the level of required knowledge of the workpiece surface integrity [89]. Table 2.3 provides a description of the three data sets.

The Minimum Surface Integrity Data Set should always be considered first in surface screening tests as it is the least expensive. It essentially provides metallographic information supplemented with microhardness measurements and conventional surface finish measurements. In published literature, for titanium alloys and nickel based superalloys, this is

by the far the most widely used integrity data set [90-93]. For more critical applications, the Standard Surface Integrity Data Set provides more in-depth information. It involves completion of the minimum surface integrity data set along with basic fatigue, stress corrosion and residual stress testing. For detailed design of components the Extended Surface Integrity Data Set should be completed. This involves completion of the Standard Surface Integrity Data Set as well as statistically designed fatigue programs and additional mechanical tests such as tensile, creep, stress rupture [89].

Minimum Surface Integrity Data Set	Surface texture	<ul style="list-style-type: none"> • Roughness measurement • Lay designation or photo • SEM images at increasing magnifications
	Macrostructure (10x or less)	<ul style="list-style-type: none"> • Macrocracks or surface imperfections • Macroetch imperfections • Chemical etchant tests
	Microstructure (cross section examination at 100x preferred)	<ul style="list-style-type: none"> • Microcracks • Plastic deformation • Phase transformations • Intergranular attack • Pits, tears, laps and protrusions • Built-up edge • Melted and deposited layers • Selective etching • Metallurgical transformations
	Microhardness alterations	<ul style="list-style-type: none"> • Heat affected zones • Plastic deformation or work hardened zones
Standard Surface Integrity Data Set	Minimum surface integrity data set	
	Residual stress profile	
	Fatigue tests (screening only using full reverse bending at room temperature using tapered area flat specimens)	
Extended Surface Integrity Data Set	Standard surface integrity data set	
	Fatigue tests – statistical data to established design	
	Stress corrosion tests at selected environmental conditions	
	Additional mechanical testing	<ul style="list-style-type: none"> • Tensile • Stress rupture • Creep • Specialised: friction, wear, sealing, bearing performance • Fracture toughness • Low cycle fatigue • Elevated or cryogenic temperature • Crack propagation • Surface chemistry

Table 2.3: Description of workpiece surface integrity data sets [89]

Almost all components are subjected to a visual inspection which sometimes involves using optical aids however this approach has a limited success in detecting visible macrocracks and other surface defects. The use of dye penetrant and magnetic particle systems, improves the detection of small cracks and defects and sometimes permits the identification of flaws that have been smeared over by a finishing operation. Eddy-current and other electromagnetic detectors can also be used however their resolution is not sufficient to measure small defects. Ultrasonic techniques can detect defects and residual stresses and plastic deformation which may exist at a considerable depth below the surface. X-ray diffraction techniques have been used for the measurement of surface residual stresses yet in-depth stress profile measurements still require removal of the surface layers using a destructive technique [88].

A table summarising the techniques used to detect and locate surface inhomogeneity in metals is provided in Appendix A. Complex and distinctive residual stress patterns are imposed on the workpiece surfaces every time a part is machined by any process. This stress pattern may be tensile or compressive with changes in magnitude depending on the depth from the machined surface. In addition, the stressed layer may be shallow or deep. There are several ways of determining the residual stress state of a material. The two most common techniques are X-ray diffraction and layer material removal processes [94].

High and low cycle fatigue are two important dynamic properties which are surface dependant. Of the two, high cycle fatigue is probably the more important. The affect of the surface condition on high cycle fatigue can be evaluated by employing an alternating stress with a mean stress of zero [88]. Whilst it is suggested that fatigue life is heavily influenced by residual stress, the metallurgical condition of the material (microstructure and microhardness) and the presence of notch-like surface irregularities by machining can play a key role [7]. The dynamic properties of a component generally result from a combination of its surface integrity effects such as surface roughness, surface hardness and residual stress. One of the most pronounced relationships that exist is the relationship between residual stress and fatigue endurance limit [95].

2.9 Machinability of gamma titanium aluminide intermetallic alloys

2.9.1 Introduction

The machinability of γ -TiAl alloys has been detailed in two review publications [6, 96]. In undertaking this literature review, the main processes considered were grinding and milling as these are two of the key processes for the production of compressor and turbine blades

however other operations such as turning, drilling or processes involving non-conventional machining are not dismissed and a review of these is also presented.

Titanium and its alloys are generally classified as “difficult to machine materials” with poor machinability [97, 98]. In 1955 Siekmann [99] stated that “machining of titanium and its alloys would always be a problem, no matter what techniques are employed to transform this metal into chips”. One of the properties that titanium alloys exhibit that leads to them being considered difficult to machine is low thermal conductivity (Ti-6Al-4V: 7.2W/m.K compared to steel: 50W/m.K). This results in a concentration of heat in the cutting zone thus increasing the temperature at the tool/workpiece interface with a subsequent reduction in tool life. Titanium alloys also have a low modulus of elasticity of 110GPa (Ti-6Al-4V), which further impairs machinability and high specific strength even at elevated temperatures. The specific strength of titanium alloys only decreases significantly at temperatures of above 850°C. Titanium is a very chemically reactive element and therefore titanium alloys have a tendency to weld to the cutting tool during machining. This leads to chipping of the tool and hence results in premature tool failure [97]. During machining, titanium alloys exhibit thermal plastic instability which leads to unique characteristics of chip formation. Non-uniform chip shear strains are localized in a narrow band that forms a serrated chip which can create fluctuations in the force and this vibration coupled with high temperature can cause micro-fatigue loading on the tool. This is reported to be partially responsible for flank wear [98]. Despite the increase in thermal conductivity of γ -TiAl alloys over standard titanium alloys such as Ti-6Al-4V, the low room temperature ductility (<2%) and fracture toughness ($\sim 20\text{MPa}\cdot\text{m}^{1/2}$) of γ -TiAl alloys means that producing workpiece surfaces with the desired integrity is extremely problematic [6]. This low value means that the workpiece surface is prone to the formation of cracks which may act as fatigue crack initiation sites and lead to part failure. In a safety critical aerospace application such as blades in the IP compressor or low pressure turbine, the presence of cracks in the workpiece surface is not acceptable and often objectives such as a minimum machining time, minimum part cost and maximum profit rate may have sacrificed in order to achieve a component with the desired integrity [5].

2.9.2 Milling processes

a) End milling

Significant operating factors and levels have been identified for the high speed end milling of the Ti-45Al-2Mn-2Nb +0.8%vol. TiB₂ alloy using Taguchi fractional factorial experimentation [100]. A single insert end mill of $\phi 12\text{mm}$ was used along with two grades of

WC (K20-30 and K15-25) and several different insert coatings (TiN, CrN and TiCN) and uncoated inserts for comparison. Preferred operating levels, (obtained from the Main Effects Plot - means for tool life (m), see Figure 2.16), for maximum tool life, involved the use of K20-30 WC, TiN coated inserts along with a cutting speed of 70m/min, depth of cut (axial and radial) of 0.2mm and a feed rate of 0.12mm/rev. Dry cutting produced the longest distance cut, however the application of high pressure fluid (27bar at 60l/min) produced an almost similar level. Fluid application, axial and radial depth of cut, feed rate and cutting speed were found to be statistically significant at the 5% level. Percentage contribution for each factor showed that cutting speed had the greatest effect at 37%. The average distance machined ~ 8.0 m was extremely short and the confirmation experiments performed using the levels which produced the longest distance machined gave a large variability from 12.7-26.22m. This short inconsistent tool life causes concerns in the economics and prediction of life in end milling.

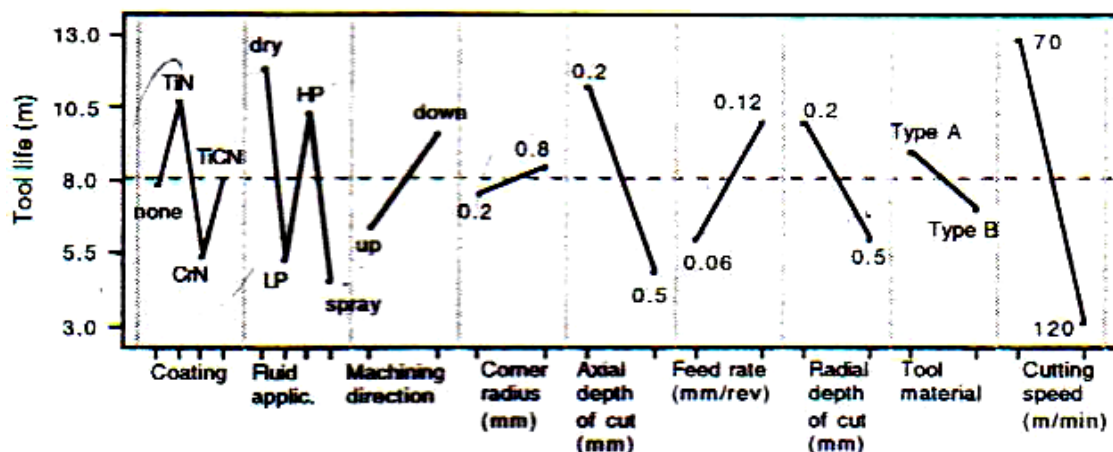


Figure 2.16: Main Effects Plot - means for tool life when high speed end milling [100]

The importance of cutting speed on tool life was shown by the extremely steep Taylor tool life curve, shown in Figure 2.17. Further work is detailed in [101] using more arduous parameters than those detailed in Figure 2.17 (stepover: 1.5-3mm, depth of cut: 1.5-3mm and feed rate: 0.1-0.2mm/tooth). Cutting speed was reduced from 70-120m/min down to 27-35m/min. Workpiece surface roughness R_a varied from 0.35-2.84 μm whilst surface integrity analysis showed the presence of a hardened layer of depth 100-140 μm with a maximum hardness increase of $\sim 140\text{-}200\text{HK}_{0.025}$ higher than bulk hardness. Cross sectional micrographs showed extensive bending of the lamellae on nearly every test. They did not however show

the high number of cracks/pullout that was evident when viewing the machined surface. Indeed, only one tear was observed in all the cross-sectional micrographs viewed.

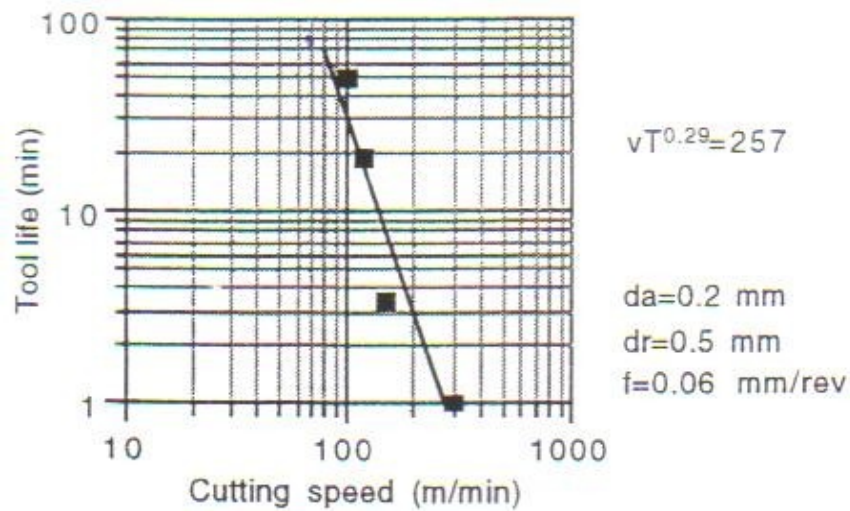


Figure 2.17: Taylor tool life curve when high speed end milling [100]

Based on the high speed milling of the side surface and bolt support head of a conrod made out of Ti-46Al-0.5Mo-0.8Cu-0.2Si, Wienert [102] recommended a cutting speed of between 30-50m/min, a feed rate of between 0.01-0.25mm/tooth and fine grain coated carbide cutting tool with emulsion as the lubricant. Tools made from PCBN and PCD were not recommended as they compared poorly, as did operation with cutting speeds >200m/min.

b) Ball nose end milling

Most of the work reported has investigated the effect of tool life when machining dry using down milling, as this was deemed to provide the 'best' results. Work by Doody [103] showed that in some cases up milling with flood coolant also produced surfaces with low surface roughness. Cutting force variation when high speed ball nose end milling (6mm diameter, WC, four flutes) is detailed in [104]. The ball nose end mills were coated with either a TiAlN (type A, 0-3° rake angle) or TiCN (type B, 13° rake angle) and the workpiece was inclined at 45° with down milling in a vertical upwards direction. The results of these tests are shown in Figures 2.18 and 2.19. When using new tools the cutting force was similar for both types of cutter and there was an increase in forces as flank wear increased up to a maximum value of 0.3mm using type A tools at identical cutting parameters as those used in Figure 2.18. Figure 2.19 (b) shows that the tool life for ball nose end milling an inclined surface was much higher

than that for end milling. Variation in cutting speed between 50-136m/min showed that cutting speed had little/no effect on the measured forces [104].

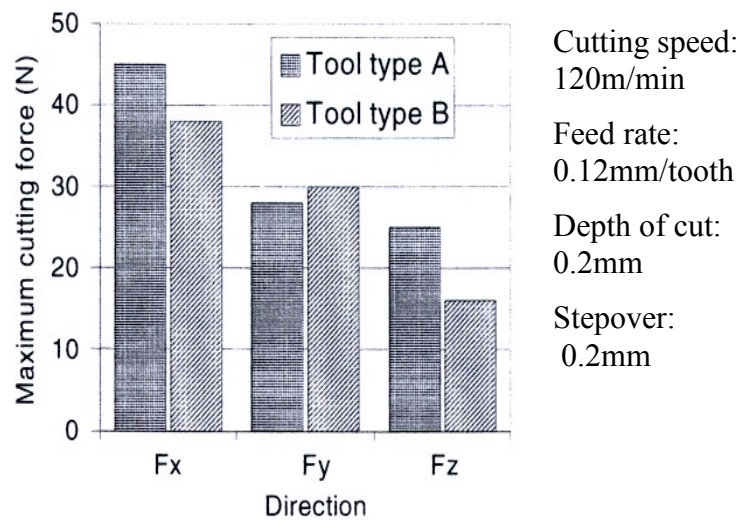


Figure 2.18: Maximum cutting forces when high speed ball nose end milling [104]

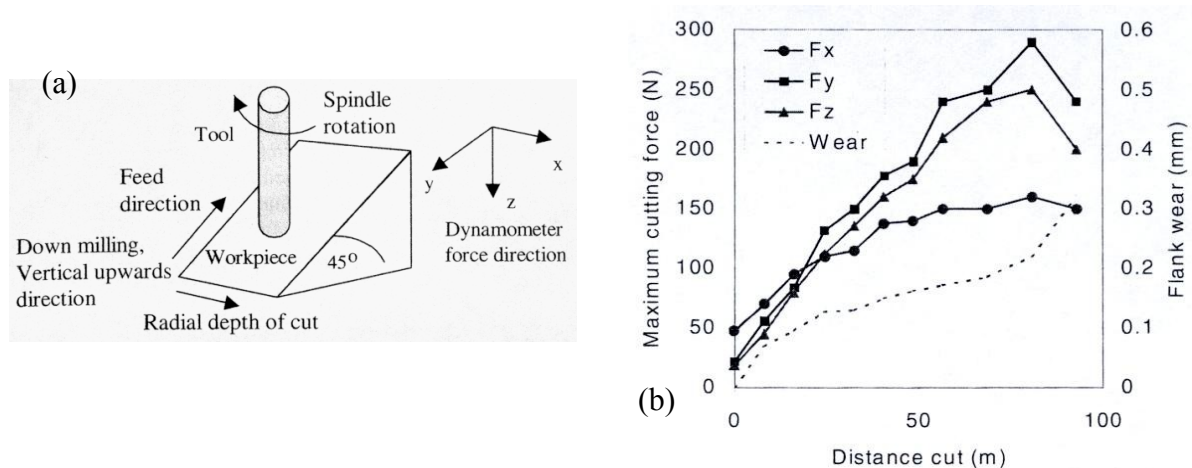


Figure 2.19: Cutting force when ball nose end milling Ti-45Al-2Mn-2Nb +0.8%vol. TiB₂ (a) schematic of the cutting process and force directions, (b) cutting force and flank wear with increasing distance cut [104]

Cutting temperature measurement of Ti-45Al-2Mn-2Nb +0.8%vol. TiB₂ using a constantan-workpiece thermocouple is detailed in [6, 105]. A looped Teflon insulated wire with a 75μm diameter core with an outer diameter of 55μm was clamped between two blocks. Both new and worn 6mm diameter TiCN coated WC ball nose end mills were used at cutting speeds of between 50-135m/min, a feed rate of 0.12mm/tooth and an axial and radial depth of cut of 0.2mm to mill the surface normal to the cutting tool using a down milling mode. Mean maximum cutting temperatures are reported to be between 137 and 252°C. Tilting the workpiece to an angle of 45° yielded an increase in temperature to 316°C for a worn tool.

Tests at a cutting speed of 345m/min gave the highest temperature of 413°C. Poor contact between the thermocouple wire caused by brittle edge fracture between the TiAl blocks was reported. Consequently implanted K type thermocouples with an overall diameter (wire and insulation) of 280µm were inserted into holes, produced by electrical discharge machining, in workpiece blocks operating at a workpiece tilt angle of 45°. Reported cutting temperatures of 234°C and 253° at a cutting speed of 70 and 120m/min respectively are in agreement with those obtained using a constantan-workpiece thermocouple.

Workpiece surface integrity evaluation when high speed ball nose end milling is detailed in [106, 107]. Table 2.4 details the operating parameters used. Finishing cuts at low cutting speed, low depths of cut with a workpiece angle of 45° and new tooling, produced surfaces with the best integrity with surface roughness values <Ra 0.8µm. Pullout was confined to a depth of 2µm and there was no cracking. The workpiece tilt angle of 45° ensured cutting speed was only slightly reduced over the tool workpiece contact area, leading to improvements in surface quality.

Cutting speed	70/120m/min
Feed rate	0.06/0.12mm/tooth
Depth of cut (axial and radial)	0.1-0.5mm
Workpiece tilt angle	0/45°
Coolant application	Dry/HP
Operation	Down milling
Flank wear level	New ($VB_B=0\mu\text{m}/\text{worn } (VB_B=300\mu\text{m})$)

Table 2.4: Operating parameters for surface integrity assessment [106, 107]

Figure 2.20 shows cross sections of the machined surface using a finishing cut with worn tooling. The micrographs, which detail fracture/pullout and plastic deformation of the workpiece surface confined to <10µm and <20µm respectively from the machined workpiece surface, are representative of all tests with the workpiece surface at 0°. Figure 2.21 illustrates the improvement in surface integrity that was achieved by using a workpiece tilt angle of 45°. Micrographs of the cross sections showed little/no cracking with pullout confined to a depth of <2µm however bending of the lamellae is observed in Figure 2.21 (a) to a depth of ~30µm [106, 107].

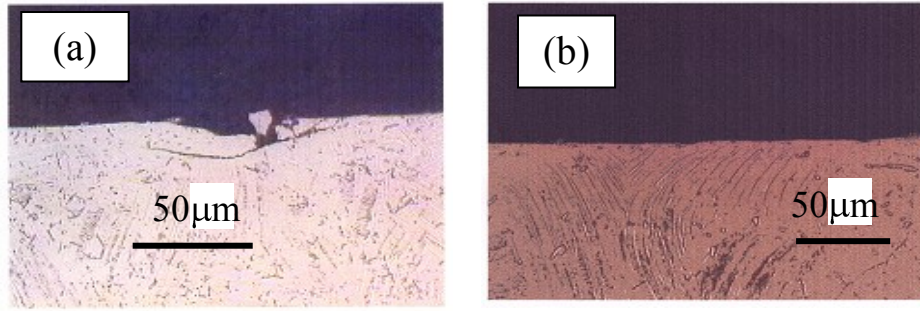


Figure 2.20: Cross sections of machined surface ($v=70\text{m/min}$, $d=0.2\text{mm}$, $a=0.2\text{mm}$, $f=0.06\text{mm/tooth}$, dry, flank wear $=300\mu\text{m}$, 0°) when ball nose end milling [106]

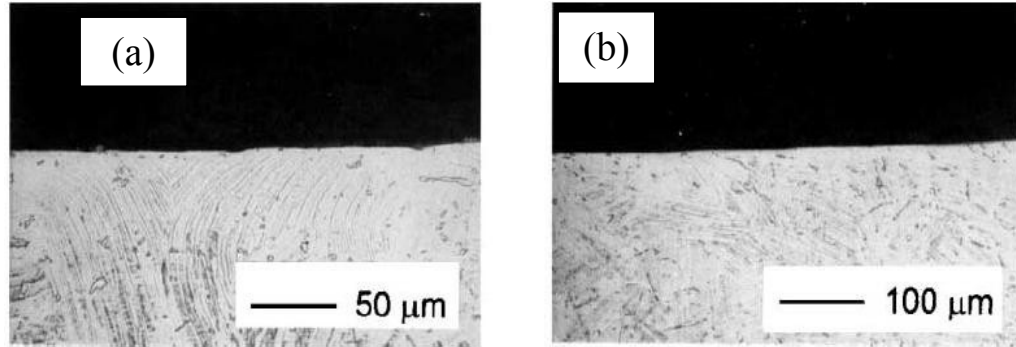


Figure 2.21: Cross sections of the machined workpiece surface, $v=70\text{m/min}$, $d=(a) 0.1\text{mm}$, (b) 0.2mm , $f=0.06\text{mm/tooth}$, dry, flank wear $=300\mu\text{m}$, 45° when ball nose end milling [106]

Hardened layers with a depth of up to $300\mu\text{m}$ were found in research by Mantle and Aspinwall [106, 107], see Figure 2.22. Extensive strain hardening occurred, with maximum hardness of $\sim 650\text{HK}_{0.025}$ at a depth of $30\mu\text{m}$ from the workpiece surface. In general, tests at 45° produce a lower microhardness as the cutting process was more efficient than at 0° resulting in lower plastic deformation.

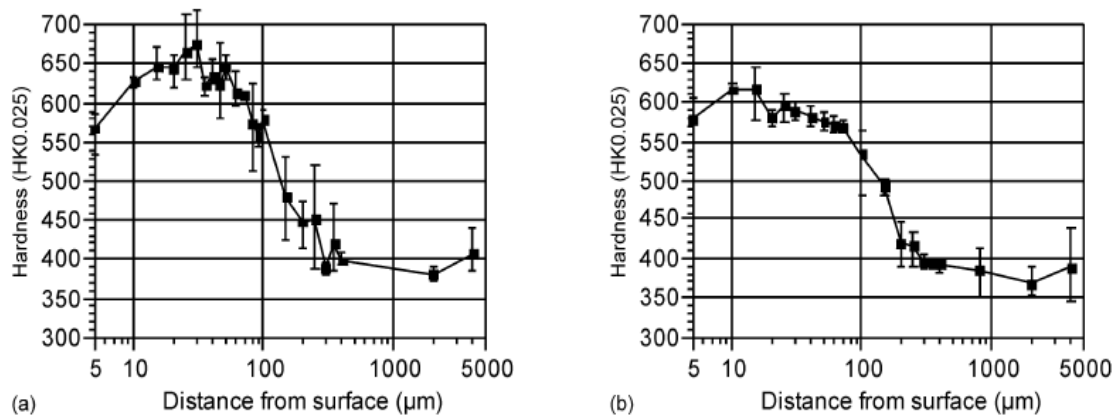


Figure 2.22: Microhardness profiles for ball nose end milling, $v=70\text{m/min}$, $d=0.2\text{mm}$, $a=0.2\text{mm}$, $f=0.06\text{mm/tooth}$, dry, flank wear $=300\mu\text{m}$, (a) 0° , (b) 45° [106]

Residual stress measurements taken of ball nose end milled surfaces using the blind hole drilling technique, showed compressive stresses $<500\text{MPa}$, which became neutral at a depth of $\sim 300\mu\text{m}$ from the machined workpiece surface [106, 107]. A Main Effects Plot- means for maximum compressive residual stress is given in Figure 2.23. The factors that had the greatest effect were cutting speed and flank wear level with the highest compressive stresses occurring with worn tooling which is consistent with greater plastic deformation. Increasing cutting speed increased cutting temperature leading to lower compressive.

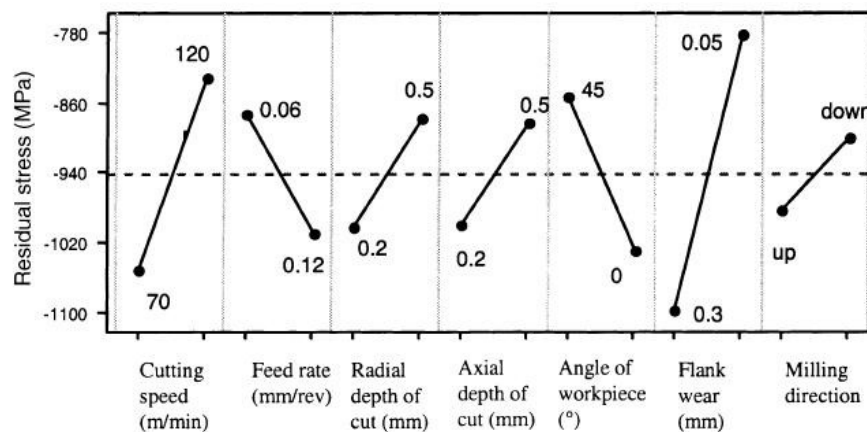


Figure 2.23: Main Effects Plot - means for residual stress when ball nose end milling [106]

Sample SN curves reporting substantially higher fatigue strength for HSM surfaces than polished or ground surfaces are shown in Figure 2.24. The increased level of cracks produced using worn HSM tools was cited as the reason for the lower performance [108, 109].

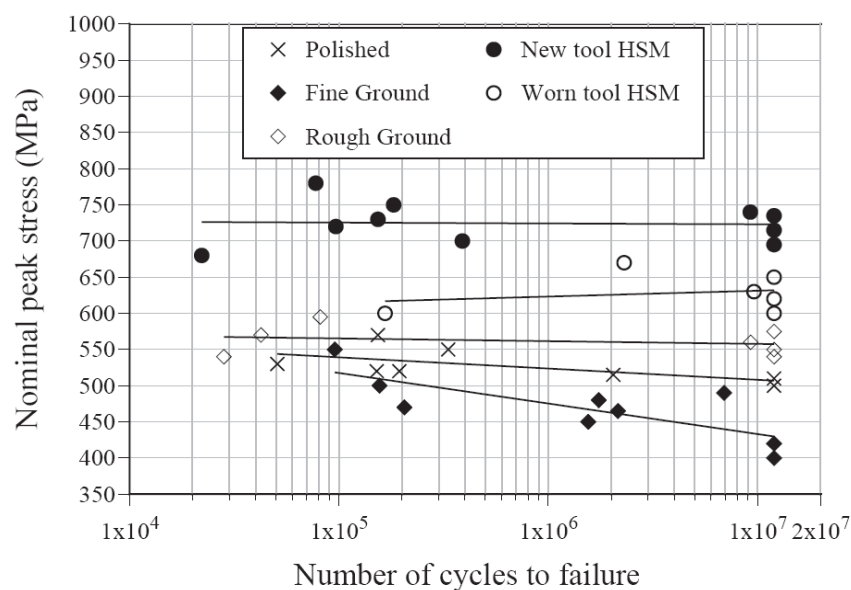


Figure 2.24: SN curves for machined surfaces [108, 109]

c) Face milling

Extruded nearly lamellar Ti-47Al-2Nb-2Mn +0.8%vol TiB₂ was used to assess the effect of face milling on tool life, cutting forces and workpiece surface roughness by Vargas Perez [110]. Conditions used for experimentation are detailed in Table 2.5. Not surprisingly, given the arduous operating parameters used, tool life was extremely short with maximum flank wear reached after less than 2m at a cutting speed of 50m/min, see Figure 2.25. No data was given for higher cutting speeds, however it is stated that at cutting speeds between 50 and 100m/min, extensive chipping of the cutting edge and very fast wear were evident. At cutting speeds above 100m/min the WC inserts failed catastrophically [110].

Cutting speed	30/50/80/100/300/400m/min
Feed rate	0.1/0.5mm/tooth
Radial depth of cut	30mm, cutter diameter: 50mm
Axial depth of cut	1mm
Operation	down milling
Cutting tools	Coarse grain: 1-2 μ m, fine grain:<1 μ m
Cutting fluid	Flood coolant using Conquest HD synthetic cutting fluid
Flank wear level	New to VB _a =300 μ m

Table 2.5: Cutting conditions for face milling Ti-47Al-2Nb-2Mn +0.8%vol. TiB₂ [110]

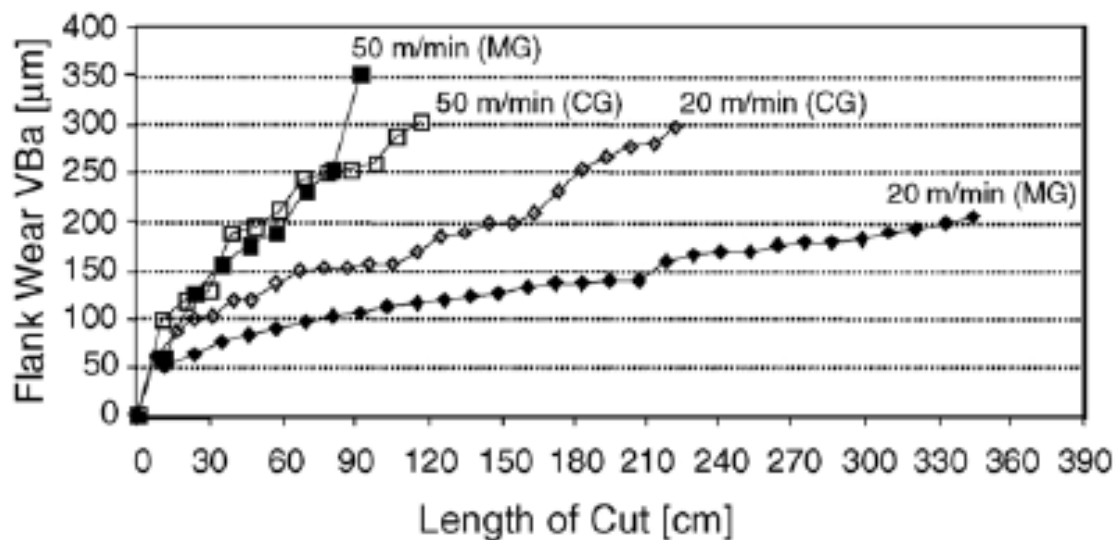


Figure 2.25: Tool life results after face milling Ti-47Al-2Nb-2Mn +0.8%vol TiB₂ (MG=micrograin, CG=coarse grain) [110]

Surface integrity assessment was performed on the basis of surface roughness measurements and microhardness measurements shown in Figure 2.26. Cutting speed used was 20m/min with the micrograin inserts used. Surface roughness varied between, Ra<0.2 μ m and 0.6 μ m for

a maximum flank wear of 300 μm . Microhardness measurements showed a hardened surface to a depth of approximately 200 μm with a maximum hardness of $\sim 800\text{HV}$. No details of microstructural damage including cracking/pullout or plastic deformation were given [110].

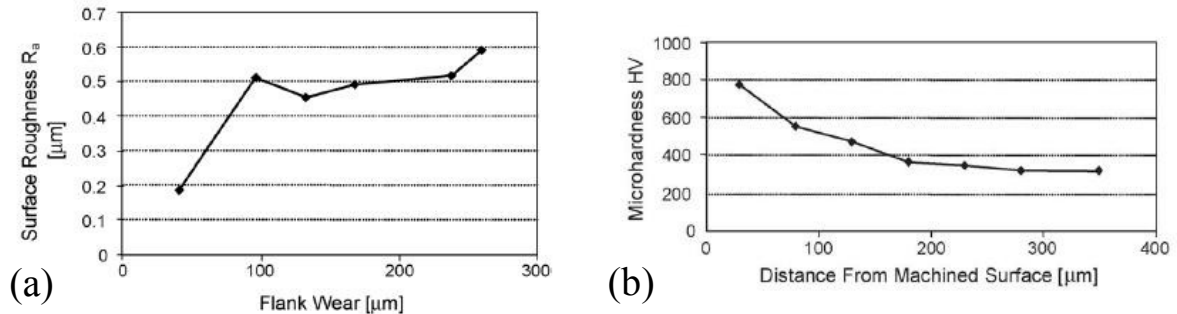


Figure 2.26: Results of face milling Ti-47Al-2Nb-2Mn +0.8%Vol TiB₂ (a) surface roughness R_a , (b) microhardness [110]

2.9.3 Abrasive processes

Grinding appears the most suitable process for manufacturing components from γ -TiAl alloys because fewer problems are presented by the alloys low room temperature ductility ($<2\%$).

a) Scratch tests

Zeppendfeld et al. [111] performed simple scratch tests to investigate the wear mechanisms when grinding Ti-45Al-2Mn-2Nb. A single diamond grit was mounted in a chuck located on the circumference of a modified grinding wheel. The machine table carrying the workpiece was moved perpendicular to the spindle axis and a scratch track is introduced into the workpiece. The grit size used was 252 μm with a rotational speed of 45m/s, a cut width of 20 μm and depth 1 μm with emulsion coolant. They found $\sim 1\mu\text{m}$ thick layers of adhered titanium aluminide which had a fine crystalline structure indicating that the workpiece material had to have been highly viscous or liquid. They also report that in-situ temperatures of up to 1400°C, which to a minor extent caused graphitisation of the diamond grit [111].

b) Surface grinding

In comparison to Ti-6Al-4V, surface grinding of Ti-45Al-2Mn-2Nb using SiC abrasives and identical operating parameters, see Table 2.6, showed a 60% reduction in tangential force, a 50% reduction in specific grinding energy, an increase in G-ratio of 3000% (45 compared to 1.5) and a reduction in surface roughness of $\sim 60\%$ (R_a 1.4 μm compared to R_a 0.6 μm . Figure

2.27, shows graphs of the surface finish and G-ratio when grinding both alloys [108, 112]. In comparison to surface grinding of Inconel 718, Nolan [113] reports G-ratios 4-10x higher with ~ 3 x lower specific grinding energy, for an undisclosed composition TiAl alloy.

Grinding wheel	GC60J7V
Wheel speed	30m/s
Feed rate	0.3m/s
Dressing	Single point diamond, feed rate: 0.15mm/rev, depth of dress 0.05mm and no of dress passes: 3
Coolant	Hocut 808 (4%) at a flowrate of 8l/min through two multi-hole flare nozzles
Depth of cut	10 μ m per down pass followed by a sparkout pass on the upstroke Crossfeed was set to zero (Operation effectively plunge grinding)

Table 2.6: Operating parameters for grinding Ti6Al4V and Ti-45Al-2Mn-2Nb [108, 112]

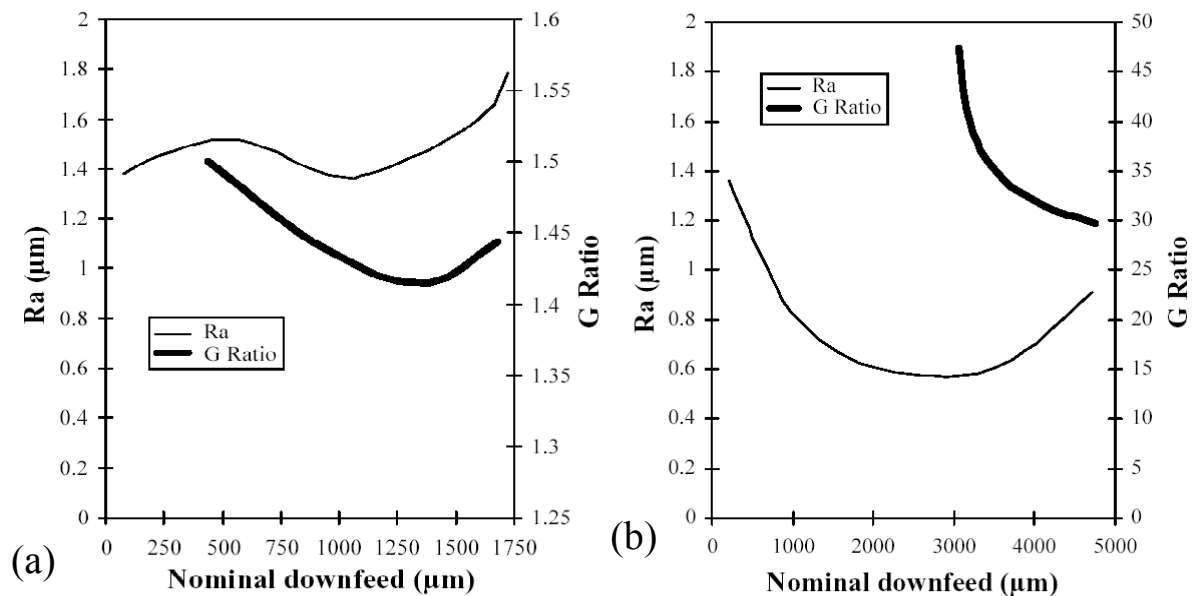


Figure 2.27: Comparison in surface finish and G-ratio when grinding (a) Ti-6Al-4V and (b) Ti-45Al-2Mn-2Nb [108, 112]

Table 2.7 details the operating parameters used when surface grinding Ti-45Al-2Mn-2Nb +0.8%vol. TiB₂ [108, 114]. In order to assess the effect of operating effect interactions, a full factorial experiment with replications was used. Four factors were investigated, grit size, wheel grade, structure and depth of cut. Force measurement results detail normal forces of 420-520N and tangential forces of 140-200N, see Figure 2.28 (a). A wide variety of workpiece surface roughness values detailed in Figure 2.28 (b) were also obtained with statistical analysis showing that the surface roughness was dependant on all operating parameters and to a greater or lesser degree their 1st and 2nd order interactions.

Grinding wheel	Grit size: 80/120, wheel grade: H/K, Structure 7/16
Wheel speed	30m/s
Feed rate	0.4m/s
Dressing	Single point diamond, feed rate: 0.15mm/rev
Coolant	Hocut 808 (4%) at a flowrate of 8l/min through two multi-hole flare nozzles
Depth of cut	10/25 μ m per down pass followed by a sparkout pass on the upstroke Crossfeed was set to zero (Operation effectively plunge grinding)

Table 2.7: Operating parameters for surface grinding
Ti-45Al-2Mn-2Nb +0.8%vol. TiB₂ [108, 114]

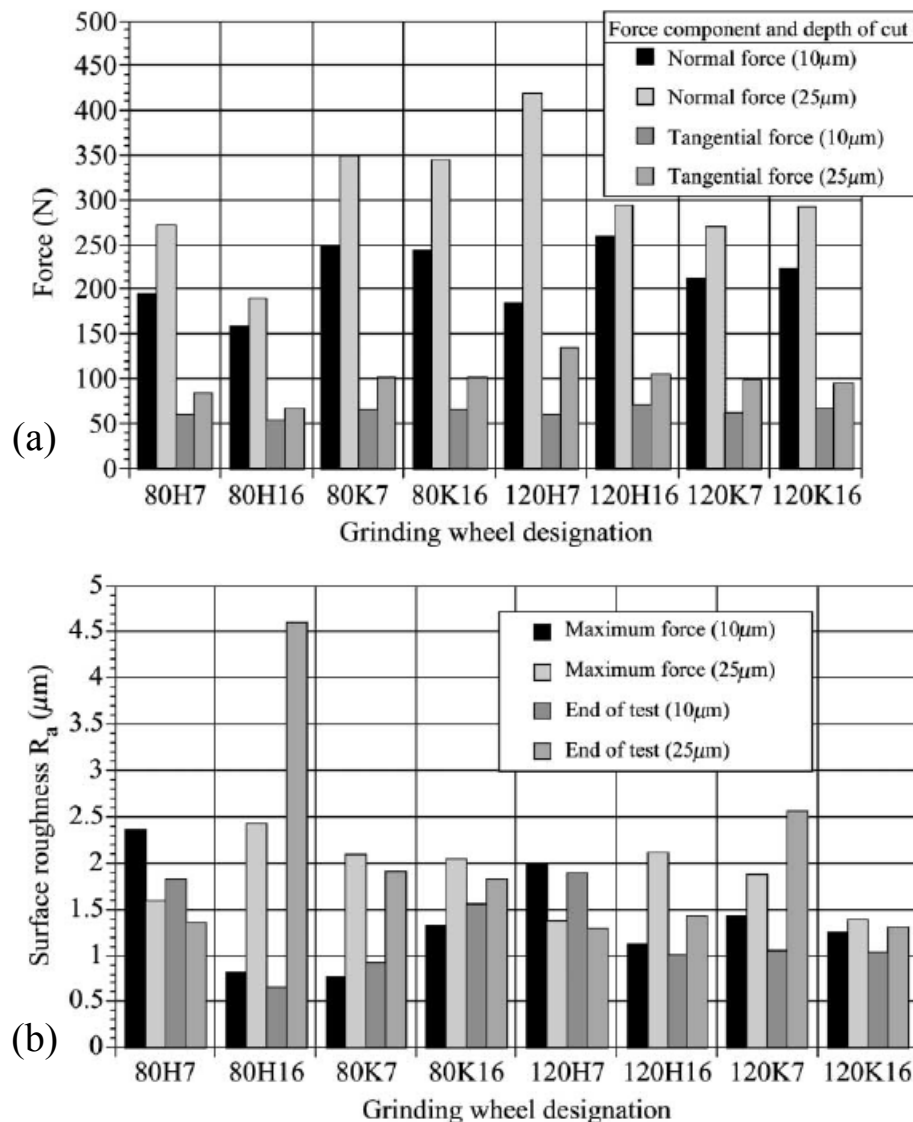


Figure 2.28: Surface grinding results (a) forces, (b) surface roughness R_a [114]

Workpiece surface integrity evaluation of the ground surfaces showed that with appropriate operating conditions, surface burn, discoloration, subsurface deformation and cracking could all be maintained within acceptable limits. Figure 2.29 (a) shows that ground surfaces

exhibited a hardened layer of depth $\sim 100\mu\text{m}$ and a maximum hardness of between 425 and 575 $\text{HK}_{0.025}$, in addition to compressive residual stresses of up to 300MPa at the workpiece surface. These stresses, shown in Figure 2.29 (b), became tensile at a depth of 100 μm from the ground surface [114].

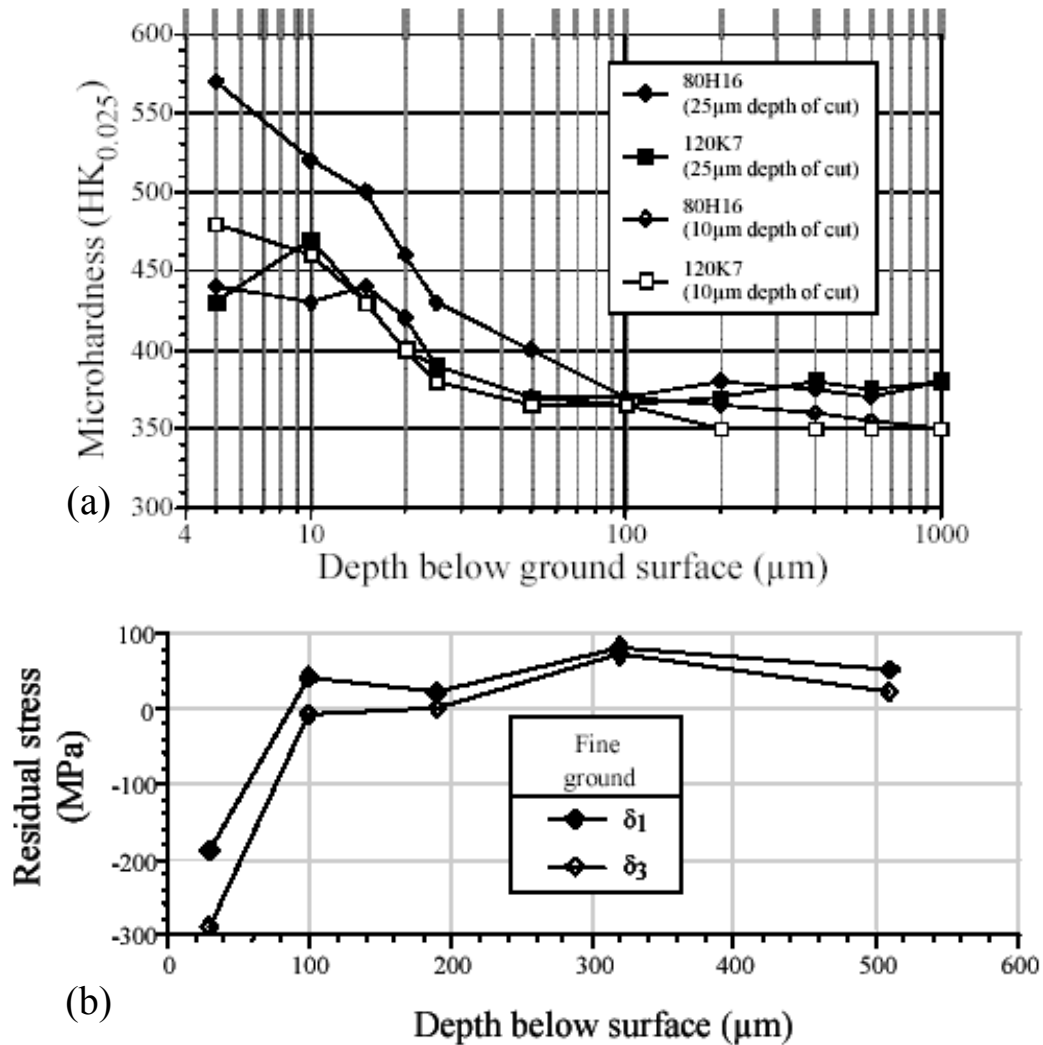


Figure 2.29: Surface grinding results (a) microhardness, (b) residual stress [114]

Further work by Bentley et al. [108, 114] focused on the effect of dressing parameters on the surface integrity of Ti-45Al-2Mn-2Nb +0.8%vol. TiB_2 . A full factorial experimental design was used to investigate the effect of wheel grade, wheel structure and dresser infeed rate. Wheel speed, feed rate, type of dressing, and coolant application were identical to those detailed in Table 2.7. The smaller grit size of 80 μm was selected as was a dress depth of 40 μm . The depth of cut, grinding mode and sparkout were identical to those detailed in Table 2.6. Wheel grade (H/K), wheel structure (7/16) and dresser infeed rate (0.1/0.3 $\mu\text{m}/\text{rev}$) were

varied. Results, Figure 2.30 (a), showed that the increase in dresser infeed rate reduced the normal force by 25%. Statistical analysis of surface roughness measurements showed that wheel grade was the most significant factor (at the 5% level) with harder grades reducing surface roughness by up to 30%. Microhardness plots, see Figure 2.30 (b), show that all ground surfaces exhibited a hardened layer of depth 50-100 μm which was 200HK_{0.025} harder than the bulk. Despite this no evidence of subsurface cracking and microstructural deformation was observed [108, 115].

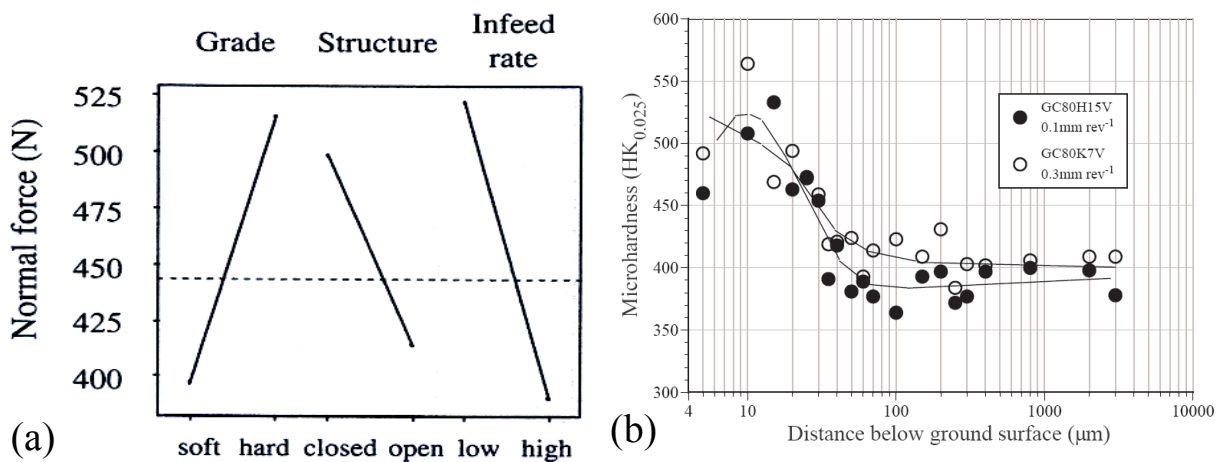


Figure 2.30: Further surface grinding results (a) Main Effects Plot – means for maximum normal force, (b) microhardness [114]

The effect of grinding on fatigue strength is detailed by Bentley et al. [108, 109]. Four point bend (tension-tension) S-N curves were generated. Tests were performed at room temperature using a R ratio of 0.1. Two different sets of grinding parameters were used, these are detailed in Table 2.8. The fatigue curves for the ground specimens are shown in Figure 2.24, along with those for polished and HSM samples. The results for fine ground specimens appeared lower than those for polished or rough ground test pieces. The absence of any microstructural difference between the test pieces suggested that tensile residual stresses were present in the subsurface, indeed residual stress measurements using the blind hole drilling technique confirmed tensile stresses [108], see Figure 2.29. Bentley [108] states that the fatigue life of a gamma alloy is greatly affected by the residual stress state of the workpiece surface: the greater the magnitude or depth of the compressive stresses the longer the fatigue life. He suggests that interlamellar de-cohesion is the main cause of the initial failure but this need not be at the workpiece surface. As long as the residual stress at the surface is sufficiently compressive to inhibit crack growth, it may be possible to tolerate surface cracks.

Parameters	Rough grinding	Finish Grinding
Wheel	GC80H7K	
Wheel speed	15m/s (30m/s used for sparkout)	30m/s
Feed rate	0.3m/s	
Depth of cut	10 μ m 1 sparkout pass on up stroke	10 μ m 2 sparkout passes on upstroke
Crossfeed	1.5mm/stroke	
Cutting fluid	Hocut 808 (4%) at a flowrate of 8l/min	
Surface roughness, Ra	1.1 μ m	0.5 μ m

Table 2.8: Parameters used for surface ground fatigue test specimens [108, 109]

Information on surface grinding of Ti-45Al-2Mn-2Nb +0.8%vol. TiB₂ using superabrasive grinding wheels is limited. Bentley [108] details only three tests performed that were part of a larger Taguchi L12 design used to assess surface grinding of Ti-45Al-2Mn-2Nb +0.8%vol. TiB₂ and Ti-44Al-8Nb-1B. Only diamond wheels of grit size 91 or 46 μ m at wheel speeds of 15 or 26m/s were used with feed rates of 0.1-0.4m/s and a depth of cut of 5 or 25 μ m, both oil and water grinding fluid were employed. Normal and tangential forces ranged from 75-1000N and 100-400N respectively depending on the test parameters used, with in general higher depths of cut and feed rates causing higher forces. Surface roughness, Ra ranged from 1.48-2.28 μ m however statistical analysis showed no factor was statistically significant at the 5% level. Surface integrity analysis showed no evidence of cracks, laps, tears or folds however, slight lamellae deformation to a depth of 3 μ m was observed.

A subsurface damage model has been generated for surface grinding of Ti-48Al to predict the depth of plastic deformation, based on the principles of indentation in brittle materials. Experimental work was presented involving force control surface grinding using the bonded interface method with a range of normal forces 15-90N, a cutting depth of 20-40 μ m and diamond, cBN and Al₂O₃ grinding wheels with water based coolant. Higher normal forces and CBN wheels caused the highest levels of plastic deformation and damage of up to ~200 μ m from the workpiece surface. Diamond wheels generated lower levels of damage (up to 80 μ m) with lower temperatures resulting in this type of grit being selected as the preferred abrasive type. As the paper is mainly concerning with modeling the depth of plastic deformation, experiments were simple with no information on wheel wear and G-ratio, workpiece surface roughness or indeed any images of the machined surface showing the damage to the lamellae or surface [116, 117].

c) Creep feed grinding

Operating parameters used to test the feasibility of creep feed grinding Ti-45Al-2Mn-2Nb +0.8%vol. TiB₂ using conventional (SiC) and superabrasive grinding (diamond and cBN) wheels are detailed in Table 2.9. Separate Taguchi L12 fractional factorial orthogonal arrays were used to investigate the effect of the operating parameters on peak current, normal and tangential forces, workpiece surface roughness and surface integrity (microstructure and microhardness).

Grinding wheel	Conventional abrasive: SiC (GC) grit size: 45/80µm, grade: F/J, structure: 20/30, Superabrasive: diamond/cBN, bond type: vitrified/metallic, grit size: 91/46µm, concentration: 70/100, porosity: 25/30%
Wheel speed	15/30m/s
Depth of cut	1/4mm
Feed rate	150/600mm/min
Dressing	Intermittent/continuous diamond wheel crush, speed ratio: +0.7, dresser infeed rate: 1.5µm/rev (continuous), 500µm/pass
Operation	Down grinding, Conventional abrasives: single pass, Superabrasives: 9 passes at 0.5mm depth of cut then either 1/4mm final pass
Coolant	Cimperial 22DB (water based) 4% concentration at a flowrate of 5l/s using either a shoe/jet nozzle

Table 2.9: Operating parameters used for creep feed grinding trials using conventional and superabrasive grinding wheels [108, 118]

For conventional abrasive tests, normal and tangential forces varied from 200-4500N and 100-1000N respectively whilst surface roughness, Ra, varied from 0.25-1.25µm. Analysis of Variance showed that with the ranges tested, for all three output measures the dressing method was significant at the 5% level with continuous dressing producing lower values. In general, lower values of depth of cut and feed rate produced lower forces and reduced workpiece surface roughness. With superabrasive tests, peak normal force varied from 140-4500N and tangential forces from 200-900N. Workpiece surface roughness also ranged from 0.5-1.2µm [108]. For both conventional and superabrasive trials, spindle stall occurred on several tests (conventional: 2 out of 12, superabrasive: 6 out of 12). For conventional tests, stall mainly occurred when using high operating parameters (depth of cut and feed rate) and intermittent dressing whilst for superabrasive trials it was thought that the lack of machine rigidity and low wheel speeds were responsible, hence a further test plan was established using higher wheel speeds. Surface integrity analysis showed that surface damage including bending of the lamellae was in general, restricted to <25µm from the machined workpiece surface [108, 118]. Microhardness plots for both sets of trials are detailed in Figures 2.30 and

2.31 respectively showing an increase in hardness of up to $250\text{HV}_{0.025}$ above bulk hardness. The depth of the hardened layer, in both cases was $\sim 100\text{-}200\mu\text{m}$ [118].

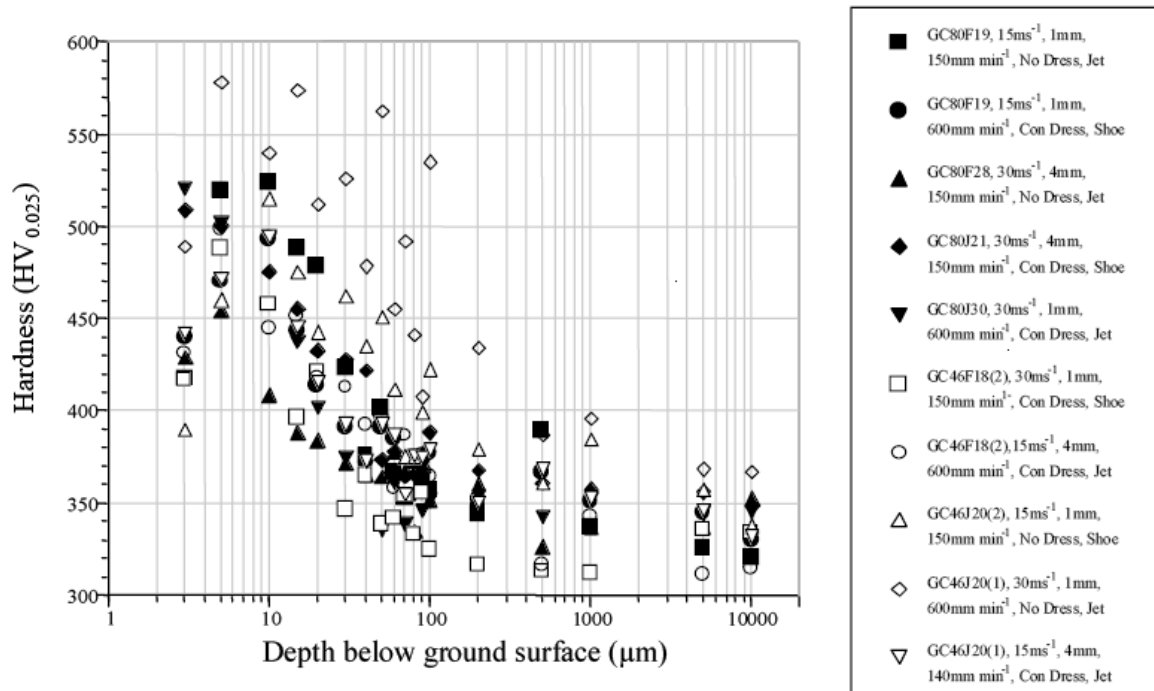


Figure 2.31: Microhardness depth profiles for conventional abrasive CFG [108]

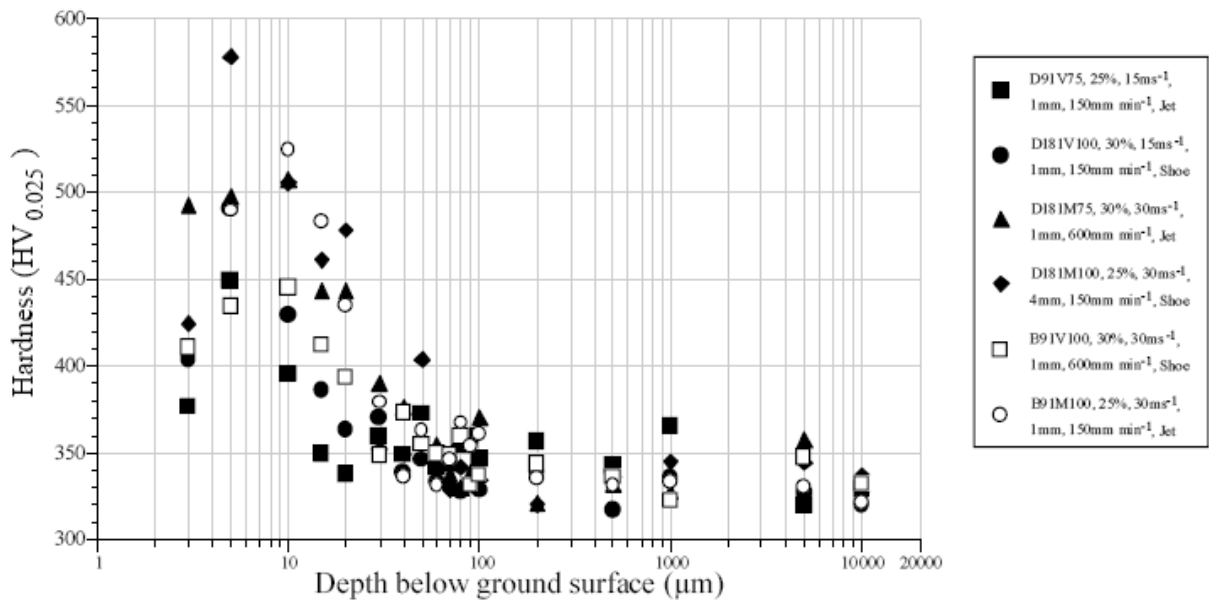


Figure 2.32: Microhardness depth profiles for superabrasive abrasive CFG [108]

Further superabrasive trials using a higher wheel speed are presented in [108]. Initially both metallic bonded diamond and CBN wheels were used however during initial testing with the diamond wheel, the high grinding forces caused breakdown of the metal matrix and loss of the grit material. Two vitrified bonded grinding wheels were substituted for the metal bonded

wheels and a Taguchi L8 orthogonal array was used for testing. The test parameters that were used are detailed in Table 2.10 [108].

Grinding wheel	Superabrasive: diamond/cBN, bond type: vitrified, grit type: 126 μ m, concentration: 75, porosity: 40%
Wheel speed	30/50m/s
Depth of cut	0.5/1.5mm
Feed rate	14/600mm/min
Dressing	No details given
Operation	Down grinding, single pass
Coolant	Water based grinding fluid at a pressure of 4/70bar

Table 2.10: Operating parameters used for creep feed grinding trials using superabrasive grinding wheels [108]

The tests only used a 4mm width of cut compared to 20-25mm width of cut in all previous trials. This reduction in width of cut resulted in a reduction in both power and normal and tangential forces, so much so that a detailed analysis was not performed. For the same reason microstructural evaluation of the machined surfaces was not undertaken [108].

A full factorial experiment was performed to establish the effect of springback passes at reduced depth of cut and dresser infeed rate. Table 2.11 lists the operating parameters used whilst Figure 2.33 shows normal and tangential forces. Normal forces increased by up to 75% when the dresser infeed rate was reduced from 1.5-0.5 μ m/rev however tangential forces increased by 25% [108, 119].

Grinding wheel	Abrasive: SiC, bond: vitrified, grit size: 80 μ m, wheel grade: J, bond structure/concentration: 30
Wheel speed	25m/s
Depth of cut	1mm
Feed rate	14/600mm/min
Dressing	Continuous using diamond wheel crush at a speed ratio of +0.7
Operation	Down grinding, single pass
Coolant	Water based grinding fluid at a pressure of 5bar through a jet nozzle
Dresser infeed rate	0.5/1.0/1.5 μ m /rev
Finishing pass depth	0/50/100 μ m

Table 2.11: Operating parameters used for creep feed grinding trails using conventional abrasive grinding wheels [108, 119]

Workpiece surface residual stress measurements, taken using the blind hole drilling technique are shown in Figure 2.34. Compressive residual stresses of up to 600MPa were measured in the transverse direction whilst tensile residual stresses of up to 700MPa were measured in the

feed direction. Both these stresses were reduced by the application of a springback pass which left a crack free surface [108, 119].

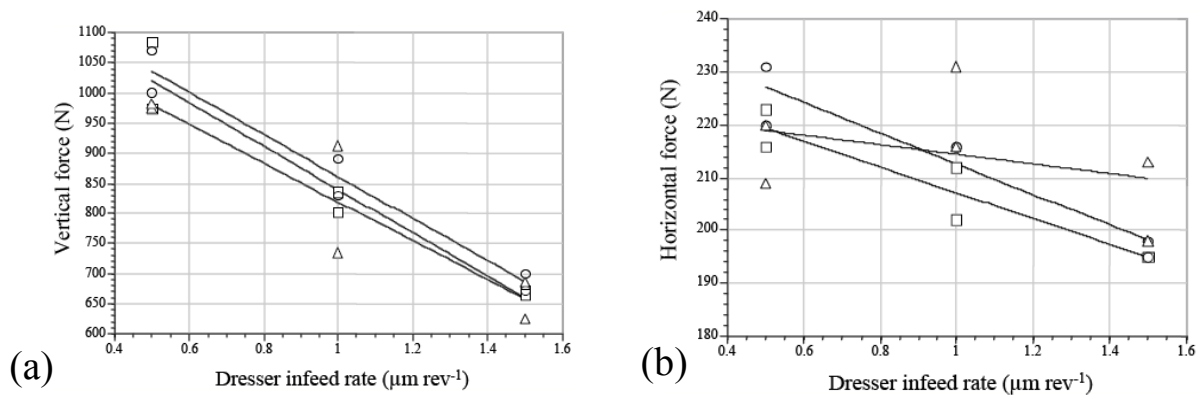


Figure 2.33: Force against dresser infeed rate when creep feed grinding using conventional abrasive wheels (a) normal, (b) tangential [108]

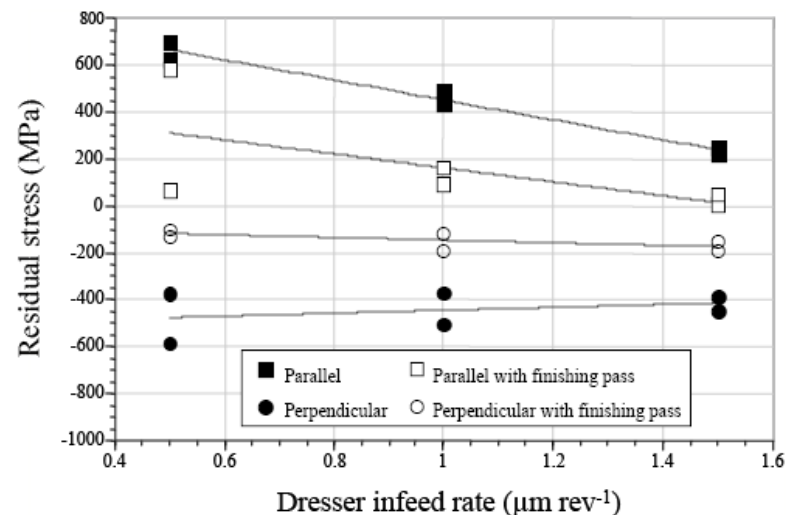


Figure 2.34: Residual stress against dresser infeed rate when creep feed grinding using conventional abrasive grinding wheels [108]

d) Speed stroke grinding

Speed stroke grinding [120, 121] utilizes vitrified bonded diamond grinding wheels, rotating at a high peripheral speed (up to 200m/s) with a low depth of cut (as low as $18\mu\text{m}$). The material removal rate is higher than conventional creep feed grinding (up to $60\text{mm}^3/\text{mm.s}$) as the machine tool used is specially designed by the addition of linear motor drives. This enables operation at very high feed rates of up to 200m/min. Operating at high wheel speeds, reduces the undeformed chip thickness which leads to reduced wear and improved surface integrity. By using a low depth of cut, the arc of contact is also kept low, which reduces the sliding length. As the feed rate is very high, the material removal rate is also high therefore the sliding length per unit volume of material removed is low. The main disadvantage is that

the undeformed chip thickness is higher at high table feeds and small depths of cut. This leads to a compromise between depth of cut and feed rate where for a given material removal rate, a value exists that minimizes wheel wear. Table 2.12 lists the operating parameters used for speed stroke grinding tests.

Grinding wheel	Abrasive: diamond, bond type: vitrified, grit size: 15 μ m, L6V600
Wheel speed	125/160/200m/s
Depth of cut	18-36 μ m, material removal rates of 30-60mm ³ /mm.s
Feed rate	50, 100, 200m/min
Dressing	Dressing overlap ratio: 4, speed ratio: +0.8, dressing infeed: 1 μ m
Operation	Down grinding
Coolant	Two component water based emulsion with an ester oil proportion of 88% of the lubricant

Table 2.12: Operating parameters used for speed stroke grinding [120, 121]

Figure 2.35 illustrates the dependency of the specific grinding energy and radial wheel wear on the table speed for different specific material removal rates and shows a critical feed rate of 120m/min where wheel wear is minimized.

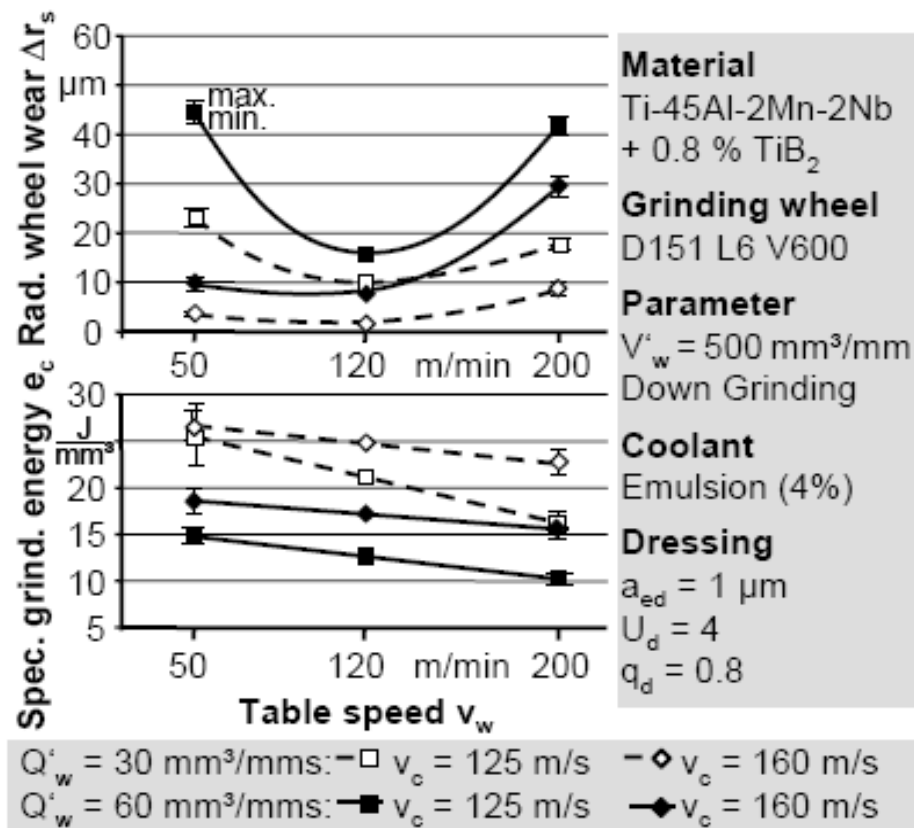


Figure 2.35: Tool wear and specific grinding energy for speed stroke grinding [120]

Figure 2.36 shows the analysis of surface samples produced at a material removal rate of $40\text{mm}^3/\text{mm.s}$. The images show no formation of cracks and deformation of the lamellae can only be observed at a feed rate of 100 and 200m/min.

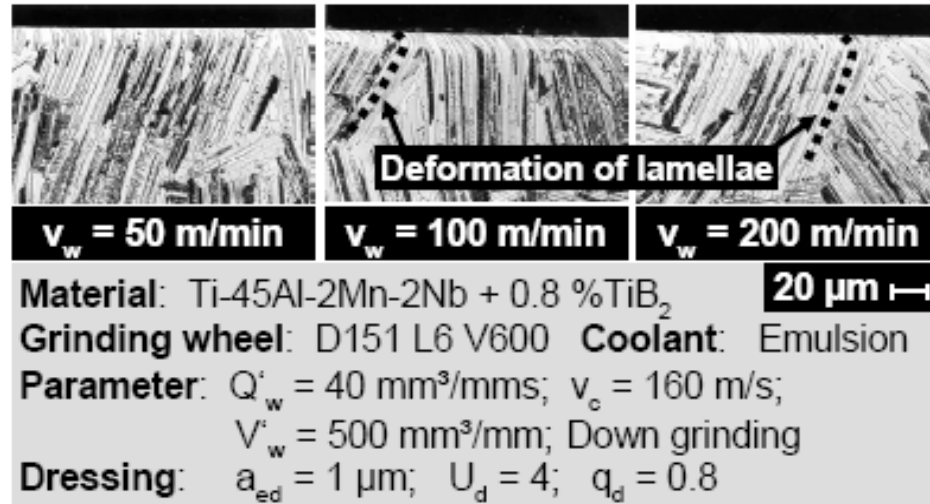


Figure 2.36: Analysis of the workpiece surface layer for speed stroke grinding [120]

Figure 2.37 shows that an increase in material removal rate to $60\text{mm}^3/\text{mm.s}$ resulted in crack formation which was caused by excessive grinding forces and stress conditions in the surface layer. Tensile residual stresses of 400MPa were measured at a table speed of 50m/min whilst increasing the feed rate to 100 and 200m/min caused compressive stresses of up to 630MPa to be measured at the workpiece surface [120].

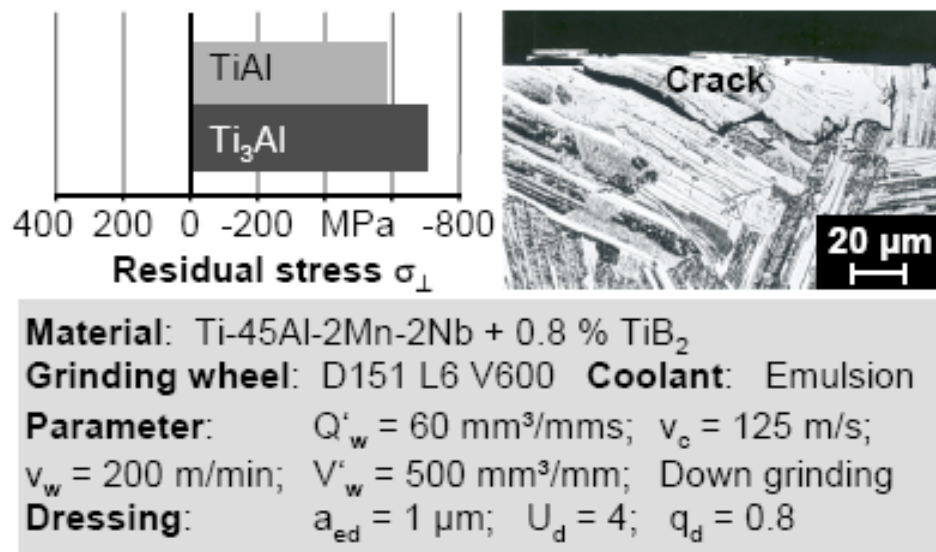


Figure 2.37: Residual stress and crack formation for speed stroke grinding [120]

2.9.4 Turning

Initial machinability investigations into a 2nd generation cast and heat-treated γ -TiAl alloy with composition Ti-48Al-2Mn-2Nb using various grades of WC tooling were performed by Zhang et al. [122-125]. Fine-grained uncoated tools (H6F-0.8 μ m grain size, 94%WC&6%Co) performed best. In general however, tool life was short with cutting times of around 17mins at a cutting speed of 20 m/min, a feed rate of 0.13mm/rev and depth of cut of 1mm. Negative rather than positive rake tool geometry improved tool life although at the expense of workpiece surface finish. Tool wear was concentrated very close to the cutting edge and consequently catastrophic failure of the tool was common. Analysis of the worn tooling showed that a built up layer of material was present on both the rake and flank faces. When high cutting speeds and feed rates were used chips were red, indicating that high temperatures were being generated and that solution wear was likely. It was however difficult to determine whether rapid failure of the tool at high feedrates and cutting speeds, was due to high flank wear or localised crater wear [123, 124]

According to Zhang et al. [122, 123] plain, mixed and whisker-reinforced aluminide based ceramics and PCBN are not suitable for the machining of titanium aluminide based intermetallics. At cutting speeds below 80m/min, alumina tools suffered significant depth of cut notch wear and although they could be used at higher cutting speeds than straight grade WC tooling, the wear rate at comparable cutting speeds was worse. At cutting speeds of above 80m/min the notch wear disappeared only to be replaced by heavy uniform flank wear resulting in a short tool life. PCBN tooling fared no better, with extremely high flank wear and a tool life of around 20s reported for a cutting speed of 100m/min, feed rate of 0.13mm/rev and depth of cut of 1mm. Microcracks (40-90 μ m long), cavities, bent lamellae and a hardened layer varying in depth from 30-60 μ m, depending on the cutting conditions used, are detailed. Measurements placed the maximum hardness of the hardened layer between 500 and 700 HV_{0.025} at a depth of 10 μ m compared to ~350HV_{0.025} for the bulk hardness [125].

Much of the published research on γ -TiAl machinability research relates to 3rd generation grain refined, fully lamellar alloys such as the Ti-45Al-2Mn-2Nb +0.8%vol. TiB₂ alloy produced by Howmet. In all cases this alloy is detailed as having been HIPed at 1260°C and 340MPa for 4 hours then subsequently heat treated at 1010°C for 50 hours to improve mechanical properties and provide a bulk hardness of 320-400HV_{0.025}. Some of the most comprehensive work on this alloy has been published by Mantle, Aspinwall and their co-

researchers [126-132]. Tool life is reported to have been low (maximum 20 min) even when using a low cutting speed of 15m/min, feed rate of 0.1mm/rev and depth of cut of 0.7mm and it is suggested that WC tooling reaches its limit of productivity at a cutting speed of 60m/min [133]. The Taylor tool life curve [126, 128] shown in Figure 2.38 suggests two distinct types of tool wear mechanism in operation: attritious wear at slower cutting speeds and solution and/or plastic deformation at higher speeds. Figure 2.38 also compares the tool life when machining Ti-45Al-2Mn-2Nb +0.8%vol. TiB₂ (45-2-2-0.8) with another γ -TiAl alloy Ti-44Al-8Nb-1B (44-8-1).

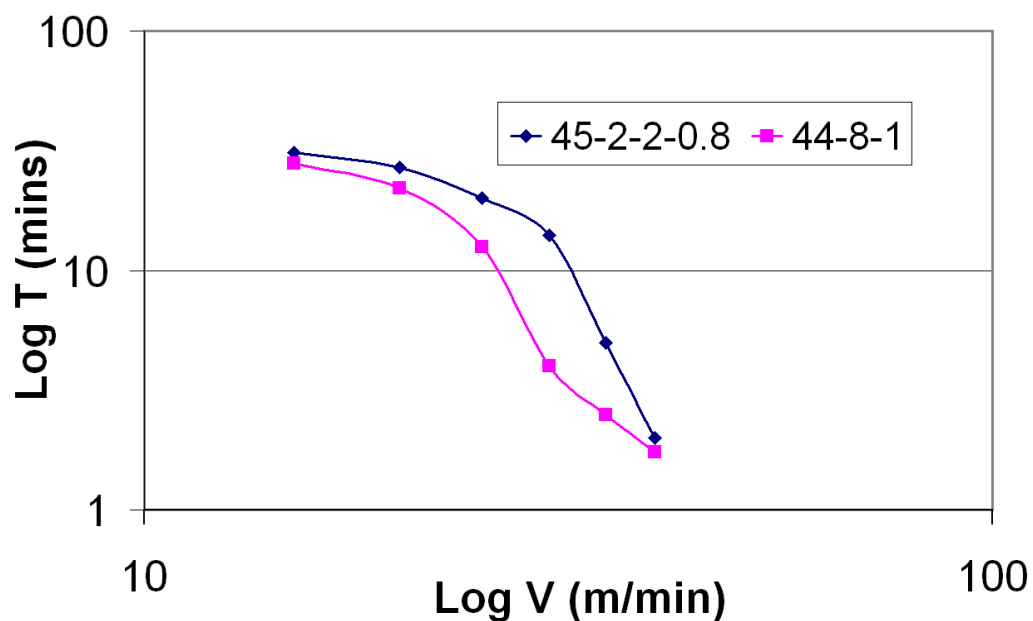


Figure 2.38: Taylor tool life curve for the turning of two different γ -TiAl alloys [126-128]

Work assessing cutting temperature using infrared pyrometry is presented by Uhlmann et al. [133] and Mantle and Aspinwall [126]. Cutting temperatures for an as-cast and extruded alloy Ti-46.8Al-1Mo-0.2Si (46.8-1-0.2) at a cutting speed of 30m/min are reported to have been 180°C and 300°C respectively [133]. Additional cutting temperature analysis is also presented using tool-workpiece and implanted thermocouple arrangements. Using the tool-workpiece thermocouple technique on Ti-45Al-2Mn-2Nb +0.8%vol. TiB₂ with a depth of cut of 0.7mm and feed rate of 0.1mm/rev, cutting temperatures at a cutting speed of 25m/min and 50m/min were reported to be ~500°C and 800°C respectively. Cutting interface temperatures were reported to be 200°C higher with worn tooling (VB_B=0.3mm) than new tooling. Cutting temperatures obtained using the implanted thermocouple technique were 450°C lower than when employing the tool workpiece thermocouple, indicating that high temperature gradients

and thermal stresses operated close to the tool edge. Temperatures when machining Ti6/4 are reported to be 100°C and 24°C lower than when cutting 45-2-2-0.8 at 30m/min and 50m/min respectively using similar cutting parameters [126].

The vast majority of researchers detail workpiece surface cracking with crack lengths of up to 40µm and depths of up to 10µm, surface drag with depths of up to 45µm and TiB₂ particulate cracking, the size and density of the cracks increasing with tool wear. In practice, it is likely that the tool life criteria ($VB_B=0.3$) used to determine tool life would have to be reduced in order to produce surfaces of acceptable integrity. Figure 2.39 shows typical cross sections of workpiece samples highlighting the cracks that in some cases appeared to extend to a full arc, resulting in total loss of part of the workpiece. Optimum parameters for producing the lowest level of cracking are reported to be a cutting speed of 25m/min, feed rate of 0.05mm/rev and depth of cut of 0.3mm. Surface roughness at these parameters was also low with a quoted value of 0.39µm Ra [134, 135].

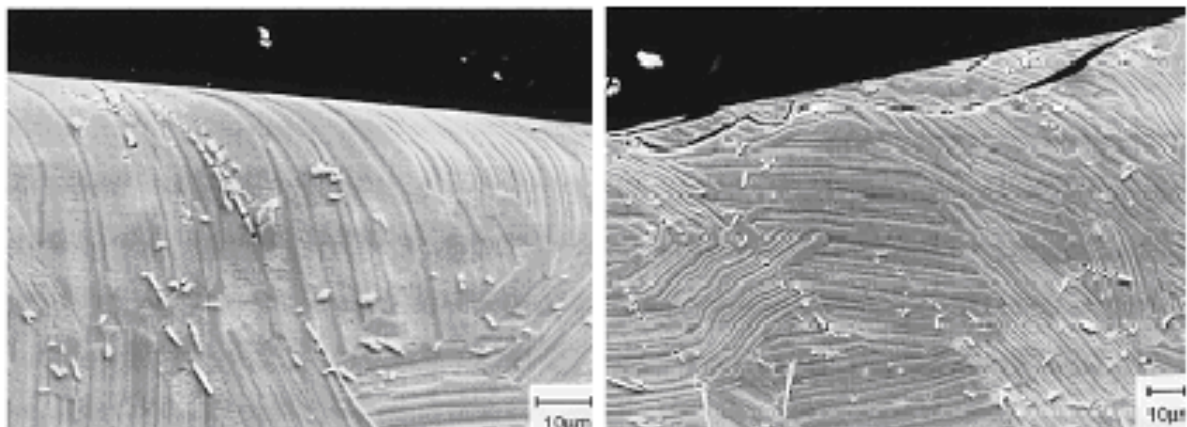


Figure 2.39: Transverse cross-sections of a turned γ -TiAl [130]

Investigations with PCBN tooling [127, 135] using higher cutting speeds (than previously reported) of up to 300m/min, found that all tool edges were subject to adhering workpiece material with wear becoming more uniform as cutting speed increased. Defect free surfaces are reported [133] on extruded 46.8-1-0.2 alloy with chips almost fully segmented, and some indication that plastic deformation and flow in the secondary shear zone had occurred. Sharman et al. [135, 136] investigated tool life and workpiece surface integrity when turning with WC, TiN/TiCN coated WC, CVD thin film diamond and PCD tooling. Cutting speeds of 25 and 40m/min, depths of cut of 0.05mm and 0.1mm, cutting environments of 65bar at 26l/min (HP) and 20bar at 6l/min (LP), with a constant feed rate of 0.05mm/rev were investigated. Tool life results, Figure 2.40 showed that, the use of the HP coolant increased

tool life by up to 300% however at both fluid pressures, increasing the depth of cut from 0.05 to 0.1mm reduced the tool life by 300%. The coated inserts performed poorly compared to the uncoated inserts because of the coatings higher chemical affinity with titanium alloys. PCD tools with a grain size of 10 μ m used with 20bar cutting fluid showed a similar performance/tool life to uncoated WC tools at 65bar. This suggested that PCD's high thermal conductivity ($\sim 540\text{Wm}^{-1}\text{K}^{-1}$) was acting to reduce the temperature at the cutting tool.

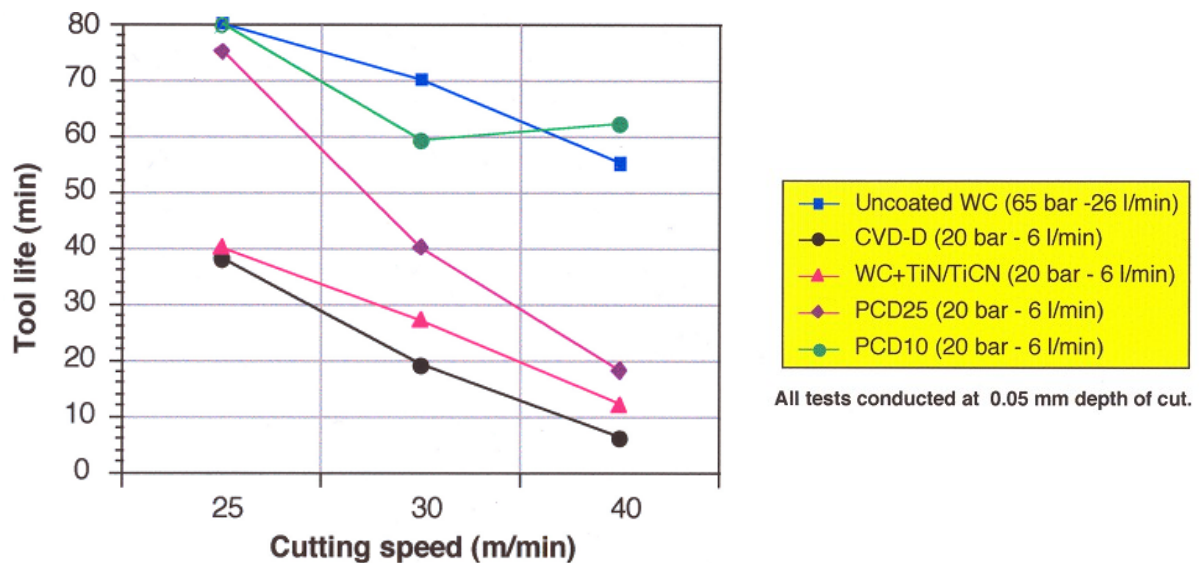


Figure 2.40: Tool life when turning Ti-45Al-2Mn-2Nb +0.8%vol. TiB₂ using various cutting tool types and fluid application methods [136]

Surface integrity evaluation [137] showed that all surfaces contained arc shaped cracks perpendicular to the feed direction. With uncoated WC tooling there was a reduction in crack size from 14 to 50 μ m and crack depth from 15-5 μ m when compared with surfaces produced by Zhang et al. [122-125] and Mantle et al. [126, 129-132, 135] using higher feed rates and depths of cut. The lowest level of cracking was observed using uncoated WC tools at a cutting speed of 40m/min and a 0.05mm depth of cut, with cutting fluid appearing not to have any effect on the level of cracking. Tension-tension fatigue tests [129] comparing samples produced using turning, electrochemical machining and electro discharge machining, showed that turned specimens benefited from highly compressive residual stresses, producing the highest run-out strength of 475MPa. Spark machined specimens with a maximum run-out strength of 357MPa suffered from the presence of tensile stresses and cracks running directly into the bulk of the material. These results are in agreement with work presented in [138, 139] where the run-out strength for turned samples was between 380 and 440MPa and Mantle and

Aspinwall [130] who determined that the endurance limit for turned samples was approximately 350MPa.

Ultrasonic assisted cutting (UAC) trials using K10 grade WC indexable inserts has been reported [135, 140]. Quoted advantages of using UAC are reduced cutting forces, which are typically only 12% of those measured when conventional turning using similar operating parameters and the replacement of fine needle chips by ~25mm long helical chips. A benefit of UAC was a reduction in the depth of lamellae deformation from 12-39 μ m for conventional turning to 5-17 μ m for UAC. In addition workpiece surface cross-sections showed the surface/subsurface contained cracks and cracked TiB₂ particles as well as an increase in workpiece microhardness. The cracks observed did not show the typical morphology seen in conventional turning and appeared to run at a shallow angle just below the machined surface. Unfortunately reported tool life was low (5-10mins) and the requirement for specialist equipment is a limiting factor [135, 140].

Laser assisted turning trials were performed to determine if improved surface integrity could be obtained by heating the workpiece to increase its ductility ahead of the cutting tool. A 1.5kW continuous wave CO₂ laser with a 1mm diameter spot size was positioned 60° ahead of the cutting tool in line with the tool nose. Cutting speeds of 20 and 40m/min and depth of cut of 0.1 and 0.2mm along with rake angle varied from +5 to -5° were used in a full factorial experimental design. Workpiece surfaces showed cracks up to 40 μ m deep which were believed to be caused by thermal stresses imparted during heating and cooling. In addition, workpiece surface roughness, Ra ranged from ~2 to 7 μ m Ra. These high values were as a result of redeposited and smeared workpiece material. Microhardness profiles were similar to those measured when using both conventional and ultrasonic assisted turning with a peak value of 610-680HK_{0.025}. In comparison to UAC, short ribbon chips (~5mm long) were produced. The chip bulk showed reduced levels of strain hardening and cracking, suggesting that the shear zone may have undergone significant heating which caused an increase in ductility of the workpiece material [135].

Turnmilling has been investigated using operating parameters similar to those detailed in Table 2.4 for ball nose end milling trials. Best results were obtained with the cutting tool positioned at 45° to the workpiece. Surfaces showed minor smearing and pullout to a depth of 2-4 μ m, lamellar deformation extending to a depth of 5-12 μ m and cracks running parallel to the workpiece surface that were 5-15 μ m long and extended to a depth of ~5 μ m. Application

of cutting fluid, reduced the level of surface deformation however as with ball nose end milling, dry cutting produced lower levels of tool wear [141].

2.9.5 Drilling, tapping and boring

Aust and Niemann [96] recommend the use of solid carbide (K10 and K20) tooling with cutting speeds in the range of 7-10m/min coupled with a feed rate of 0.033mm/rev when drilling a cast γ -TiAl. Problems concerning breakout on exit are reported, however no further integrity data is discussed. Mantle et al. [142] present similar work using 8mm solid WC drills (H10F). Here, tool life was unpredictable even at low cutting speeds and feed rates, as a result of tool chipping. Recommended operating conditions include a cutting speed of 15m/min with a feed rate of 0.05mm/rev. Figure 2.41 shows that whilst entry fracture was limited, extensive exit fracture was observed. Wienert et al. [102] drilling and tapping the alloy Ti-46Al-0.5Mo-0.8Cu-0.2Si recommend the use of uncoated straight fluted drilling tools with a 0° rake angle operating at a cutting speed of 30-50m/min and a feed rate of 0.05mm/rev. Tapping tests showed best results with a -5° rake angle, 3 or 5 rows of cutting edges, fine grain WC tools with oil used as a lubricant. No details are given of the integrity of any surface produced by either drilling or tapping [102].

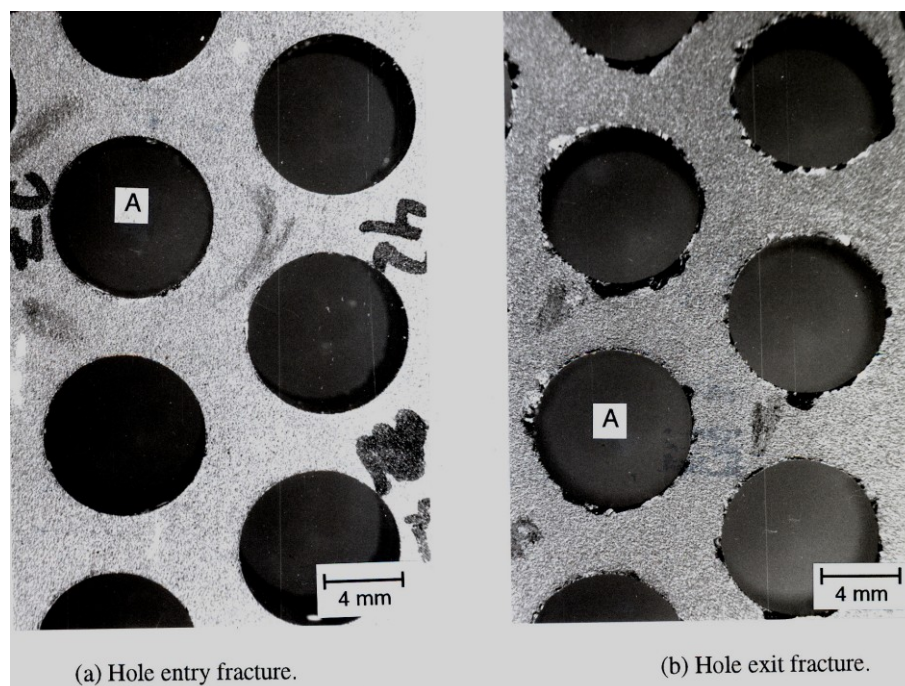


Figure 2.41: Entry and exit fracture when twist drilling [142]

Improvements in hole integrity have been obtained using ultrasonic machining [143]. Productivity was low when machining from solid, although ultrasonically counter boring pre-drilled holes dramatically reduced cutting times. Whilst some exit fracture was still evident, there was a dramatic improvement in it with only limited breakthrough. Figure 2.42 shows the ultrasonically machined holes. It is evident to see the improvements that ultrasonic machining could make to the visual quality of the hole. Surface integrity analysis showed shallow strain hardened layers (30-50 μm) with a maximum hardness of 550HK_{0.025} and tensile residual stresses of below 39MPa [143].

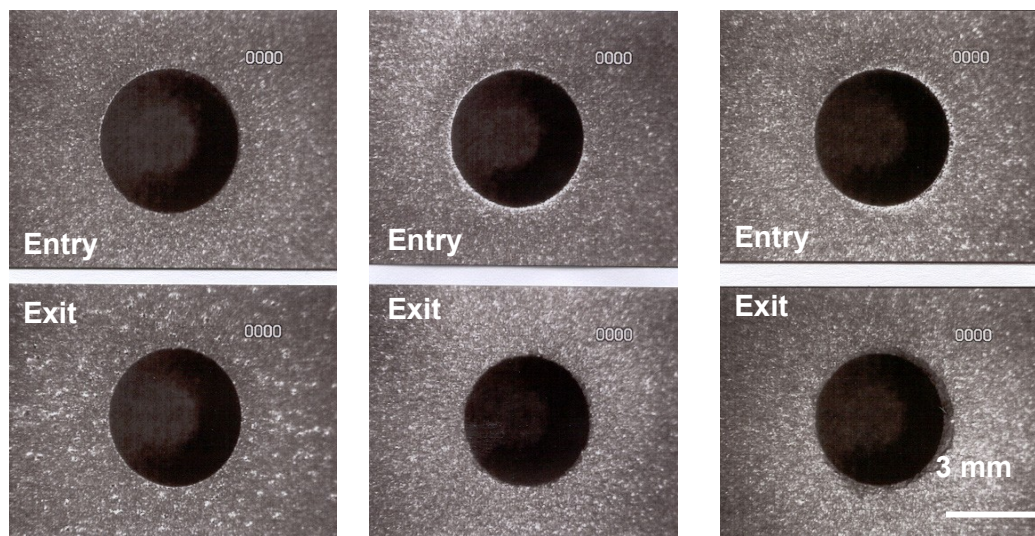


Figure 2.42: Images showing entry and exit of ultrasonically machined holes [143]

2.9.6 Non-conventional machining processes

a) Electrical discharge wire machining

Cutting speeds of 6.6mm/min with a surface roughness of $\sim\text{Ra } 3.6\mu\text{m}$ are possible when electro discharge wire machining 10mm thick samples [144]. Surface roughness was reduced to $\sim 1.7\mu\text{m Ra}$ by reducing the discharge energy (capacitance and current) however this was at the expense of cutting speed which reduced to 0.7mm/min. Achieving the desired surface integrity was difficult no matter what discharge energy was used, as recast layers with a maximum depth of 15 μm and microcracks of length and depth 37 μm and 33 μm respectively, were reported [144-146]. A sample showing the extent to which these cracks run into the workpiece surface is shown in Figure 2.43. The results were comparable to results presented by Aust and Niemann who detail cracks $\sim 0.1\text{mm}$ deep [96].

**Test 2 results.**

Cutting speed = 5.4mm/min

Surface roughness, R_a =
2.9-3.5 μm Max. recast depth = 13 μm Average recast depth = 7 μm Max. crack length = 30 μm Crack depth = 24 μm

Figure 2.43: Sample EDM'd surface showing cracks and HAZ [144]

Sarkar et al. [147] performed an investigation into single pass WEDM of the alloy Ti-45Al-2Cr-2Nb -0.3B (at.%). The focus of the work was mainly on developing an additive model to select optimum parameters so that the appropriate wire offset can be used in order to get the desired surface finish and dimensional accuracy. Unfortunately the paper details the model development process and does not include any information on the effect of the EDM process on the workpiece surface integrity.

b) Electrochemical machining

Electrochemical machining (ECM) is an attractive process for manufacturing components out of γ -TiAl alloy as it is able to machine a material irrespective of hardness at a high material removal rate giving a excellent surface finish with no surface hardening, no tensile residual stresses or micro fracture damage of the workpiece surface. Clifton et al. [148] detail results using both perchlorate and chloride electrolytes and reports conditions under which stable ECM is viable with conditions parameterised in terms of stoichmetry machining parameters generated from chronoamperometric analysis. In the case of the chloride system stable dissolution is limited by surface passivation and in the perchlorate system, choking was the cause. The authors also report that the surfaces machined were of high integrity with no evidence of microstructural defects and a hardened layer that was shown to have decreased by 46% when compared to a conventionally machined surface [148].

c) Water jet cutting

Kong and Axinte [149] established the results of abrasive water jet cutting of a γ -TiAl alloy. The main findings of their work were that using a pressure of 50kspi, an abrasive flowrate of 0.773kg/min and a standoff distance of 1mm, a material removal rate of 220mm³/min could be obtained. These parameters also gave the best kerf in terms of geometrical accuracy and

surface quality. The instant oxidation of Ti at the workpiece surface level caused a thermal related phenomenon, bubble like TiO_2 –based spots. However the authors state that no white layer or cracks were observed indicating that this exothermic reaction caused no significant damage to the workpiece surface. Side embedded particles were observed in the cut surface. A cleaning method was developed involving sweeping and tilting the nozzle head with stepover to eliminate these particles. The ability to produce surfaces that are crack free using abrasive waterjet cutting could lead to this becoming more prevalent as a manufacturing process for components made out of γ -TiAl alloys. The main concern is that abrasive water jet cutting tends to be expensive process as capital equipment and maintenance costs are high. In addition, this process has generally been used for applications such as cutting plate and has limited success when machining jet engine blades, a major application for γ -TiAl alloys.

2.10 Machinability of burn resistant titanium alloys

Few publications exist detailing the machinability of the BuRTi alloy, vT curves given in [6] suggest it falls between standard titanium alloys such as Ti-6Al-4V and γ -TiAl alloys. An initial assessment of machinability of BuRTi when milling is presented in [150, 151]. Trials mainly involved $\phi 8\text{mm}$ diameter, 4 flute solid coated (Al, Ti) N micrograin tungsten carbide (WC) ball nose end mills although limited trials were also performed with single edge polycrystalline diamond ball nose end mills. Operating parameters were a cutting speed of 100-150m/min, feed rate of 0.05 to 0.2mm/tooth using 25-70bar (5-17l/min) coolant. Depth of cut and stepover were kept constant with values of 0.5 and 2mm respectively. A workpiece tilt angle of 45° was used. Figure 2.44 shows a graph of maximum flank wear against length cut. The coated WC tools significantly outperformed the PCD tools due to significant notching of the PCD tools.

Creep feed grinding trials also presented in [150] established G-ratios ranging from 0.16 to 1.53 for conventional abrasive (SiC) grinding wheels. The presence of numerous brittle titanium carbides caused significant damage to the surface including material pullout, workpiece smearing, crater formation after carbide pullout to a depth up to $8\mu\text{m}$ from the workpiece surface, fractured carbides and debonding, see Figure 2.45. Despite such problems the microstructure and microhardness of the workpiece remained largely unaffected, with no appreciable microstructural deformation or change in microhardness from the surface into the bulk with compressive residual stress regimes produced by both processes at the conditions specified.

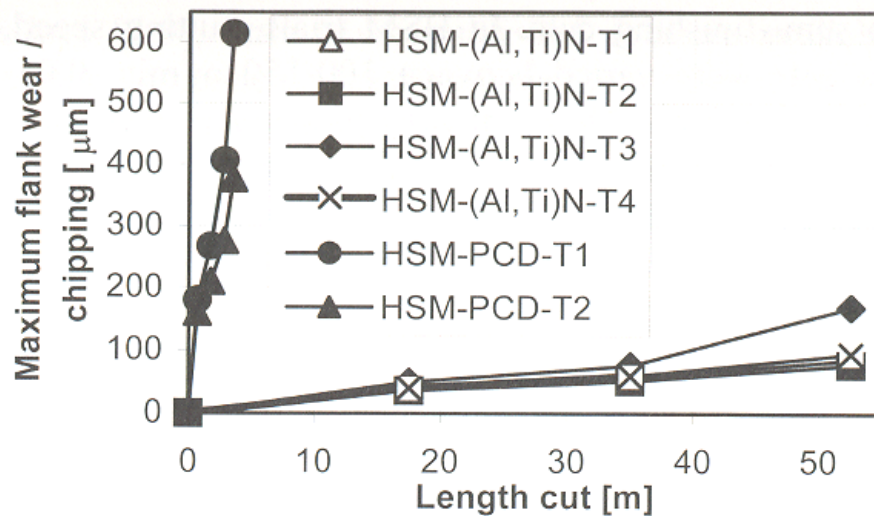


Figure 2.44: Tool wear in high speed ball nose end milling trials [150]

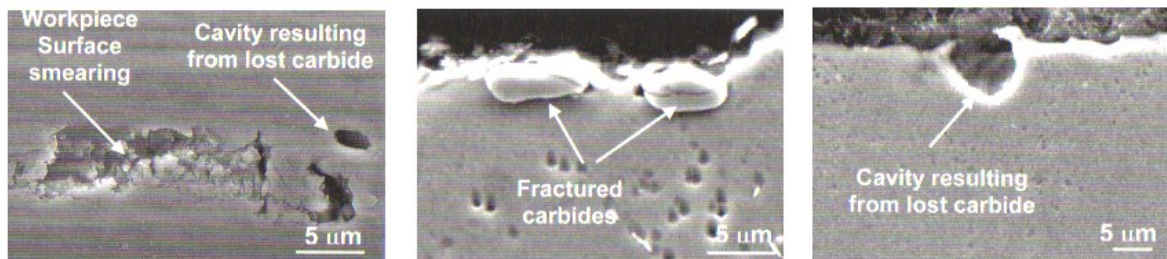


Figure 2.45: SEM images of workpiece surface damage and cross sections after HSM [150]

2.11 Machinability of orthorhombic TiAl alloys

Machinability assessment when grinding, milling, turning and drilling the orthorhombic TiAl alloy, Ti-23Al-25Nb-0.35Si (at %) is presented in [152] and [153]. In general, the tool/wheel life was lower than for γ -TiAl alloys however improved workpiece surface integrity could be achieved. Results of surface grinding trials established that G-ratio for the TiAl alloy, Ti-48Al-2Mn-2Nb was approximately 5 times higher than for the orthorhombic TiAl alloy. In contrast, the conventional titanium alloy, Ti-6Al-4V showed lower performance with a G-ratio of 1-2 when compared to the orthorhombic TiAl alloy's value of 5-8. Cross-sectional micrographs of the workpiece surface of the orthorhombic TiAl alloys, showed no significant cracking or microstructural deformation however there was evidence of a discontinuous, non-uniform white layer with a thickness of 2-3 μ m. The depth of the white layer increased as wheel wear increased. Microhardness results the presence of a shallow hardened layer 50 μ m deep, with a maximum hardness only 50HK_{0.025} higher than bulk hardness. This suggested a much lower level of strain hardening occurred when machining orthorhombic TiAl alloy than

when grinding γ -TiAl alloy, Ti-45Al-2Mn-2Nb +0.8vol. TiB₂ (Ti-45-2-2-0.8) where the surface hardness was typically 140HK_{0.025} higher than the bulk value [152].

As with γ -TiAl alloys, tool life when milling the orthorhombic alloy was low with a steep gradient to the Taylor tool life curve indicating that the choice of cutting speed is vital to prolong tool life. Indeed, at higher cutting speeds (120-140m/min) tool life was extremely low (<1minute) due to excessive flank wear and chipping. Orthorhombic TiAl alloy also produced a shorter tool life than the γ -TiAl alloy, Ti-45Al-2Mn-2Nb-0.8% vol. TiB₂, see Figure 2.46.

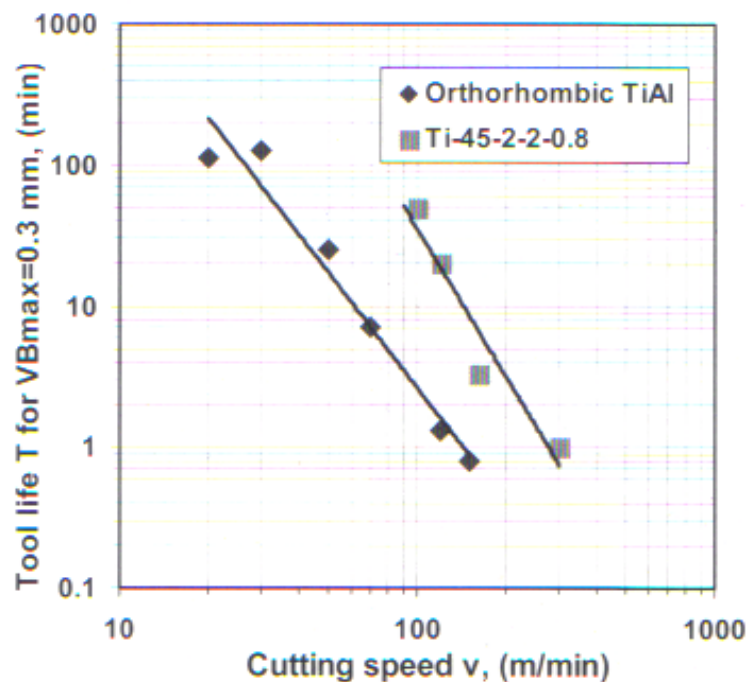


Figure 2.46: v-T curves when high speed end milling orthorhombic TiAl and Ti-45Al-2Mn-2Nb +0.8%vol. TiB₂ [152]

As with grinding, workpiece surface cross-sections taken using cutting speeds of 20-70m/min showed no cracking or microstructural deformation of the subsurface and a minimal strain hardened region as indicated by a microhardness profile similar to the one reported for grinding. In contrast to γ -TiAl alloys, no breakout occurred on exit of the cutter from the workpiece [152].

For turning orthorhombic TiAl alloy, a K25 cutting tool is recommended with a maximum feasible cutting speed of 20m/min. Even at this low speed, tool life was extremely low with a reported tool life ($VB_{Bmax} = 0.3\text{mm}$) of ~7minutes when using a depth of cut of 0.7mm, a feed rate of 0.1mm/rev and Houghton Hocut 3280 cutting fluid supplied at 6l/min and 20bar. Tool life when drilling orthorhombic TiAl, mirrored that of turning, with <10

holes produced at cutting speed of 10m/min using the same operating parameters as turning. As with milling, minimal entry/exit workpiece damage was observed with limited burr formation. In addition, helical chips were produced which could present problems with flute packing. For both drilling and turning, cross-sectional microstructure images showed no significant cracking however, there was evidence of a cutting speed and tool wear dependant intermittent discontinuous white layer with a depth of up to 20 μ m. Reported strain hardening is consistent with levels reported for grinding and milling, with only a minimal increase in workpiece surface hardness and a much lower magnitude and depth than those reported for γ -TiAl alloys [153].

2.12 Experimental design

The purpose of experimentation is to understand how to reduce and control variation of a product or process. This means that decisions must be made concerning the parameters affecting the performance of the product or process. Ross [154] describes an approach based on the use of Taguchi orthogonal arrays to conduct small, highly fractional experiments up to larger, full factorial experiments. He suggests that an experiment is the simultaneous evaluation of two or more factors chosen for their ability to affect the resultant average or variability of a particular product or process characteristic. To accomplish this in an effective and statistically proper fashion, the levels of the factors are varied in a strategic manner. The complete set of results is analysed to determine the influential factors and preferred levels and whether an increase or decrease in the levels will lead to further improvement. Experimental design is described as an iterative process, where the first round of experimentation, often called a screening experiment, finds the important and influential factors which then lead to further rounds of experimentation. In each of these rounds, there are three main phases, involving the planning, conducting the tests and analysis [154].

The planning phase identifies and sets the factors and levels and is therefore the most important stage of experimentation. The correct selection of factors and levels is non-statistical in nature and more dependant upon product or process expertise. It is noted that the determination of significant factors and their relative strengths is based on the levels chosen for these factors. Any factor would tend to look more important if the levels chosen for it were further apart [154].

The second most important phase, concerns the collection of results. The experimental analysis is normally the easiest phase and if a good planning process is followed and the experiment conducted well, the analysis is more likely to give an indication of which

factors and levels lead to product or process improvement (positive information). The analysis phase is the least important in terms of whether the experiment will yield good results however it is the most statistical in nature of the three phases. The three phases of experimentation are fundamentally identical irrespective of the design employed. The major steps to conduct an effective designed experiment are detailed below [154]:

1. State the problem or area of concern.
2. State the objectives of the experiment.
3. Select the quality characteristics and measurement systems.
4. Select the factors that may influence the selected quality characteristics.
5. Identify noise control and noise factors.
6. Select levels for the factors.
7. Select the appropriate orthogonal array
8. Select interactions that may influence the selected quality characteristics.
9. Assign factors to orthogonal arrays and locate interactions.
10. Conduct tests described by trials in orthogonal array.
11. Analyse and interpret results of the experimental trials.
12. Conduct confirmation experiment.

A full factorial experimental design is generally only acceptable when only a few factors are to be investigated and not when a large number of factors are involved. If a full factorial design is to be used then for say n factors at 2 levels, a 2^n test must be conducted not counting replications. This can lead to an inefficient experimental design as a typical engineering application may involve many factors. Fractional factorial experiments have been designed to be more efficient as they use only a portion of the total possible combinations to estimate the main factor effects and in some cases, but not all, interactions. This type of experimental design is much more appealing to the experimenter from a time and cost standpoint. Taguchi developed a family of Fractional Factorial Orthogonal Arrays that can be utilised. This is a relatively straightforward technique that can be applied to many engineering situations. Emphasis is placed on a mean performance characteristic value close to the target value rather than a value within certain specification limits. Experimentation using the orthogonal arrays can be used to quickly narrow down the scope of a research project. Experimental design using this technique allows for the analysis of many different parameters without a high level of experimentation having to be performed. For example, a process with 7 variables, each at 2 levels, would require 128 experiments to test all variables not including replications. Using

Taguchi's orthogonal arrays, only 8 experiments are necessary, or 6.25% of the total number of tests. In this way, it allows for the identification of key parameters that have the most effect on the performance characteristic value so that further experimentation on these parameters can be performed and the parameters that have little effect can be ignored [155, 156].

The main limitation of the Taguchi method is that the results obtained are only relative and do not exactly indicate which parameter has the largest effect on the performance characteristic value. Another limitation is that they have difficulty in accounting for interactions between parameters. Since orthogonal arrays do not test all variable combinations, this method should not be used when all relationships between all variables are needed. Taguchi methods are typically applied most effectively at the early stages of process development [155, 156].

The selection of an orthogonal array depends on the number of factors and interactions of interest, the number of levels for the factors and the desired experimental resolution or cost limitations. It is recommended that the screening experiment is performed using the smallest orthogonal array that will accommodate the number of factors under evaluation. The resolution of this initial round of experimentation is therefore low however significant factors should be identified that can then be evaluated further using a higher resolution experiment such as a larger fractional or a fully factorial array. In an experiment, pairs of factors may interact with one another to provide a synergistic effect on a quality characteristic being studied [154].

Analysis of Variance (ANOVA) is the most objective statistical method used to interpret experimental data and make necessary decisions, other methods such as observation method, ranking method, column effect method and plotting method should be considered for supporting and reinforcing techniques. ANOVA is a statistically based, objective decision making tool that detects differences in average performance of a group of items tested. In its simplest form, it breaks total variation down into accountable sources, the variation of the average of all the data points relative to zero and the variation of the individual data point around the average [154]. A confirmation experiment is the final step in the experimental process. Its purpose is to validate the conclusions drawn during the analysis phase and it is performed by conducting a test using a specific combination of the factors and levels previously evaluated [154].

3. EXPERIMENTAL WORK

3.1 Workpiece materials

The machinability of two different gamma titanium aluminide intermetallic (γ -TiAl) alloys was investigated. The first had the nominal composition Ti-45Al-8Nb-0.2C (%at.) and was produced as a cast cylindrical billet $\phi 225\text{mm} \times 275\text{mm}$ high, which was Hot Isostatically Pressed (HIP'ed) at 1260°C and 150MPa for 4 hours, resulting in a bulk hardness of $\sim 365\text{HV}_{30}$. Attempts were made to thermomechanically process the alloy to produce a convoluted microstructure similar to that detailed by Saage et al. [157] however after processing, analysis of the workpiece microstructure showed that the alloy had not transformed and that there had been no reduction in grain size, see Figure 3.1. Doubts were raised over the exact elemental composition of the ingot therefore testing was performed by IncoTest to provide clarification. The results identified a reduction in aluminium content of 0.7 % (vol.) resulting in a value of 44.3% (vol.) when compared with the nominal level of 45% (vol.) and 0.136% (vol.) oxygen. Concerns were raised concerning the findings [158] and it was felt that either the low aluminium or the high oxygen content could have been responsible for the lack of microstructural transformation. A decision was made to undertake machinability studies with the alloy despite the compromised microstructure, due to the high financial cost of procuring new workpiece material. Additionally it was suggested that the difference in mechanical properties between an alloy with the correct grain size and the alloy as supplied would only be $\sim 5\%$ [158]. For the purposes of this report the alloy is referred to by its nominal composition, Ti-45Al-8Nb-0.2C.

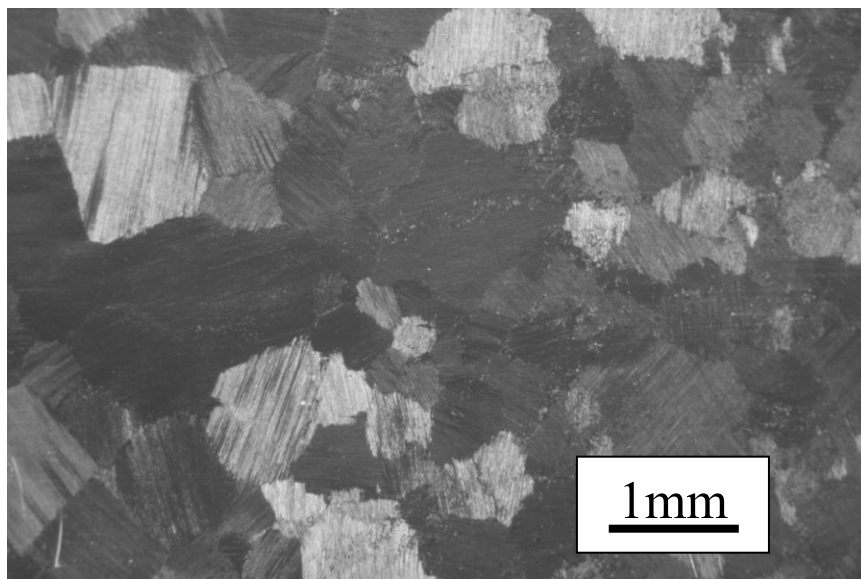


Figure 3.1: Ti-45Al-8Nb-0.2C workpiece microstructure

The second γ -TiAl alloy used had the composition Ti-45Al-2Mn-2Nb +0.8% vol. TiB₂ XDTM (Referred to as Ti-45Al-2Mn-2Nb +0.8%vol. TiB₂). The material was investment cast, HIP'ed at 1260°C and 170MPa for 4hours followed by heat treatment at 1010°C for 50h resulting in a bulk hardness of $\sim 365\text{HV}_{30}$. This material was remaining from EPSRC IMI project GR/K66970 and GR/L33993 (1.2.96 to 31.1.00). Only a single block, $\sim 80\text{mm} \times 80\text{mm} \times 20\text{mm}$ was available which meant that only limited benchmarking tests could be completed. This alloy had a lamellar microstructure with a grain size of ~ 50 to $100\mu\text{m}$, see Figure 3.2.

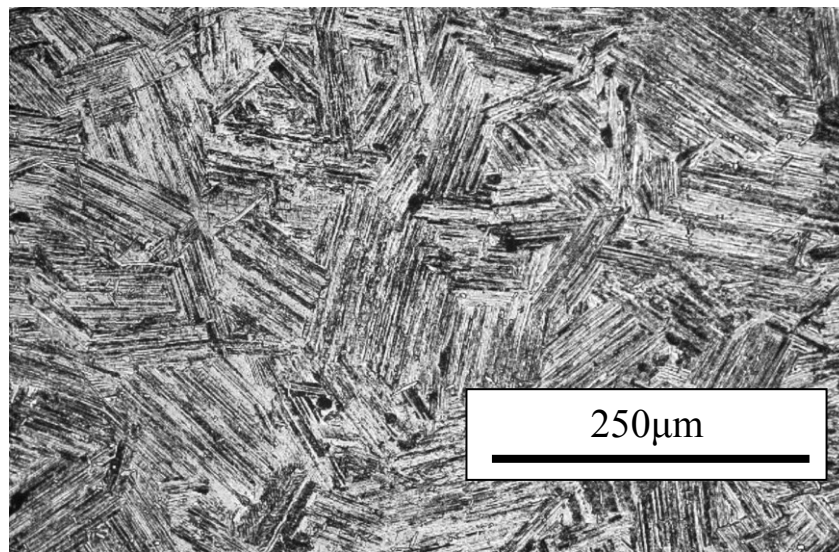


Figure 3.2: Ti-45Al-2Mn-2Nb +0.8% vol. TiB₂ workpiece microstructure

The burn resistant titanium (BuRTi) workpiece material was provided in the shape of compressor blades produced via open die forging extruded ingots, see Figure 3.3 (a). The alloy, which was a β phase alloy, composition Ti-25V-15Cr-2Al-0.2C (%wt), was subjected to a heat treatment cycle of 600°C for 2 hours. Prior to the start of tests, the root of the blade samples were initially prepared via a combination of face milling, side milling and electrical discharge wire machining (EDWM) to produce a rectangular section suitable for milling and grinding trials, see Figure 3.3 (b). Microstructural analysis showed that the typical grain size was $30\text{--}50\mu\text{m}$ with randomly distributed carbide particles having a length of up to $15\mu\text{m}$, see Figure 3.3 (c). Bulk hardness was measured at $\sim 330\text{HV}_{30}$.

The standard α/β titanium alloy, Ti-6Al-4V was used to provide limited comparative benchmarking data. The material was supplied in the annealed condition and had a bulk hardness of $\sim 350\text{HV}_{30}$. Blocks typically, $80\text{mm} \times 40\text{mm} \times 20\text{mm}$ that had been electrical discharge wire machined from a larger ingot were used for grinding trials.

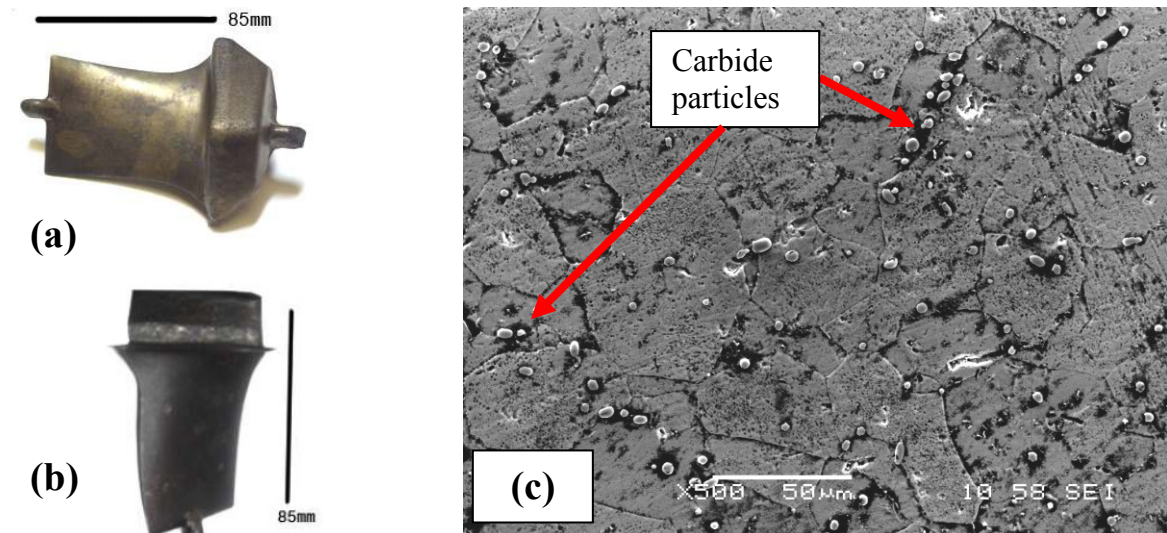


Figure 3.3: (a) BuRTi blade in the received state, (b) BuRTi blade machined to create section for tests and (c) bulk microstructure

3.2 Machine tools, fixturing and equipment

3.2.1 Phase 1, high speed ball nose end milling

Phase 1, high speed ball nose end milling tests were conducted on either a Matsuura FX5 vertical machining centre or a Matsuura LX1 vertical machining centre. Figure 3.4 shows images of each machine tool. Cutting tools were held in MST Mizoguchi HSK shrink fit tool holders for the Matsuura LX1 and BT40-CT10-90 tool holders with MST collet holders (CTH10 – $\varnothing 2.6$ -10mm) and associated collets for the Matsuura FX5.

(a) Matsuura LX1 machining centre



Spindle speed: 200-60,000rpm

Maximum spindle power: 5kW

Maximum cutting feed rate: 10m/min

(b) Matsuura FX5 machining centre



Spindle speed: 200-20,000rpm

Maximum spindle power: 15kW

Maximum cutting feed rate: 4m/min

Figure 3.4: Machining centres used for Phase 1, high speed ball nose end milling tests

Figure 3.5 shows the experimental setup that was used for all Phase 1, high speed ball nose end milling trials. For those involving Ti-45Al-8Nb-0.2C, three blocks were prepared including one with dimensions 220mm x 80mm x 60mm which was used for the majority of workpiece material removal. A second block 100mm x 80mm x 20mm was mounted on a Kistler platform dynamometer for force measurements. The third block had dimensions of 200mm x 80mm x 5mm and was used for workpiece surface integrity evaluation once the tool had reached the selected wear criterion. For trials involving Ti-45Al-2Mn-2Nb +0.8%vol. TiB₂, the 80mm x 80mm x 20mm workpiece was electrical discharge wire machined into two smaller blocks with one being used for the majority of workpiece material removal and the second being used for workpiece surface integrity evaluation. The large vice shown in Figure 3.5 (a) was used to hold both Ti-45Al-2Mn-2Nb +0.8%vol. TiB₂ workpieces. A bespoke fixture was produced for holding the BuRTi blades by the aerofoil section, see Figure 3.6.

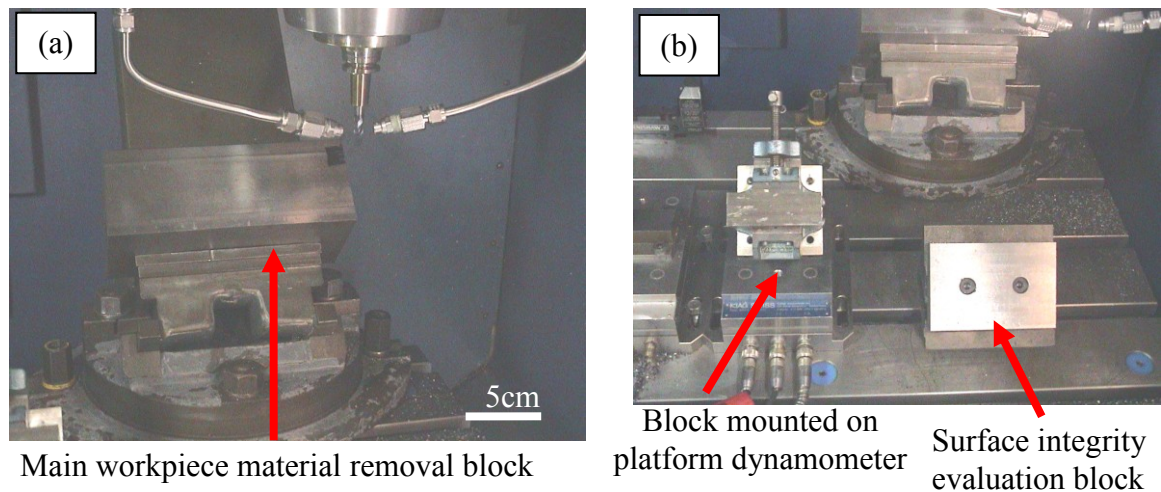


Figure 3.5: γ -TiAl workpiece, nozzle and cutting tool holder setup

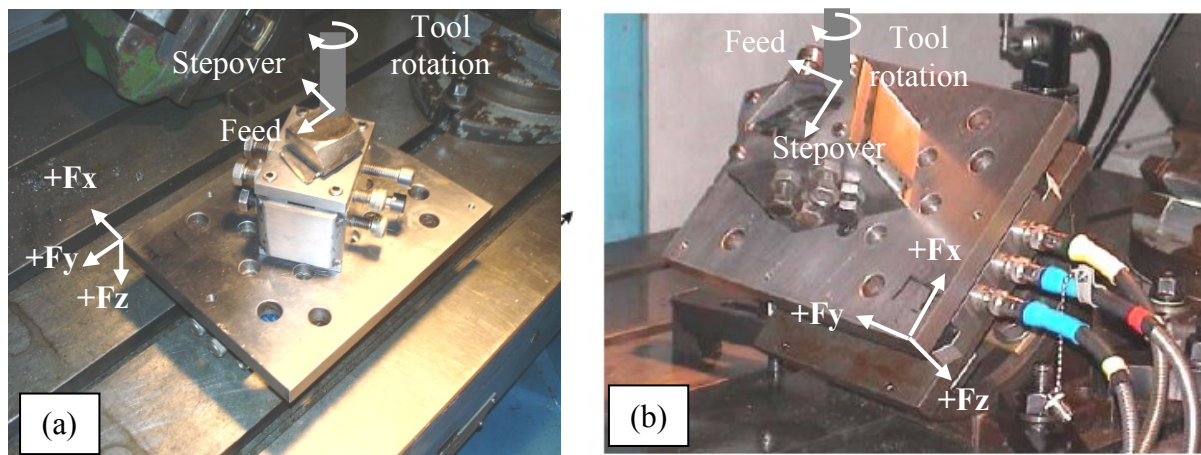


Figure 3.6: BuRTi workpiece and fixture at an angle of (a) 0°, (b) 45°

Houghton Vaughan Hocut 3380 soluble oil with a concentration of 5% cutting fluid was used in all tests where cutting fluid was required. The fluid was supplied at high pressure by a Hydrajel G15 pump which had a maximum supply pressure of 70bar with a flowrate of 26l/min through twin nozzles. The positioning of these twin nozzles is shown in Figure 3.5. For tests with dry cutting, compressed air was used to remove swarf and prevent secondary cutting.

3.2.2 Phase 2, creep feed grinding

All Phase 2, creep feed grinding tests were carried out on a Bridgeport FGC1000 flexible grinding centre. It had maximum spindle speed of 6000rpm and a maximum continuous power rating of 28kW. Figure 3.7 shows the Bridgeport FGC1000 along with the power/torque curve for its spindle. All grinding wheels were held using MST BT40 FMSB32-60 tool holders with associated blotters and flanges.

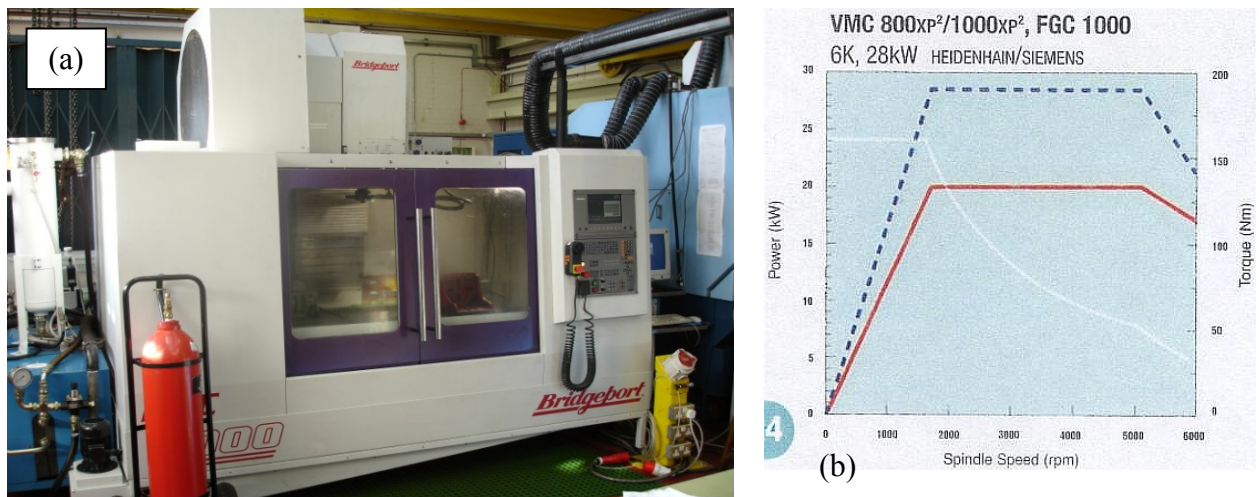


Figure 3.7: (a) Bridgeport FGC1000, (b) spindle power/torque curve

Rectangular workpieces with approximate dimensions 80mm x 80mm x 20mm were prepared by electrical discharge wire machining for all γ -TiAl creep feed grinding tests. The workpiece was drilled with four holes so that it could be mounted directly onto the Kistler platform dynamometer, Figure 3.8 (a) illustrates the arrangement used. For all creep feed grinding tests involving BuRTi, the bespoke fixture, see Figure 3.6, was used to hold the BuRTi blade by the aerofoil section, see Figure 3.8 (b).

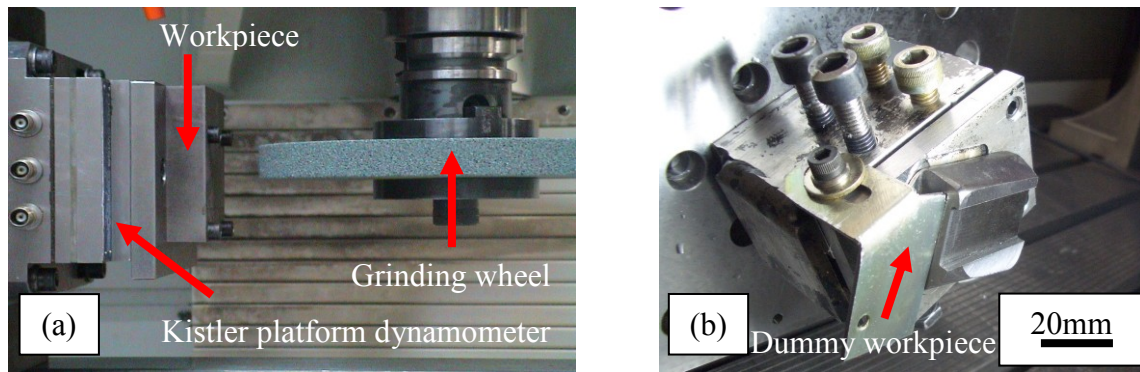


Figure 3.8: Grinding arrangements (a) γ -TiAl and Ti-6Al-4V (b) BuRTi workpieces

Two Hydra jet G25 pumping systems provided grinding fluid for both the cleaning and cooling jets with free jet nozzles, which had a rectangular cross section and a slot height of 20mm used to supply the fluid. The design of these nozzles was as described by Webster and his co-researchers [61, 77]. Four different nozzle widths, 0.5, 1.0, 1.5 and 2.0mm were supplied by St-Gobain Abrasives, see Figure 3.9 (a)

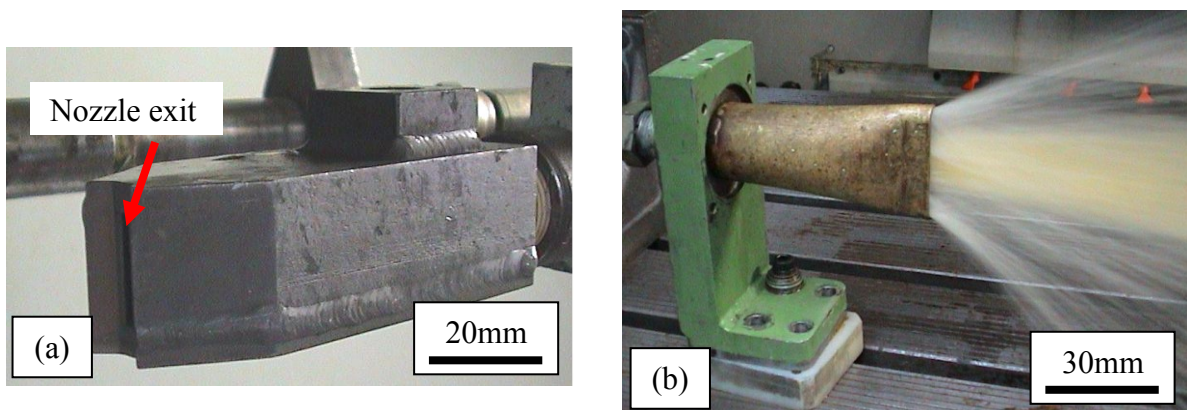


Figure 3.9: Nozzles (a) Free jet nozzle, (b) low pressure spark suppression nozzle

When tests involved the use of neat oil as the grinding fluid, the large amount of sparks produced required the addition of a fire suppression system, consisting of a manually operated CO₂ cylinder with a nozzle mounted near the grinding wheel. A low pressure (<1bar), high flowrate (200l/min) jet was used to suppress the sparks produced, see Figure 3.9 (b). For conventional abrasives, the grinding fluid used was a water based synthetic product, Trim C270 having a concentration of 7-10%, whilst for superabrasive wheels, in addition to Trim C270, a neat oil, Sintogrind IN, Poly Alpha Olefin supplied by Oel-Held was used.

For all grinding tests, dressing of the grinding wheels was carried out using an intermittent hydraulic diamond roller dresser mounted on the bed of the machine tool. A plain profile, hand set sintered diamond roll (ϕ 105mm) with a diamond size of \sim 800 μ m and spacing

of $\sim 1.5\text{mm}$ was used for the majority of tests. Figure 3.10 (a) shows the dresser arrangement with a close up of the diamond spacing shown in Figure 3.10 (b). Figure 3.10 (c) shows the lobe type profile diamond roller dresser that was used for trials with a profiled workpiece.

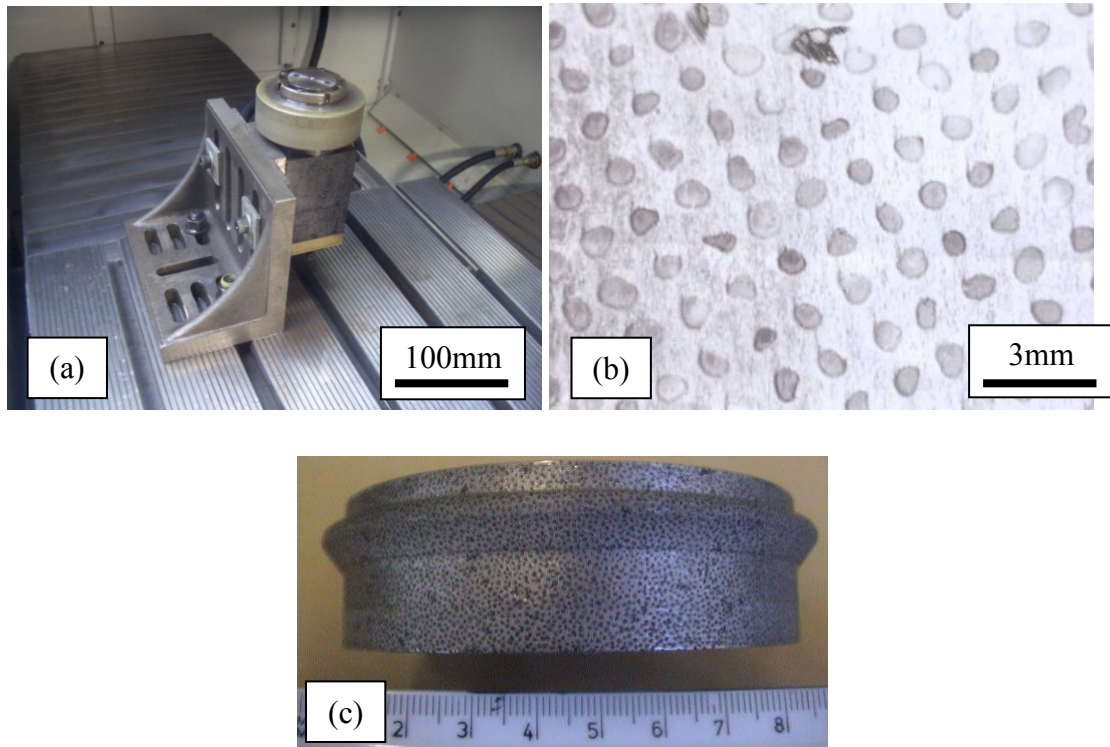


Figure 3.10: (a) Hydraulic diamond roller dresser and plain profile hand set sintered diamond roll, (b) hand set sintered diamond roll, (c) “lobe” type diamond roller dresser

3.3 Cutting tools

All cutting tools used were 4 flute, 8mm diameter, tungsten carbide (WC) coated ball nose end mills. Two different cutting tools were supplied by Iscar Tools Ltd and were designated IC900 and IC903. They were identical in terms of tool geometry and coating however, the IC903 used a finer grade carbide substrate material.

- Iscar IC900 - A tough sub-micron ($\sim 0.8\mu\text{m}$) PVD AlTiN coated grade. The tool was suitable for use with a medium to high cutting speed and was designed for machining of heat resistant alloys, austenitic stainless steel, hard alloys and carbon steel at interrupted cuts. It had an ISO range –P/M/K: (P15-P40) [159]. Figure 3.11 shows a micrograph of the carbide substrate. The tool had a single layer coating with a thickness of $\sim 2\mu\text{m}$.
- Iscar IC903 - Ultra-fine sub-micron ($0.3\text{-}0.5\mu\text{m}$) carbide grain with 12% cobalt, AlTiN PVD coated. The coating and geometry were identical to the Iscar IC900 tool with only the substrate altered. The tool had high wear resistance and toughness and was suitable for

high speed with a medium feed rate. It is intended for use on hardened steel (up to 62HRC), titanium, nickel-based alloys and stainless steel. It had an ISO range –P/M/K: (P05-P15) [159].

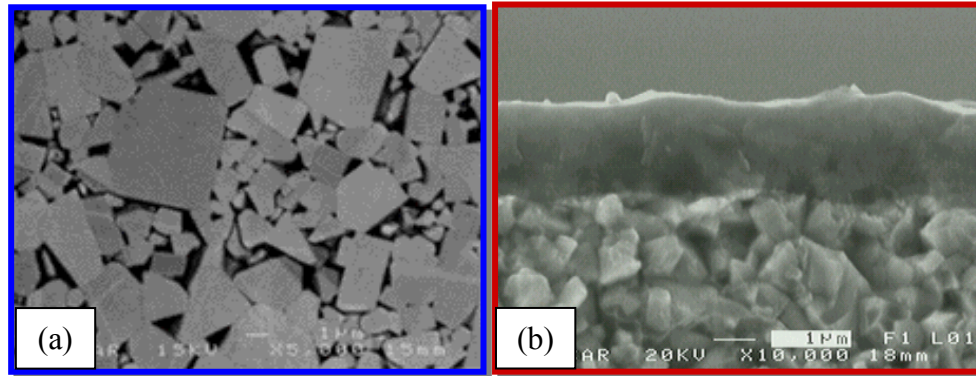


Figure 3.11: IC900 cutting tool (a) micrograph of substrate, (b) cross-section [159]

An AlTiN coating was recommended by Iscar Tools Ltd for the milling of titanium alloys which was in agreement with several authors [160, 161] when compared to other cutting tool coatings. Although uncoated WC carbide tools are generally recommended for the milling of titanium alloys [29], it has been shown that TiN and TiCN coatings improved tool life when end milling γ -TiAl. Ceramic, PCD and CBN tools were dismissed as Wienart [102] suggests performance compares poorly with WC tools.

3.4 Creep feed grinding wheels

All grinding wheels were supplied by Saint-Gobain Abrasives. Wheels A, B and C contained SiC grit and had a nominal diameter of 220mm with a wheel width of 20mm. Wheels D, E and F containing superabrasive grits had a nominal diameter of 175mm with a wheel width of 20mm. Table 3.1 details the specifications of all grinding wheels used. Initially Wheel A was supplied for testing. This wheel had a fairly high percentage of grit material and bond material with a low level of porosity. It was not a typical creep feed grinding wheel which are detailed as mostly being softer grade with an open structure to keep temperatures low and improve surface finish [69]. Wheels B and C were however typical creep feed grinding wheels with a more open wheel structure and less grit material.

For superabrasive trials, initially Wheels D and E were supplied. Lower porosity was originally planned for Wheel D with diamond grit, however, this could not be achieved with the aspect ratio of the test wheels (wheel width to abrasive layer height). The increase in porosity was also expected to help with dressing. The higher grit content of Wheel D with

CBN grit was designed to compensate for its lower hardness and wear resistance. Superabrasive Wheel F was supplied during May 2007. The main aim in producing this wheel was to improve the workpiece surface integrity previously obtained using Wheel D but at higher feed rates (600mm/min). At this feed rate surfaces produced using Wheels D & E showed significant workpiece surface burn and cracking. By increasing the porosity of the wheel, the useful coolant flowrate was expected to increase, resulting in lower temperatures and less workpiece damage [162]. It was envisaged that there would also be a decrease in grinding performance as by increasing the porosity there would be a reduction in the amount of bond material thereby making the wheel too ‘soft’ and liable to wear by a bond fracture mechanism.

Wheel coding	Wheel specification	Grit type	Grit mesh size/size	Grit material	Bond	Porosity
				%	%	%
A	GC 601 J 45 VKRNN [#]	SiC	60grit*	54.2	6	39.8
B	GC 601 J 62 VKRNN	SiC	60grit	43.7	5.9	50.5
C	GC 601 H 62 VKRNN	SiC	60grit	43.6	4.2	52.1
D		Diamond	91 μ m	31.25	30	38.75
E		cBN	91 μ m	40	37	23
F		Diamond	91 μ m	31.25	27.75	41

Table 3.1: Conventional abrasive and superabrasive grinding wheel specifications (*FEPA designation, # St-Gobain designation)

3.5 Analysis equipment

a) Tool wear

Cutting tool wear was measured using a JVC TKC1380 colour video camera with Naviar macrozoom lens attachment, connected to a JVC 14” monitor and laptop with image capture software and a Mitutoyo digital micrometer measuring platform, having a resolution of 0.001mm.

b) Grinding wheel wear

Grinding wheel diameter was measured using a Swift coordinate measurement machine using Delcam Power Inspect software. Sixteen points around the grinding wheel periphery were measured and the computer software calculated the diameter of the grinding wheel using a least squares method. Three measurements of the wheel diameter were taken with the average being used. G-ratio was calculated using Equation 12.

c) Cutting/grinding forces, power and specific energy

Cutting forces, when both milling and grinding were measured using a Kistler 9257A three-component piezo-electric platform dynamometer (resonant frequency of 2.3kHz and a recommended operating frequency <760Hz) attached to a series of Kistler 5011 charge amplifiers which were in turn connected to a PC running Kistler Dynaware software for signal analysis and force output. Figure 3.12 shows the force orientations for high speed ball nose end milling γ -TiAl alloys whilst Figure 3.6 shows the force orientations for high speed ball nose end milling of BuRTi. Force orientations for creep feed grinding tests can be found in Figure 2.8. Equations 5 and 6 were used to calculate the normal and tangential forces at the point where the line of action of the total resultant force intersects the grinding zone [42].

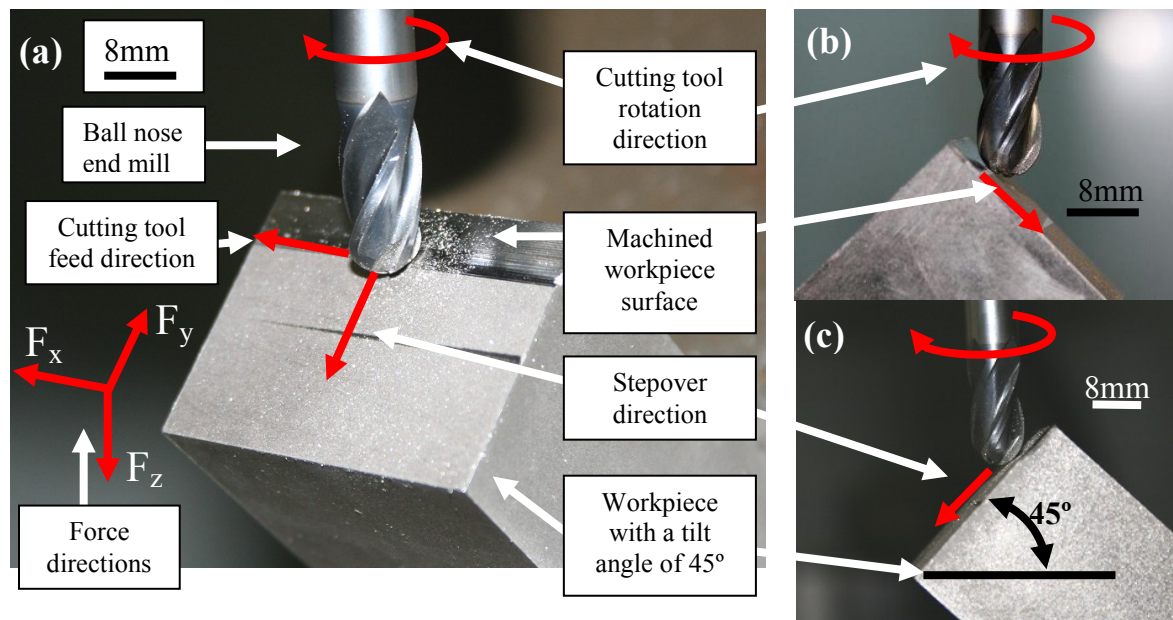


Figure 3.12: Images showing the orientation used for milling tests, (a) Isometric view, (b) Left side view (Cutting tool feed direction: out of paper), (c) Right side view (Cutting tool feed direction: into the paper)

Grinding power was measured directly from the Heidenhain power meter that was integrated into the controller of the Bridgeport FGC1000. This gave the percentage of spindle power used and could be converted into units of kilowatts using Figure 3.5 (b). The specific energy was calculated using Equation 10.

d) Temperature measurement

The FLIR THERMACAM SC3000 used for temperature measurement when high speed ball nose end milling, was loaned from EPSRC Engineering Equipment Pool (27th May – 20th July 2007). Figure 3.13 shows the Thermacam SC3000 along with a bracket that was made to

fit the camera to the machine tool. This bracket ensured the camera was located in a constant position to the cutting tool so that the image of the cutting tool was in focus. The camera had a temperature range of -20° to $+2000^{\circ}$ C and an accuracy of $\pm 1\%$ or 1° C for measurements up to $+150^{\circ}$ C and $\pm 2\%$ or 2° C for above. It acquired images in real time and could take 750 pictures per second with a reduction in picture size. The information acquired was analysed using the ThermaCAM researcher software installed on the accompanying PC. The system had a thermal sensitivity of 20mK at 30° C, a spectral range of 8 to $9\mu\text{m}$ and a resolution of 320 X 240 pixels.



Figure 3.13: FLIR Thermacam SC3000 and mounting bracket

e) Workpiece surface roughness

Machined workpiece surface roughness R_a was measured using a Taylor Hobson Form Talysurf 120L unit with a vertical resolution of 10nm, a stylus angle of 60° and a stylus tip radius of $2\mu\text{m}$. A cut off length of 0.8mm and an evaluation length of 4.0mm were used.

f) Machined workpiece surface

Photographs of the milled or ground surfaces were taken using a Sony Digital Handycam. Surface samples were analyzed using a Leica DMLM microscope with pictures taken using a Pixilink Colour Camera (1.3 megapixels) which was coupled to PC using Buelher Omnimet software with a JEOL 6060 scanning electron microscope used to provide a more detailed view.

g) Workpiece surface/subsurface cross-sectional analysis

Selected surface samples were produced using electrical discharge wire machining (EDWM). A schematic showing the location and nomenclature for both high speed ball nose end milled and creep feed ground samples are shown in Figures 3.14 and 3.15.

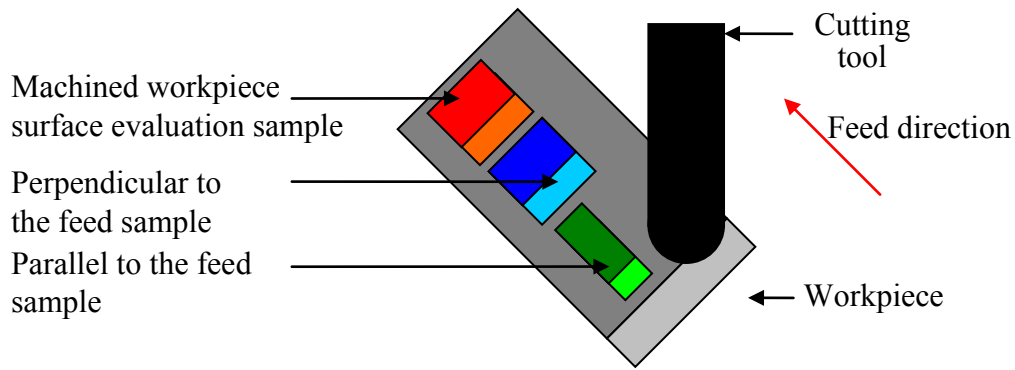


Figure 3.14: Schematic showing location and nomenclature of samples used for high speed milled workpiece surface integrity assessment

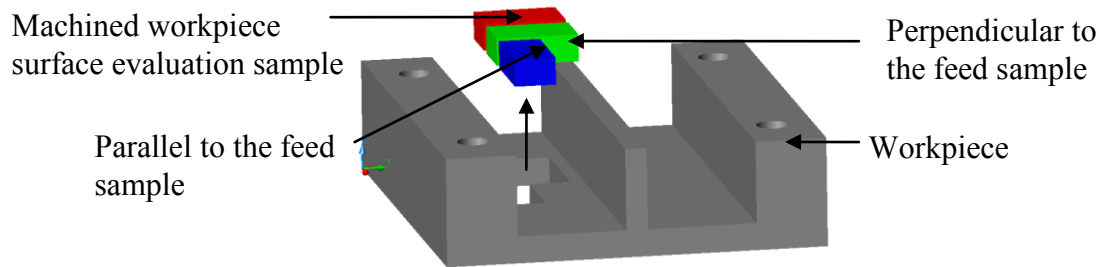


Figure 3.15: Schematic showing location and nomenclature of samples used for creep feed ground workpiece surface integrity assessment

The samples were hot mounted in Buehler Epiomat edge retentive bakelite, ground using silicon carbide (SiC) paper and polished on a Buehler Beta Vector grinder-polisher. Samples were then immersion etched using a solution of 2%HF, 10%HNO₃ with balance water for 8-10seconds. The grinding, polishing and etching regime for γ -TiAl alloys is detailed in Table 3.2 and was identical to that used by Mantle and Aspinwall [107], who investigated different regimes to ensure that repeatability between samples was achieved. Table 3.3 gives the grinding, polishing and etching regime for the BuRTi alloy.

Step	Force	Time	Rotation
	N	min	
SiC paper (120grit)	20	Until plane	Complimentary
SiC paper (240grit)	20	4	Complimentary
SiC paper (600grit)	20	4	Complimentary
SiC paper (1200grit)	20	4	Complimentary
Buelher UltraPol polishing cloth with ~0.06 μ m OP-s colloidal silica	20	8	Complimentary
Etched used 2%HF, 10%HNO ₃ with balance water for 8-10 seconds.			

Table 3.2: Grinding, polishing and etching regime for γ -TiAl alloys

Operation	Force	Time	Rotation
	N	min	
SiC paper (120grit)	40	Until plane	Complimentary
9 μ m diamond wheel grit	40	4	Complimentary
3 μ m diamond wheel grit	40	4	Complimentary
Buelher UltraPol polishing cloth with ~0.06 μ m OP-s colloidal silica	25	5	Complimentary
Etched using 7%HF, 10%HNO ₃ with balance water for ~30 seconds			

Table 3.3: Grinding, polishing and etching regime for BuRTi alloy

h) Microhardness

Microhardness measurements of the workpiece (depth profile) were taken using a Mitutoyo MVK G3 or Mitutoyo 800 microhardness testing machine. A 25g load and indent time of 15s were used with three measurements taken, each set at 10 μ m intervals from the surface until bulk hardness was achieved. The average for each depth was calculated and plotted. In order to improve the reliability of the data, the indent test-point centres were kept at a minimum distance of 30 μ m from each other in order to avoid the influence of previous indents on the new reading.

i) Statistical analysis

Statistical analysis including the production of main effects plots, interaction plots and ANOVA tables was performed using Minitab version 14.

3.6 Experimental programmes

Two phases of experimental design were developed, Phase 1 covered high speed ball nose end milling whilst Phase 2 covered creep feed grinding using both conventional and superabrasive grinding wheels. Each phase was broken down into a series of sub phases designed to establish the affect of various operating parameters on the machinability of the new γ -TiAl alloy, Ti-45Al-8Nb-0.2C and can be traced to the objectives detailed in Section 1.2: Aims and Objectives of the project. Figure 3.16 shows a chart which allows visualisation of the phases of the work that were conducted. The next sections detail these experiments including the objectives of the experiment, variable factors and levels investigated, fixed factors and the output measures with an explanation of the reasoning behind each experiment.

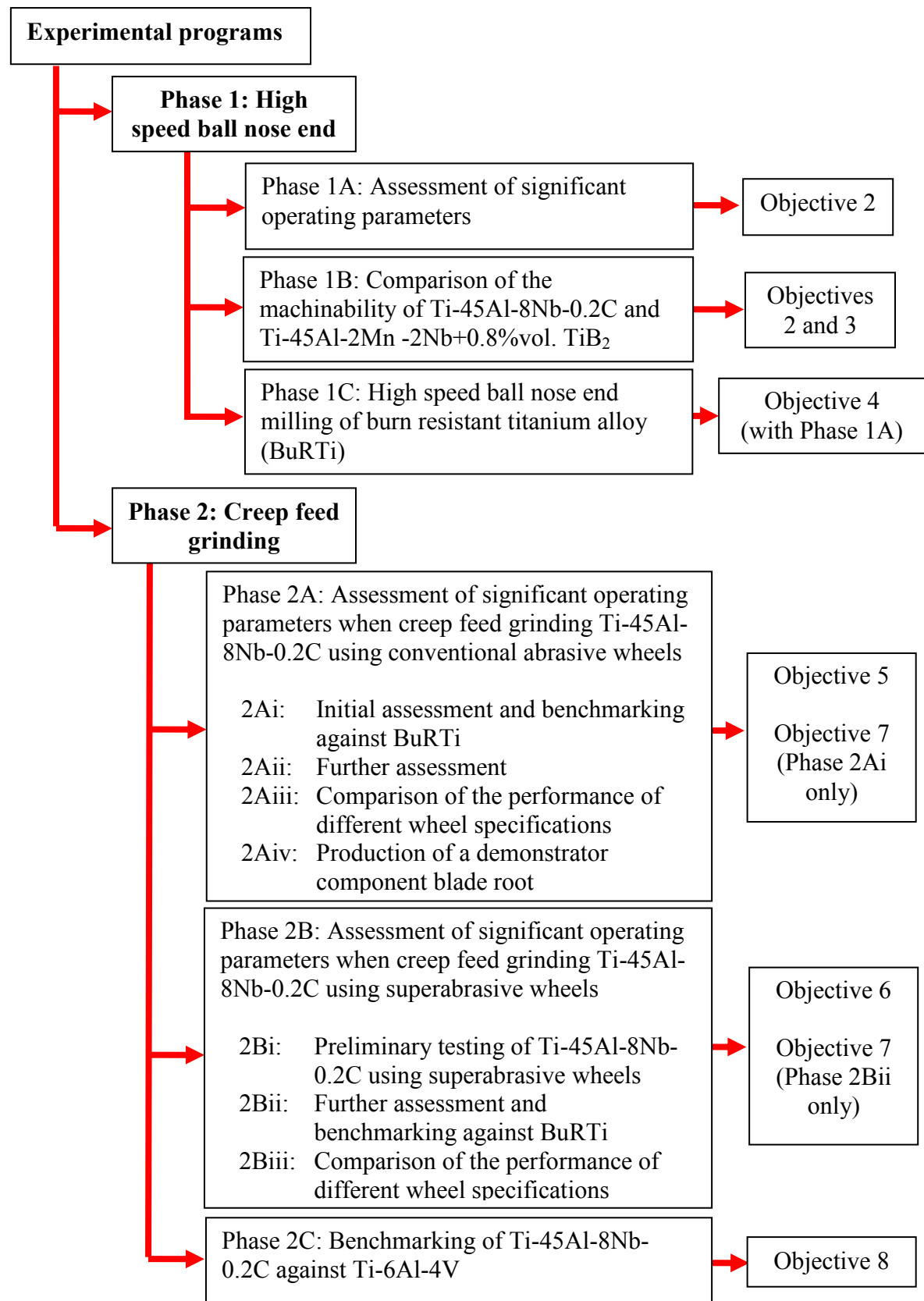


Figure 3.16: Phases of work chart
(Refer to section 1.2 for details of the objectives)

3.6.1 Phase 1, high speed ball nose end milling

3.6.1.1 Phase 1A: Assessment of significant operating parameters

The main objective of this phase was to fulfil Objective 2, see Section 1.3 and to provide an assessment of selected significant operating parameters when high speed ball nose end milling Ti-45Al-8Nb-0.2C using Iscar tools. An initial appraisal of the factors and levels that could be investigated to determine their affect is detailed in Table 3.4.

Factors		Levels
Cutting tool	Tool material and number of grades / products	Carbide (10grades/products) / Cermet (5grades/products) / Conventional ceramic (2grades/products) / PCBN (8grades / products)
	Coating	None / TiN / TiCN / TiAlN / TiN-AlN
	Type of cutter	End mill / ball nose / radius end mill / face mill
	Cutting edge(s)	Solid / Brazed / Inserts
	Diameter (mm)	6 / 10 / 32
	Length	Standard / Long
	No of teeth	1 / 2 / 4
	Geometry – axial rake angle and radial rake angle	+6° / 0° / -6°
	Toolholder	ISO / HSK / Collet / Hydraulic / Shrink-fit
	Runout (µm)	1 / 5 / 10
	Balance quality	G1 / G2.5 / G6.3
Workpiece	Surface condition	As cast / EDM / Face milled / Previous test
Machining parameters	Cutting speed (m/min)	50 / 100 / 200 / 400 / 600 / 800 / 1000
	Axial depth of cut (mm)	0.1 / 0.5 / 1.0 / 2.0 / 10.0
	Radial depth of cut (mm)	0.1 / 0.2 / 0.5 / 1.0 / 2.0 / 10.0
	Feed per tooth (mm/tooth)	0.05 / 0.1 / 0.2
	Type of cut	Peripheral / Slotting
	Approach to workpiece	Horizontal / Plunge / Ramp (5°)
	Direction of cut angle (β angle)	+ β_v , - β_v , + β_v and - β_v
	Angle of workpiece from horizontal	0° / 30° / 60° / 89° / 90°
	Milling direction	Up (conventional) / Down (climb)
	Cutting fluid	None / Compressed air / Flood standard pressure / Flood high pressure / Spray mist

Table 3.4: List of possible factors and levels for Phase 1, high speed ball nose end milling [163]

Investigation of all the factors detailed in the table would require an extensive and time consuming test program. This was unrealistic and therefore it was decided to keep certain factors constant with others varied at several levels. The literature review showed the importance of

factors such as cutting speed, feed rate and axial and radial depth of cut, therefore this experiment was designed to include these as variable factors at as many levels as possible. Indeed these four factors were all determined statistically significant at the 5% level when end milling Ti-45Al-2Mn-2Nb +0.8%vol. TiB₂ [100]. The Taylor tool life curve shown in Figure 2.6 had a steep gradient indicating that a small increase in cutting speed caused a significant reduction in tool life. Published information concerning high speed ball nose end milling on which to base the levels for the current series of tests was scarce. Indeed, the literature review identified only two sources of information including the work of Mantle and Aspinwall [104] and the work of Doody [103], Figure 2.8 (b) is from the former publication.

Ross [154] suggests that experimental design is an iterative process, where the first round of experimentation, often called a screening experiment, finds the important and influential factors which then can lead to further rounds of experimentation. See Appendix A, section A8 for further details concerning experimental design techniques. A Taguchi L16 fractional factorial orthogonal array was used to reduce the number of tests that were required to be performed. This array was modified to allow four factors at 4 levels and two factors at 2 levels with a spare column that could be used as the residual. Table 3.5 shows the orthogonal array used. A factorial design with the same number of factors and levels would require 1024 tests to be performed whereas only 16 were performed using the Taguchi design. No assessment of interactions between factors was possible with the array used. The 4 level factors were established as cutting speed, feed rate and axial and radial depth of cut. In addition, the two different tool substrates were investigated as one of the two level factors to determine the affect of reducing the carbide grain size on tool life. Work by Mantle and Aspinwall [100], Figure 2.5, showed that whilst cutting dry produced the longest tool life, a long tool life was also produced using high-pressure coolant therefore the final factor that was selected was cutting environment. It was decided to take the two best performing levels from Figure 2.5, dry and HP cutting fluid as the two levels for this experiment. These factors and levels used for this phase of experimentation are shown in Table 3.5.

Levels were predominately based on the work of Mantle and Aspinwall [100, 104, 106, 107] along with Doody [103] but took into account improvements in cutting tool technology since the previous work had been performed, hence the maximum cutting speed of 120m/min used with previous work was increased to 160/min for the present study. The axial and radial depths of cut levels were low due to the net shape nature of the blade manufacturing process and a maximum of 1mm used. Only small amounts of material needed to be removed therefore it was not necessary to assess the affect of larger depths of cut. In

addition, Harding [101] showed that at higher axial and radial depths of cut (1.5-3mm) and feed rates of 0.1-0.2mm/tooth tool life was reduced when end milling Ti-45Al-2Mn-2Nb +0.8%vol. TiB₂.

Test	Cutting speed (v)	Feed rate (f)	Axial depth of cut (a)	Radial depth of cut (d)	Cutting tool	Environment
	m/min	mm/tooth	mm	mm		
1	70	0.06	0.1	0.1	IC900	HP
2	70	0.09	0.25	0.25	IC900	dry
3*	70	0.12	0.5	0.5	IC903	Dry
4*	70	0.15	1	1	IC903	HP
5	100	0.06	0.25	0.1	IC903	HP
6	100	0.09	0.1	0.25	IC903	dry
7	100	0.12	1	1	IC900	HP
8*	100	0.15	0.5	0.5	IC900	dry
9*	130	0.06	0.5	1	IC900	dry
10	130	0.09	1	0.5	IC900	HP
11	130	0.12	0.1	0.25	IC903	dry
12	130	0.15	0.25	0.1	IC903	HP
13*	160	0.06	1	0.25	IC903	HP
14	160	0.09	0.5	0.1	IC903	dry
15	160	0.12	0.25	1	IC900	HP
16	160	0.15	0.1	0.5	IC900	dry

Table 3.5: Phase 1A test details

*Indicates test replication performed using Matsuura FX5 machining centre.

A workpiece tilt angle of 45° was used to remove the effect of rubbing at the centre of the ball which has been shown to cause extensive cracking/surface pullout, see Figure 2.9 [106]. The milling mode and orientation were held constant for all tests with down milling in a horizontal downwards direction being used. Despite a vertical upwards orientation being used in work published by Mantle and Aspinwall [106, 107] the horizontal downwards direction was selected in the present study as Ng et al. [164] suggest that this was the preferred cutting direction to maximise tool life and reduce forces due to a reduced level of tool vibration. Down milling was used for all trials in order to allow a comparison with previous work. Appendix B provides a review of milling modes together with information concerning the milling orientation used, whilst Figure 3.12 shows a schematic of the tool/workpiece arrangement detailing the cutting tool rotation and workpiece feed directions. Tool overhang was maintained at 28mm, to improve the rigidity of the experiment setup with a tool run out of <10µm. Entry and exit into the workpiece were performed using separate tools to those

used for testing to ensure test conditions were fair. Due to scheduling commitments, the Matsuura LX1 machine tool used for the testing program was not available for any test replications to be performed. The Matsuura FX5 machining centre therefore had to be used for selected replication and all future testing involving high speed ball nose end milling. Tests marked with an asterisk in Table 3.5 were replicated. Apart from the machine tool and associated tool holder all other parameters were identical including tool overhang and runout, workpiece orientation and cutting tool geometry and coating.

Tool life including plots of distance machined, machining time and volume of workpiece material removed were produced. A tool life criteria of 0.3mm maximum flank wear and maximum notch wear of 0.6mm was selected to be in accordance with ISO8688-2 as far as possible [54]. Based on the information in Figure 2.19 (b) [104], a maximum distance machined of ~200m to reach the tool life criteria was expected. A significant proportion of the tests did not reach the tool life criteria within 200m therefore in order to conserve workpiece material and time, a maximum distance machined criteria of 200m had to be employed. Selected milling passes at certain cutting tool maximum flank wear levels had their cutting forces (F_x , F_y and F_z) measured with the maximum for each pass recorded.

As this was an initial experiment to assess the machinability of the new γ -TiAl alloy using factors from previous research that had been identified as being significant, only the “Minimum Workpiece Surface Integrity Data Set” was performed [89]. This included workpiece surface roughness R_a measurement undertaken in the direction perpendicular to the feed, assessment of the workpiece surface, microhardness depth profiles in the direction perpendicular to the feed and assessment of the workpiece surface/subsurface. The assessed surface was the one produced at the end of the test which was decided by either the tool life criteria or the distance machined criteria.

3.6.1.2 Phase 1B: Comparison of the machinability of Ti-45Al-8Nb-0.2C and Ti-45Al-2Mn-2Nb+0.8%vol. TiB₂

This phase had two main objectives, firstly benchmarking of Ti-45Al-8Nb-0.2C against Ti-45Al-2Mn-2Nb +0.8%vol. TiB₂ using Iscar IC903 tooling to fulfil Objective 3 (see Section 1.2). The secondary objective was the determination of the affect of cutting speed and tool flank wear on the surface integrity of the machined surface which was further work undertaken to achieve Objective 2. A full factorial experimental design, rather than the Taguchi experimental design that was used for Phase 1A, was developed because of the lower number of factors to be investigated. A full factorial experimental design allowed the

assessment of interactions between factors which was not possible with a Taguchi design. Phase 1A showed that at a cutting speed of $<160\text{m/min}$ tool life would be very high with the potential for a distance machined of $>1000\text{m}$ if low values of feed rate and depth of cut were used. Higher cutting speeds of 160, 250 and 340m/min were therefore selected so that tool life criteria would be based on maximum flank wear rather than distance machined. Table 3.6 details the tests that were performed including the variable factors and levels.

Test	Workpiece material	Cutting speed (v)	Cutting tool
		m/min	
1*	Ti-45Al8Nb-0.2C	160	Iscar IC903
2*	Ti-45Al8Nb-0.2C	250	Iscar IC903
3*	Ti-45Al8Nb-0.2C	340	Iscar IC903
4	Ti-45Al-2Mn-2Nb +0.8%vol. TiB_2	160	Iscar IC903
5	Ti-45Al-2Mn-2Nb +0.8%vol. TiB_2	250	Iscar IC903
6	Ti-45Al-2Mn-2Nb +0.8%vol. TiB_2	340	Iscar IC903

Table 3.6: Phase 1B test details

* Replication performed

Based on the results of Phase 1A, feed rate was held constant at 0.06mm/tooth with axial and radial depth of cut held constant at 0.25mm . These were chosen as the size and number of surface defects/damage including fracture/pullout was observed to be relatively low whilst a reasonable material removal rate was maintained. Phase 1A showed that the Iscar IC903 tool outperformed the IC900 tool and this was therefore selected for these tests. Dry cutting was selected as it was deemed to be preferable when compared to operating with high pressure (70bar) cutting fluid and also allowed cutting temperature measurement using infra red pyrometry to be performed. All other fixed factors were identical to Phase 1A including using down milling mode in a horizontal downwards direction with workpiece title angle of 45° . The Matsuura FX5 machine tool was used for all tests in this phase of experimentation.

Tool life was measured until a maximum flank wear criteria of 0.3mm on any single cutting edge was reached. Tests 1 to 3 using Ti-45Al-8Nb-0.2C workpiece material were replicated so that cutting temperature using infra red pyrometry at selected maximum flank wear levels could be measured. Limited availability of the thermal camera precluded further temperature measurement trials. Emissivity calibration was performed using a hotplate able to produce temperatures of up to 400°C . Several pieces of gamma TiAl material (chips and small blocks) were placed on the hotplate and then heated to a specified temperature in accordance with the procedure detailed by Mantle and Aspinwall [126]. The temperature of the surface was measured using a thermocouple (K-type, -50°C to $+1300^\circ\text{C}$ with a resolution of 0.1°C

and an accuracy of $<2^{\circ}\text{C}$). The emissivity of the camera was adjusted to register agreement to the temperature of the surface.

Cutting force measurement (F_x , F_y and F_z) was undertaken on passes at selected flank wear levels with the maximum value recorded. Insufficient Ti-45Al-2Mn-2Nb +0.8%vol. TiB_2 workpiece material precluded it from the assessment of cutting force. As with Phase 1A, measurements involved the Minimum Workpiece Surface Integrity Data Set [89]. Assessed surfaces for both workpiece materials were produced using a tool with a maximum flank wear criteria of 0, 100, 200 and $300\mu\text{m}$ so that the affect of tool flank wear on surface integrity could be established.

3.6.1.3 Phase 1C: High speed ball nose end milling of burn resistant titanium alloy (BuRTi)

Due to limited workpiece material supply and cost of sample preparation, a fractional factorial experimental design employing a Taguchi L8 Orthogonal Array was used to investigate the affect of six factors, each at two levels. This phase of work was performed to achieve Objective 4 (see Section 1.2) and was essentially a replication of Phase 1A therefore the factors and levels reflected this. As with Phase 1A, the two different carbide grades, IC900 and IC903 were selected as one of the factors along with either a dry or HP cutting fluid cutting environment. Operating parameters including feed rate and axial and radial depth of cut were selected as factors, with levels selected based on the levels used for Phase 1A to allow benchmarking between the γ -TiAl and BuRTi alloys. Workpiece tilt angle was selected as a factor to identify if operating at 45° reduced the level of surface smearing resulting from operating with a cutting tool with zero cutting speed at the centre of the ball. Table 3.7 shows the Taguchi orthogonal array used as well as the factors and levels selected.

In order to ensure conditions were identical between tests, i.e. a constant depth and width of cut, entry into and exit from the workpiece was performed using a separate IC900 cutting tool. Peripheral cutting speed was fixed at 100m/min for all tests while analysis of the results was restricted to main effects rather than interactions between the factors. No replication of the test program was performed however a confirmation trial to validate the results at the end of the experiment, detailed as Test 9 in Table 3.7 was performed. The Matsuura FX5 machine tool was used for all tests in this phase of experimentation.

Test	Cutting tool	Feed rate (f)	Axial depth of cut (a)	Radial depth of cut (d)	Environment	Orientation
		mm/min	mm	mm		(°)
1	IC900	0.06	0.25	0.25	Dry	0
2	IC900	0.06	0.25	0.5	HP	45
3	IC900	0.12	0.5	0.25	Dry	45
4	IC900	0.12	0.5	0.5	HP	0
5	IC903	0.06	0.5	0.25	HP	45
6	IC903	0.06	0.5	0.5	Dry	0
7	IC903	0.12	0.25	0.25	HP	0
8	IC903	0.12	0.25	0.5	Dry	45
9	IC903	0.06	0.25	0.25	HP	45

Table 3.7: Phase 1C test details

Tool life criterion was selected in accordance with ISO standard 8688-2 (0.3mm flank / 0.6mm notch) [104]. Cutting forces, F_x , F_y and F_z were measured on selected cutting passes. Measurements were taken in accordance with the Minimum Surface Integrity Data Set [89]. Following completion of all trials, the resulting workpiece surface roughness R_a was measured parallel and perpendicular to the feed as was surface/subsurface damage on selected samples. Finally microhardness depth profile measurements on the surface perpendicular to the feed direction were conducted.

This phase of experimentation was conducted with the help of Colin Johnson, 4th year undergraduate, Mechanical Engineering, University of Birmingham who assisted with the testing program including tool wear, force and surface roughness measurements, sample preparation and microhardness assessment.

3.6.2 Phase 2, creep feed grinding

3.6.2.1 Phase 2A: Assessment of significant operating parameters when creep feed grinding Ti 45Al-8Nb-0.2C using conventional abrasive wheels

Phase 2Ai: Initial assessment and benchmarking against BuRTi

The main objective of this phase of work was to provide an initial assessment of selected significant operating parameters when creep feed grinding Ti-45Al-8Nb-0.2C using conventional abrasive (SiC) wheels. The work was performed so that Objective 5 could be achieved, see Section 1.2. An initial appraisal of the factors and levels that could be utilised during experimental design is detailed in Table 3.8. As with milling, a testing program that assessed the affect of all the factors detailed, at several levels would have consumed a large

volume of workpiece material and required extensive time to perform. It was therefore decided to investigate the affect of main factors that were established from published literature as being the most significant with other factors fixed using “best practice” values identified from the published literature.

Initially only a single specification SiC wheel - Wheel A, was supplied by Saint-Gobain abrasives, therefore it was not possible to investigate any other wheel specifications during this experiment. Additional wheels for assessment in subsequent phases were produced based on the performance of Wheel A during this phase of experimentation.

	Factors	Levels
Wheel	Grit material	SiC, cBN, diamond
	Grit size (conv. abrasives)	46 - 600 mesh (508 – 8 μm)
	Grit size (diamond and cBN)	430 – 8 μm
	Wheel grade / friability	Soft (A) – Hard (Z)
	Bond type	Resin, Metal, Vitrified, Electroplated
	Bond structure:	Dense – Open
	Concentration (conv. abrasives)	1 – 30
	Concentration (diamond, cBN)	50 – 200
	Wheel profile	Plain, Profiled
	Wheel diameter	50 – 400 mm
	Wheel width	10 – 50 mm
Operation	Surface speed	15 – 60 m/s
	Depth of cut (CFG)	0.01 – 10 mm
	Feed rate	10 – 1000 mm/min
	Wheel direction	Up, Down
Dressing	Dressing method	Intermittent, Continuous
	Dresser type	Single point diamond Diamond wheel crush Brake truer
	Dresser speed, cont. dressing	-1.5 – +1.5 $\times v_s$
	Dresser feed rate, cont. dressing	1.5 $\mu\text{m}/\text{rev.}$
	Infeed rate, intermittent dressing	5 – 500 μm
Fluid	Fluid type	Water based, Oil, Synthetics
	Fluid application	Jet, Shoe
	Fluid flow rate and pressure	1 – 360 l/min; 0 – 100 bar

Table: 3.8: List of possible factors and levels for Phase 2, creep feed grinding [108]

Bentley and Aspinwall [118] established that when creep feed grinding Ti-45Al-8Nb-0.2C using SiC abrasives, wheel speed, depth of cut, feed rate, dressing method and fluid application were statistically significant variables for output measures including normal and tangential forces, power, surface roughness R_a and microhardness. Several of these parameters were therefore investigated when grinding the new γ -TiAl alloy, Ti-45Al-8Nb-

0.2C. It was decided to investigate the affect of the operating parameters, wheel speed, feed rate and depth of cut on grinding performance with dressing and fluid application remaining constant for all tests. The choice of levels for these three factors was predominately based on earlier work [108, 118, 119] which were the only three publications that were found that detailed creep feed grinding of γ -TiAl alloys. A Taguchi L9 fractional factorial orthogonal array was selected for this experiment. Using this technique the number of tests required to be performed reduced from 27 for a full factorial experimental design to 9 for the Taguchi design employed, however this was at the expense of the assessment of interactions between factors. High and low levels for wheel speed and feed rate were identical in the work of Bentley [108, 118] with a further value selected for the middle level. For depth of cut, the maximum depth of cut that could be used with the Bridgeport FGC1000 was 5mm therefore this was selected as the high level. A value of 2.5mm was selected for the middle value whilst for the lowest level 1.25mm was selected. This allowed a comparative assessment after a fixed amount of workpiece material had been removed. Table 3.9 shows the Taguchi L9 Fractional Factorial Orthogonal Array used along with the factors and levels.

Test	Wheel speed (v)	Depth of cut (d)	Feed rate (f)
	m/s	mm	mm/min
1	15	1.25	150
2	15	2.5	375
3	15	5	600
4	25	1.25	375
5	25	2.5	600
6	25	5	150
7	35	1.25	600
8	35	2.5	150
9	35	5	375

Table 3.9: Phase 2Ai test details

With the current research, it was not possible to assess the affect of continuous dressing as Bentley and Aspinwall [118] had done, as this facility was not available on the Bridgeport FGC1000. Intermittent dressing was therefore performed prior to every test with a dresser/wheel ratio of +0.8 in order to provide a sharp wheel suitable for high stock removal. The infeed of the dresser per revolution of the grinding wheel was $2.0\mu\text{m}$ with a dress depth of $500\mu\text{m}$. These are typical values for conventional abrasive wheels [40]. Similar parameters were used by Bentley [108] for selected tests requiring intermittent dressing and therefore a

comparison could be made between the grinding performances of the two γ -TiAl alloys. In order to simplify experiments, plain profile grinding wheels were used.

When grinding titanium alloys wear has been reported to be extensive with reported G-ratios of <30 [113]. If a shoe nozzle had been used there would have been a requirement to develop an active nozzle system [73] which took into account the change in diameter of the grinding wheel and adjusted the shoe nozzle position accordingly. This was judged to add unnecessary complexity when free jet nozzles offer improved performance. A free jet nozzle with a rectangular exit slot width of 2mm and a height of 20mm was used to supply grinding fluid to the workpiece/contact zone interface for cooling and lubrication. This slot width allowed the maximum achievable flowrate of 90 l/min at a pressure of 7bar. Flow at this pressure allowed the fluid velocity to approximately match the wheel velocity. Where possible the recommendations of Webster and his co-researchers [61, 77] were followed, including the use of large contraction ratios, limited bends and elbows and long straight sections of pipe to reduce the turbulence of the flow. Figure 3.17 shows a photograph of the arrangement.

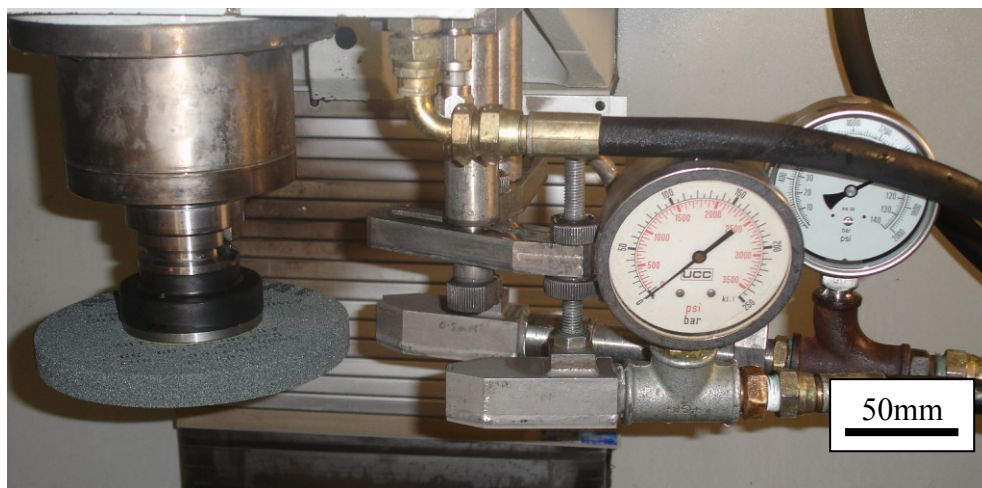


Figure 3.17: Grinding wheel and nozzle arrangement

The location of the nozzle relative to the grinding zone and workpiece is shown in Figure 3.18 with the nozzle positioned a distance of ~ 170 mm away from the point of first contact between the wheel and the workpiece at a tangential angle to the wheel. The nozzle position was adjusted as the grinding wheel radius reduced due to dressing or wheel wear.

A free jet nozzle with a rectangular exit slot width of 0.5mm and a height of 20mm was used to remove the air barrier that forms when the grinding wheel rotates, to preload the grinding wheel with fluid before entering the contact zone and for cleaning of the grinding wheel. Consideration was given to using a close fitting scraper plate to eliminate the air

barrier and to remove the debris from the grinding wheel, however this approach was dismissed in favour of the high pressure cleaning jet because of the need to adjust the scraper plate as the wheel diameter reduced. The high pressure nozzle was placed $\sim 20\text{mm}$ from the grinding wheel and aimed towards the rear of the wheel at a slight angle of $10\text{-}15^\circ$ from normal to reduce interference with the cooling jet. The location of the cleaning jet in relation to the workpiece/contact zone jet is shown in Figure 3.18. The pressure of the cleaning jet was 64bar just before the nozzle and equated to a pressure of 70bar at the pump which was the pumps maximum permissible pressure. A flowrate of 35 l/min was achieved for this pressure.

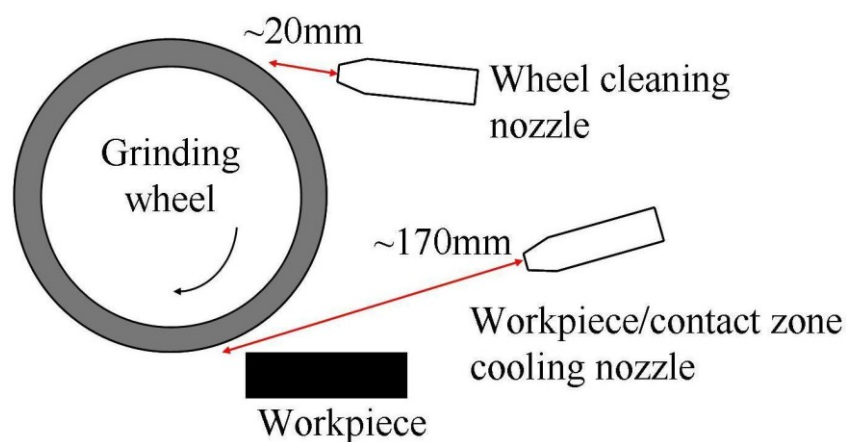


Figure 3.18: Nozzle disposition schematic

Down grinding was selected for all tests as the fluid was applied at the point of highest material removal and highest temperature. No dummy workpiece/nip or low pressure cooling nozzle at the rear of the workpiece was used as the workpiece had a cutting length of 80mm. A slot 20mm wide, 80mm long and 15mm deep was ground into the workpiece using the operating parameters detailed in Table 3.9 with no sparkout passes performed in accordance with the work detailed in [118].

Wheel wear was measured after every grinding pass with all tests stopped once $\sim 24,000\text{mm}^3$ of material had been removed. Normal and tangential grinding forces, power, specific energy and workpiece surface images (extent of surface burn) were also measured/taken for selected volumes of material removed. For surface integrity assessment, only the Minimum Surface Integrity Data Set was performed. Surface roughness R_a measurements were undertaken on the workpiece surface in the direction perpendicular to the feed once the full volume of workpiece material had been removed. Workpiece surface, microhardness depth profile measurements in a direction perpendicular to the feed and workpiece surface/subsurface assessment was undertaken on this surface.

Benchmarking of the γ -TiAl alloy against the performance of BuRTi was also conducted during this phase with the whole experiment replicated for the BuRTi material. This achieved the first part of Objective 7, see Section 1.2. All test details including tests levels and factors, dressing, fluid application and analysis techniques were identical except that the nozzle applying grinding fluid for workpiece/contact zone cooling and lubrication was located a distance of 100mm away from the point of first contact between the wheel and the workpiece at a tangential angle to the wheel. This was because the length of the BuRTi workpiece was ~ 40 mm compared to ~ 80 mm for the γ -TiAl. This reduction in workpiece length also had an affect on the volume of workpiece material removed. For BuRTi tests $\sim 12000\text{mm}^3$ removed. The testing of the BuRTi alloy during this phase of experimentation was conducted in partnership with Frederik Lechner, University of Munich who was a Visiting Scholar at the University of Birmingham.

Phase 2Aii: Further assessment

The objective of Phase 2Aii was to provide further assessment of significant operating parameters (depth of cut and feed rate) on output measures at a wheel speed of 15m/s. Phase 2Aii showed increased levels of cracking and workpiece surface burn at wheel speeds of greater than 15m/s. This phase was conducted under Phase 2A which was designed to achieve Objective 5, see Section 1.2. A factorial experiment was therefore designed with 2 factors each at 2 levels to gather more information on the performance of SiC abrasives when a lower wheel speed was used. Wheel speed was held constant at 15m/s whilst depth of cut and feed rate were varied from 1.25mm to 5mm and 150mm/min to 600mm/min respectively in accordance with Phase 1A. Table 3.10 details the tests performed.

Test	Depth of cut (d)	Feed rate (f)
	mm	mm/min
1	1.25	150
2	1.25	600
3	5	150
4	5	600

Table 3.10: Phase 2Aii test details

Tests 1 and 4 used identical operating parameters to those detailed in Table 3.9 for Phase 2Ai Tests 1 and 3 and allowed replication to be performed. All other experimental details including the grinding wheel specification, dressing and fluid application were identical to those

detailed for Phase 2Ai. The grinding performance was assessed in the same manner to that of Phase 2Ai. Tests were only conducted on Ti-45Al-8Nb-0.2C workpiece material.

Phase 2Aiii: Comparison of the performance of different wheel specifications

This phase had the main objective of establishing if different wheel specifications with increased porosity could improve the performance when grinding Ti-45Al-8Nb-0.2C. As with Phase 2Ai and 2Aii, this phase was conducted in order to achieve Objective 5, see Section 1.2. Two new specification conventional (SiC) abrasive wheels; Wheels B and C, were supplied by Saint-Gobain Abrasives. A factorial design was developed to assess the performance of the two new wheel specifications, relative to Wheel A. In addition, the affect of wheel speed was also investigated to determine if the levels of workpiece surface damage could be reduced at higher wheel speeds with a wheel having an increased level of porosity. The three wheel speeds chosen were identical to those used for Phase 2A and are detailed in Table 3.11.

Test	Wheel specification	Wheel speed (v)
		m/s
1	A	15
2	A	25
3	A	35
4	B	15
5	B	25
6	B	35
7	C	15
8	C	25
9	C	35

Table 3.11: Phase 2Aiii test details

Depth of cut and feed rate were fixed at 1.25mm and 150mm respectively as Phases 2A and 2B established that they gave the “best results” with the highest G-ratio, lowest forces and surfaces which showed the highest level of integrity. All other experimental details including dressing and fluid application were identical to those detailed for Phase 2Ai. Tests were only conducted on Ti-45Al-8Nb-0.2C workpiece material and no replications were performed. Output measures were also identical to those used for Phase 2Ai, however the volume of material removed was reduced from 24000mm³ to 6000mm³ to conserve workpiece material. No workpiece surface/subsurface or microhardness assessment was undertaken.

Phase 2Aiv: Production of a demonstrator component blade root

The main objective of Phase 2Aiv was to produce a demonstrator component blade root using conventional abrasive grinding wheels. This was the final phase conducted as part of Phase 2A which was designed to achieve Objective 5, see Section 1.2. Up to this point in the research, all grinding trials had involved a plain flat profile grinding wheel, here the ‘lobe type’ profiled diamond dresser was used. Unfortunately, no specification details for the diamond dresser could be obtained resulting in a component that could only ‘look the part’. Two tests were performed with a wheel speed of 15m/s and a feed rate of 150mm/min, with one test having a sparkout pass and the other not. The demonstrator component was ground from solid using a depth of cut of 1.25mm. All other experimental parameters including the dressing infeed rate and depth and fluid application were identical to those detailed for Phase 2A. Analysis encompassed images of the workpiece surface, surface roughness R_a measurements parallel to the feed direction and assessment of surface/subsurface damage.

3.6.2.2 Phase 2B: Assessment of significant operating parameters when creep feed grinding Ti 45Al-8Nb-0.2C using superabrasive wheels

Phase 2Bi: Preliminary testing of Ti-45Al-8Nb-0.2C using superabrasive wheels

The main objective of this phase was to perform initial tests at a low material removal rate ($d=1.25\text{mm}$ and $f=150\text{mm/min}$) and wheel speed ($v=35\text{m/s}$) with superabrasive grinding wheels to establish their affects on output measures without performing an extensive evaluation using factorial or Taguchi fractional factorial experimental designs. This was the initial phase of work which was designed to achieve Objective 6 (see Section 1.2). Wheel type was selected as one of the factors with Wheel D (diamond grit) and Wheel E (cBN grit) as the two levels. The second factor was fluid type with water and oil based grinding fluids selected. There was a concern that when operating with superabrasives and oil based grinding fluid, there was a chance of fire or an explosion occurring. Tests were therefore initially performed with the water based fluid followed by repeat tests with the oil based fluid. Table 3.12 details the tests that were performed for this experiment.

Test	Wheel specification	Fluid
1	D	Water
2	E	Water
3	D	Oil
4	E	Oil

Table 3.12: Phase 2Bi test details

Grinding fluid application was identical to that detailed for Experiment 2Ai except that for this experiment and all subsequent experiments involving superabrasive grinding wheels, the wheel cleaning pressure was lowered from 63bar to 40bar. This was based on a recommendation from Saint-Gobain Abrasives, so that the risk of grit removal by the high pressure fluid was minimised. In addition, the low pressure (<1bar), high flowrate (200 l/min) spark suppression nozzle was used to reduce the incidence of sparks and to prevent fire, see Figure 3.9. This was used for all tests involving either water or oil based grinding fluid. Dressing was carried out using the same equipment as for the conventional abrasives with a dress depth of 5 μ m, a dresser infeed rate of 2 μ m/rev and a dresser speed ratio of +0.8. The low dressing depth was also anticipated to reduce dressing forces so that there would be limited pullout of grains, resulting in less bond material being left at the surface. The grinding performance was assessed in an identical way to that of Phase 2Ai with tests conducted on only Ti-45Al-8Nb-0.2C workpiece material

Phase 2Bii: Further assessment and benchmarking against BuRTi

The main objective of this phase was to develop Phase 2Bii experimentation further and establish the affect of significant operating parameters including wheel speed, depth of cut and feed rate in addition to wheel specification and fluid type to achieve Objective 6 (see section 1.2) Variable factors and levels were chosen based on earlier work performed in Phase 2Ai and 2Bi and constraints imposed by the equipment available. Depth of cut and feed rate were selected as factors with levels identical to those used for Phase 2Ai so that a direct comparison could be made between conventional and superabrasive wheels. Only the 1.25 and 2.5mm depths of cut were selected. Wheel speed was also chosen as a factor with levels of 35 and 50m/s. These were higher than those used for conventional abrasives and reflected the increased hardness and thermal conductivity of the abrasive grit. It was decided to keep all factors at two levels and therefore a Taguchi L8 fractional factorial experimental design was developed which allowed the assessment of 5 factors each at 2 levels with a spare column used for the residual. Only 8 tests were performed instead of the 32 tests required for a full factorial design with the same factors and levels, however the use of this experimental design did not allow interactions to be investigated. Table 3.13 details the tests that were performed for this phase of work. As with Phase 2E, the wheel cleaning pressure was lowered from 63bar to 40bar and the spark suppression nozzle was used for all tests. All other fluid application arrangements were identical to those detailed for Phase 2Ai.

Test	Wheel specification	Wheel speed (v)	Depth of cut (d)	Feed rate (f)	Fluid
		m/s	mm	mm/min	
1 *	D	35	1.25	150	Water
2	D	35	1.25	600	Oil
3	D	50	2.5	150	Water
4	D	50	2.5	600	Oil
5	E	35	2.5	150	Oil
6	E	35	2.5	600	Water
7	E	50	1.25	150	Oil
8	E	50	1.25	600	Water

Table 3.13: Phase 2Bii test details

Note: Test 1 was conducted as part of Phase 2Bi (γ -TiAl only)

Benchmarking of the γ -TiAl alloy against the performance of BuRTi was also conducted during this phase with the whole experiment replicated for the BuRTi material, however time restrictions meant that no workpiece surface integrity assessment was undertaken. This coupled with Phase 2Ai would achieve Objective 7. As with Phase 2Ai benchmarking tests, the volume of BuRTi ground was reduced and the workpiece/contact zone nozzle was positioned closer to the point of first contact. The testing of the BuRTi alloy during this phase of experimentation was conducted with the help of Mathieu Lanette, an undergraduate student from INSA Toulouse, who was a Visiting Scholar at the University of Birmingham and assisted with the testing program including grinding wheel wear and surface roughness measurements.

Phase 2Biii) Comparison of the performance of different wheel specifications

The main objective of this phase was to benchmark the performance of a new specification diamond wheel against the one that had been previously used for Phases 2Bi and 2Bii and to further fulfil Objective 6, see Section 1.2. The idea behind the new wheel was to improve the workpiece surface integrity previously obtained using Wheel D but at higher feed rates (600mm/min). Table 3.14 details the tests that were performed for this experiment. All other fixed factors including the dressing and grinding fluid application were identical to those used in Experiment 2Bi or Phase 2Bii. Grinding performance was assessed in an identical way to that of Phase 2Ai however, no workpiece surface/subsurface or microhardness assessment was undertaken. Tests were only conducted on Ti-45Al-8Nb-0.2C workpiece material.

Test number	Wheel type	Wheel speed (v)	Depth of cut (d)	Feed rate (f)
		m/s	mm	mm/min
1*	D	35	1.25	150
2	D	35	1.25	600
3*	D	50	2.5	150
4	F	35	1.25	150
5	F	35	1.25	600
6	F	50	2.5	150

Table 3.14: Phase 2Biii test details

*Note: Tests 1 and 3 were conducted as part of Experiment 2E and 2F

3.6.2.3 Phase 2C: Benchmarking of Ti-45Al-8Nb-0.2C against Ti-6Al-4V

The main objective of this phase was to benchmark the new γ -TiAl material against that of the conventional titanium alloy; Ti-6Al-4V, using both conventional and superabrasives so as to fulfil Objective 8. This was achieved using a series of tests involving the two workpiece materials and two different wheel speeds for conventional abrasives and a single wheel speed for the superabrasive wheels. This meant a total of 3 tests for each workpiece material. The factors and levels selected were the preferred operating parameters identified from Phases 2A to 2G which gave the preferred combination of highest G-ratio, lowest workpiece surface roughness Ra and highest workpiece integrity. Wheel speeds of 15m/s and 25m/s were employed with the SiC abrasive Wheel A while 35m/s was used with Wheel D. Table 3.15 details the tests that were performed for this experiment.

Test	Wheel specification	Wheel speed (v)	Workpiece material
		m/s	
1	A	15	γ -TiAl
2	A	15	Ti-6Al-4V
3	A	25	γ -TiAl
4	A	25	Ti-6Al-4V
5	D	35	γ -TiAl
6	D	35	Ti-6Al-4V

Table 3.15: Phase 2C test details

The depth of cut and feed rate were held constant at 1.25mm and 150mm/min respectively. These two factors were not selected for assessment during this phase of work as Phases 2A and 2B showed that in general, improved performance was achieved at a lower material removal rate. All other operating parameters including fluid application and dressing were

identical to those detailed in Phases 2A (Wheel A) for conventional abrasives and 2B for superabrasives (Wheel D). Due to the high wear level of Ti-6Al-4V with both types of abrasive wheel the material removal rate was limited to 3 passes of a workpiece ~75mm long which resulted in a total of 5625mm³ of material removed. The grinding performance was assessed in an identical way to that of Phase 2A however, only wheel wear measurement, grinding force assessment and a visual evaluation of the workpiece surface were performed.

4. RESULTS AND DISCUSSION:

PHASE 1, HIGH SPEED BALL NOSE END MILLING

4.1 Phase 1A: Assessment of significant operating parameters

a) Tool life

In general, the results for tool life, see Figure 4.1, were encouraging with a significant proportion of tests reaching the end criteria of a distance machined of 200m before reaching the maximum flank wear criteria of 300 μ m. Several tests however, typically those using higher operating parameter levels, produced a considerably shorter distance machined of <50m. Without subsequent statistical analysis however it is difficult to draw conclusions as to the effect of each operating parameter on tool life solely on the basis of such graphical data, as the Taguchi approach involves factors changing their levels for each test.

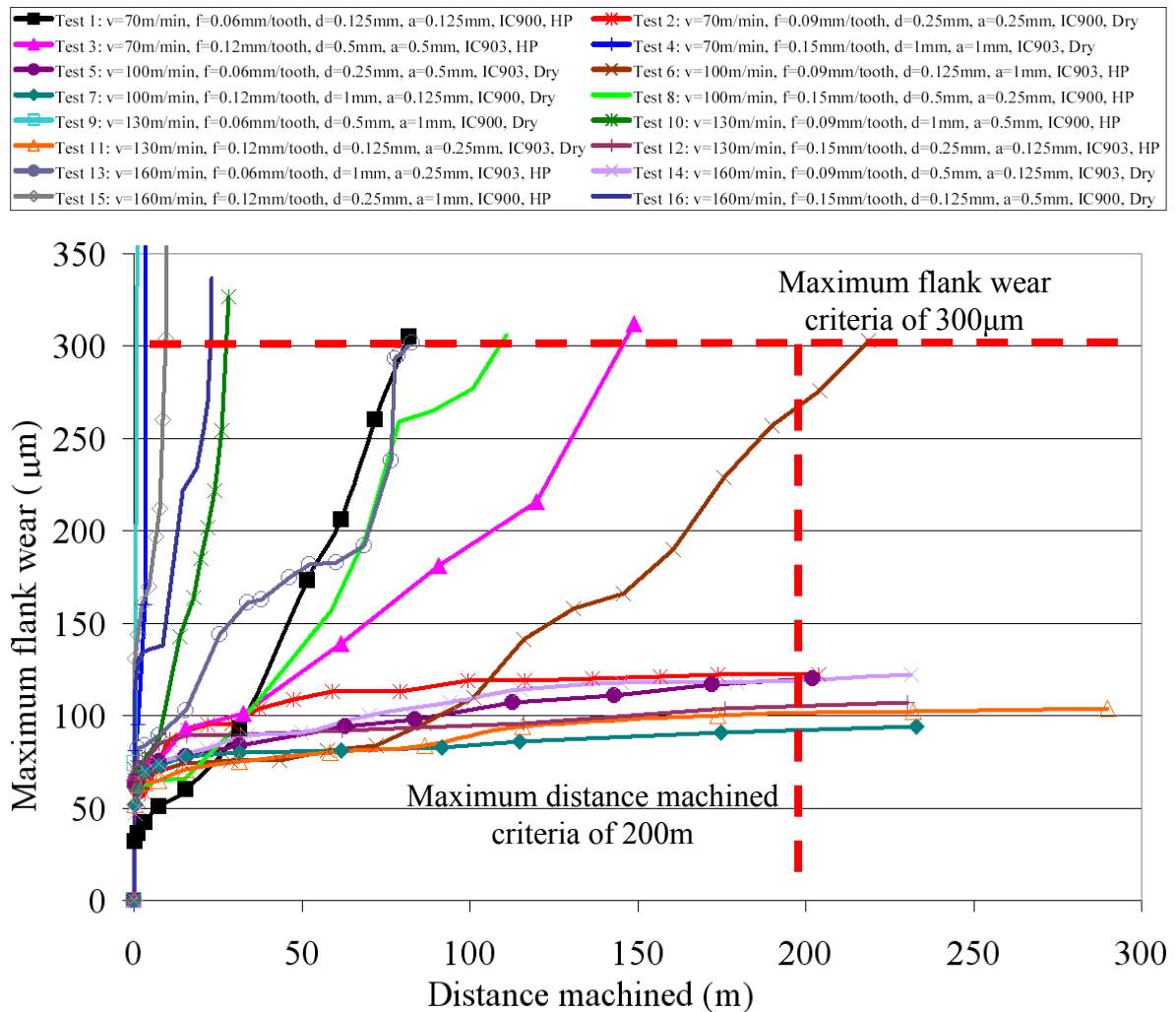


Figure 4.1: Maximum flank wear against distance machined for all tests (Phase 1A)

Additional graphs showing maximum flank wear against machining time and volume of workpiece material removed are detailed in Appendix C, Figures C1 and C2 respectively. A graph of distance machined against material removal rate is shown in Figure 4.2 whilst Figures C3 and C4 in Appendix C show graphs of machining time and material removed against material removal rate. Results showed a reasonable level of consistency between all three graphs and as expected, long tool life was generally achieved at a low material removal rate with much shorter tool life at a higher material removal rate. The region below a material removal rate of $\sim 500 \text{ mm}^3/\text{min}$ was observed to provide optimum operating conditions with tool life of over 200m machined and a volume of workpiece material removed of over 20000 mm^3 . All tests which did not reach the maximum flank wear criterion, $VB_{\text{max}}=0.3 \text{ mm}$, were below a material removal rate of $500 \text{ mm}^3/\text{min}$.

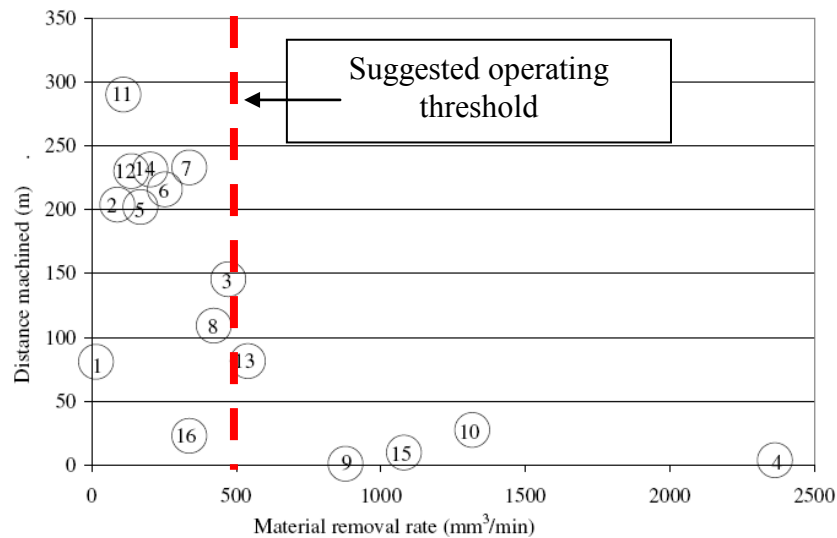
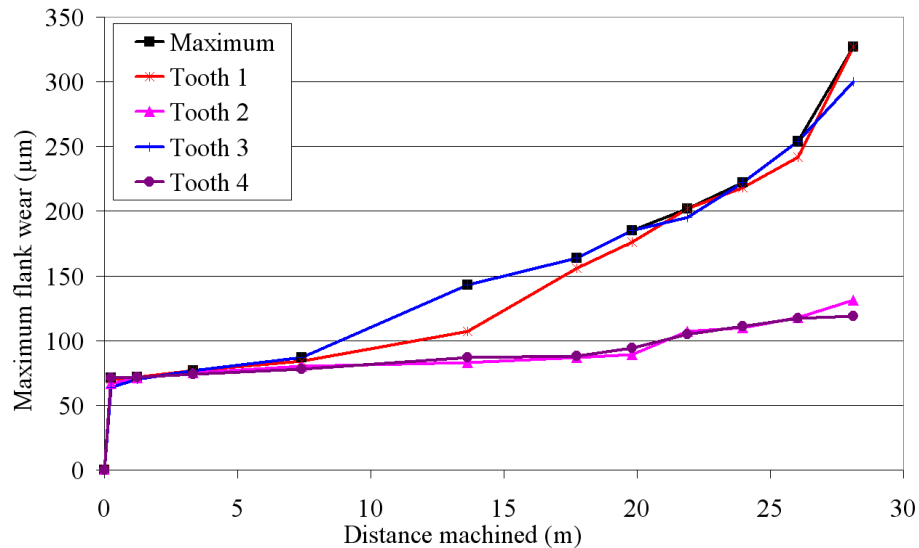


Figure 4.2: Distance machined against material removal rate (Phase 1A)

Individual graphs showing maximum flank wear against distance machined for selected tests are shown in Appendix C, Figures C5 to C13. Shaw [30] suggests that a typical wear curve starts with a period of heavy initial wear followed by a period of steady wear before increasing wear and catastrophic failure of the cutting edge. The initial period of heavy wear was observed for all tests, with maximum flank wear of between 30 and $150 \mu\text{m}$ seen after a relatively short distance machined. Several of the tests showed the period of steady then catastrophic wear including Tests 4 and 15 shown in Figures C4 and C12 respectively. The tests that were stopped because they reached a distance machined of 200m would probably exhibit the typical profile if they had been allowed to continue. Test 2 was one of these tests and its wear profile, Figure C6, showed an initial period of heavy wear which resulted in the

tool having a maximum flank wear of $\sim 50\mu\text{m}$ after a distance machined of $\sim 1\text{m}$. Over the next $\sim 100\text{m}$ the maximum flank wear rate reduced until a plateau was reached. Doody [103] details ball nose end milling of the γ -TiAl alloy Ti-45Al-2Mn-2Nb +0.8%vol. TiB_2 with a workpiece tilt angle of 45° . The ‘best’ result achieved was a maximum distance machined of only $\sim 120\text{m}$ for a maximum flank wear criteria of $300\mu\text{m}$. Operating parameters to reach this result are detailed as finishing parameters with axial and radial depths of cut of only 0.2mm , along with a cutting speed of 93m/min and a feed rate of 0.12mm/tooth . The increased performance in terms of distance machined with the current work can be attributed to developments in cutting tool technology including the use of a finer grade carbide substrate, alternative geometry and the TiAlN coating which showed improved hardness and oxidation resistance in addition to the difference between the two γ -TiAl alloys.

In general, the majority of tests showed consistent tool wear over the four cutting edges of each cutting tool, however, several of the tests including Tests 3 and 10 using a higher axial depth of cut of 1mm showed extensive wear on odd numbered cutting edges whilst even numbered cutting edges had a reduced level of wear. A graph showing maximum flank wear against distance machined for Test 10 is detailed in Figure 4.3 and shows that when the maximum flank wear criteria of $300\mu\text{m}$ was achieved, the difference in flank wear level between odd and even numbered cutting edges was $\sim 160\mu\text{m}$.



Test 10: $v=130\text{m/min}$, $f=0.09\text{mm/tooth}$, $a=1.0\text{mm}$, $d=0.5\text{mm}$, IC900, HP

Figure 4.3: Maximum flank wear against distance machined for Test 10

Figure 4.4 shows selected wear scar photographs for Test 10 whilst Appendix C, Figures C14 to C22 show selected wear scar photographs for other tests. The vast majority of tests

exhibited uniform flank wear (VB 1) (see Figure 2.12) at the start of the tests with non-uniform flank wear (VB 2), localised flank wear (VB 3) and in some instances catastrophic failure (CF) towards the end of the test as the tool reached the test end criteria. Only one instance of possible chipping (CH 1) was observed for Test 13, shown in Figure C20. No other instances of chipping were observed, nor were any visible cracks on any cutting edges. Possible adhered workpiece material was seen on every test, with in general, the highest levels when cutting dry with higher levels of operating parameters. Assessment of the wear scar photographs for Test 10, Figure 4.4 showed flank wear was initially uniform (VB 1) across the wear land on all four cutting edges, however after a distance machined of $\sim 15\text{m}$ had been machined, non uniform flank wear was observed on odd numbered cutting edges whilst uniform flank wear continued on even numbered cutting edges. The photographs taken at the end of the test after a distance of 28.12m show CF had occurred in one region of the odd numbered cutting edges whilst VB 1 was still evident on even numbered cutting edges. Test 4 showed a similar type of wear behaviour however the higher operating parameter levels used caused fracture of all four cutting edges.

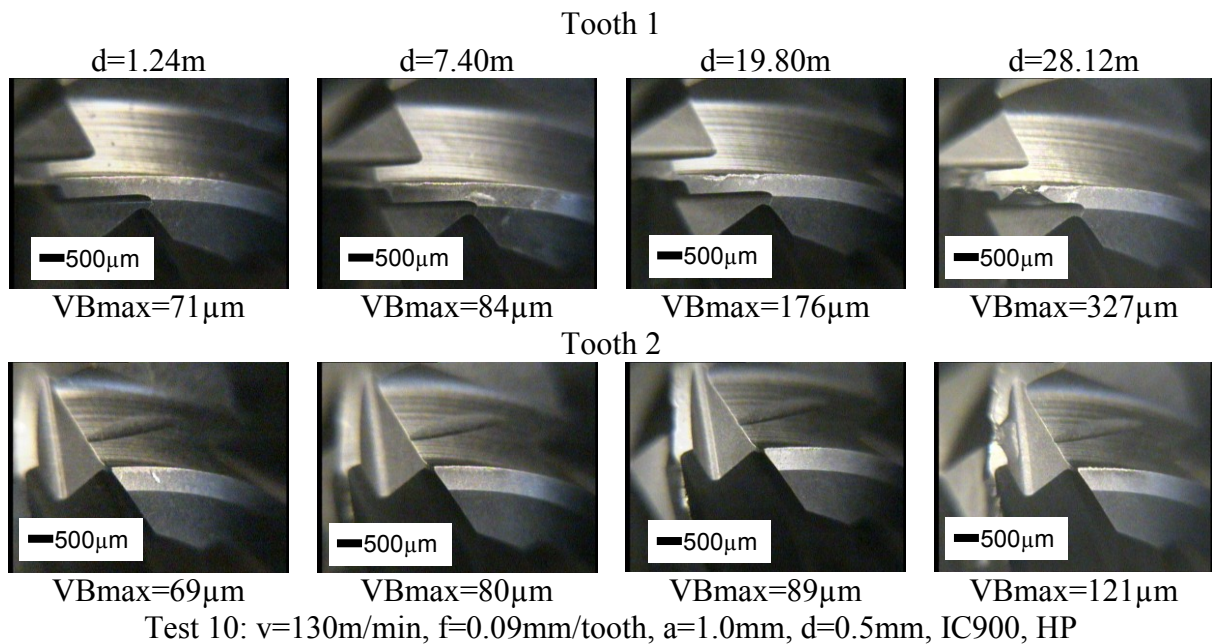


Figure 4.4: Test 10 wear scar photographs

Examination of the ball nose end mills used for this project showed that there was a region of the cutting edge present on odd numbered cutting edges that were not present on even numbered cutting edges, see Figure 4.5. Tooth 1 and 3 (odd) number edges join at the centre of the ball whereas Tooth 2 and 4 (even) numbered do not. The design of the cutter is further illustrated in Figures 4.6 and 4.7 which show side views of the cutting edges. These figures

also show the machined workpiece surface, the axial depth of cut, the tool feed direction and the stepover direction.

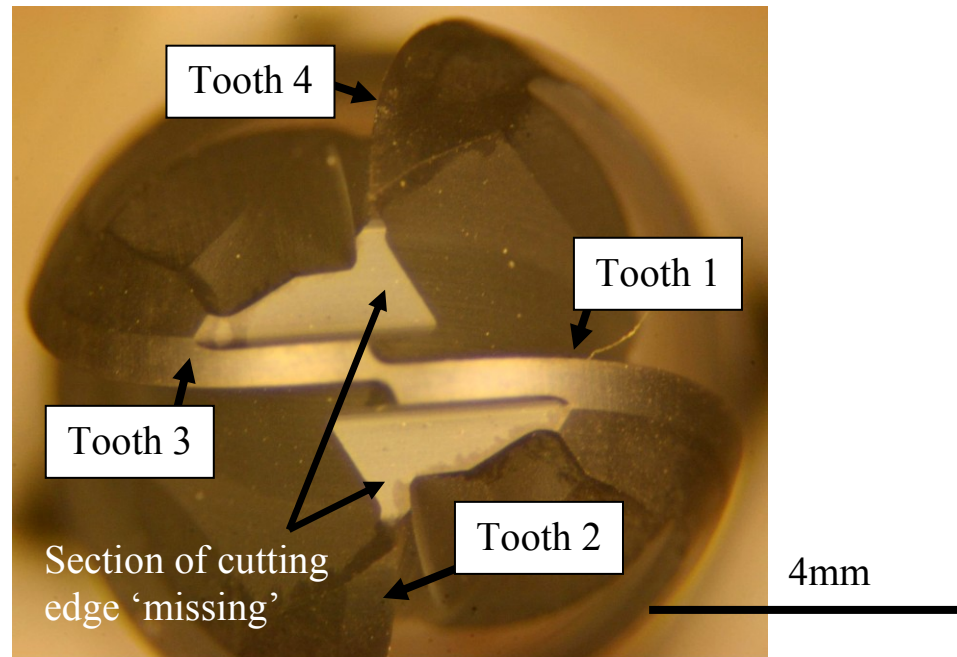


Figure 4.5: View of ball nose end mill showing four cutting edges

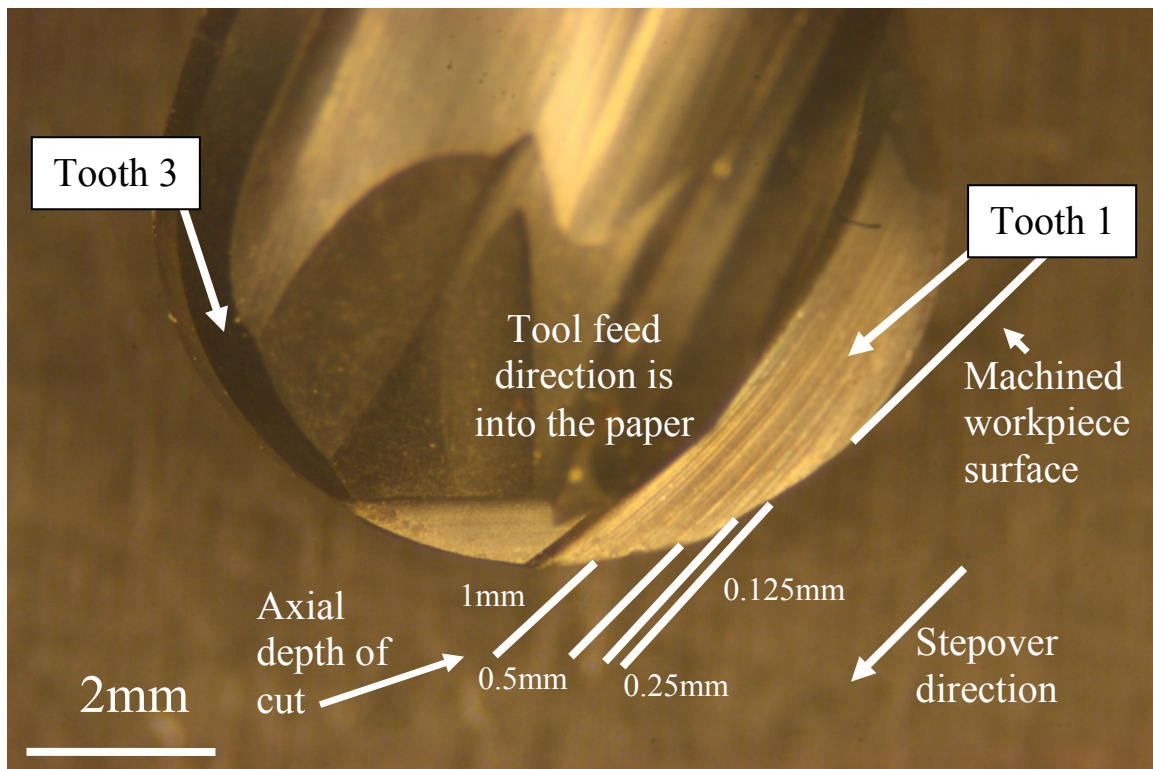


Figure 4.6: Side view of the cutters (Tooth 1 and 3 (odd))

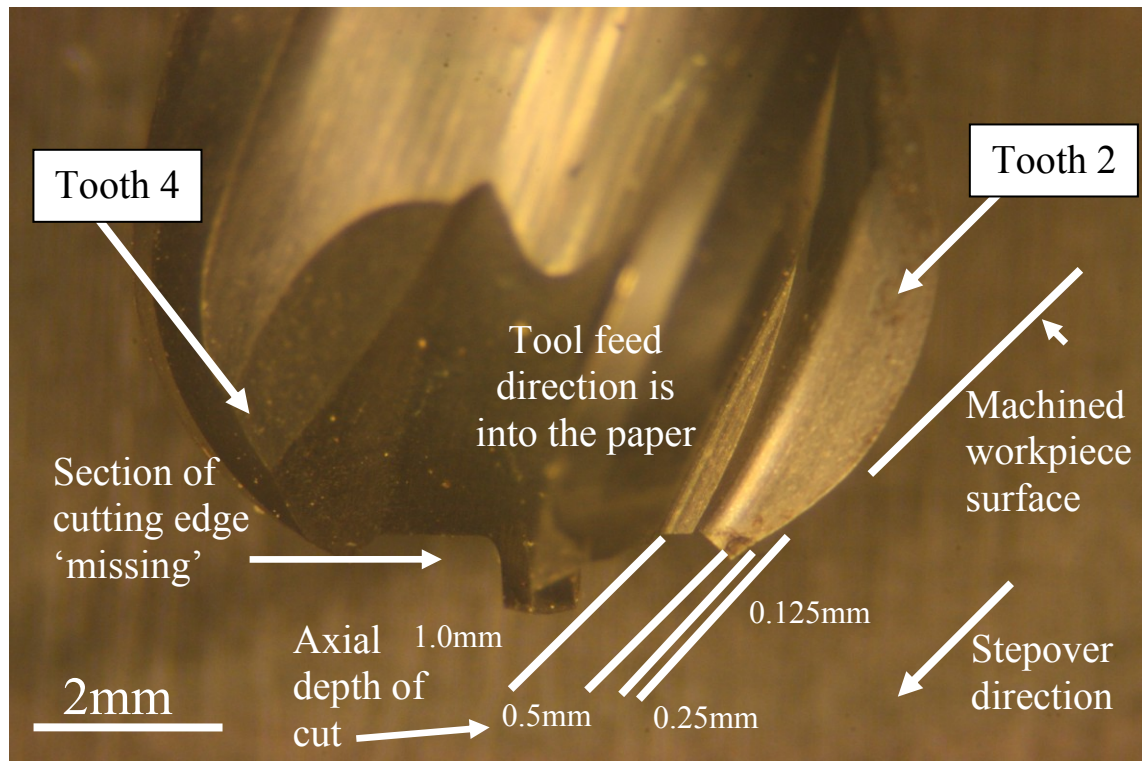
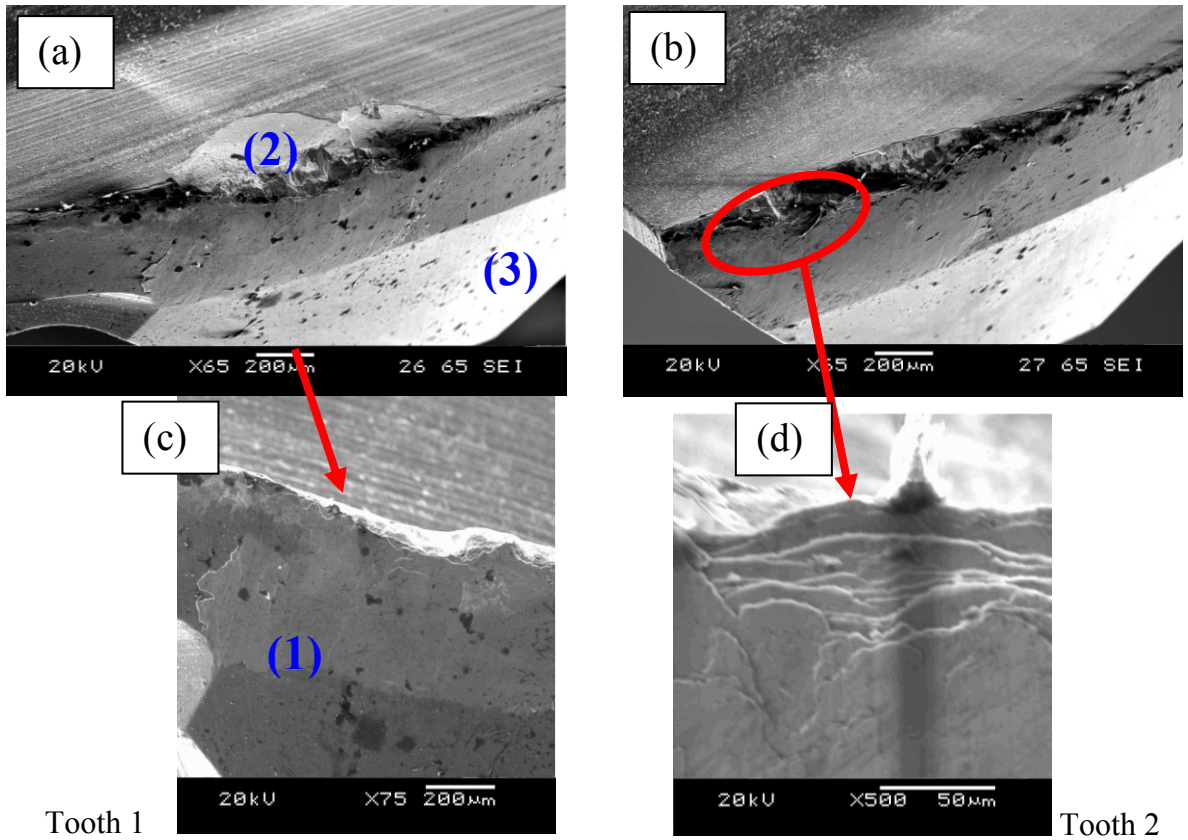


Figure 4.7: Side view of the cutting tool (Tooth 2 and 4 (even))

When a depth of cut of 1mm was used, the feed rate per tooth on odd numbered cutting edges was effectively doubled in the region where the cutting edge was missing, see Figures 4.6 and 4.7. This resulted in an increase in undeformed chip thickness which is proportional to the feed rate [29]. As a consequence the force on the cutter tooth increased [29] and explains why heavy wear and subsequent failure of the cutting edge was observed in the wear scar photographs, see Figure 4.4. At lower depths of cut, the feed rate per tooth over all four cutting edges was uniform and this type of wear was not observed.

Assessment of selected cutting tools was undertaken using a scanning electron microscope (SEM) to provide higher magnification. The results are shown in Figure 4.8 for Test 9 and Figures C23 to C27 in Appendix C. In addition, to the visible wear types observed using optical microscopy, the SEM images showed rake face wear consisting of stair-formed face wear (KT 2) and not notch wear (KT 1) on several of the cutting tools. SEM images for Test 9 show a possible region of adhered material on the flank face of the tool however limited visible adhered material on the rake face of the cutting tool which made measurement of flank wear extremely difficult. The adhered material on the flank face appears to be built up in several layers. In some cases it has been shown that adhered material can help provide a protective layer to the surface of the cutting tool [29]. Energy Dispersive Spectrometry (EDX)

was performed on the adhered material for confirmation. Figure 4.9 shows EDX traces with the graphs corresponding to region (1), (2) and (3) from Figure 4.6 (a) and (c).



Test 9: $v=130\text{m/min}$, $f=0.06\text{mm/tooth}$, $a=0.5\text{mm}$, $d=1.0\text{mm}$, IC900, dry

Figure 4.8: SEM images of cutting tools from Test 9

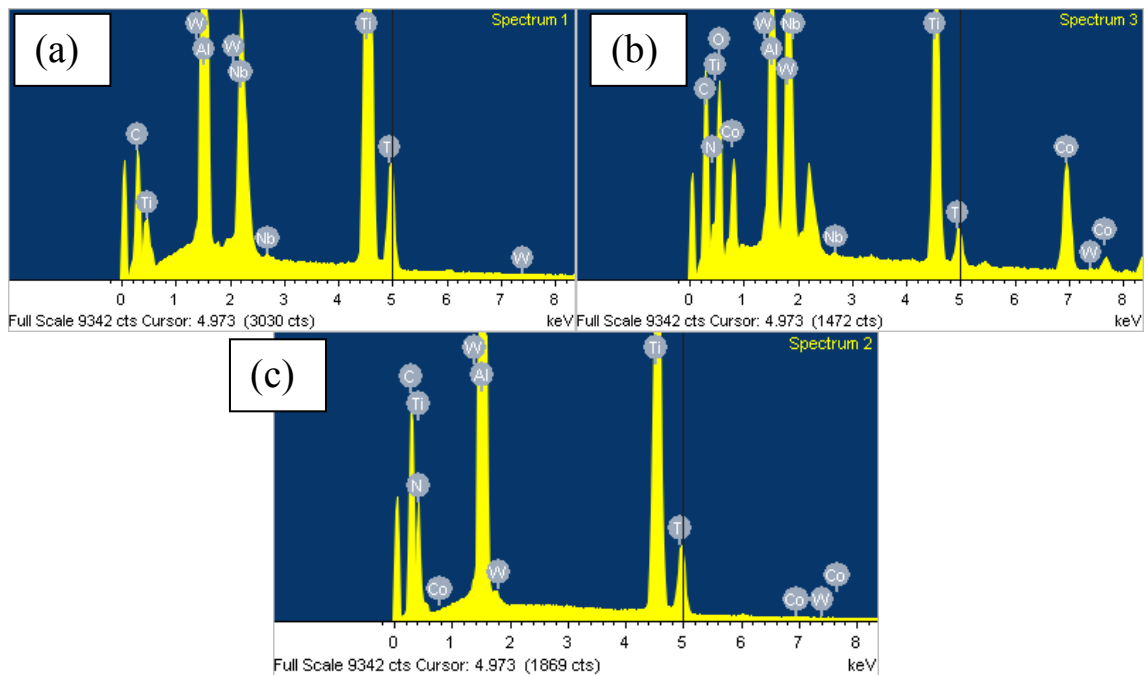


Figure 4.9: EDX analysis of worn tools used in Test 9. From Figure 4.8 (a) and (c): (a) Region 1, (b) Region 2, (c) Region 3

In region (1) niobium material was present indicating that the adhered material was indeed from the workpiece. Region (2) on the rake face showed removal of AlTiN coating with limited adhered material, as well as WC and Co substrate material. An unworn area of the cutting tool, region (3) was analysed for a baseline. This area of the tool showed the presence of the AlTiN (coating) and tungsten carbide with a cobalt binder phase. No niobium was present indicating that there was no adhered workpiece material on this section of the tool.

End milling Ti-45Al-2Mn-2Nb +0.8%vol. TiB₂ is detailed by Mantle and Aspinwall [100] with tool flank wear detailed as being typically uniform (VB 1) at the start of the test, becoming less uniform as wear increased. Wear was concentrated at the tool edge as stair formed rake face wear (KT 2) and not crater wear (KT 1). A built up layer of workpiece material which made tool life measurement extremely difficult was found on both the flank and rake faces. Chipping that was found to contribute to tool wear was also observed, however no comb cracks (CR 1), parallel cracks (CR 2) or irregular cracks (CR 3) were observed. Current work showed almost identical trends including the adhered material and stair formed face wear. The instances of CF in the present work were not reported to have occurred in previous work and were a consequence of the cutting tool design and the high operating parameters including feed rate and axial and radial depth of cut that were used with the current work.

It was clear from the wear scar photographs and SEM images that several different wear mechanisms were evident including both attritious and diffusive wear however it was difficult to establish conclusions as several different operating parameters changing between each test. At low cutting speeds and material removal rates similar to those detailed for Test 2, cutting temperatures would be expected to be lower and therefore thermal damage wear mechanisms such as diffusive wear and plastic deformation should be low so that mechanical damage and attritious wear predominate. As the cutting speed and material removal rate were increased, (although axial depth of cut was kept low) it was anticipated that diffusive wear should increase [47] and tool life reduce and this was the case in Tests 15 and 16, where a cutting speed of 160m/min was used. Ginting and Nouari [165] suggest when ball nose end milling Ti-6242S using dry cutting, that visible wear of the alloyed carbide tool used for lower operating parameters was predominately VB1 with an adhesive wear mechanism predominating. For higher operating parameters visible wear was mostly VB3 which was followed by plastic deformation and brittle fracture. It was suggested that besides adhesive wear dissolution-diffusion also occurred [165]. Jawaaid et al. [166] when face milling Ti-6Al-4V using coated WC inserts suggest that coating delamination was found to be the initial wear

mechanism even after 10s of machining, which may be responsible for the heavy initial flank wear observed with the current work. Once the coating had been removed tool wear was found to involve a complex combination of adhesion of workpiece material to the flank face, attritious wear with the removal of grains of tool material and diffusion between the tool and workpiece together with plastic deformation at the cutting edge. They suggest that diffusion wear was present even at a low cutting speed of 55m/min as indicated by smooth wear at the flank and rake faces.

Very fine needle chips were produced for all tests as a consequence of the low room temperature ductility (<2%) of γ -TiAl alloys [29]. A similar type of chip was reported by both Mantle and Aspinwall [100] and Doody [103].

The Main Effects Plot - means for distance machined, is shown in Figure 4.10 and established using the results detailed in Figure 4.1 with a distance of 200m used for tests that did not reach the maximum flank wear criteria. In order to achieve the longest distance machined a cutting speed of 100m/min, a feed rate of 0.09mm/tooth an axial depth of cut of 0.25, a radial depth of cut of 0.125mm, IC903 cutting tool and dry machining should be used.

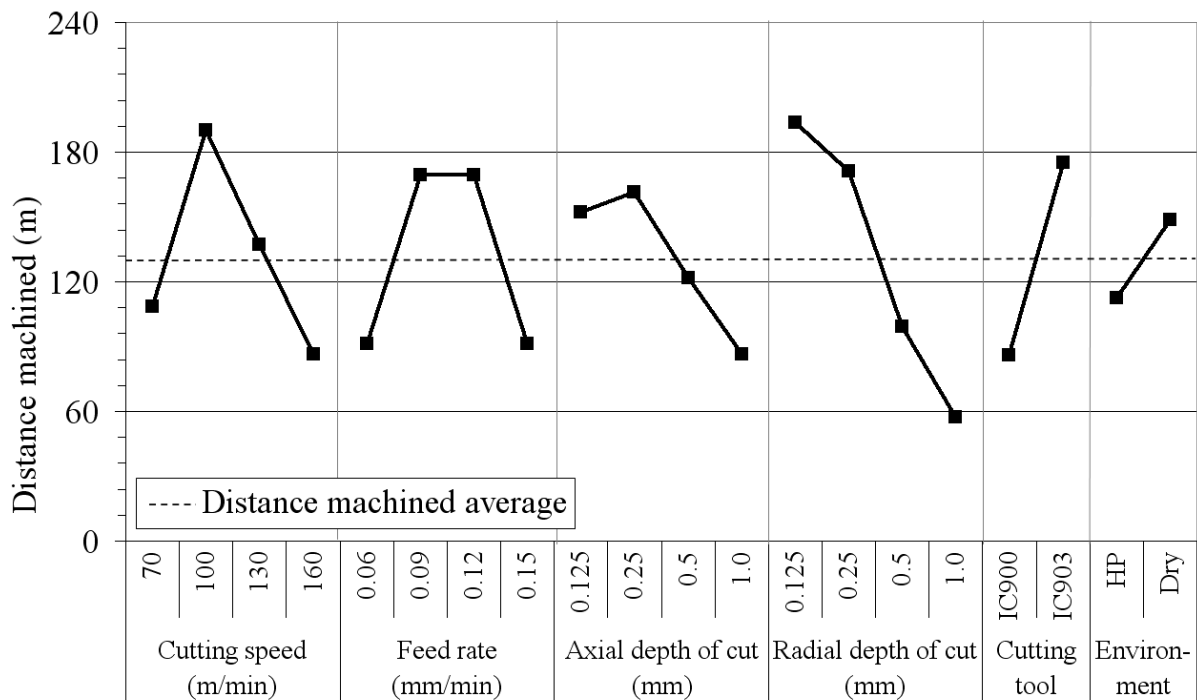


Figure 4.10: Main Effects Plot - means for distance machined

An increase in cutting speed in the range of 100-160m/min caused a reduction in the distance machined. Cutting speed is generally considered to have the most considerable influence on tool life [97] and an increase is likely to cause an increase in cutting temperature [29]. Figure

2.16 details the Main Effects Plot - means for distance machined for end milling of Ti-45Al-2Mn-2Nb +0.8%vol. TiB₂ [100] and shows that increasing the cutting speed from 70m/min to 120m/min caused a reduction in distance machined from on average 13m to 3m. In addition, the Taylor tool life curve in Figure 2.17 shows a similar trend with a reduction in tool life at higher cutting speeds. It was difficult to explain the low value for distance machined at 70m/min as the cutting temperature should be the lowest for this cutting speed. It is possible that this result could be unrepresentative due to the reduced number of tests performed as part of the Taguchi experimental design, furthermore not all tests reached identical end criteria.

Figure 4.10 shows that the preferred feedrate to give the longest distance machined was between 0.09mm/tooth and 0.12mm/tooth. Tool life when machining steels is generally considered to be affected more by cutting speed than feed rate however, titanium alloys are deemed to be very sensitive to changes in feed rate [97]. Operation at higher feed rates is generally recommended as it is often desirable to increase productivity. Lopez de Lacalle et al. [167] suggest an optimum feed rate for distance machined within the range of 0.08 and 0.12mm/tooth when end milling Ti-6Al-4V. At a higher feed rate, thicker chips cause an increase in the cutting loads and thus cutting temperatures. The affect of increasing either axial or radial depth of cut on the distance machined was almost identical and caused a reduction in distance machined. Increasing both of these parameters will cause an increase in the chip thickness, cutting forces and temperature, thus reducing tool life. Ezugwu [97] suggests that this effect occurs when turning titanium alloys and results in a decrease in tool life. As with cutting speed, Figure 2.16 shows similar trends, with increasing either axial or radial depth of cut from 0.2mm to 0.5mm causing a reduction in tool life [100].

The IC903 cutting tool with the finer grade carbide substrate (0.3-0.5 μ m) outperformed the IC900 cutting tool which had a grain size of 0.8 μ m. Improved performance was found by Perez [110] when face milling γ -TiAl using a micrograin WC tool when compared to a coarse grain tool. Shaw [30] suggests that the finer the grade of carbide, the higher the wear resistance and hardness. In addition, Antoniadis et al. [168] studied the fatigue properties of cemented carbides and found that hardmetals having a finer WC grain size possessed improved fatigue behaviour. These reasons are likely to be the cause of the improved performance with the IC903 cutting tool. Thermal shock was probably responsible for the reduced tool life using HP fluid despite the absence of cracks on the cutting edges. A similar trend has been reported where a 15% increase in tool life was achieved with dry cutting over HP fluid application [100].

Composite Main Effects Plots - means for machining time and means for volume of workpiece material removed are shown in Appendix C, Figure C28. In general, the graphs give similar trends to that of the Main Effects Plot - means for distance machined, except for axial and radial depth of cut and cutting environment in respect of material removed.

The Analysis of Variance (ANOVA) table for distance machined is shown in Table 4.1 whilst ANOVA tables for machining time and volume of workpiece material are shown in Appendix C, Tables C1 and C2. As $F_{0.05;3;1} = 216$ and $F_{0.05;1;1} = 161$ [154] none of the factors for either of the three output measures were determined as being statistically significant at the 5% level. The Percentage Contribution Ratios (PCR (%)) to some extent matched the Main Effects Plot with depth of cut having the highest PCR (%) value for both output measures. The residual error PCR (%) for distance machined and machining time were 9.42 and 6.24 which was lower than the value of ~15% or less that Ross [154] suggests for acceptable noise. The extremely high value of 53.10% for material removed indicates that either important factors were omitted, conditions were not precisely controlled, measurement error was excessive or interactions were present [154]. Interactions diagrams of which Figure C29 in Appendix C for distance machined is an example, showed crossover indicating that there were interactions between factors.

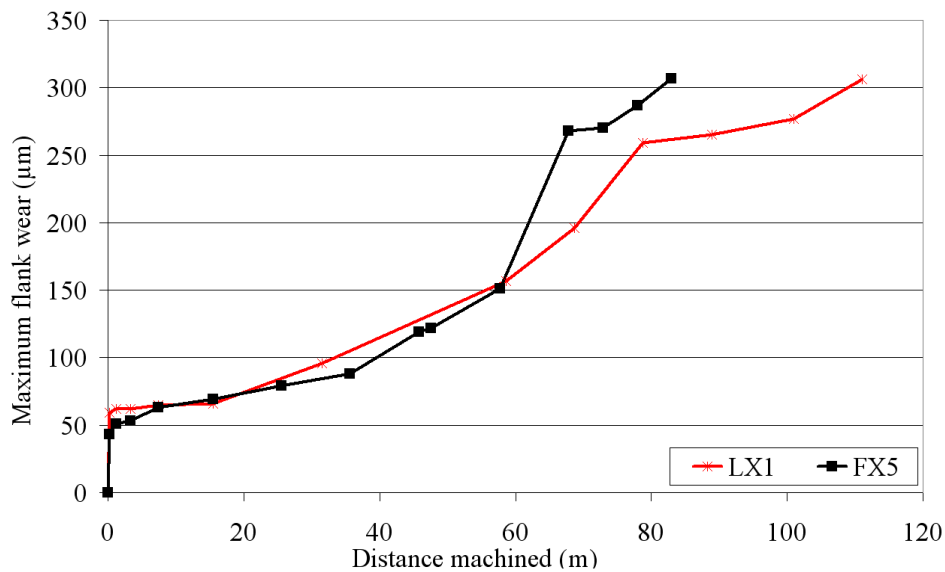
Source	SS	DOF	MSS	F _{calc}	PCR (%)
Cutting speed	24097	3	8032	4.00	14.81
Feed rate	24467	3	8156	4.06	15.06
Axial depth of cut	13842	3	4614	2.30	7.94
Radial depth of cut	47810	3	15937	7.94	30.71
Cutting tool	31718	1	31718	15.80	19.92
Cutting fluid	5190	1	5190	2.59	2.13
Error	2007	1	2007	-	9.42
Total	149132	15	-	-	-

Table 4.1: ANOVA table for distance machined (Phase 1A)

Confidence intervals were not established due to the enforced use of a distance machined tool life criteria, which could to some extent, cloud the statistical analysis. If the distance machined tool life criteria had not been used and the tests which typically used lower operating parameters had been allowed to reach a maximum flank wear criteria of 300µm, then ANOVA may have shown that more factors were statistically significant at the 5% level in accordance with the work of Mantle and Aspinwall [100]. They used similar operating parameters to the current work and established that cutting speed, feed rate, axial and radial

depth of cut and fluid application were statistically significant at the 5% level when end milling Ti-45Al-2Mn-2Nb +0.8%vol. TiB₂.

Selected replication was performed in order to determine the effect of changing the machine tool on tool life and involved five tests from the Taguchi L16 fractional factorial array. Figure 4.11 shows the graph of maximum flank wear against distance machined for Test 8 whilst additional graphs for the other 4 replicated tests are shown in Appendix C, Figures C30 to C33.



Test 8: $v=100\text{m/min}$, $f=0.15\text{mm/tooth}$, $a=0.5\text{mm}$, $d=0.25\text{mm}$, IC900, HP.

Figure 4.11: Maximum flank wear against distance machined for Test 8

All graphs showed similar trends for both the original test and its replication, irrespective of the machine tool used, with in general, tests using the FX5 (collet holders) showing slightly reduced tool life over tests performed with the LX1 (shrink fit). This was probably due to the lower tool runout ($<3\mu\text{m}$) when compared to the collet holder ($<3\mu\text{m}$ as opposed to $<10\mu\text{m}$).

b) Cutting forces

Figure 4.12 shows composite Main Effects Plots - means for F_x , F_y and F_z respectively for a tool in the new condition. As expected increasing the material removal rate, by increasing either the feed rate or axial and radial depth of cut, caused each force component to increase by up to 400% in some cases. This was most evident for the axial depth of cut, mainly because of the high range of values chosen (0.125mm to 1.0mm). Cutting force was measured to be highest at the lowest cutting speed of 70m/min. This increase in force over the other cutting speeds may have caused the slight reduction in tool life observed at a cutting speed of

70m/min. Changing the cutting tool appeared to have a limited effect on the cutting force. This was expected as only the substrate material was different between the two tools (no tool geometry or coating changes). As all measurements were taken with a new tool, cutting tool flank wear was not able to affect the results. Using high pressure cutting fluid increased the F_y and F_z forces by $\sim 10\%$ and was probably caused by the twin jets impinging on the workpiece, as it was mounted at 45° in this experiment. A marginal increase in cutting force in the x direction was observed. This was because of the location of the twin jets, shown in Figure 3.5 (a) where the force caused by the jets effectively cancelled each other out.

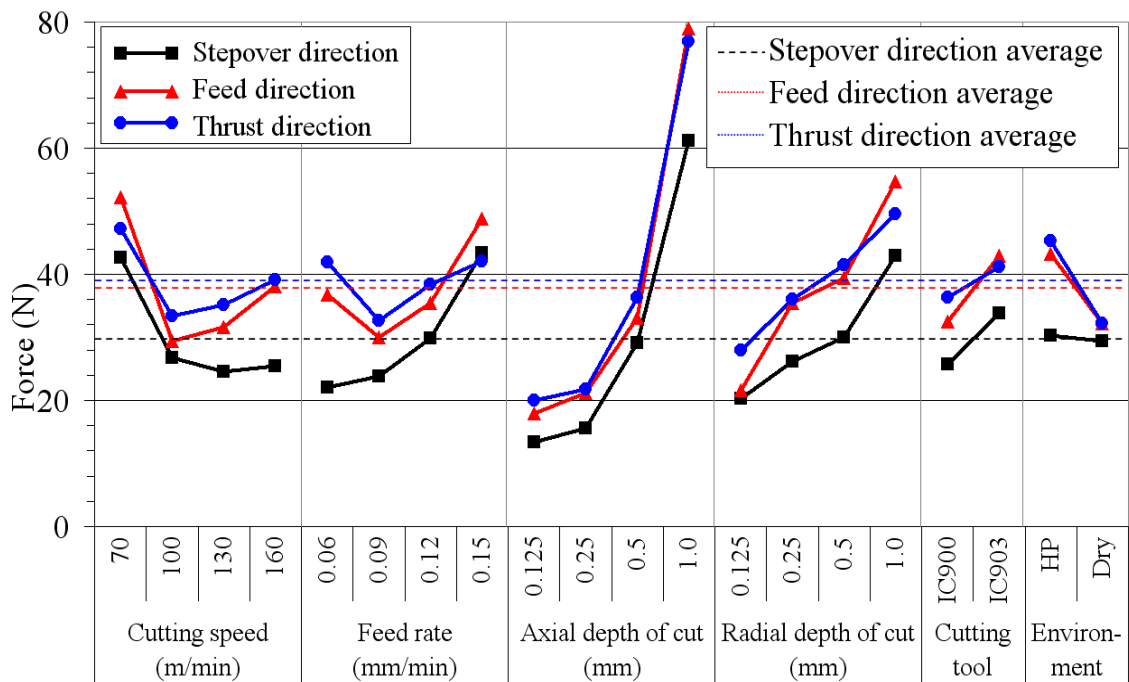


Figure 4.12: Main Effects Plot - means for forces

Cutting force evaluation when ball nose end milling Ti-45Al-2Mn-2Nb +0.8%vol. TiB_2 is presented in [104]. For new tools, forces were within the range of 25N to 45N, using a cutting speed of 120m/min, a feed rate of 0.12mm/tooth, an axial & radial depth of cut of 0.2m and dry cutting. The average force levels from the Main Effects Plot were within the range of 30N to 40N and were similar to those obtained for previous ball nose end milling of a γ -TiAl alloy when the effect of using a higher axial and radial depth of cut of 1mm with the current work are taken into account. ANOVA for the forces in the three directions are given in Tables 4.2, 4.3 and 4.4 respectively. The only significant factors at the 5% level, identified from the statistical analysis, were the axial and radial depths of cut for F_z . All other factors were deemed to be non significant at the 5% level with no statistical difference between factors. Residual error percentage contribution ratios were in the most part low for F_y and F_z with

values of 10.35% and 4.16% obtained. The marginally higher value of 18.20% for Fx over the 15%, may again be due to either important factors being omitted, conditions not being precisely controlled, excessive measurement errors or the presence of interactions [154]. As with ANOVA for tool life it was likely that measurement errors and interactions between factors were responsible.

Source	SS	DOF	MSS	Fcalc	PCR (%)
Cutting speed	878.3	3	292.8	1.00	6.20
Feed rate	1119.6	3	373.2	1.28	8.75
Axial depth of cut	5805.8	3	1935.3	6.64	58.29
Radial depth of cut	1101.0	3	367.0	1.26	8.56
Cutting tool	260.7	1	260.7	0.89	0.00
Cutting fluid	2.6	1	2.6	0.01	0.00
Error	291.6	1	291.6	-	18.20
Total	9459.6	15	-	-	-

Table 4.2: ANOVA table for Fx

Source	SS	DOF	MSS	Fcalc	PCR (%)
Cutting speed	1263.0	3	421.0	1.91	6.99
Feed rate	755.7	3	251.9	1.14	3.59
Axial depth of cut	9544.7	3	3181.6	14.41	62.49
Radial depth of cut	2214.5	3	738.2	3.34	13.36
Cutting tool	436.7	1	436.7	1.98	1.45
Cutting fluid	486.3	1	486.3	2.20	1.78
Error	220.7	1	220.7	-	10.35
Total	14921.6	15	-	-	-

Table 4.3: ANOVA table for Fy

Source	SS	DOF	MSS	Fcalc	PCR (%)
Cutting speed	455.45	3	151.82	34.84	4.16
Feed rate	228.25	3	76.08	17.46	2.06
Axial depth of cut	8395.41	3	2798.47	642.20	77.33
Radial depth of cut	989.90	3	329.97	75.72	9.08
Cutting tool	96.68	1	96.68	22.19	0.85
Cutting fluid	681.60	1	681.60	156.41	6.24
Error	4.36	1	3.36	-	0.28
Total	10851.65	15	-	-	-

Table 4.4: ANOVA table for Fz

c) Workpiece surface roughness

Workpiece surface roughness Ra results are presented in a bar chart, see Figure C34 in Appendix C and the Main Effects Plot - means for workpiece surface Ra, in Figure 4.13. A wide range of surface roughness Ra values, from 0.29 μ m to 3.2 μ m were measured depending

on the operating parameters used. Comparable surface roughness R_a values of $0.6\mu\text{m}$ to $1.2\mu\text{m}$ are reported in [107] for ball nose end milling Ti-45Al-2Mn-2Nb +0.8%vol. TiB_2 with a workpiece tilt angle of 45° whilst values of R_a $0.42\mu\text{m}$ to $0.71\mu\text{m}$ have been reported when high speed ball nose end milling burn resistant titanium (BuRTi), using similar operating parameters to those detailed for Test 2 [150]. The lower level of surface smearing expected with the less ductile γ -TiAl alloy would be expected to have caused the lower values. Figure 4.13 established that radial depth of cut was the most significant factor. An increase from 0.125 to 1.0mm caused a significant increase in workpiece surface roughness R_a by over 600%. This was probably due to the increased spacing of the scallops [169] which are caused when a ball nose end cutter mills the surface. Compared to radial depth of cut, all other factors showed a limited effect on the workpiece surface roughness R_a .

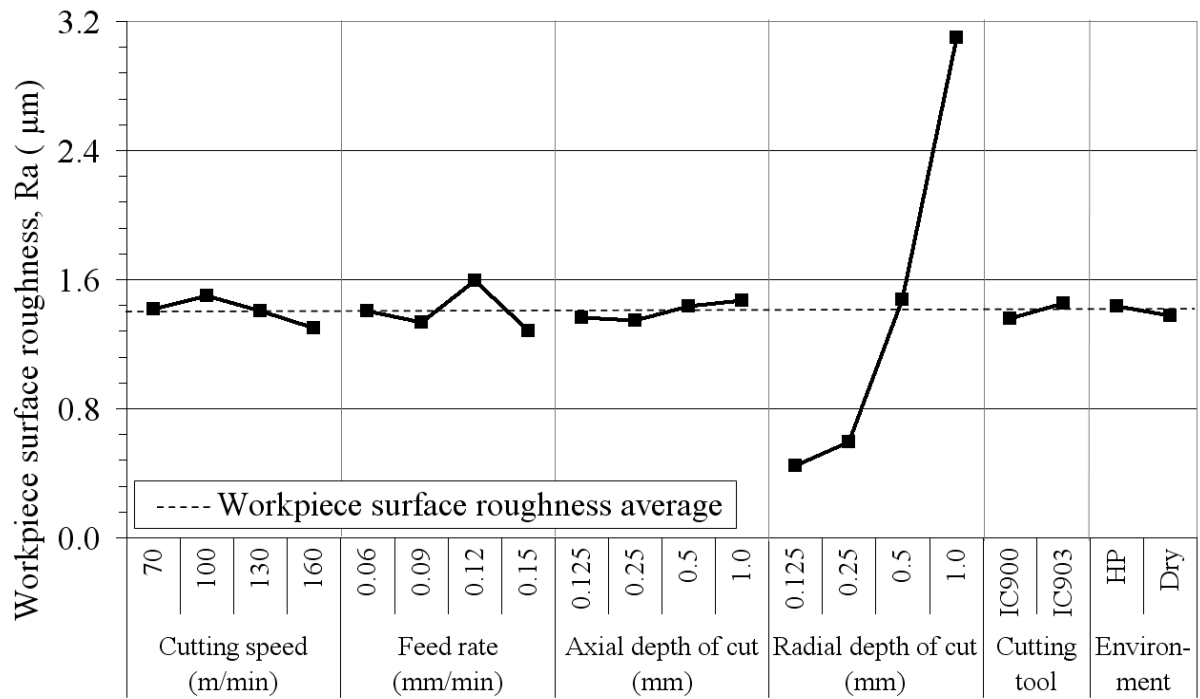


Figure 4.13: Main Effects Plot - means for workpiece surface roughness (Phase 1A)

Not surprisingly given the trends detailed in Figure 4.13, radial depth of cut was the only statistically significant factor at the 5% level. See Table 4.5 for the ANOVA table. In addition the residual error percentage contribution ratio was extremely low with a value of 0.84.

Source	SS	DOF	MSS	Fcalc	PCR (%)
Cutting speed	0.0818	3	0.0273	1.19	0.32
Feed rate	0.2246	3	0.0749	3.27	1.11
Axial depth of cut	0.0396	3	0.0132	0.58	0.09
Radial depth of cut	17.8084	3	5.9361	259.43	97.57
Cutting tool	0.0357	1	0.0357	1.56	0.07
Cutting fluid	0.0151	1	0.0151	0.66	0.00
Error	0.0229	1	0.0229	-	0.84
Total	18.2281	15	-	-	

Table 4.5: ANOVA table for workpiece surface roughness (Phase 1A)

d) Workpiece surface

The quality of the machined workpiece surface was a concern as the low room temperature ductility of γ -TiAl alloys means that producing surfaces that are crack and defect free is extremely problematic [6]. Figure 4.14 shows the surface of the workpiece used for integrity evaluation before the evaluation surfaces had been machined. This surface was prepared using a milling operation with operating parameters including a cutting speed of 70m/min, a feed rate of 0.12mm/tooth, an axial and radial depth of cut of 0.125mm, IC900 tooling and dry cutting. Two complete passes across the block were performed to remove defects and cracking from previous passes. The quality of the surface was a concern as damage was observed consisting of possible fracture/pullout at random locations over the entire surface. There also appeared to be no trend/rationale between the locations of the surface defects, as some areas of the block had an extensive number of defects whereas other areas of the block showed limited damage. Figure 4.15 shows the workpiece surface after machining the 16 surfaces required for the Taguchi L16 experimental design. It was intended to use tools that had reached the maximum flank wear criteria of 300 μ m, however, the tools that were used for Tests 4 and 10 were unsafe to use because high flank wear and fracture of the tool resulted in a danger of stalling the spindle. For surface integrity assessment, new tooling was used as a replacement. All surfaces showed some regenerative effects caused by the previous machining operation to clear the workpiece surface, however in general, tests with the higher operating parameters showed higher levels of damage. Edge chipping was also evident with the intensity depending on the severity of the operating parameters.

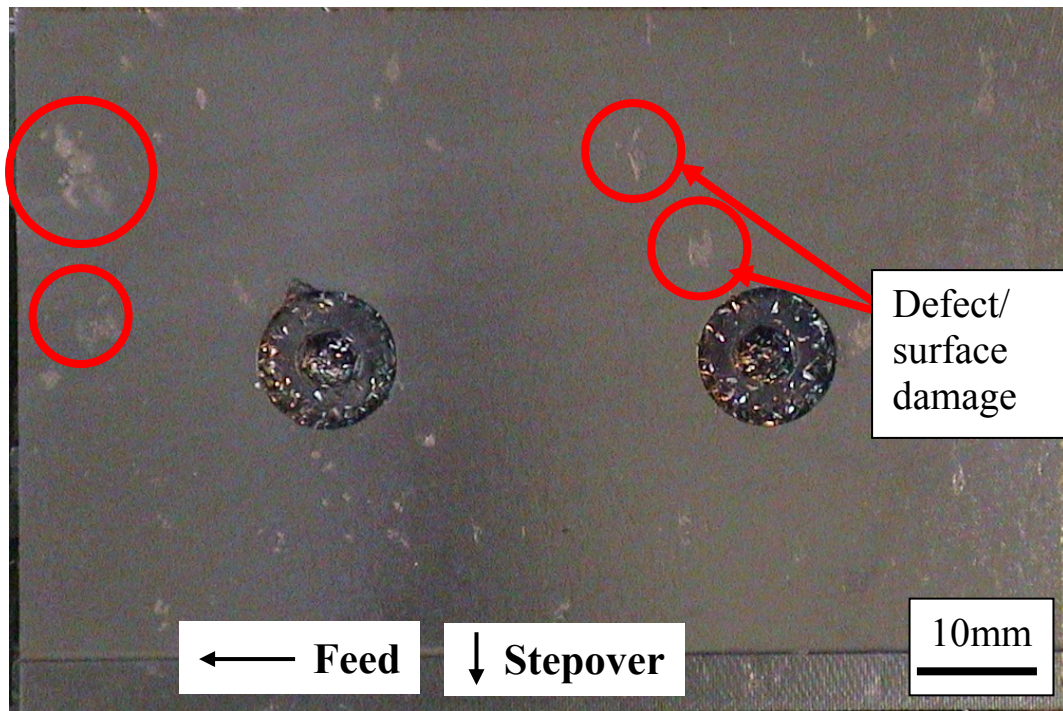


Figure 4.14: Workpiece surface after the initial preparation stage

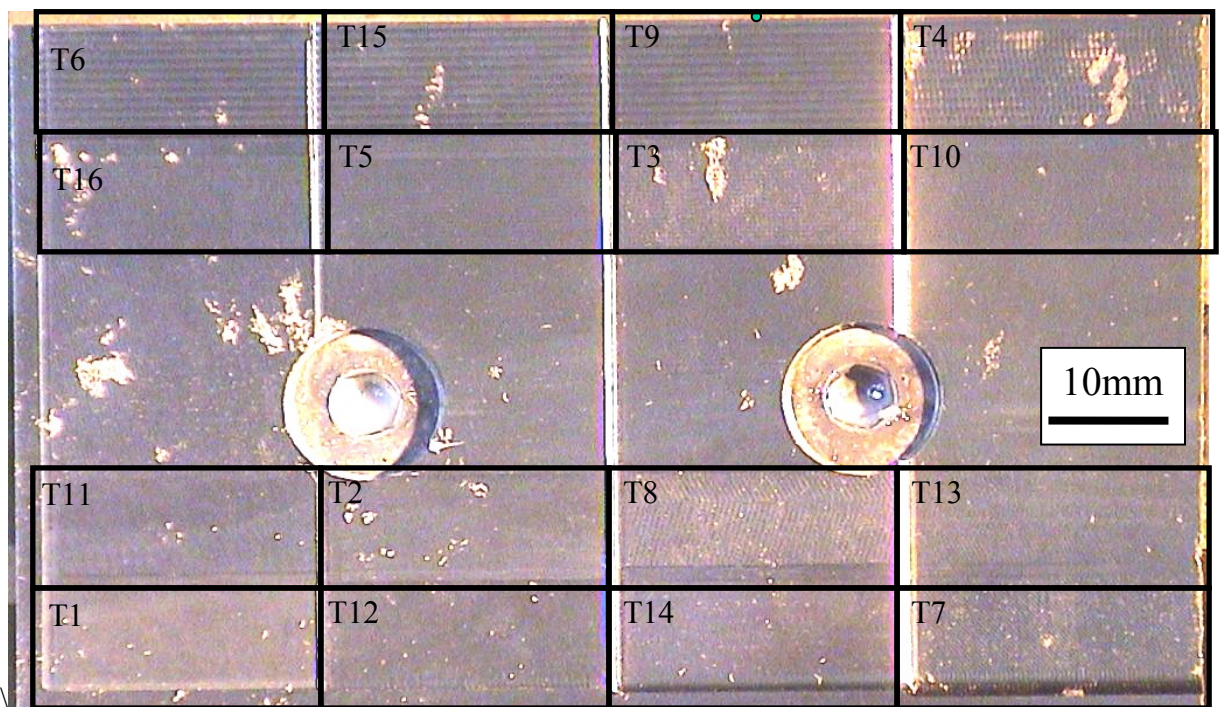
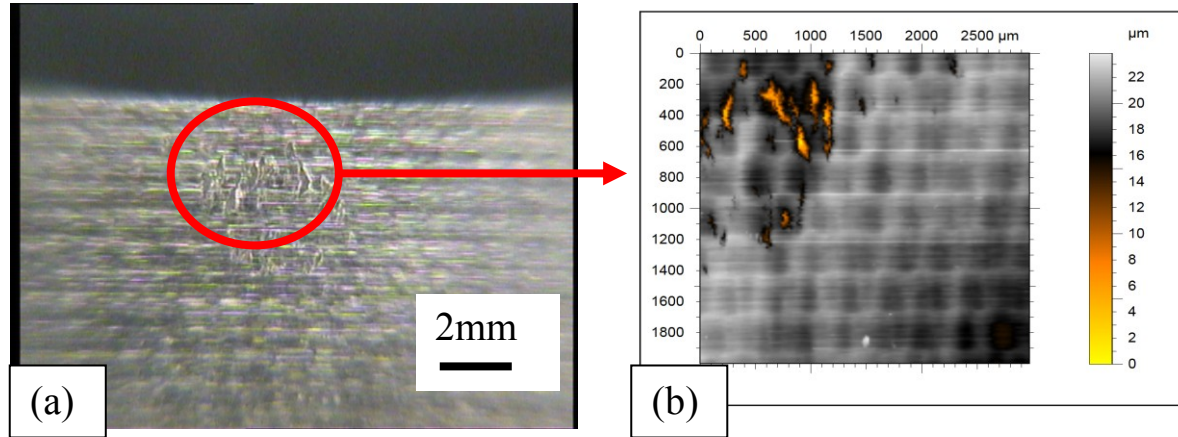


Figure 4.15: Machined workpiece surfaces

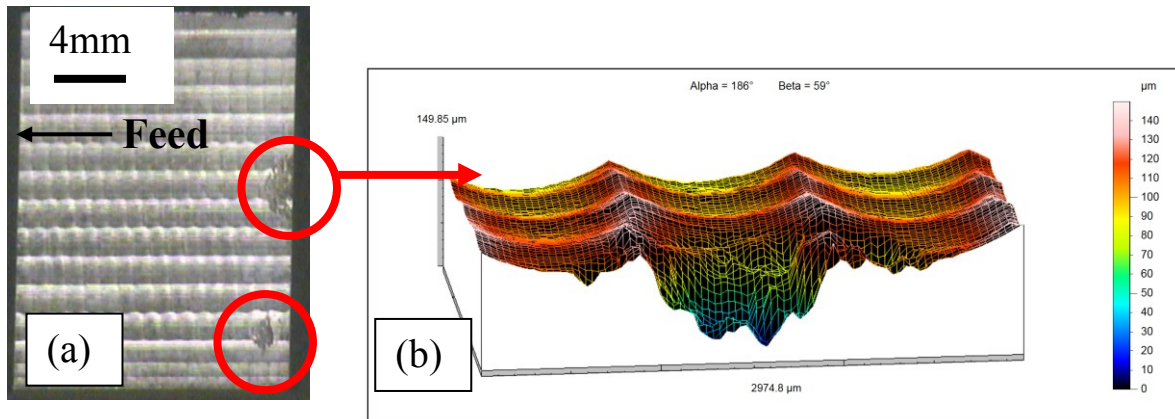
Limited smeared material was observed on machined workpiece surfaces, however some instances of adhered material (chips) were found on surfaces machined using a dry environment. Further analysis of the workpiece surfaces including higher magnification images of the workpiece surface and form talysurf plots in order to determine the depth and

size of the damage are shown in Figures 4.16 and 4.17. The talysurf plot for the surface produced using Test 2 operating parameters, Figure 4.16 (b) shows a region with fracture/pullout up to depth $\sim 22\mu\text{m}$ and a size of $200\mu\text{m}$ by $50\mu\text{m}$. In contrast, the workpiece surface produced by Test 4 operating parameters, see Figure 4.17, showed two regions of fracture/pullout, the largest of which was $\sim 80\mu\text{m}$ deep and had a diameter of $\sim 1\text{mm}$.



Test 2: $v=70\text{m/min}$, $f=0.09\text{mm/tooth}$, $a=0.25\text{mm}$, $d=0.25\text{mm}$, IC900, dry, $\text{VB}_{\text{max}}=122\mu\text{m}$.

Figure 4.16: Machined workpiece surface and surface damage from Test 2

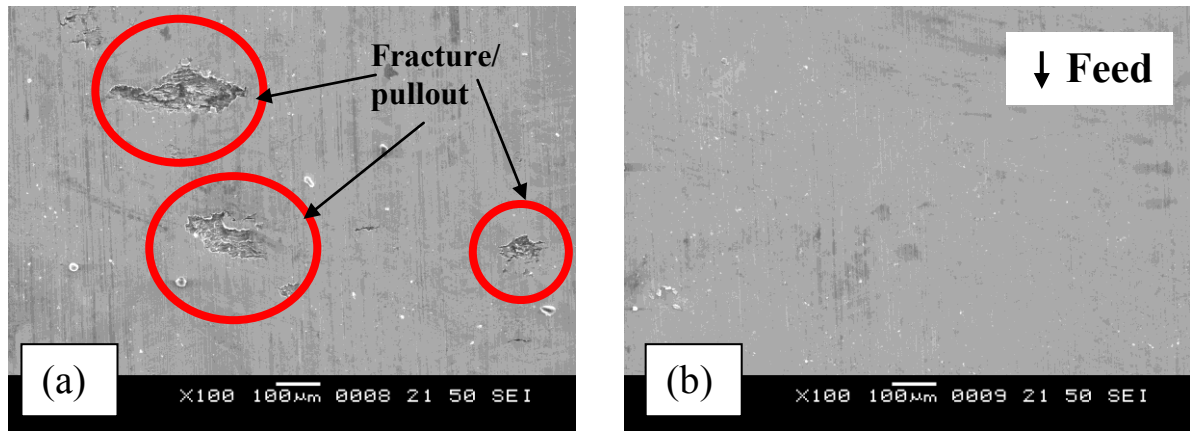


Test 4: $v=70\text{m/min}$, $f=0.15\text{mm/tooth}$, $a=1.0\text{mm}$, $d=1.0\text{mm}$, IC903, dry, new tool

Figure 4.17: Machined workpiece surface and surface damage from Test 4

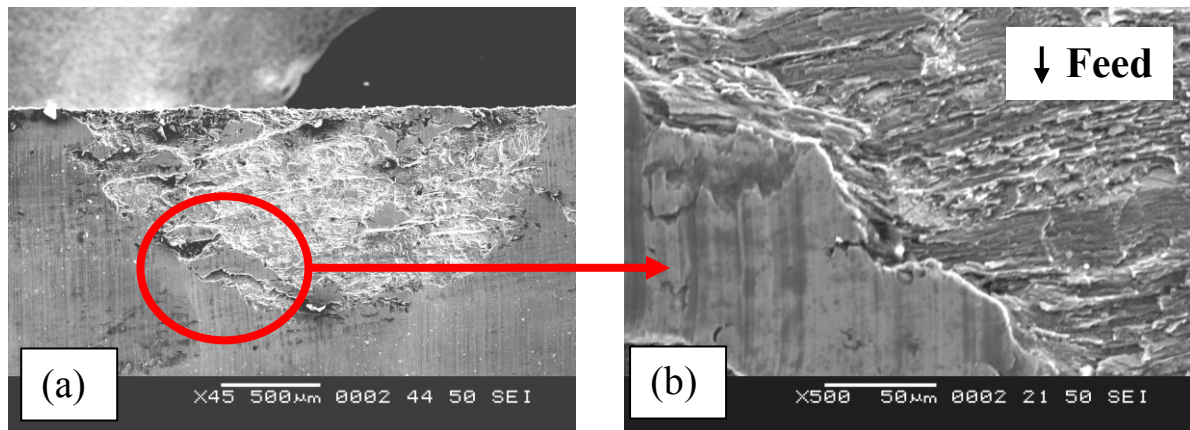
Figure 4.18 details two SEM images of the surface produced using Test 2 operating parameters. The image on the left (a) shows three areas of fracture/pullout with a size of up to $200 \times 50\mu\text{m}$. On the right (b), the surface appears free of damages and defects. This was difficult to explain and no reason could be found as to why one particular area of the surface was prone to defects/damage and why another was not. SEM images of the surface from Test 4 showed extensive fracture/pullout see Figure 4.19. Similar workpiece fracture/pullout was reported by Mantle and Aspinwall [107] to a depth of $<10\mu\text{m}$ from the workpiece surface

when high speed ball nose end milling Ti-45Al-2Mn-2Nb+0.8% vol. TiB₂ and when turning the same material by Sharman et al. [134].



Test 2: $v=70\text{m/min}$, $f=0.09\text{mm/tooth}$, $a=0.25\text{mm}$, $d=0.25\text{mm}$, IC900, dry

Figure 4.18: SEM views showing machined workpiece surface from Test 2



Test 4: $v=70\text{m/min}$, $f=0.15\text{mm/tooth}$, $a=1.0\text{mm}$, $d=1.0\text{mm}$, IC903, dry

Figure 4.19: SEM views showing the machined workpiece surface from Test 4

Sharman [135] suggests that the larger cracks and lack of plastic deformation seen in the cavity are indicative of the low ductility of the γ -TiAl material. Attempts to generate high temperatures in the shear zone in order to exceed the brittle to ductile transition temperature and increase the ductility of the chip are detailed [127, 133]. When using polycrystalline cubic boron nitride tools at high cutting speeds of 200m/min, surface analysis showed less cracking when compared to WC tooling however, the cracks were larger with a depth of 0.2 to 0.6mm from the surface. The relaxation of thermal stresses in the surface layers upon cooling created by the alloys low thermal conductivity was believed to have caused these cracks. Uhlmann et al. [133], detail surfaces that are absolutely free from cracks and break-offs when turning Ti-52Al-46.8-1Mo-0.2Si, using a cutting speed of 300m/min and a low feedrate of 0.02mm/rev

with CBN tooling. Chips were reported as being fully segmented, with a smooth lower face indicating that plastic deformation had occurred in the secondary shear zone. Material removal from machining ceramics occurs when stresses build up ahead of the advancing tool around grain boundary interactions, dislocation pile ups, inclusions and other stress raisers. Rapidly growing cracks leading to fracture and chip formation are caused by these stresses. Ductile mode machining of ceramics has been investigated and there was a suggestion that a fracture loading limit exists below which cracks will not develop and the workpiece material will be removed by plastic flow [170]. Crack free surfaces have been produced using grinding [114] and ball nose end milling [106]. A characteristic of these two processes are the low cutting forces and levels of stress generated in the cutting zone [135] which suggests that to produce a crack free surface, these stresses should be reduced. It was therefore no coincidence that surfaces that had the largest levels of fracture/pullout used the higher levels of feed rate and both axial and radial depth of cut which gave rise to higher levels of cutting force. A similar type of damage has been reported when milling other brittle materials such as the in the micro milling of glass by Matsumura et al. [171]. Observed damage was significantly smaller ($<5\mu\text{m}$ in diameter) than the fracture/pullout observed with the current work and reflected the micro nature of the cutting. Ductile mode cutting was suggested to occur when milling glass at an undeformed chip thickness of $<1\mu\text{m}$.

e) Microhardness

Microhardness profiles showing hardness against distance from the machined workpiece surface for all 16 tests are shown in Figure 4.20. This shows a summary of all the tests, however with Appendix C: Figures C35 and C36 showing individual profiles for each test. A hardened layer was found for every surface/subsurface which generally had a depth of $\sim 300\mu\text{m}$ and a maximum hardness of up to $590\text{HK}_{0.025}$. Compared to the previous research of Mantle and Aspinwall [106], who when ball nose end milling the alloy Ti-45Al-2Nb-2Mn +0.8%vol. TiB_2 showed that surfaces milled with a tilt angle of 0° had a maximum hardness of up to $650\text{HK}_{0.025}$ while at 45° the maximum hardness was up to $600\text{HK}_{0.025}$, these hardened layers were found up to $400\mu\text{m}$ from the machined surface. At similar operating parameters the present work showed a similar hardened layer, however it was $\sim 100\text{HK}_{0.025}$ lower using part worn tools ($122\mu\text{m}$ max flank wear) than in the previous work with more arduous operating parameters (a combination of higher cutting speed, feed rate and depth of cut) and with using worn tooling, a hardened layer with maximum hardness from $\sim 550\text{--}600\text{HK}_{0.025}$ was found. The results obtained also have a lower maximum value when compared to work

on face milling of Ti-47Al-2Mn-2Nb +0.8%TiB₂ [110]. Here a hardened layer up to 3x higher than the bulk value extending to a depth of 300µm from the workpiece surface was found. The present results reflect the lower forces and temperatures expected when using a high speed machining technique.

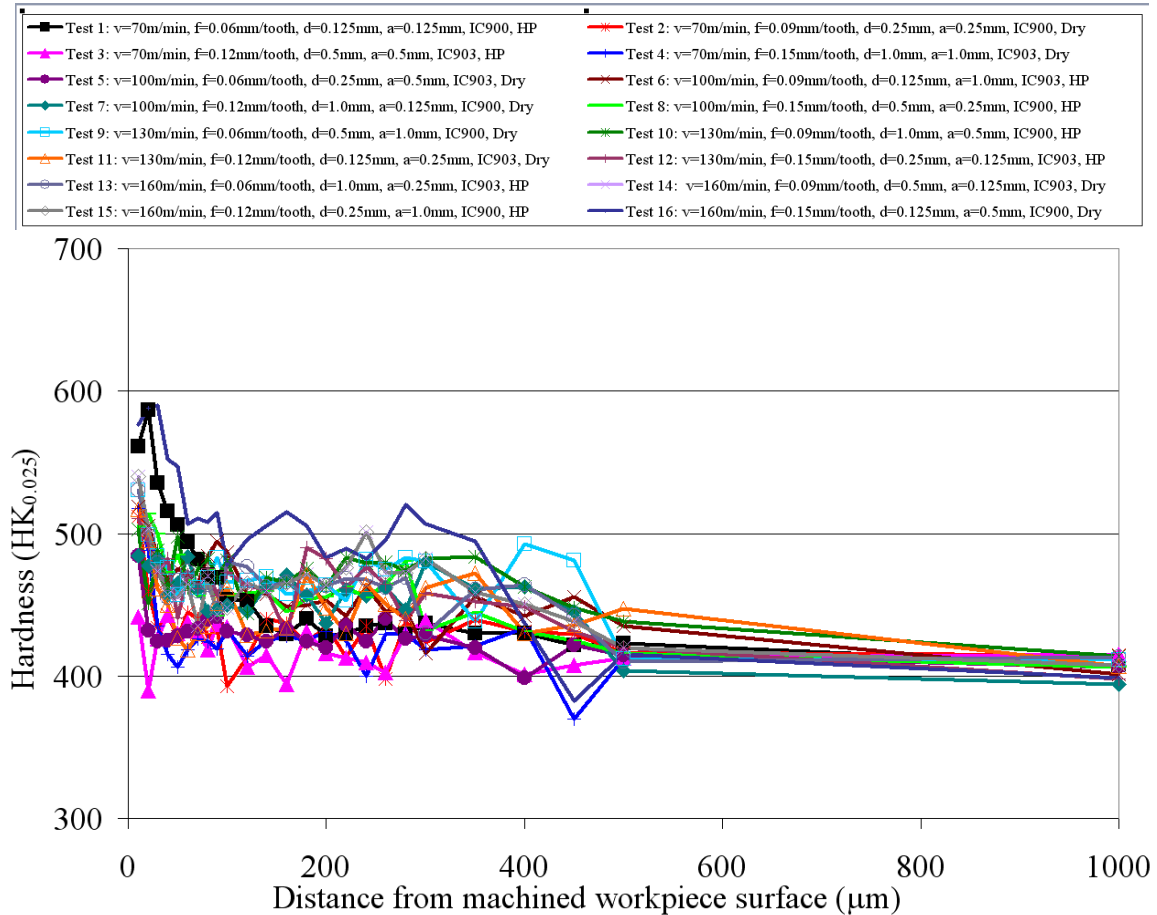


Figure 4.20: Microhardness depth profiles (Phase 1A)

f) Workpiece surface/subsurface

Surface/subsurface micrographs for two electrical discharge wire machined surfaces are shown in Figure 4.21. These are included in order to benchmark Ti-45Al-8Nb-0.2C against Ti-45Al-2Mn-2Nb +0.8%vol. TiB₂ [144] and also allow comparison with milled and ground surfaces for reference. Both micrographs show a continuous recast layer with an average depth of ~5µm and a maximum depth of up to ~10µm. Figure 4.21 (a) shows cracks running through the recast material and stopping at the bulk material however, Figure 4.21 (b) shows a crack running through the recast layer and extending to a depth of ~20µm from the machined workpiece surface. This type of crack causes concern because it could act as an initiation site for fatigue cracks. In addition, it is likely that the workpiece surface/subsurface is subjected to

tensile residual stress as these generally occur with electrical discharge machining processes [95].

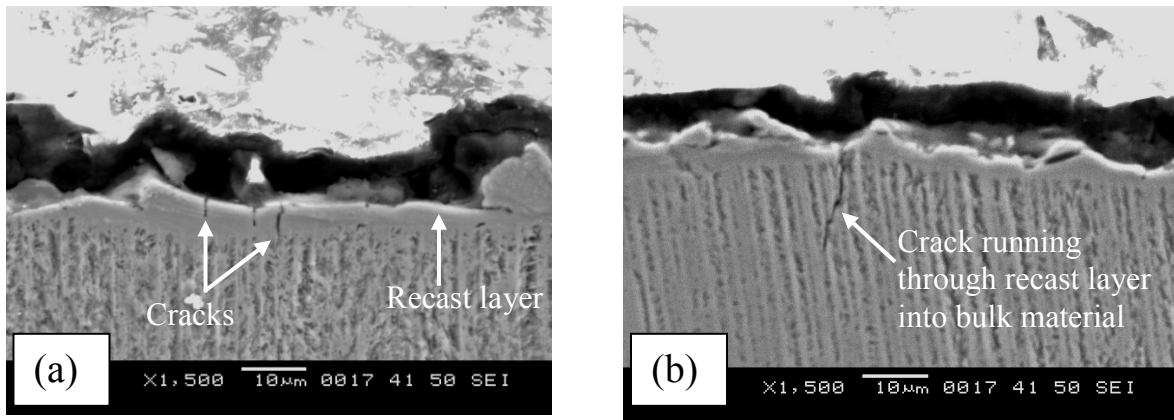
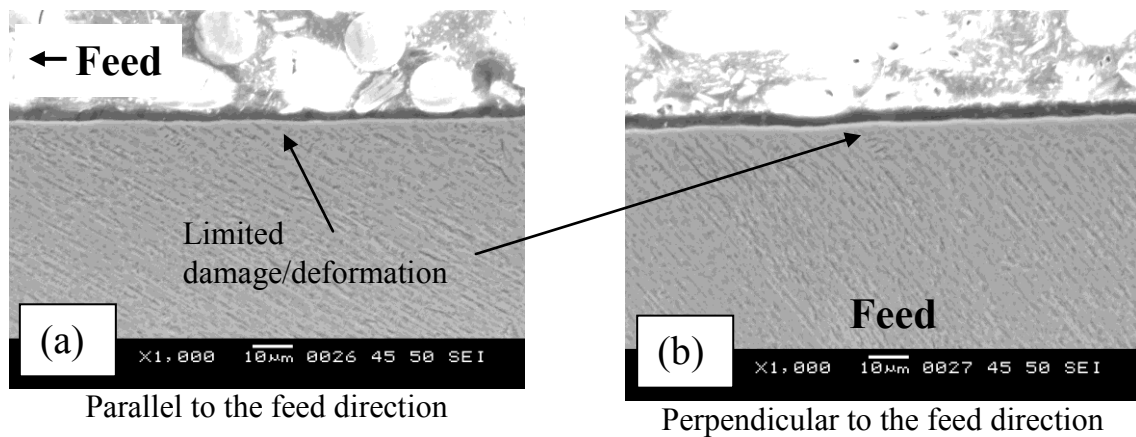


Figure 4.21: Surface/subsurface micrographs of electrical discharge wire machined surfaces

The current results are almost identical to work performed on Ti-45Al-2Mn-2Nb +0.8%vol. TiB₂ where a recast layer with an average depth of 4-7 μm was reported and a maximum depth of 17 μm was found using the most abusive cuts. As with the present work, cracking was not only restricted to just the recast layer but also entered the bulk workpiece material. The maximum depth of these cracks was reported to be 33 μm from the workpiece surface which was slightly higher than the current work but comparable given the different operating parameters used.

Surface damage on the high speed ball nose milled surface/subsurfaces was mainly in the form of fracture/pullout, deformation/bending of the lamellae up to a depth of ~30 μm from the machined workpiece surface. Possible microcracks, <1 μm wide running between the lamellae were observed in certain micrographs. The effect of such cracks on fatigue life has yet to be ascertained, however S-N curves for high speed milled samples of Ti-45Al-2Mn-2Nb +0.8%vol. TiB₂ compared favorably to fine ground and polished samples [109]. Indeed, samples produced using worn tools (VB_{max}=300 μm) which surface/subsurface analysis indicated had deformed lamellae and cracking extending to a depth of up to 20 μm from the workpiece surface, had on average, reduced performance of only 15% when compared to surfaces produced using identical parameters and new tools. It was suggested that the substantially higher fatigue strength with milled surfaces when compared to ground or polished samples was due to increased sub-surface hardness and deformation causing higher levels of compressive residual stress at the workpiece surface [107, 109].

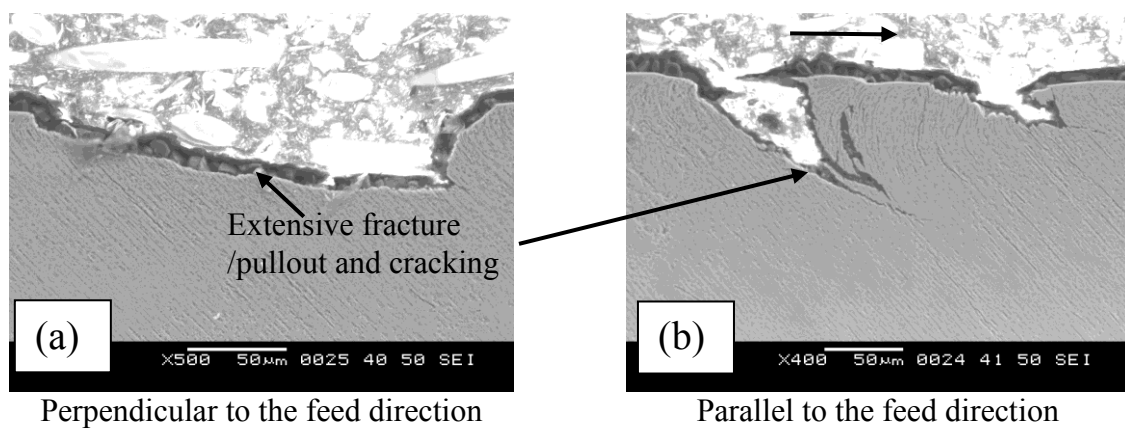
Micrographs in Figure 4.22 show limited damage on the surface/subsurface of Test 2. This was established as the “best” surface with only two regions of deformation/bending of the lamellae in parallel and perpendicular to the feed samples. In general, Test 2 had a combination of lower operating parameters along with a maximum flank wear level of $\sim 120\mu\text{m}$. Mantle and Aspinwall [107] report similar findings when milling Ti-45Al-2Mn-2Nb +0.8%vol. TiB_2 using very fine and fine finishing cuts [107]. Micrographs presented for surfaces machined at 45° showed pullout confined to a depth of $<2\mu\text{m}$ and limited cracking.



Test 2: $v=70\text{m/min}$, $f=0.09\text{mm/tooth}$, $a=0.25\text{mm}$, $d=0.25\text{mm}$, IC900, dry

Figure 4.22: Cross sectional micrographs of the workpiece surface/subsurface from Test 2

Cross-sectional micrographs of typical surface damage in Test 4 are shown in Figure 4.23. The left hand micrograph shows a single area of damage $60\mu\text{m}$ deep and $250\mu\text{m}$ wide, while the right hand micrograph shows two areas of damage with cracks. This test used a combination of the highest feed rate and axial and radial depth of cut and resulted in one of the shortest tool lives.



Test 4: $v=70\text{m/min}$, $f=0.15\text{mm/tooth}$, $a=1.0\text{mm}$, $d=1.0\text{mm}$, IC903, dry

Figure 4.23: Cross sectional micrographs of the workpiece surface/subsurface from Test 4

The high level of operating parameters caused a large chip thickness and as a consequence high forces that led to the high levels of fracture/pullout observed. Bending of the lamellae can be observed to a depth of up to $\sim 10\mu\text{m}$ for the surfaces machined with Test 5 and Test 8 operating parameters, see Figure 4.24. It was expected that the higher operating parameters caused an increase in the strain hardening of the workpiece.

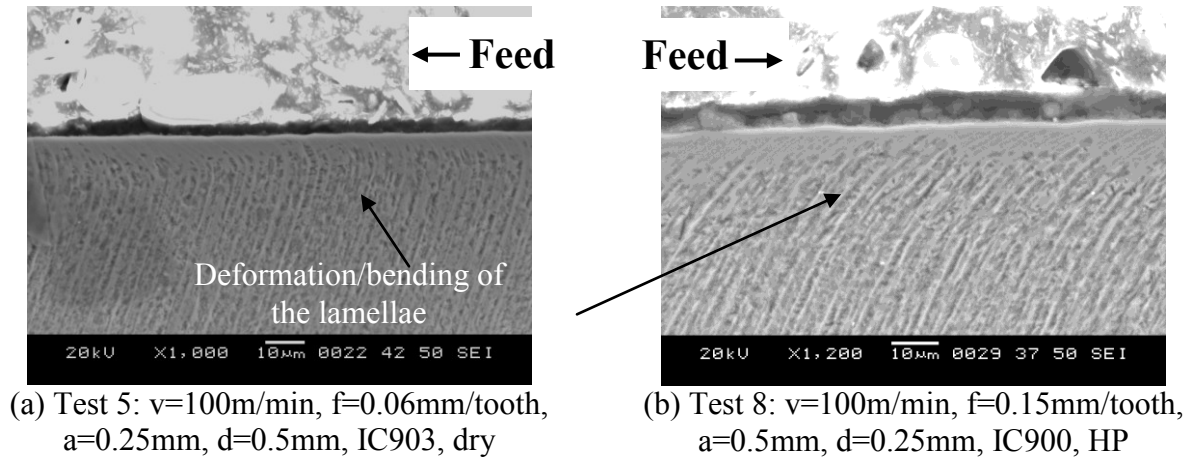


Figure 4.24: Cross sectional micrographs of the workpiece surface/subsurface in a direction parallel to the feed direction

The micrograph in Figure 4.25 shows part of the surface/subsurface from Test 15 with limited damage. Highest cutting speed was used for this test along with a mix of operating parameters. Harding [101] reports that whilst a high number of cracks/pullout was evident when viewing the machined surface, very few instances were found when viewing surface/subsurface cross-sectional micrographs. Measurement of surface integrity was taken in accordance with standard operating practice, however the results relate to that section of the workpiece analysed and may not necessarily be representative of all areas machined.

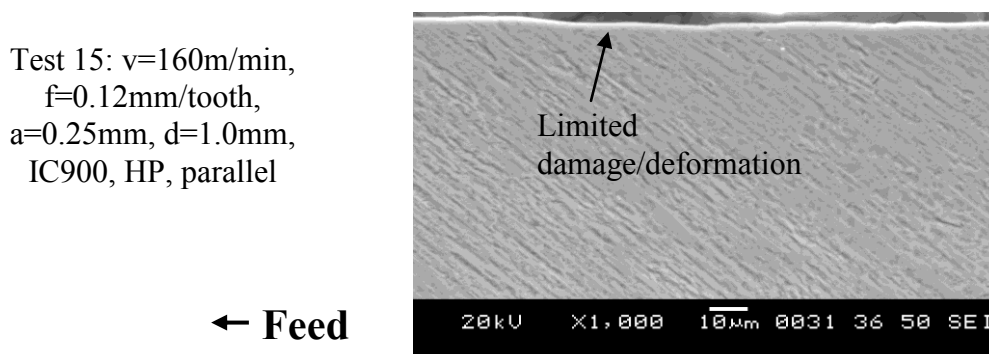
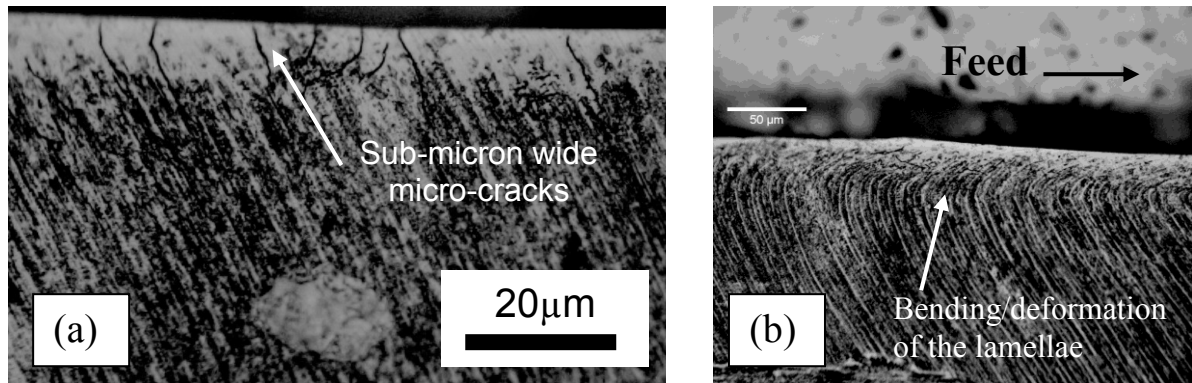


Figure 4.25: Cross sectional micrograph of the workpiece surface/subsurface from Test 15

Possible microcracks between lamellae were evident in the surface/surface micrographs from Test 16. Bending of the lamellae was also observed with several regions to a depth of up to $\sim 30\mu\text{m}$. Figure 4.26 shows examples of both the cracks and bending of the lamellae in surfaces parallel to the feed direction. It is likely that the white layers near the surface were un-etched areas rather than a HAZ.



Test 16: $v=160\text{m/min}$, $f=0.15\text{mm/tooth}$, $a=0.125\text{mm}$, $d=0.5\text{mm}$, IC900, dry, (a) perpendicular, (b) parallel

Figure 4.26: Cross sectional micrographs of the workpiece surface/subsurface from Test 16

The grain size of the current alloy was large when compared to previous γ -TiAl alloys. The alloy had been HIPped to remove porosity however, no further heat-treatment had been performed. Tests to allow comparison with the previous alloy Ti-45Al-2Mn-2Nb +0.8%vol. TiB_2 using identical operating parameters and conditions were therefore scheduled as part of Phase 1B work to allow a more direct comparison. These tests also allowed the assessment of flank wear (at a given level) on surface integrity.

4.2 Phase 1B: Comparison of the machinability of Ti-45Al-8Nb-0.2C and Ti-45Al- 2Mn-2Nb +0.8%vol. TiB_2 .

a) Tool life

Tool life at a cutting speed of 160m/min was extremely good with a distance machined of over 800m and a machining time of 400min achieved before the maximum flank wear criterion of $300\mu\text{m}$ was reached. Figure 4.27 shows maximum flank wear against distance machined when comparing the machinability of two different γ -TiAl alloys, Ti-45Al-8Nb-0.2C against Ti-45Al-2Mn-2Nb +0.8%vol. TiB_2 . In contrast to Phase 1A, all tests reached the maximum flank wear criteria of $300\mu\text{m}$ with relatively consistent wear across each of the four cutting edges observed. No (CF) occurred as a result of using a low axial depth of cut. For

both alloys the higher the cutting speed, the shorter the tool life. This trend was expected as increased cutting speed generally produces increased cutting temperatures. Additional graphs showing maximum flank wear against machining time and volume of workpiece material removed, are shown in Appendix C, Figures C37 and C38.

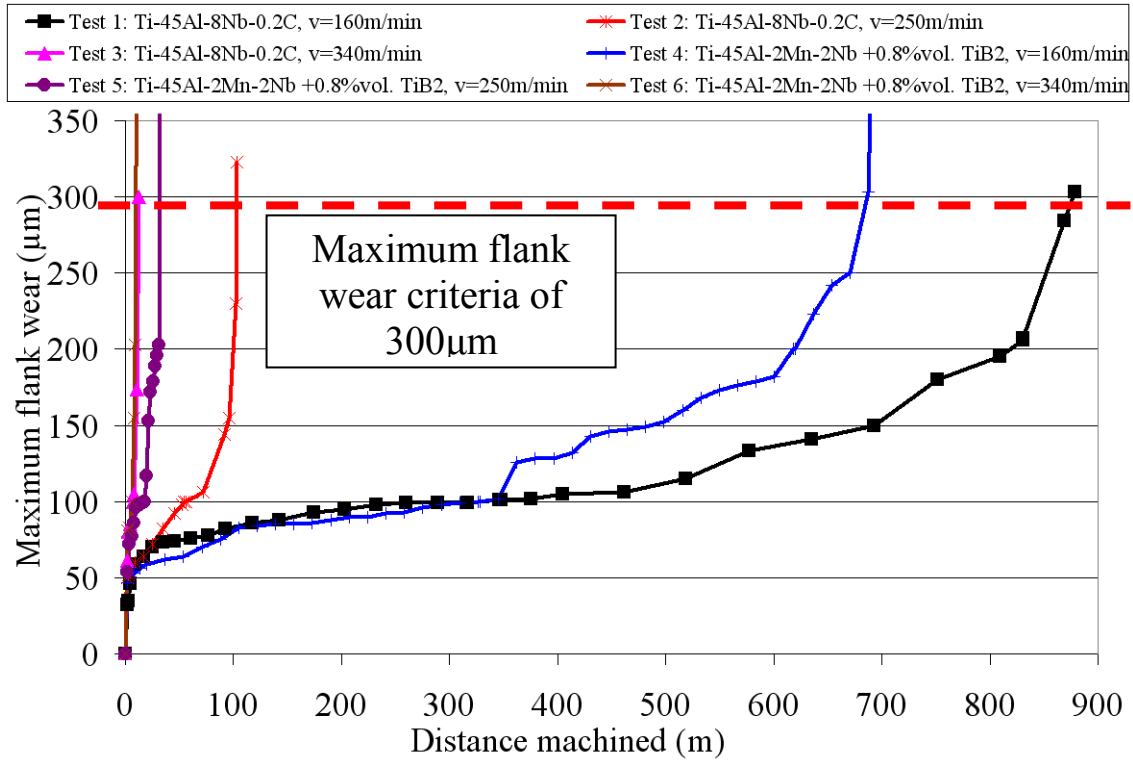


Figure 4.27: Maximum flank wear against distance machined (Phase 1B)

Tool wear scar photographs are shown in Appendix C, Figures C39 to C44 and detail similar results for both alloys at each cutting speed. Initial wear consisted of VB 1 which progressed to VB 2 at the central point of the wear scar. Stair-formed face wear was also evident on the rake face. At higher cutting speeds of 250 and 340m/min, wear progression with both alloys was extremely fast once a flank wear of $\sim 200\mu\text{m}$ had been reached. The format of the wear scars (smooth) suggests diffusion as the prime wear mechanism together with adhesion. Perez [110] suggests that abrasion wear due to the abrasive action of TiB_2 ceramic particles was observed when end milling the alloy $\text{Ti-47Al-2Mn-2Nb} + 0.8\%\text{vol. TiB}_2$.

The Taylor tool life curve (vT curve) for a maximum flank wear criteria of $300\mu\text{m}$ is shown in Figure 4.28. The performance in terms of machining time of $\text{Ti-45Al-2Mn-2Nb} + 0.8\%\text{vol. TiB}_2$ was established as being $\sim 25\%$ lower than for Ti-45Al-8Nb-0.2C . No significant differences in bulk hardness were found between the two alloys. It would be expected that the Ti-45Al-8Nb-0.2C alloy with a grain size greater than $2\mu\text{m}$ compared to a

grain size of 50 to 100 μm for Ti-45Al-2Mn-2Nb +0.8%vol. TiB₂ would have the lower tensile strength [22].

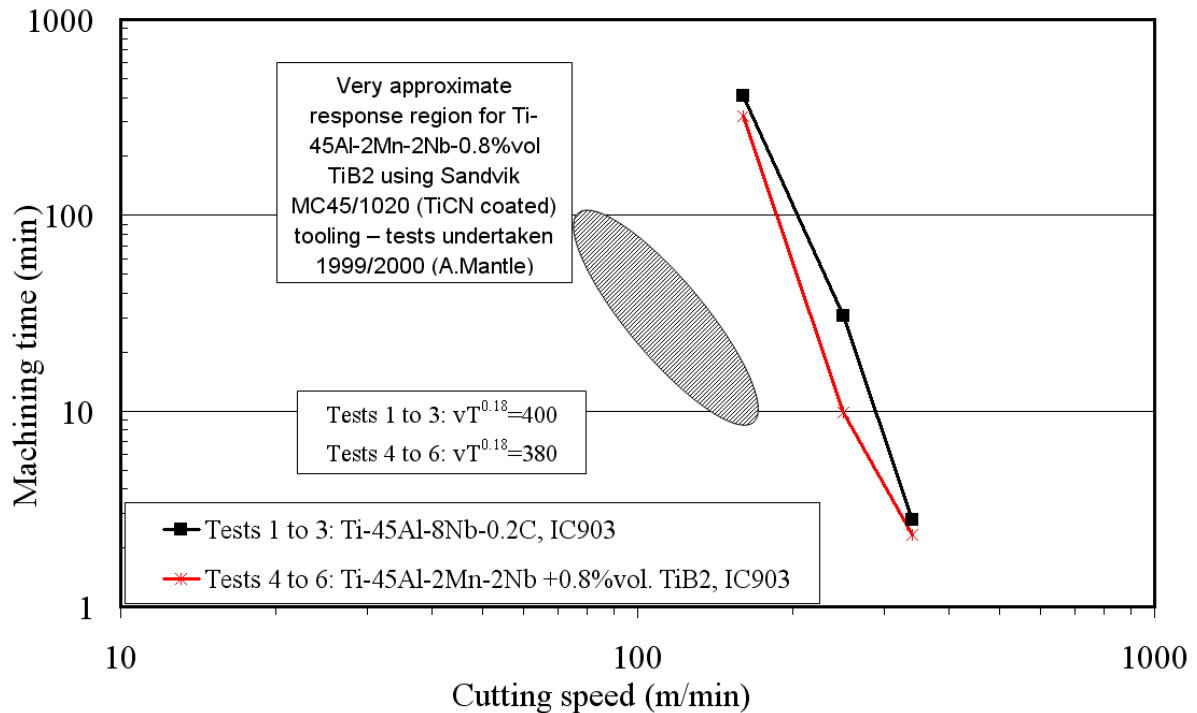


Figure 4.28: Taylor tool life (vT) curve

Although published data comparing the tool life of Ti-45Al-2Mn-2Nb +0.8%vol. TiB₂ against that of the higher tensile strength alloy, Ti-44Al-8Nb-1B when turning [128] are reported as similar, the tool life for the latter γ alloy was 10% lower than for the former. In addition, the action of the ceramic TiB₂ particles could also reduce tool life through an abrasion wear mechanism [110]. The machining time for both γ -TiAl alloys was heavily dependant on the cutting speed with a steep gradient which was likely to be caused by higher cutting temperatures occurring at higher cutting speeds.

It was difficult to compare the results to those achieved from Phase 1A as higher cutting speeds were used for this phase in order to allow the cutting tool to reach the maximum flank wear criterion. Phase 1A, Test 2 probably used the closest match in operating parameters with an identical depth of cut and dry cutting. The feed rate was slightly higher for Test 2 in Phase 1A, however an IC900 cutting tool was used rather than the IC903. Extrapolating the vT curve to give the machining time at a cutting speed of 70m/min and assuming a linear relationship between cutting speed and tool life gives a tool life of ~10000m or over 7 days. Even if the relationship between cutting speed and tool life at lower cutting speeds is not a linear relationship and the gradient of the curve reduces at low cutting speeds

due to being in the brittle or tough domain rather than the Taylor domain (plastic deformation) as shown by Mantle and Aspinwall [126] when turning Ti-45Al-2Mn-2Nb +0.8%vol. TiB₂, it is suggested that the distance machined would be at least 1000m.

Figure 4.28 also shows a very approximate response region for unpublished research into high speed ball nose end milling Ti-45Al-2Mn-2Nb-0.8%vol TiB₂ using Sandvik MC45/1020 (TiCN coated) tooling with a workpiece tilt angle of 45° and end milling using uncoated carbide inserts detailed in [100]. The tests were undertaken during 1999/2000 by A. Mantle at the University of Birmingham. Operating parameters including feed rate and depth of cut were similar between the previous and current research. In order to reach a maximum flank wear criteria of 300µm with a machining time of 10min using the TiCN coated tooling, a cutting speed of ~170m/min would have been required whereas with the current research the same machining time could be achieved at a cutting speed of ~250m/min. This increase in cutting speed was as a result of improvements in tool substrate material including the use of a finer grain carbide and the AlTiN coating which is reported as having a hardness of 3500HV and oxidation resistance of 800°C when compared to values of 3000HV and 400°C for TiCN [172].

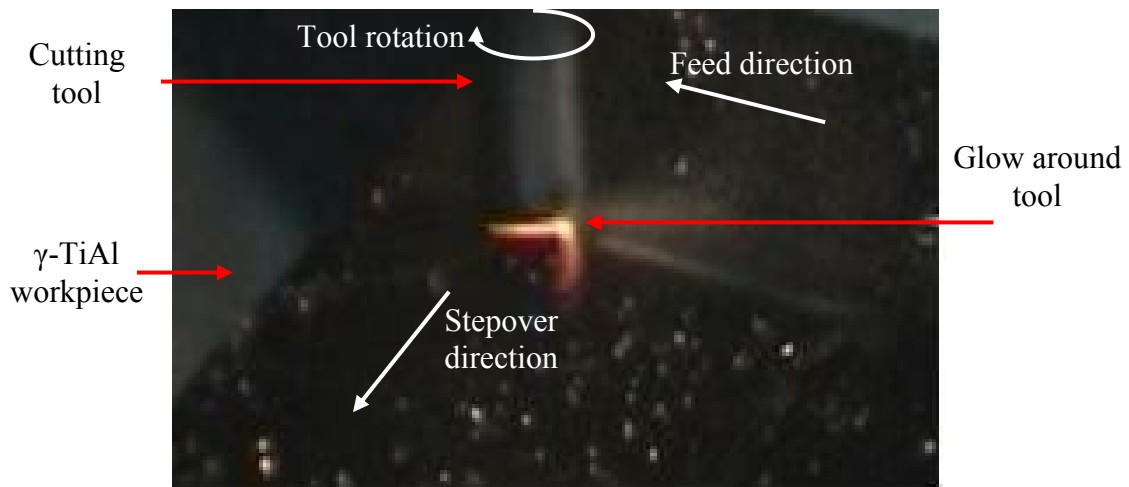
The combination of the two different γ -TiAl alloys and 3 different cutting speeds was considered as a factorial experimental design. Analysis of Variance (ANOVA) was performed to determine which of the factors was statistically significant. The workpiece material/cutting speed interaction had the lowest Sum of Squares (SS) and was therefore used for the residual error, see Table 4.6. Table C3 in Appendix C details the original ANOVA table on which Table 4.6 was based. As $F_{0.05;1;2} = 18.5$ and $F_{0.05;2;2} = 19.0$ [154], not surprisingly the cutting speed was determined as being statistically significant at the 5% level with the workpiece material being non-significant. The residual error (PCR (%)) had a low value of 4.7 which was within the 15% that Ross [154] suggests for acceptable noise.

Source	SS	DOF	MSS	Fcalc	PCR (%)
Workpiece material	11408	1	11408	2.54	0.3
Cutting speed	741908	2	741908	92.69	95.0
Error (Workpiece material/cutting speed interaction)	8973	2	8973	-	4.7
Total	762288	5	-	-	-

Table 4.6: Modified ANOVA table for machining time

b) Cutting temperature measurement

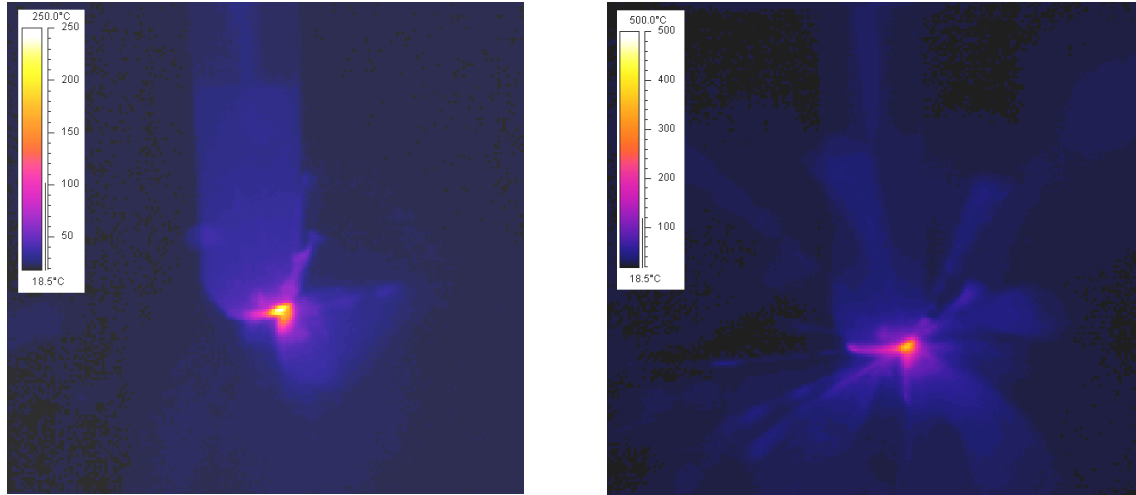
Figure 4.29 shows a digital photograph of the cutting tool whilst milling at a cutting speed of 340m/min with a new tool. It shows a bright glow around the end of the tool indicating that high cutting temperatures had occurred. In general, with a new tool a similar glow was observed at a cutting speed of 250m/min. An increase in the maximum flank wear level at either a cutting speed of 250 or 340m/min caused an increase in the intensity of the red glow. At a cutting speed of 160m/min, with a new tool, no glow was seen around the cutting tool however, a red glow appeared once a maximum flank wear level of $\sim 200\mu\text{m}$ was reached.



Test 3: Ti-45Al-8Nb-0.2C, $v=340\text{m/min}$, new tool.

Figure 4.29: Digital image of the cutting tool when machining Test 3

An average value of 0.81 was obtained for the emissivity of Ti-45Al-8Nb-0.2C as the temperature of the material/swarf either increased or decreased for either a heating or cooling cycle. The results obtained with the current work are in agreement with Mantle and Aspinwall [126] who used a Williamson Viewtemp 2200D FOV2 infra red camera to determine the emissivity of γ -TiAl swarf at 100°C and 200°C and report a value of 0.82. Figure 4.30 shows selected images taken for Tests 1 to 3 using Ti-45Al-8Nb-0.2C with both new and worn tools that had reached the maximum flank wear criteria of $300\mu\text{m}$. The images show that the maximum cutting temperature was located at the interface, with values of $\sim 250^\circ\text{C}$ at a cutting speed of 160m/min for a new tool, rising to $\sim 430^\circ\text{C}$ at a cutting speed of 340m/min with a tool that had $300\mu\text{m}$ of flank wear. The high number of chips formed at higher speeds was problematic in that they obscured the observation region and may have effected measurements.



(a) Test 1: Ti-45Al-8Nb-0.2C, $v=160\text{m/min}$, $VB_{\text{max}}=0\mu\text{m}$

(b) Test 3: Ti-45Al-8Nb-0.2C, $v=340\text{m/min}$, $VB_{\text{max}}=300\mu\text{m}$

Figure 4.30: Images showing the cutting temperatures

Figure 4.31 shows a summary of the cutting temperatures obtained for Tests 1 to 3 with both new and worn ($VB_{\text{max}}=300\mu\text{m}$) tools. The graph also shows the results of replications performed for Tests 1 to 3 as cutting temperature measurement occurred after mainstream tool life testing had occurred. These replications are in general agreement with the results detailed in Figure 4.27 and contrast with the work detailed in [100] which found a wide range in the distance machined for replications using the same operating parameters.

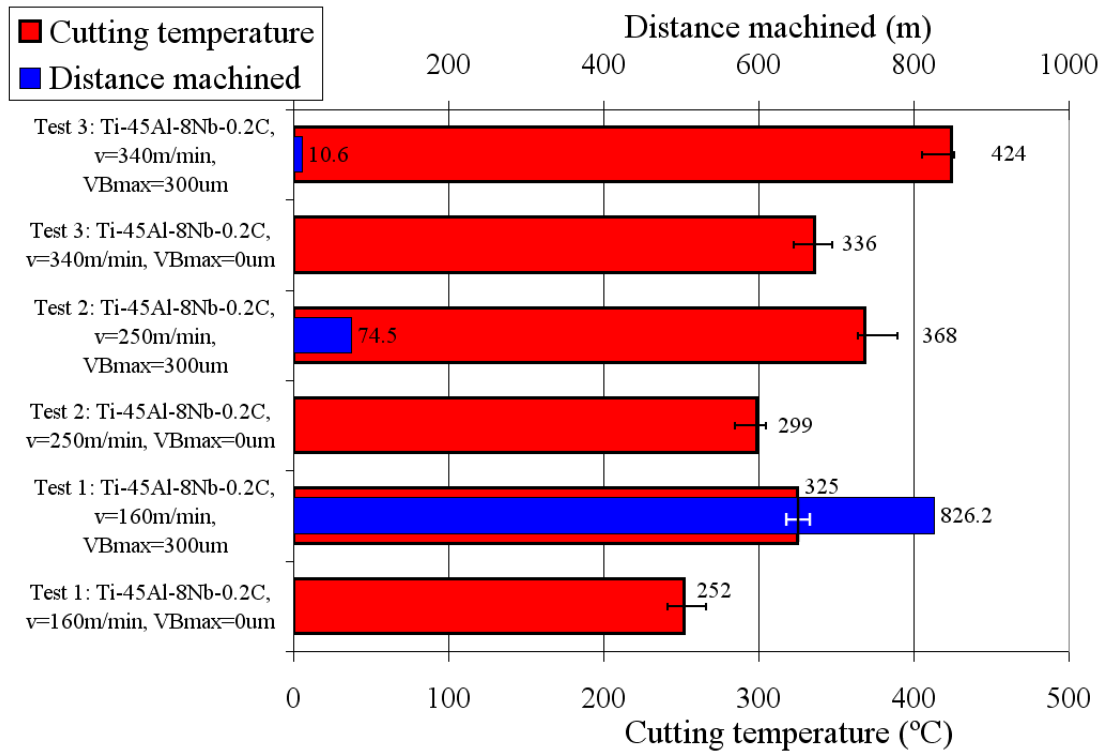


Figure 4.31: A bar chart showing cutting temperature

The cutting temperature results for the current work are in agreement to previously published research where a cutting temperature of 316°C was measured using constantan-workpiece thermocouples with a worn tool ($VB_{max}=300\mu m$), when using a cutting speed 135m/min, a feed rate of 0.12mm/min, axial and radial depths of cut of 0.2mm with the workpiece orientated at 45°. A subsequent increase in the cutting speed to 345m/min caused the cutting temperature to increase to 413°C [6, 105].

Figure 4.32 shows the Main Effects Plot - means for maximum cutting temperature. Both maximum flank wear and cutting speed caused an increase in cutting temperatures with an almost linear increase in cutting temperature occurring with a linear increase in cutting speed. Increased flank wear leads to increased rubbing between the cutting tool and workpiece material thus leading to the increase in cutting temperatures [173]. A similar response with an increase in cutting temperature caused by an increase in flank wear level when turning Ti-45Al-2Mn-2Nb +0.8%vol. TiB_2 has been reported [126].

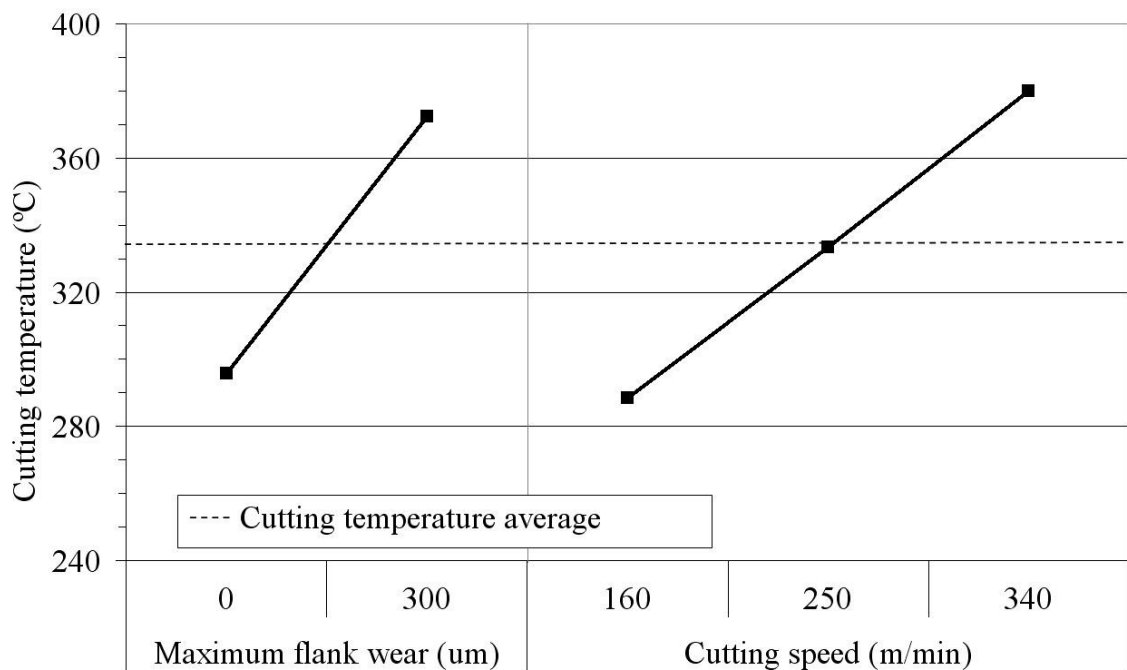


Figure 4.32: Main Effects Plot - means for maximum cutting temperature

The combination of the two different maximum flank wear levels and 3 different cutting speeds was considered as a factorial experimental design. Analysis of Variance was performed to determine which of the factors were statistically significant. Table C4 in Appendix C shows the ANOVA table for cutting temperature. The workpiece material/cutting speed interaction had the lowest Sum of Squares (SS) and was used for the residual error. Table 4.7 shows the resulting modified ANOVA table for cutting temperature. As $F_{0.05;1;2}$

$=18.5$ and $F_{0.05;2;2} = 19.0$ [154] both maximum flank wear and cutting speed were determined as being statistically significant at the 5% level. The residual error (PCR) had a low value of 1.4 which was less than the 15% recommended by Ross [154] for acceptable noise.

Source	S.S.	D.O.F.	M.S.S.	F _{calc}	PCR (%)
Maximum flank wear	8816.7	1	8816.7	175.75	50.7
Cutting speed	8373.0	2	4186.5	93.45	47.9
Error (Maximum flank wear/cutting speed interaction)	100.3	2	50.2	-	1.4
Total	17290.0	5	-	-	-

Table 4.7: Modified ANOVA table for cutting temperature

c) Cutting forces

A graph showing each force component F_x , F_y and F_z and distance machined against distance machined for Test 1 is shown in Figure 4.33. An increase in cutting force was measured with increasing distance machined and thus maximum flank wear as a consequence of the increased contact and rubbing between the flank face and the workpiece [174]. Insufficient Ti-45Al-2Mn-2Nb +0.8% vol. TiB_2 workpiece material was available to allow a comparison between γ -TiAl alloys, as tool life performance and surface integrity analysis were deemed more important.

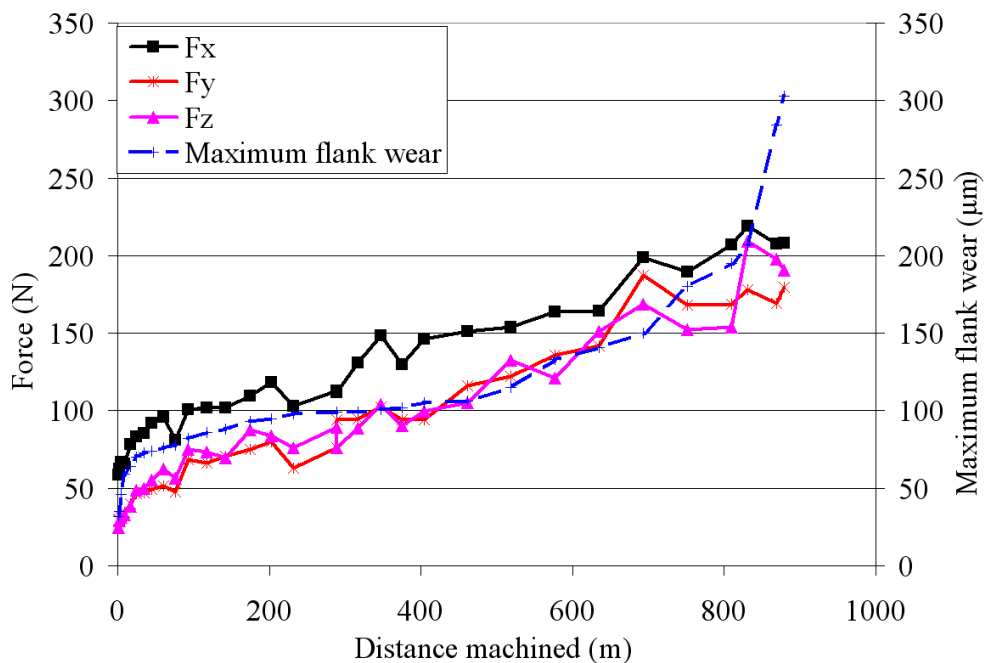


Figure 4.33: Cutting forces and maximum flank wear against distance machined for Test 1: $v=160\text{m/min}$

Figure 2.19 (b), taken from the work of Mantle and Aspinwall [104] when ball nose end milling Ti-45Al-2Mn-2Nb +0.8%vol. TiB₂ shows a similar graphical response to that detailed in Figure 4.33. Operating parameters detailed for the published work were a cutting speed of 120m/min a feed rate of 0.12mm/tooth and an axial and radial depth of cut of 0.2mm. The magnitudes of F_x, F_y and F_z are almost identical between the two graphs when the different feed and stepover directions are taken into account. For the present work, F_x is the feed force and F_y the force in the stepover direction whilst in the published research F_y was the feed force and F_x is the force in the stepover direction. The feed force for both the present and published research was established as being the highest with values of ~200N. The marginally lower force in the feed direction measured with the current work was probably due to a lower feed rate of 0.06mm/tooth. Difficulties were encountered when obtaining force measurements at higher cutting speeds (Tests 2 and 3 using cutting speeds of 250 and 340m/min) as tool wear progressed extremely quickly. In general, forces for a similar flank wear level were comparative, see Appendix C, Figures C45 and C46. Mantle and Aspinwall [104] report that at cutting speeds of 240m/min and 300m/min, problems were encountered on reaching the natural frequency of the dynamometer/workpiece assembly and thus the accuracy of the force measurements was questionable. In the current work, the force traces for Tests 2 and 3 became sinusoidal suggesting similar resonance problems [174].

d) Workpiece surface roughness

A bar chart showing workpiece surface roughness Ra for each test and flank wear level is shown in Figure 4.34. Values ranged from Ra 0.25µm to Ra 1.25µm although the majority of readings were between Ra 0.3µm and 0.6 µm. Results for Ti-45Al-2Mn-2Nb +0.8%vol.TiB₂ are ~ Ra 0.1 to 0.2µm lower for the current work when compared to those previously presented [106], when ball nose end milling the same γ-TiAl alloy. This was likely to be due to the increased rigidity of the cutting tool caused by using a larger diameter tool and the differences in milling orientations, in addition to the differences in tool geometry. Ng et al. [164] reported reduced vibrations and ~25% lower surface roughness for the horizontal downwards cutting direction (which was used for the current work) when compared to a vertical upwards direction which was used for previous research.

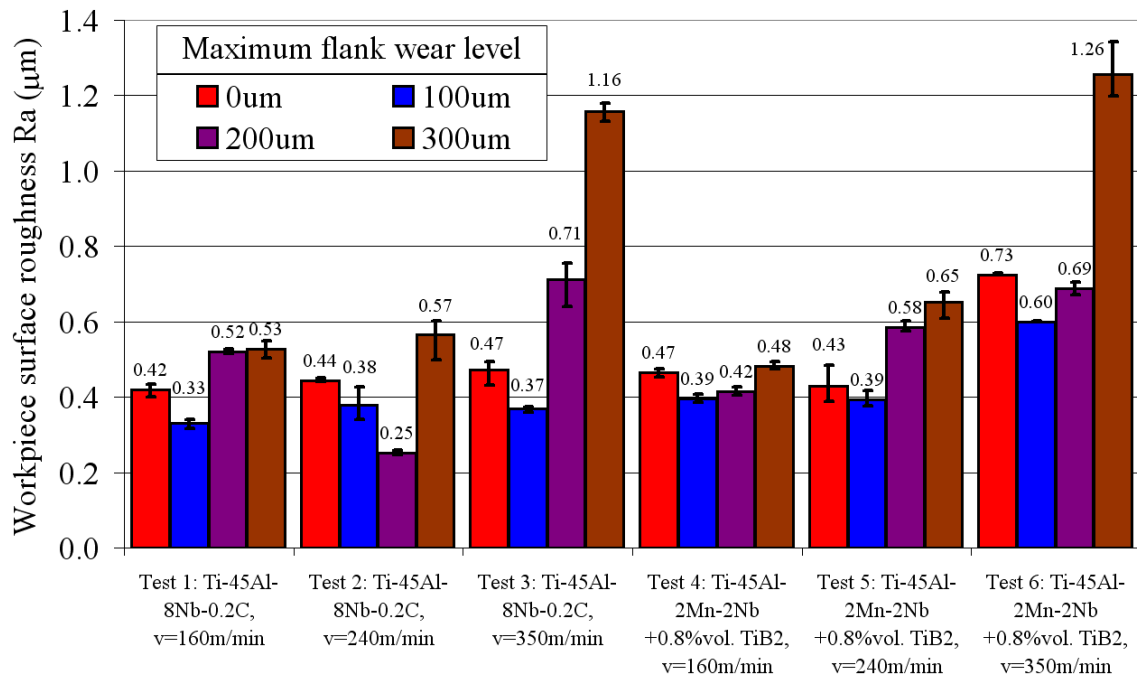
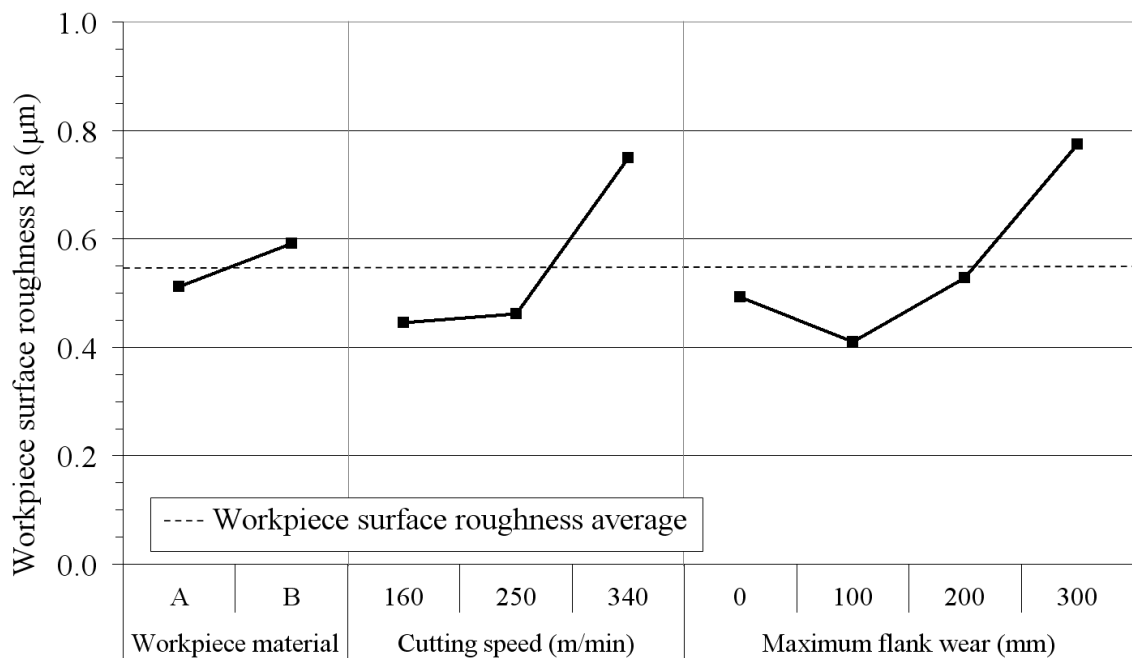


Figure 4.34: Workpiece surface roughness R_a (Phase 1B)

The Main Effects Plot - means for workpiece surface roughness R_a is shown in Figure 4.35. On average Ti-45Al-2Mn-2Nb +0.8%vol. TiB_2 had a surface roughness R_a of $\sim 0.1\mu\text{m}$ higher than Ti-45Al-8Nb-0.2C.



Workpiece A: Ti-45Al-8Nb-0.2C, B: Ti-45Al-2Mn-2Nb +0.8%vol. TiB_2

Figure 4.35: Main Effects Plot - means for workpiece surface roughness R_a (Phase 1B)

Increasing the cutting speed from 160 to 340m/min caused an increase in the surface roughness of ~100%, however, a greater increase was identified between a cutting speed of 250m/min and 340m/min than between 160m/min and 250m/min. A turning point was observed with the maximum flank wear factor. The curve shows that lowest surface roughness R_a was measured on the surface produced using a maximum flank wear of 100 μ m with a subsequent increase in maximum flank wear to 300 μ m causing an increase in surface roughness R_a of ~100%.

The combination of the two different γ -TiAl alloys, 3 different cutting speeds and 4 different flank wear levels was considered as a factorial experimental design. Analysis of Variance (ANOVA) was performed to determine which of the factors was statistically significant. The workpiece material/cutting speed/flank wear interaction (3rd order) was used for the residual error. The corresponding modified ANOVA table for workpiece surface roughness is shown in Table 4.8 whilst Table C5 in Appendix C shows the ANOVA table on which Table 4.8 was based. As $F_{0.05;1;6} = 5.99$, $F_{0.05;2;6} = 5.14$, $F_{0.05;3;6} = 4.76$ and $F_{0.05;6;6} = 4.28$ [154], cutting speed and flank wear were determined as being statistically significant at the 5% level whilst the workpiece material and interactions between the three factors were determined as being non-significant. The residual error (PCR) had a value of 18.5.

Source	SS	DOF	MSS	F _{calc}	PCR (%)
Workpiece material	0.036817	1	0.036817	3.28	2.0
Cutting speed	0.467158	2	0.233579	20.82	33.3
Flank wear	0.443367	3	0.147789	13.17	31.6
Workpiece material/cutting speed interaction	0.025008	2	0.012504	1.11	0.20
Cutting speed/flank wear interaction	0.003350	3	0.001117	0.10	0
Workpiece material/flank wear interaction	0.254708	6	0.042451	3.78	14.4
Error	0.067325	6	0.011221	-	18.5
Total	1.297733	23	-	-	-

Table 4.8: Modified ANOVA table for workpiece surface roughness R_a

e) Workpiece surface

Selected images of the machined workpiece surfaces produced using the three different cutting speeds for Ti-45Al-8Nb-0.2C and Ti-45Al-2Mn-2Nb + 0.8% vol. TiB₂ are shown in Figure 4.36. All machined surfaces showed evidence of surface damage including possible fracture/pullout of the workpiece surface. These regions were randomly distributed across the workpiece and varied in size from 20 μ m to 500 μ m. In general, increasing the cutting speed

caused a marginal increase in the number of surface defects with the quality of the surface using a new tool considerably better than that produced with a worn tool as found previously [107]. The size of the fractured material/pullout was in general smaller for Ti-45Al-2Mn-2Nb + 0.8% vol. TiB₂ than for Ti-45Al-8Nb-0.2C suggesting that grain size has an influence on the size of the damage. The smaller grain size alloy should be the more ductile alloy [14] and therefore a reduced level of fracture should be observed. A limited difference was observed in the number and distribution of the defects observed for each alloy. Some instances of smeared material were observed with an increase in cutting speed or maximum flank wear level. Adhered material was visible on the workpiece surface of every test.

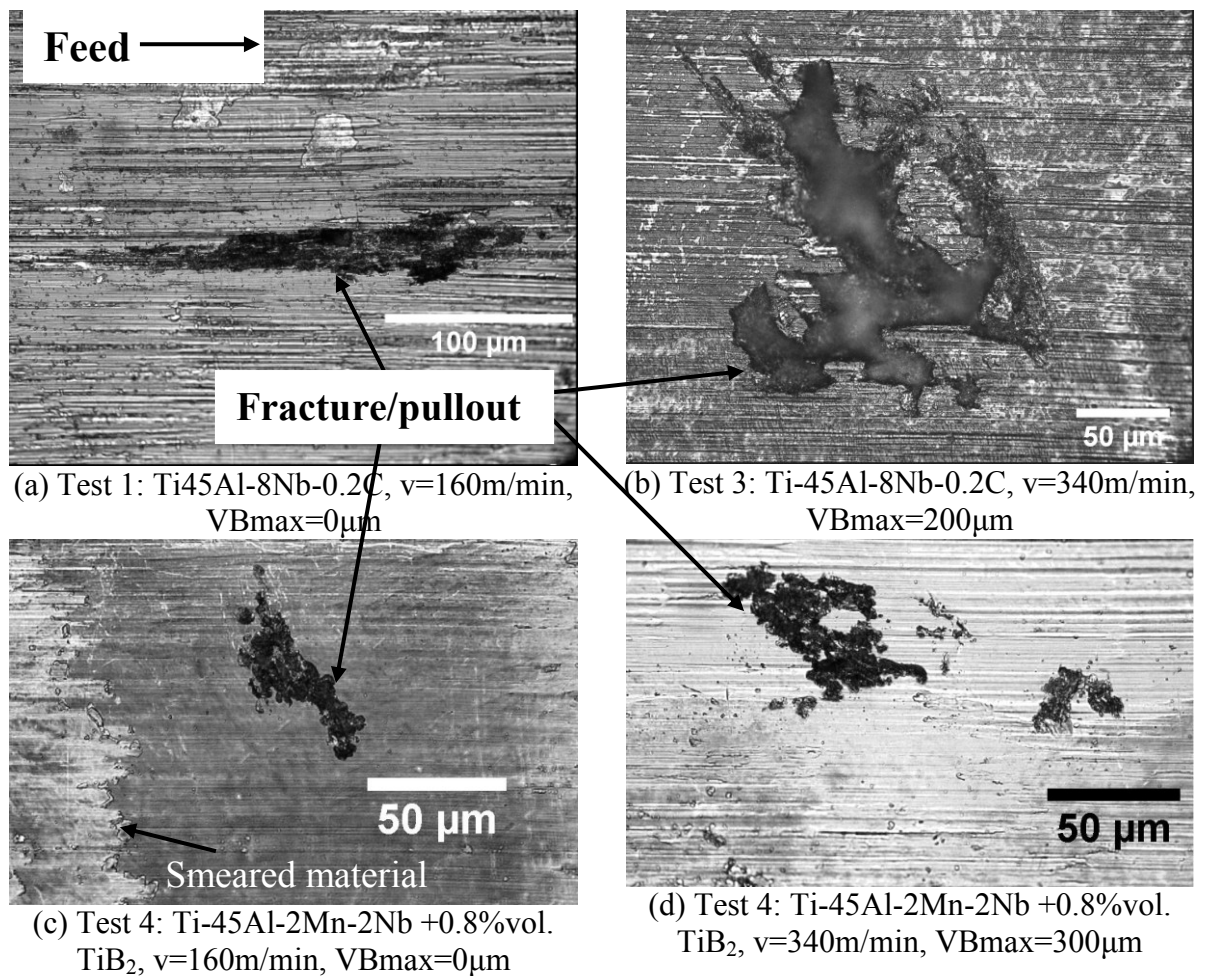


Figure 4.36: Images of machined workpiece surface (Phase 1B)

f) Microhardness

Microhardness profiles showing hardness against distance from the machined workpiece surface are shown in Figures 4.37 and 4.38. Individual microhardness profiles for each test and tool wear level are shown in Appendix C, Figures C47 to C50. All samples for Ti-45Al-2Mn-2Nb+0.8% vol. TiB₂ showed the presence of a strain hardened layer to a depth of

~300 μm with the increase in workpiece hardness ranging from 100 $\text{HK}_{0.025}$ up to 250 $\text{HK}_{0.025}$ above bulk hardness depending on operating conditions. Similar results in terms of the depth of the hardened layer were obtained for Ti-45Al-8Nb-0.2C, however, maximum hardness was ~50 $\text{HK}_{0.025}$ lower. The highest flank wear level caused the largest increase in microhardness with in general, increasing flank wear by an increment of 100 μm causing an increase in hardness of up to ~25 $\text{HK}_{0.025}$. This was probably because a greater amount of rubbing and plastic deformation occurred with a worn tool.

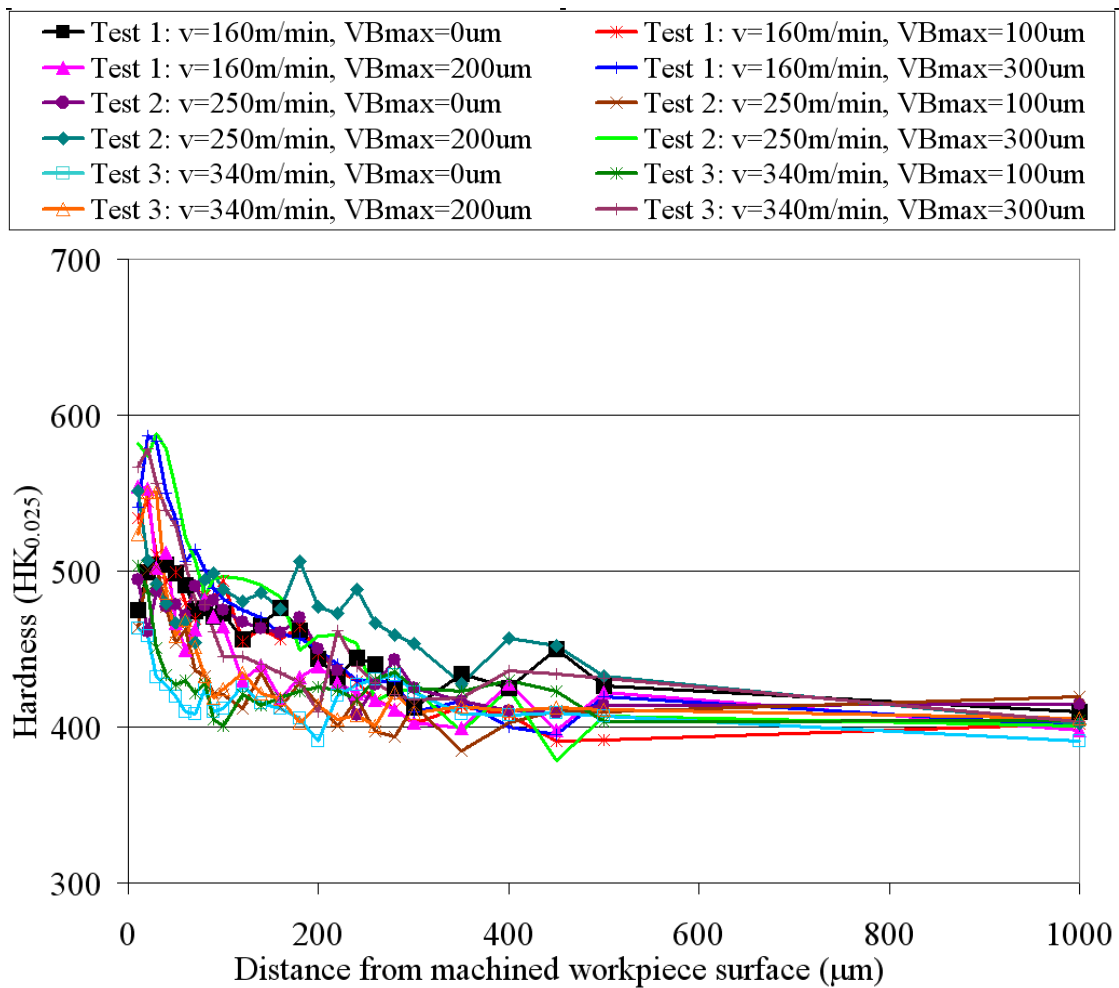


Figure 4.37: Microhardness depth profiles for Tests 1 to 3 (Ti-45Al-8Nb-0.2C)

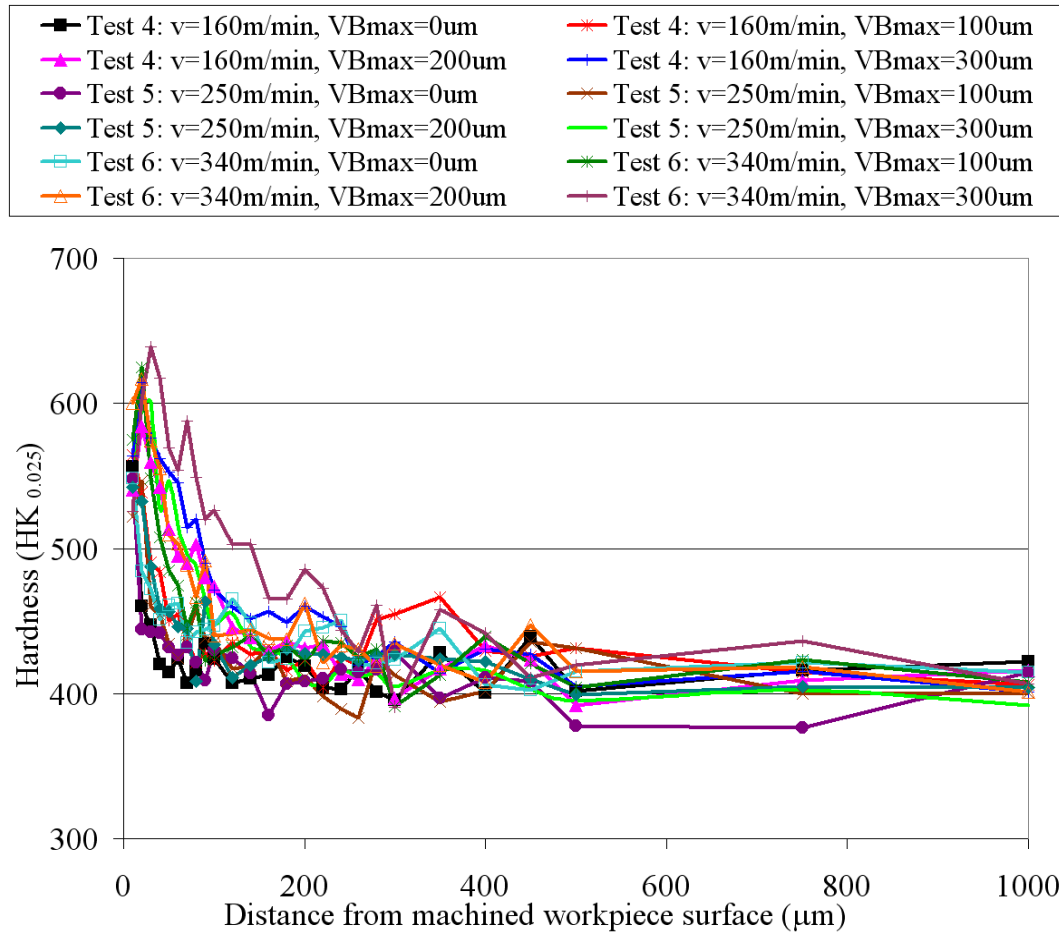
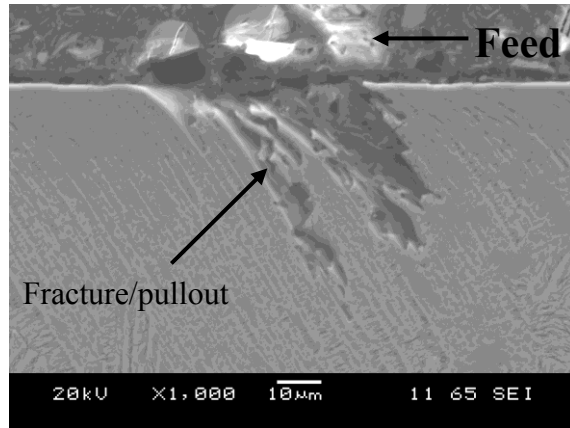


Figure 4.38: Microhardness depth profiles for Tests 4 to 6
(Ti-45Al-2Mn-2Nb +0.8%vol. TiB_2)

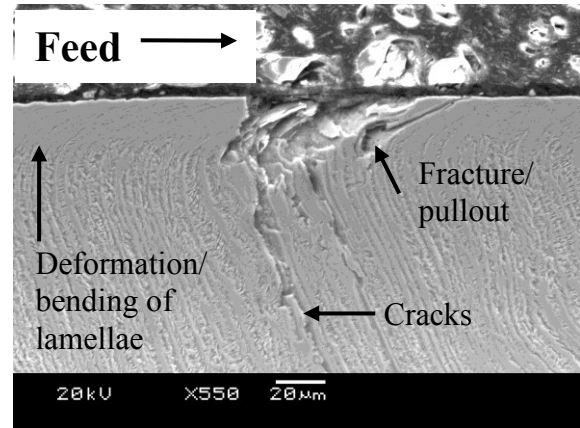
g) Workpiece surface/subsurface

Assessment of the machined surface/subsurface established the presence of material fracture/pullout in accordance with the assessment of the machined workpiece surface. Workpiece surface/subsurface cross-sectional micrographs showing the extent of this damage are detailed in Figure 4.39. In general, the depth of the fracture/pullout was restricted to $<50\mu\text{m}$ from the machined workpiece surface, however one single large region $\sim 100\mu\text{m}$ was found for Test 3 using the Ti-45Al-8Nb-0.2C alloy at a cutting speed of 340m/min and a maximum flank wear level of $200\mu\text{m}$ in a direction perpendicular to the feed. No differences in the size, location or depth of the fracture/pullout were observed between longitudinal or transverse analysis directions. No correlation could be found linking the size and depth of the damage to cutting speed or maximum flank wear within the range tested. This was probably due to the fracture/pullout being observed at random locations on the workpiece surface, consequently it was possible that cross-sectional micrographs missed significant portions of the damage as they reflected a ‘snap shot’ of the workpiece surface/subsurface at a particular

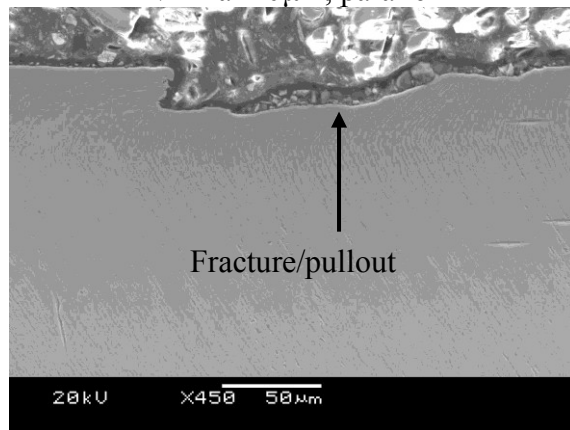
position. Harding [101] reported a similar trend when end milling a γ -TiAl alloy with analysis of the machined surface showing extensive fracture/pullout yet only two cross-sectional micrographs showed this occurring.



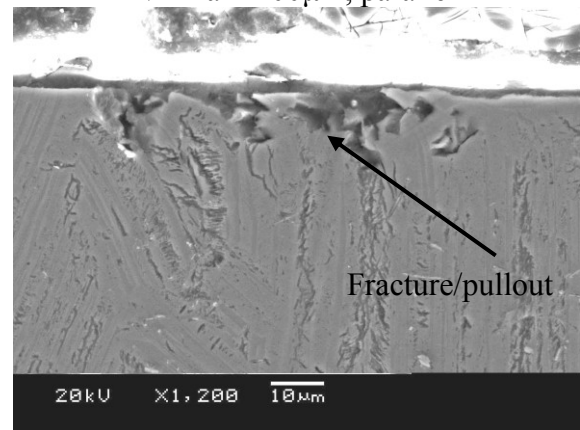
(a) Test 2: Ti-45Al-8Nb-0.2C, $v=250\text{m/min}$, $VB_{\text{max}}=0\mu\text{m}$, parallel



(b) Test 3: Ti-45Al-8Nb-0.2C, $v=340\text{m/min}$, $VB_{\text{max}}=200\mu\text{m}$, parallel



(c) Test 3: Ti-45Al-8Nb-0.2C, $v=340\text{m/min}$, $VB_{\text{max}}=200\mu\text{m}$, perpendicular



(d) Test: 4: Ti-45Al-2Mn-2Nb +0.8vol. TiB_2 , $v=160\text{m/min}$, $VB_{\text{max}}=100\mu\text{m}$, perpendicular

Figure 4.39: Workpiece surface/subsurface cross-sectional images (Phase 1B) (1)

In general, Ti-45Al-8Nb-0.2C cross-sectional micrographs showed surface damage appearing to be larger in terms of size, depth and observed incidence than Ti-45Al-2Mn-2Nb+0.8% vol. TiB_2 cross-sections and was possibly due to the larger grain size of the former alloy. Similar workpiece fracture/pullout is reported by Mantle and Aspinwall [107] to a depth of $<10\mu\text{m}$ from the workpiece surface when high speed ball nose end milling Ti-45Al-2Mn-2Nb+0.8% vol. TiB_2 . Plastic deformation was visible in the form of bending of the lamellae. In general, trends for cutting speed and maximum flank wear level appeared to mimic the hardness depth profiles. Higher hardness levels were caused by higher flank wear and cutting speed had the greatest influence on bending of the lamellae, extending a depth of up to $100\mu\text{m}$ for Ti-45Al-8Nb-0.2C, see Figure 4.40 (a).

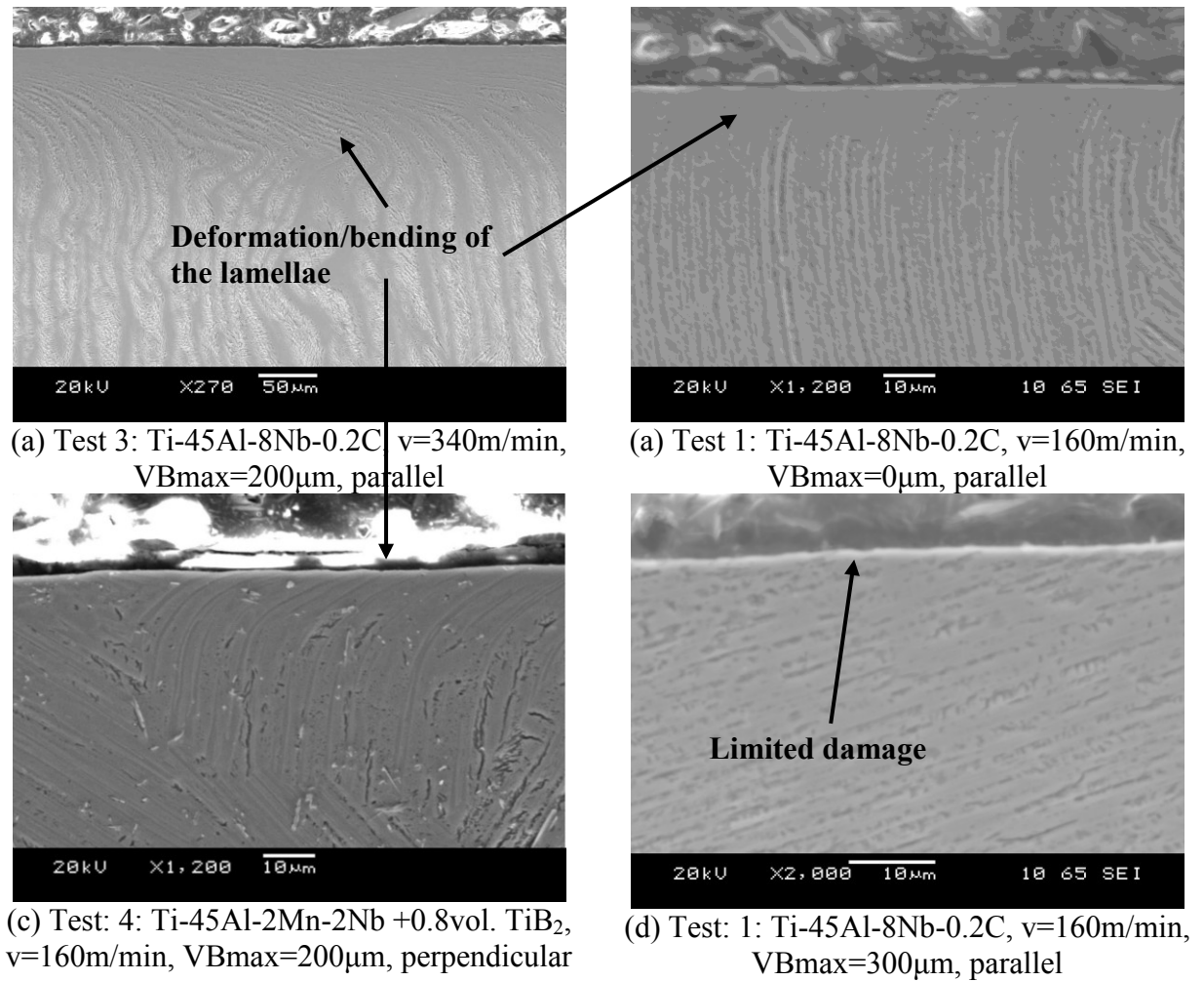


Figure 4.40: Workpiece surface/subsurface cross-sectional images (Phase 1B) (2)

Bending of the lamellae at lower operating parameters was restricted to $<20\mu\text{m}$ from the workpiece surface, see Figure 4.40 (b). Ti-45Al-2Mn-2Nb-0.8% vol. TiB_2 with a smaller, more uniform grain size appeared to show marginally lower levels of lamellae bending than Ti-45Al-8Nb-0.2C at lower cutting speeds, see Figure 4.40 (c). Figure 4.40 (d) shows the surface produced that had no visible damage including fracture/pullout and/or bending of the lamellae and indicates that it was possible to produce surfaces of acceptable integrity with minimum damage.

4.3 Phase 1C: High speed ball nose end milling of burn resistant titanium alloy (BuRTi)

a) Tool life

Tool life results for distance machined are shown in Figure 4.41. A wide range of values from 2m to 68m were obtained for a maximum flank wear criteria of $300\mu\text{m}$ indicating that careful selection of operating parameters is required. Of the 8 tests performed as part of the initial

experimental design (excluding the confirmation test), Test 5 produced the longest distance machined at 68m. In general, this test used the lower levels of feed rate and radial depth of cut, along with the finer grade IC903 substrate material, HP cutting fluid and a workpiece tilt angle of 45°. It was difficult to draw conclusions directly from Figure 4.41 as with the experimental design used, several factors were different for each test.

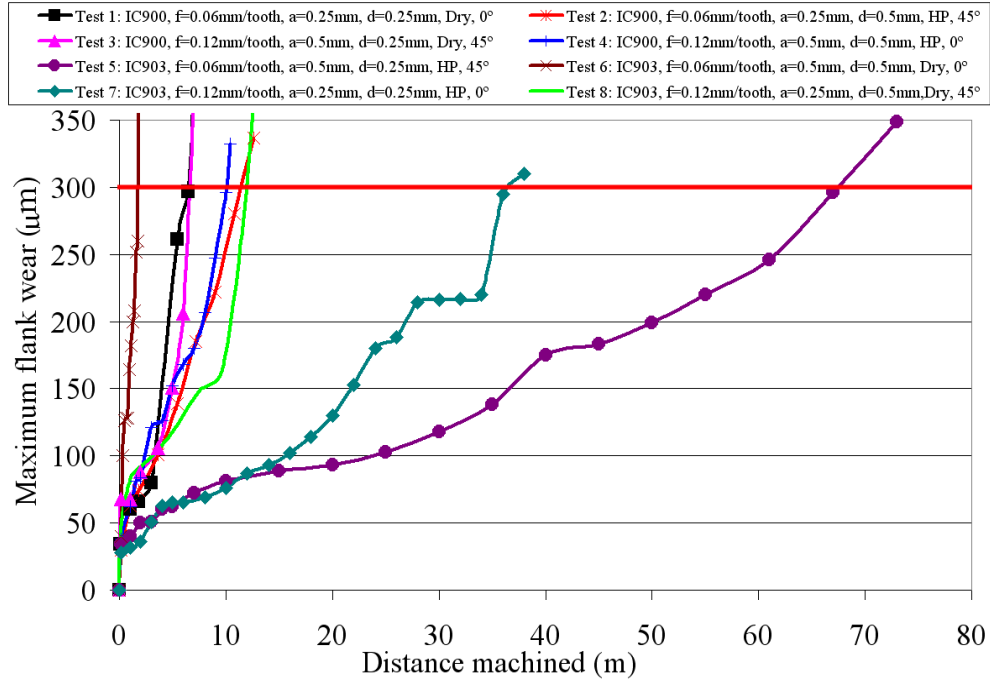


Figure 4.41: Maximum flank wear against distance machined (Phase 1C)

Figure 4.42 shows the Main Effects Plot - means for tool life using a 300µm maximum flank wear tool life criterion. The figure shows distance machined, machining time and material removed as exhibiting almost identical trends with the longest tool life using IC903 tooling, a feed rate of 0.06mm/tooth, an axial depth of cut of 0.5mm, a radial depth of cut of 0.25mm, HP fluid and a workpiece tilt angle of 45°. These operating parameters were used for Test 5. The coating and geometry of the two types of cutting tool, IC900 and IC903 was identical therefore the increased performance for IC903 was attributed to the finer grain size, higher hardness and increased resistance to fatigue of the carbide substrate [30, 168]. A similar result was found for γ -TiAl during Phase 1A. The reduction in tool life observed when increasing both the feed rate and radial depth of cut was as expected, as a higher material removal rate should increase the cutting forces and temperatures resulting in an increase in tool flank wear, again a similar result was found during Phase 1A.

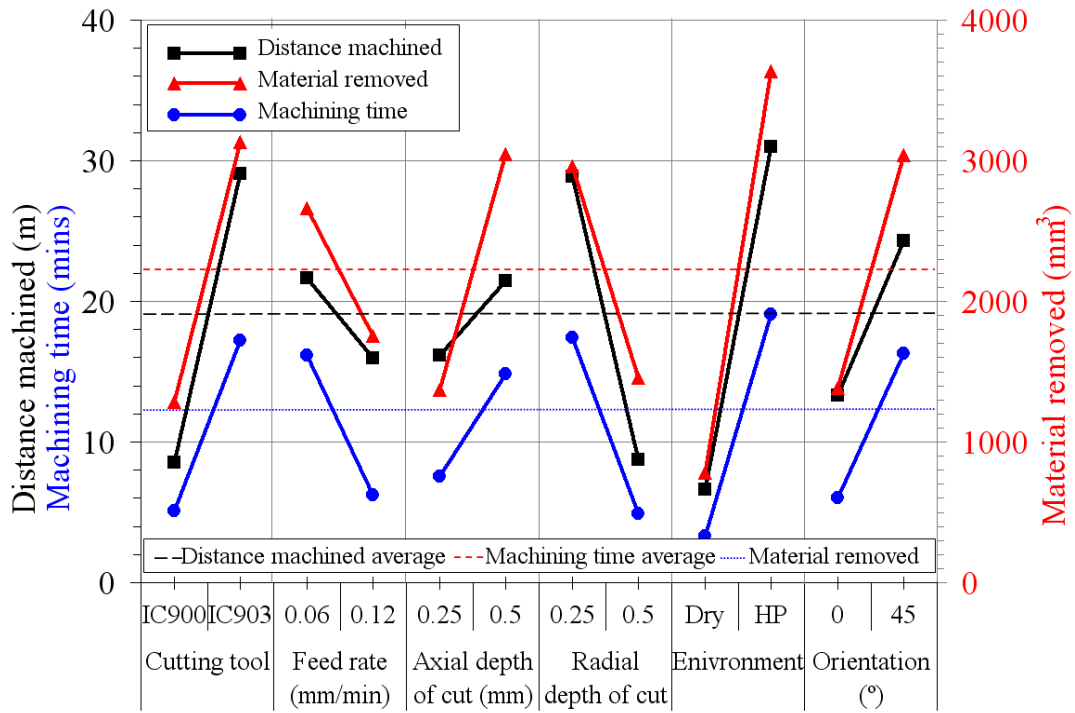
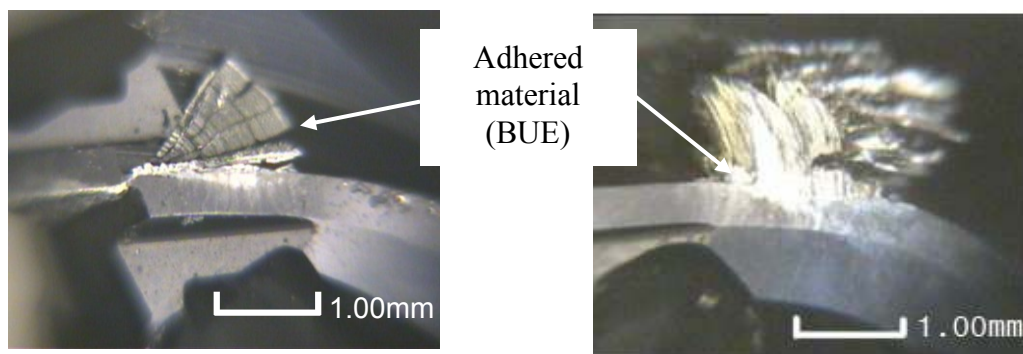


Figure 4.42: Main Effects Plot - means for tool life

A high instance of built-up-edge (BUE) and adhered material was observed when machining dry. High pressure (HP) cutting fluid helped to reduce the level however it did not eliminate BUE. Figure 4.43 shows the BUE and adhered material on part worn tools ($VB_{max} \approx 200 \mu m$) for Tests 6 and 8. Su et al. [175] report a similar tendency for the workpiece material to adhere to the surface of the cutting tool when milling Ti-6Al-4V dry or under a variety of cooling/lubrication conditions. Ezugwu et al [97] state that cutting fluid acts as both a coolant and lubricant reducing the tool temperature and chip welding that are commonly experienced with titanium alloys. Temperatures are reported to be $\sim 200^\circ$ lower using HP cutting fluid than dry cutting when machining Inconel 718 [56].



(a) Test 6: IC903, $f=0.06 \text{ mm/tooth}$, $a=0.5 \text{ mm}$, $d=0.5 \text{ mm}$, dry, 0°

(b) Test 8: IC903, $f=0.12 \text{ mm/tooth}$, $a=0.25 \text{ mm}$, $d=0.5 \text{ mm}$, dry, 45°

Figure 4.43: Wear scar photographs showing adhered material (Phase 1C)

Operating with a workpiece tilt angle of 45° eliminated the ploughing at the centre of the ball, caused by an effective cutting speed of zero that occurs when the cutting tool axis was perpendicular to the workpiece surface. Figure 4.44 illustrates this point, with images showing SEM images of cutting tools used to machine in both workpiece orientations.

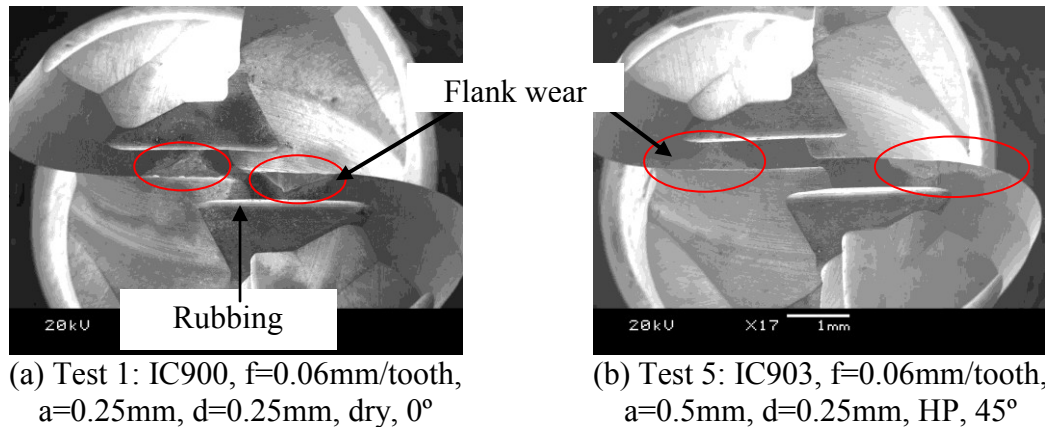


Figure 4.44: Wear scar photographs show wear location (Phase 1C)

The Main Effects Plot - means for tool life, Figure 4.42 indicated, somewhat surprisingly, improved tool life with increasing axial depth of cut. On closer inspection of individual tool wear scars, tests employing a 0.25mm axial depth of cut, in general, provided better tool life. The contradictory observation was thought to be due to interactions between factors that were not accounted for in the Taguchi design. As the levels of factors that produced the “best” tool life had been completed as part of Test 5, a confirmation test Test 9, using exactly the same parameters as Test 5 except a 0.25mm axial depth of cut was felt necessary. Figure 4.45 shows that Test 9 when compared to Test 5, achieved a $\sim 10\%$ increase in the distance machined before the maximum flank wear criterion was reached. This increase was not large enough however to affect the result of material removed, where almost twice as much workpiece material was removed by Test 5 in contrast to Test 9 with identical flank wear levels.

The results presented in Figure 4.45 show a marginally lower performance for the current trials compared to the previous work of Novovic et al. [150]. Maximum flank wear for a distance machined of 50m ranged from $150\text{--}200\mu\text{m}$, compared to $100\text{--}150\mu\text{m}$ for the previously reported work. As the operating parameters were similar, this reduction in tool life could have been due to slight differences in workpiece material, however it was more probably due to the differences in the cutting tools. As the substrate, geometry and coating were different between the two products, it was difficult to assess which factor was

responsible. Phases 1B and C used an identical feed rate, axial and radial depth of cut, cutting tool and orientation, however, the cutting environment was different with each workpiece material having their preferred conditions (γ -TiAl: dry, BuRTi: HP). the BuRTi alloy would also be expected to cause a reduction in tool life for BuRTi.

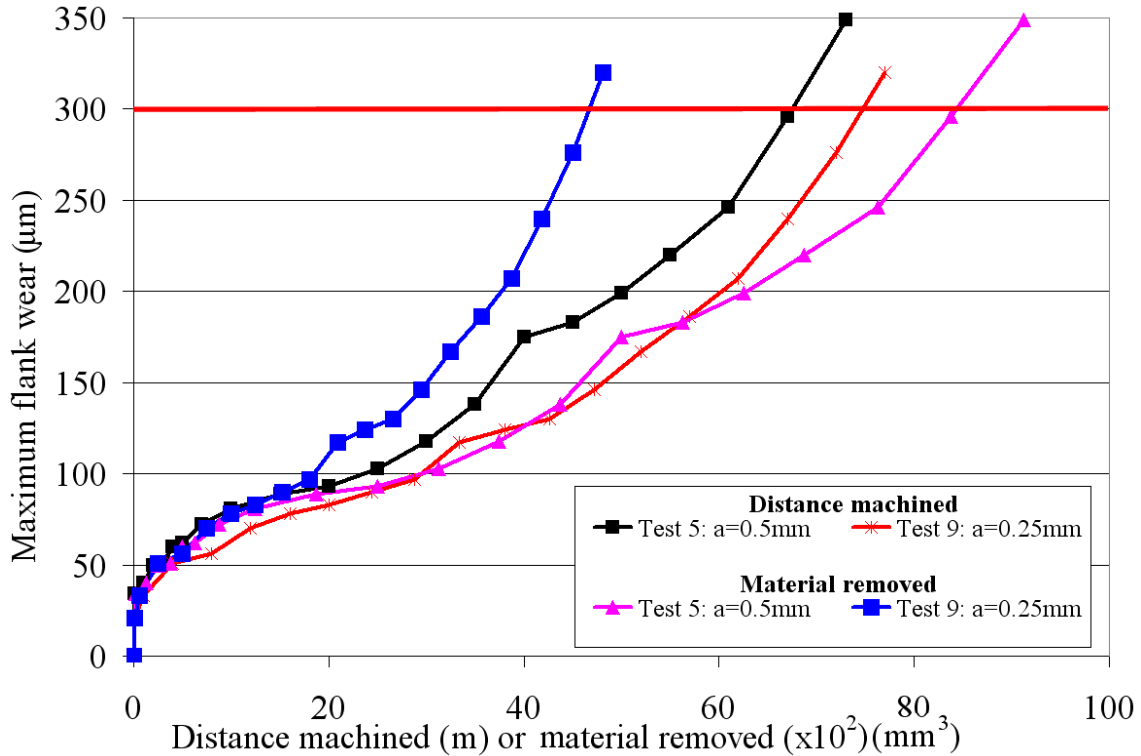


Figure 4.45: Maximum flank wear against distance machined or material removed

The distance machined before the maximum flank wear criteria was reached for γ -TiAl was $\sim 10\times$ higher than for BuRTi despite the cutting speed for γ -TiAl being 60% higher than for BuRTi. This is a significant improvement in tool life for the γ -TiAl workpiece material and contrasts with vT curves detailed in [6] which suggest BuRTi is easier to machine than γ -TiAl alloys when turning. The lower cutting speed could be responsible for the difference, as increased levels of BUE are generally found at lower cutting speeds and subsequently an increase in cutting speed could produce longer life. The 30% higher tensile strength, the increased room temperature ductility and the presence of carbide particles in

Analysis of Variance (ANOVA) for distance machined is shown in Table 4.9 whilst ANOVA tables for machining time and volume of material removed are shown in Tables C6 and C7 in Appendix C. $F_{5\%(1, 1)}=111$ therefore no factors were identified as being statistically significant at the 5% level [154]. The tables also revealed that cutting environment had the greatest influence on tool life with a percentage contribution ratio (PCR (%)) ranging from

17.2 to 28.7% followed by tool grade 18.5%, radial depth of cut 17.7% and orientation 1.0%. Residual error levels were also high indicating that factors were omitted, measurement errors were present or most likely, that there were interactions between factors [154].

	S.S.	D.O.F.	M.S.S.	F _{calc}	PCR (%)
Cutting tool	839.3	1	839.3	4.03	18.5
Feed rate	65.8	1	65.8	0.32	0.00
Axial depth of cut	55.4	1	55.4	0.27	0.00
Radial depth of cut	810.4	1	810.4	3.89	17.7
Environment	1187.8	1	1187.8	5.71	28.7
Orientation	242.0	1	242.0	1.16	1.0
Error	208.1	1	208.1	-	34.1
Total	3408.8	7	-	-	-

Table 4.9: ANOVA table for distance machined (Phase 1C)

b) Cutting forces

The Main Effects Plot - means for maximum resultant force, detailed in Figure 4.46 shows values for both new and worn tooling. Using worn tooling caused the resultant force on average to increase by 160%. Not surprisingly, increasing the material removal rate by changing the feed rate, axial and radial depth of cut caused an increase in the resultant force by up to 60N for a new tool and 160N for a worn tool.

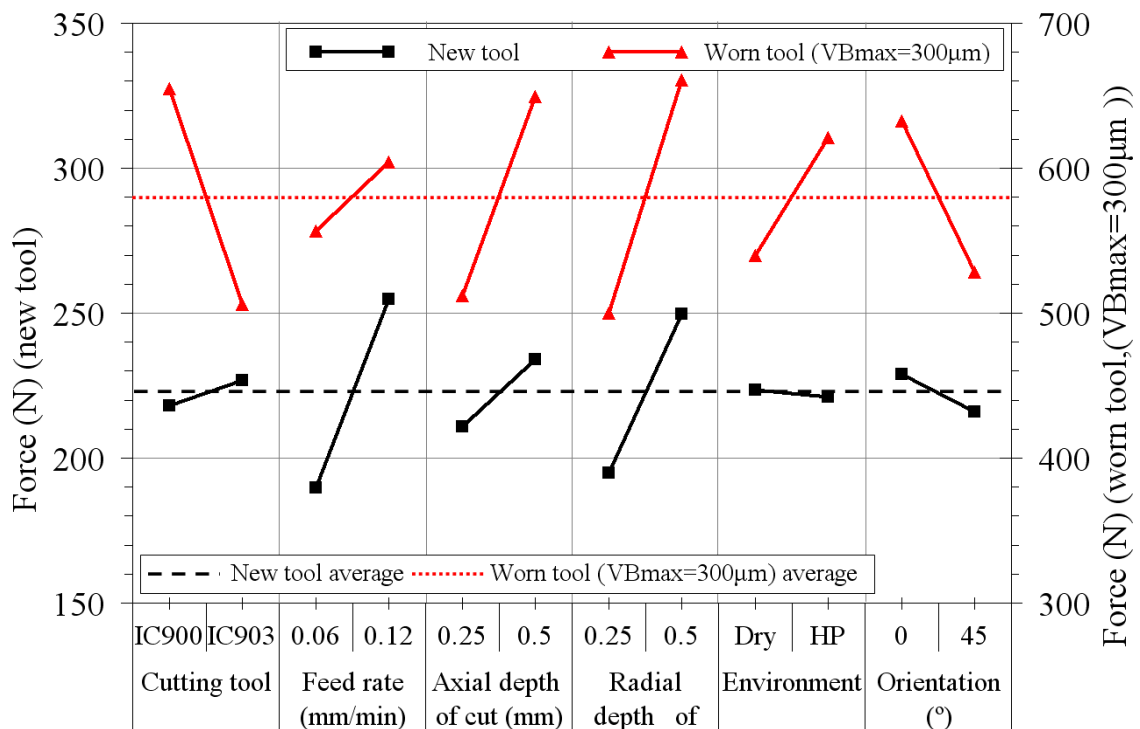


Figure 4.46: Main Effects Plot - means for resultant force

In terms of workpiece orientation the lowest resultant force occurred with the workpiece at 45° . This was probably because of the reduced level of ploughing compared with the workpiece at 0° and the more favourable cutting configuration. With a new tool, changing the cutting tool and environment had little effect on force, however, with worn tools both factors assumed greater significance. In the case of the cutting tool, a worn IC903 produced a 150N lower value than a worn IC900. Ng et al. [164] reported resultant forces of $\sim 300\text{N}$ when milling Inconel 718 using down milling in a horizontal downwards direction using new TiAlN tools. The slightly lower values obtained for the current work are a result of the reduced hardness of the workpiece and the reduction in the radial depth of cut from 2mm to 0.25-0.5mm.

A comparison of the cutting force components F_x , F_y and F_z measured for Tests 5 and 9 (confirmation experiment) is shown in Figure 4.47. For each test, the graph shows all three components increasing by up to 400% over the transition from a new tool to a worn tool. Increasing the axial depth of cut from 0.25mm to 0.5mm caused a slight increase ($\sim 10\%$) in the F_x and F_y force components with both a new tool and a worn tool. Despite these differences all three components showed similar values for the forces at intermediate flank wear levels ($VB_{\max} = 50\text{-}250\mu\text{m}$). Several of the tests showed a peak force value at a flank wear level of between $200\text{-}250\mu\text{m}$ with a slightly lower value for a flank wear of $300\mu\text{m}$.

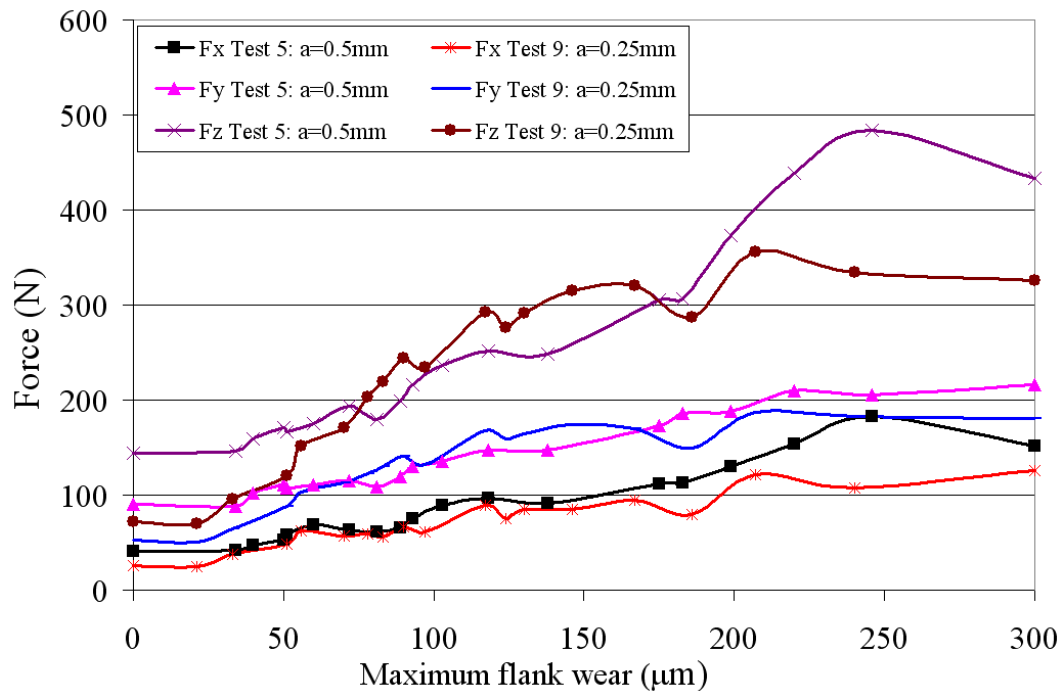


Figure 4.47: Force against maximum flank wear for Tests 5 and 9

c) Workpiece surface roughness

The Main Effects Plot - means for workpiece surface roughness, Figure 4.48 shows that the workpiece surface roughness R_a was on average 33% higher perpendicular to the feed direction than in the parallel directions. The cutting tool type showed limited difference between levels however this was expected, as the cutting tool geometry and coating were identical for both tool types. Other notable trends are that workpiece tilt angle (orientation) and feed rate had the greatest influence in improving the roughness of the machined surface. Tests which were carried out with the workpiece horizontally mounted showed higher surface roughness (average of $3.89\mu\text{m}$ R_a over 4 tests) when compared against those performed with a 45° tilt angle (average of $1.45\mu\text{m}$ R_a). Mantle and Aspinwall [100] report a similar finding with the workpiece orientation having a greater effect on the workpiece surface roughness in a direction perpendicular to the feed direction rather than parallel. Despite the higher room temperature ductility of the BuRTi alloy, surface roughness results, in the direction perpendicular to the feed were comparable ($R_a \sim 0.5\mu\text{m}$) for γ -TiAl and BuRTi alloys when using a worn tool ($VB_{\text{max}}=300\mu\text{m}$).

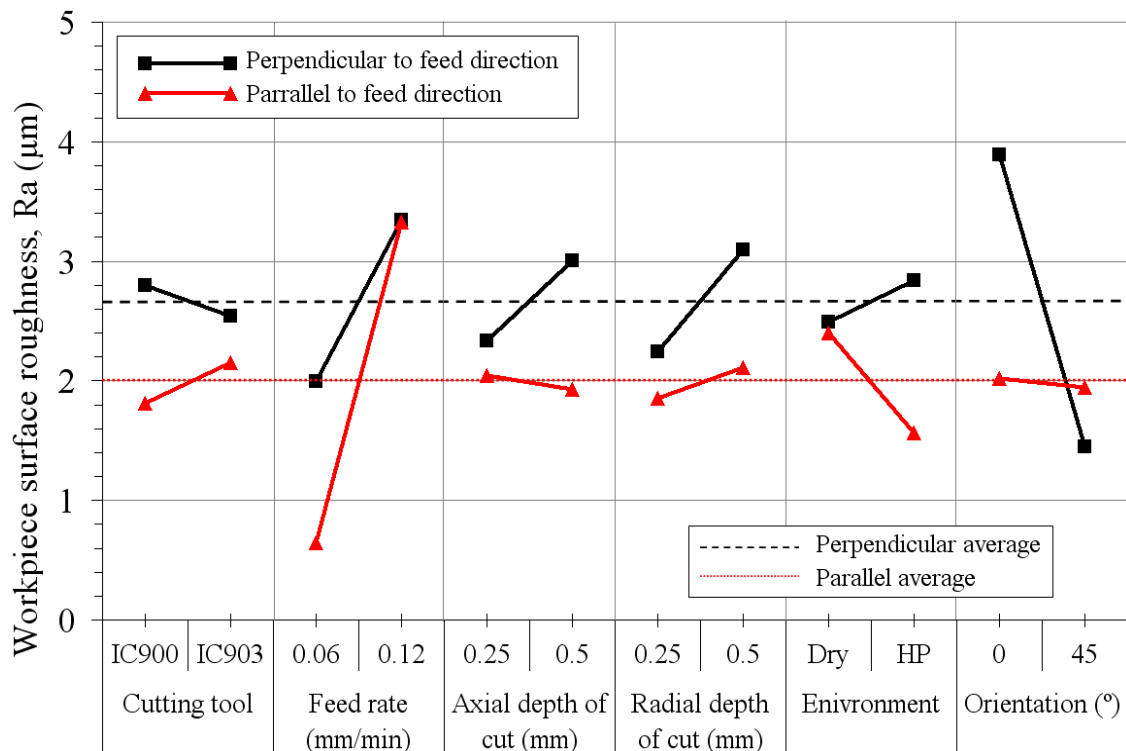


Figure 4.48: Main Effects Plot - means for workpiece surface roughness R_a (Phase 1C)

ANOVA analysis of workpiece surface roughness perpendicular to the feed direction is given in, Table 4.10. As $F_{0.05;1;1} = 161$ [154] none of the factors for surface roughness R_a

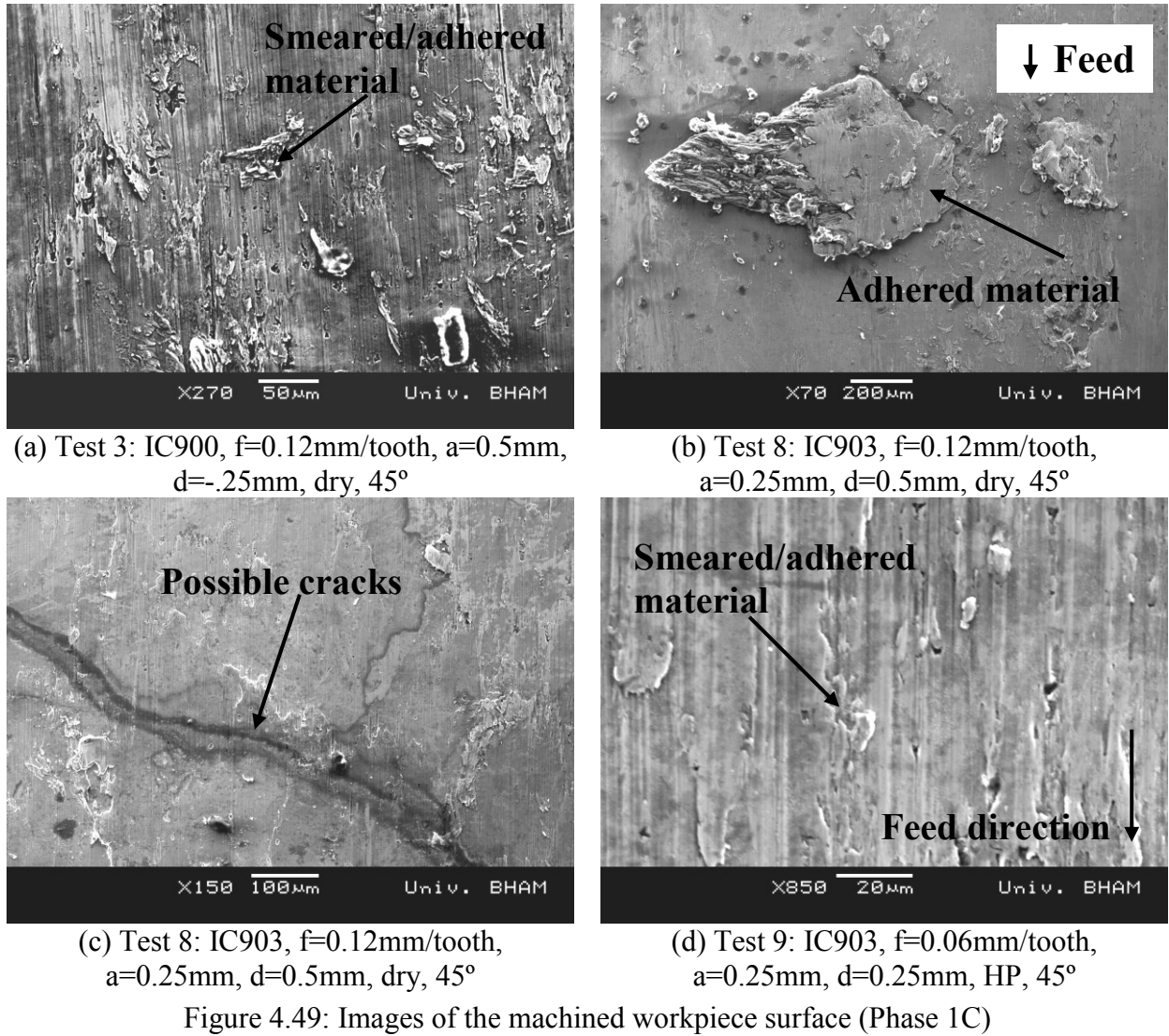
perpendicular to the feed direction were determined as being statistically significant at the 5% level. The largest percentage contribution of 58.39% is attributed to the workpiece angle, 14.77% to the feed rate and 0.50% and 3.34% to axial and radial depths of cut respectively. The residual error level of 23.01% was higher than the 15% recommended by Ross [154] for acceptable noise. The ANOVA table for surface roughness Ra parallel to the feed direction is shown in Appendix C, Figure C10. Feed rate and environment were determined as being statistically significant at the 5% level.

Source	S.S.	D.O.F.	M.S.S.	F _{calc}	PCR (%)
Cutting tool	0.1281	1	0.1281	0.16	0
Feed rate	3.6133	1	3.6133	4.50	14.77
Axial depth of cut	0.8976	1	0.8976	1.12	0.50
Radial depth of cut	1.4380	1	1.4380	1.79	3.34
Environment	0.2402	1	0.2402	0.30	0.00
Orientation	11.9167	1	11.9167	14.86	58.39
Error	0.8022	1	0.8022	-	23.01
Total	19.0361	7	-	-	-

Table 4.10: ANOVA table for surface roughness Ra perpendicular to the feed direction

d) Workpiece surface

Figure 4.49 shows examples of workpiece surfaces produced using worn tools ($VB_{max}=300\mu m$). Adhered material was found on all surfaces of varying size (up to 1mm) and frequency depending on operating parameters, see Figures 4.49 (a) and (b). Surfaces of tests using high pressure cutting fluid had reduced levels of adhered material and smearing which was also observed on tests where a large step-over was implemented, whilst tests at 45° showed lower levels of smearing as a consequence of the improved cutting speed distribution over the cutting edge. Holes/ pull out which were possible sites of fractured/removed carbides were found in the top region of all surfaces whilst possible microcracks were found on the worst surfaces (Test 3 and 8), see Figure 4.49 (c). The confirmation test, Test 9 showed the “best” surface, with smeared/adhered material reduced to $\sim 20\mu m$ in size. Due to limited workpiece material availability no workpiece surfaces were produced using new tools. It was expected that these surfaces would show lower levels of damage including adhered material, smearing, cracks and voids. Burring was observed on the exit from the workpiece of each pass however, high pressure cutting fluid reduced the severity



e) Microhardness

Microhardness profiles were taken for all samples perpendicular to the feed direction. Figure 4.50 shows all the microhardness depth profiles. Most samples show an increased hardness of up to $80\text{HK}_{0.025}$ higher than the bulk hardness of $\sim 370\text{HK}_{0.025}$ to a depth of up to $500\mu\text{m}$. It was found that samples for Tests 3, 5 and 8 had increased hardness over the entire depth measured. The presence of non-uniformly distributed carbide particles of up to $\sim 12\mu\text{m}$ in size made the measurement of microhardness difficult. A comparison can be drawn between Test 5 and 9 (confirmation experiment) surfaces. Here axial depth of cut was the only operating parameter that was varied with Test 5 (using a 0.5mm axial depth of cut) experiencing an increased microhardness of up to $\sim 100\text{HK}_{0.025}$ higher than bulk hardness to a depth of around $400\mu\text{m}$. Test 9 (using a 0.25mm axial depth) showed both a reduction in hardness and depth of the hardened layer. These latter are in agreement with the work of Novovic et al. [150], who report limited change in the microhardness from the surface into the bulk workpiece.

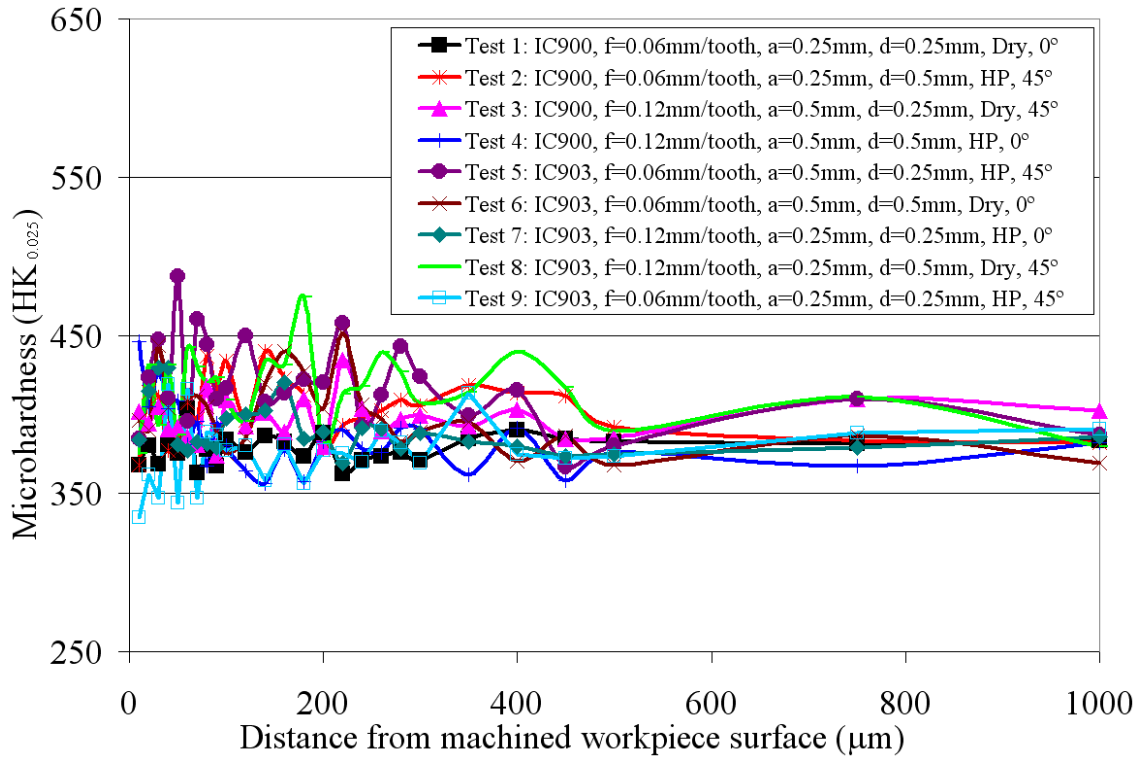
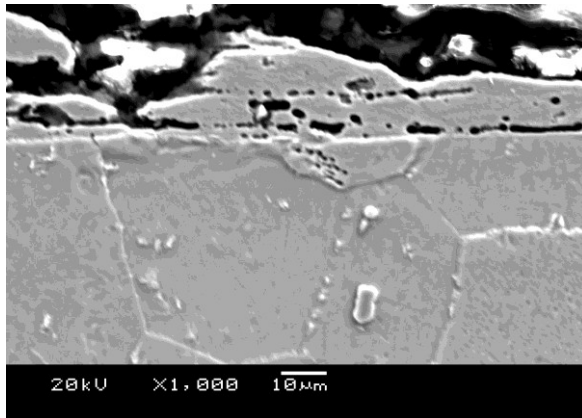


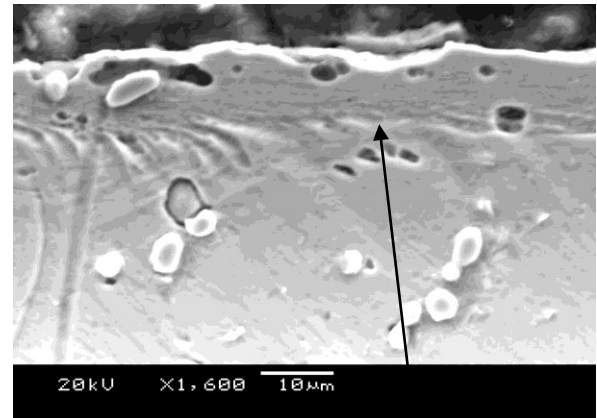
Figure 4.50: Microhardness depth profiles (Phase 1C)

f) Workpiece surface/subsurface

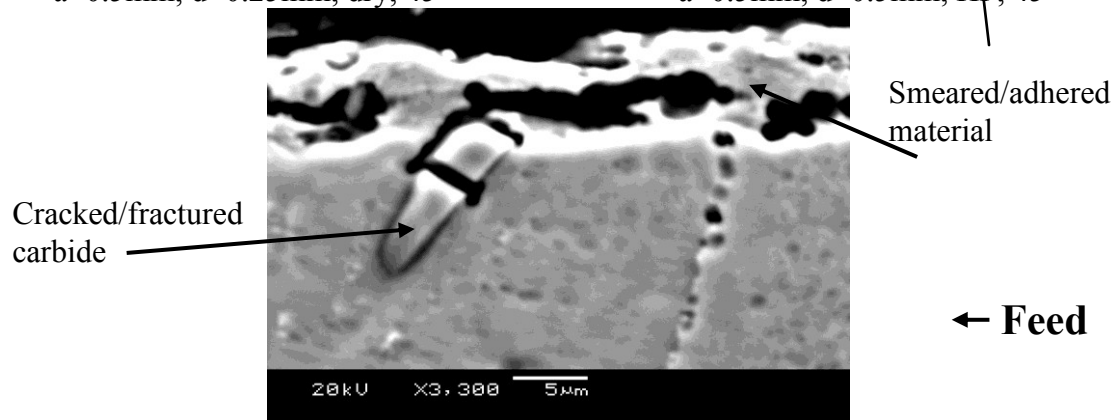
Figure 4.51 shows a range of surface/subsurface cross-sectional micrographs in a direction parallel to the feed. As with the analysis of the machined workpiece surface, adhered material up to a depth of $\sim 20\mu m$ was seen on the surface of every cross-section, the depth and frequency of which depended on the operating parameters. In general, an orientation of 45° , HP cutting fluid and lowest feed, depth of cut and stepover produced the lowest levels. Surface smearing and ploughing was also observed. Material pullout at the surface and voids were found in “reformed” material. Carbide fracture or removal was also observed occurring at the workpiece surface. Figure 4.51 (c) details a sample cross-section from Test 5 showing fracturing of a carbide as well as material with voids adhered to the workpiece surface. Comparative levels of damage to the surface/subsurface were found by Novovic et al. [150], including fractured carbides near to the surface.



(a) Test 3: IC900, $f=0.12\text{mm/tooth}$, $a=0.5\text{mm}$, $d=0.25\text{mm}$, dry, 45°



(b) Test 4: IC900, $f=0.12\text{mm/tooth}$, $a=0.5\text{mm}$, $d=0.5\text{mm}$, HP, 45°



(c) Test 5: IC903, $f=0.06\text{mm/tooth}$, $a=0.5\text{mm}$, $d=0.25\text{mm}$, HP, 45°

Figure 4.51: Images of the machined workpiece surface/subsurface (Phase 1C)

5. RESULTS AND DISCUSSION:

PHASE 2, CREEP FEED GRINDING

5.1 Phase 2A: Assessment of significant operating parameters when creep feed grinding Ti-45Al-8Nb-0.2C using conventional abrasive wheels

5.1.1 Phase 2Ai: Initial assessment and benchmarking against BuRTi

a) Wheel wear, surface roughness, forces, power and specific energy

In general, the best combination of results including highest G-ratio of ~35, low workpiece surface roughness R_a of $1.48\mu\text{m}$ and lowest forces and power were obtained when operating with Test 1 parameters (wheel speed of 15m/s, a depth of cut of 1.25mm and a feed rate of 150mm/min). Bentley and Aspinwall [112] report comparative G-ratios of up to 50 when surface grinding the alloy Ti-45Al-2Mn-2Nb +0.8%vol. TiB_2 with conventional abrasive SiC wheels. Figure 5.1 shows a graph of G-ratio against volume of workpiece material removed for γ -TiAl. Compared to Test 1, all other tests showed a higher wheel wear rate with G-ratios in general, ranging from 5 to 10.

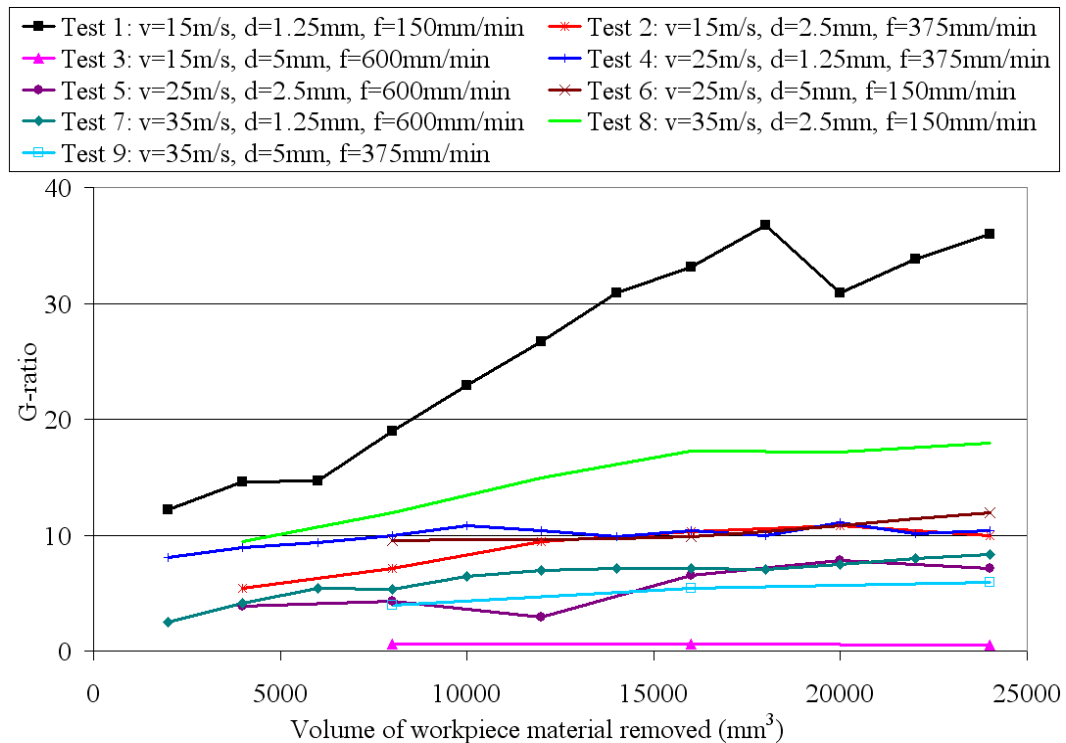


Figure 5.1: G-ratio against volume of workpiece material removed (Phase 2Ai, γ -TiAl)

Test 3, which had the highest combination of feed rate and depth of cut at the lowest wheel speed, produced the lowest G-ratio of <1 which implies an equal amount of material was removed from the wheel and the workpiece with a ‘contra’ grinding operating occurring. Novovic [151] describes a similar result occurring when creep feed grinding BuRTi with vitrified bonded SiC abrasive wheels using a cutting speed of 25m/s, a feed rate of 60-500mm/min and a depth of cut of 1mm. Kumar [176], describes G-ratios of ~ 1 when grinding Ti-6Al-4V with SiC wheels.

Liao et al. [60] suggest that typical wheel wear behaviour consists of a first regime of high initial wear, as the dressed grinding wheel grains become duller as a consequence of attritious wear, followed by a steady state regime with a nearly constant wear rate, where a parity is achieved between wear flat and new cutting edge generation, then a third regime of accelerating wear and a subsequent requirement to redress the wheel. Figure 5.1 showed that when the test end criteria had been reached, Test 1 was still in the initial phase with high initial wear. The majority of other tests reached the second regime with steady state wear caused by parity being reached between wear flat and new cutting edge generation. Malkin et al. [44] describes a similar shape curve with increased G-ratio against grinding time when grinding silicon nitride with electroplated diamond wheels. The wear rate for Test 3 was so high that the dressing operation did not have any influence on the grinding process and therefore no change in the wear rate was observed. Additionally extensive radial wheel wear of up to 3mm was observed on the wheel used for Test 3 using the lowest wheel speed and the highest depth of cut and feed rate. Figure 5.2 (a) shows the wheel profile with extensive ‘radiusing’ of the corners. During a grinding operation a wheel may act “soft” or “hard” regardless of its grade with this behavior being a function of the force on the grain, with a tendency for grains to fracture or dislodge when the grain force is higher [29].

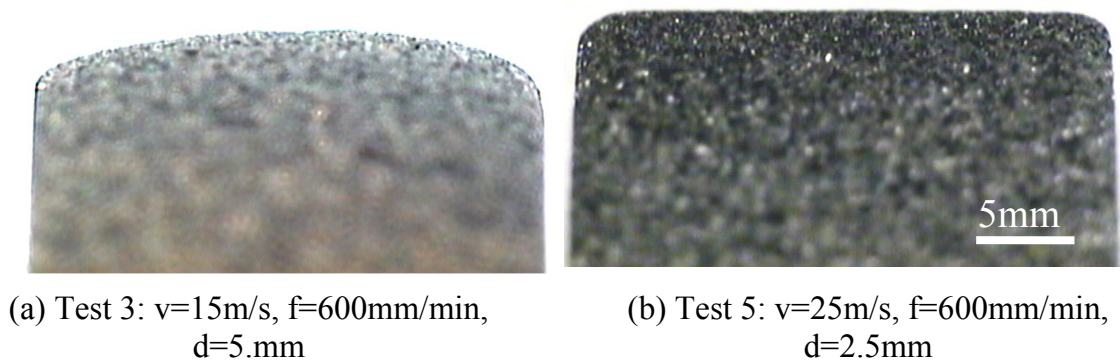


Figure 5.2: Wheel profile wear

The relative grain force is defined as being proportional to the feed rate and depth of cut whilst being inversely proportional to the wheel speed, thus in the case of Test 3, the wheel was acting “soft” and as a consequence the lowest G-ratio was measured. All other tests exhibited ‘radiusing’ of the grinding wheel corners however, at a much lower level ($\sim 1\text{mm}$), to that of Test 3, see Figure 5.2 (b). Similar wheel ‘radiusing’ for each test was also observed for the BuRTi alloy however at a slightly increased level. Sunarto [177] reports a similar “radiusing” effect when grinding deep rectangular shaped slots. Andrew et al. [40] states that when conventional abrasive wheels are used for creep feed grinding (CFG), the main wheel wear mode is attritious with wear occurring by the rubbing of the wear flats on the individual grits, resulting in even wear across the profile. In reality, it is unlikely that a compressor or turbine blade produced from a γ -TiAl alloy would have a slot 20mm wide and 15mm deep ground into it. It was decided therefore when developing this phase of experimentation to grind the slot so that the largest volume of workpiece material could be removed, as no data was found during the literature review on wheel wear rates for CFG of γ -TiAl alloys. For both alloys, limited workpiece material was found adhering to the surface of the grinding wheel.

Additional graphs showing normal and tangential forces, power and specific energy against volume of workpiece material removed for γ -TiAl are shown Appendix C, Figures C51 to C54. At the end of each test normal forces ranged from 800N to 2500N, tangential forces from 320N to 850N and power levels from 5kW to 23kW, depending on the operating parameters used. In general, tests that had the highest G-ratio also had the lowest force and power levels. The majority of tests showed an increase in the force and power levels as the volume of workpiece material removed increased. It is suggested that this was due to attritious wear causing increased generation of wear flats leading to greater rubbing and sliding components of the total force and power [42]. This also suggests that the dressing conditions used did indeed give a “sharp wheel” that was suitable for stock material removal. Comparable forces of 2000N to 3000N for normal force and 300N to 500N for tangential force are presented by Bentley and Aspinwall [118] when intermittent creep feed grinding Ti-45Al-2Mn-2Nb +0.8%vol. TiB_2 with similar operating parameters and SiC wheels.

The results of workpiece surface roughness R_a measurements taken on the surface parallel to the feed direction made at the end of each test are shown in Appendix C, Figure C55. The majority of values were in the range R_a $1.2\mu\text{m}$ to $1.8\mu\text{m}$, however Test 3 which had the lowest G-ratio had the highest surface roughness, with an R_a value of $3.60\mu\text{m}$. Both Bentley and Aspinwall [118] and Novovic [151] report comparable values ranging from R_a

0.6 μ m to 1.5 μ m depending on the operating parameters used when CFG γ -TiAl and BuRTi alloys.

It was difficult to draw conclusions concerning the effect of the different levels of each operating parameter directly from the graphs of output measure against volume of workpiece material removed. This was because several factors changed with each test as a result of the Taguchi design. Only when the “main effects” are considered can the effect of operating parameters be established. Figure 5.3 shows the Main Effects Plot - means for G-ratio for both γ -TiAl and BuRTi alloys. BuRTi alloy data for all main effects plots was based on the graphs detailed in Appendix C, Figures C56 to C61. The average value for γ -TiAl was $\sim 10\times$ higher than that for BuRTi. Trends for γ -TiAl were as expected with highest G-ratio obtained using a wheel speed of 15m/s, a feed rate of 1.25mm and a feed rate of 150mm/min. Wheel speed had almost the same effect on G-ratio for both alloys, however trends for depth of cut and feed rate differed for the two materials.

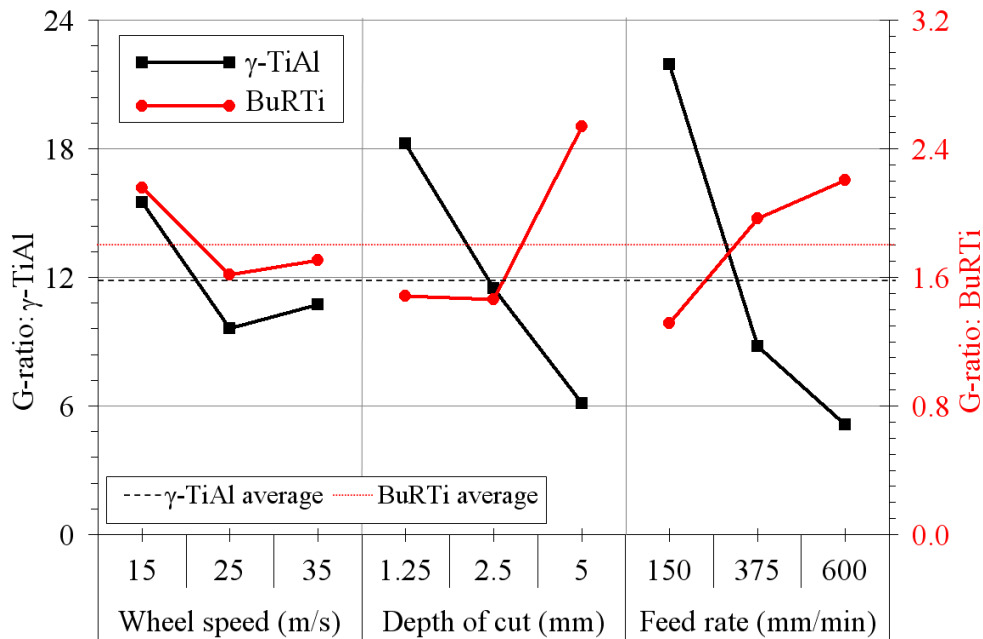


Figure 5.3: Main Effects Plot - means for G-ratio (Phase 2Ai)

Main effects plots - means for normal force and tangential force for both alloys are shown in Figures 5.4 and 5.5 respectively. Average tangential force was 50% lower for γ -TiAl than for BuRTi however average normal force for BuRTi was ~ 100 N lower than for γ -TiAl. Trends for γ -TiAl appeared more consistent with a higher depth of cut and feed rate causing an increase in both force components. Increasing wheel speed caused an increase in normal force but a decrease in tangential force. The BuRTi trends are in part more difficult to explain as

altering the feed rate and depth of cut had very little effect on normal force. Similarly, tangential force when increasing both depth of cut and feed rate showed a reduction in force. In the absence of grinding temperature data and a possible correlation with material strength, the reasons for this are unclear. The significantly lower thermal conductivity value for BuRTi of $\sim 10\text{W/m.K}$ compared with $\sim 22\text{W/m.K}$ for $\gamma\text{-TiAl}$ would be expected to give greatly increased temperatures when grinding the former.

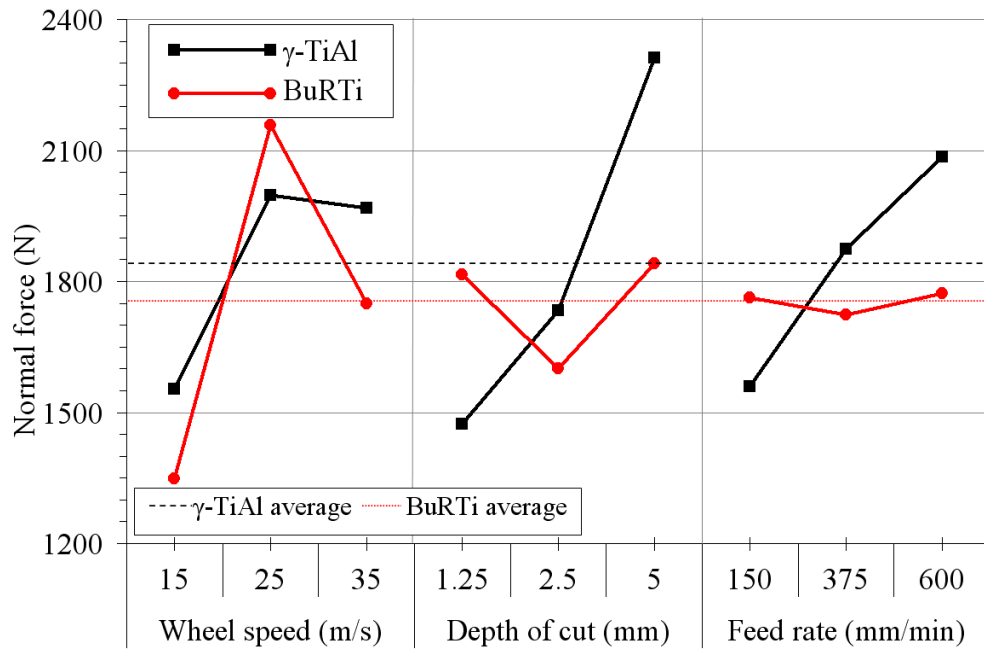


Figure 5.4: Main Effects Plot - means for normal force (Phase 2Ai)

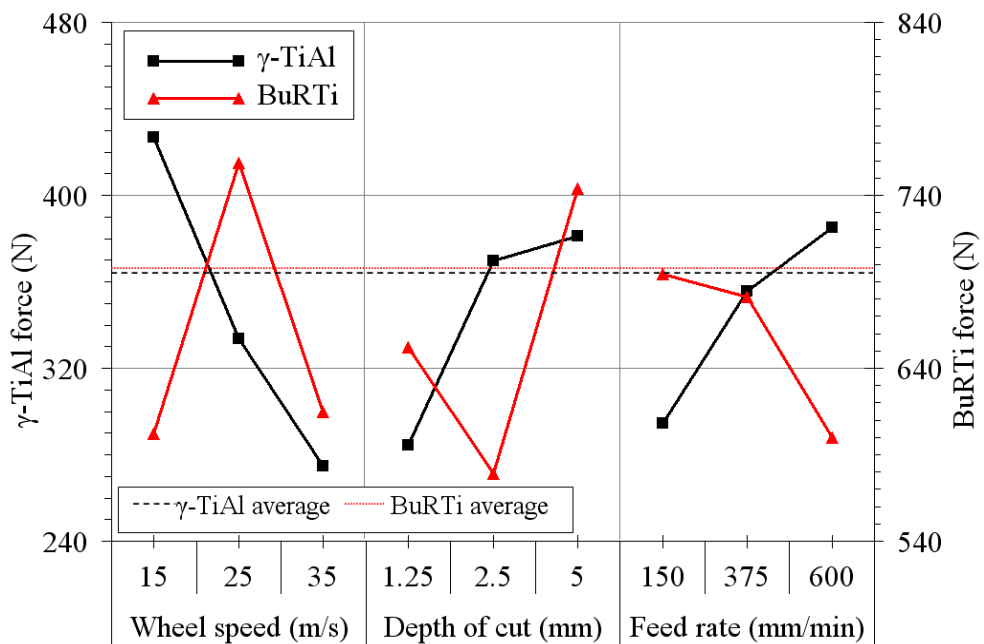


Figure 5.5: Main Effects Plot - means for tangential force (Phase 2Ai)

The Main Effects Plot - means for power is shown in Figure 5.6. Average power for γ -TiAl was 42% lower than for BuRTi and in general, trends for each output measure were identical for either alloy, with increasing wheel speed and depth of cut generally causing an increase in power levels. Power level remained approximately constant for changes in feed rate with both alloys.

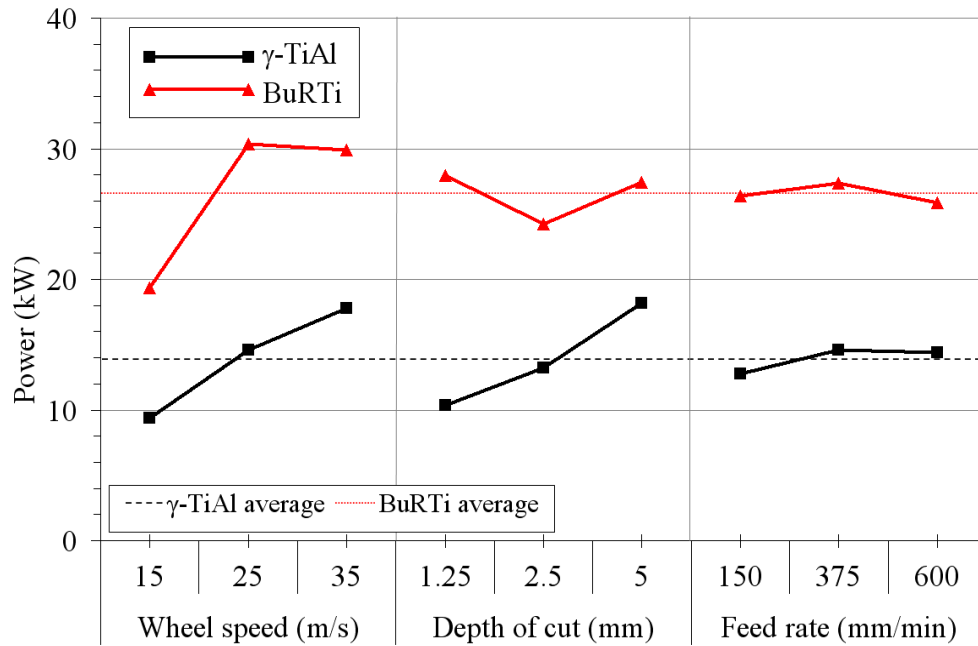


Figure 5.6: Main Effects Plot - means for power (Phase 2Ai)

The Main Effects Plot - means for specific energy is shown in Figure 5.7. In keeping with the power results, the average for γ -TiAl was 60% lower than for BuRTi. Trends for depth of cut and feed rate were almost identical between alloys with an increase in either factor causing a reduction in specific energy. An increase in specific energy was observed with an increase in wheel speed for γ -TiAl however wheel speed had a limited effect for BuRTi.

Figure 5.8 shows the Main Effects Plot - means for workpiece surface roughness R_a for both alloys. On average a 28% lower value was measured for γ -TiAl than for BuRTi and in contrast to the G-ratio results, both alloys showed almost identical trends with lowest surface roughness obtained using a wheel speed of 25m/s with lowest depth of cut and feed rate.

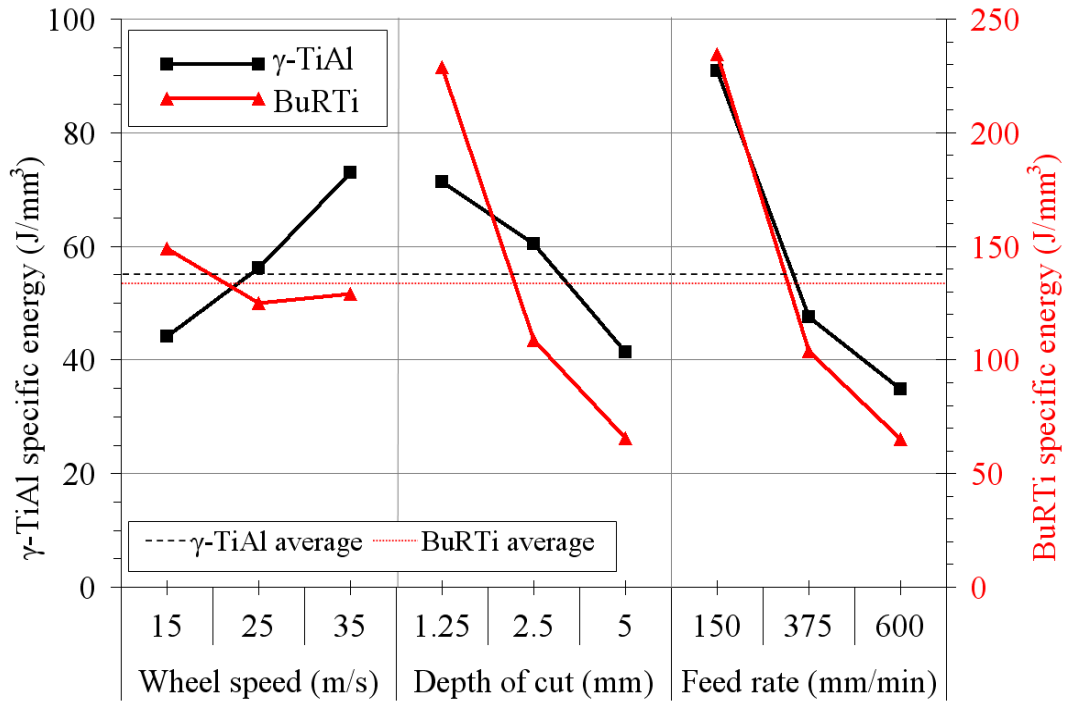


Figure 5.7: Main Effects Plot - means for specific energy (Phase 2Ai)

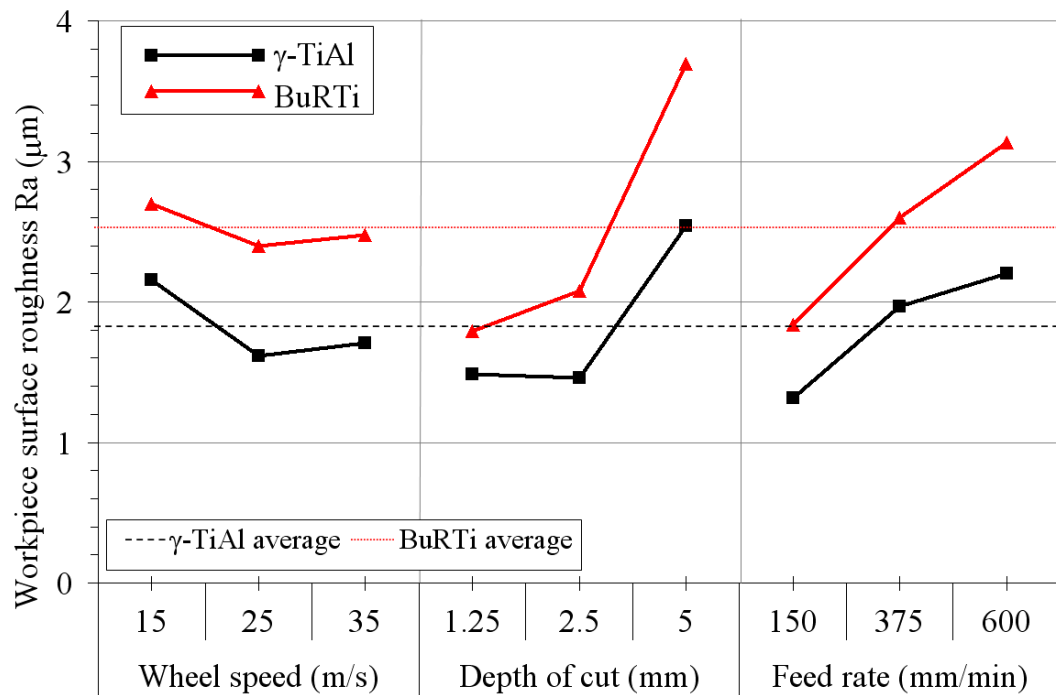


Figure 5.8: Main Effects Plot - means for surface roughness Ra (Phase 2Ai)

In general, γ -TiAl results for the majority of factors were as expected, with increasing depth of cut and feed rate increasing the normal and tangential forces and power because of an increase in both the undeformed chip thickness and the actual area of contact, leading to increased sliding forces [39, 42]. The higher forces experienced at higher depths of cut are

likely to have been coupled with higher temperatures, leading to increased attritious wear along with grain and bond fracture and a lower G-ratio.

Accepting that wheel speed is inversely proportional to the undeformed chip thickness squared [42], an increase in the former would be expected to reduce the latter, leading to a potential reduction in forces, longer wheel life and improved surface integrity [42]. Workpiece surface roughness and tangential force appear to follow this trend with an increase in wheel speed causing a reduction, however for G-ratio, normal force, power and subsequently specific energy, this was not the case. A possible reason for this is suggested by Malkin et al. [44] who report that the use of faster wheel speeds is associated with an increase in the sliding length per unit volume of material removed. This leads to the increased generation of wear flats, and hence an increase in the rubbing and sliding component of force with increased power and specific energy levels. An associated increase in grinding temperature would also be expected and thus higher levels of wheel wear with lower G-ratio. In addition, hydrodynamic lift or hydroplaning that can be experienced by a non porous wheel as the cutting fluid becomes compressed in the gap between the workpiece and grinding wheel, may have been experienced as the grinding wheel used for this phase of work had low porosity. Andrew et al. [40] also report an increase in power levels as wheel speed increased when grinding a nickel based superalloy. Apart from the force results, the γ -TiAl alloy outperformed the BuRTi alloy with higher G-ratio and lower workpiece surface roughness Ra. Key contributory factors in this were the 20-30% higher strength of the BuRTi alloy over γ -TiAl, the significantly higher ductility of BuRTi (~20% at room temperature) and the presence of Ti_2C and TiC carbides in the BuRTi microstructure.

The Analysis of Variance (ANOVA) tables for G-ratio for γ -TiAl is shown in Table 5.1 with other ANOVA tables for all other output measures shown in Appendix C, Figures C11 to C15 for γ -TiAl and Figures C16 to C21 for BuRTi. As $F_{0.05;2,2} = 19.0$ [154] no factors for any output measure for γ -TiAl were determined as being statistically significant at the 5% level and only wheel speed for normal force was significant for BuRTi. High Percentage Contribution Ratios ranging from 20.8% to 56.1% were obtained for nearly every output measure, the only exception was for power, where a value of 14.0% was calculated. The 35.8% error level shown in Table 5.1 suggests that important factors were omitted, conditions were not precisely controlled, measurement error was excessive or interactions were present [154]. Measurement errors could exist for wheel wear as the radius of the wheel was not taken into account, however interactions between factors were the more likely reason. One

such interaction was the effect of the grinding wheel acting “soft” in the case of Test 3 with a low wheel speed and highest material removal rate. At higher wheel speeds, the wheel stops acting soft and therefore the effect of increasing the material removal rate was less pronounced. An interaction plot for G-ratio is shown in Appendix C, Figure C62 where crossover indicates the presence of interactions between factors.

Source	SS	DOF	MSS	Fcalc	PCR (%)
Cutting speed	58.75	2	29.37	0.74	0
Depth of cut	222.13	2	111.07	2.80	17.2
Feed rate	469.20	2	236.40	5.92	47.0
Error	79.28	2	39.64	-	35.8
Total	829.36	8	-	-	-

Table 5.1: ANOVA table for G-ratio (Phase 2Ai)

b) Workpiece surface

Images of the machined workpiece surface at the end of each test for γ -TiAl are shown in Figure 5.9. In general, tests at the lowest wheel speed of 15m/s showed limited surface burn, tests at a wheel speed of 25m/s showed an increased level of workpiece surface burn and cracking whilst tests at the highest wheel speed of 35m/s showed extensive workpiece surface burn and high levels of cracking. Changes in the depth of cut and feed rate cloud the results to some extent. Limited cracking through the centre of workpiece was felt may have been due to the grinding configuration/clamping arrangements employed and the higher grinding temperatures causing tensile residual stresses. The high level of cracking may also have influenced the surface roughness Ra measurements.

The intensity of the workpiece surface burn and cracking for tests at a wheel speed of 25m/s generally showed an increase, with an increase in the volume of material removed, whereas for tests using a wheel speed of 35m/s, increasing the volume of material removed appeared to have a limited effect on the level of workpiece surface burn. An increase in wheel speed should allow an increased volume of grinding fluid to enter the contact zone [77], however it appears in this case the higher wheel speeds and increased sliding velocity caused an increase in the rubbing and sliding components of normal force and power [42], leading to higher levels of power and specific energy. Figure 5.7 confirms the increase of specific energy with increasing wheel speed. Andrews et al. [40] also found a similar result and suggested that when grinding the nickel based superalloy C0123 using aluminium oxide wheels, although higher wheel speeds aided the transfer of heat from the grinding zone, the rapid development of wear flats on the grinding grits produced higher rubbing forces [40].

The increase in power generated as a consequence of the increased rubbing energy was greater than the heat transfer from the grinding zone with the increased energy causing a rise in temperature.

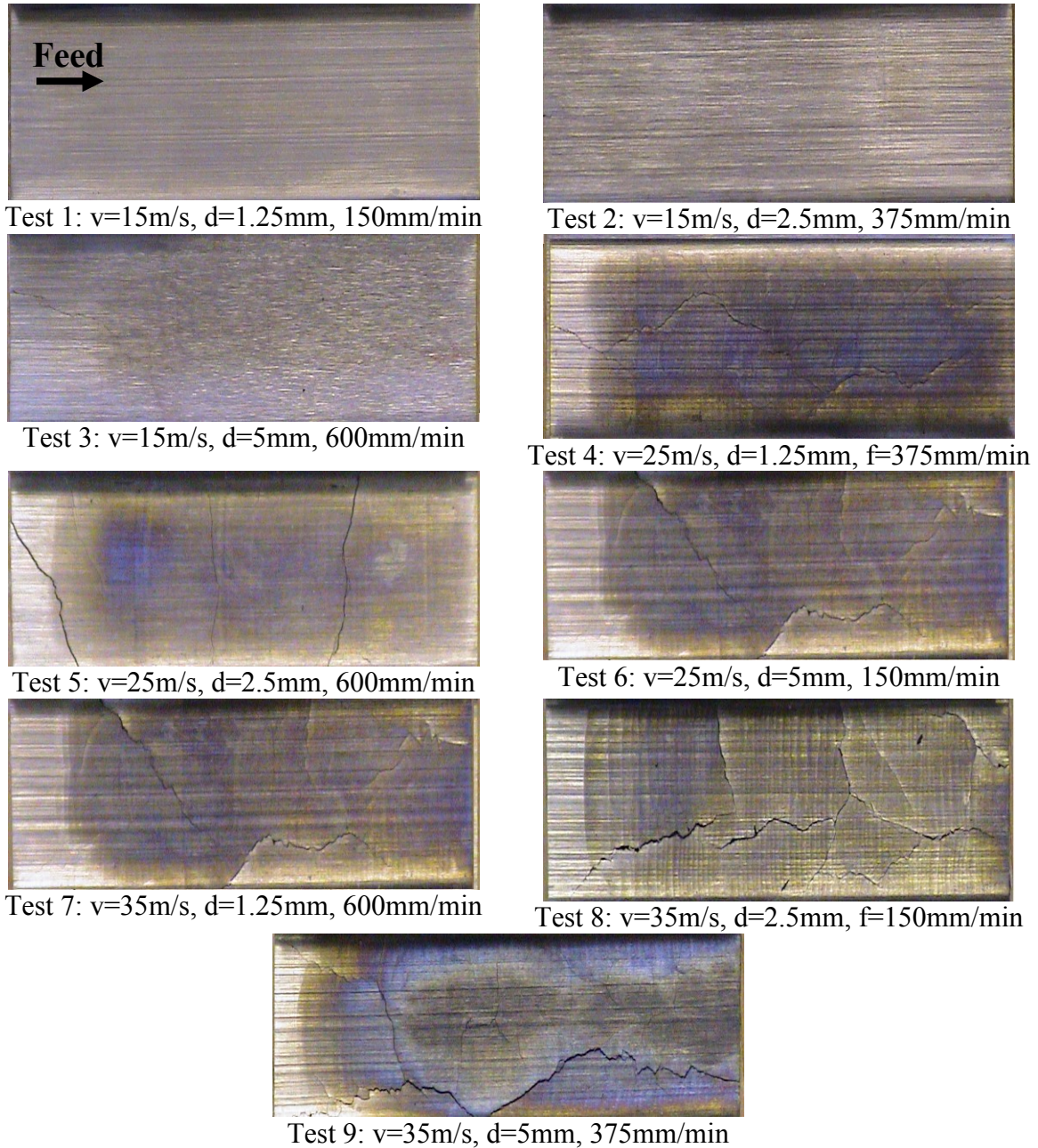


Figure 5.9: Selected γ -TiAl workpiece surface images (Phase 2Ai, γ -TiAl)

A critical burnout temperature of 140°C has been established for water based fluids when grinding steels [178]. Below this temperature, nucleate boiling which is a very efficient method of heat transfer occurs, however, above this temperature film boiling takes place in which bubbles coalesce to form a vapour blanket on the workpiece surface and thus heat transfer is much more difficult [178]. This results in a rapid rise in grinding temperature up to

1000°C or more. Novovic [151] reported grinding temperatures measured using implanted thermocouples of above 400°C when grinding BuRTi using SiC abrasive grinding wheels and similar parameters to those used for the current study. The surfaces produced at these temperatures were characterised as having significant levels of workpiece surface burn.

Bentley and Aspinwall [118] reported high levels of cracking and workpiece burn when intermittent dress creep feed grinding Ti-45Al-2Mn-2Nb +0.8% TiB₂ using SiC abrasive wheels even after an initial pass. Even at a low wheel speed of 15m/s, surface discolouration was described by the authors as being “distinct” and the level of cracking as “bad”. This suggests that an improvement in useful coolant flow was achieved in the current work by use of free jet nozzles. It should be noted that Bentley and Aspinwall [118] state that elimination of cracking and workpiece surface burn was only achieved through the application of continuous dressing which kept the wheel continually ‘sharp’ and did not allow attritious wear and wear flat generation to occur. Aust and Niemann [96] also suggest that the largest influence on surface quality involved the continuous dress process. Continuous dressing was not available on the Bridgeport FGC1000 therefore this could not be assessed, however it should be considered for future work when grinding of γ -TiAl alloys.

Steffen et al. [63] state that the highest material removal rate before workpiece burn occurs is called the critical material removal rate (CMRR). They used an angled workpiece to determine the depth of cut and thus CMRR at which workpiece surface burn occurred when intermittent dress creep feed grinding a nickel based superalloy with aluminium oxide wheels. Workpiece burn was evident at some point in every test and an increase in the depth of cut led to increased burn. The actual results for the CMRR may be inaccurate due to non-consideration of transient effects and the effect of grinding wheel wear against the volume of material removed [178].

Images of the machined surface at the end of each test are shown in Figure 5.10 for BuRTi. In general, the levels of workpiece surface burn observed matched those for γ -TiAl, however, the lower thermal conductivity of the BuRTi alloy (10W/m.K) when compared to γ -TiAl (22W/m.K) produced differences in the intensity of the burn. Similar levels of workpiece surface burn were reported by Novovic [151] when grinding BuRTi. The temper colours for Ti-6Al-4V [179] are a useful guide to temperature although they were produced over a period of many hours, when in comparison a grinding pass takes a few seconds. Typically, ‘bluish’ colours like those found on Tests 4 to 9 occurred at temperatures of 500°C and upwards.

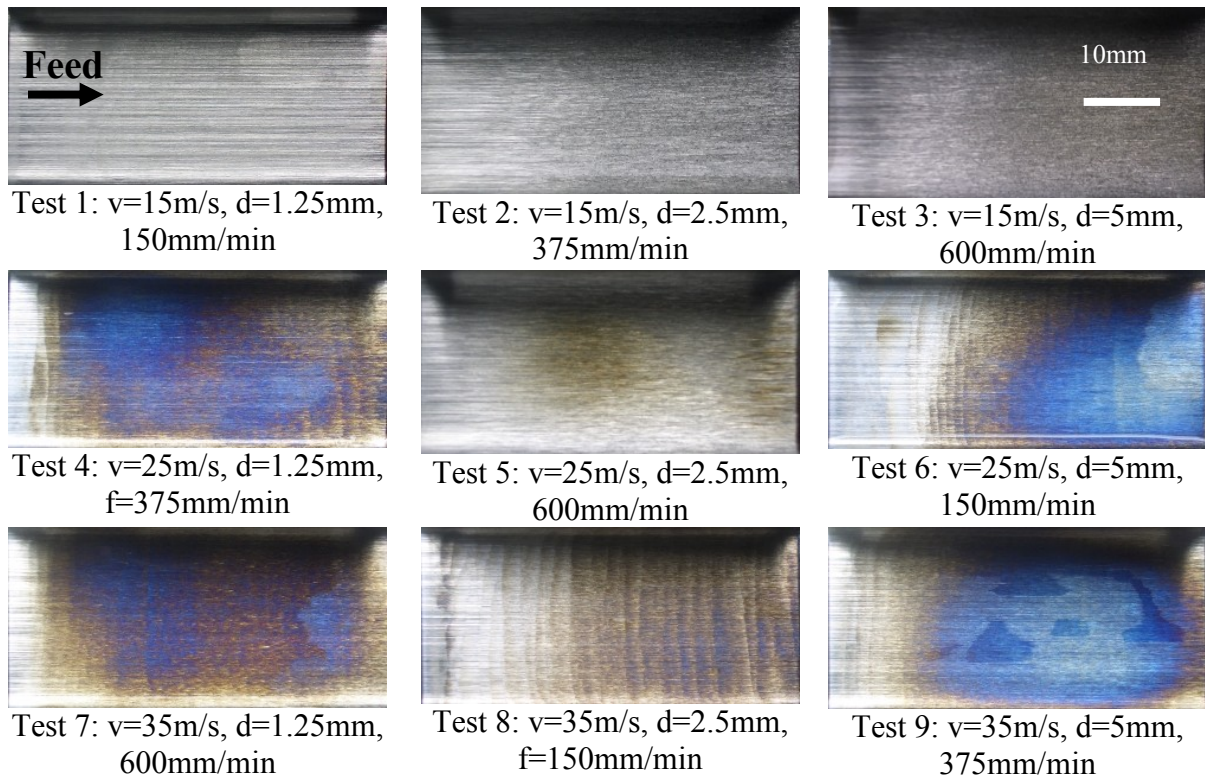


Figure 5.10: Selected BuRTi workpiece surface images (Phase 2Ai, BuRTi)

Selected higher magnification images of the γ -TiAl ground surface are shown in Figure 5.11. The surface produced using Test 1 operating parameters was in the most part, free of damage including cracks or smeared material, however, a single region of fracture/pullout was observed. When compared to similar fracture/pullout produced with a high speed ball nose end milling operation, this region was significantly smaller ($<25\mu\text{m}$) in diameter and was probably due to the reduced size of the grinding chip thickness [29]. At higher operating parameters, a network of cracks covering the majority of the surface was observed. The surface of Test 9 showed a level of fracture/pullout with a similar size to one found on the Test 1 surface, see Figure 5.11 (b). Comparable fracture/pullout was not found on other workpiece surfaces. Published data [108, 118, 119] provides very little information concerning the analysis performed on the machined surface therefore it was difficult to compare the current work. Some adhered/smeared material (sideflow) was also observed, which generally increase in level as operating parameters increased.

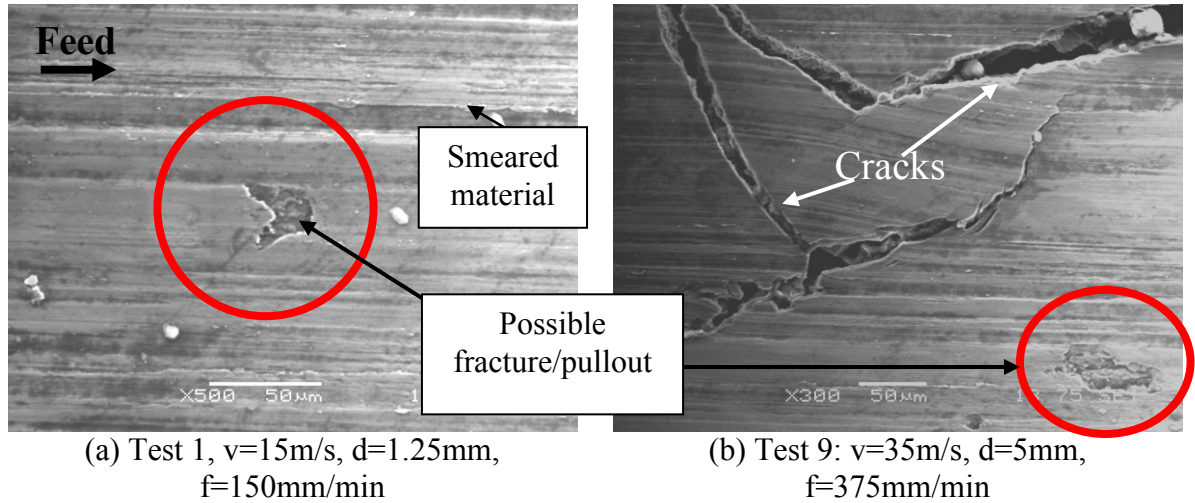


Figure 5.11: Higher magnification images of the ground surface (Phase 2Ai, γ -TiAl)

In contrast, BuRTi surfaces had high levels of surface smearing, adhered material and possible pullout as a consequence of the higher ductility of the alloy. Figure 5.12 provides images of the workpiece surface for selected tests and shows that workpiece surface smearing together with laps and folds where present on most BuRTi surfaces. Similar workpiece surface smearing was also found in work by Novovic [151].

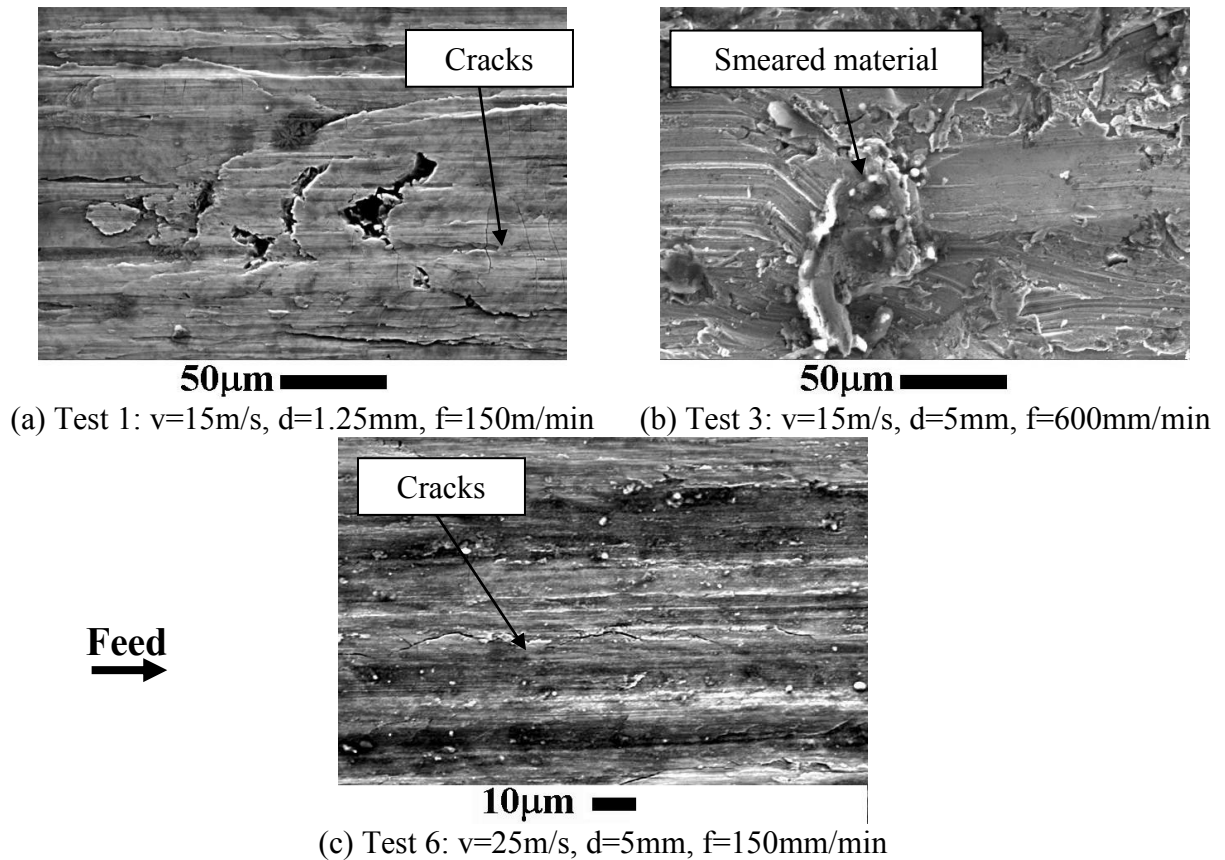


Figure 5.12: Higher magnification images of the ground surface (Phase 2Ai, BuRTi)

Often the surface showed cracks both parallel and perpendicular to the feed direction. Usually in grinding, thermal cracking is perpendicular to the feed direction, however, under severe grinding conditions, cracks parallel to the grinding direction may also develop. In general, the highest level of workpiece cracking occurred with the most severe operating parameters (i.e. highest wheel speed, feed rate and depth of cut), resulting in intensive surface burn and the highest normal force.

c) Microhardness

Microhardness depth profiles for all γ -TiAl tests are shown in Figure 5.13 whilst graphs showing the profile obtained from each individual test are shown in Appendix C2, Figures C63 and C64. In general, all tests showed the presence of a hardened layer extending to a depth of up to 300 μ m from the machined surface. Tests 8 and 9 had the highest value for this hardened layer with values of up to $\sim 600\text{HK}_{0.025}$ which was $\sim 150\text{HK}_{0.025}$ higher than bulk hardness.

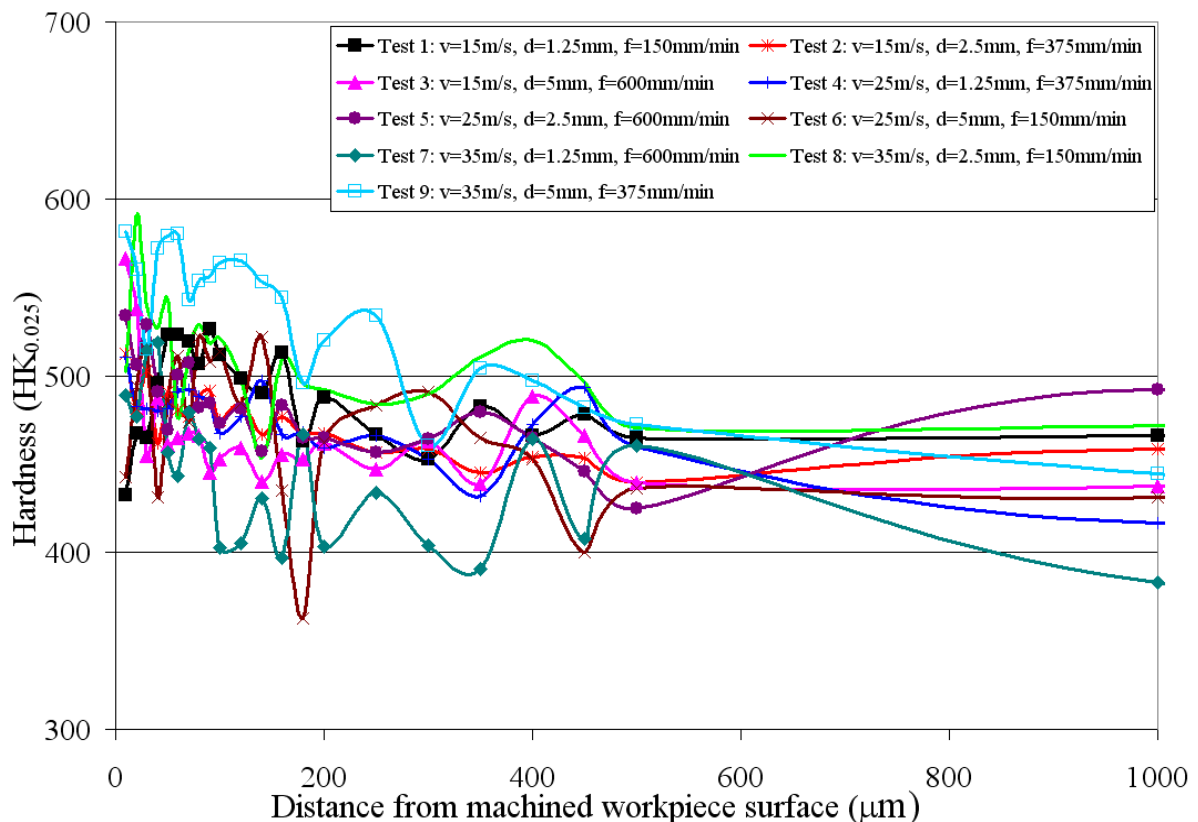


Figure 5.13: Microhardness depth profiles (Phase 2Ai, γ -TiAl)

Bentley and Aspinwall [118] also found a hardened layer when creep feed grinding Ti-45A-2Mn-2Nb +0.8%vol TiB₂ using SiC abrasives with intermittent dressing. The depth of the

hardened layer was reported to be up to $\sim 200\mu\text{m}$ with a maximum hardness of $250\text{HV}_{0.025}$ above bulk hardness for tests that had workpiece surface burn and cracking described as “severe”. They also detail a hardened layer of up to $100\text{HV}_{0.025}$ higher to depth of up to $\sim 200\mu\text{m}$ from the machined workpiece surface for tests where no burn and/or cracking were observed. In comparison to this Test 1 which had both the highest G-ratio and lowest forces and presented a similar level of workpiece surface burn with no cracking or burn had a similar depth hardened layer with a reduced magnitude of only $50\text{HK}_{0.025}$ higher than bulk hardness. When grinding steel, (quenched and tempered, 50Rc), abusive grinding conditions result in higher grinding temperatures and are generally the cause of thicker hardened layers with increased hardness whereas conventional conditions normally yield a workpiece surface with limited hardness variation [95]. The thickness of the hardened layer for Test 9 was $\sim 500\mu\text{m}$ and the high hardness of $\sim 550\text{HK}_{0.025}$ at a depth of $200\mu\text{m}$ suggests that high temperatures had penetrated deep into the workpiece surface. Similar results were obtained when high speed ball nose end milling Ti-45Al-8Nb-0.2C, where a hardened layer up to $150\text{HK}_{0.025}$ greater than the bulk hardness was found, however the depth of the layer was reduced.

Microhardness depth profiles for BuRTi are shown in Figure 5.14. Tests 4 and 6 exhibited slight workpiece softening close to the machined face at a depth of 5-15 μm . Similar microhardness results were reported by Novovic [151] including softening in the first 15 μm from the machined BuRTi surface. These instances could be caused by edge effects due to a lack of support rather than surface softening. Some surfaces showed an increase in hardness of 50-60 $\text{HK}_{0.025}$ from the bulk value of 370 $\text{HK}_{0.025}$ at between 30-50 μm from the workpiece face and on one occasion a value of $\sim 575\text{HK}_{0.025}$ was recorded, due possibly to the formation of the oxide layer. In addition, the presence of carbide particles with a diameter of up to 14 μm made microhardness measurement for BuRTi problematic.

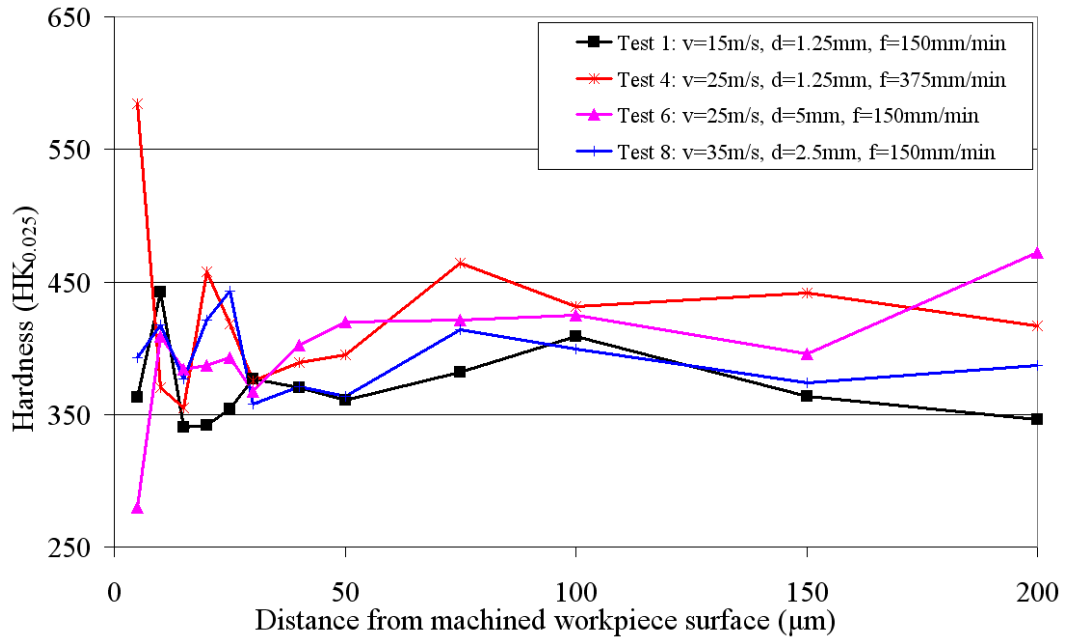


Figure 5.14: Microhardness depth profiles (Phase 2Ai, BuRTi)

d) Workpiece surface/subsurface

Analysis of the workpiece surface/subsurface showed that surfaces perpendicular to the feed direction appeared considerably rougher than parallel surfaces due to visible wear tracks caused by each grinding grit, see Figure 5.15 (a). Tests 1 and 2 produced similar surfaces with damage consisting of intermittent deformation/bending of the lamellae to a depth of $\sim 4\mu\text{m}$ on parallel sections and $\sim 2\mu\text{m}$ on perpendicular sections. Both parallel and perpendicular surface/subsurface cross-sections for all other tests showed both intergranular and transgranular cracks. These ranged from $\sim 2\mu\text{m}$ to $>1\text{mm}$ wide and $\sim 100\mu\text{m}$ to $>5\text{mm}$ deep. The majority of these surfaces also showed increased intermittent deformation/bending of the lamellae covering up to 60% of the machined surface/subsurface to a depth of up to $20\mu\text{m}$ on surfaces parallel to the feed direction, see Figure 5.15 (b).

Several of the workpiece surfaces showed possible fracture/pullout to a depth of up to $\sim 20\mu\text{m}$, however, no fracture/pullout was observed in Test 1 and 9 surface/subsurface micrographs. Only the perpendicular surface produced using Test 3 operating parameters showed folding of workpiece material which was restricted to a depth of $\sim 3\mu\text{m}$. Surfaces showing the highest levels of damage were produced by Test 9 operating parameters, where extensive cracking and a suspected heat affected zone (HAZ) was found, which had a depth of $\sim 800\mu\text{m}$ parallel to the feed direction. The transverse cross-section showed a lower level of damage with the largest depth of $\sim 300\mu\text{m}$ found at the centre of the slot. The workpiece

surface burn was observed to be the most intense with this surface where temperatures were expected to approach 1000°C.

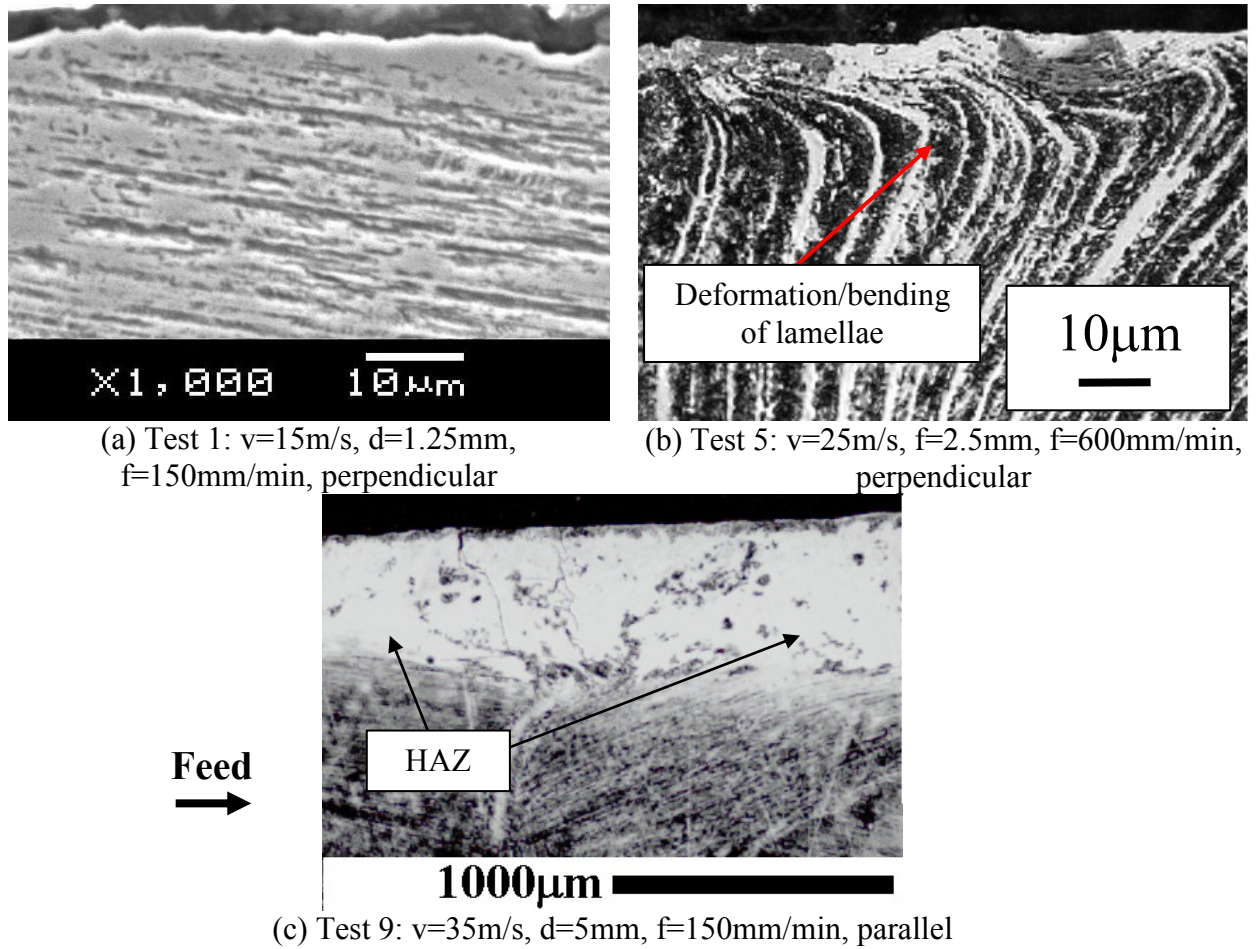


Figure 5.15: Surface/subsurface cross-sectional micrographs (Phase 2Ai, γ -TiAl)

When using SiC abrasives to creep feed grind Ti-45Al-2Mn-2Nb +0.8%vol. TiB_2 , Bentley [108] found no evidence of pits, tears or laps, however no tests were performed with a high ratio of material removal rate to wheel speed (Test 3 in the present work). Both intergranular and transgranular cracks are reported which are described as severe and of the order of 2 to 3mm in length. The maximum deformed lamella depth was seen to be $25\mu\text{m}$ which corresponds well with deformation/bending of the lamellae observed on the surface of Test 5. Two samples also showed recrystallisation to a maximum depth of 3mm. In the absence of any details/images concerning these surfaces it is assumed that they were produced using intermittent dressing, surface burn is described as “severe” which is consistent with Test 9 surfaces in the present work.

Sample surface/subsurface cross-sectional micrographs for BuRTi are shown in Figure 5.16. Extensive carbide fracture and/or cavities due to lost carbides, reported earlier by

Novovic et al. [150] were not found, although with the high level of smearing experienced this was difficult to assess. Surface cross sections in the direction of the feed revealed further surface and subsurface damage with a possible heat-affected zone (HAZ) occurring in some tests however, damage was in general, restricted to $<10\mu\text{m}$ from the ground surface.

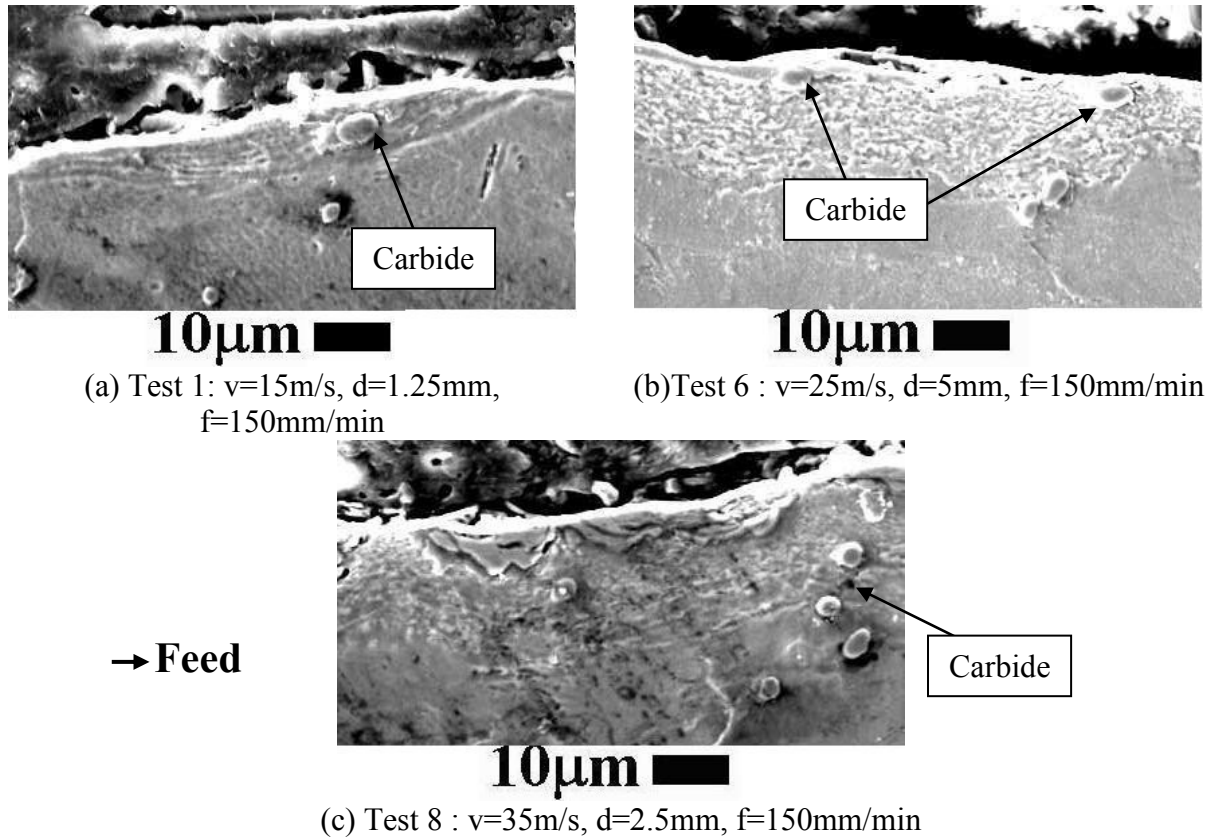


Figure 5.16: Surface/subsurface cross-sectional micrographs (Phase 2Ai, BuRTi)

5.1.2 Phase 2Aii: Further assessment

a) Wheel wear, surface roughness, force, power and specific energy

Replication of Phase 2Ai, Tests 1 and 3 showed almost identical results for G-ratio indicating reasonable repeatability. The results for G-ratio and workpiece surface roughness R_a are shown in Figure 5.17. For Tests 1 to 3, G-ratio increased with the volume of workpiece material removed as observed in Phase 2Ai. As with Phase 2Ai, the highest G-ratios were obtained at the lowest operating parameters and increasing the material removal rate by increasing either the feed rate or depth of cut caused a reduction. Increasing the feed rate from 150 to 600mm/min (Test 1 to 2) had a lower effect on G-ratio reduction when compared to increasing the depth of cut from 1.25 to 5mm (Test 1 to 3). Tests 2 and 3 did however, have the same material removal rate.

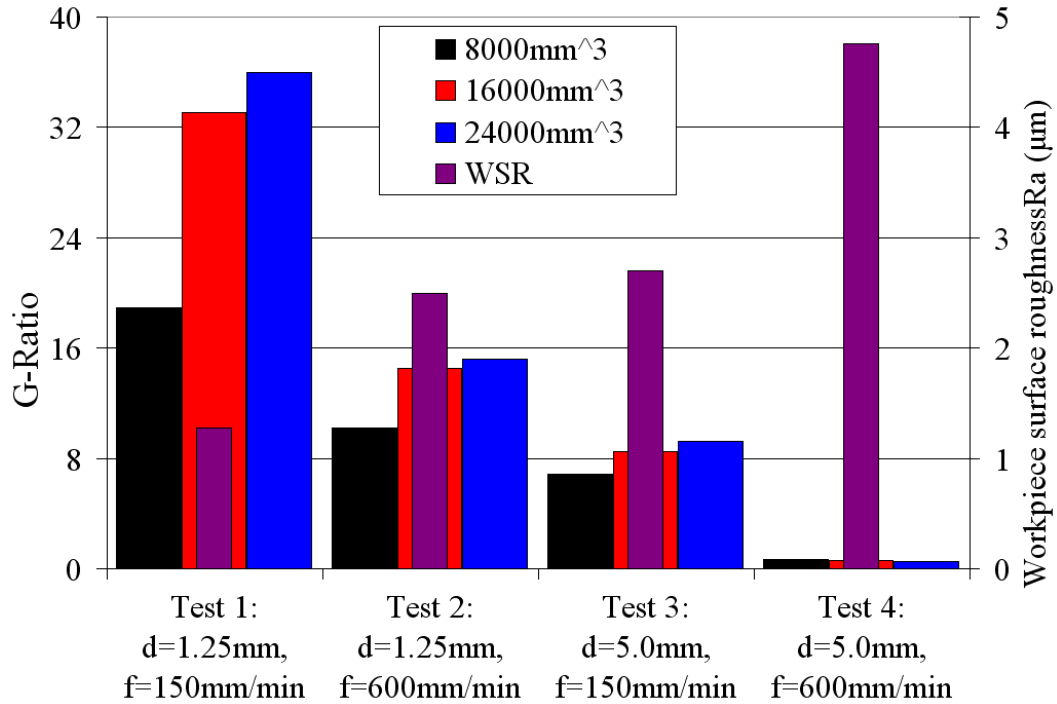


Figure 5.17: G-ratio and workpiece surface roughness Ra (Phase 2Aii)

An increase in the depth of cut whilst decreasing the feed rate (in order to keep a constant material removal rate), will cause an increase in the sliding length and an increase in the sliding length per unit volume of material removal has been shown to cause more attritious wear and dulling of the abrasive grains [44]. Speed stroke grinding [120, 121] takes this principle to the extreme by using a depth of cut of just a few microns with a very high feed rate of up to 200m/min. With the material removal rate kept constant, the undeformed chip thickness increases at a faster rate with a higher feed rate than depth of cut and therefore there is a limit to how high the feed rate can be increased. At the highest operating parameters, as with Phase 2Ai, Test 3, G-ratio was the lowest with a value <1 obtained as the wheel was acting “soft” and the ratio of material removal rate to wheel speed was too high. Surface roughness trends were similar to those obtained for G-ratio but in reverse, with the lowest value of $Ra \sim 1.45\mu m$ when operating at a depth of cut of 1.25mm and a feed rate of 150m/min. Test 2 and 3 which had an identical material removal rate showed similar surface roughness Ra values of $\sim 2.5\mu m$, whilst the highest surface roughness value of $Ra \sim 4.5\mu m$ was measured from the surface of Test 4 which used the highest operating parameters.

Normal and tangential force results for each test are shown in Figure 5.18. The majority of forces showed an increase in the force level as the volume of material removed increased due to increased wear flat generation. Test 1 using the lowest operating parameters, showed the lowest levels of forces with normal forces of $\sim 800N$ and tangential forces of

~300N. An increase in the feed rate from 150mm/min to 600mm/min whilst depth of cut was kept constant at 1.25mm, caused an increase in the normal and tangential forces of ~800N and ~100N respectively. Increasing the depth of cut from 1.25mm to 5mm whilst keeping feed rate constant at 150mm/min, caused an increase in normal and tangential forces of ~1600N and ~200N respectively. At the higher depth of cut of 5mm, increasing the feed rate from 150mm/min to 600mm/min caused a slight reduction in the normal force of ~100N whilst the tangential force increased by ~50N.

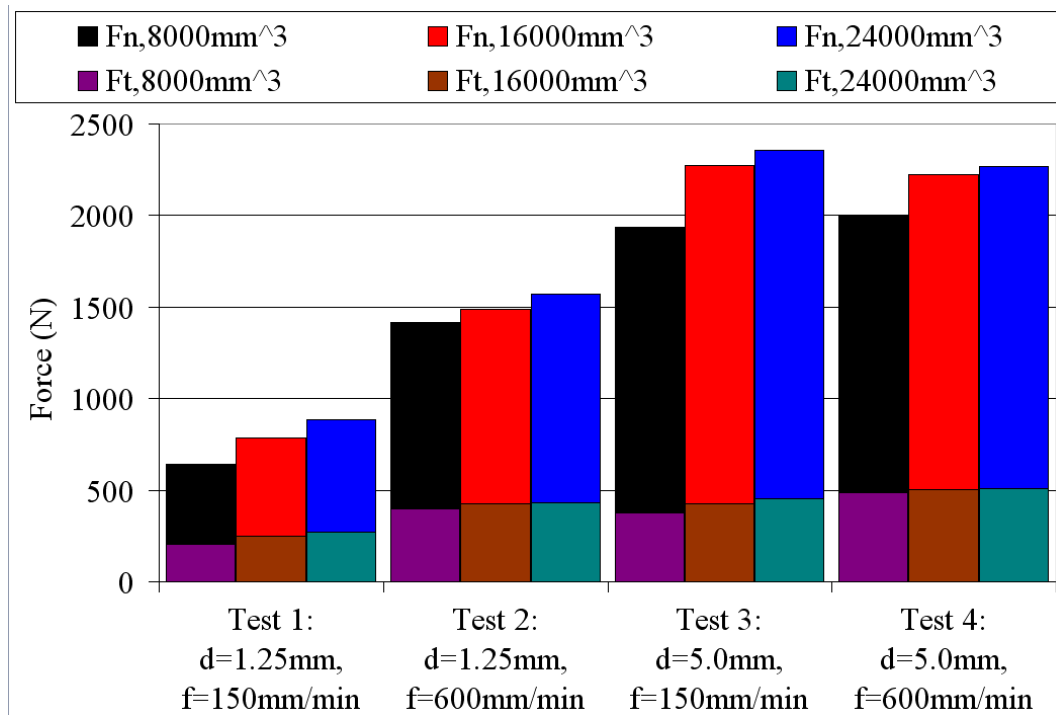


Figure 5.18: Normal and tangential force (Phase 2Aii)

The trends for power, shown in Figure 5.19 are almost identical to those obtained for normal and tangential forces with lowest power levels of ~10kW obtained using the lowest operating parameters (Test 1) whilst highest power levels of 30kW were obtained when operating with the highest operating parameters. Increasing the depth of cut from 1.25 to 5mm at a constant feed rate appeared to cause a greater increase in power when compared to increasing the feed rate from 150mm/min to 600mm/min at a constant depth of cut. Highest specific energy levels of 180J/mm³ were measured when operating with Test 1 parameters, whilst lowest values were measured when using Test 4 parameters.

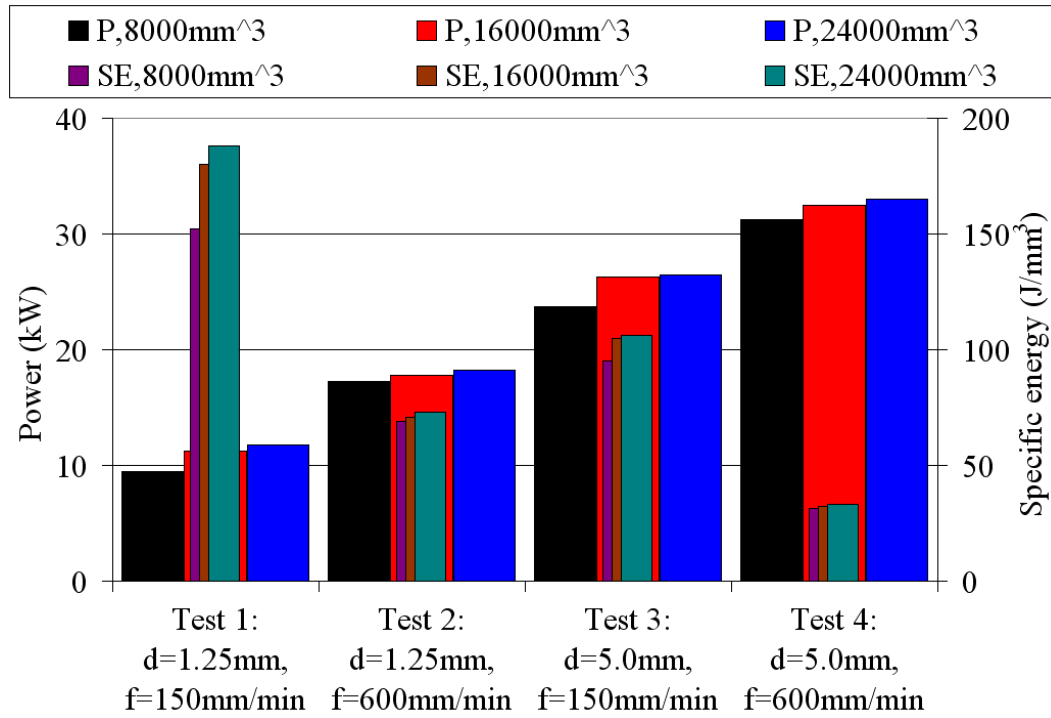


Figure 5.19: Power and specific energy (Phase 2Aii)

b) Workpiece surface

In the main, the workpiece surfaces of Tests 1 and 2, shown in Figure 5.20 were free of burn and chatter, in contrast to results reported by Bentley et al. [118]. Test 3, performed at the higher depth of cut and lower feed rate showed cracking with some workpiece surface burn which increased in severity as the material removed increased, Test 4 surfaces showed a similar surface to other tests until full depth of cut had been reached (cut in), then the surface became extremely rough as a consequence of the increased chip thickness leading to an increased chip load. At a low depth of cut, the surfaces produced looked similar irrespective of the feed rate. Andrew et al. [40] found the surface finish to be generally insensitive to feed rate so that the surface finish requirement is not normally limited by the feed rate. No further details or explanation were given as to the reasons why this should occur. Kuriyagawa et al. [180] performed temperature measurement when grinding cermet ((Ti(C,N) using a diamond wheel at a wheel speed of 14.7m/s, a depth of cut of 0.5mm and water based grinding fluid using a range of feed rates from 40 to 80mm/min. A maximum grinding temperature of ~100°C was reported at feed rates of 40 and 50mm/min whilst at a feed rate of 60 or 70mm/min the grinding temperature increased to 400°C. This research suggests that below the critical burnout temperature, the surface will be free of workpiece surface burn but that a rapid rise in temperature will occur if the temperature exceeds the critical burnout temperature.

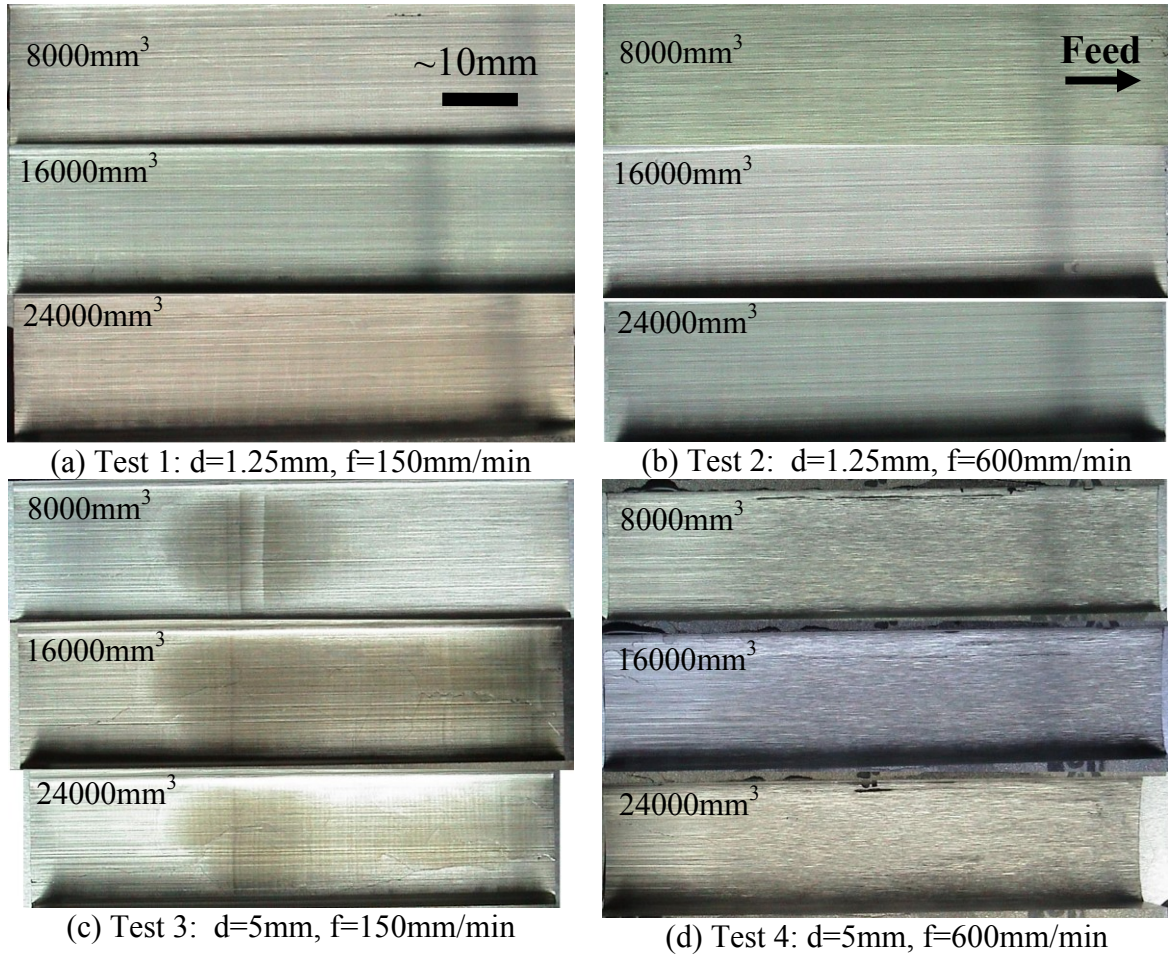


Figure 5.20: Workpiece surface images (Phase 2Aii)

Higher magnification analysis of the workpiece surface produced using Test 1 and 2 operating parameters showed almost identical surfaces with no evidence of any fracture/pullout or microcracking of the workpiece surface. The surfaces were characterised as having visible scratches running along the length of the surface which were created by the individual overlapping grits. Limited sideways displacement from the scratches by ploughing was also visible. Malkin [42] suggests that the degree of sideflow depends upon the particular workpiece material being ground with metals that are more adhesive such as titanium alloys, tending to exhibit a greater amount of sideways flow. Figure 5.21 (b) shows the surface from Test 4 at an identical magnification to that used for Figure 5.21 (a). The effect of increasing the depth of cut on sideflow is clearly evident.

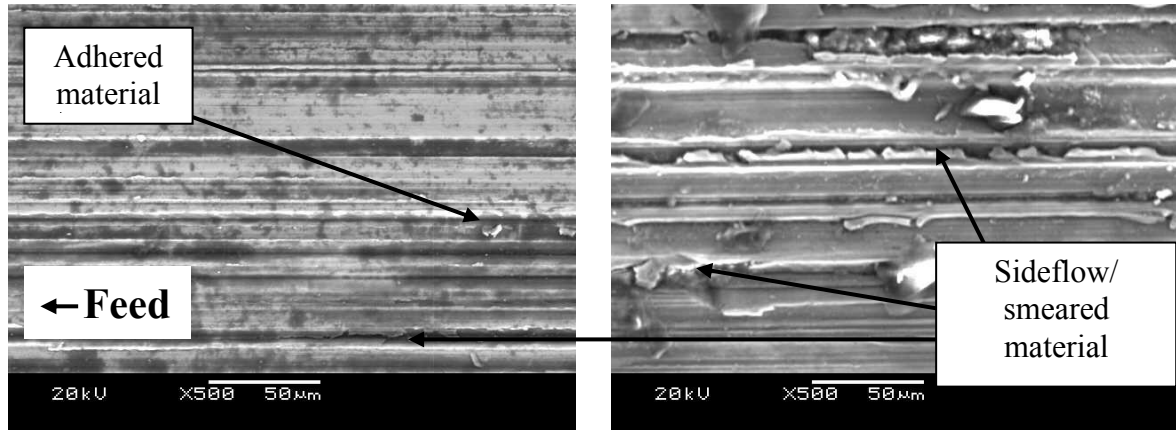
(a) Test 2: $d=1.25\text{mm}$, $f=600\text{mm/min}$ (b) Test 4: $d=5\text{mm}$, $f=600\text{mm/min}$

Figure 5.21: High magnification workpiece surface images (Phase 2Aii)

c) Microhardness

Microhardness depth profiles are given in Figure 5.22 with individual profiles shown in Appendix C, Figure C65. In general, Tests 1 and 2 using a lower depth of cut show a marginal/slight hardened layer however Tests 3 and 4 at the higher depth of cut show a more pronounced hardened layer with a maximum hardness of between $550\text{HK}_{0.025}$ and $575\text{HK}_{0.025}$. Phase 2Aii. As with previous microhardness results for creep feed grinding, the more arduous operating parameters, namely the increase in depth of cut, caused an increase in the sliding length and thus forces, power and grinding temperature, resulting in an increase in the maximum hardness.

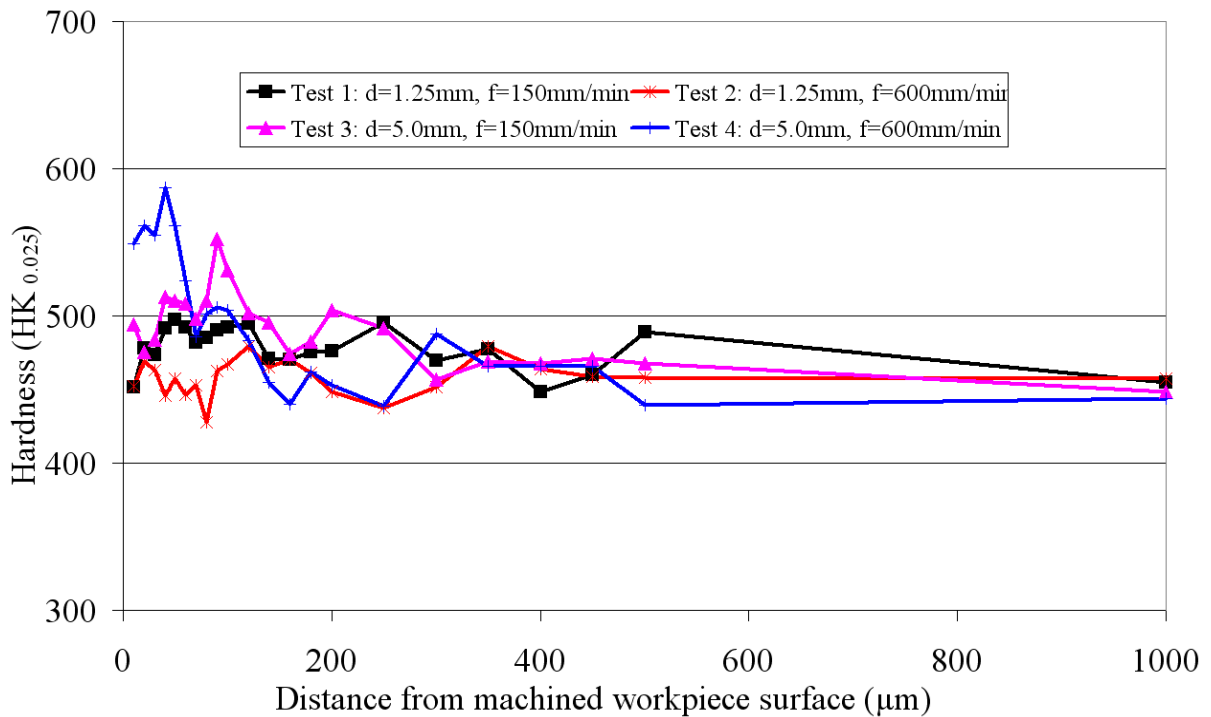


Figure 5.22: Microhardness depth profiles (Phase 2Aii)

d) Workpiece surface/subsurface

Workpiece surface/subsurface damage including deformation/bending of the lamellae and fracture/pullout could be controlled to within $\sim 10\mu\text{m}$ of the surface using a 1.25mm depth of cut and a feed rate of 150 or 600mm/min. A marginal increase in the deformation/bending of the lamellae of $\sim 3\mu\text{m}$ was observed on the cross-section parallel to the feed direction at the higher feed rate. Figure 5.23 shows cross-sections of workpiece surfaces machined using a 5mm depth of cut at the low feed rate (a) and high feed rate (b). Extensive deformation/bending of the lamellae to a depth of $\sim 20\mu\text{m}$ and cracks were observed on both working surfaces in directions parallel to the feed direction. Figure 5.23 (a) shows a crack $\sim 10\mu\text{m}$ wide and 2mm deep and was consistent with surface/subsurfaces produced using Phase 2Ai, Tests 4 to 9. Figure 5.23 (b) shows an image of the subsurface produced using Test 4 operating parameters in a direction perpendicular to the feed. Extensive bending of the lamellae to a depth of $\sim 20\mu\text{m}$ was visible in addition to folding of workpiece material to a depth of $\sim 3\mu\text{m}$ and which corresponded to the size of the sideflow observed in the workpiece surface analysis.

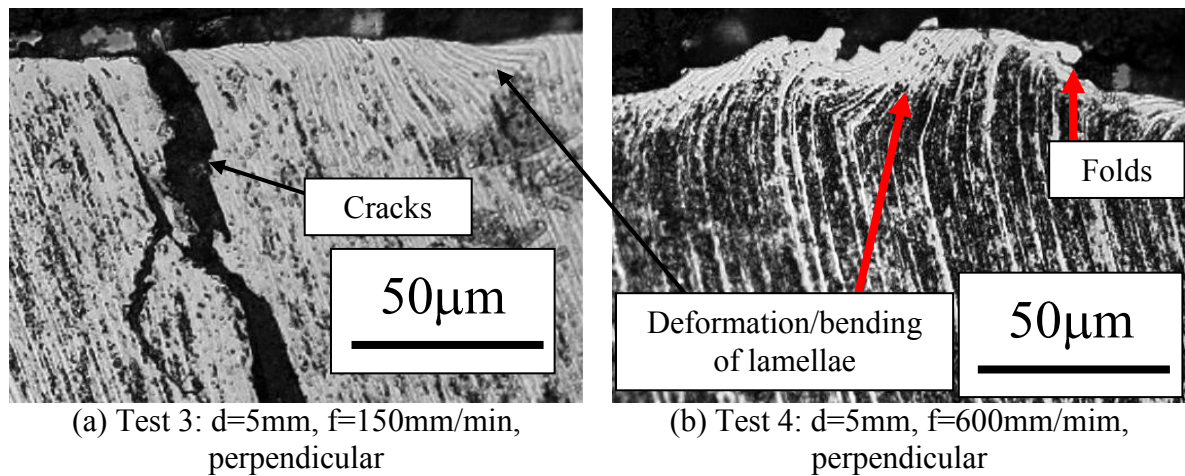


Figure 5.23: Workpiece surface/subsurface cross-sectional images (Phase 2Aii)

5.1.3 Phase 2Aiii: Comparison of the performance of different wheel specifications

a) Wheel wear, surface roughness, force, power and specific energy

Results for G-ratio and workpiece surface roughness are shown in Figure 5.24 whilst results for normal and tangential forces and power are shown in Figure 5.25. Wheel A operating at the lowest wheel speed produced the best combination of results with G-ratios ~ 15 , low average workpiece surface roughness of $\sim \text{Ra } 1.2\mu\text{m}$, limited profile wear and surfaces free of

cracking and burn, despite having higher values of force and power when compared to the other two wheel types at a comparable wheel speed.

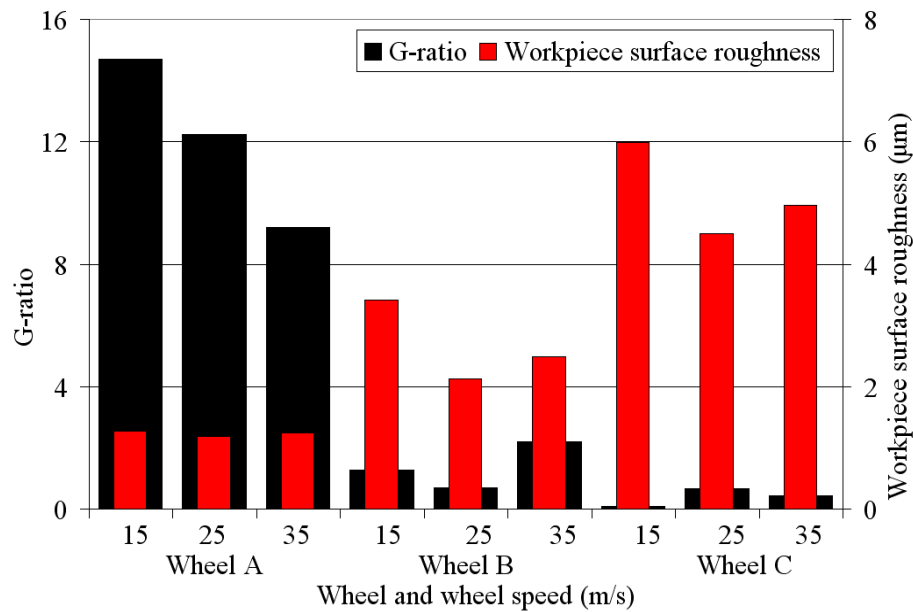


Figure 5.24: G-ratio and surface roughness (Phase 2Aiii)

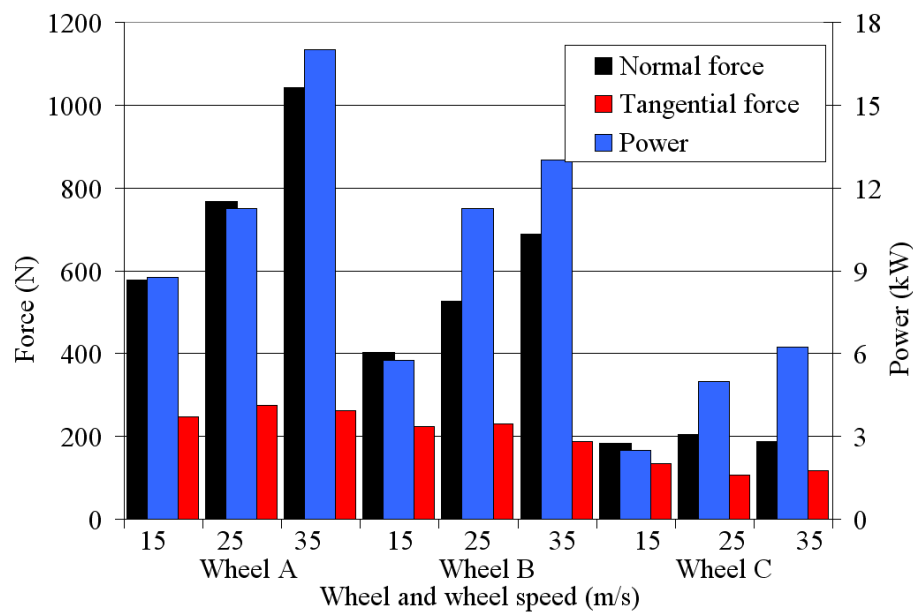


Figure 5.25: Forces and power (Phase 2Aiii)

When compared to Wheel A, Wheel B had a greatly reduced G-ratio of <3 and increased surface roughness R_a of $2\mu\text{m}$ to $3.5\mu\text{m}$. Wheel C had the worst performance including a G-ratio of <0.5 with contra grinding occurring (more wheel material being removed than on the workpiece) and a surface roughness R_a greater than $4\mu\text{m}$. Increasing the wheel speed caused a reduction in the G-ratio for Wheel A whilst for Wheels B and C higher G-ratios were measured. For Wheels A and B, increasing the wheel speed caused the normal force and

power levels to almost double. Power for Wheel C also mimicked this trend however normal force showed a limited difference between wheel speeds.

Assuming wheel speed is inversely proportional to the undeformed chip thickness, higher wheel speeds would be expected to yield a smaller undeformed chip thickness resulting in lower forces, better surface integrity and longer wheel life [119]. As with Phases 2A and 2B, it was likely that faster wheel speeds caused an increase in the sliding length per unit volume of material removed [42] and resulted in more attritious wear and dulling of the abrasive grits hence, the higher forces and power observed with higher wheel speeds.

Compared to Wheel A, Wheel B had a lower percentage of grit material along with higher porosity, resulting in an increase in force per grit (relative grain force) which caused an increase in attritious grain wear and grain fracture. Wheel C had a lower percentage of bond material along with increased porosity over Wheel B. This reduced bond strength caused the wheel wear mechanisms to switch from attritious grain wear and grain fracture to a combination of attritious grain wear, grain fracture and bond fracture. The force per grit for Wheels A and B was not sufficient to cause bond posts to rupture, however this was likely to have occurred with Wheel C as there was no difference in the concentration of grit material between Wheels B and C. Figure A8 [45] supports the results showing that a reduction in bond hardness (amount of bond) or grit concentration causes the cutting forces, G-ratio and cutting temperature to decrease whilst the workpiece surface roughness increases.

Bentley and Aspinwall [118] found that wheel grade (F, J) and structure (20-30) had limited effect on output measures including force and workpiece surface roughness which was in contrast to the current work. Grit size, grade and structure were similar for the published study and the present work, therefore it is difficult to explain the contrasting results. The published study used both intermittent and continuous dressing in a Taguchi fractional factorial experimental design may have affected the statistical analysis. In contrast, for surface grinding of Ti-45Al-2Mn-2Nb +0.8%vol. TiB_2 using SiC wheels, wheel grade had the largest effect with a harder wheel grade causing normal forces to increase by 25% and surface roughness R_a to reduce by 30% due to the reduced rate of self dressing, with grit pullout resulting in increased wear flat generation [114].

b) Workpiece surface

Workpieces produced using Wheel C, shown in Figure 5.26 appeared visually crack and burn free because bond fracture was the predominant wheel wear mechanism with the wheel effectively self-dressing and wear flat generation minimised. The increased porosity of Wheel

C would be expected to improve cooling by allowing an increase in the useful coolant flow, in addition to a reduction in the specific energy as a consequence of reduced grit and bond material.

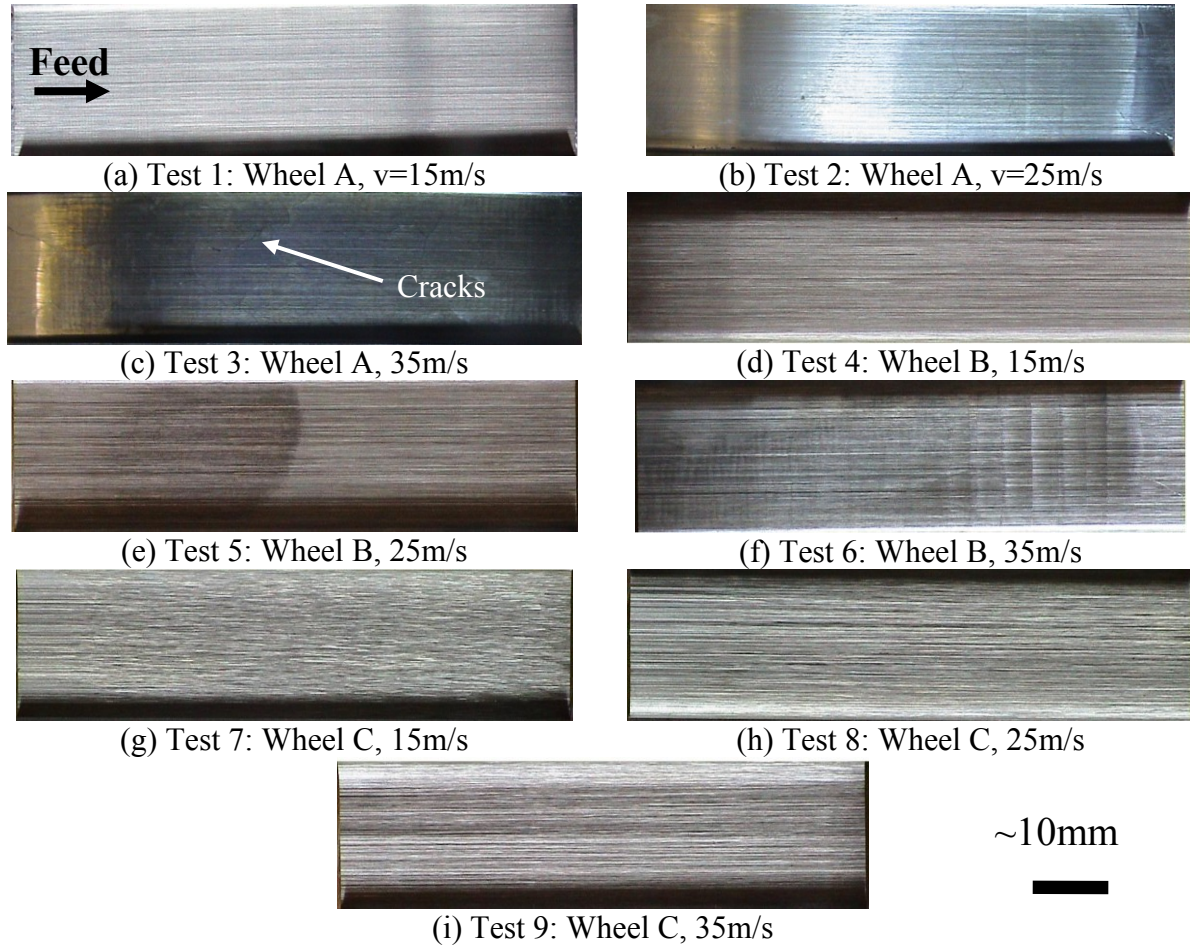


Figure 5.26: Workpiece surface images (Phase 2Aiii)

Malkin and Guo [178] suggest that 95% of the energy during creep grinding is removed by the grinding fluid therefore any increase in useful coolant flow should allow grinding temperatures to be reduced. This increase in cooling was however traded against an increase in wheel wear as a consequence of having a lower level of grit and bond material. Only surfaces produced with low wheel speeds for either Wheel A or B appeared visually crack and burn free, with at higher wheel speeds cracks up to 1mm deep were evident with extreme workpiece surface burn. This was because an increase in the wheel speed is associated with an increase in the sliding length per unit volume of material removed leading to higher forces, power and grinding temperature [44]. Visible chatter was also visible on the surface produced using Test 6 operating parameters which used a combination of high wheel speed and low depth of cut together with a relatively open wheel.

5.1.4 Phase 2Aiv: Production of a demonstrator component blade root

The demonstrator ‘lobe-type’ blade root ground using Wheel A at a speed of 15m/s, a depth of cut of 1.25mm (x4) and a feed rate of 150mm/min, had a workpiece surface which appeared visually free from defects and burn, see Figure 5.27 (a). Workpiece surface roughness R_a for Test 1 was measured to be $R_a 1.31\mu\text{m}$ which with a single spark out pass (Test 2) reduced to $R_a 1.23 \mu\text{m}$. The surface roughness results are comparable to those produced for Phases 2Ai and Aii, Test 1 which had an average value of $R_a 1.28\mu\text{m}$. The improvement in surface finish obtained by using spark-out was attributed to an increased number of wheel profiles passing the same location on the workpiece [42]. Bentley and Aspinwall [119] also detail that a sparkout pass reduced tensile residual stresses produced in the direction parallel to the feed and compressive residual stresses in the direction perpendicular to the feed by $\sim 200\text{MPa}$ when CFG Ti-45Al-2Mn-2Nb +0.8%vol. TiB_2 using soft to medium grade vitrified bonded SiC wheel at conventional wheel speeds with a low depth of cut and slow feed rate.

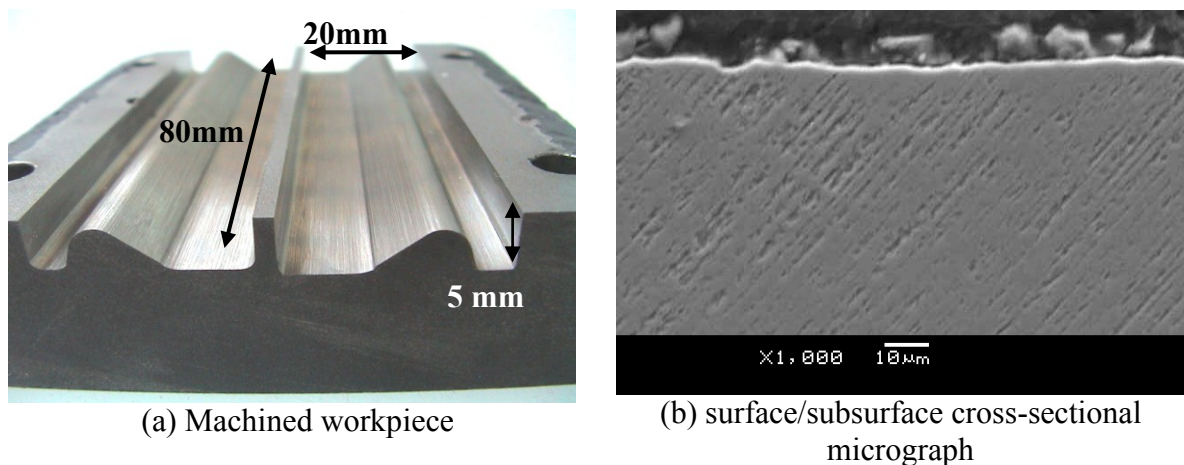


Figure 5.27: Demonstrator blade root

Analysis of workpiece surface/subsurface showed similar results to those obtained in Experiment 2B using identical operating parameters, see Figure 5.27 (b). No cracking, whether involving arc shaped cracks or visible heat affected zone were observed and there was only limited deformation/bending of the lamellae in both tests. For surface/subsurface cross-sections parallel to the feed direction this occurred to a depth of $\sim 5\mu\text{m}$ which reduced to a depth of $\sim 3\mu\text{m}$ with the addition of the sparkout pass. On surfaces perpendicular to the feed direction, bending/deformation of the lamellae occurred on the angled surfaces of the lobe to a depth of $\sim 2\mu\text{m}$. Several regions of possible fracture/pullout were observed on both sections to a depth of $\sim 2\mu\text{m}$.

5.2 Phase 2B: Assessment of significant operating parameters when creep feed grinding Ti-45Al-8Nb-0.2C using superabrasive wheels

5.2.1 Phase 2Bi: Preliminary testing of Ti-45Al-8Nb-0.2C using superabrasive wheels

a) Wheel wear, surface roughness, force, power and specific energy

Preliminary testing of Wheels D (diamond) and E (cBN) showed that compared to SiC abrasives with identical operating parameters, the superabrasive wheels provided an increase in G-ratio of ~2000% due to the improved wear resistance and thermal conductivity of the superabrasive grits over the SiC grit material. Figure 5.28 details the results of the trials and shows that in the majority of tests, when the test was stopped, (due to the removal of the prerequisite amount of workpiece material), G-ratio was still increasing as parity had not been reached between the rate at which wear flats are generated by attritious wear and grit and bond fracture.

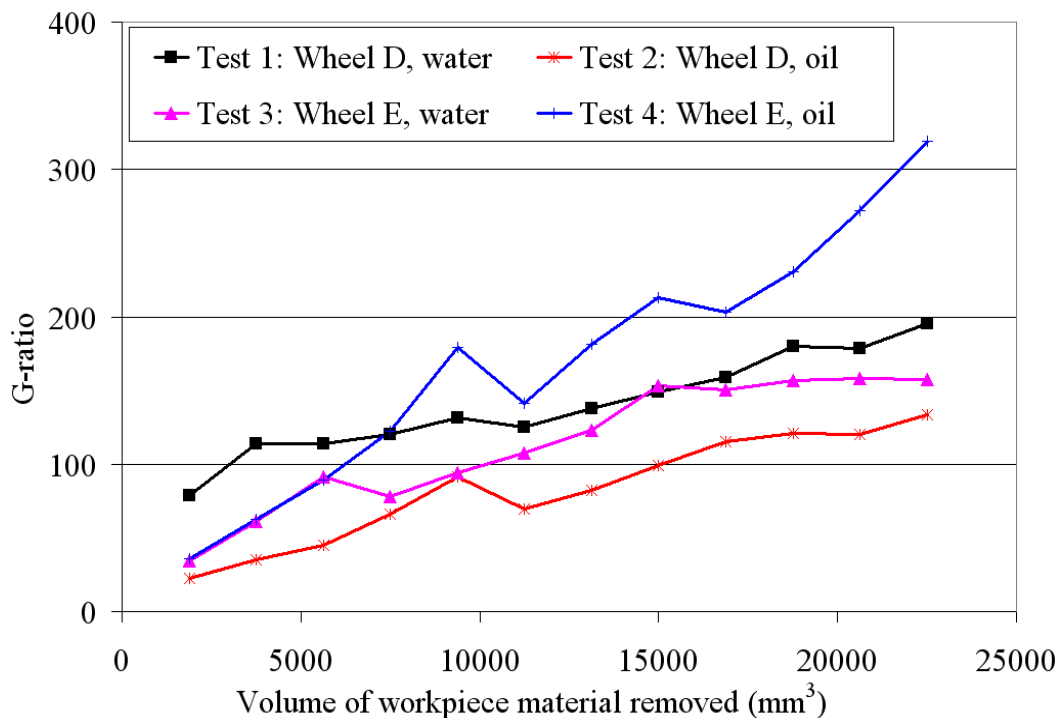


Figure 5.28: G-ratio against volume of workpiece material removed (Phase 2Bi)

Both wheels showed a similar performance when grinding with water based fluid. This was possibly due to a balance being reached between the increased hardness and thermal conductivity of the diamond grit in Wheel D and the increased volume of the CBN grit material in Wheel E. The two wheels differed greatly in their performance with an oil based fluid, with an increase in the G-ratio of Wheel E (CBN grit), and a reduction in G-ratio for Wheel D (diamond grit). Brinksmeier et al. [72] state that when grinding with CBN grit,

improved performance with lower surface roughness and wheel wear (higher G-ratio) is generally observed with oil rather than water. The poor performance of CBN and water based grinding fluid has been generally attributed to the chemical affinity between CBN and water [72]. Oliveira et al. [181] performed surface grinding tests on hardened steel (52HRC) and compared the performance of water based and oil based grinding fluid. The major findings of their research were that the chemical reactions between CBN grains and water resulting in boron oxide formation on the surface of the CBN grains were not one of the significant factors in the wheel wear mechanism and that water based fluids are as good as neat oils.

Andrew et al. [40] provides an alternative explanation for the improved performance with cBN grit and oil based fluids. They suggest that a reduction in wheel porosity may have more of an effect on the useful coolant flowrate with water than with oil and that the presence of induced porosity was much more necessary for high stock removal rates when the fluid was water based. This provides an explanation as to why the more open, porous Wheel D had a worse performance with the oil based fluid than water based product and why Wheel E (with an increased proportion of CBN grit) had increased performance with the oil based grinding fluid.

Plots for maximum normal force, tangential force and power are shown in Figure 5.29. A decrease in the forces, power and specific energy would be expected due to the lubricating properties of oil which would cause the sliding and rubbing components of force and power to reduce. Indeed Monici et al. [182] report up to a 20% reduction in tangential force and specific energy levels when using neat oil compared to a water based fluid when cylindrical grinding using a nozzle similar to the one that used for the current work. The graph in Figure 5.29 shows that a reduction in forces did not occur when using oil as the grinding fluid, indeed for normal force and power an increase was observed when using oil. A possible reason for the increase is presented by Klocke et al. [183], who suggest that the motion of the grinding wheel continuously draws grinding fluid into the grinding gap, which subsequently builds up hydrodynamic pressure between the wheel and workpiece in a similar way as the supporting force in a hydrodynamic bearing. This results in a rise in the normal force by the so called coolant induced force. A model was presented that indicated that the force increased with wheel speed, coolant flow rate and the viscosity of the grinding fluid. Oil based grinding fluids typically have higher (at least an order of magnitude) viscosities than water based grinding fluids and as a consequence coolant induced forces would be expected to be higher with oil.

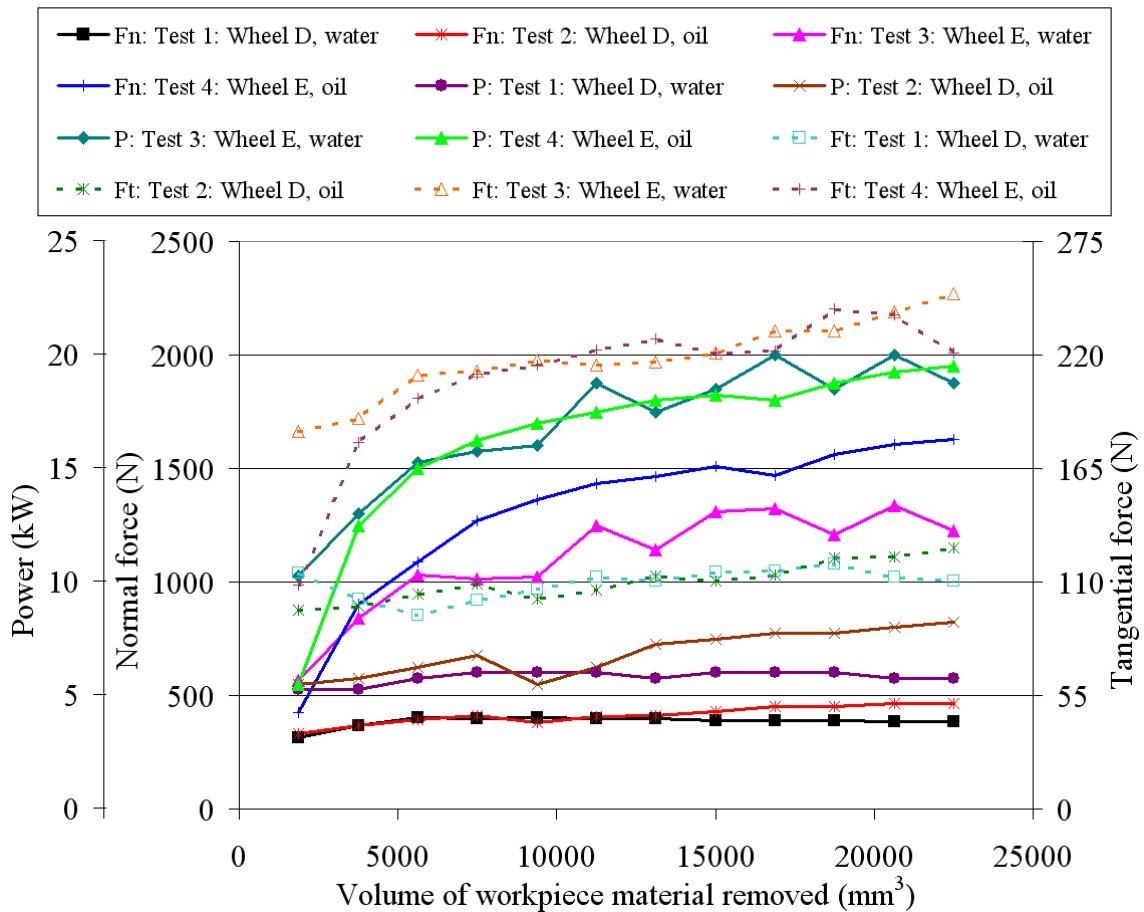


Figure 5.29: Forces and power against volume of material removed (Phase 2Bi)

Possibly of greater significance was the different performance of the two grinding wheels. After dressing, at the beginning of the test, the performance of both wheels was fairly similar however, as the test progressed and volume of material removed increased Wheel E with CBN grit showed a rapid initial increase of up to 200% in grinding forces and power before increasing linearly. Wheel D on the other hand with diamond grit showed a marginal 10% increase in response values from the start of the test to the end of the test. A higher level of forces and power would be expected from Wheel E due to its higher abrasive content [45]. The initial rapid increase in forces and power with Wheel E could have been due the differences in dressing. Wheel E was probably sharper after dressing than Wheel D and as increased wear flats were generated, the forces and power increased. Unfortunately, it was extremely difficult to provide a direct comparison between the two wheels as they differed in other aspects of composition as well as abrasive grit type (based on comments from Saint-Gobain).

Figure 5.30 shows a graph of workpiece surface roughness Ra at the end of each test after 22,500mm³ of workpiece material had been removed. Despite not reducing the forces or

power, the use of oil reduced surface roughness by ~20% as a result of improved lubrication and a reduction in sliding and rubbing. Workpiece surfaces produced using Wheel E had a lower workpiece surface roughness than Wheel D and was because Wheel E had more grit material, resulting in more cutting edges and lower porosity: less “empty space”. Brinksmeier et al [72] state that no entirely uniform statements can be made as to the comparison of oils and emulsions concerning workpiece roughness, only that a reduction in tool wear through the use of oil due to increased lubrication, is clear. In comparison to results using SiC abrasives, surface roughness, when using comparable operating parameters and conditions was 25% lower for Wheel D and 70% lower for Wheel E. The smaller grit size and lower levels of porosity of the superabrasive wheels are expected to have had an influence on this.

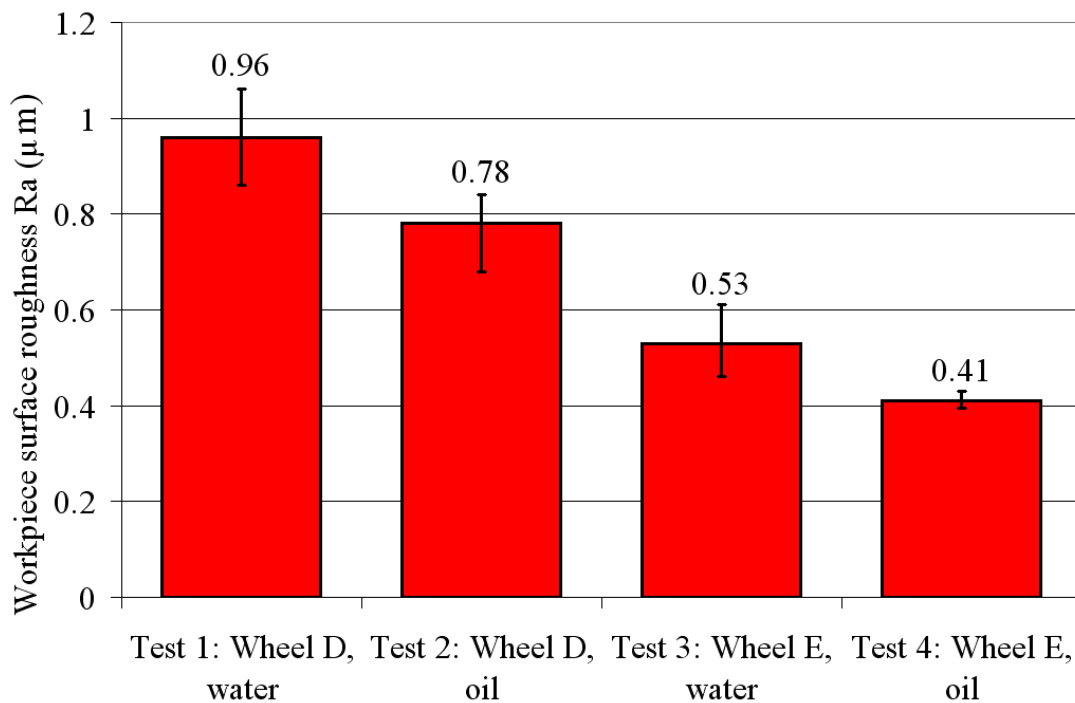


Figure 5.30: Workpiece surface roughness Ra (Phase 2Bi)

b) Workpiece surface

Images of the workpiece surface are shown in Figure 5.31. Tests with Wheel D showed surfaces free of workpiece surface burn and cracking whereas tests with Wheel E showed low levels of workpiece surface burn with cracks running along the length of the workpiece. Water based fluids are considered better coolants than oils since their specific heats are typically two times higher and their thermal conductivities about four times higher than for oils [178].

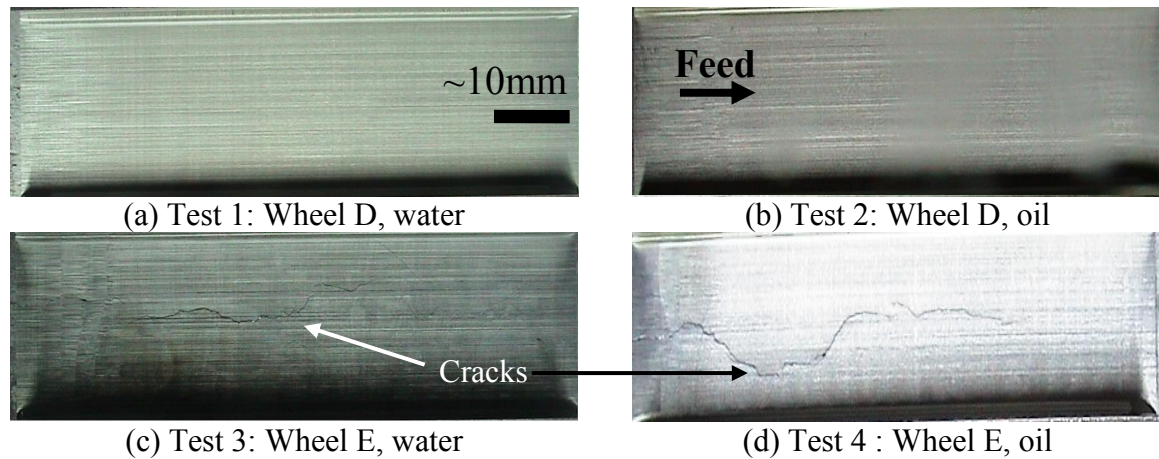


Figure 5.31: Workpiece surface images (Phase 2Bi)

Phase 2, Experiments 2Ai to Aiii showed that when grinding with wheels employing SiC grit material, at low wheel speeds of 15m/s, surfaces appeared free of cracks and workpiece surface burn, while at higher speeds up to 35m/s, extensive workpiece surface burn was evident. The higher thermal conductivity of the superabrasive grits ($\sim 2000\text{W/m.K}$ for diamond and $\sim 1300\text{W/m.K}$ for CBN) when compared with SiC grit material ($\sim 42\text{W/m.K}$) allowed for an increase in wheel speed before the occurrence of surface burn [184] as the superabrasive grit removed a much larger fraction of the total grinding energy. A similar result was reported by Novovic [151] when grinding burn resistant titanium, whilst Aust and Niemann [96] reported that surface quality could be improved by 15-20% using a diamond wheel rather than a SiC wheel, under comparable conditions.

The workpiece surface burn and cracking observed on the surfaces ground using Wheel E, has been largely attributed to the increased percentage of grit and bond material and the subsequent reduction in porosity of the grinding wheel. An increase in the percentage of grit in the wheel would be expected to remove more heat as there is a greater volume into which the heat can be conducted. The reduction in the percentage of porosity caused a lower level of useful coolant flowrate and as a consequence less heat was conducted to the grinding fluid. As it is suggested that 95% of the heat in creep feed grinding is conducted to the grinding fluid [178], any reduction in flow passing through the contact zone would result in less heat being transferred to the fluid and as a consequence more heat was channeled to the workpiece leading to increased temperatures. No significant difference in the visual quality of the workpiece surface were observed when using water based grinding fluid compared to oil for wheel D, however, an increase in surface burn was observed for Wheel D when grinding using water based fluid. This could help support the suggestion by Andrew et al. [40] that low porosity wheels have better performance with oil based fluids than more open grinding

wheels. Cracks observed running through the centre of the surfaces of Tests 3 and 4 were probably caused by high stress operating conditions leading to tensile residual stresses.

Higher magnification analysis of the workpiece surface produced using either Wheel D or E showed a surface similar in type to those produced using Phase 2Aii, Test 1 and 2 operating parameters, see Figure 5.32. Surfaces typically consisted of visible scratches running from one side of the surface to the other. In general, Tests 2 and 4 which used oil as the grinding fluid had a lower level of sideflow which was probably through a reduction in plowing due to improved lubrication. An increased amount of adhered material was found on surfaces produced using Wheel E, due possibly to the increased amount of abrasive and reduced porosity of this wheel compared to Wheel D. This would be expected to increase the grinding temperature and also reduce the amount of useful coolant flow that is able to remove the grinding chips. No incidences of fracture/pullout were observed on any of the assessed surfaces.

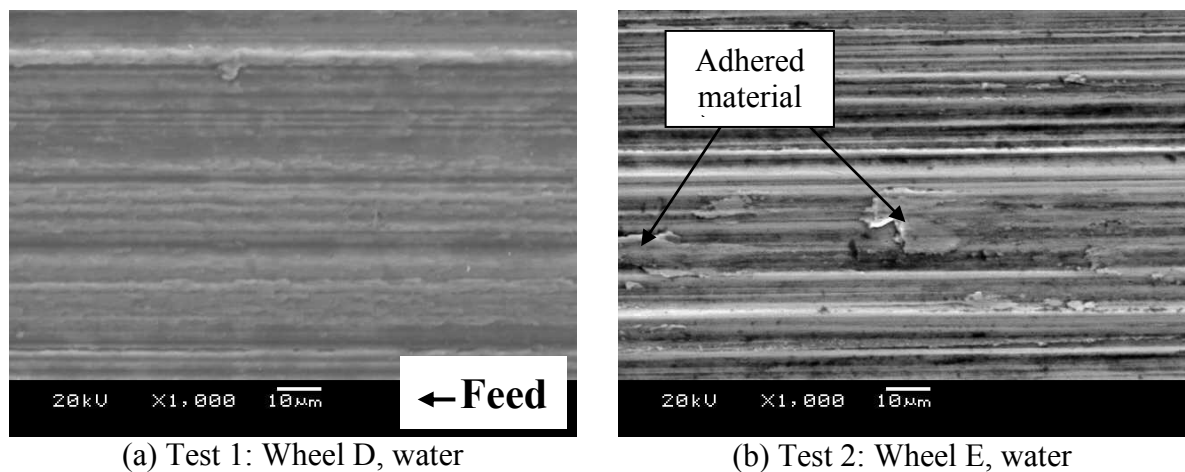


Figure 5.32: Higher magnification images of the machined workpiece surface (Phase 2Bi)

c) Microhardness

Microhardness depth profiles for the four tests are shown in Figure 5.33, Appendix C, Figure C66 gives individual profiles. All tests showed a hardened layer extending to a depth of $\sim 500\mu\text{m}$ from the workpiece surface. Test 1 using Wheel D and water based fluid showed the highest level of hardness with a maximum value of $\sim 550\text{HK}_{0.025}$. Test 3 showed a similar performance although with a minor reduction in maximum hardness. Both tests using oil based grinding fluid showed similar peak hardness values of $\sim 475\text{HK}_{0.025}$ however Test 4 showed softening within the first $30\mu\text{m}$ of the workpiece surface. The graph also shows that a higher level of strain hardening was caused when using water as a grinding fluid. It is suggested that the use of a water based fluid over oil leads to compressive residual stresses as

a result of its greater heat removal capacity [72]. An increase in microhardness with associated plastic deformation of the workpiece surface at a relatively low temperature has been shown to cause an increase in compressive residual stresses in milling γ -TiAl [107]. Workpiece surface images of surfaces produced using Wheel E showed instances of workpiece surface burn indicating that higher temperatures were caused by a combination of the lower thermal conductivity of the grit and the reduced porosity, even though the higher grit concentration would be expected to offset this aspect.

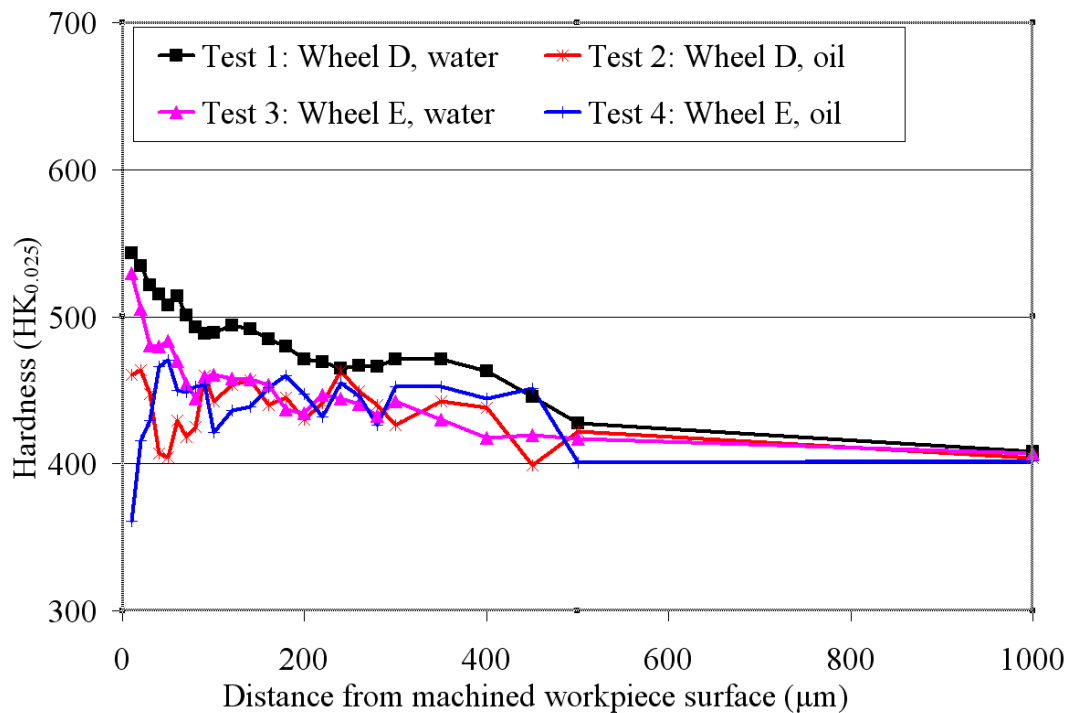


Figure 5.33: Microhardness depth profiles (Phase 2Bi)

d) Workpiece surface/subsurface

Surface/subsurface cross-sections parallel to the feed direction were observed to be smoother than surfaces perpendicular with the greatest disparity between them observed when using Test 1 operating parameters, see Figure 5.34 (a) and (b). In contrast, Test 4 surfaces showed only a marginal difference between parallel and perpendicular sections. In general these results are consistent with the surface roughness R_a results detailed in Figure 5.30. Visible damage consisting of intermittent deformation/bending of the lamellae which was observed on all surface/subsurfaces assessed both parallel and perpendicular to the feed direction. In the parallel direction deformation/bending of the lamellae covered up to 70% of the surface with to a maximum depth of $\sim 12\mu\text{m}$ and an average depth of ~ 5 to $8\mu\text{m}$, irrespective of the operating conditions used to produce the surface. Figure 5.34 (b) shows a cross-sectional

micrograph from Test 1 workpiece. The depth of deformation/bending perpendicular to the feed direction was consistently $<5\mu\text{m}$ and covered no more than 10% of the surface that was assessed.

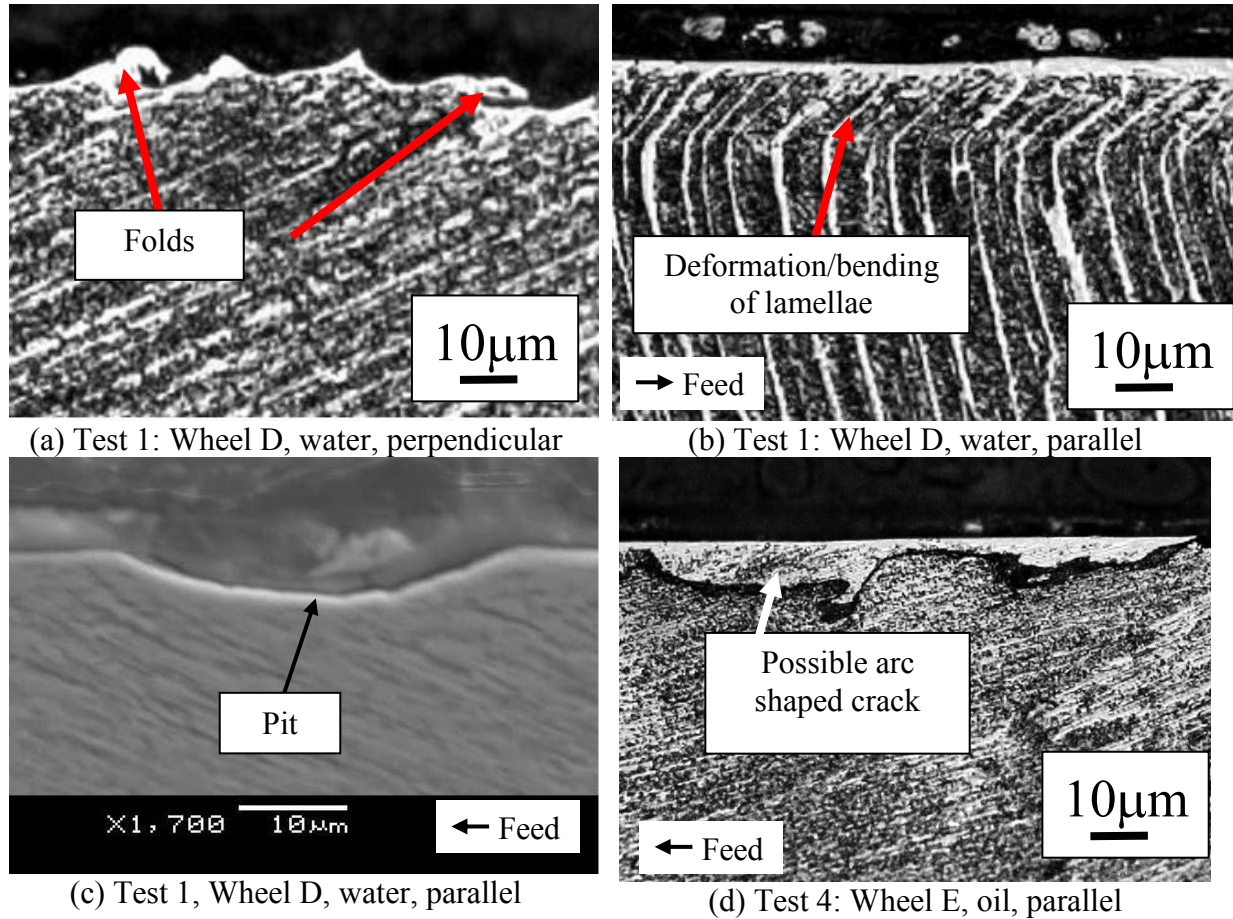


Figure 5.34: Workpiece surface/subsurface cross-sectional images (Phase 2Bi)

No evidence of any significant microstructural change including a heat affected zone was observed on any surface. With workpiece samples sectioned perpendicular to the feed direction, evidence of laps and folds was found whether involving Wheels D or E, see Figure 5.34 (a). This was generally to a depth of $<3\mu\text{m}$ from the workpiece surface as with Phase 2Ai, Test 3. Three areas of possible fracture/pullout (pits) were observed in the sample sectioned parallel to the feed direction produced using Wheel D and water based grinding fluid. These had a depth of $<5\mu\text{m}$ with a width ranging from 5 to $15\mu\text{m}$. No evidence of similar size damage was observed, however, smaller areas of possible fracture/pullout, $<2\mu\text{m}$ in depth were observed on all other cross-sections. Workpiece cross-sections perpendicular to the feed direction produced using Wheel E with either oil or water based grinding fluid showed an extensive network of cracks up to $\sim 15\mu\text{m}$ wide and 5mm deep. A possible arc shaped crack is visible in Figure 5.34 (d) with a depth of $\sim 10\mu\text{m}$ and a width of $\sim 100\mu\text{m}$, the

machined surface utilize Wheel E and oil based fluid. Analysis of the microstructure of creep feed ground surfaces of Ti-45Al-2Mn-2Nb +0.8%vol. TiB₂ showed no evidence of pits, tears or laps, however, cracking was seen to be severe and both intergranular and transgranular. The maximum depth of the deformed layer was 25µm. Zeppendfeld and Klocke [120] report deformation/bending of the lamellae to a depth of up to ~20µm with an arc shaped crack similar to that shown in Figure 5.34 (d) also reported which had a depth of ~20µm and width of ~100µm. They suggest that such crack formation was caused by enhanced grinding forces and stress conditions in the surface layer.

5.2.2 Phase 2Bii: Further assessment and benchmarking against BuRTi

a) Wheel wear, surface roughness, power, forces and specific energy

G-ratios obtained for γ-TiAl during this phase of experimentation ranged from ~80 to ~340. In comparison to conventional abrasives, every test showed an increase in G-ratio of up to ~600% from the first to the last grinding passes and in several of tests, G-ratio was still increasing when the test was stopped indicating that parity had not been reached between the development of wear flats and new cutting edges, see Figure 5.35. Additional graphs showing γ-TiAl normal and tangential force, power and specific energy are shown in Appendix C, Figures C67 to C71. For γ-TiAl, normal forces ranged from 400N to 3000N, tangential forces from 100N to 400N, power from 15kW to 37.5kW and specific energy from 70J/mm³ to 600J/mm³ depending of the operating parameters used for each test. In contrast to the γ-TiAl G-ratio results, other output measures for the γ-TiAl alloy showed only a marginal increase with the volume of workpiece material removed. This was probably due to reduced wear flat generation resulting from the increased hardness and thermal conductivity of the superabrasive wheels over the SiC wheels [40]. Results for Phase 2Ai showed that tests with the highest G-ratio had the lowest normal and tangential forces and power levels, however this trend was not observed for this phase of work using superabrasive wheels. The results of γ-TiAl workpiece surface roughness Ra measurements of the surface parallel to the feed direction taken at the end of each test are shown in Appendix C, Figure C76. The lowest value of Ra 0.19µm was observed for Test 8 whilst the highest value of Ra 1.01µm was observed for Test 2. All tests involving superabrasive grit showed a lower surface roughness Ra, even when grinding using higher operating parameter levels. This was possibly due to the increased grit size of the conventional wheels.

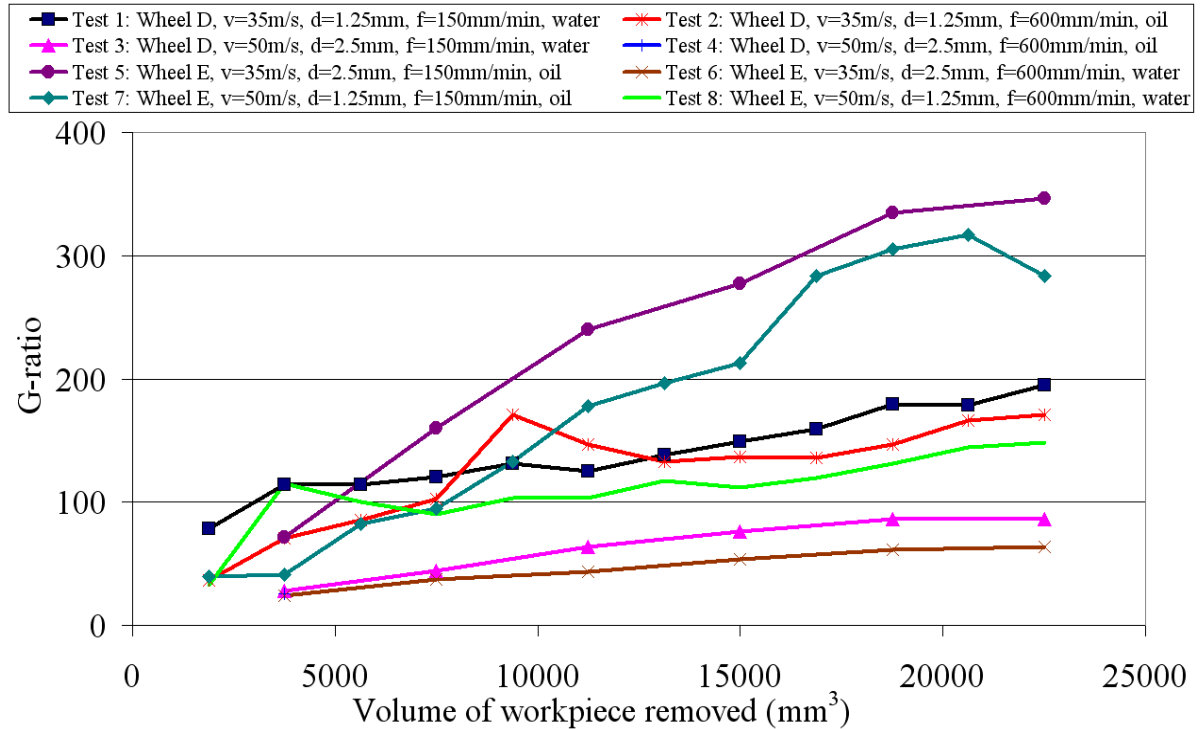


Figure 5.35: G-ratio against volume of workpiece material removed (Phase 2Bii)

As with Phase 2Ai, it is only when the main effects are considered that conclusions can be made regarding the effect of the operating parameters on each output measure. The Main Effects Plot - means for G-ratio for both alloys is shown in Figure 5.36. BuRTi alloy data was based on the graphs detailed in Appendix C, Figures C72 to C77. Average G-ratio for γ -TiAl was ~4times higher than for BuRTi and all factors apart from depth of cut showed almost identical trends for the two alloys. For γ -TiAl, increasing the wheel speed, depth of cut or feed rate caused a reduction in G-ratio by up to 50%. These trends were as expected and the reasons for the results are essentially the same as those given for the conventional abrasives in Phases 2Ai to 2Aiii. The G-ratio of Wheel D was over double that of Wheel E and was probably due to the increased grit content of Wheel D which was ~8.75% higher. The composition of the two wheels was such that a direct comparison proved difficult. Producing two wheels of the same composition except for the type of grit would have been straightforward if the chemical reactivity of the two materials were the same however the diamond and CBN grit behaved quite different chemically making comparison difficult.

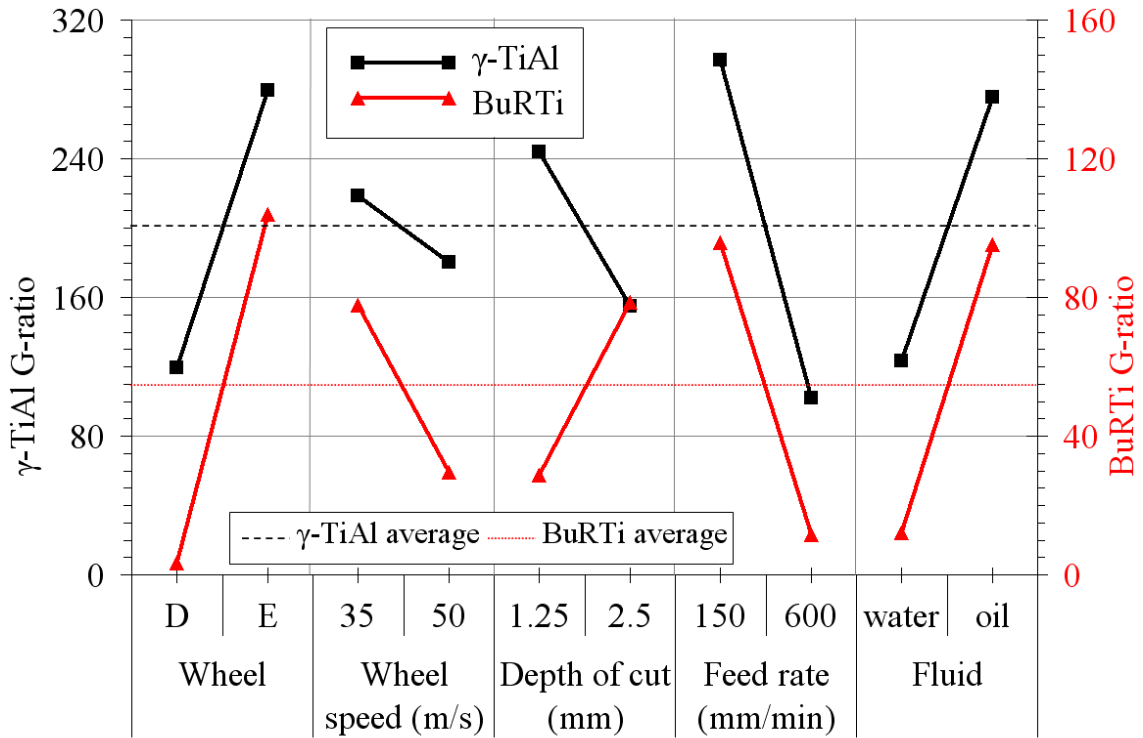


Figure 5.36: Main Effects Plot - means for G-ratio (Phase 2Bii)

Main Effect Plots means for normal and tangential forces and power for both alloys are shown in Figures 5.37, 5.38 and 5.39 respectively. On average, γ -TiAl showed 8% lower normal force, 36% lower tangential force and 4.5% lower power than BuRTi and was due to the lower ductility and tensile strength of γ -TiAl which would be expected to reduce the sliding and rubbing components of force and power. Trends for both alloys were almost identical with increasing the depth of cut or feed rate causing an increase in either force or power level. As these factors are proportional to the relative grain force, increasing them would be expected to cause an increase. Changes in wheel speed had a lower impact on force or power levels for γ -TiAl, than for BuRTi. Wheel E showed higher normal and tangential forces because of the increased abrasive contact area over that of Wheel D. It would be expected that lower forces would be measured for oil based grinding fluid rather than for water based, however the opposite was true. This could be due to an increase in the hydrodynamic force leading to coolant induced forces [183].

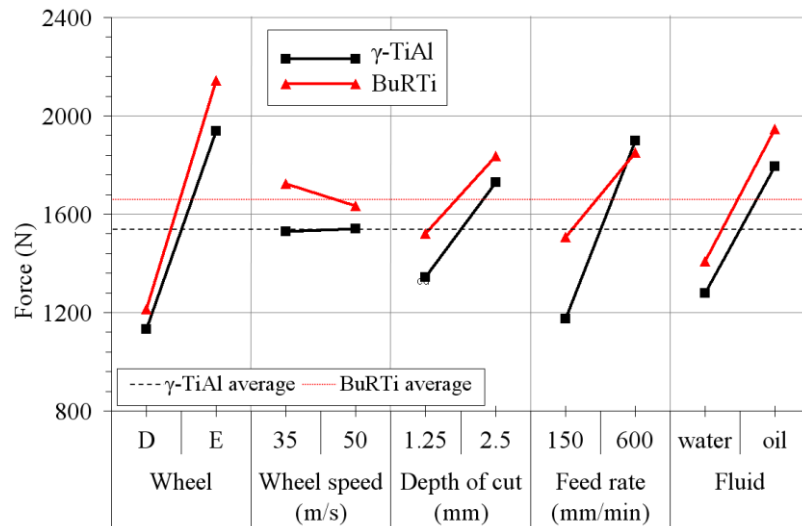


Figure 5.37: Main Effects Plot - means for normal force (Phase 2Bii)

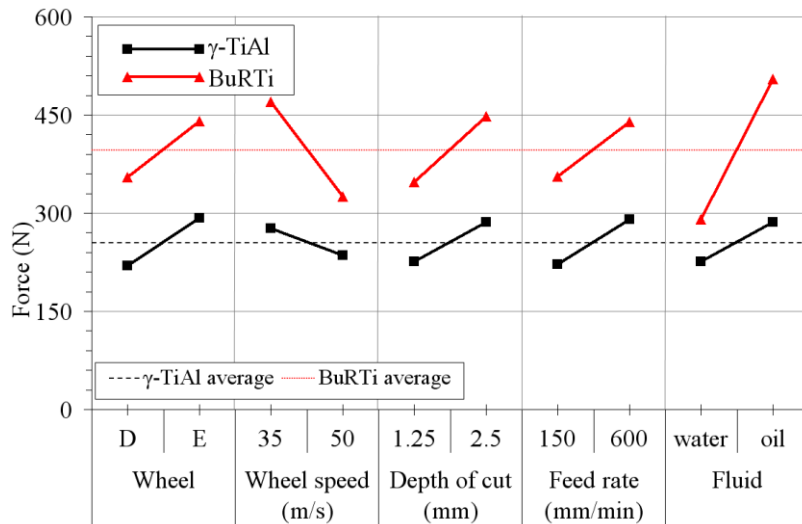


Figure 5.38: Main Effects Plot - means for tangential force (Phase 2Bii)

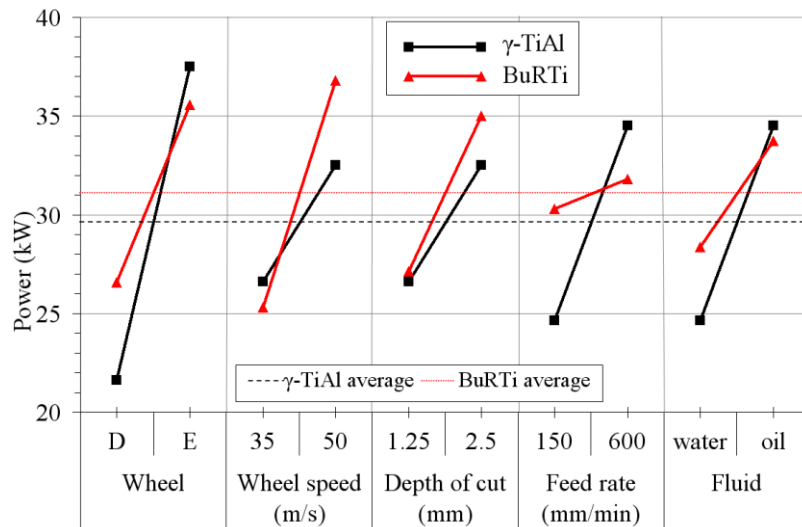


Figure 5.39: Main Effects Plot - means for power (Phase 2Bii)

The Main Effects Plot - means for specific energy is shown in Figure 5.40. On average a 14% lower value was obtained for γ -TiAl than for BuRTi with identical trends observed between alloys for each factor.

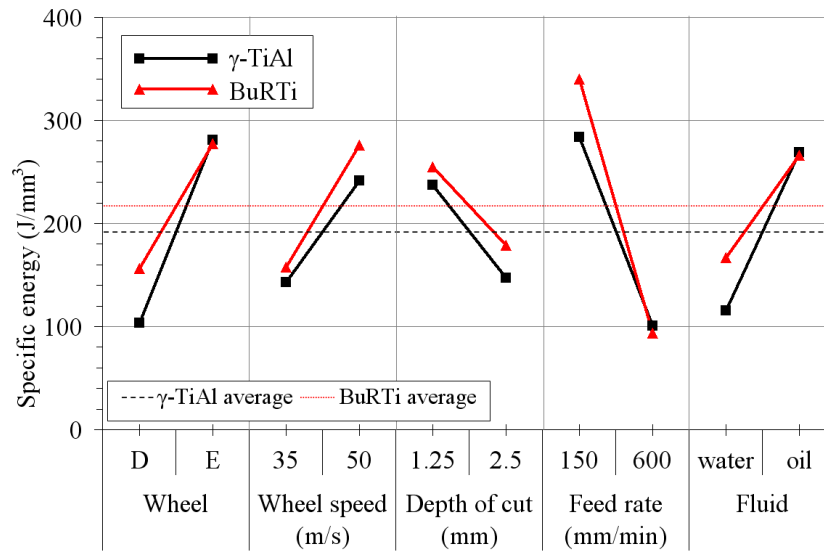


Figure 5.40: Main Effects Plot - means for specific energy (Phase 2Bii)

Surface roughness was on average $\sim 40\%$ lower for γ -TiAl than for BuRTi and is in agreement with results obtained for conventional abrasives (Phase 2Ai), see Figure 5.41. The effect of the wheel and wheel speed was almost identical for the two alloys, with lower surface roughness Ra achieved using Wheel E at a higher wheel speed, however the trends for depth of cut, feed rate and fluid differed between the two alloys.

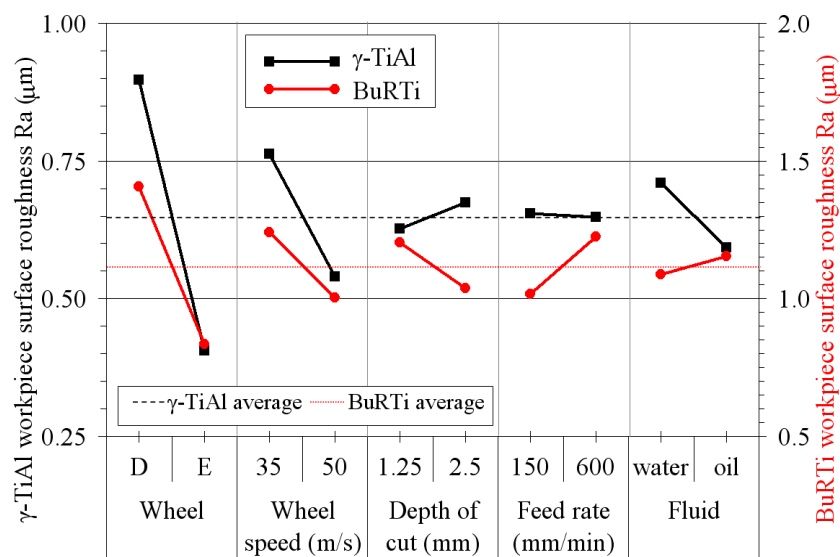


Figure 5.41: Main Effects Plot - means for workpiece surface roughness Ra (Phase 2Bii)

The Analysis of Variance (ANOVA) table for γ -TiAl G-ratio is shown in Table 5.2. ANOVA tables for γ -TiAl normal and tangential force, power, specific energy and workpiece surface roughness are shown in Appendix C, Tables C22 to C26 whilst ANOVA tables for BuRTi G-ratio, normal and tangential force, power, specific energy and workpiece surface roughness are shown in Appendix C, Tables C27 to C32. As $F_{0.05;1;2} = 18.5$, for γ -TiAl, all factors except wheel speed were statistically significant for G-ratio. Wheel type and feed rate were significant for normal force and all factors were significant for power. For BuRTi only wheel type and fluid type were significant for normal force. A large proportion of the output measures assessed for both γ -TiAl and BuRTi alloys had large residual error percentage contribution ratios indicating that either factors were omitted, measurement errors occurred or there was interactions between factors. As with Phase 2Ai, interactions plots showed extensive cross-over indicating that there were interactions between factors. Unfortunately the array used only allowed analysis of main effects, not interactions.

Source	S.S.	D.F.	M.S.S.	F_{calc}	PCR (%)
Wheel type	51267	1	51267	68.41	26.0
Wheel speed	2948	1	2948	3.93	1.1
Depth of cut	15810	1	15810	21.10	7.8
Feed rate	75980	1	75980	101.38	38.8
Fluid type	46495	1	46495	62.04	23.6
Error	1499	2	749	-	2.7
Total	193999	7	-	-	

Table 5.2: ANOVA table for G-ratio (Phase 2Bii)

b) Workpiece surface

Figures 5.42 shows workpiece surfaces for each of the γ -TiAl tests at the end of the test with the maximum volume of material removed. Test 4 was the only exception to this which was stopped after a single pass due to dangerous operating conditions including spindle stall and excessive smoke production which filled the machine tool enclosure. The surface produced for Tests 1 and 3 appeared visually free of defects and burn, whilst the Test 2 surface exhibited very slight burning with limited cracking. The marks where the spindle stalled are clearly evident on the images of the surface produced using Test 4 operating parameters. In contrast, all surfaces produced using Wheel D showed burn and cracking but to a lesser or greater extent, due to the different levels of operating factors. Test 6 appears to be the worst case with extensive burn covering >75% of the workpiece surface and a network of cracks running throughout the surface. It was difficult to assign which factor was causing the increase in workpiece surface burn and cracking as several factors changed for each test,

however in addition to the effect of the wheel, increasing the wheel speed, feed rate and depth of cut all appeared to cause an increase in surface burn and cracking. These trends were expected as an increase in these three operating parameters will generally increase the grinding temperatures leading to higher levels of surface damage [45]. As with Phase 2Bi, the lower porosity level and higher abrasive content of Wheel D was likely to have reduced the useful coolant flowrate and therefore reduced heat removal.

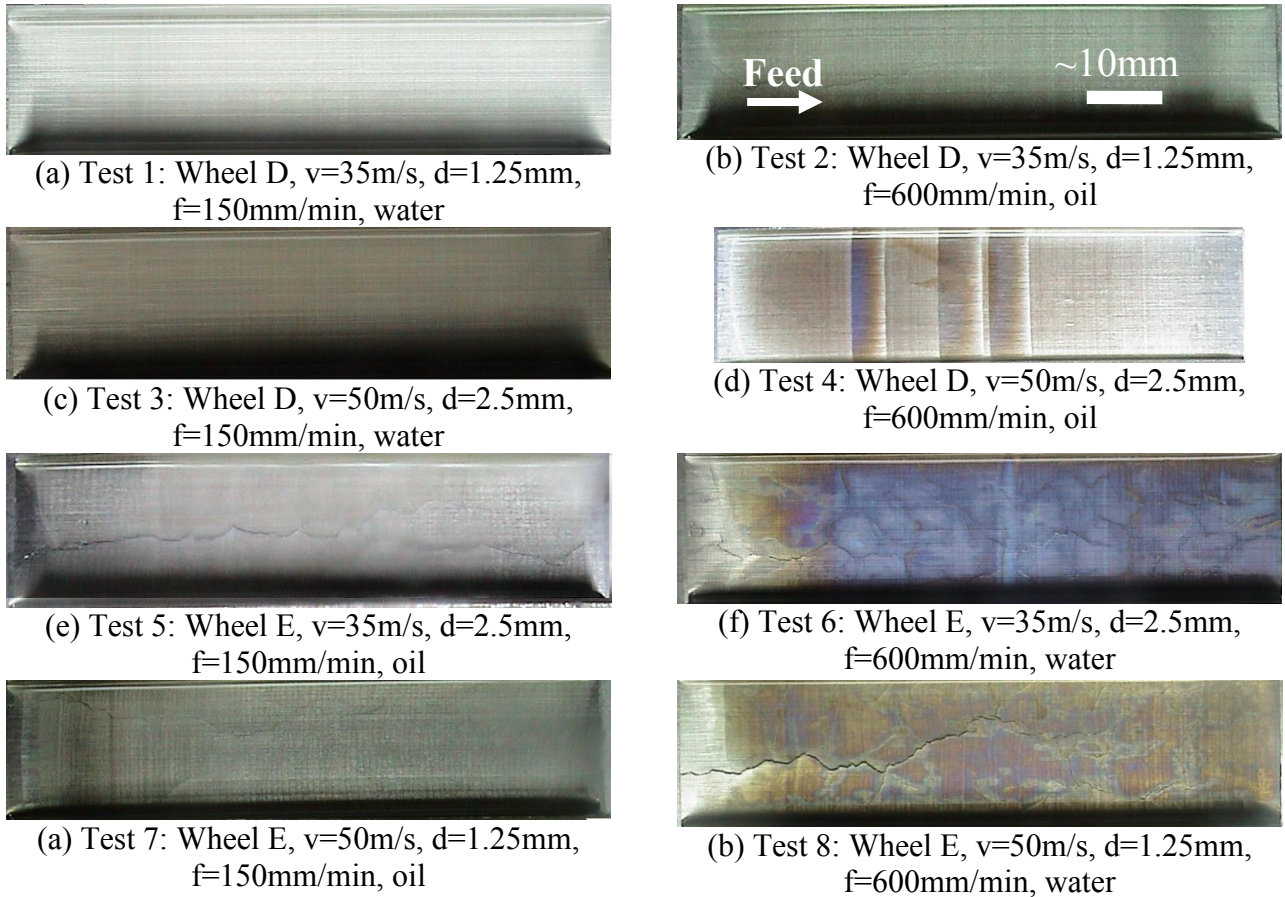


Figure 5.42: Workpiece surface images (Phase 2Bii, γ -TiAl)

The surfaces of tests that produced extensive workpiece surface burn, Tests 6 and 7, showed an initial period of limited workpiece surface burn during cut-in, as the depth of wheel engagement in the feed direction increased from zero to the specified depth of cut. The grinding temperature would also be expected to show a rapid rise during cut-in as the material removal rate increased to its steady state value [178]. It is also suggested that during cut-out, as the grinding wheel leaves the workpiece and there is a reduction in the workpiece material available to conduct heat, the grinding temperature may exceed its steady state value and the level of workpiece surface burn may increase [178]. With respect to the images for this and other phases of experimentation, this trend was not observed on any workpiece surface.

As with the benchmarking trials of γ -TiAl against BuRTi detailed in Phase 2Ai, the surface images for BuRTi given in Figure 5.43 show similar trends to those for γ -TiAl with Test 1 and 3 surfaces appearing to be visually free of burn, whilst all four tests performed using Wheel D showed high levels of surface burn. In addition, the lack of visible surface cracking as a consequence of the higher room temperature ductility of the BuRTi alloy was also consistent with Phase 2Ai trials.

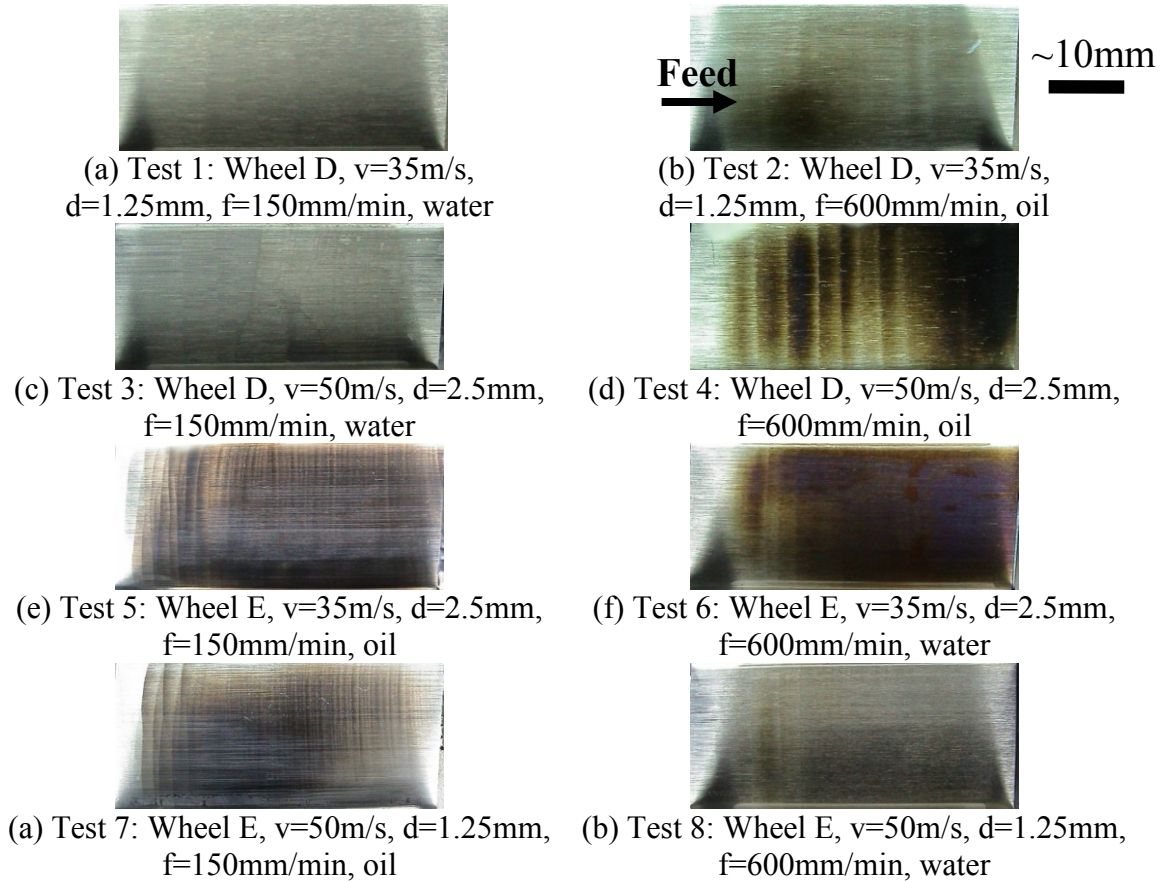
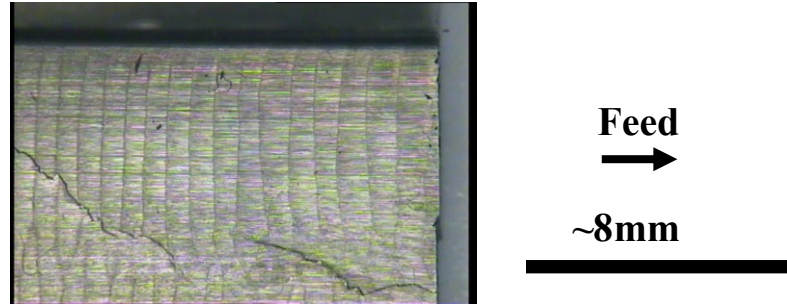


Figure 5.43: Workpiece surface images (Phase 2Bii, BuRTi)

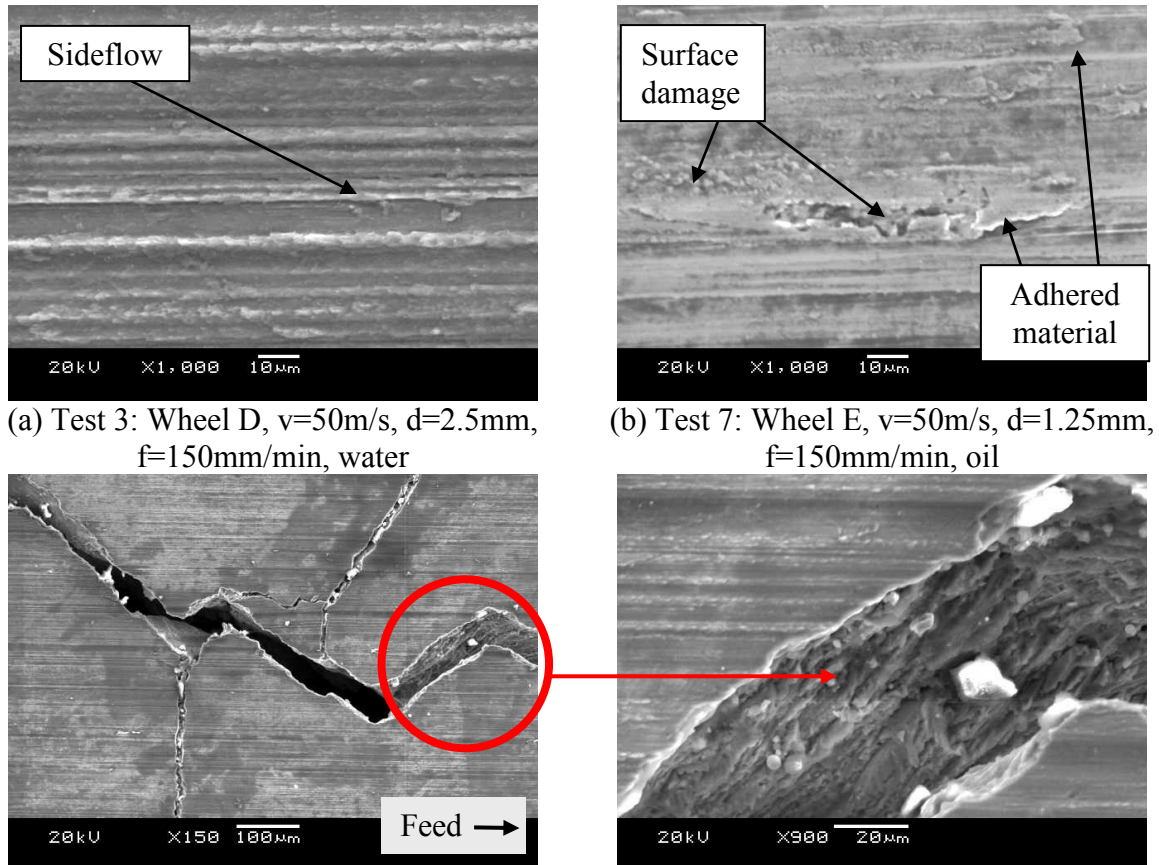
Figure 5.44 shows a magnified view of the γ -TiAl workpiece surface produced using Test 7 operating parameters with the surface burn characterised by a succession of ‘surges’. Andrew et al. [40] suggests that during a surge the workpiece temperature rises from a steady state value to a higher value then returns to the steady state value. At the critical burnout temperature there is a breakdown in the heat transfer mechanism which results in a rapid temperature rise. It is suggested that the wheel self-sharpens during the surge as the specific energy has been measured to be lower after the surge than before it. The lowering of specific energy then permits grinding temperatures to return to pre-surge cooler levels [40].



Test 7: Wheel E, $v=50\text{m/s}$, $d=1.25\text{mm}$, $f=150\text{mm/min}$, oil

Figure 5.44: Higher magnification image of the surface produced using Test 7 parameters

Analysis of the $\gamma\text{-TiAl}$ ground surfaces under higher magnification showed that surfaces produced using Test 1 and 3 operating parameters were free from damage including cracks, however Test 3 using a higher wheel speed and depth of cut than in Test 1, showed a greater amount of sideflow, see Figure 5.45 (a).



(c) and (d) Test 8: Wheel E, $v=50\text{m/s}$, $d=1.25\text{mm}$, $f=600\text{mm/min}$, water

Figure 5.45: Higher magnification images of the machined workpiece surface (Phase 2Bii)

Cracks up to 1mm wide were observed running in directions both parallel and perpendicular to the feed direction for all other tests. Figure 5.45 (c) and (d) show a typical crack with a width of up to $100\mu\text{m}$. The fractured surface of the crack walls is typical of a brittle fracture

mechanism. In general, as with other ground surfaces, fracture/pullout of the workpiece surface was limited however some instances where this occurred were observed, see Figure 5.45 (b). In general, an increase in the levels for operating parameters increased the occurrence of this damage and also the level of adhered material, however no trend could be identified for its location.

c) Microhardness

Microhardness depth profiles for all γ -TiAl tests are shown in Figure 5.46 with individual graphs shown in Appendix C, Figure C78. All tests exhibited workpiece surface hardening to different degrees depending on test operating parameters levels used. Phase 2Ai and 2Aii results showed that a similar hardened layer was present with a maximum hardness of $\sim 600\text{HK}_{0.025}$ when grinding with SiC abrasives using wheel speeds from 15-35m/s. The lower maximum hardness of $\sim 550\text{HK}_{0.025}$ for tests using the superabrasive wheels was probably as a result of the improved thermal conductivity of the superabrasive grits. In comparison, to Phase 2Ai where the surface produced using the higher operating levels, had a hardened layer with the highest hardness, this phase of work showed that Test 1 with the lowest operating parameters had a hardened layer with the highest hardness. Unfortunately lack of time precluded replication of the test to assess if this trend is correct.

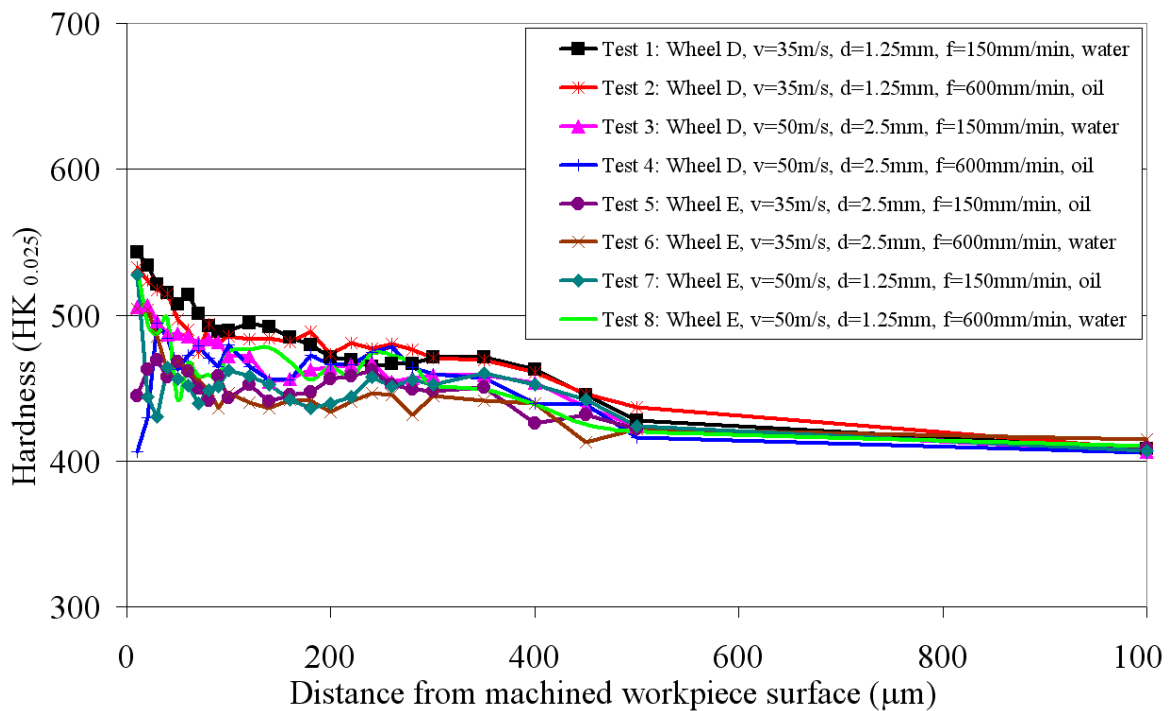
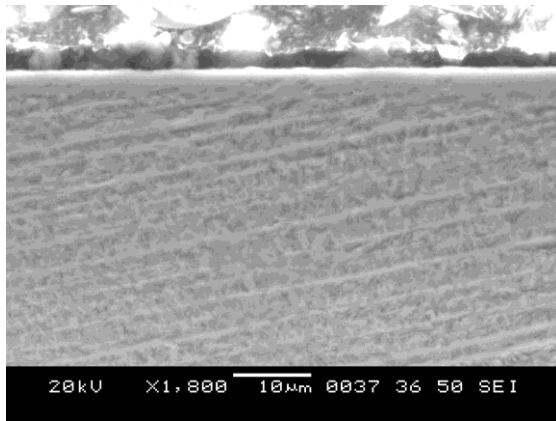


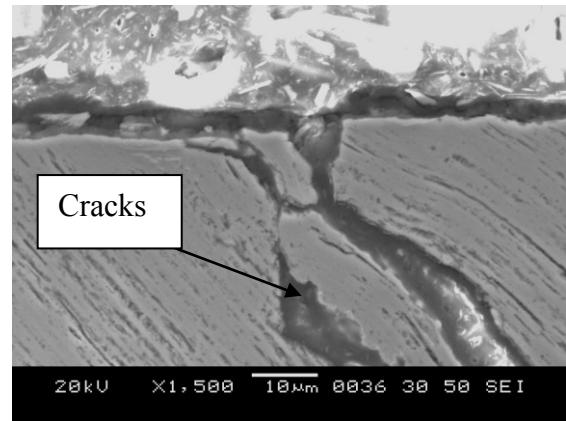
Figure 5.46: Microhardness depth profiles (Phase 2Bii)

d) Workpiece surface/subsurface

Surface/subsurface integrity evaluation of Tests 1 and 3 showed surfaces that appeared to be free of defects including macro cracking, HAZ and bending of the lamellae, see Figure 5.47 (a). These tests also produced the lowest normal and tangential forces of $\sim 500\text{N}$ and $\sim 200\text{N}$ respectively. Not surprisingly, cross sections parallel to the feed showed smoother surfaces than those perpendicular to the feed. It was difficult to draw conclusions concerning which surface appeared the most damaged, however all tests with Wheel D produced surfaces characterized by having extensive networks of cracks of up to $\sim 10\mu\text{m}$ wide and $>1\text{mm}$ deep, see Figure 5.47 (b). The increased force and power levels shown in the Main Effect Plots would be expected to cause increased grinding temperatures and stresses leading to tensile residual stresses in the machined workpiece surface.



Test 4: Wheel D, $v=50\text{m/s}$, $d=2.5\text{mm}$, $f=600\text{mm/min}$, oil, parallel



Test 8: Wheel E, $v=50\text{m/s}$, $d=1.25\text{mm}$, $f=600\text{mm/min}$, water, perpendicular

Figure 5.47: Workpiece surface/subsurface cross-sectional images (Phase 2Bii)

5.2.3 Phase 2Biii) Comparison of the performance of different wheel specifications

In comparison with Wheel D, the new specification grinding wheel (Wheel F) which employed increased porosity and reduced bond material, had on average a G-ratio that was 50% of the G-ratio measured for tests using Wheel D for the same operating parameters, see Figure 5.48. Appendix C, Figures C79 to C82 show graphs of normal and tangential force, power and specific energy against volume of workpiece material removed for Phase 2Biii. In general, Wheel D had a normal force up 100% higher, a tangential force up to 60% higher, 33% higher power and 25% higher specific energy than Wheel F when using the same test parameter levels. Andrew et al. [40] states that the size of the wear flats generated are

dependant on the grade of the wheel. Wear flats build up to a level that will either fracture the grit or remove it from the bond faster with a softer grade wheel. This means that a softer grade wheel will give a lower wear flat area and hence lower rubbing energy than a hard wheel and hence lower forces and power. In Phase 2Aiii, Wheel C had a considerably lower force and power level than Wheel B.

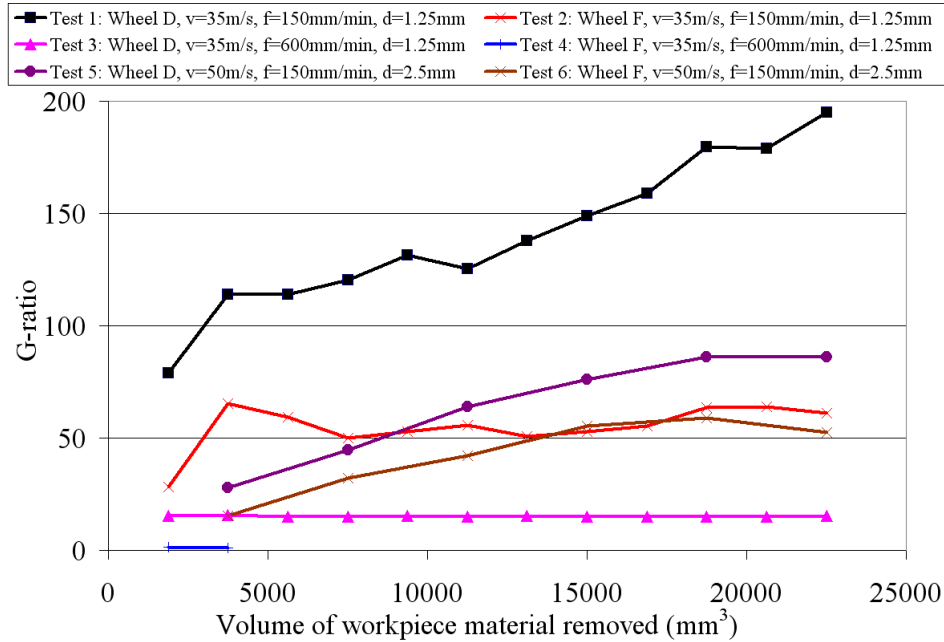


Figure 5.48: G-ratio against volume of workpiece material removed (Phase 2Biii)

Workpiece surface images for Tests 2, 4, 5, 6 are shown in Figure 5.49 whilst Tests 1 and 3 were shown in Figure 5.42. They show that at a high feed rate, the increased porosity of Wheel F allowed an improvement in coolant to enter the grinding zone which would be expected to reduce the grinding temperatures and diminish the likelihood of workpiece surface burn and cracking. Workpiece surfaces produced at the higher feed rate (600mm/min) using wheel F showed extensive chatter. In order to increase the porosity, the amount of bond material was reduced. Operating at high feed rate produced a larger undeformed chip thickness and subsequently higher forces, causing increased bond post rupture and the loss of grit material with radial wheel wear of up to $\sim 150\mu\text{m}$. The main aim using Wheel F was to increase the critical material removal rate before workpiece burn occurred and this was achieved, however the unstable operating conditions and high wear rates made it impossible to operate with this wheel. At lower material removal rates, Wheel D produced better results with higher G-ratios and similar workpiece surface images. Cross-sectional micrographs of

surfaces produced using Wheel D showed limited surface damage caused by the machining process, therefore Wheel D would be the more suitable wheel with which to operate.

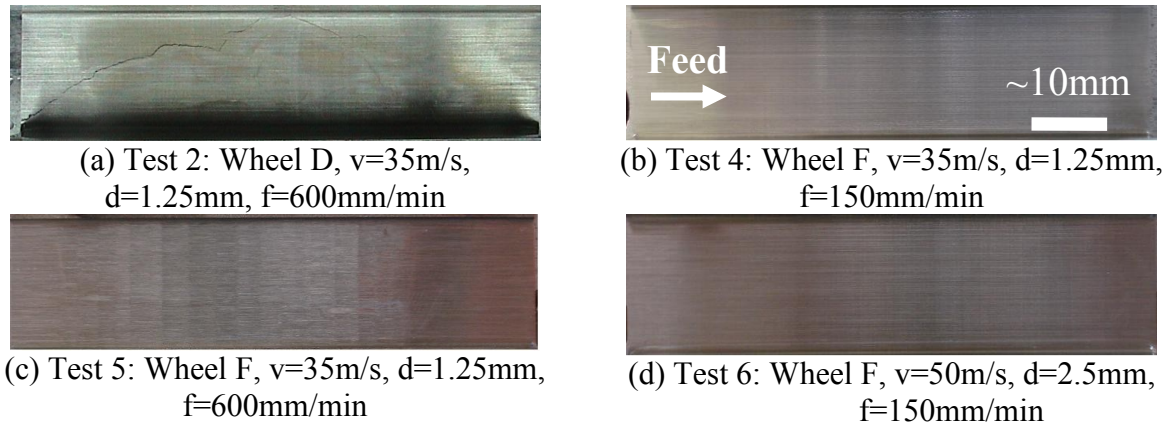


Figure 5.49: Workpiece surface images (Phase 2Biii)

5.3 Phase 2C: Benchmarking of Ti-45Al-8Nb-0.2C against Ti-6Al-4V

Benchmarking of the γ -TiAl alloy Ti-45Al-8Nb-0.2C against Ti-6Al-4V was performed using Wheel A (SiC grit) and Wheel D (diamond superabrasive grit). The results in Figure 5.50 showed quite convincingly that the more ductile ($>10\%$ when compared to $<2\%$ for γ -TiAl), Ti-6Al-4V was extremely difficult to grind when compared to γ -TiAl alloys. Indeed, the G-ratio for all tests involving Ti-6Al-4V was very low with a maximum value of ~ 1.2 for SiC abrasive rising to only 1.5 for the test with a superabrasive wheel. In contrast, values for γ -TiAl alloys were typically 9 times higher for SiC abrasives and ~ 71 times higher for superabrasives. Ti-6Al-4V tests showed extensive regenerative chatter which increased in magnitude with each grinding pass. This was a consequence of the extremely high level of wheel wear which caused the grinding wheel grits to rapidly lose sharpness with consequent deterioration in the wheel roundness. This chatter caused a rapid change in force of up to 600N in a time period of less than 1s and caused a ringing sound to be heard with the superabrasive wheels, see Figure 5.51 and 5.52. Limited workpiece surface burn was observed on the ground surfaces, however, the extensive regenerative chatter caused the workpiece surface to vary in different regions by up to $40\mu\text{m}$. The heavy wheel wear and poor surface finish/geometrical accuracy found in the present work and that of other researchers suggests that it may never be technically viable or economically feasible to process Ti-6Al-4V by creep feed grinding

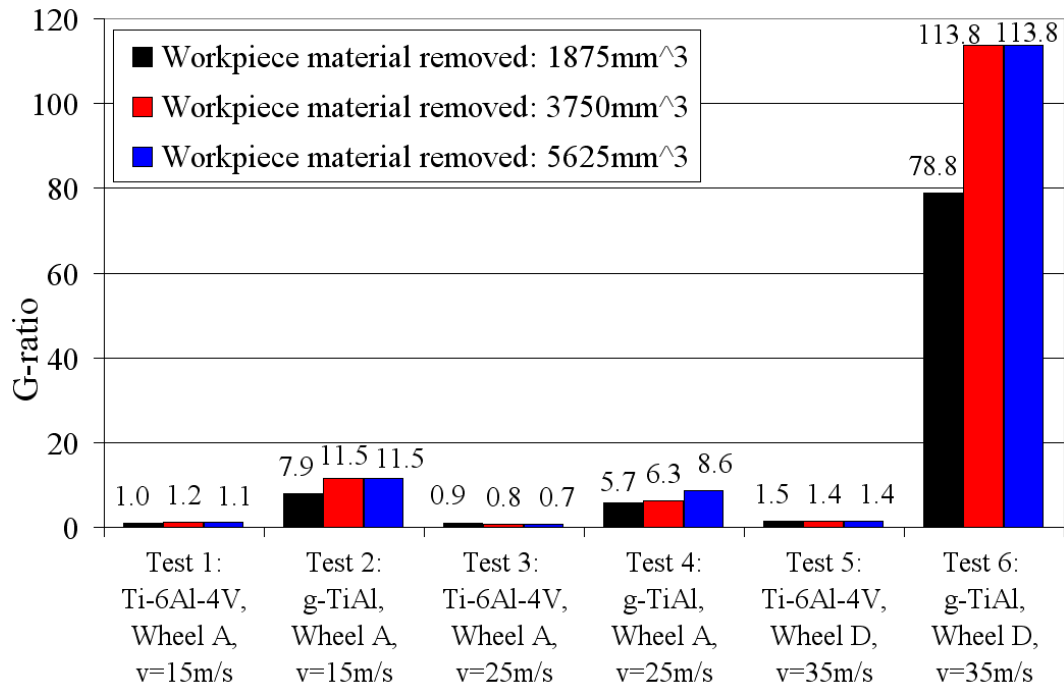


Figure 5.50: Bar chart showing G-ratio against material removed for γ -TiAl and Ti-6Al-4V

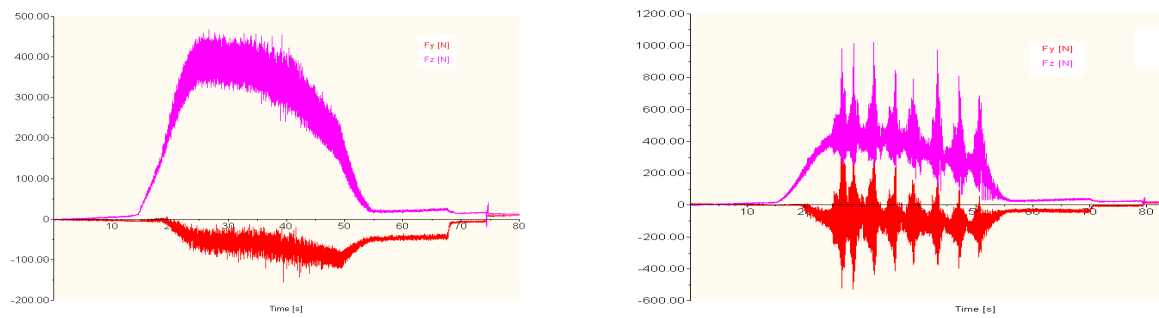


Figure 5.51: Force profiles for Test 5 (a) and Test 6 (b)

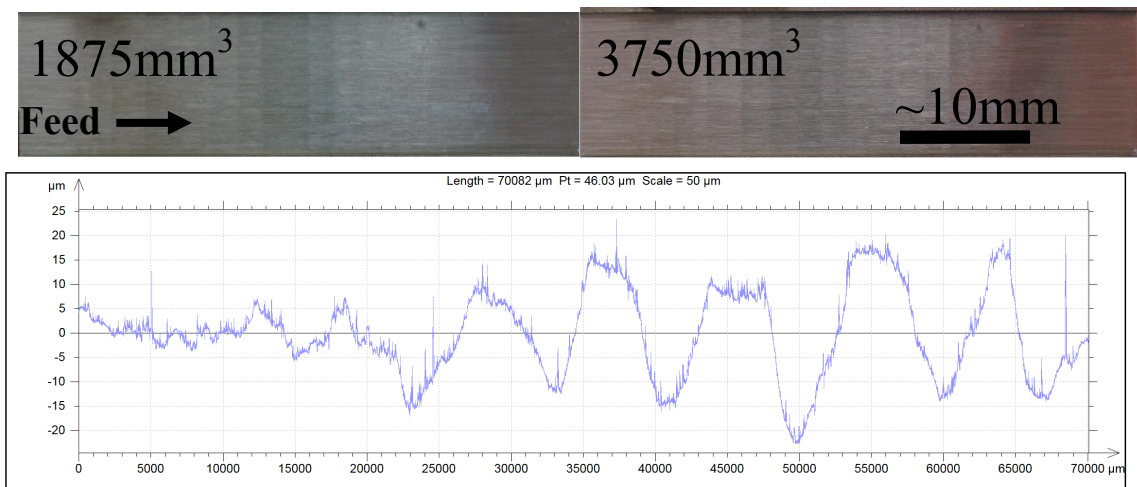


Figure 5.52: Workpiece surface images and talysurf plot

6. CONCLUSIONS

This chapter should be read with reference to the research objectives detailed in section 1.2: Aims and objectives of the project.

- 1. Perform a literature review to determine the current status of information on the machinability of advanced titanium alloys such as gamma titanium aluminide intermetallic, burn resistant and orthorhombic titanium alloys.**

Some ~50 references were found detailing the machinability of γ -TiAl alloys which covered a ~20 year period. Key processes identified were grinding and high speed milling for the production of compressor and turbine blades however literature was also found concerning other operations such as turning, drilling, EDM and ECM. In addition to the difficulties faced when machining conventional titanium alloys, γ -TiAl alloys suffer from low room temperature ductility (<2%) and low fracture toughness ($\sim 20\text{MPa}\cdot\text{m}^{1/2}$). Consequently producing workpiece surfaces with the desired integrity has proved problematic. In contrast only limited sources were found concerning the machinability of burn resistant titanium and orthorhombic titanium aluminide alloys.

- 2. Determine preferred tooling, operating parameters and conditions when high speed ball nose end milling Ti-45Al-8Nb-0.2C for assessment criteria tool life: workpiece surface roughness and workpiece surface integrity.**

This objective was completed. Accepting that a factorial design (with the factors and levels selected necessitating a minimum of 1024 experiments without replication) would have provided a high level of confidence/reduced error in identifying preferred parameters, the Taguchi approach (or similar) was the only feasible option. Faced with the high cost of experimental testing and minimal workpiece material only 16 tests (1.56% of the number required for a factorial design) were performed.

Tool life for Ti-45Al-8Nb-0.2C was generally excellent with a distance machined, in excess of 200m, even at a cutting speed of 160m/min. However, when using high levels of operating parameters including typically, a feed rate of 0.12 to 0.15mm/tooth and axial and radial depth of cuts of 0.5 to 1mm, tool life, in some cases, was extremely short (<10m). This suggests that care should be taken when selecting operating parameters to maximise tool life. Despite the large differences in tool life, none of the factors investigated in Phase 1A within the ranges tested were found to be statistically significant at the 5% level. Only when a smaller factorial experiment in Phase 1B was performed was cutting speed (160, 250 and 340m/min) found to be statistically significant at the 5% level. For workpiece surface

roughness, Ra in a direction perpendicular to the feed, radial depth of cut (0.125 to 1mm) was the only factor found to be statistically significant at the 5% level for Phase 1A whilst Phase 1B showed that cutting speed (160, 250 and 340m/min) was significant. All other factors were established as being non-significant. Surface damage on the high speed ball nose milled surface/subsurfaces was mainly in the form of fracture/pullout with deformation/bending of the lamellae up to a depth of $\sim 30\mu\text{m}$ from the machined workpiece surface.

3. Benchmark Ti-45Al-8Nb-0.2C against the previously investigated γ -TiAl alloy Ti-45Al-2Mn-2Nb +0.8%vol. TiB₂ when high speed ball nose end milling for assessment criteria: tool life, workpiece surface roughness and workpiece surface integrity.

In completion of this objective, benchmarking trials (Phase 1B) established alloy Ti-45Al-8Nb-0.2C as providing a $\sim 25\%$ increase in tool life based on a maximum flank wear criteria of $300\mu\text{m}$. Despite this difference, the workpiece material was found not statistically significant at the 5% level when compared to the cutting speed (160, 250 and 340m/min). On average Ti-45Al-2Mn-2Nb +0.8%vol. TiB₂ had a surface roughness Ra of $\sim 0.1\mu\text{m}$ higher than Ti-45Al-8Nb-0.2C with values $< 0.6\mu\text{m}$ Ra possible depending on the operating parameters used however as with tool life, the workpiece material was found not to be statistically significant at the 5% level. For both γ -TiAl alloys, fracture/pullout was observed on every milled surface that was assessed. The size of the fracture/pullout varied from a few microns to millimeters depending on test operating levels, with higher cutting speeds and tool flank wear levels causing increased damage. In general, marginally less fracture/pullout was observed for Ti-45Al-2Mn-2Nb +0.8%vol. TiB₂, as a consequence of the alloys smaller grain size. The results of Phase 1A and 1B which fulfilled Objectives 2 and 3 were compiled to produce Tables 6.1 and 6.2 which detail the fixed operating parameters and levels and preferred cutting tool, operating parameters and levels for high speed ball nose end milling Ti-45Al-8Nb-0.2C respectively. Output measures include the longest distance machined and machining time, largest volume of material removed, lowest workpiece surface roughness and ‘best’ workpiece surface integrity. Tool life was based on a maximum flank wear of $300\mu\text{m}$ therefore the majority of tests performed as part of Phase 1A which did not reach this criterion were discounted.

Operation	Down milling in a horizontal downwards direction
Workpiece orientation	45°
Tool overhang and runout	28mm and <10µm

Table 6.1: Fixed operating parameters and levels (γ -TiAl)

Output measure	Cutting speed	Cutting tool	Feed rate	Axial depth of cut	Radial depth of cut	Environment
	(m/min)		(mm/tooth)	(mm)	(mm)	
Longest distance machined	<160	IC903	0.06	0.25	0.25	Dry
Longest machining time	<160	IC903	0.09	0.25	0.25	Dry
Largest material removed	<160	IC903	0.12	1.0	0.5	HP ¹
Lowest workpiece surface roughness Ra	<160	IC900	0.09	0.25	0.125	Dry
‘Best’ workpiece surface integrity	<160	IC903	0.06	0.25	0.25	Dry

Table 6.2: List of preferred operating parameters for each output measure (γ -TiAl)

¹70bar - 25l/min through twin nozzles

4. Benchmark Ti-45Al-8Nb-0.2C against BuRTi when high speed ball nose end milling for assessment criteria: tool life, workpiece surface roughness and workpiece surface integrity.

This objective was successfully completed with the results obtained in Phases 1A and 1B for Ti-45Al-8Nb-0.2C benchmarked against BuRTi results in Phase 1C. Tables 6.3 and 6.4 detail the preferred cutting tool, operating parameters and levels for the output measures longest distance machined and machining time, largest volume of material removed, lowest workpiece surface roughness and ‘best’ workpiece surface integrity for BuRTi. Tool life using the same life criteria and almost identical operating parameters was 10 times longer for Ti-45Al-8Nb-0.2C than BuRTi. This significant improvement in tool life for the γ -TiAl workpiece material contrasts sharply with previous turning research which suggested that BuRTi was the easier of the two alloys to machine [6]. The 30% higher tensile strength, increased room temperature ductility and the presence of carbide particles for the BuRTi alloy would have been expected to cause the reduction in tool life.

When machining BuRTi, surface roughness Ra was poor with an average value of ~2µm due to the presence of smeared/adhered material. In contrast the surface roughness of

Ti-45Al-8Nb-0.2C showed a lower average value of $\sim 1.5\mu\text{m}$ Ra despite using more arduous operating parameters. Workpiece surface/subsurface damage was experienced in all BuRTi tests. This included carbide pullout or fracture, smeared material and micro cracks, the severity of which depended on the levels of operating parameters used with higher levels, in general yielding more damage.

Cutting speed	100m/min
Operation	Down milling in a horizontal downwards direction
Tool overhang and runout	28mm and $<10\mu\text{m}$

Table 6.3: Fixed operating parameters and levels (BuRTi)

Output measure	Cutting tool	Feed rate	Axial depth of cut	Radial depth of cut	Environment	Orientation
		(mm/tooth)	(mm)	(mm)		(°)
Longest distance machined	IC903	0.06	0.25	0.25	HP ¹	45
Longest machining time	IC903	0.06	0.25	0.25	HP ¹	45
Largest material removed	IC903	0.06	0.5	0.25	HP ¹	45
Lowest workpiece surface roughness Ra	IC903	0.06	0.25	0.25	Dry	45
‘Best’ workpiece surface integrity	IC903	0.06	0.25	0.25	HP ¹	45

Table 6.4: List of preferred operating parameters for each output measure (BuRTi)

¹70bar - 25l/min through twin nozzles

5. Determine the preferred grinding wheel specification, operating parameters and conditions when creep feed grinding Ti-45Al-8Nb-0.2C using conventional abrasive (SiC) grinding wheels for assessment criteria: wheel life, workpiece surface roughness and workpiece surface integrity.

This objective was completed as part of Phase 2A and sub phases 2Ai, 2Aii, 2Aiii and 2Aiv. A maximum G-ratio of ~ 30 was achieved using Wheel A (SiC abrasive) at a low wheel speed of 15m/s, a depth of cut of 1.25mm and a feed rate of 150mm/min. Operating under the conditions produced a workpiece surface roughness Ra value of $1.1\mu\text{m}$. Increasing the wheel speed to 25 and 35m/s reduced the surface roughness Ra level, but at the expense of surface burn was found. Assessment of surfaces produced using SiC abrasives at lower operating parameter levels showed that damage consisted of intermittent deformation/bending of the

lamellae to a depth of $\sim 4\mu\text{m}$ on parallel sections and $\sim 2\mu\text{m}$ on perpendicular sections with no visible cracking or fracture/pullout. At higher operating levels, increased bending of the lamellae up to $\sim 20\mu\text{m}$ from the surface was observed which covered up to 60% of the machined surface. Phase 2Ai Test 9 produced the most intensive workpiece surface burn, with a thermally damaged layer (HAZ) of up to $\sim 800\mu\text{m}$ from the ground surface.

The low levels of fracture/pullout observed compared favourably with surfaces produced using high speed ball nose end milling as a result of the lower stress operating conditions and the lower chip thickness associated with abrasive processes. Tables 6.5 and 6.6 detail the preferred grinding wheel specification, operating parameters and levels for creep feed grinding Ti-45Al-8Nb-0.2C using conventional abrasive wheels. Factors and levels are given for the highest G-ratio, lowest workpiece surface roughness and ‘best’ workpiece surface integrity.

Operation	Wheel direction	Down
	Sparkout	Yes
Dressing	Dressing method	Intermittent
	Dresser type	Hydraulic diamond roller dresser
	Dresser speed	+0.8
	Dresser feed rate	$2\mu\text{m/rev}$
	Infeed rate	Conventional abrasive: $500\mu\text{m}$ Superabrasive: $5\mu\text{m}$
Fluid	Workpiece/contact zone cooling	Type: Free jet nozzle (2x20mm), pressure: 7bar, flowrate: 90 l/min
	Wheel cleaning	Type: Free jet nozzle (0.5x20mm), pressure: 63bar (SiC), 40bar (superabrasive), flowrate: 35 l/min

Table 6.5: Fixed operating parameters and levels (γ -TiAl and BuRTi)

	Wheel specification	Wheel speed	Depth of cut	Feed rate	Fluid type
		(m/s)	(mm)	(mm/min)	
Highest G-ratio	Wheel A	15	γ -TiAl: 1.25 BuRTi: 5	γ -TiAl: 150 BuRTi: 600	Water
Lowest workpiece surface roughness R_a	Wheel A	15	1.25	150	Water
‘Best’ workpiece surface integrity	Wheel A	15	1.25	150	Water

Table 6.6: List of preferred operating parameters for each output measure (γ -TiAl and BuRTi, SiC wheels)

No improvement in G-ratio or a reduction in workpiece surface roughness Ra was obtained using a softer or a more open wheel and as a consequence workpiece surface integrity evaluation was not completed on surfaces produced using those wheels. The production of a complex demonstrator blade root showed that it was possible to utilise the research findings using plane profile wheels. Whilst no details of the geometrical accuracy of the demonstrator component was obtained, the surface roughness Ra levels and surface/subsurface assessment were consistent with Phases 2Ai, 2Aii & 2Aiii results.

6. Determine the preferred grinding wheel specification operating parameters and conditions when creep feed grinding Ti-45Al-8Nb-0.2C using superabrasive grinding wheels for assessment criteria: wheel life, workpiece surface roughness and workpiece surface integrity.

This objective was only partially completed as part of Phase 2B. G-ratios using superabrasive grinding wheels were ~10 times higher than for SiC abrasive wheels when using similar operating parameter levels as consequence of the increased grit hardness and thermal conductivity (2000W/m.K for diamond and ~1300W/m.K for CBN when compared with SiC grit material ~40W/m.K). These properties allowed surfaces to be produced that were free of surface burn and cracking even at wheel speeds of up to 50m/s. In comparison to results using SiC abrasives, surface roughness, when using comparable operating parameters and conditions was 25% lower for Wheel D (diamond grit) and 70% lower for Wheel E (CBN grit). The smaller grit size and lower levels of porosity of the superabrasive wheels are expected to have had an influence on this. Due to time and workpiece material restrictions the full benefits of being able to operate at higher wheel speeds such as increased material removal rates and lower workpiece surface roughness. Tables 6.5 and 6.7 detail the preferred grinding wheel specification, operating parameters and levels for creep feed grinding Ti-45Al-8Nb-0.2C using superabrasive wheels. Factors and levels are given for the highest G-ratio, lowest workpiece surface roughness and ‘best’ workpiece surface integrity.

	Wheel specification	Wheel speed	Depth of cut	Feed rate	Fluid type
		(m/s)	(mm)	(mm/min)	
Highest G-ratio	Wheel F	35	1.25	150	Oil
Lowest workpiece surface roughness Ra	Wheel F	50	γ -TiAl: 1.25 BuRTi: 2.5	γ -TiAl: 600 BuRTi: 150	γ -TiAl: Oil BuRTi: Water
‘Best’ workpiece surface integrity	Wheel D	35	1.25	150	Water

Table: 6.7: List of preferred operating parameters for each output measure (γ -TiAl and BuRTi, superabrasive wheels)

7. Benchmark Ti-45Al-8Nb-0.2C against burn resistant titanium alloy (BuRTi) when creep feed grinding for assessment criteria: wheel life, workpiece surface roughness and workpiece surface integrity.

This objective was completed as part of Phases 2Ai and 2Bii. The γ -TiAl alloy Ti-45Al-8Nb-0.2C was easier to grind than the BuRTi alloy with on average, for Wheel A (SiC abrasive) a 10 fold increase in G-ratio, 10% lower maximum power, 25% lower maximum specific energy, 28% lower tangential force and 15% lower average workpiece surface roughness Ra. Similar results were also obtained for superabrasive wheels which produced a 4 fold increase in G-ratio, 4.5% lower maximum power, 14% lower maximum specific energy, 8% lower normal force, 36% lower tangential force and 40% lower average workpiece surface roughness Ra. Key contributory factors in this are the 30% higher tensile strength, the increased room temperature ductility and the presence of carbide particles for the BuRTi alloy. Surface integrity assessment of BuRTi surfaces established a high level of surface smearing, adhered material and possible pullout as a consequence of the higher ductility of the alloy. Often the surface showed cracks both parallel and perpendicular to the feed direction which were probably as a result of the high grinding temperatures caused by the high level of wear flat generation and low workpiece thermal conductivity (10Wm/K). Microhardness depth profiles for BuRTi showed slight workpiece softening close to the machined face at a depth of 5-15 μ m. Tables 6.5, 6.6 and 6.7 detail the preferred operating parameters and levels for creep feed grinding Ti-45Al-8Nb-0.2C using superabrasive wheels. Factors and levels are given for the highest G-ratio, lowest workpiece surface roughness and ‘best’ workpiece surface integrity.

8. Benchmark Ti-45Al-8Nb-0.2C against the conventional titanium alloy Ti-6Al-4V when creep feed grinding for assessment criteria: wheel life.

This objective was completed within work package Phase 2C. The G-ratio measured for Ti-45Al-8Nb-0.2C was ~9 times higher when using conventional abrasives and ~71 times higher when using superabrasives than those measured when grinding Ti-6Al-4V. With the current experimental set-up it was not possible to diamond grind Ti-6Al-4V (technically and economically) due to the alloys high strength, low thermal conductivity ($\sim 7.2\text{W/m.K}$), high ductility ($>10\%$) and high chemical reactivity.

7. SUGGESTIONS FOR FUTURE WORK

- Selected high speed ball nose end milling and creep feed grinding tests should be performed on a γ -TiAl alloy Ti-45Al-8Nb-0.2C which is 'true to specimen' and includes a reduced grain size of $\sim 250\mu\text{m}$, so that the alloy can be benchmarked against the current work.
- Only limited test replications were performed, therefore, a number of tests should be completed using identical operating parameters to confirm tool life/wheel life and the effect of operating parameters on workpiece surface integrity.
- Phase 1, high speed ball nose end milling tests did not produce a surface that was free of defects including fracture/pullout. As a consequence, testing should be performed with a lower level of operating parameters, including cutting speed, feed rate and depth of cut (axial and radial), to determine if a lower stress milling regime will improve surface integrity.
- Phase 2, creep feed grinding experiments established a preferred conventional and superabrasive grinding wheel. Acceptable workpiece surface integrity was only achieved at lower operating parameter levels. Further investigation should focus on a wider variety of grinding wheel specifications, especially with superabrasive grit material, in order to determine if improved surface integrity can be achieved at higher material removal rates.
- Investigation should be performed into the effect of wheel dressing technique/parameters and fluid application methods including the use of different pressures, flowrates, etc to determine if improvements in wheel life and surface integrity can be achieved.
- High Efficiency Deep Grinding (HEDG) of γ -TiAl, BuRTi and standard titanium alloys such as Ti-6Al-4V should be investigated to establish if wheel life and workpiece surface integrity can be improved. This should involve the use of electroplated grinding wheels, rotating at a high speed ($\sim 200\text{m/s}$) with a high feed rate and depth of cut.
- Investigation of the temperature distribution within the workpiece during the grinding process by means of implanted split foil thermocouples and PVD coatings should be undertaken. The results should be related back to changes in the surface integrity of the workpiece.

- At the outset of the project, work was planned involving residual stress measurements with the new γ -TiAl alloy, Ti-45Al-8Nb-0.2C. In the event, this was not undertaken as the reliability of blind hole drilling and conventional x-ray diffraction methods present problems with γ -TiAl materials in the latter case due to significant line broadening [119]. Mantle and Aspinwall [106] performed residual stress measurements using the blind hole drilling technique. They suggest that some of the data appeared spurious and indicated surfaces containing compressive residual stresses at levels above the material ultimate tensile strength. The data presented was therefore only used for comparative purposes as this technique is generally not recommended for measuring residual stresses which exceed 50% of the yield stress. A special residual X-ray diffraction unit was developed to take into account of line broadening problems (EPSRC IMI project GR/K66970 and GR/L33993 (1.2.96 to 31.1.00)), however, during the period of the present investigation the machine was inoperable and subsequently decommissioned. It is understood that suitable X-ray diffraction equipment now exists at The University of Manchester and measurements should be made using this facility.
- Assessment of fatigue performance was not undertaken due to the limited supply of quality workpiece material with a suitable grain size. Attempts were undertaken to procure workpiece material with the composition Ti-45Al-2Mn-2Nb +0.8%vol. TiB₂ which had the preferred physical and mechanical properties, however this was not possible within the timeframe of this project. Testing should therefore be undertaken to determine fatigue performance after machining and likely in-service performance using preferred operating parameters, however this should only be performed on a γ -TiAl alloy with the required mechanical and physical properties.
- Grinding tests using a small diameter wheel/point with a surface of electroplated diamond should be undertaken on γ -TiAl. Tests should involve plain or ball end grinding points. A milling operation would leave ~10-50 μ m of workpiece to be removed by this operation.
- Ultrasonic assisted machining (point grinding and milling) should be considered. This is the kinematic overlapping of rotation with added oscillation in the axial direction of a tool. It is suggested that this processes results in a 3 fold productivity increase for hard machining of advanced materials [185] with reduced forces and improved workpiece surface integrity. No literature concerning ultrasonic assisted milling or grinding of γ -

TiAl material could be found however work has investigated ultrasonic assisted turning and ultrasonic drilling of Ti-45Al-2Mn-2Nb +0.8vol. TiB₂ [140, 143] with reported benefits in terms of significantly reduced cutting forces and improved workpiece integrity.

8. REFERENCES

- [1] D. Rugg, (2003). The Current Status of Titanium Alloy Use in Aero-Engines, Proceedings of the 10th World Conference on Titanium (Ti-2003). Hamburg, Germany, Vol. IV, pp. 2727-2735, ISBN: 3-257-30306-5.
- [2] W.E. Voice, M. Henderson, E.F.J. Shelton and X. Wu, (2005). Gamma Titanium Aluminide - TNB, Intermetallics, Vol. 13, pp. 959-964, ISSN: 0966-9795.
- [3] J. Eblinger and D. Helm, (2003). Titanium in Aero-Engines, Proceedings of the 10th World Conference on Titanium (Ti-2003). Hamburg, Germany, Vol. IV, pp. 2845-2850, ISBN: 3-257-30306-5.
- [4] W. Voice, (2003). Burn Resistant Titanium Alloy (BuRTi). Proceedings of the 10th World Conference on Titanium (Ti-2003). Hamburg, Germany, Vol. IV, pp. 2915-2922, ISBN: 3-257-30306-5.
- [5] Personal communication with Dr. A.L Mantle of Rolls-Royce Plc, February 2009.
- [6] D.K. Aspinwall, R.C. Dewes and A.L. Mantle, (2005). The Machining of γ -TiAl Intermetallic Alloys, Annals of CIRP, Vol. 54/1, pp. 99-104, ISSN: 007 8506.
- [7] R. Boyer, G. Welsch and E.W. Collings, (1994). Materials Properties Handbook: Titanium Alloys, ASM International, ISBN: 0-87170-481-1.
- [8] D. M. Dimiduk, (1999). Gamma titanium aluminide alloys - an assessment within the competition of aerospace structural materials, Materials Science and Engineering A, Vol. 263/2, pp, 281-288, ISSN: 0921-5093.
- [9] Baucio, (1993). ASM Metals reference book, 3rd Edition, ASM International, 614, ISBN 0-87170-478-1.
- [10] J.C. Williams, (1995). Titanium alloys: production behavior and application, High Performance Materials in Aerospace eds. H.M. Flower, Chapman and Hall Publishers, pp, 85-134, ISBN: 0412533502.
- [11] R.E. Schafrik, (2001). A perspective on intermetallic commercialization for aero-turbine applications, 3rd International Symposium on Structural Intermetallics (ISSI-3). The MS, Jackson Hole, Wyoming, USA, The Minerals, Metals & Materials Society's, TMS.
- [12] P.A. Bartolotta and D.L. Krause, (1999). Titanium Aluminide Applications in the High Speed Civil Transport, NASA/TM-1999-209071, International Symposium on Gamma Titanium Aluminides Sponsored by The Minerals and Materials Society, San Diego, California, February 28th to March 4th, 1999.
- [13] M. Yamaguchi, (1992). High temperature intermetallics – with particular emphasis on TiAl, Materials Science and Technology, Vol. 8, pp, 299-307, ISSN: 0921-5093.
- [14] F. Appel, U. Brossmann, U. Christoph, S. Eggert, P. Janschek, U. Lorenz, J. Mullauer, M. Oehring and J. Paul, (2000). Recent Progress in the Development of Gamma Titanium Aluminide Alloys, Advanced Engineering Materials, Vol. 2, Number: 2, pp, 699-720, ISSN: 1527-2648.
- [15] P.A. McQuay, (2001). Cast gamma TiAl alloys: are we there yet? 3rd International Symposium on Structural Intermetallics (ISSI-3). The MS, Jackson Hole, Wyoming, USA, The Minerals, Metals & Materials Society's, TMS. pp, 83–90.
- [16] Guy Norris, (2006). Flight International Magazine, Issue dated: 13/06/06.
- [17] C. McCullough, J.J. Valencia, C.G. Levi and R. Mehrabian, (1989). Phase equilibria and solidification in Ti-Al alloys. Acta Materialia, Vol. 37, pp, 1321-1336, ISSN: 1359-6454.
- [18] E.A. Loria, (2001). Quo Vadis gamma titanium aluminide, Intermetallics, Vol. 9/12, pp, 997-1001, ISSN: 0966-9795.

- [19] Y.W. Kim and D.M. Dimiduk, (1991). Progress in the Understanding of Gamma Titanium Aluminides, pp, 40-47, ISSN 1833-122X.
- [20] K.S. Chan and Y.W. Kim, (1995). Effects of lamellae spacing and colony size on the fracture resistance of fully lamellar TiAl alloy, *Acta Metallurgica Materiala*, Vol. 43, Number: 2, pp, 439-451, ISSN: 1359-6454.
- [21] A. Partridge and M.R. Winstone, (1997). γ -TiAl alloys: Current status and future potential, *Proceedings of the 4th International Charles Parsons Turbine Conference: Advanced in Turbine Materials, Design and Manufacture*, 4-6 November, Newcastle, UK, pp, 358-377, ISBN: 1861250533.
- [22] K.S. Kumar, J.A.S. Green, D.E. Larsen and L.D. Kamar, (1995). XD titanium aluminide composites, *Advanced Materials and Processes*, Vol. 4, pp, 35-38.
- [23] K.S. Chan and Y-W Kim, (1992). Influence of microstructure on crack tip micromechanics and fracture behaviours of two phase TiAl Alloy, *Metallurgical and Material Transactions A*, Vol. 23, pp, 1663-1677, ISSN: 1543-1940.
- [24] M.H. Loretto, P.A. Blenkinsop, W. Voice, D. Rugg and N.A. Walker, (2000). The development of burn-resistant titanium for aeroengine applications, *Proceedings of the Rolls-Royce Conference on Advanced Engine Technology*, Tiejieng, China.
- [25] Y.G.Li and P.A. Blenkinsop, (2000). A beta titanium alloy, European Patent Number: EP1002882 (A1).
- [26] Y.G.Li, P.A. Blenkinsop, M.H. Loretto and N.A. Walker, (1999). Effect of aluminium on deformation structure of highly stabilised β -Ti-V-Cr alloys, *Materials Science and Technology*, Vol. 15, pp. 151-155, ISSN: 0267-0836.
- [27] Y.G. Li, P.A. Blenkinsop, M.H. Loretto, D.Rugg and W.Voice, (1999). Effect of Carbon and Oxygen on Microstructure and Mechanical Properties of Ti-25V-15Cr-2Al (wt%) Alloys, *Acta Materialia*, Vol. 47/10, pp. 2889-2905, ISSN: 1359-6454.
- [28] E.M. Trent and P.K. Wright, (1991). *Metal Cutting*, 4th Edition, Butterworth-Heinemann, ISBN: 0-7506-7069-X.
- [29] S. Kalpakjian and S. R. Schmid, (2002). *Manufacturing Processes for Engineering Materials*, 4th Edition, Pearson Education, ISBN: 0130453730.
- [30] M.C. Shaw, (1997). *Metal Cutting Principles*, Oxford Science Publications, ISBN: 0-7506-1068-9.
- [31] Sandvik Coromant, (1994). *Modern Metal Cutting – A Practical Handbook*, AB Sandvik Coromant, ISBN: 91-97 22 99-0-3.
- [32] B.Mills and A.H. Redford, (1983), *Machinability of Engineering Materials*, Applied Science Publishers Ltd, ISBN: 0-85334-183-4.
- [33] E.J.A. Armarego and R.H. Brown, (1969), *The Machining of Metals*, Prentice-Hall, Inc, Library of Congress Catalog Number: 69-10532
- [34] P.Lee and Y. Altintas, (1995), Prediction of Ball-End Milling Forces From Orthogonal Cutting Data, *International Journal of Machine Tools and Manufacture*, Volume: 36, No. 8, pp. 1059-1072, ISSN: 0890-6955.
- [35] N. Liu and M. Loftus, (2006), Prediction of Surface Quality From Ball-Nose Milling in High-Speed Machining Applications, *Proceedings of the IMechE*, Vol. 220, Part: B, *Journal of Engineering Manufacture*, IMechE, pp. 571-578, ISSN: 0954-4054.
- [36] K.D. Bouzakis, P. Aichouh and K. Efstathiou, (2003), Determination of the Chip Geometry, Cutting Force and Roughness in Free Form Surfaces Finishing Milling, With Ball End Tools, *International Journal of Machine Tools and Manufacture*, Vol. 43, pp. 499-514, ISSN: 0890-6955.
- [37] O.E.E.K. Omar, T.El-Wardany, E. Ng and M.A. Elbestawi, (2007), An Improved Cutting Force and Surface Topography Prediction in End Milling, *International*

- Journal of Machine Tools and Manufacture, Vol. 47, pp. 1263-1275, ISSN: 0890-6955.
- [38] M. Fontaine, A. Moufki, A. Devillez and D. Dudzinski, (2007), Modeling of Cutting Forces in Ball-End Milling With Tool-Surface Inclination Part I: Predictive Force Model and Experimental Validation, Journal of Materials Processing Technology, Vol. 189, pp. 73-84, ISSN: 0924-0136.
 - [39] M. Shaw, (1996). Principles of Abrasive Processing, Oxford University Press, ISBN: 0 19 859021 0.
 - [40] C. Andrew, T.D. Howes and T.R.A. Pearce, (1985). Creep Feed Grinding, Holt, Rinehart and Winston Ltd, ISBN: 0-8311-1167-4.
 - [41] J. R. Besse, (1987). Practical Creep Feed Grinding, SME Technical Paper, MR87-820.
 - [42] S. Malkin, (1989). Grinding Technology: Theory and Application of Machining with Abrasives, Society of Manufacturing Engineers, ISBN 0-85312-756-5.
 - [43] T. Jin and D.J. Stephenson, (2006). Heat Flux Distributions and Convective Heat Transfer in Deep Grinding, International Journal of Machine Tools and Manufacture, Vol. 46, pp. 1862-1868, ISSN: 0890-6955.
 - [44] H.J. Hwang, C.J. Evans, E.P. Whifton and S.Malkin, (2000). High Speed Grinding of Silicon Nitride with Electroplated Diamond Wheels, Part 1: Wear and Wheel Life, Journal of Engineering for Industry - Transactions of the ASME, Vol. 122, pp. 32-41, ISSN: 0022-1481.
 - [45] R. Holz and J. Sauren, (1998). Grinding with Diamond and CBN, Ernst Winter and Sohn .
 - [46] BS 5623: 1979/ISO 3685: (1977). Tool-Life Testing with Single Point Turning Tools.
 - [47] T.H.C Childs, K. Maekawa, T. Obikawa and Y. Yamane, (2000). Metal Machining Theory and Applications, Arnold, ISBN: 0 340 69159X
 - [48] D. A. Stephenson and J.S. Agapiou, (1996). Metal Cutting Theory and Practice, Marcel Dekker Inc, 0824795792.
 - [49] H. El-Hofy, (2007). Machining Processes Conventional and Nonconventional Processes, ISBN: 0-8493-7288-7.
 - [50] H.R. Krain, A.R.C. Sharman and K. Ridgway, (2007). Optimisation of Tool Life and Productivity when End Milling Inconel 718™, Journal of Materials Processing Technology, Vol. 189, pp. 153-161, ISSN: 0924-0136.
 - [51] A. Sharman, R.C.Dewes, D.K.Aspinwall, (2001). Tool Life when High Speed Ball Nose End Milling Inconel 718™, Journal of Materials Processing Technology, Vol. 118, pp. 29-35, ISSN: 0924-0136.
 - [52] Z.A. Zoya and R. Krishnamurthy, (2000). The performance of CBN tools in the machining of titanium alloys, Journal of Materials Processing Technology, Vol. 100, pp. 80-86, ISSN: 0924-0136.
 - [53] P.J. Arrazola, A. Garay, L. M Iriarte, M. Armendia, S. Marya and F. Le Maitre, (2008). Machinability of titanium alloys (Ti-6Al-4V and Ti555.3). Journal of Materials Processing Technology, Vol. 205/5, pp. 2223-2230, ISSN: 0924-0136.
 - [54] ISO Organization, (1989). Tool life testing in milling-Part 2: End milling, International Standard ISO8688-2.
 - [55] J. Paulo Davim, (2008). Machining Fundamentals and Recent Advances, Springer, ISBN: 978-1-84800-212-8.
 - [56] E.G.Ng, D.W.Lee, R.C.Dewes, D.K.Aspinwall, (2000). The Effect of Cutting Environments When High Speed Ball Nose End Milling Inconel 718, Intermetallics and Superalloys Euromat, Vol. 10, Wiley-VCH, pp. 71-76, ISBN 3-527-30192-5.

- [57] K.A. Venugopal, S. Paul and A.B. Chattopadhyay, (2007). Growth of Tool Wear in Turning Ti-6Al-4V Alloy Under Cryogenic Cooling, *Wear*, Vol. 262, pp. 1071-1078, ISSN: 0043-1648.
- [58] Z. Shi and S. Malkin, (2006). Wear of Electroplated CBN Grinding Wheels, *Journal of Engineering for Industry- Transactions of the ASME*, Vol. 128, pp. 110-118, ISSN: 0022-1481.
- [59] S. Ebbrell, N.H. Woolley, Y.D. Tridimas, D.R. Allanson and W.B. Rowe, (2000). The Effects of Cutting Fluid Application Methods on the Grinding Process, *International Journal of Machine Tools and Manufacture*, Vol. 40, pp. 209-223, ISSN: 0890-6955.
- [60] T.W. Liao, K. Li and S.B. McSpadden Jr., (2000). Wear Mechanisms of Diamond Abrasives During Transition and Steady Stages in Creep-Feed Grinding of Structural Ceramics, *Wear*, Vol. 242, pp. 28-37, ISSN: 0043-1648.
- [61] J. A. Webster, (2007). Improving surface integrity and economics of grinding by optimum coolant application, with consideration of abrasive tool and process regime. *Proceedings of the Institution of Mechanical Engineers, Part B: Journal of Engineering Manufacture*, pp. 1665-1675, 0954-4054.
- [62] R.A. Irani, R.J. Bauer and A. Warkentin, (2005). A Review of Cutting Fluid Application in the Grinding Process, *International Journal of Machine Tools and Manufacture*, Vol. 45, pp. 1696-1705, ISSN: 0890-6955.
- [63] J. Steffen, A. Warkentin, R.J. Bauer and C. Becze, (2005). Effect of Jet Coherency on Workpiece Burn for Non-continuous dress creep feed grinding of Inconel 718, *Journal of Advanced Manufacturing Systems*, Vol. 4/2, pp. 117-130, ISSN: 1793-6896.
- [64] S.B. Wang and H.S. Kou, (1997). Cooling Effectiveness of Cutting Fluid in Creep Feed Grinding, *International Communications in Heat Mass Transfer*, Vol. 24/6, pp. 771-783, ISSN: 0735-1933.
- [65] E. Minke, (1999). Contribution to the Role of Coolants on Grinding Process and Work Results, *SME Technical Paper*, MR99-227.
- [66] N.E.Ye and T.R.A. Pearce, (1983). Some Observations on Profile Wear in Creep-Feed Grinding, *Wear*, Vol. 92, pp. 51-66, ISSN: 0043-1648.
- [67] A.K. Chattopadhyay and H.E. Hintermann, (1994). On Performance of Brazed Single-Layer CBN Wheel, *Annals of the CIRP*, Vol. 43/1, pp. 313-317, ISSN: 1726-0604.
- [68] S. Shaji and V. Radhakrishnan, (2003). Analysis of Process Parameters in Surface Grinding with Graphite as Lubricant Based on the Taguchi Method, *Journal of Materials Processing Technology*, Vol. 141, pp. 51-59, ISSN: 0924-0136.
- [69] V.K. Gviniashvili, N.H. Woolley and W.B. Rowe, (2004). Useful Coolant Flowrate in Grinding, *International Journal of Machine Tools and Manufacture*, Vol. 44, pp. 629-636, ISSN: 0890-6955.
- [70] M.N. Morgan, A.R.Jackson, H.Wu, V. Baines-Jones, A. Batako and W.B. Rowe, (2008). Optimisation of fluid application in grinding, *Annals of the CIRP*, Vol. 57/1, pp. 363-366, ISSN: 0007-8506.
- [71] S.C. Salmon, (1992). *Modern Grinding Process Technology*, McGraw Hill, 0070545006.
- [72] E. Brinksmeier, C. Heinzl and M. Wittmann, (1999). Friction, Cooling and Lubrication in Grinding, *Annals of the CIRP*, Vol. 48/2, pp. 581-598, ISSN: 007-8506.
- [73] J.A. Webster, (2005). Current Global Research Projects in Fixed Abrasive Grinding, *Cool-Grind Technologies*.
- [74] S. Ninomiya, M. Iwai, T. Uematsu, K. Suzuki and R. Mukai, (2003). Effect of the Floating Nozzle in Grinding of Mild Steels with Vitrified CBN Wheel, *Proceedings of*

- the 6th International Symposium on Advances in Abrasive Technology (ISAAT). Bristol, England.
- [75] K. Ramesh, S.H. Yeo, Z.W. Zhong and K.C. Sim, (2001). Coolant Shoe Development of High Efficiency Grinding, *Journal of Materials Processing Technology*, Vol. 114, pp. 240-245, ISSN: 0924-0136.
 - [76] J. Webster, E. Brinksmeier, C. Heinzl, M. Wittmann and K. Thoens, (2002). Assessment of Grinding Fluid Effectiveness in Continuous-Dress Creep Feed Grinding, Vol. 51/1, pp. 235-240, ISSN: 1726-0604.
 - [77] J.A. Webster, C. Cui, R.B. Mindek Jr, (1995). Grinding Fluid Application System Design, *Annals of the CIRP*, Vol. 44/1, pp. 333-338, ISSN: 1726-0604.
 - [78] F. C. Gift Jr, W.Z. Misiolek and E. Force II, (2004). Fluid Performance Study for Groove Grinding a Nickel-Based Superalloy Using Electroplated Cubic Boron Nitride (CBN) Grinding Wheels, *Journal of Manufacturing Science and Engineering*, Vol. 126, pp. 451-458, ISSN: 1087-1357.
 - [79] C.P.R. Hill, J.R. Watkins, C. Ray and S. Ray, (1999). Method and apparatus for grinding, *European Patent Specification*, EP 0 924 028 B1.
 - [80] M. Hitchiner, (2007). Grinding in the Aerospace Industry, *Proceedings of the Precision Grinding and Abrasive Technology at SME International Grinding Conference (ISAAT2007)*. *Advanced in Abrasive Technology X*, pp. 491-497, ISBN: 087263853-7.
 - [81] R. Kovacevic and R. Mohan, (1995). Effect of high speed grinding fluid on surface grinding performance, *Technical Papers of the First International Machining and Grinding Conference*, Dearborn, Michigan, pp. 917-931.
 - [82] H.J. Xu, Y.C. Fu, F.H. Sun, (2001). Research on Enhancing Heat Transfer in Grinding Contact Zone with Radial Water Jet Impinging Cooling, *Key Engineering Materials*, Vol. 202-203, pp. 53-56, ISSN: 1013-9826.
 - [83] S. Ray and C. Ray, *Method and Apparatus for Grinding*, UK Patent, Application number: GB 2391 1188B.
 - [84] S. Okuyama, Y. Nakamura and S. Kawamura, (1993). Cooling action of grinding fluid in shallow grinding, *International Journal of Machine Tools and Manufacture*, Vol. 33/1, pp. 13-23, ISSN: 0890-6955.
 - [85] M. Yokogawa and K. Yokogawa, (1993). Improving Grinding Performance of CBN-Wheels by Dual-Fluid Supply Method, *International Journal of the Japan Society for Precision Engineering*, Vol. 27/1,
 - [86] R.A. Irani, R.J. Bauer and A. Warkentin, (2007). Development of a New Cutting Fluid Delivery System for Creepfeed Grinding, *International Journal of Manufacturing Technology and Management*, Vol. 12/1/2/3, pp. 60-71, ISSN: 1368-2148.
 - [87] M. Field and J.F. Kahles, (1971). Review of Surface Integrity of Machined Components, *Annals of the CIRP*, Vol. 20/2, pp. 153-163.
 - [88] M. Field, J.F. Kahles and J.T. Cammett, (1972). A Review of Measuring Methods for Surface Integrity, *Annals of the CIRP*, Vol. 21/2, pp. 219-238.
 - [89] J.F. Kahles and M. Field, (1971). Surface integrity guidelines for machining, Paper Number: IQ71-240, *Society of Manufacturing Engineers*.
 - [90] C.H. Che-Haron, (2001). Tool Life and Surface Integrity in Turning Titanium Alloy, *Journal of Materials Processing Technology*, Vol. 118, pp. 231-237, ISSN: 0924-0136.
 - [91] J. Hughes, A.R.C. Sharman and K. Ridgway, (2004). The Effect of Tool Edge Preparation on Tool Life and Workpiece Surface Integrity, *Proceedings of the Institution of Mechanical Engineers, Part B: Journal of Engineering Manufacture*, Vol. 218, pp. 1113-1123, ISSN: 0954-4054.

- [92] A. Ginting and M. Nouari, (2009). Surface Integrity of Dry Machined Titanium Alloys, *International Journal of Machine Tools and Manufacture*, Vol. 49, pp. 325-332, ISSN: 0890-6955.
- [93] C.H. Che-Haron and A. Jawaid, (2005). The Effect of Machining on Surface Integrity of Titanium Alloy Ti-6% Al-4%V, *Journal of Materials Processing Technology*, Vol. 166, pp. 188-192, ISSN: 0924-0136.
- [94] P.J. Withers, (2007). Residual stress and its role in failure, *Reports in Progress in Physics*, Vol. 70/12, pp. 2211-2264, ISSN 1361-6633.
- [95] Metcut Research Associates Inc, (1980). *Machining Data Handbook*, 3rd Edition, Vol. 2, Metcut Research Associates Inc, ISBN: 0-936974-02-8.
- [96] E. Aust and H-R. Niemann, (1999). Machining of γ -TiAl, *Advanced Engineering Materials*, Vol. 1/1, pp. 53-57, ISSN: 78-296.
- [97] E.O. Ezugwu and Z.M. Wang, (1997). Titanium Alloys and their Machinability – A Review, *Journal of Materials Processing Technology*, Vol. 68, pp. 262-274, ISSN: 0924-0136.
- [98] M. Rahman, Z-G. Wang and Y-S. Wong, (2006). A Review on High-Speed Machining of Titanium Alloys, *JSME International Journal*, Series: C, Vol. 49, Number: 1, pp. 11-20, ISSN: 1347-538X.
- [99] H.J. Siekman, (1955). How to Machine Titanium, *Tool Engineer*, pp. 78-82.
- [100] A.L. Mantle and D.K. Aspinwall, (1998). Tool Life and Workpiece Surface Roughness When High Speed Machining a Gamma Titanium Aluminide, *Proceedings of the 4th International Conference on Progress of Cutting and Grinding (ICPCG '98)*. China, pp. 89-94, ISBN: 7-80003-429-1.
- [101] R.S. Harding, (1997). Machinability of Titanium Aluminide, (Conventional End Milling). Final Year Project Report, School of Manufacturing and Mechanical Engineering, University of Birmingham.
- [102] K. Wienert, S. Bergmann, C. Kempmann, (2006). Machining Sequence to Manufacture a γ -TiAl-Conrod for Application in Combustion Engines, *Advanced Engineering Materials*, Vol. 8/1-2, pp. 41-47, ISBN: 78-296.
- [103] S. Doody, (1998). The Application of Coolant when High Speed Milling Gamma Titanium Aluminides, Final Year Project Report, School of Manufacturing and Mechanical Engineering, University of Birmingham.
- [104] A.L. Mantle and D.K. Aspinwall, (2000). Cutting force evaluation when high speed end milling a gamma titanium aluminide intermetallic alloy. *Proceedings of the EUROMAT 99*, Vol. 10, pp. 209-215, ISBN: 3527 30575.
- [105] W.K. Chan, (1998). Temperature Analysis When High Speed Machining Gamma Titanium Aluminide, Undergraduate Final Year Report, School of Mechanical Engineering, University of Birmingham.
- [106] A.L. Mantle and D.K. Aspinwall, (1999). Surface integrity of a high speed milled gamma titanium aluminide. *Proceedings of the International Conference on Advanced in Materials and processing Technologies, AMPT '99 and 16th Annual Conference of the Irish Manufacturing Committee, IMC16*, Dublin, Ireland, pp. 447-456.
- [107] A.L. Mantle and D.K. Aspinwall, (2001). Surface Integrity of a High Speed Milled Gamma Titanium Aluminide, *Journal of Materials Processing Technology*, Vol. 118, pp. 143-150, ISSN: 0924-0136.
- [108] S.A. Bentley, (2000). Surface and creep feed grinding of gamma titanium aluminide, Doctoral Thesis, School of Manufacturing and Mechanical Engineering, The University of Birmingham.

- [109] S.A. Bentley, A.L. Mantle and D.K. Aspinwall, (1999). The Effect of Machining on the Fatigue Strength of a Gamma Titanium Aluminide Intermetallic Alloy, *Intermetallics*, Vol. 7, pp. 967-969, ISSN: 0966-9795.
- [110] R.G. Vargas Perez, (2005). Wear Mechanisms of WC Inserts in Face Milling of Gamma Titanium Aluminides, *Wear*, Vol. 259, pp. 124-131, ISSN: 0044-288.
- [111] C. Zeppenfeld, F. Klocke and H. Groning, (2004). Micro-Analysis of Material Adhesion on Diamond Grinding Grits, *Industrial Diamond Review*, Vol. 4, pp. 56-63, ISSN: 0019-89.
- [112] S.A. Bentley and D.K. Aspinwall, (1997). A Comparison of the Grinding of IMI318 Titanium Alloy and a Gamma Titanium Aluminide Intermetallic, *Proceedings of the 32nd International MATADOR Conference*, UMIST, Manchester, pp. 331-336, ISBN: 1-333-7295-8.
- [113] T.C. Nolan, (1991). Wet Surface Grinding NiAl 809, 817, TiAl, GE Industrial Internal Correspondence, Library number: 91112, Evaluation Bulletin number: AD-9144.
- [114] S.A. Bentley, N.P. Goh and D.K. Aspinwall, (2001). Reciprocating Surface Grinding of a Gamma Titanium Aluminide Intermetallic Alloy, *Journal of Materials Processing Technology*, Vol. 53, pp. 22-28, ISSN: 0924-0136.
- [115] S.A. Bentley, S.Z. Lim and D.K. Aspinwall, (2000). The Effect of Wheel Dressing Parameters on the Surface Integrity of Surface Ground Gamma Titanium Aluminide Intermetallic Alloy, *Intermetallics and Superalloys*, *Proceedings of the EUROMAT 99*, Vol. 10, pp. 216-221, ISBN: 3527 30575
- [116] W. Stone and T. Kurfess, (2007). Grinding Titanium Aluminide: Subsurface Damage, *International Journal of Manufacturing Technology and Management*, Vol. 12/1/2/3, pp. 60-71, ISSN: 1368-212.
- [117] H. Ali Razavi, T.R. Kurfess and S. Danyluk, (2003). Force Control Grinding of Gamma Titanium Aluminide, *International Journal of Machining Tools & Manufacture*, Vol. 44, pp. 50-56, ISSN: 0890-6955.
- [118] S.A. Bentley and D.K. Aspinwall, (1997). Identification of Significant Operating Factors when Conventional Abrasive Creep Feed Grinding of a Gamma Titanium Aluminide Intermetallic. *Proceedings of the 4th International Charles Parsons Turbine Conference*, 'Advances in Turbine Materials, Design and Manufacturing', Newcastle, pp. 474-488, ISBN: 511250533.
- [119] S.A. Bentley and D.K. Aspinwall, (2000). Creep Feed Grinding of γ -TiAl, *Proceedings of the 33rd MATADOR Conference*, Manchester, pp. 449-446, ISBN: 50233 3235.
- [120] C. Zeppenfeld and F. Klocke, (2006). Speed Stroke Grinding of γ -Titanium Aluminides, *Annals of the CIRP*, Vol. 55/1, pp. 333-338, ISSN: 366-0604.
- [121] F.Klocke, C. Zeppenfeld and Z. Nachmani, (2007). Advanced grinding of titanium aluminides, *International Journal of Manufacturing Technology and Management*, Vol. 12/1/2/3, pp. 200-224, ISSN: 1368-212.
- [122] H. Zhang, (1995). Investigation of machinability of titanium aluminide, School of Manufacturing and Mechanical Engineering, The University of Birmingham.
- [123] H. Zhang, M.L.H. Wise and D.K. Aspinwall, (1993). The Machining of TiAl Based Intermetallics, *Proceedings of the 30th International MATADOR Conference*, UMIST, Manchester, pp. 111-1118, ISBN: 502338806.
- [124] H. Zhang, M.L.H. Wise, D.K. Aspinwall and E.M. Aspinwall, (1994). Investigation of Machinability of HIP-ed Gamma Titanium Aluminide, *Proceedings of the Materials Issues in Machining II and the Physics of Machining Processes II*, Chicago, Illinois, USA, pp. 89-104, ISBN: 0-87339-242-6.

- [125] H. Zhang, M.L.H. Wise, D.K. Aspinwall, (1995). The Surface Quality of Hipped Gamma Titanium Aluminide Bar after Turning, Proceedings of the 31st MATADOR Conference, UMIST, Manchester, pp. 217-221.
- [126] A.L. Mantle and D.K. Aspinwall, (1996). Temperature Measurement and Tool Wear When Turning Gamma Titanium Aluminide Intermetallic, Proceedings of the 13th Conference of the Irish Manufacturing Committee (IMC-13). Re-Engineering for World Class Manufacturing, Limerick, Ireland, pp. 427-446, ISBN: 524653-38-0.
- [127] A.L. Mantle and D.K. Aspinwall, (1996). Tool Wear and Surface Integrity when Turning Gamma Titanium Aluminide Intermetallics, Proceedings of the 3rd International Conference on Progress of Cutting and Grinding, Vol. 3, Osaka, Japan, pp. 63-68.
- [128] A.L. Mantle, S.A. Bentley, and D.K. Aspinwall, (1998). A Comparison of tool Wear When Turning Ti-45Al-2Mn-2Nb +0.8 Vol% TiB₂ and Ti-44Al-8Nb-1B Titanium Aluminide Intermetallics, Proceedings of the International Conference on Behaviour of Materials in Machining: Opportunities and Prospects for Improved Operations, Stratford-upon-Avon, UK, pp. 300-308, ISBN: 1-86125-086-X.
- [129] A.L. Mantle, (1998). The machining of gamma titanium aluminide intermetallics School of Manufacturing and Mechanical Engineering, The University of Birmingham.
- [130] A.L. Mantle and D.K. Aspinwall, (1997). Surface Integrity and Fatigue Life of Turned Gamma Titanium Aluminide, Journal of Materials Processing Technology, Vol. 72, pp. 413-420, ISSN: 0924-0136.
- [131] A.L. Mantle and D.K. Aspinwall, (1997). Machining of Titanium Intermetallic, Proceedings of the 30th International Symposium on Automotive Technology and Automation, Materials for Energy Efficient Vehicles, Florence, Italy, pp. 619-626.
- [132] A.L. Mantle, D.K. Aspinwall, M.L.H. Wise, (1995). Single Point Turning of Gamma Titanium Aluminide Intermetallics. Proceedings of 8th World Titanium Conf. (Titanium '95) October, pp. 248-255, ISBN: 1-86125-005-3.
- [133] E.Uhlmann, G.Frommeyer, S.Herter, S.Knippscheer and J.M.Lischka, (2003). Studies on the Conventional Machining of TiAl-Based Alloys, Proceedings of the 10th World Conference on Titanium, Ti-2003, Hamburg, July 2003, pp. 2293-2300.
- [134] A.R.C. Sharman, D.K. Aspinwall, R.C. Dewes and P. Bowen, (2001). Workpiece surface integrity considerations when finish turning gamma titanium aluminide. Wear, Vol. 249, pp. 473-481, ISSN: 0044-288.
- [135] A.R.C. Sharman, (2001). An investigation into the effects of machining on the surface integrity and fatigue life of gamma based titanium aluminides, School of Manufacturing and Mechanical Engineering, The University of Birmingham.
- [136] A.C. Sharman, D.K. Aspinwall, R.C. Dewes and P. Bowen, (2000). Tool life when turning gamma titanium aluminide using carbide and PCD tools with reduced depths of cut and high pressure cutting fluid. Trans. Of the North American Manufacturing Research Institution of SME, Vol. 28, pp. 25-30, ISBN: 08726 3518X.
- [137] A.R.C. Sharman, D.K. Aspinwall, R.C. Dewes, D. Clifton and P. Bowen, (2001). The effects of machined workpiece surface integrity on the fatigue life of γ -titanium aluminide (short communication). International Journal of Machine Tools and Manufacture, Vol. 41, pp. 321-325, ISSN: 0890-6955.
- [138] P.E. Jones, D.Eylon, (1999). Effect of conventional machining on high cycle fatigue behavior of the intermetallic alloy Ti-47Al-2Nb-2Cr, Materials Science and Engineering, Issue: A263, pp. 296-304, ISSN: 0921-5093.

- [139] P.E. Jones, (1997). Effects of Conventional Machining on High Cycle Fatigue Behavior of the Intermetallic Alloy Ti-47Al-2Nb-2Cr (at%). School of Engineering, The University of Dayton.
- [140] A.R.C. Sharman, X.P. Li, M. Rahman, P. Bowen, R.C. Dewes and D.K. Aspinwall, (2001). Ultrasonic Assisted Turning of Gamma Titanium Aluminide, Proceedings of the 13th International Symposium for Electromachining (ISEM XIII). Bilbao, Spain, Vol. II, Bilbao, Spain, pp. 939-951, ISBN: 93206407.
- [141] I.J. Howitt, (2001). Turnmilling of Gamma Titanium Aluminide Using Small Diameter Ball Nose End Mills, Final Year Project Report, School of Manufacturing and Mechanical Engineering, University of Birmingham.
- [142] A.L. Mantle, D.K. Aspinwall and O. Wollenhofer, (1995). Twist Drilling of Gamma Titanium Aluminide Intermetallics, Proceedings of the 12th Conference of the Irish Manufacturing Committee, IMC-12, Cork, Ireland, pp. 229-236.
- [143] D.K. Aspinwall, Y. Kasuga and A.L. Mantle, (2001). The Use of Ultrasonic Machining for the Production of Holes in γ -TiAl, Proceedings of the 13th International Symposium for Electromachining (ISEM XIII). Bilbao, Spain, Vol. II, pp. 925-937, ISBN: 93206407.
- [144] A.L. Mantle, E. Abboud and D.K. Aspinwall, (1997). Productivity and Workpiece Surface Integrity Effects When Electrical Discharge Wire Machining a Gamma Titanium Aluminide, Proceedings of the 14th Conference of the Irish Manufacturing Committee, IMC-14, Dublin, Ireland, pp. 444-450, ISBN: 1-89760632.
- [145] E.C. Abboud, (1997). Electrical Discharge Wire Machining of Gamma Titanium Aluminide, Final Year Project Report, School of Manufacturing and Mechanical Engineering, University of Birmingham.
- [146] A.L. Mantle, D.K. Aspinwall and M.L.H. Wise, (1994). Electrical Discharge Wire Machining of Titanium Aluminide Inter-Metallic, Proceedings of the 3rd International Conference on the Behavior of Materials in Machining, Warwick, Institute of Materials, pp. 138-151.
- [147] S. Sarkar, S. Mitra and B. Bhattacharyya, (2005). Parametric Analysis and Optimization of Wire Electrical Discharge Machining of γ -Titanium Aluminide Alloy, Journal of Materials Processing Technology, Vol. 23, pp. 286-294, ISSN: 0924-0136.
- [148] D. Clifton, A.R. Mount, D.J. Jardine and R. Roth, (2001). Electrochemical Machining of Gamma Titanium Aluminide Intermetallics, Journal of Materials Processing Technology, Vol. 108, pp. 338-348, ISSN: 0924-0136.
- [149] M.C. Kong and D. Axinte, (2009). Response of Titanium Aluminide Alloy to Abrasive Waterjet Cutting, Proceedings of the IMechE, Vol. 223, Part: B, Journal of Engineering Manufacture, IMechE, pp. 20-42, ISSN: 0954-4054.
- [150] D. Novovic, D.K. Aspinwall, R.C. Dewes, W. Voice and P. Bowen, (2003). The surface Integrity of a Burn Resistant Titanium Alloy (Ti-25V-15Cr-2Al-0.2C wt%) after High Speed Milling and Creep Feed Grinding, Proceedings of the 10th World Conference. on Titanium, pp. 2817-2824, ISBN: 3-257303065.
- [151] D. Novovic, (2004). The Effect of Machined Workpiece Surface Integrity and Topography on Fatigue Life, Doctoral Thesis, The University of Birmingham.
- [152] J.M.T. Simao, DK Aspinwall, RC Dewes and WE Voice, (2004). High speed milling and surface grinding of an orthorhombic TiAl alloy Ti-23Al25Nb, 13-18 July 2003, Proceedings of the 10th World Conference on Titanium, Vol. IV, pp. 2185-2192, ISBN: 3527303065.
- [153] J.M.T. Simao, DK Aspinwall, RC Dewes and W Voice, (2002). Machinability assessment of an orthorhombic TiAl alloy Ti-23AL-25Nb for aerospace applications, Proceedings of the 5th International Conference on Behaviour of Materials in

- Machining, Chester, UK/2002, London, UK, IOM Communications, pp. 35-42, ISBN: 51125204.
- [154] P.J. Ross, (1988). Taguchi Techniques for Quality Engineering, 2nd Edition, McGraw-Hill, ISBN: 0-07-053958-8.
 - [155] J. Pignatiello and J.S. Ramberg, (1991-1992), Top Ten Triumphs and Tragedies of Genichi Taguchi, Quality Engineering, Vol. 4-2, pp. 211-225.
 - [156] G. Taguchi, S. Chowdhury and Y. Wu, (2005), Taguchi's Quality Engineering Handbook, J. Wiley and Sons, ISBN: 0-471-41334-8.
 - [157] H. Saage, A.J. Haung, D. Hu, M.H. Loretto and X. Wu, (2009). Microstructures and tensile properties of massively transformed and aged Ti-46Al8Nb and Ti-46Al8Ta Alloys, Intermetallics, Vol. 17, pp. 32-38, ISSN: 0966-9795
 - [158] Personal communication with Wayne Voice, Rolls-Royce Plc, Machinability of Gamma Titanium Aluminide Intermetallic/Machinability of Burn-Resistant Titanium Formal Project Meeting 10, Thursday 12th July 2007, University of Birmingham.
 - [159] Mike Jones, (2007). Solid Carbide Substrate Presentation, Iscar Tools UK Ltd.
 - [160] M. Sokovic J. Kopac, L.A. Dobrzanski and M. Adamiak, (2004). Wear of PVD-Coated Solid Carbide End Mills in Dry High-Speed Cutting, Journal of Materials Processing Technology, Vol. 157-158, pp. 422-426, ISSN: 0924-0136.
 - [161] H. Niemann, E.G. Ng, H. Loftus, A. Sharman, R. Dewes and D. Aspinwall, (2001). The Effect of Cutting Environment and Tool Coating When High Speed Ball Nose End Milling Titanium Alloy, 3rd International Conference on Metal Cutting and High Speed Machining, Metz, France, June 27-29, pp. 74-80.
 - [162] S. Ebbrell, N.H. Woolley, Y.D. Tridimas, D.R. Allanson and W.B. Rowe, (2000). The Effects of Cutting Fluid Application Methods on the Grinding Process, International Journal of Machine Tools and Manufacture, Vol. 40, pp. 209-223, ISSN: 0890-6955.
 - [163] D.K. Aspinwall, R.C. Dewes, A.L. Mantle and E.G. Ng, (1998). High Speed Milling of Advanced Aerospace Alloys and Hardened Mould/Die Steels, Sharing Tomorrow's Technology Today, ISBN: 09073480401.
 - [164] E.G. Ng, D.W. Lee, D.K. Aspinwall, R.C. Dewes, (2000). Analysis of Cutting Direction When High Speed Ball Nose End Milling a Nickel Based Superalloy, Intermetallics and Superalloys Euromat, Vol. 10, Wiley-VCH, pp. 64-70, ISBN 3-527-30192-5.
 - [165] A. Ginting and M. Nouari, (2007). Optimal cutting conditions when dry end milling the aeroengine material Ti-6242S, Journal of Materials Processing Technology, Vol. 184, pp. 319-324, ISSN: 0924-0136.
 - [166] A. Jawaid, S. Sharif and S. Koksai, (2000). Evaluation of Wear Mechanisms in Coated Carbide Tools When Face Milling Titanium Alloy, Journal of Materials Processing Technology, Vol. 99, pp. 266-274, ISSN: 0924-0136.
 - [167] L. Lopez de Lacalle, J. Perez, J. Llorente and J. Sanchez, (2000). Advanced cutting conditions for the milling of aeronautical alloys, Journal of Materials Processing Technology, Vol. 100, pp. 1-11, ISSN: 0924-0136.
 - [168] A. Antoniadis, N. Vidakis and N. Bilalis, (2002). Fatigue Fracture Investigation of Cemented Carbide Tools in Gear Hobbing, Transactions of the ASME, Part: 1, pp. 784-791.
 - [169] A. Warkentin, S. Bedi and F. Ismail, (1996). Five Axis Milling of Spherical Surfaces, International Journal of Machine Tools and Manufacture, Vol. 36/2, pp. 229-243, ISSN: 0890-6955.
 - [170] G.M. Zang, D.K. Anand, S. Ghosh, W.F. Ko, (1993). Study of the Formation of Macro and Micro Cracks During Machining of Ceramics, Proceedings of the International Conference on Machining of Advanced Materials, Maryland, USA, NIST special publication, pp. 465-478.

- [171] T. Matsumura, T. Hiramatsu and T. Shirakashi, (2005). A Study on Cutting Force in the Milling Process of Glass, *Journal of Manufacturing Processes*, Vol. 7/2, pp. 102-108, ISSN: 1526-6125.
- [172] S. PalDey and S.C. Deevi, (2003). Single Layer and Multilayer Wear Resistant Coatings of (Ti,Al)N: A Review, *Materials Science and Engineering*, Vol. A342, pp. 58-79, ISSN: 0921-5093.
- [173] H.T. Young, (1996). Cutting Temperature Responses to Flank Wear, *Wear*, Vol. 201, pp. 117-120, ISSN: 0043-1648.
- [174] R.C. Dewes, (1997). High-Speed Machining of Hardened Ferrous Alloys, Doctoral Thesis, The University of Birmingham.
- [175] Y. Su, N. he, L. Li and X.L. Li, (2006). An experimental investigation of effects of cooling/lubrication conditions on tool wear in high-speed end milling of Ti-6Al-4V, *Wear*, Vol. 261, pp. 760-766, ISSN: 0043-1648.
- [176] K.V. Kumar, (1990). Superabrasive Grinding of Titanium Alloys, SME Technical Paper, Code: MR90-505, pp. 1-17.
- [177] Y.I. Sunarto, (2001). Creep Feed Grinding of Ni-Based Superalloys with Ultrafine-Polycrystalline cBN Abrasive Grits, *Precision Engineering, Journal of the International Societies for Precision Engineering and Nanotechnology*, Vol. 25, pp. 274-283, ISSN: 0141-6359.
- [178] S. Malkin and C. Guo, (2007). Thermal Analysis of Grinding, *Annals of the CIRP*, *Annals of the CIRP*, Vol. 56/2, pp. 760-782, ISSN: 1726-0604.
- [179] Rolls-Royce plc, (Date unknown). Titanium (IMI 318) Temper Colours, Rolls-Royce Image Resource, Derby, Document number: D00.1230.5.
- [180] T. Kuriyagawa, K. Syoji and H. Ohshita, (2003). Grinding Temperature Within Contact Arc Between Wheel and Workpiece in High-Efficiency Grinding of Ultrahard Cutting Tool Materials, *Journal of Materials Processing Technology*, Vol. 136, pp. 39-47, ISSN: 0924-0136.
- [181] J.F.G Oliveira and S.M. Alves, (2006). Development of Environmentally Friendly Fluid for CBN Grinding, *Annals of the CIRP*, Vol. 55/1, pp. 343-346, ISSN: 007-8506.
- [182] R.D. Monici, E.C.Bianchi, R. Catai and P.R. de Aguiar, (2006). Analysis of the Different Forms of Application and Types of Cutting Fluid Used in Plunge Cylindrical Grinding Using Conventional and Superabrasive CBN grinding wheels, *International Journal of Machine Tools and Manufacture*, Vol. 46, pp. 122-131, ISSN: 0890-6955.
- [183] F.Klocke, A. Baus and T. Beck, (2000). Coolant Induced Forces in CBN Grinding with Shoe Nozzles, *Annals of the CIRP*, Vol. 49/1, pp. 241-244, ISSN: 007-8506.
- [184] S.F. Krar and E. Ratterman, (1990). Superabrasives- Grinding and Machining, McGraw Hill, ISBN: 0-07-035587-8.
- [185] DMG | DECKEL MAHO | GILDEMEISTER Website, <http://www.dmguk.com/en,advanced-technologies,ultrasonic>, accessed 18.6.2008

APPENDIX A: Workpiece surface integrity

Table A1 details the techniques used to detect inhomogeneity in metals.

Metallurgical inhomogeneity	Commonly employed	Specialized	Possible with further development	Destructive techniques
Macrocracks	Visual inspection, binocular inspection, magnetic particle, eddy current, acid macroetch	Ultrasonic, automatic optical scanning	Acoustic impact	Optical metallography
Microcracks	Binocular inspection High sensitively fluorescent penetrant Magnetic particle	Ultrasonic	Radioactive gas penetrant, high frequency ultrasonic acoustic impact, surface electrical resistance	Optical metallography, scanning or transmission electron microscopy
Tears, laps and pits	Visual with etch Magnetic particle Eddy current penetrant	Automatic optical scanning	Radioactive gas penetrant	Optical metallography, scanning electron microscopy
IGA and selected etch		High sensitivity florescent penetrant		Macroetch, scanning or transmission electron microscopy
Surface phase transformation	Macroetch	X-ray diffraction, magnetic particle	Ultrasonic velocity, surface electrical resistance, eddy current	Optical metallography
Compositions			Laser probe, mass spectrometry, X-ray spectroscopy	Wet chemical analysis, electron microprobe
Surface hardness changes	Superficial or ultrasonic hardness testing	Eddy current	Beta backscatter	Microhardness traverse
Redeposited and resolidified material	Macroetch Visual inspection			Optical metallography
Recrystallisation and grain growth		Ultrasonic	Radioactive gas penetrant	Optical metallography
Plastic deformation	Superficial hardness testing	Eddy current, magnetic particle	Beta backscatter, radioactive gas penetrant, ultrasonic velocity	Optical metallography, microhardness traverse
Inclusion and voids	Ultrasonic Penetrant X-ray radiography Eddy current Magnetic particle	Gamma radiography, neutron radiography	Radioactive gas penetrant	Optical metallography
Residual stresses	X-ray diffraction	Ultrasonic velocity	Eddy current, electrochemical potential, ultrasonic attenuation, magento-absorption	Parting out, layer removal, X-ray diffraction
Distortion	Visual inspection	Metrology		

Table A1: The techniques used to detect and locate surface inhomogeneity in metals [87]

APPENDIX B: Milling modes

The milling cutter rotates while the workpiece is fed against it or vice versa. A cut is defined by the various parameters involved. There are two ways that this can be achieved depending of the rotation of the cutter in relation to the workpiece. This difference is fundamental to milling and considerably affects the process.

The first mode is up milling, which is also known as conventional milling [29, 31, 49] or orthodox milling [28] and is shown in Figure B1. In this mode, the rotation and motion of the cutter is such that:

- Maximum chip thickness is at the end of the cut [29, 49]. The cycle of operating to remove the chip is first one of sliding with a crushing action taking place which is followed by the actual cutting action [49]
- The feed on each tooth is very small at first and reaches a maximum where the tooth breaks contact with the work surface [28]
- The direction of the rotation of the cutter at the area of cut is opposing the direction of the feed of the workpiece (with the feed of the cutter) [30, 31, 49]

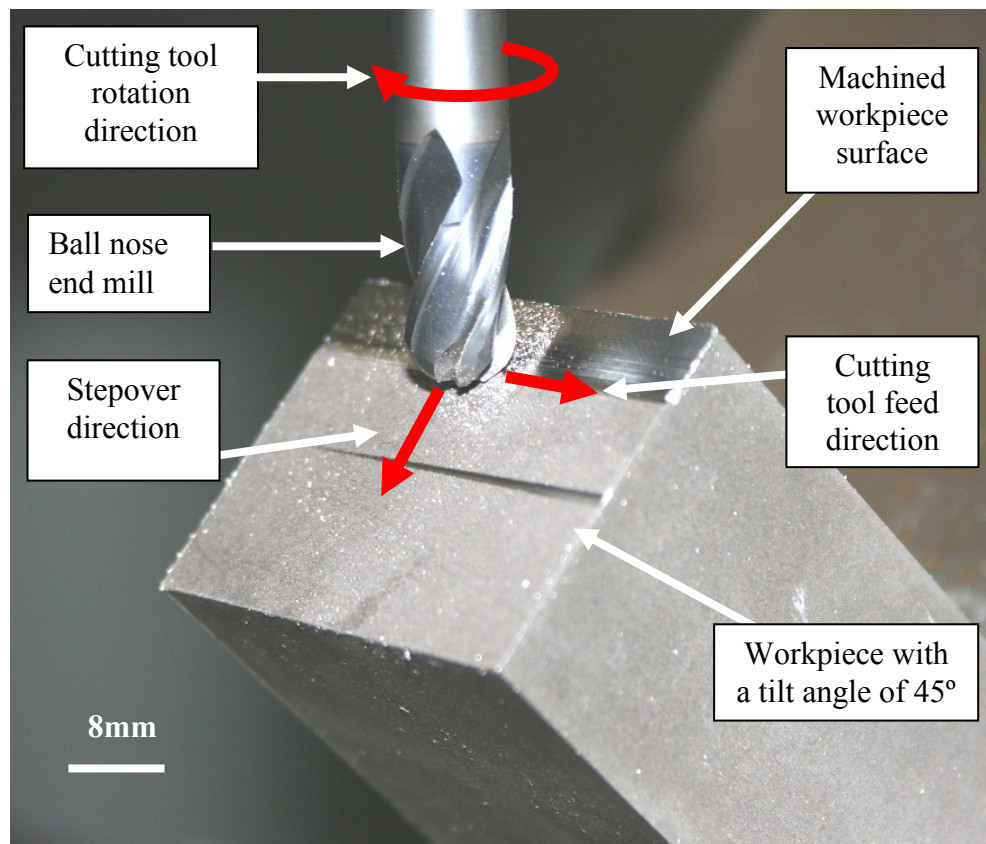


Figure B1: Schematic showing up milling in a horizontal downwards direction using a ball nose end milling and a workpiece tilt angle of 45°

The advantages of up milling include:

- Tooth engagement is not a function of workpiece surface characteristics [29]
- Contamination or scale on the workpiece surface does not effect tool life [29, 49]
- The machine tool does not require a backlash eliminator [49]
- It is generally considered that this mode is safer in operation as the cutter does not climb into the workpiece [49]
- The loads on the teeth are acting gradually [49]
- Built-up-edge (BUE) fragments are absent from the machined surface [49]

The disadvantages of up milling include:

- There is a tendency for the cutter to chatter [29]
- There is a tendency of the workpiece to be pulled upward therefore proper clamping is required [29, 31]
- This milling mode can lead to strain hardening of the machined surface and also chattering with excessive teeth blunting [49]
- High cutting forces are often measured [31]
- The insert/cutting edge has to be forced into the cut creating a rubbing or burnishing effect with excessive friction, high temperatures and often contact with a work hardened surface caused by the preceding insert/cutting edge [31]
- The chip can be trapped or wedged between the insert and workpiece which can result in insert breakage [31]

The second milling mode is commonly known as down or climb milling, see Figure B2 [28, 29, 49]. In this mode, the rotation and motion of the cutter is such that:

- The cut starts with the chip at its thickest location [29, 31, 49] and will decrease until it is zero at the end of the cut in peripheral milling [31]
- The feed on each tooth is greatest at the point of initial contact [28]
- The cutter rotation at the area of cut is in the same direction as the workpiece feed (against the cutter feed) [28, 30, 31]
- The cutter attempts to climb the workpiece [49]

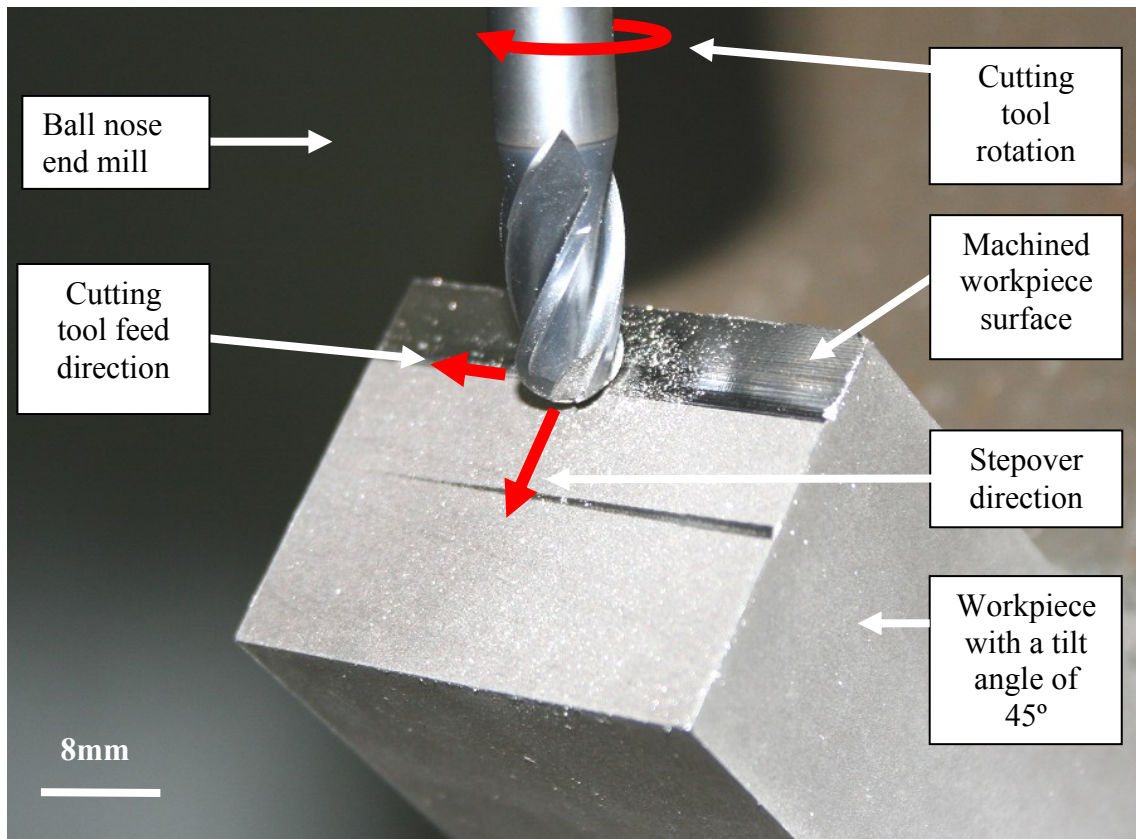


Figure B2: Schematic showing down milling in a horizontal downwards direction using a ball nose end mill and a workpiece tilt angle of 45°

The advantages of down milling include:

- The downward component of cutting forces holds the workpiece in place. This is useful for slender parts [29, 31, 49]. Flat workpieces or plates that cannot be firmly held can be machined by down-milling [49]
- Fixtures tend to be simpler and less costly as cutting forces are acting downward [49]
- A cutter with a high rake angle can be used. This can decrease the power requirement [49]
- Tool blunting is less likely [49]
- Improved surface finish as less tendency to chatter and vibrate [49]
- Less burnishing effect with less heat and minimal work hardening tendencies [31]
- In down milling, the same chip produced in up milling would be cut in half and not damage the workpiece [31]

The disadvantages of down milling include:

- High impact forces are often measured when the tooth engages the cut workpiece therefore this operation must have a rigid setup and backlash eliminated [29, 31, 49]
- Excessive wear is often caused by harder cast or scaled surfaces [29].

Figures B3 and B4 show a scale drawing of a ball nose end mill ($\phi 8\text{mm}$) when using a depth of cut of 0.25mm , a stepover of 0.25mm and a feed rate of 0.06mm/tooth . Both figures show the cutting tool rotation (clockwise when viewed from above), the cutting tool feed and the workpiece feed (opposite to the tool feed). A horizontal downwards milling mode has been used with the workpiece orientated at 45° . This was used for all Phase 1A and Phase 1B tests as well as half the tests performed during Phase 1C. The only difference between the two figures is the milling mode with Figure B3 showing up milling and Figure B4 showing down milling. Figure B3 shows that at the area of cut, the tool rotation is in an opposite direction to the workpiece feed and also that the cut starts at the point of minimum chip thickness and increases to a maximum at the end of cut. This is in agreement with the definitions given in [28, 29, 31, 49] for up milling.

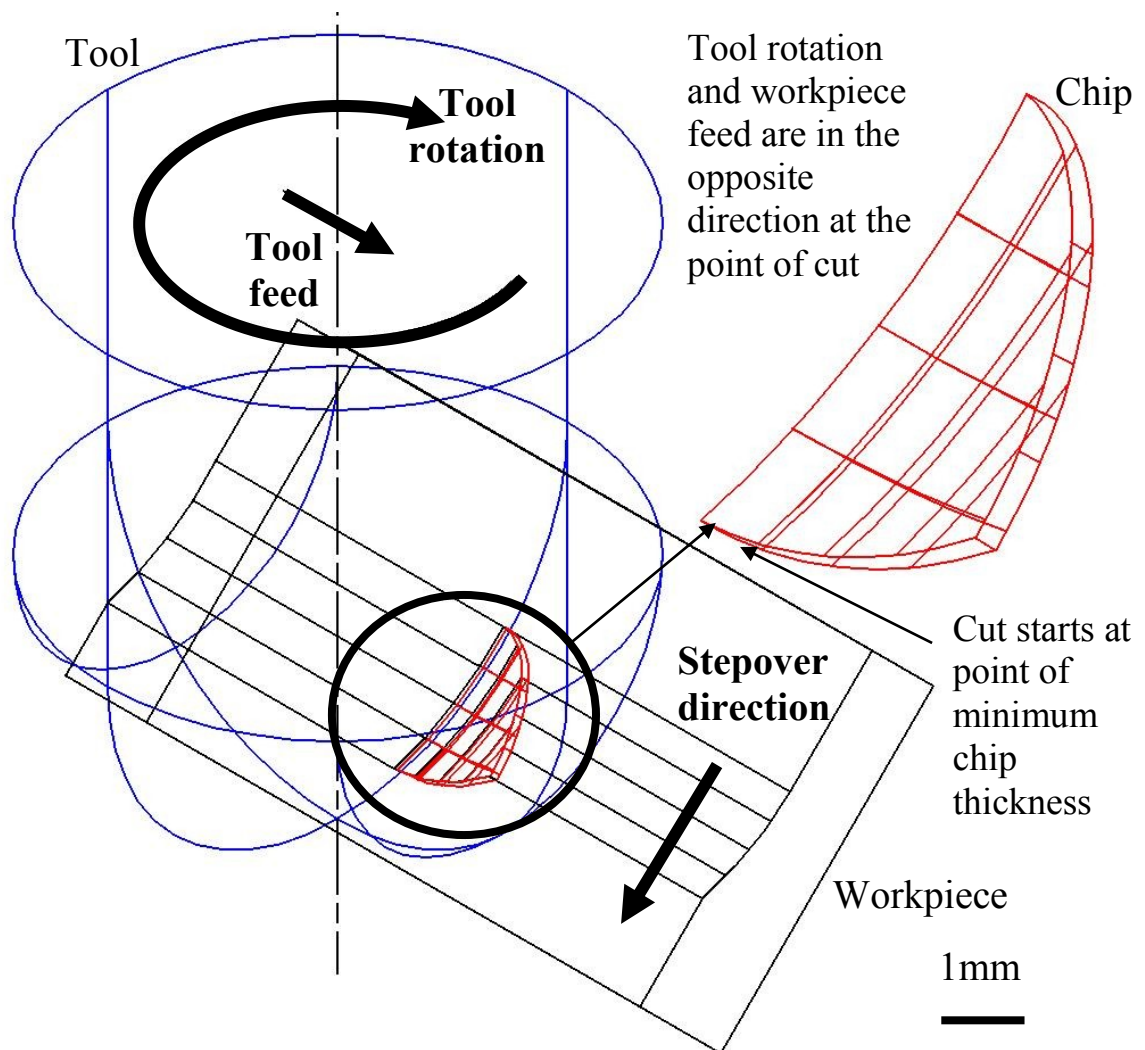


Figure B3: Schematic of up milling in a horizontal downwards direction

Figure B4 shows the workpiece feed and tool feed in the opposite direction to Figure B3. The figure shows that at the area of cut, the tool rotation is in the same direction as the workpiece feed direction and that the cut starts at the point of thickest chip thickness and reduces to zero at the end of the cut. This is in agreement with the definitions given in [28, 29, 31, 49] for down milling. The maximum chip thickness is identical for either milling mode therefore mathematical assessment of the chip shape/thickness cannot be used to determine the milling mode [29]. A change in the operating parameters such as cutting speed, feed rate, depth of cut (axial and radial) does not change the milling mode and only by changing the workpiece feed direction or tool rotation will the milling mode be altered.

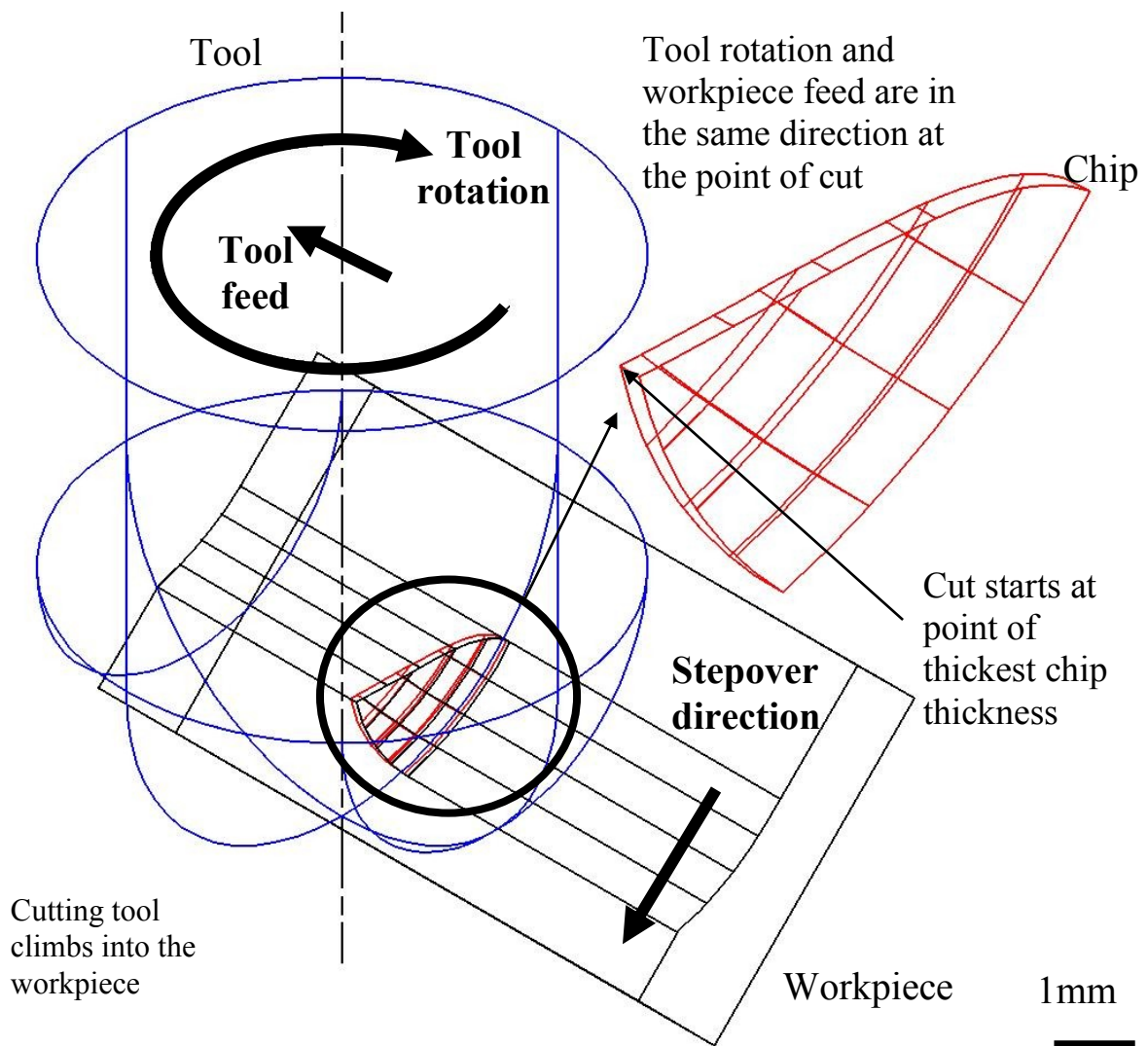


Figure B4: Schematic of down milling in a horizontal downwards direction

APPENDIX C: Additional Experimental Results

C1 Phase 1, high speed milling

a) Phase 1A: Initial assessment of significant operating parameters

Figure C1 shows maximum flank wear against machining time.

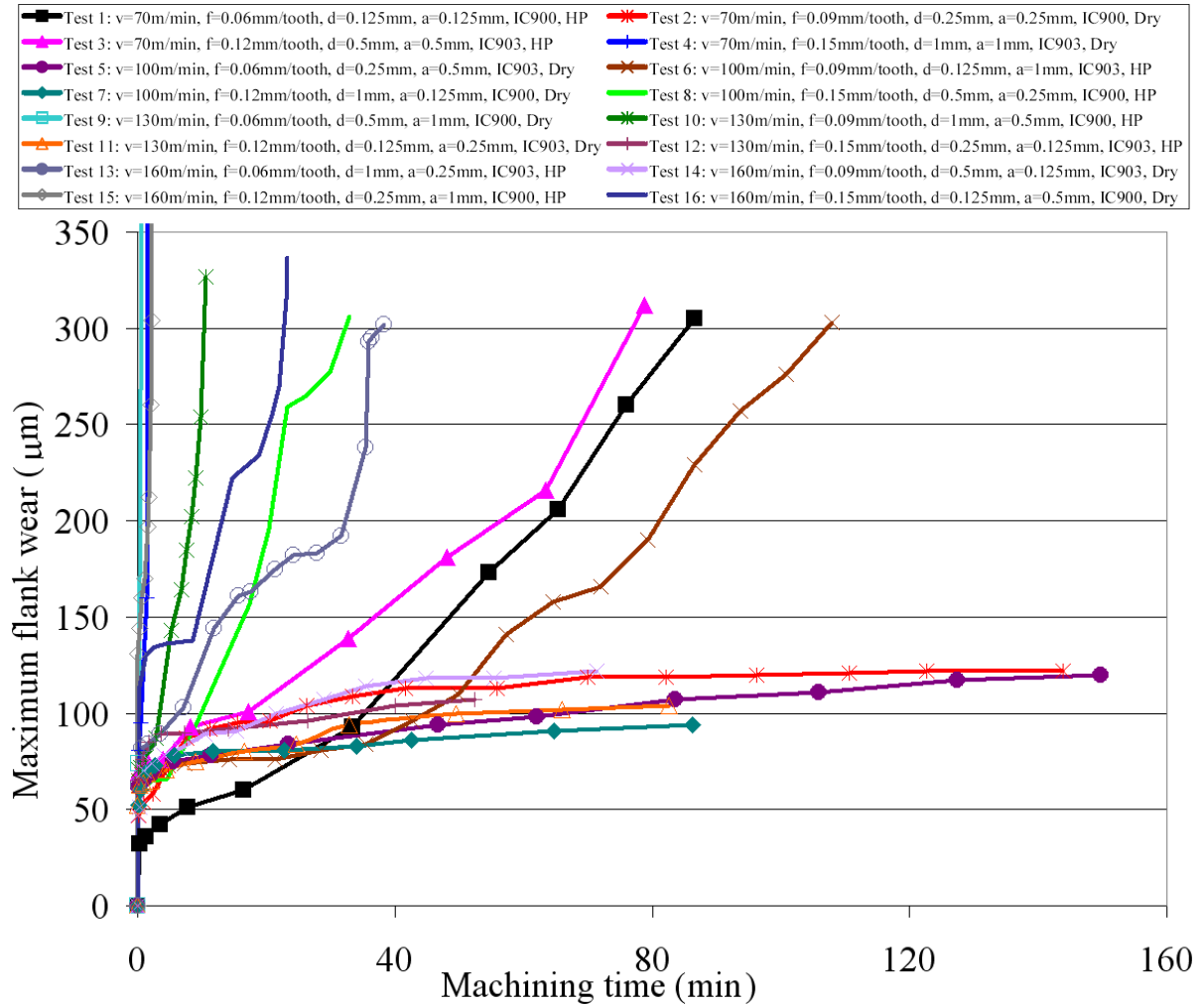


Figure C1: Maximum flank wear against machining time (Phase 1A)

Figure C2 shows maximum flank wear against volume of workpiece material removed.

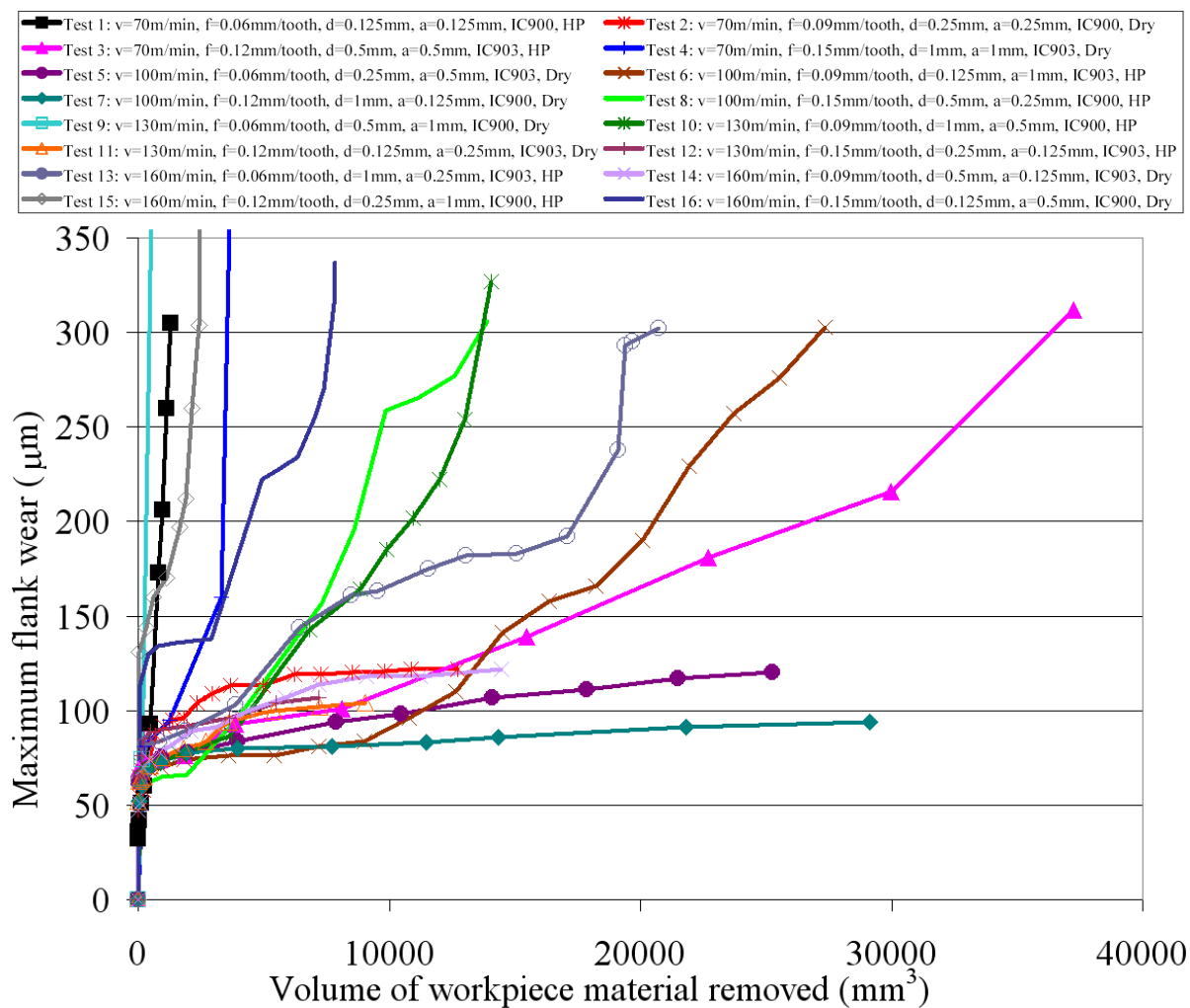


Figure C2: Maximum flank wear against volume of workpiece material removed (Phase 1A)

Figure C3 shows machining time against material removal rate.

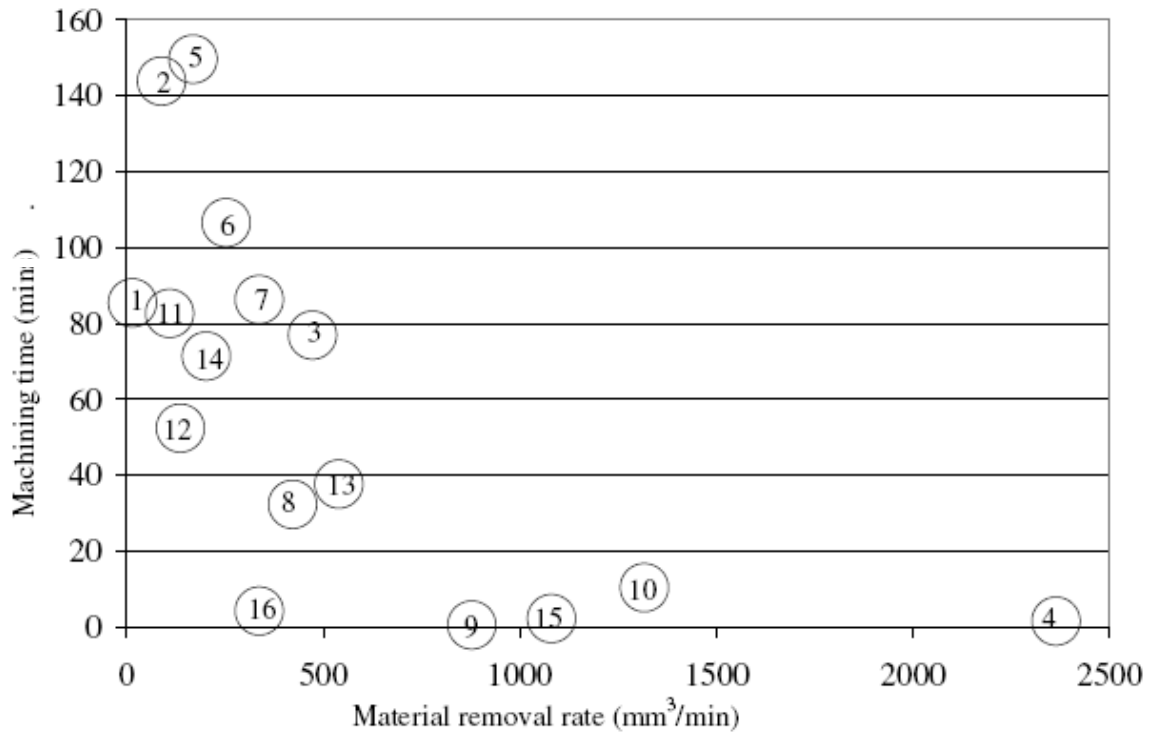


Figure C3: Machining time against material removal rate

Figure C4 shows volume of workpiece material removed against material removal rate.

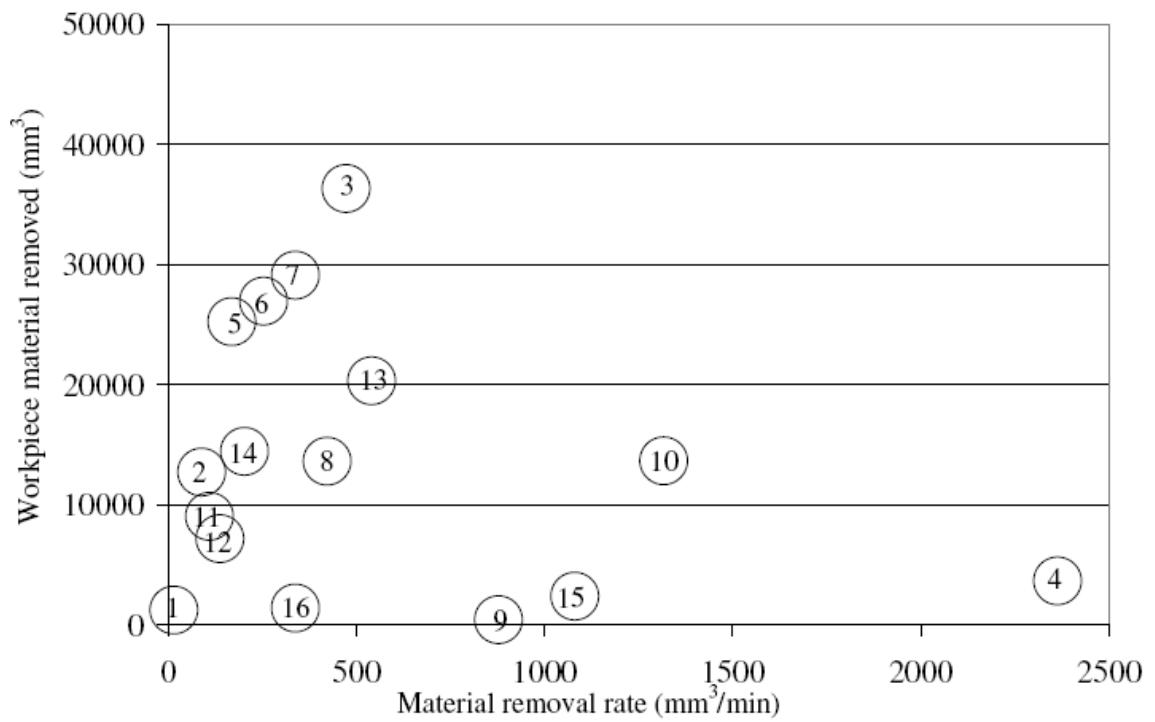
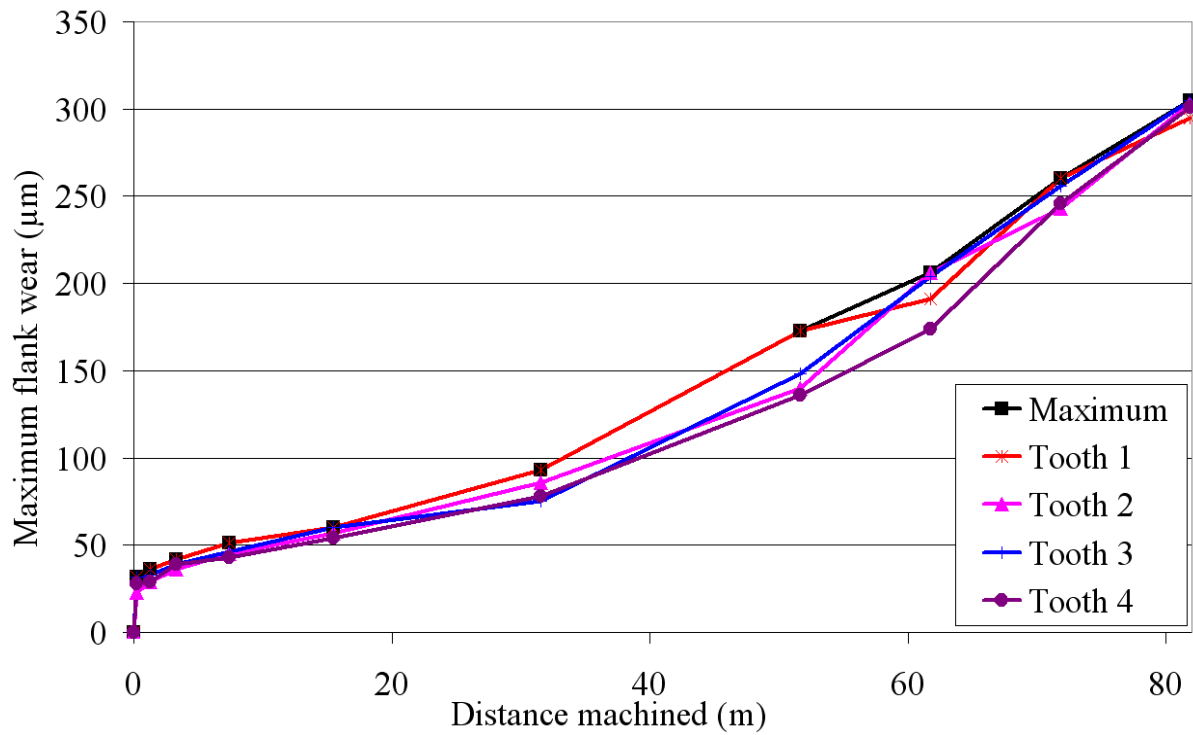


Figure C4: Workpiece material removed against material removal rate

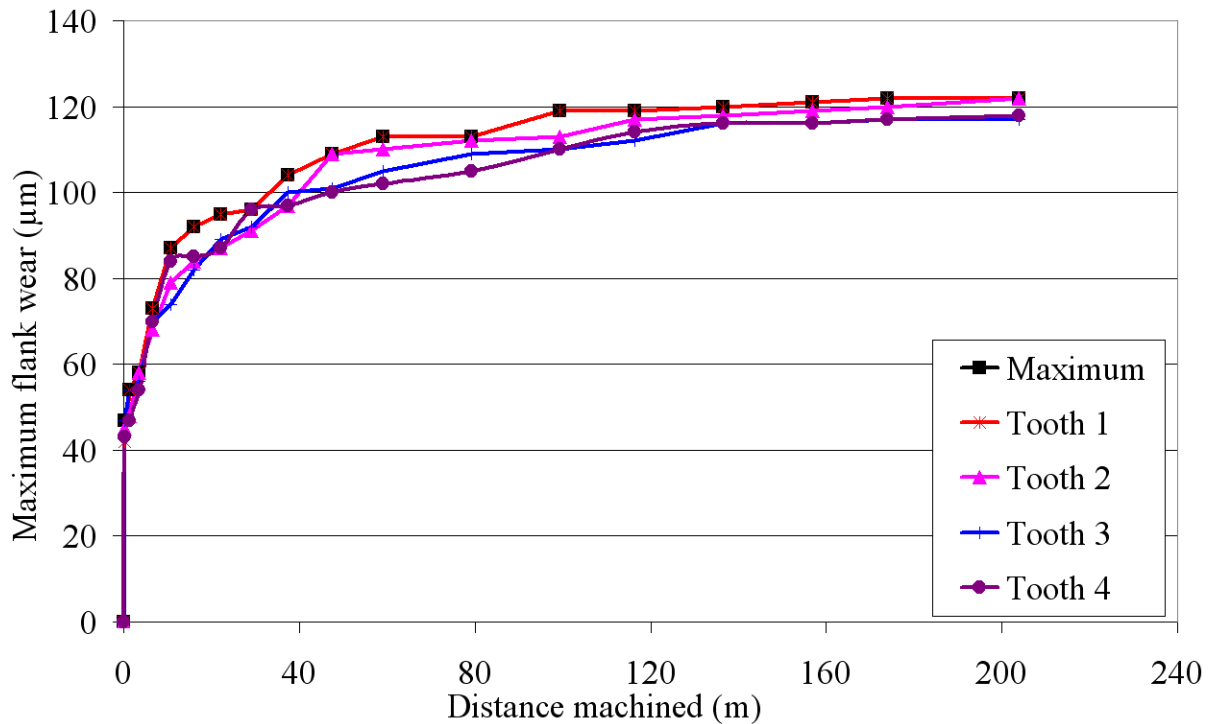
Figure C5 shows maximum flank wear against distance machined for Test 1.



Test 1: $v=70\text{m/min}$, $f=0.06\text{mm/tooth}$, $a=0.125\text{mm}$, $d=0.125\text{mm}$, IC900, HP

Figure C5: Maximum flank wear against distance machined for Test 1

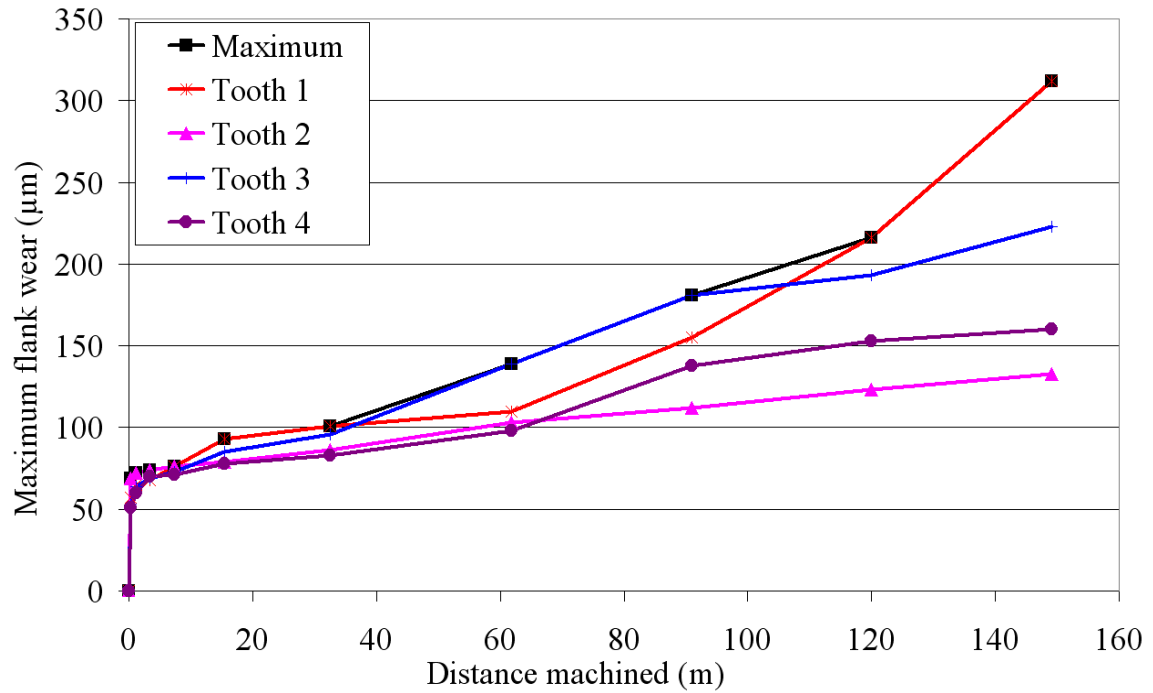
Figure C6 shows maximum flank wear against distance machined for Test 2.



Test 2: $v=70\text{m/min}$, $f=0.09\text{mm/tooth}$, $a=0.25\text{mm}$, $d=0.25\text{mm}$, IC900, dry

Figure C6: Maximum flank wear against distance machined for Test 2

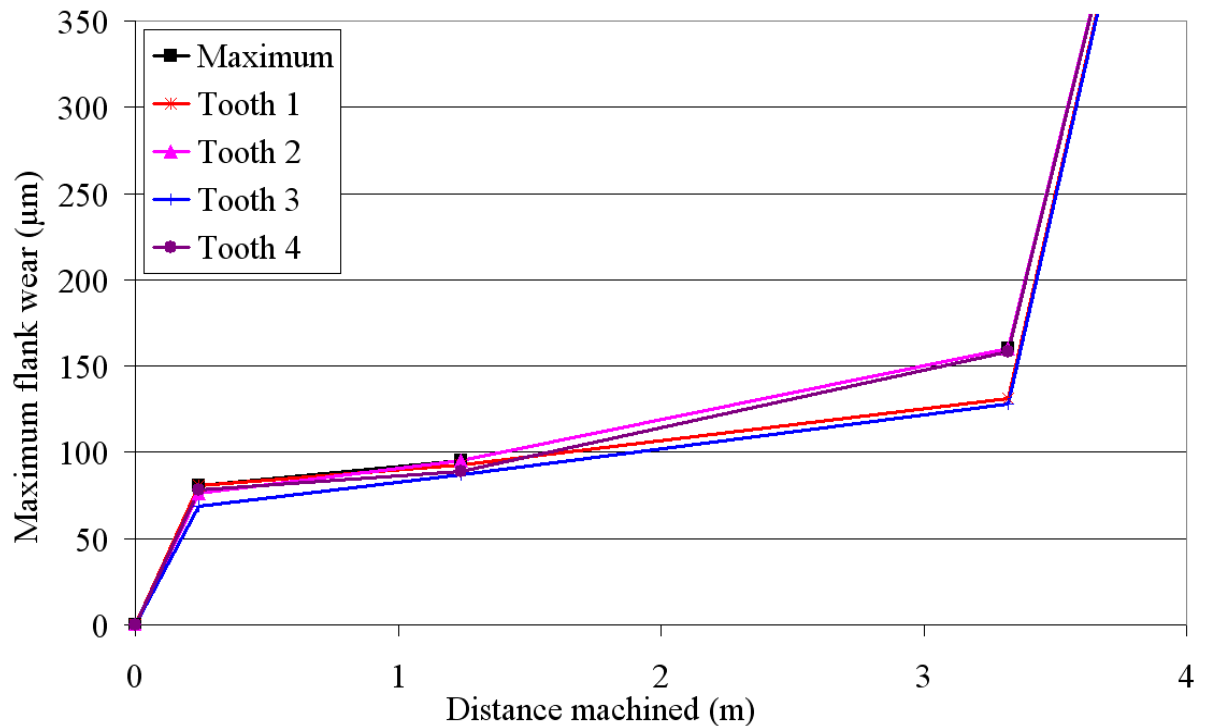
Figure C7 shows maximum flank wear against distance machined for Test 2.



Test 3: $v=70\text{m/min}$, $f=0.12\text{mm/tooth}$, $a=0.5\text{mm}$, $d=0.5\text{mm}$, IC903, HP

Figure C7: Maximum flank wear against distance machined for Test 3

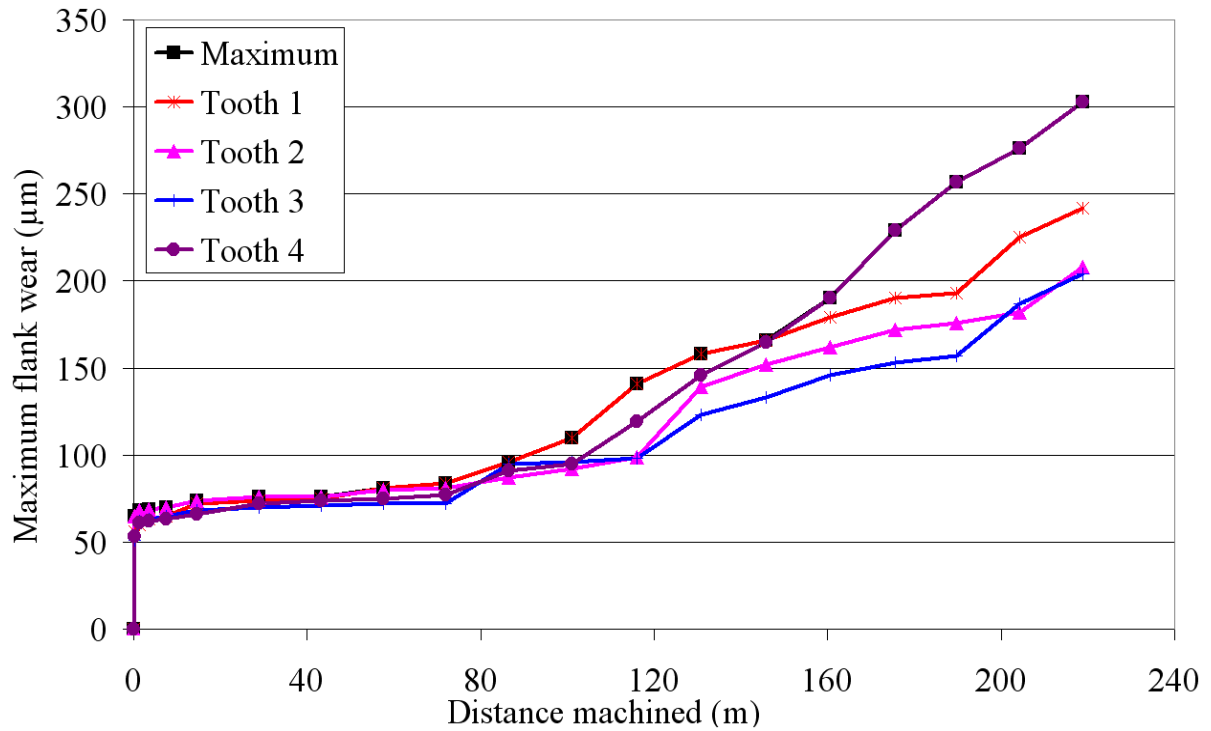
Figure C8 shows maximum flank wear against distance machined for Test 4.



Test 4: $v=70\text{m/min}$, $f=0.15\text{mm/tooth}$, $a=1.0\text{mm}$, $d=1.0\text{mm}$, IC903, dry.

Figure C8: Maximum flank wear against distance machined for Test 4

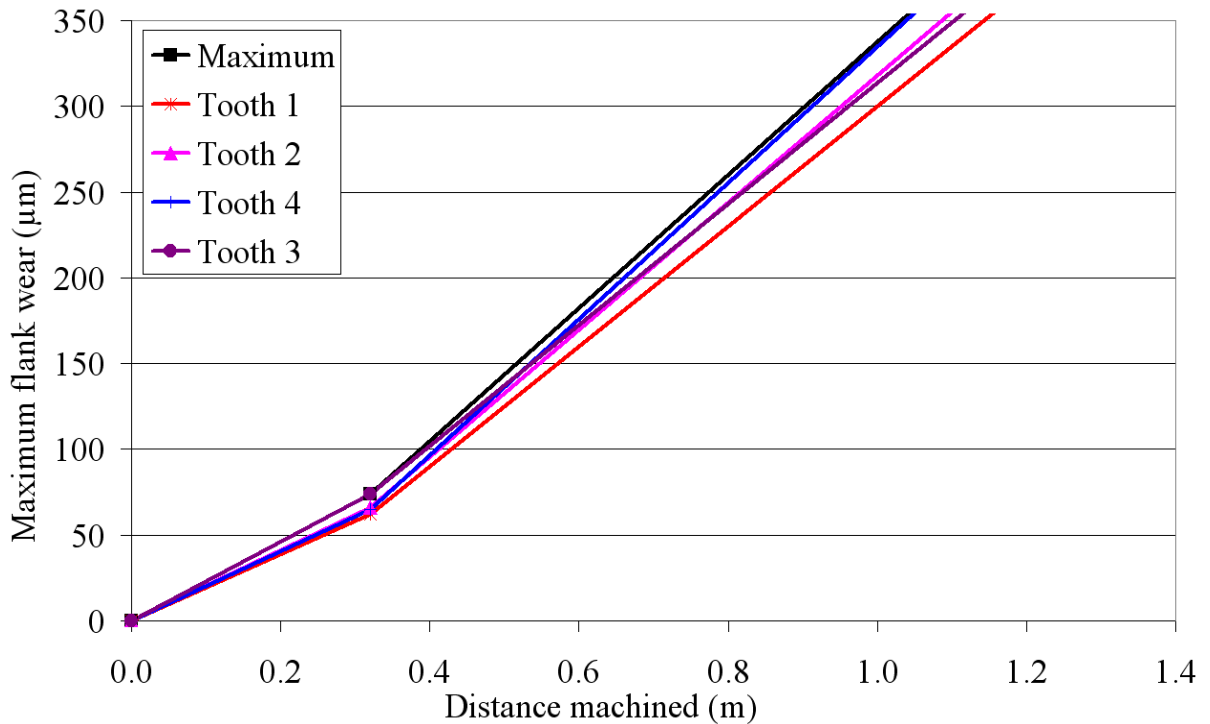
Figure C9 shows maximum flank wear against distance machined for Test 6.



Test 6: $v=100\text{m/min}$, $f=0.09\text{mm/tooth}$, $a=0.125\text{mm}$, $d=1.0\text{mm}$, IC903, HP

Figure C9: Maximum flank wear against distance machined for Test 6

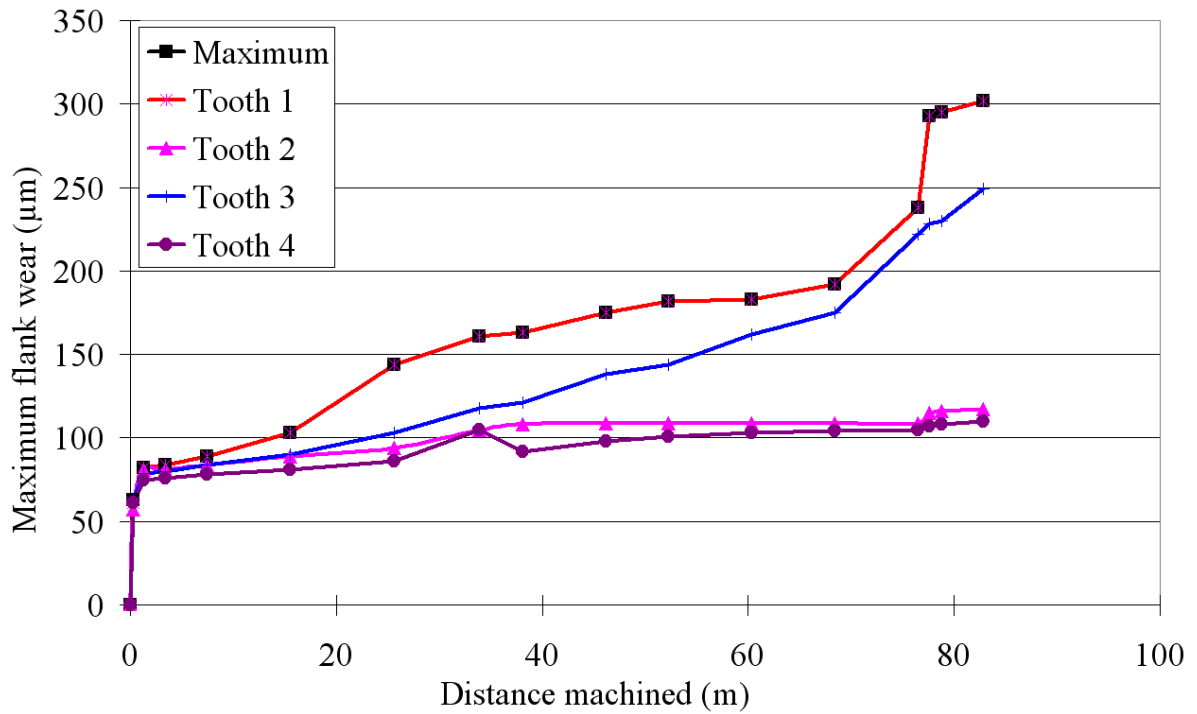
Figure C10 shows maximum flank wear against distance machined for Test 9.



Test 9: $v=130\text{m/min}$, $f=0.06\text{mm/tooth}$, $a=0.5\text{mm}$, $d=1.0\text{mm}$, IC900, dry

Figure C10: Maximum flank wear against distance machined for Test 9

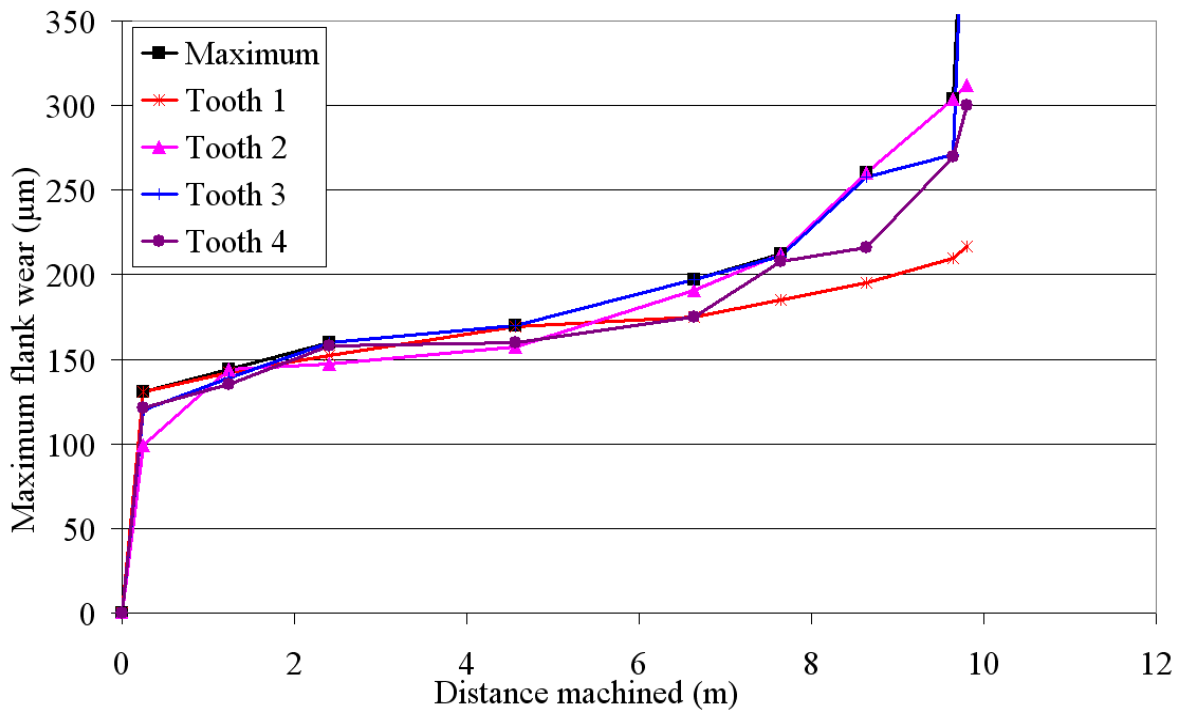
Figure C11 shows maximum flank wear against distance machined for Test 13.



Test 13: $v=160\text{m/min}$, $f=0.06\text{mm/tooth}$, $a=1.0\text{mm}$, $d=0.25\text{mm}$, IC903, HP

Figure C11: Maximum flank wear against distance machined for Test 13

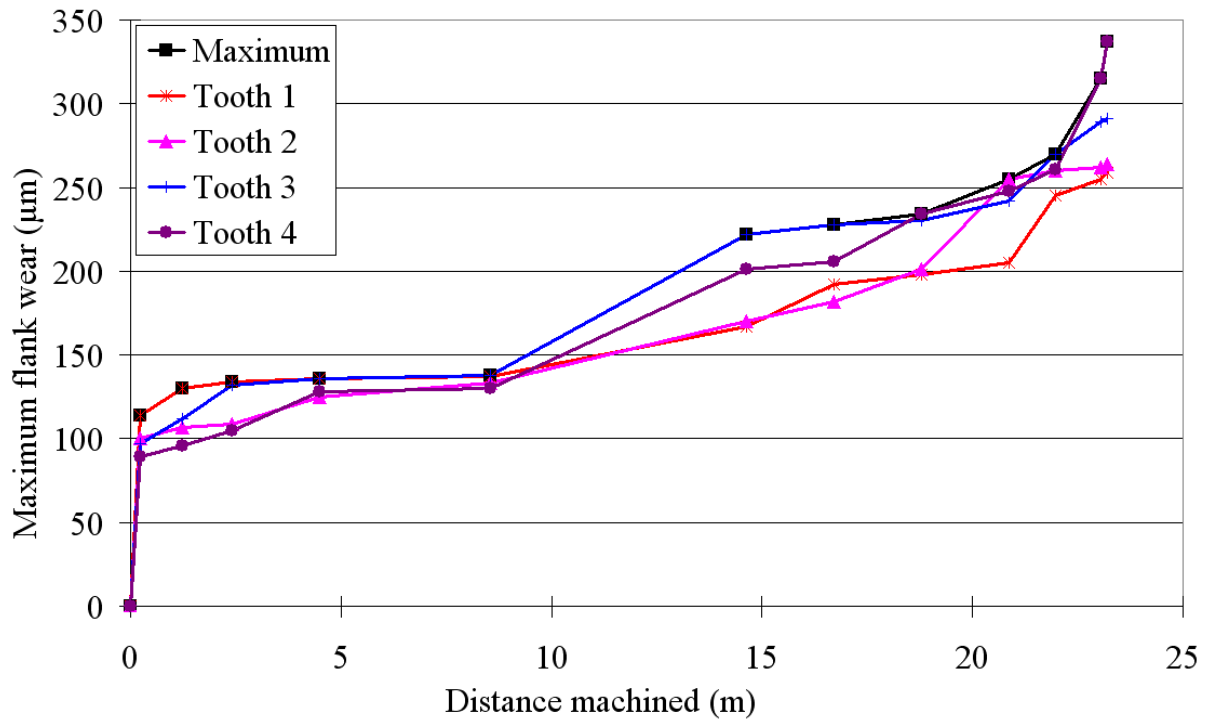
Figure C12 shows maximum flank wear against distance machined for Test 15.



Test 15: $v=160\text{m/min}$, $f=0.12\text{mm/tooth}$, $a=0.25\text{mm}$, $d=1.0\text{mm}$, IC900, HP

Figure C12: Maximum flank wear against distance machined for Test 15

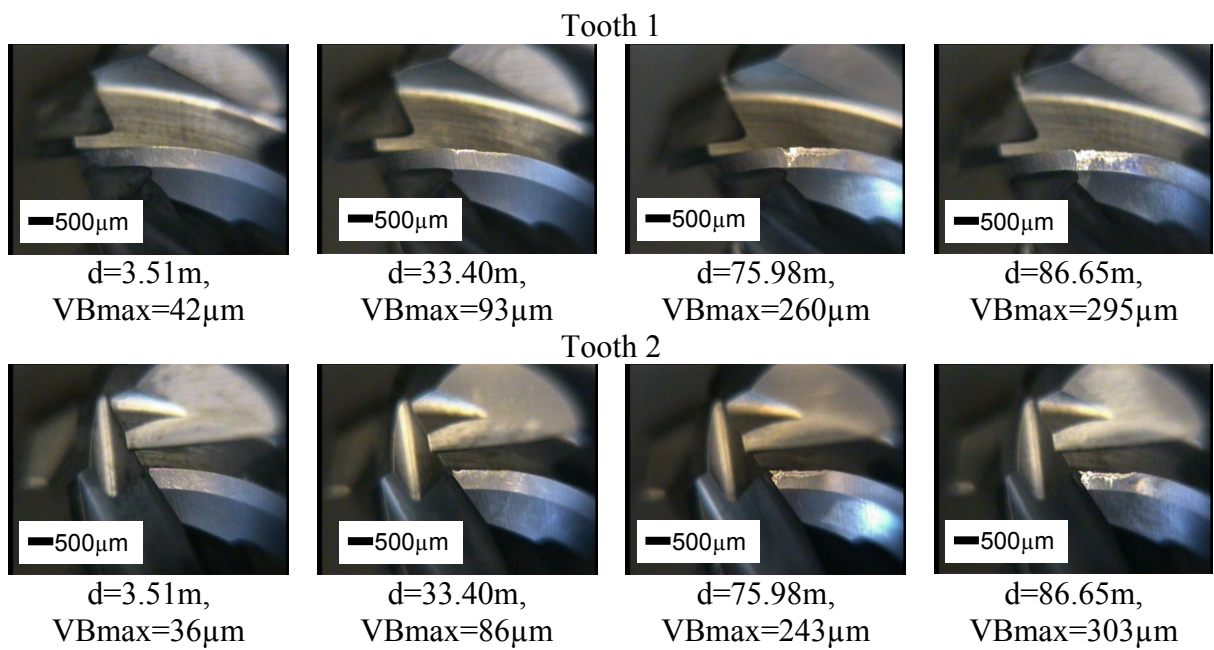
Figure C13 shows maximum flank wear against distance machined for Test 16.



Test 16: $v=160\text{m/min}$, $f=0.15\text{mm/tooth}$, $a=0.125\text{mm}$, $d=0.5\text{mm}$, IC900, dry

Figure C13: Maximum flank wear against distance machined for Test 16

Figure C14 shows selected wear scar photographs for Test 1



Test 1: $v=70\text{m/min}$, $f=0.06\text{mm/tooth}$, $a=0.125\text{mm}$, $d=0.125\text{mm}$, IC900, HP.

Figure C14: Test 1 wear scar photographs (Phase 1A)

Figure C15 shows selected wear scar photographs for Test 2.

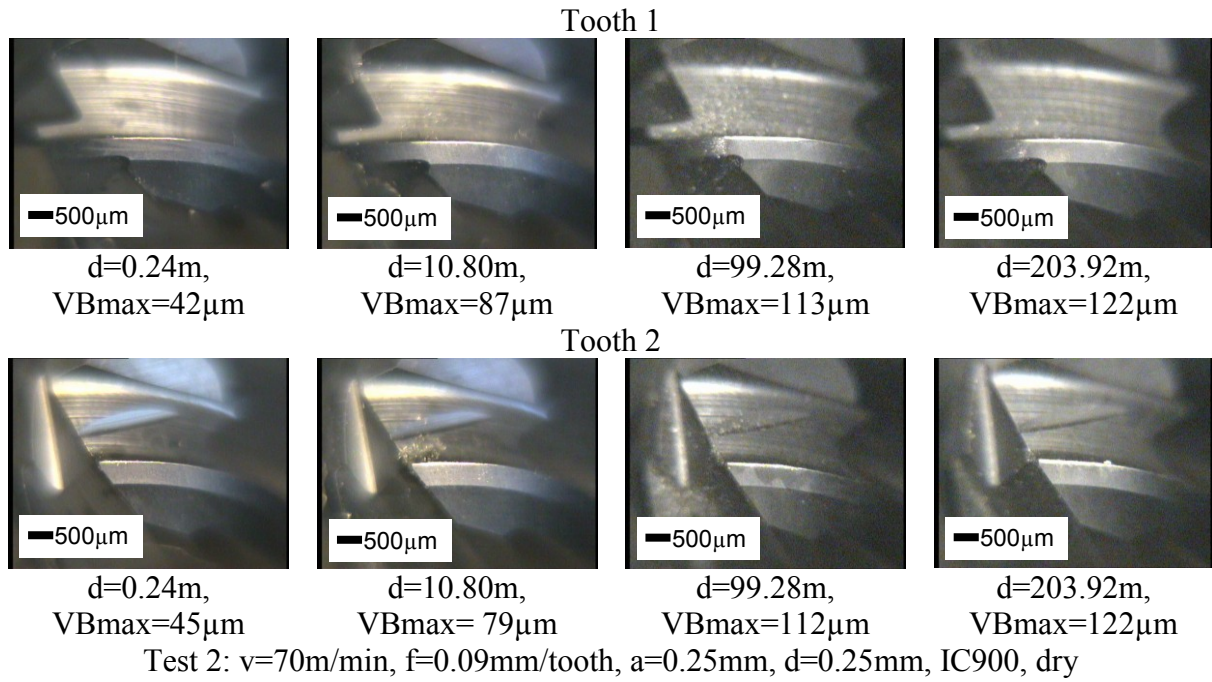


Figure C15: Test 2 wear scar photographs (Phase 1A)

Figure C16 shows selected wear scar photographs for Test 3.

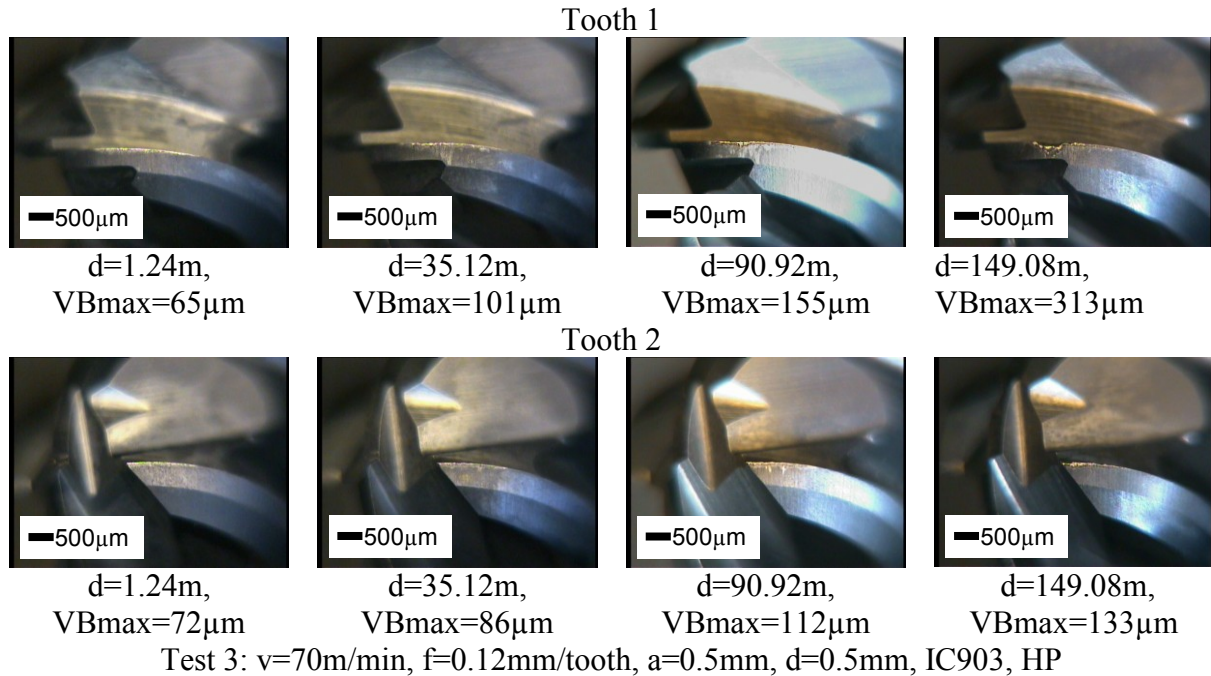


Figure C16: Test 3 wear scar photographs(Phase 1A)

Figure C17 shows selected wear scar photographs for Test 3.

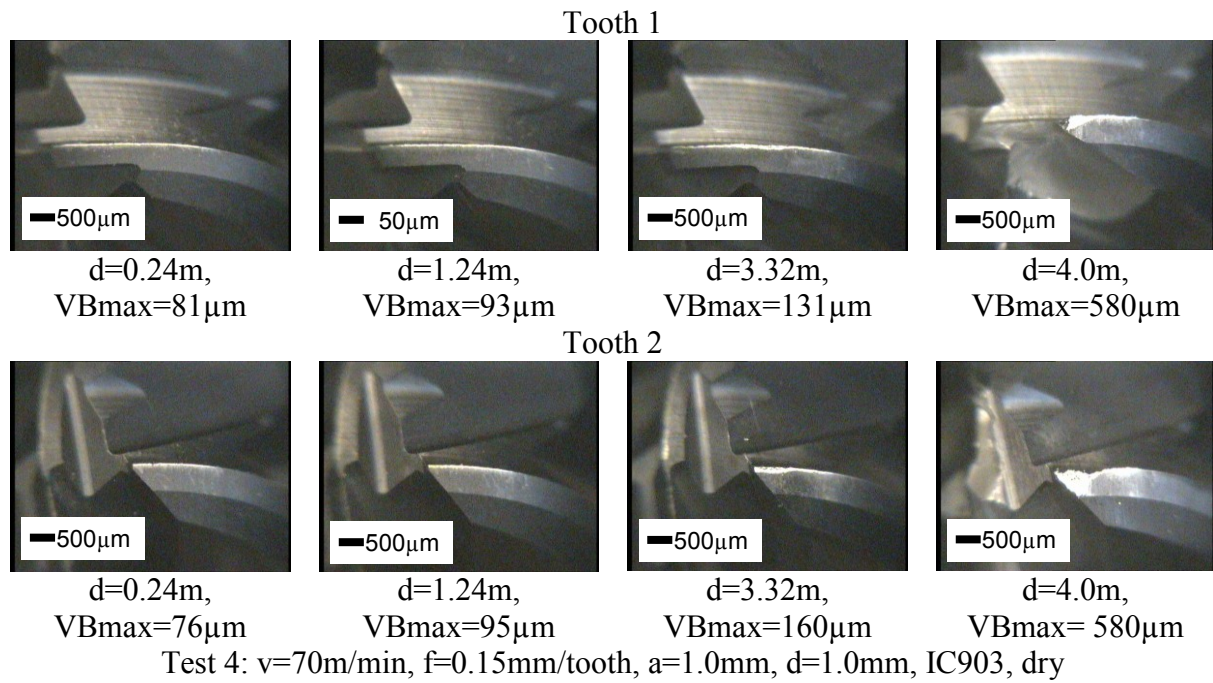


Figure C17: Test 4 wear scar photographs (Phase 1A)

Figure C18 shows selected wear scar photographs for Test 6.

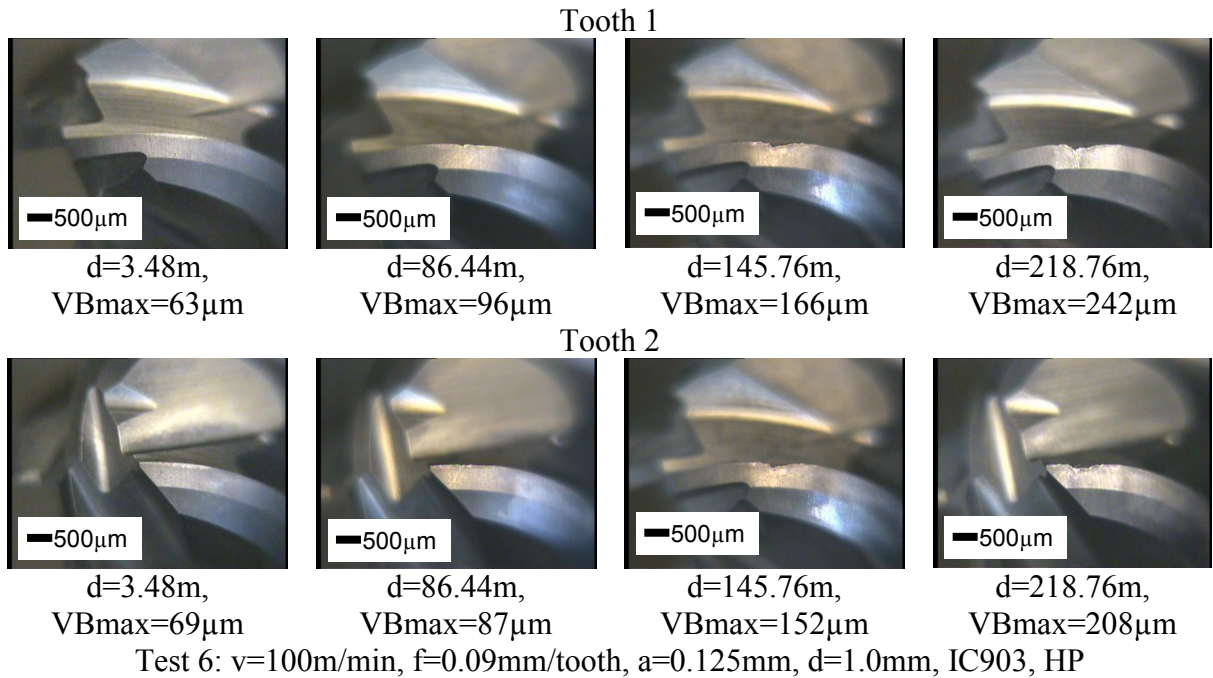


Figure C18: Test 6 wear scar photographs (Phase 1A)

Figure C19 shows selected wear scar photographs for Test 9.

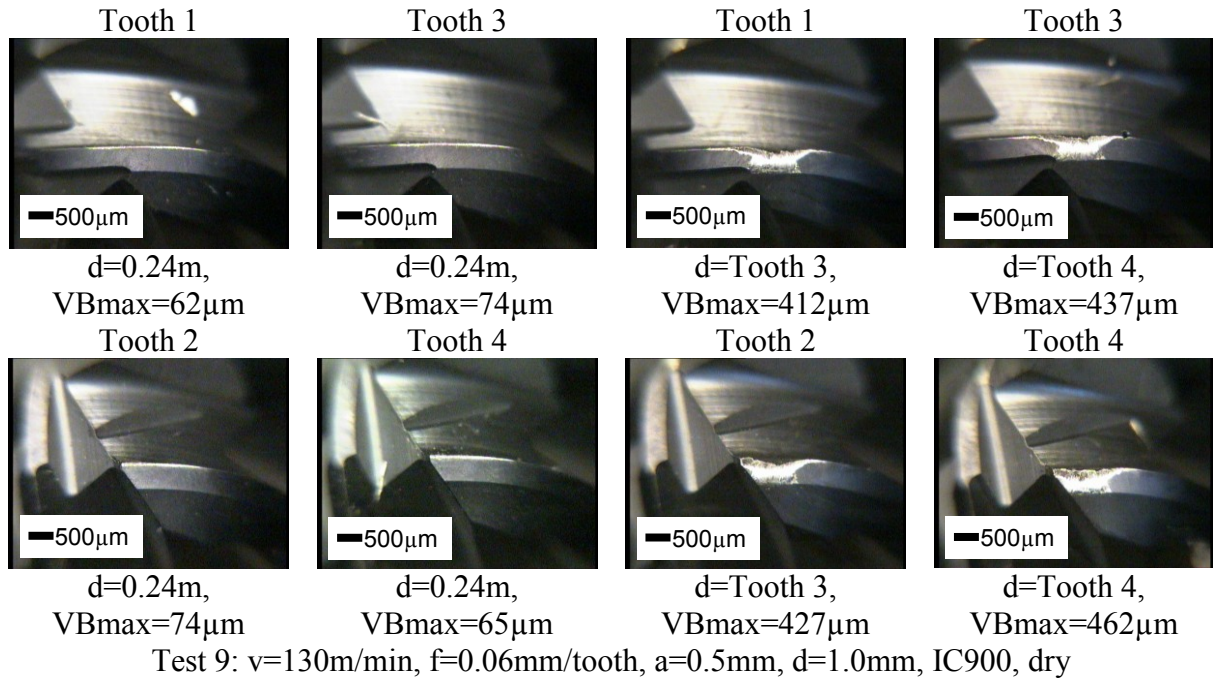


Figure C19: Test 9 wear scar photographs (Phase 1A)

Figure C20 shows selected wear scar photographs for Test 13.

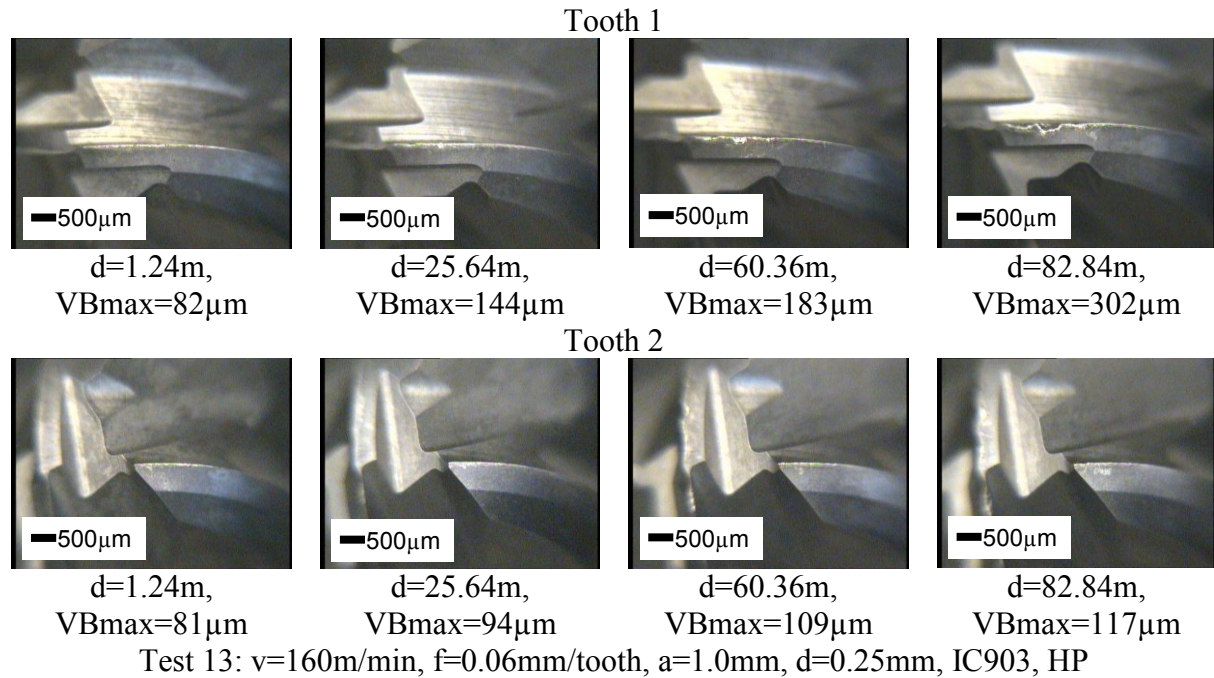


Figure C20: Test 13 wear scar photographs (Phase 1A)

Figure C21 shows selected wear scar photographs for Test 15.

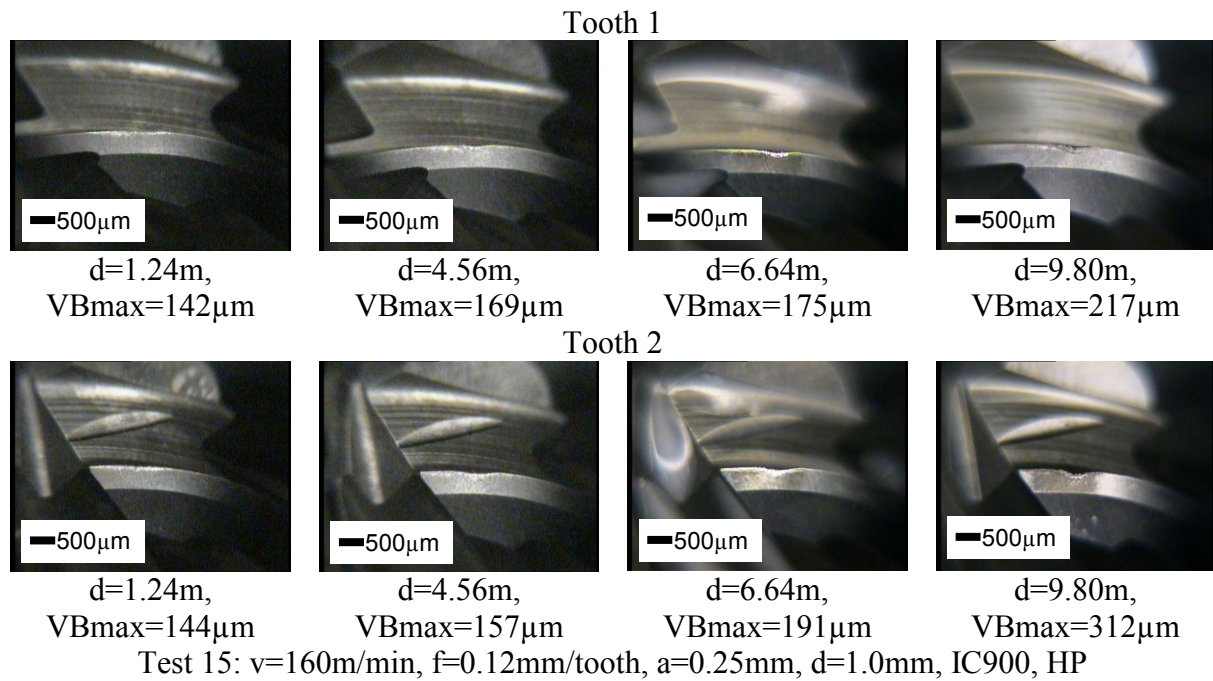


Figure C21: Test 15 wear scar photographs (Phase 1A)

Figure C22 shows selected wear scar photographs for Test 16.

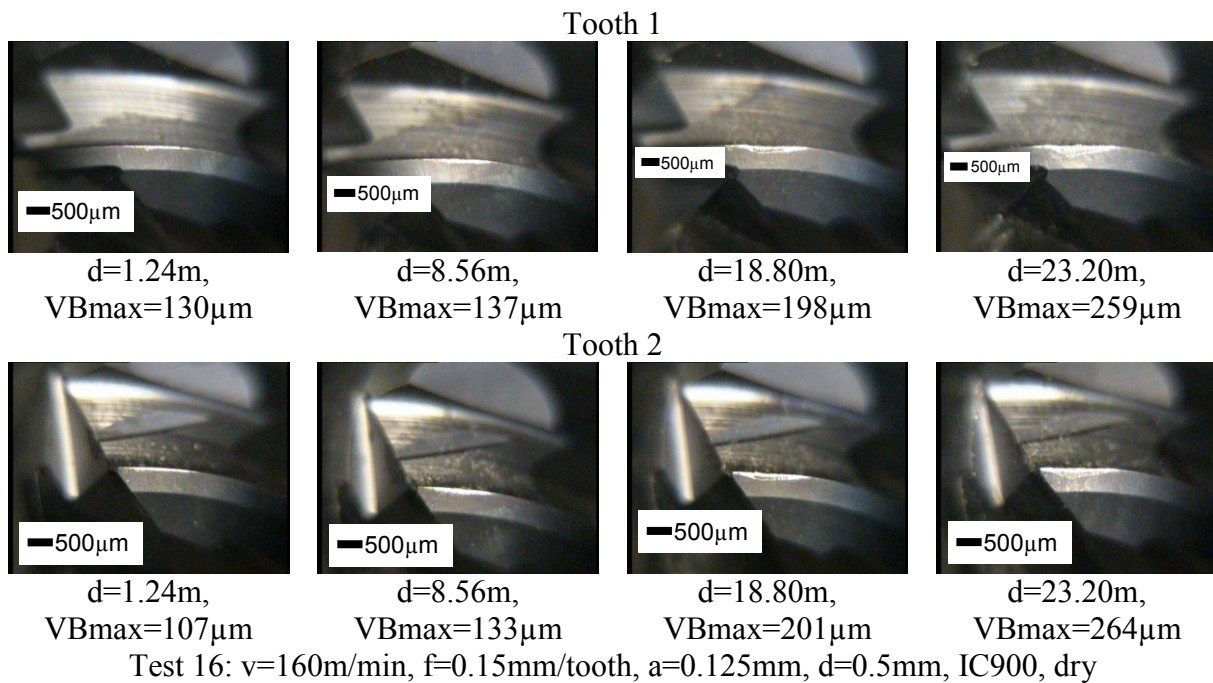
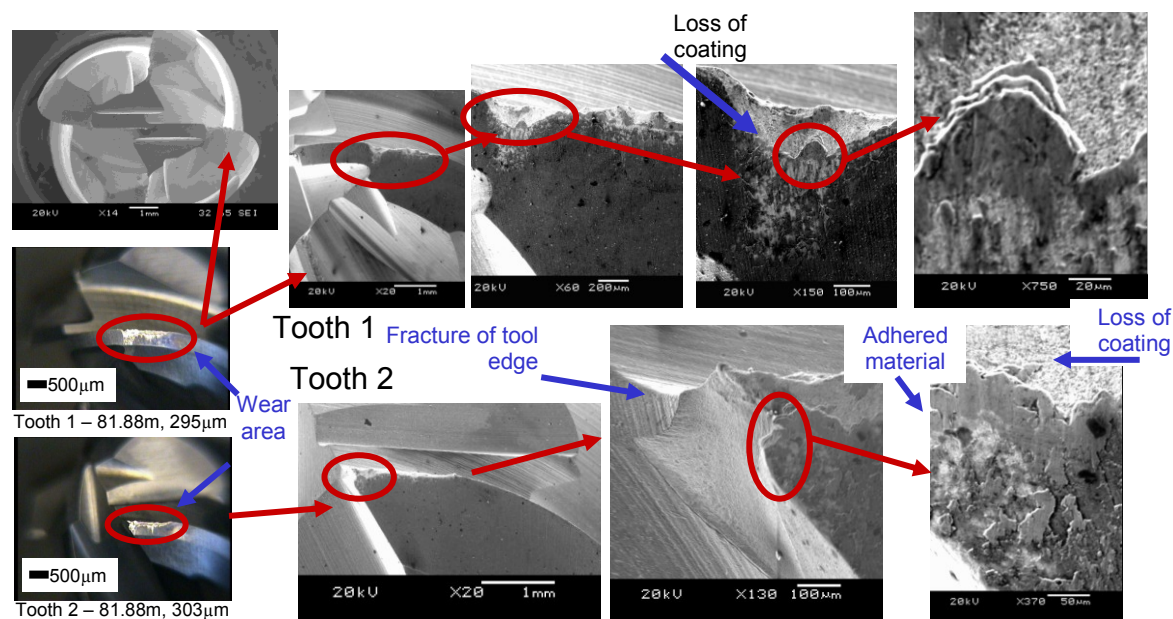


Figure C22: Test 16 wear scar photographs (Phase 1A)

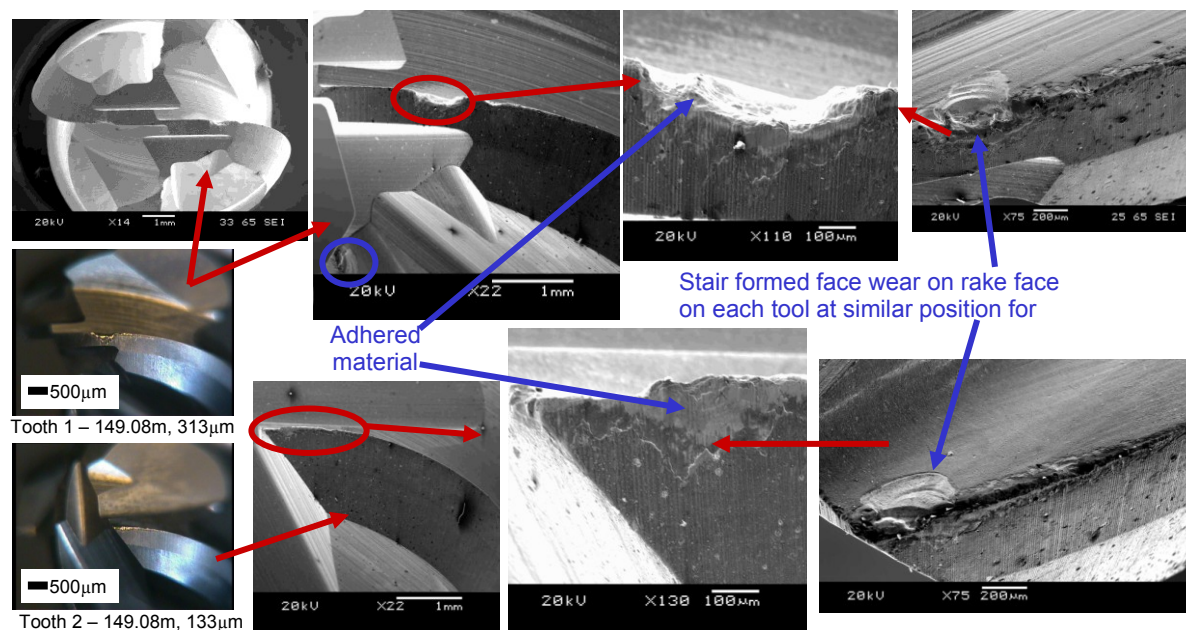
Figure C23 shows Scanning Electron Microscope (SEM) images of the tools from Test 1.



Test 1: $v=70\text{m/min}$, $f=0.06\text{mm/tooth}$, $a=0.125\text{mm}$, $d=0.125\text{mm}$, IC900, HP

Figure C23: SEM analysis of worn tooling from Test 1

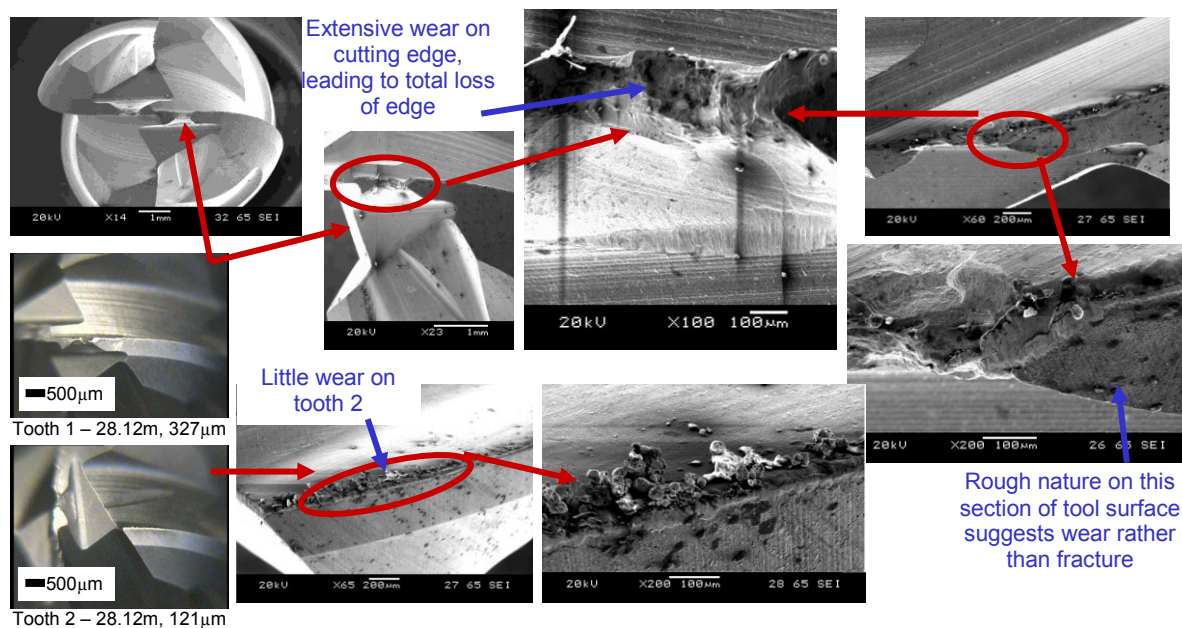
Figure C24 shows Scanning Electron Microscope (SEM) images of the tool from Test 3.



Test 3: $v=70\text{m/min}$, $f=0.12\text{mm/tooth}$, $a=0.5\text{mm}$, $d=0.5\text{mm}$, IC903, HP

Figure C24: SEM analysis of worn tooling used in Test 3

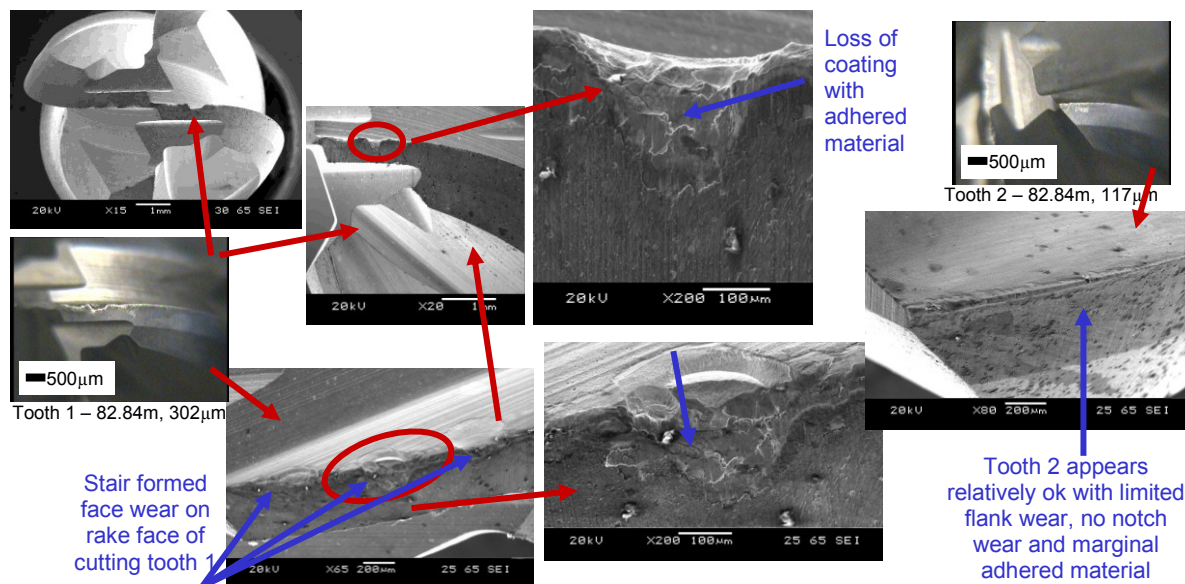
Figure C25 shows Scanning Electron Microscope (SEM) images of the tool from Test 10.



Test 10: $v=130\text{m/min}$, $f=0.09\text{mm/tooth}$, $a=1.0\text{mm}$, $d=0.5\text{mm}$, IC900, HP

Figure C25: SEM analysis of worn tooling used in Test 10

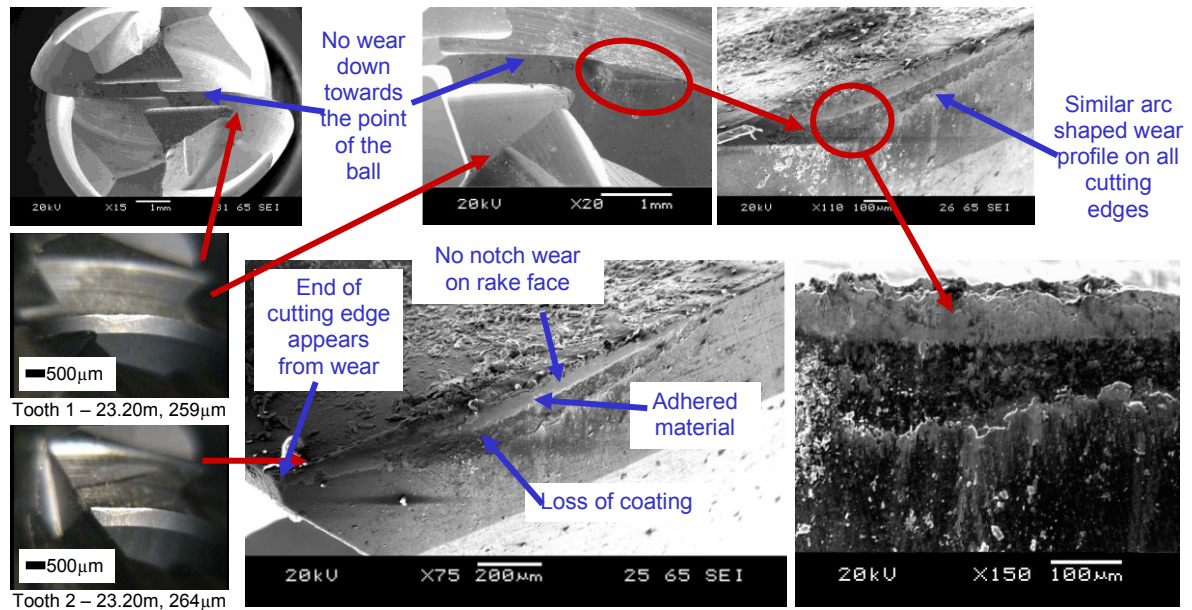
Figure C26 shows Scanning Electron Microscope (SEM) images of the tool from Test 13.



Test 13: $v=160\text{m/min}$, $f=0.06\text{mm/tooth}$, $a=1.0\text{mm}$, $d=0.25\text{mm}$, IC903, HP

Figure C26: SEM analysis of worn tooling used in Test 13

Figure C27 shows Scanning Electron Microscope (SEM) images of the tool from Test 16.



Test 16: $v=160\text{m/min}$, $f=0.15\text{mm/tooth}$, $a=0.125\text{mm}$, $d=0.5\text{mm}$, IC900, dry

Figure C27: SEM analysis of worn tooling used in Test 16

Figure C28 shows the main effects plot means for machining time and volume of workpiece material removed.

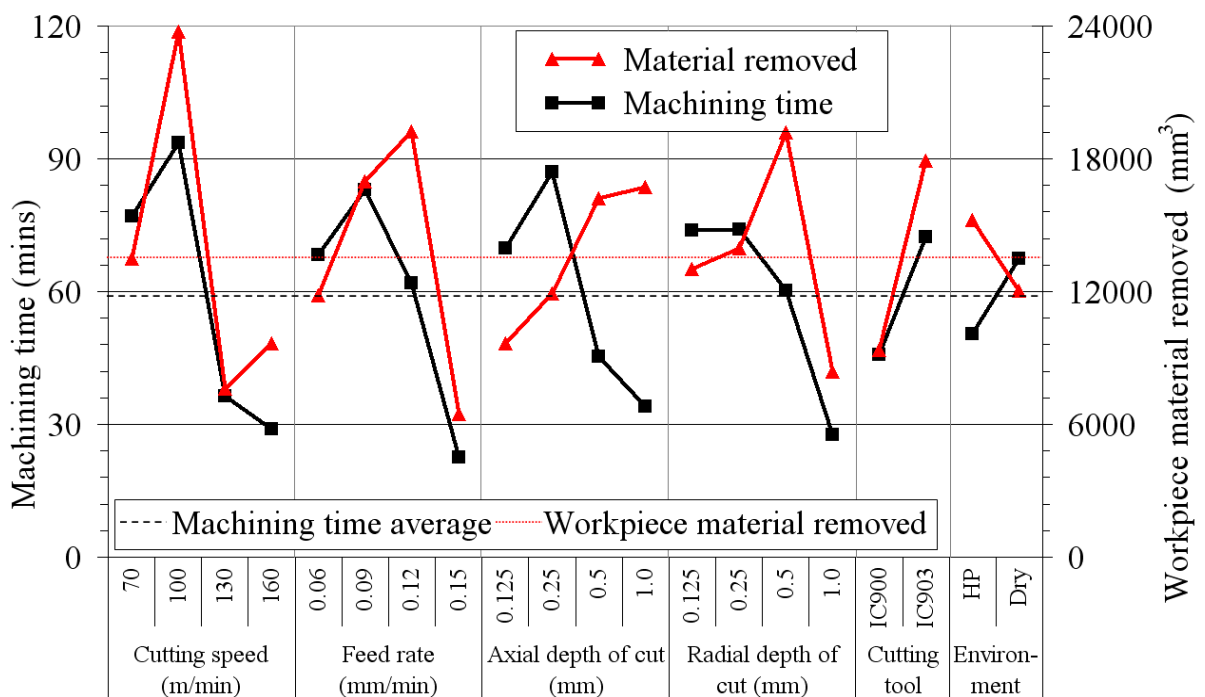


Figure C28: Main effects plot - means for machining time and volume of workpiece material removed

Tables C1 and C2 show ANOVA tables for machining time and volume of workpiece material removed.

Source	SS	DOF	MSS	Fcalc	PCR%
Cutting speed	11731.0	3	3910.3	11.98	31.16
Feed rate	8005.6	3	2668.5	8.17	20.98
Axial depth of cut	6832.6	3	2277.5	6.98	17.78
Radial depth of cut	5719.4	3	1906.5	5.84	14.73
Cutting tool	2836.1	1	2836.1	8.69	6.6
Cutting fluid	1148.9	1	1148.9	3.52	2.25
Error	326.5	1	326.5	-	6.24
Total	36600.1	15	-	-	-

Table C1: ANOVA table for machining time (Phase 1A)

Source	SS	DOF	MSS	Fcalc	PCR%
Cutting speed	618219505	3	206073168	1.26	24.21
Feed rate	387197608	3	129065869	0.79	11.91
Axial depth of cut	139208808	3	46402936	0.28	0.00
Radial depth of cut	235176149	3	78392050	0.48	3.82
Cutting tool	294023381	1	294023381	1.80	6.95
Cutting fluid	41045036	1	41045036	0.25	0
Error	163430272	1	163430272	-	53.10
Total	1878300761	15	-	-	-

Table C2: ANOVA table for workpiece material removed (Phase 1A)

Figure C29 shows the interactions plot for distance machined.

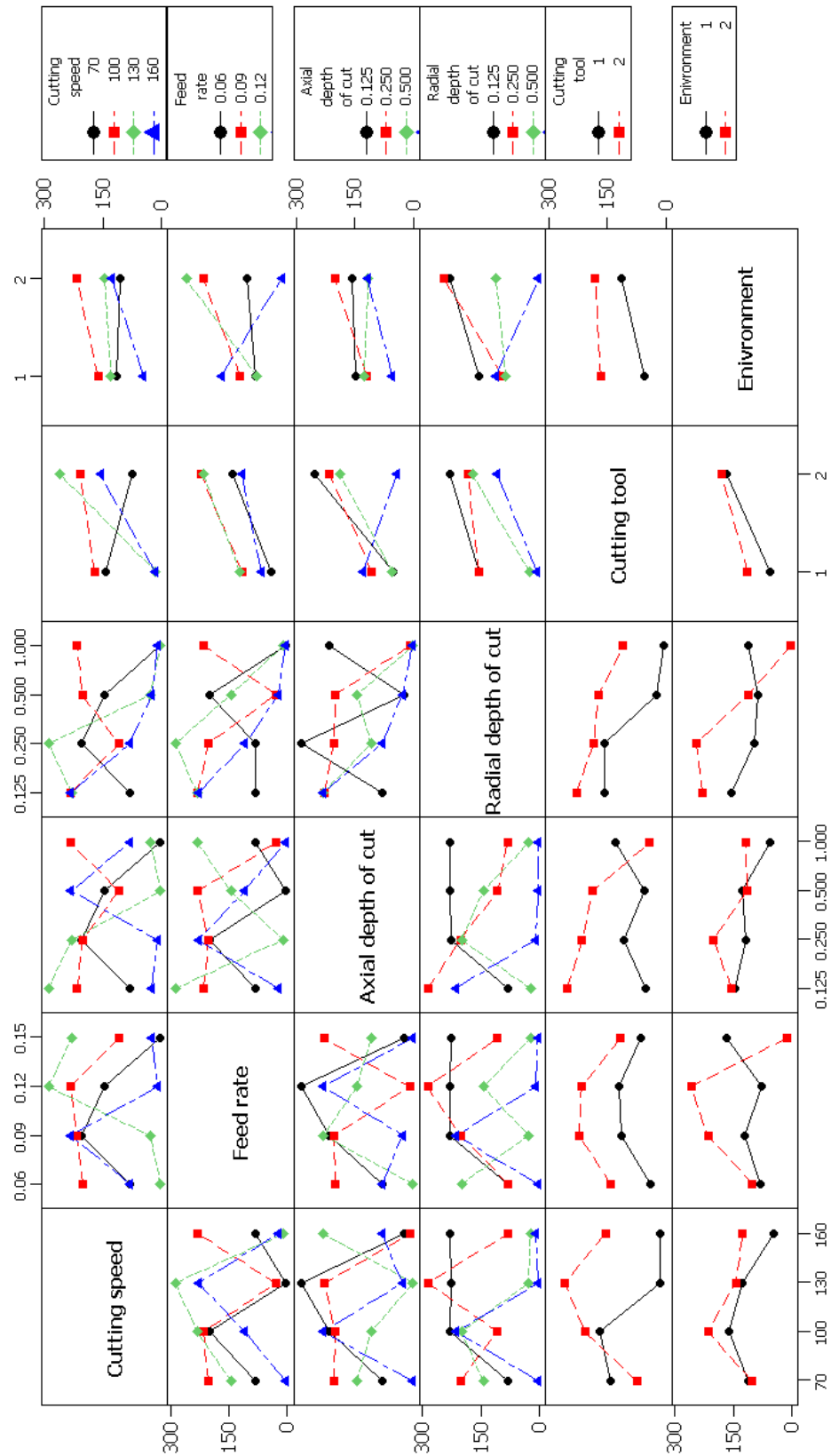
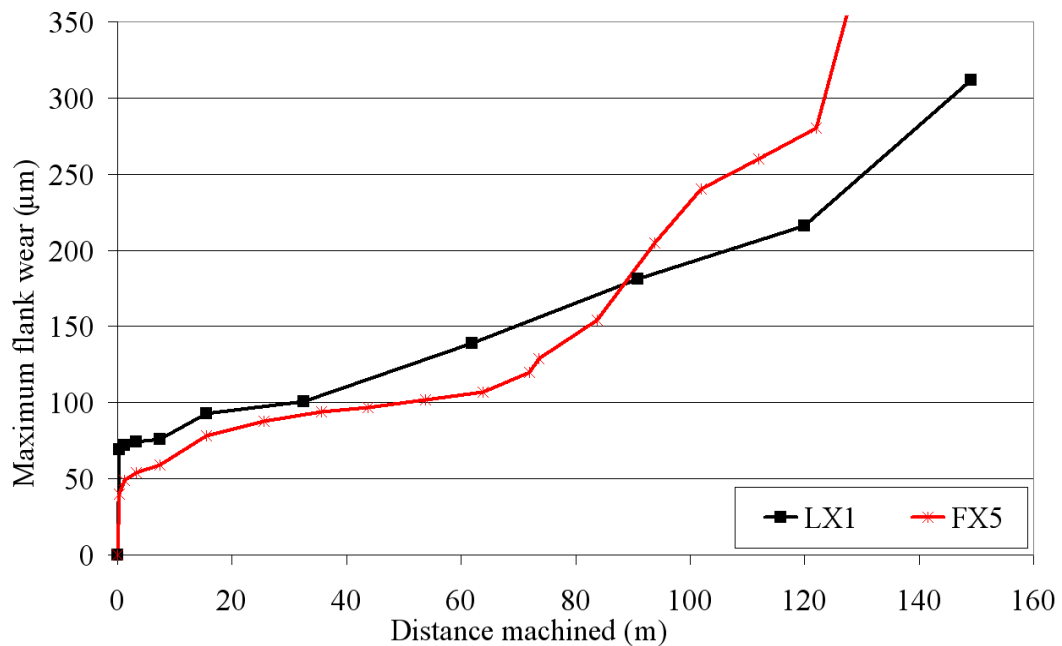


Figure C29: Interactions plot for distance machined

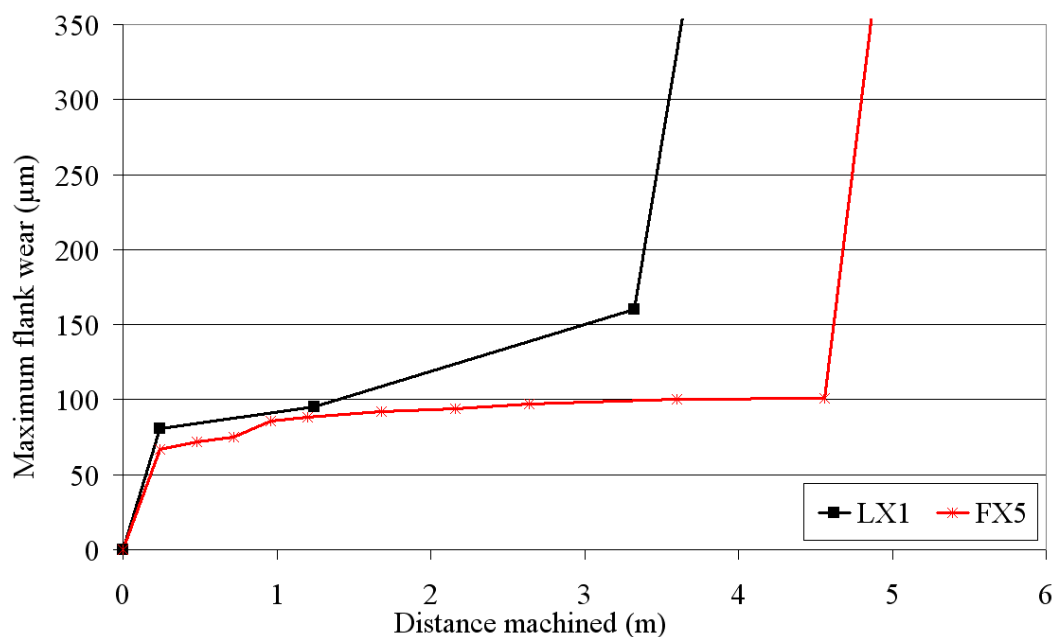
Figure C30 shows maximum flank wear against distance machined for the replication of Test 3 conducted using the Matsuura FX5 machining centre.



Test 3: $v=70\text{m/min}$, $f=0.12\text{mm/tooth}$, $a=0.5\text{mm}$, $d=0.5\text{mm}$, IC903, HP

Figure C30: Maximum flank wear against distance machined for Test 3 (replication)

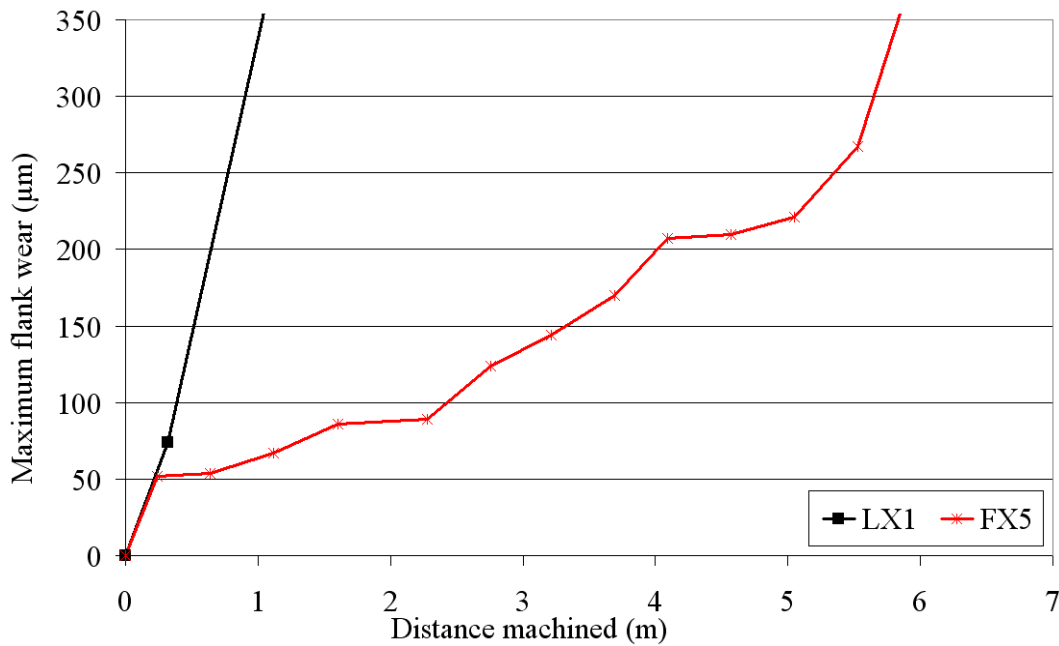
Figure C31 shows maximum flank wear against distance machined for the replication of Test 4 conducted using the Matsuura FX5 machining centre.



Test 4: $v=70\text{m/min}$, $f=0.15\text{mm/tooth}$, $a=1.0\text{mm}$, $d=1.0\text{mm}$, IC903, dry

Figure C31: Maximum flank wear against distance machined for Test 4 (replication)

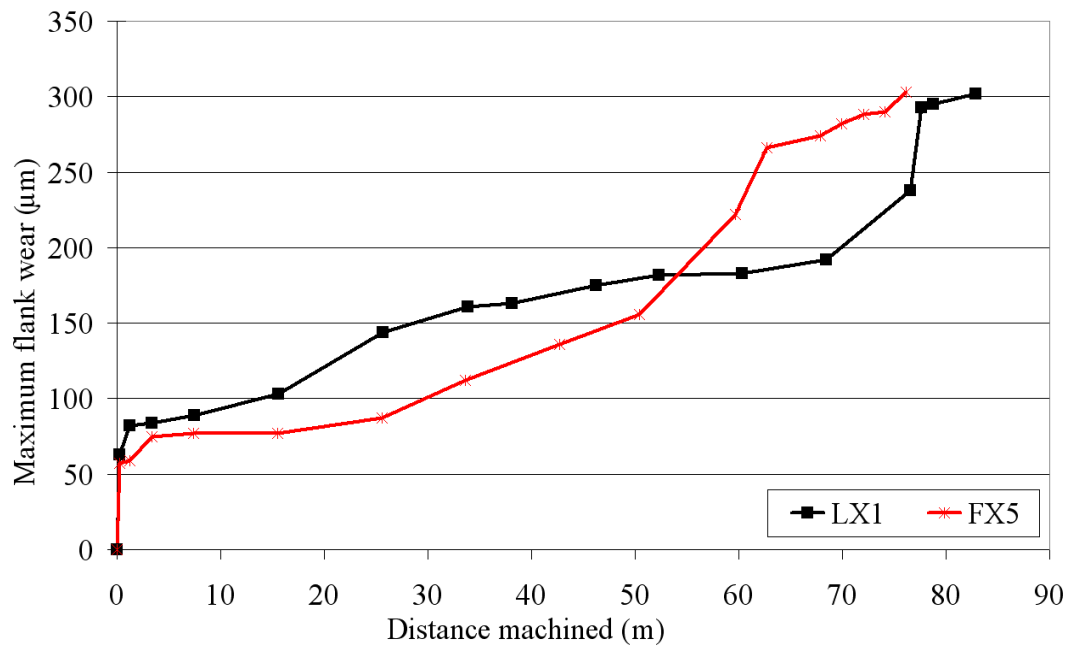
Figure C32 shows maximum flank wear against distance machined for the replication of Test 9 conducted using the Matsuura FX5 machining centre.



Test 9: $v=130\text{m/min}$, $f=0.06\text{mm/tooth}$, $a=0.5\text{mm}$, $d=1.0\text{mm}$, IC900, dry

Figure C32: Maximum flank wear against distance machined for Test 9 (replication)

Figure C33 shows maximum flank wear against distance machined for the replication of Test 13 conducted using the Matsuura FX5 machining centre.



Test 13: $v=160\text{m/min}$, $f=0.06\text{mm/tooth}$, $a=1.0\text{mm}$, $d=0.25\text{mm}$, IC903, HP

Figure C33: Maximum flank wear against distance machined for Test 13 (replication)

Figure C34 shows a bar chart detailing workpiece surface roughness Ra.

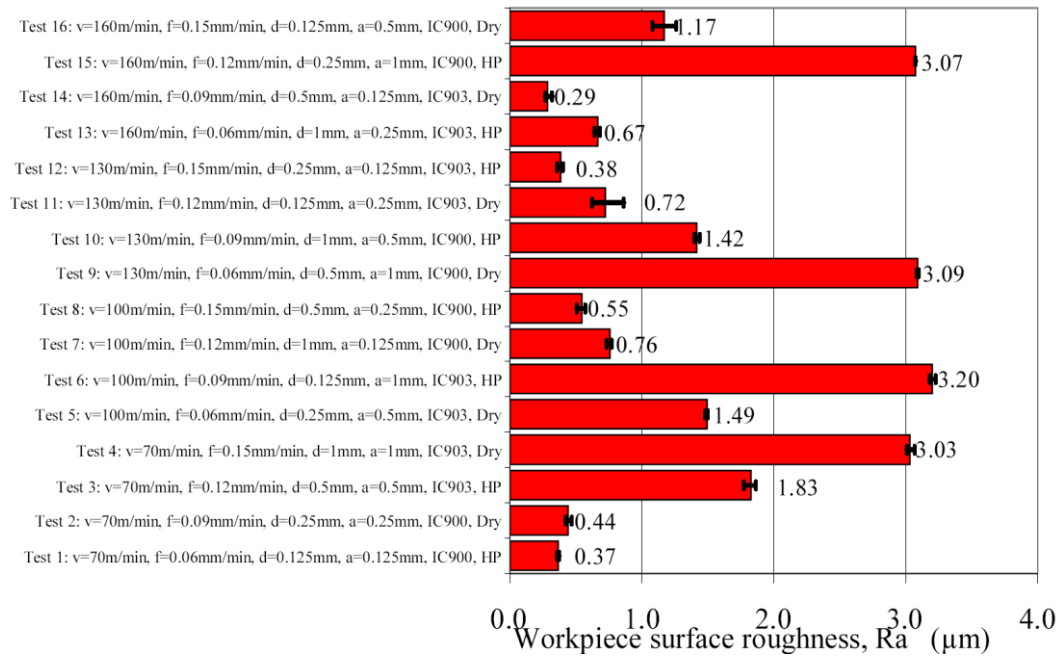
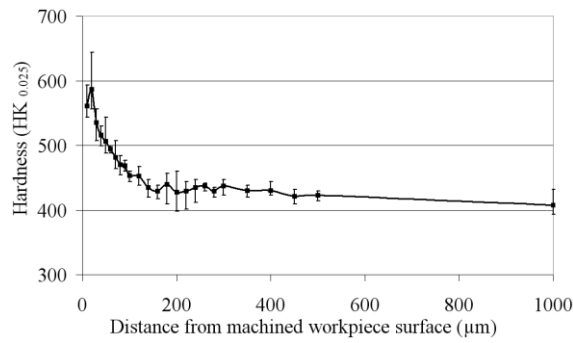
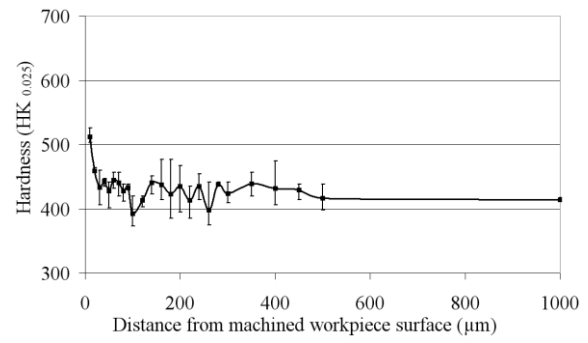


Figure C34: Workpiece surface roughness bar chart (Phase 1A)

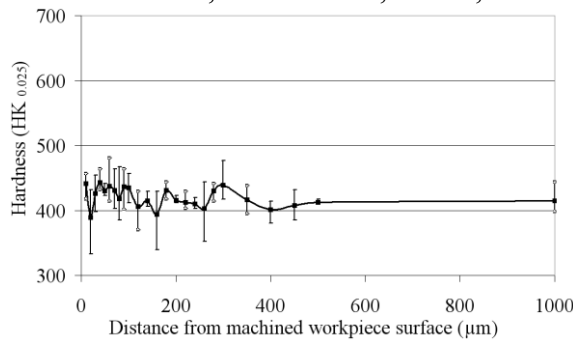
Figures C35 and C36 show individual hardness depth profiles.



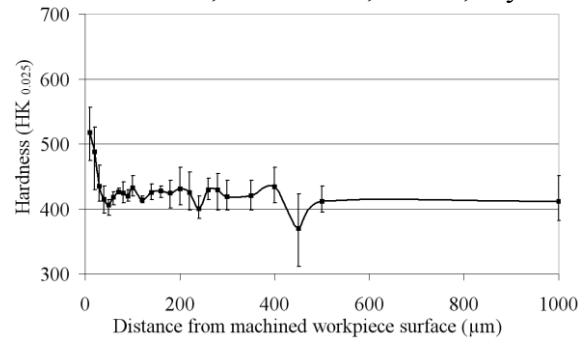
(a) Test 1: $v=70\text{m/min}$, $f=0.06\text{mm/tooth}$, $a=0.125\text{mm}$, $d=0.125\text{mm}$, IC900, HP



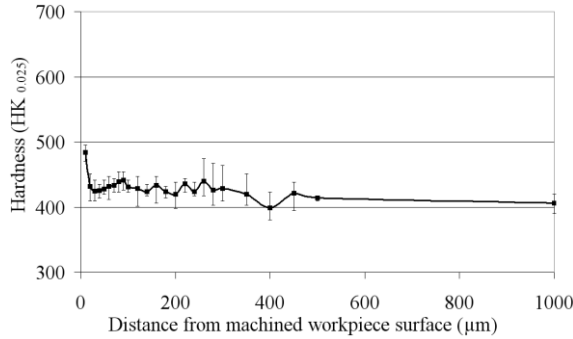
(b) Test 2: $v=70\text{m/min}$, $f=0.09\text{mm/tooth}$, $a=0.25\text{mm}$, $d=0.25\text{mm}$, IC900, dry



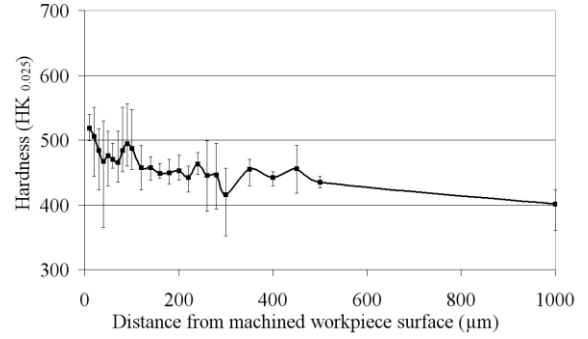
(c) Test 3: $v=70\text{m/min}$, $f=0.12\text{mm/tooth}$, $a=0.5\text{mm}$, $d=0.5\text{mm}$, IC903, HP



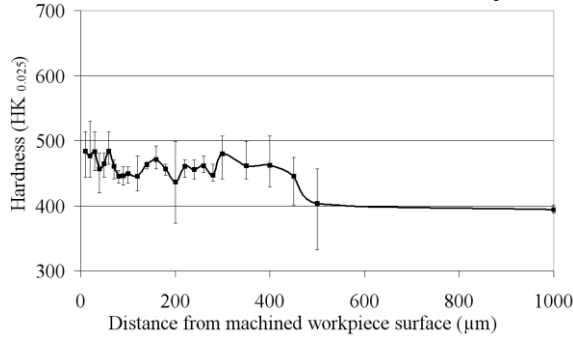
(d) Test 4: $v=70\text{m/min}$, $f=0.15\text{mm/tooth}$, $a=1.0\text{mm}$, $d=1.0\text{mm}$, IC903, dry



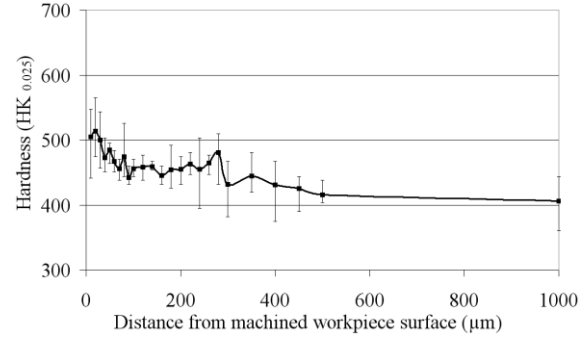
(e) Test 5: $v=100\text{m/min}$, $f=0.06\text{mm/tooth}$, $a=0.25\text{mm}$, $d=0.5\text{mm}$, IC903, dry



(f) Test 6: $v=100\text{m/min}$, $f=0.09\text{mm/tooth}$, $a=0.125\text{mm}$, $d=1.0\text{mm}$, IC903, HP

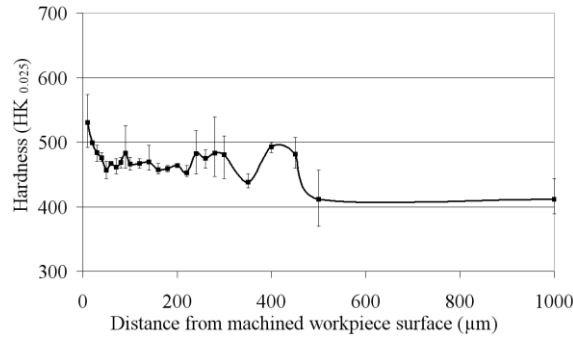


(g) Test 7: $v=100\text{m/min}$, $f=0.12\text{mm/tooth}$, $a=1.0\text{mm}$, $d=0.125\text{mm}$, IC900, dry

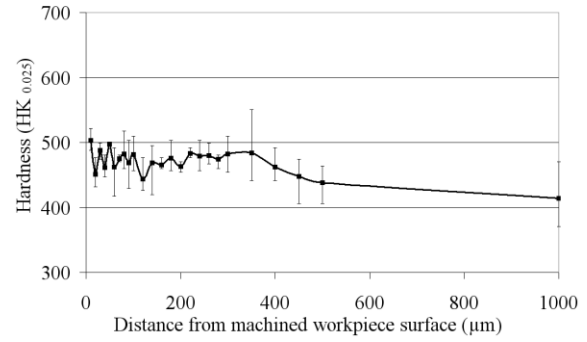


(h) Test 8: $v=100\text{m/min}$, $f=0.15\text{mm/tooth}$, $a=0.5\text{mm}$, $d=0.25\text{mm}$, IC900, HP

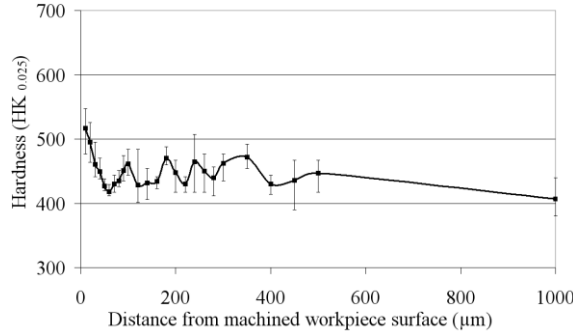
Figure C35: Individual microhardness profiles for Tests 1 to 8 (Phase 1A)



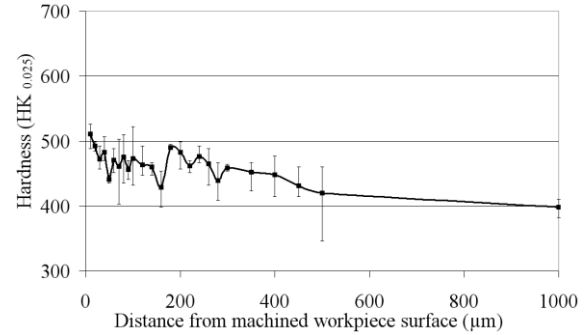
(a) Test 9: $v=130\text{m/min}$, $f=0.06\text{mm/tooth}$, $a=0.5\text{mm}$, $d=1.0\text{mm}$, IC900, dry



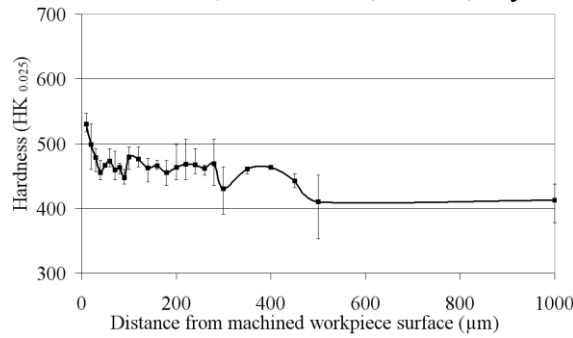
(b) Test 10: $v=130\text{m/min}$, $f=0.09\text{mm/tooth}$, $a=1.0\text{mm}$, $d=0.5\text{mm}$, IC900, HP



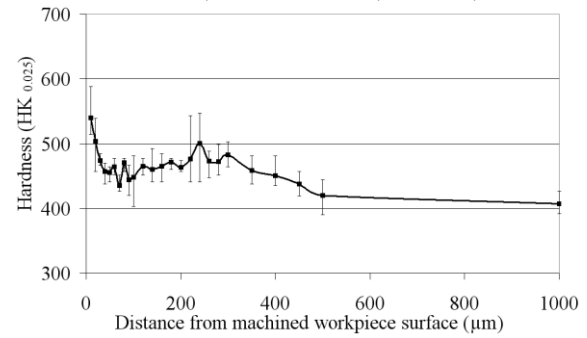
(c) Test 11: $v=130\text{m/min}$, $f=0.12\text{mm/tooth}$, $a=0.125\text{mm}$, $d=0.25\text{mm}$, IC903, dry



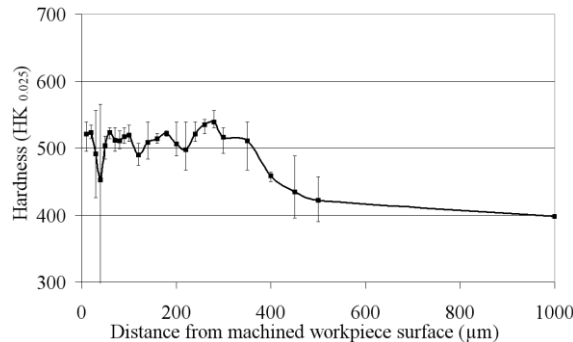
(d) Test 12: $v=130\text{m/min}$, $f=0.15\text{mm/tooth}$, $a=0.25\text{mm}$, $d=0.125\text{mm}$, IC903, HP



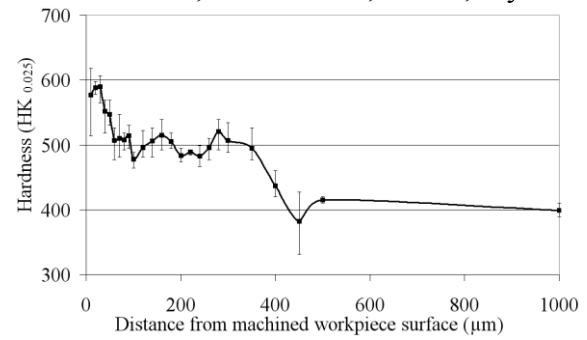
(e) Test 13: $v=160\text{m/min}$, $f=0.06\text{mm/tooth}$, $a=1.0\text{mm}$, $d=0.25\text{mm}$, IC903, HP



(f) Test 14: $v=160\text{m/min}$, $f=0.09\text{mm/tooth}$, $a=0.5\text{mm}$, $d=0.125\text{mm}$, IC903, dry



(g) Test 15: $v=160\text{m/min}$, $f=0.12\text{mm/tooth}$, $a=0.25\text{mm}$, $d=1.0\text{mm}$, IC900, HP



(h) Test 16: $v=160\text{m/min}$, $f=0.15\text{mm/tooth}$, $a=0.125\text{mm}$, $d=0.5\text{mm}$, IC900, dry

Figure C36: Individual microhardness profiles for Tests 9 to 16 (Phase 1A)

b) Phase 1B: Comparison of the machinability of Ti-45Al-8Nb-0.2C and Ti-45Al-2Mn-2Nb +0.8%vol. TiB₂

Figures C37 and C38 show graphs of maximum flank wear against machining time and volume of workpiece material removed.

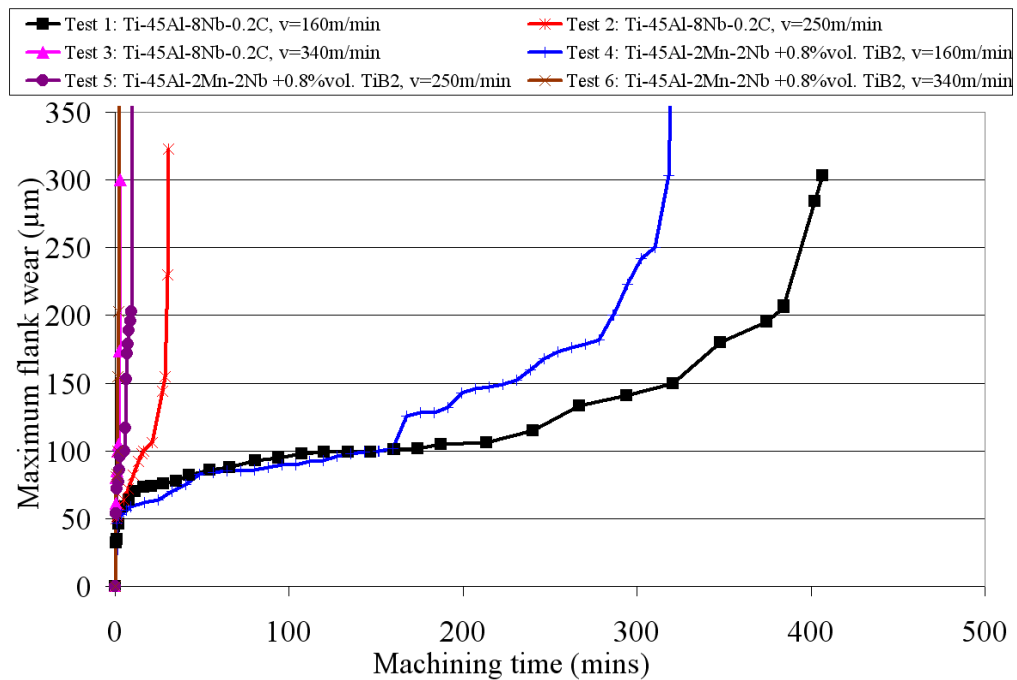


Figure C37: Maximum flank wear against machining time (Phase 1B)

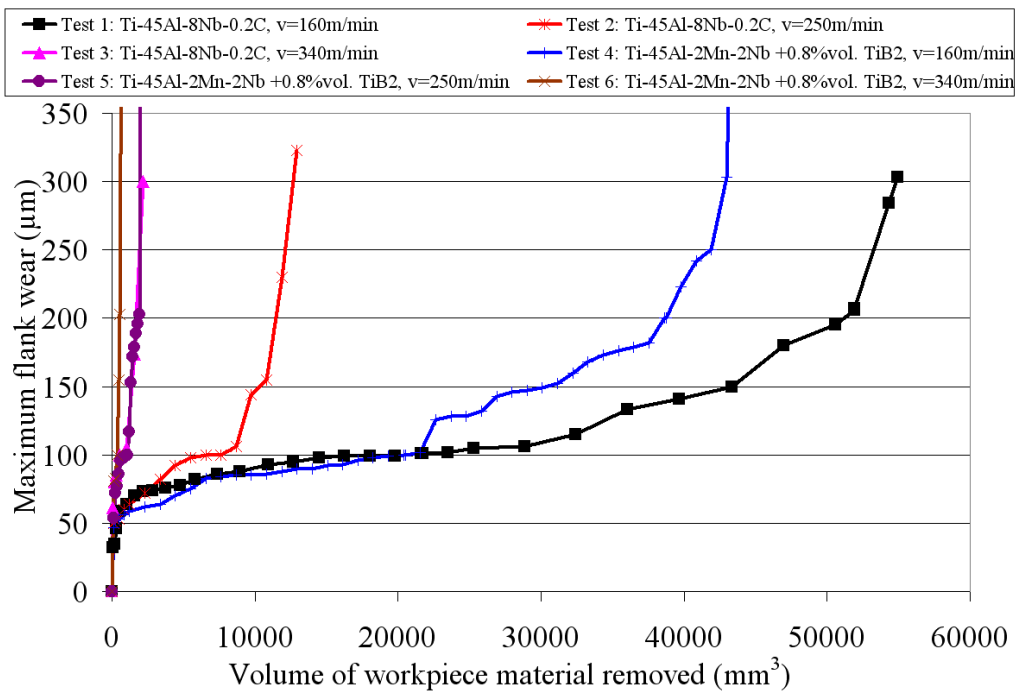
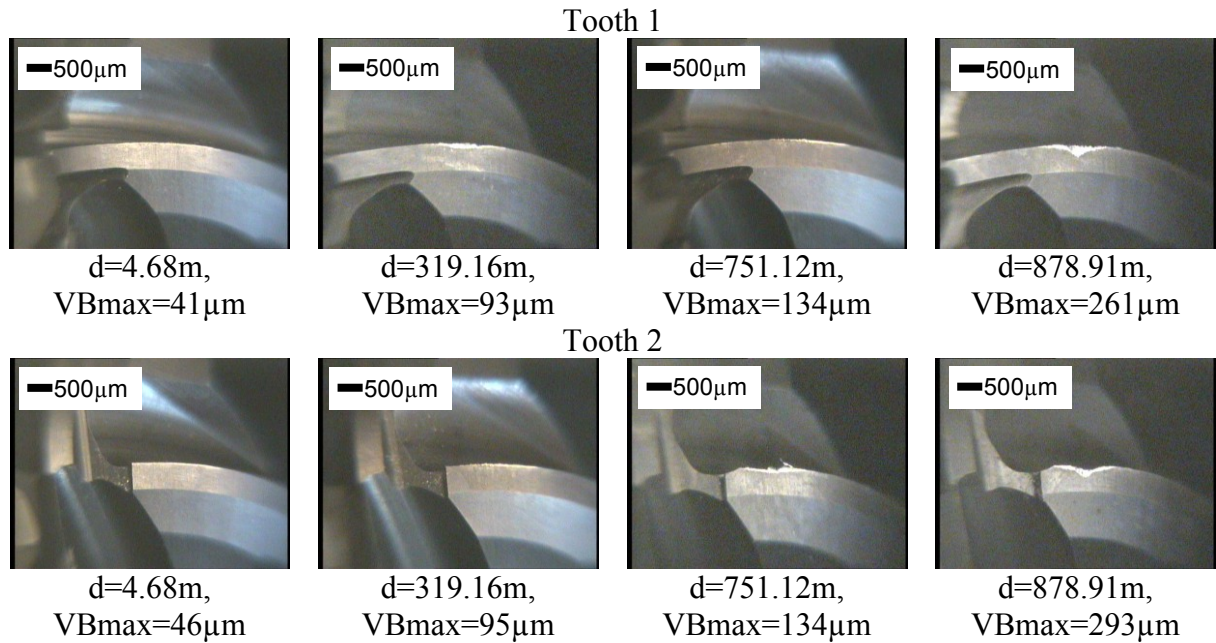


Figure C38: Maximum flank wear against volume of workpiece material removed against (Phase 1B)

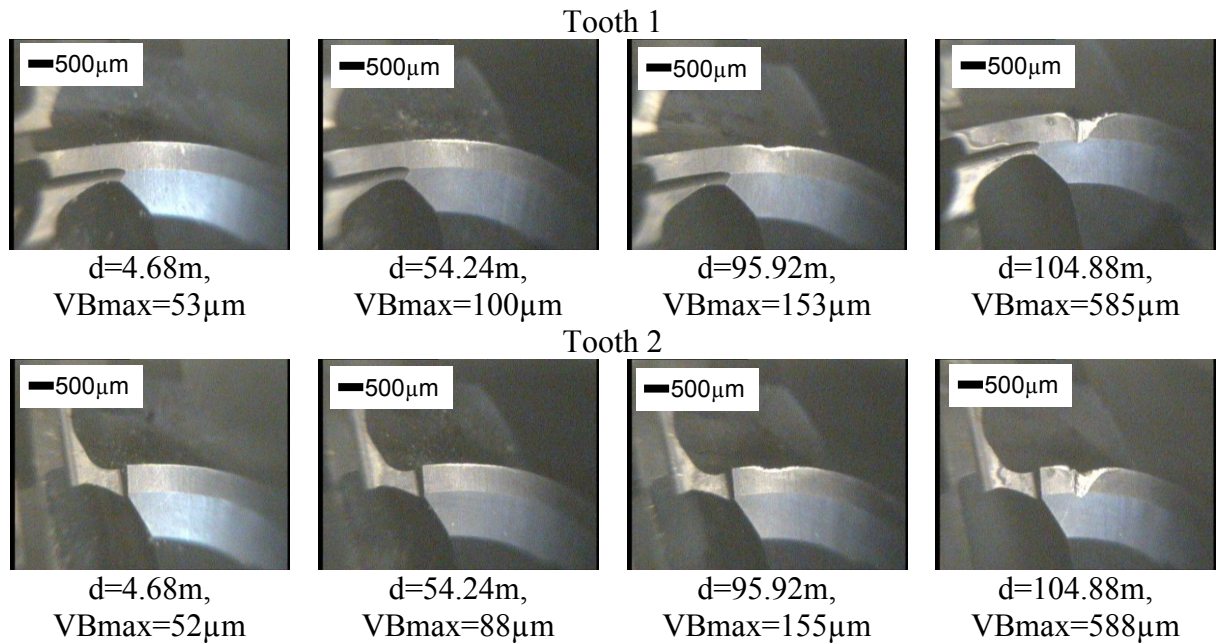
Figure C39 shows selected wear scar photographs for Test 1.



Test 1: Ti-45A-8Nb-0.2C, $v=160\text{m/min}$, IC903.

Figure C39: Test 1 wear scar photographs (Phase 1B)

Figure C40 shows selected wear scar photographs for Test 2.



Test 2: Ti-45A-8Nb-0.2C, $v=250\text{m/min}$, IC903

Figure C40: Test 2 wear scar photographs (Phase 1B)

Figure C41 shows selected wear scar photographs for Test 3.

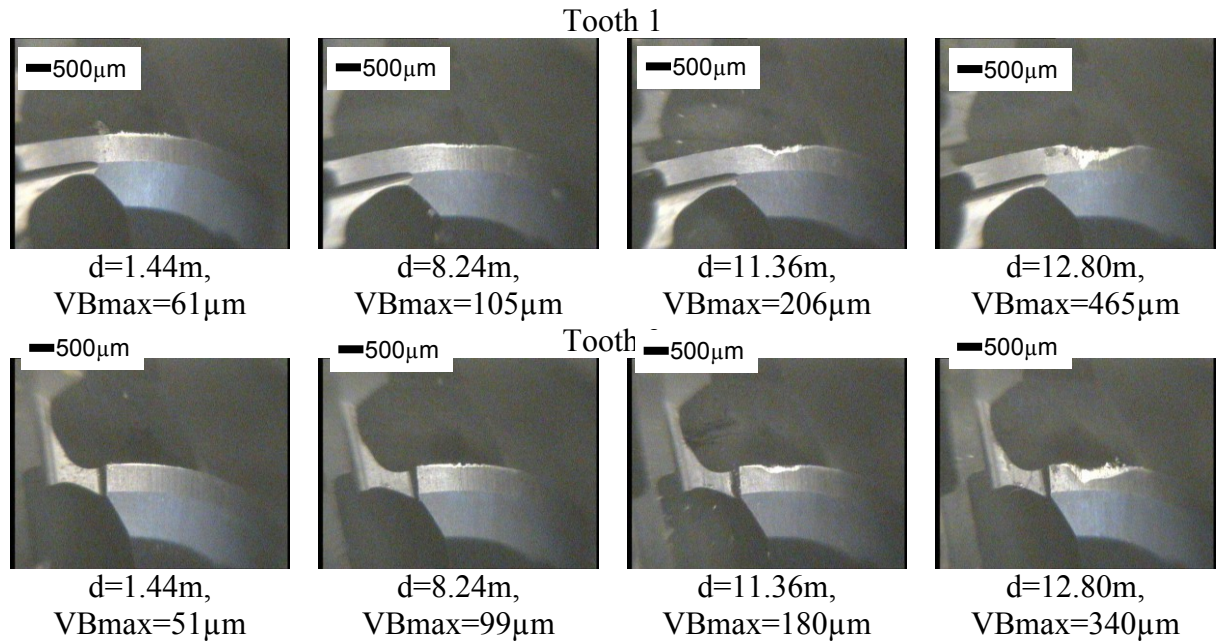


Figure C41: Test 3 wear scar photographs (Phase 1B)

Figure C42 shows selected wear scar photographs for Test 4.

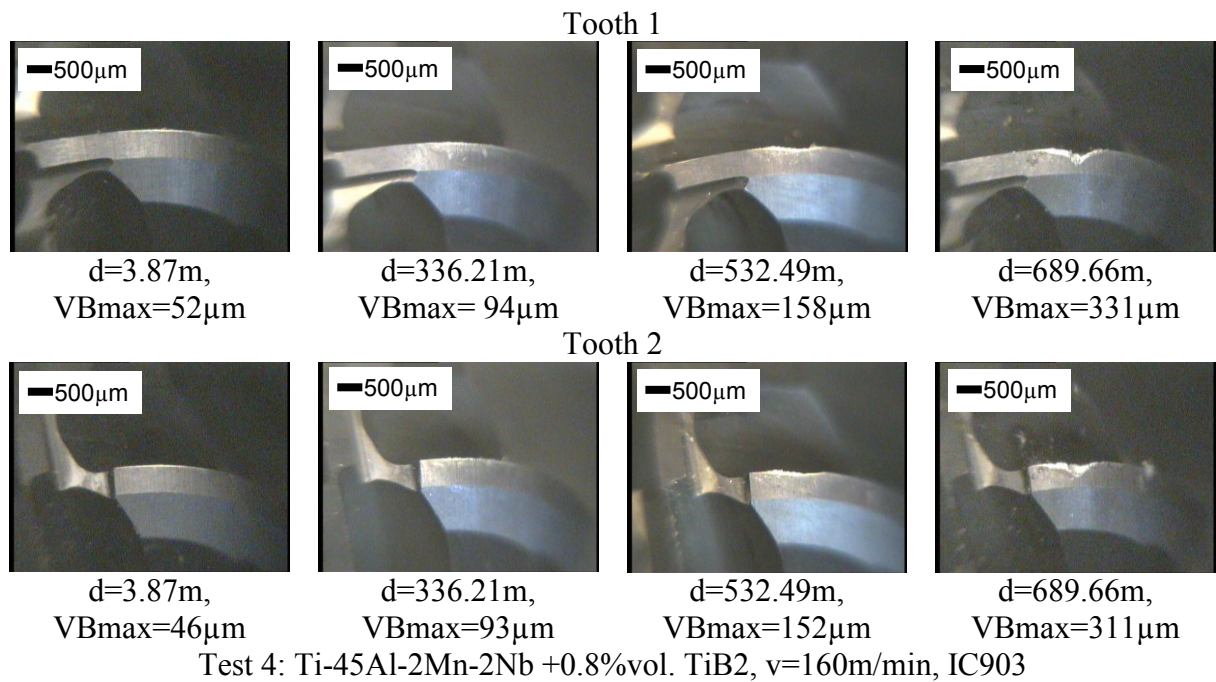


Figure C42: Test 4 wear scar photographs (Phase 1B)

Figure C43 shows selected wear scar photographs for Test 5.

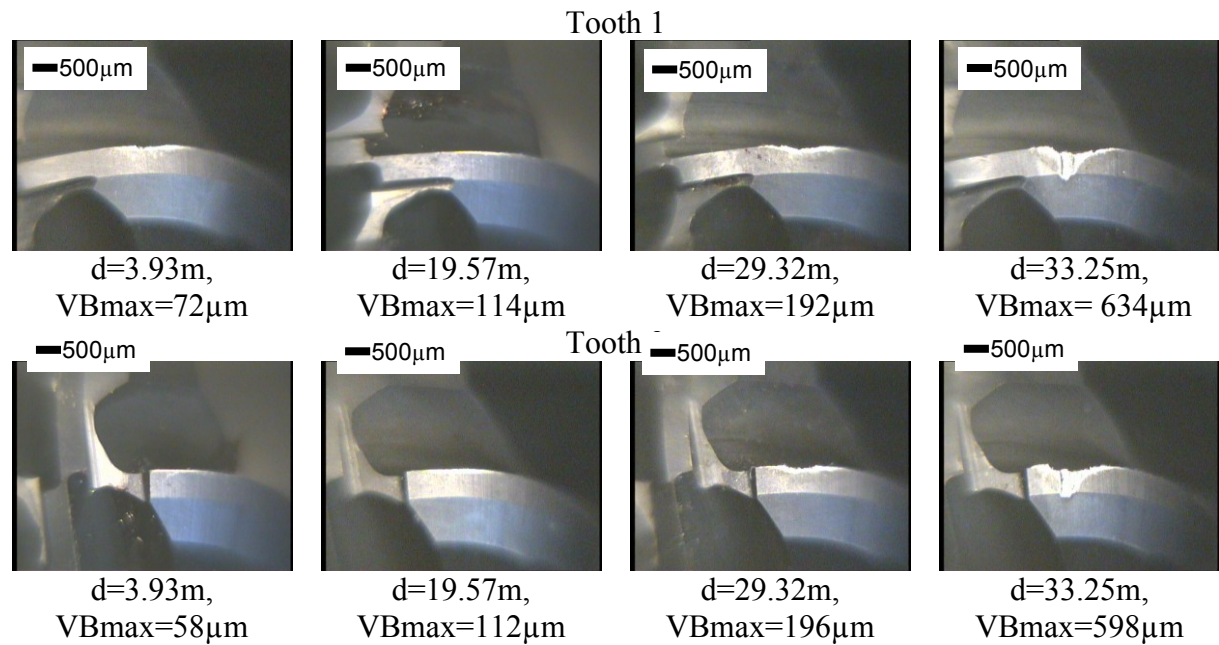


Figure C43: Test 5 wear scar photographs (Phase 1B)

Figure C44 shows selected wear scar photographs for Test 6.

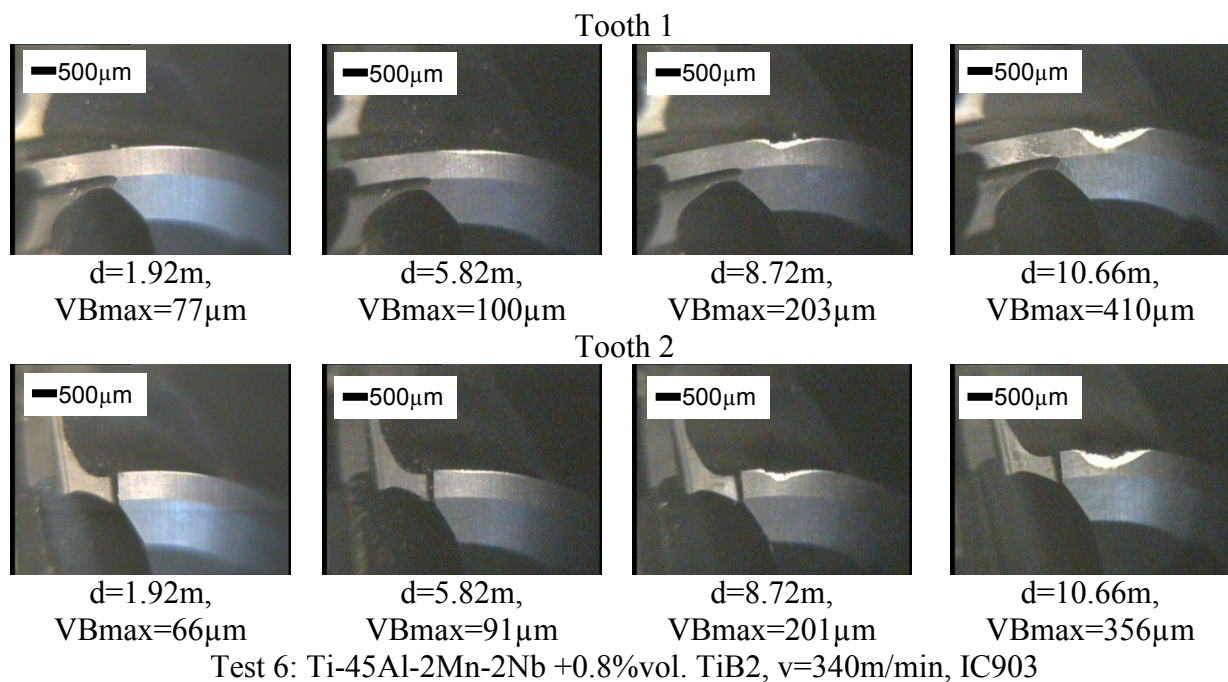


Figure C44: Test 6 wear scar photographs (Phase 1B)

Table C3 shows ANOVA table for machining time.

Source	S.S.	D.O.F.	M.S.S.	F _{calc}	PCR%
Workpiece material	11408	1	11408	-	-
Cutting speed	741908	2	370954	-	-
Workpiece material/cutting speed interaction	8973	2	4486	-	-
Error	-	0	-	-	-
Total	762288	23	-	-	-

Table C3: ANOVA table machining time (Phase 1B)

Table C4 shows ANOVA table for cutting temperature.

Source	S.S.	D.O.F.	M.S.S.	F _{calc}	PCR%
Maximum flank wear	8816.7	1	8816.7	-	-
Cutting speed	8373.0	2	4186.5	-	-
Maximum flank wear/cutting speed interaction	100.3	2	50.2	-	-
Error	-	-	-	-	-
Total	17290.0	23	-	-	-

Table C4: ANOVA table for cutting temperature (Phase 1B)

Figure C45 shows force and maximum flank wear against distance machined for Test 2.

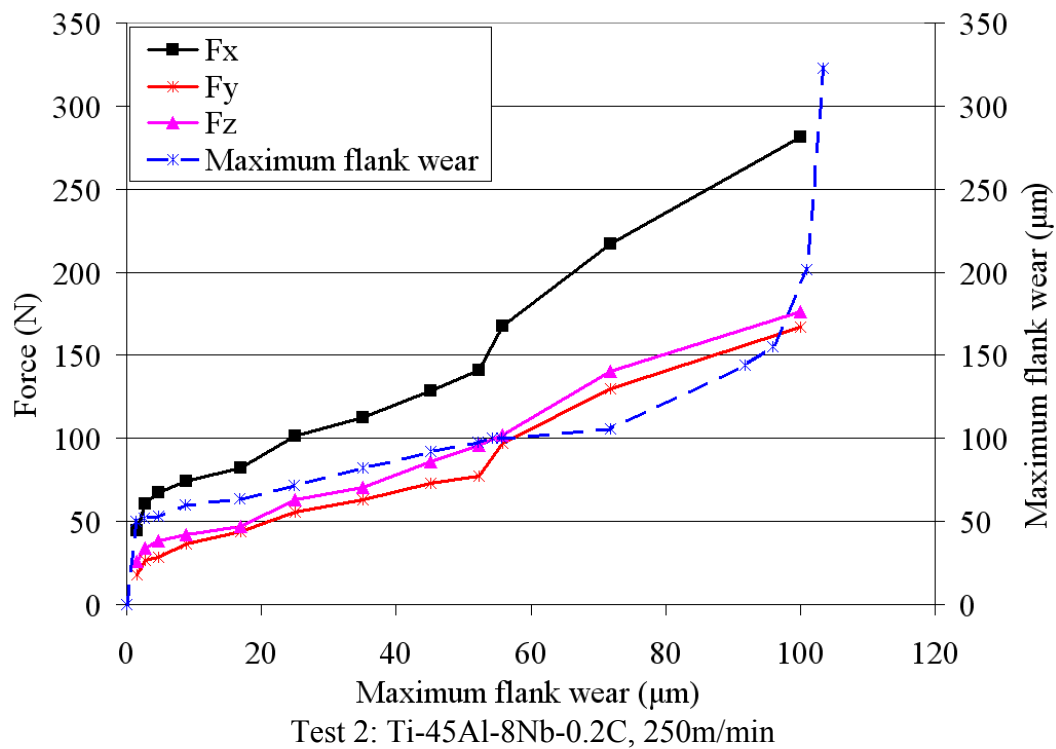
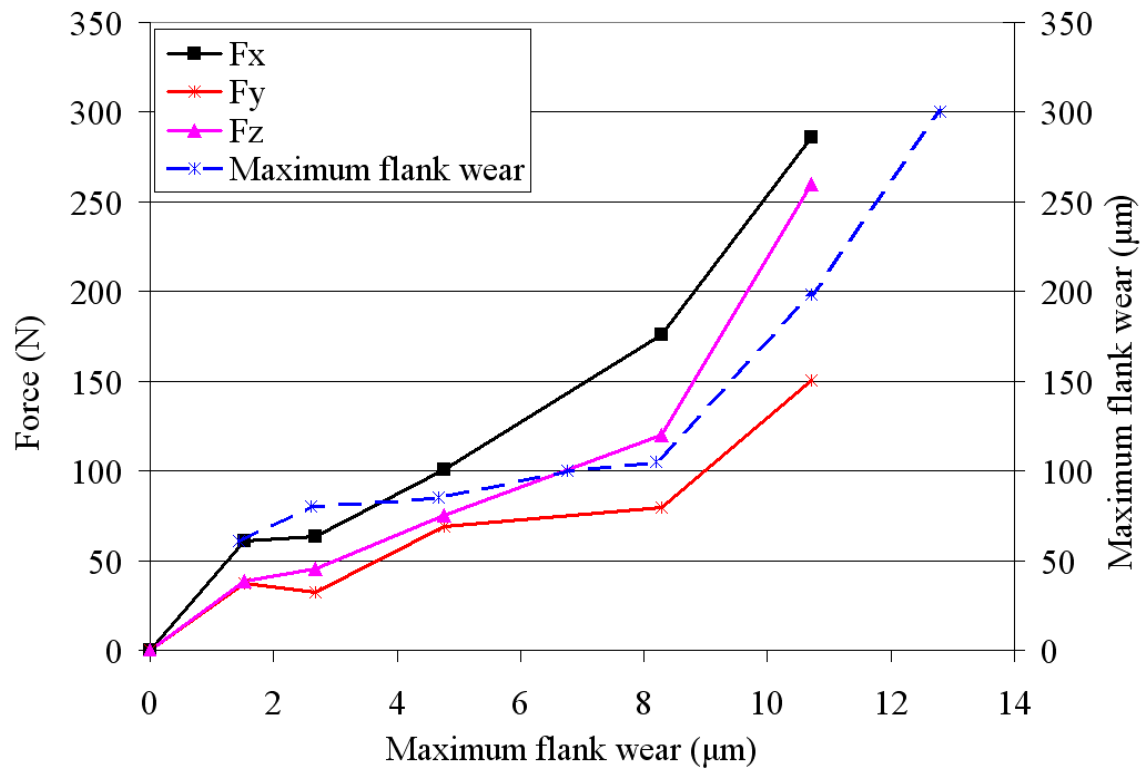


Figure C45: Graph showing cutting forces and maximum flank wear against distance machined for Test 2

Figure C46 shows force and maximum flank wear against distance machined for Test 3.



Test 3: Ti-45Al-8Nb-0.2C, 340m/min

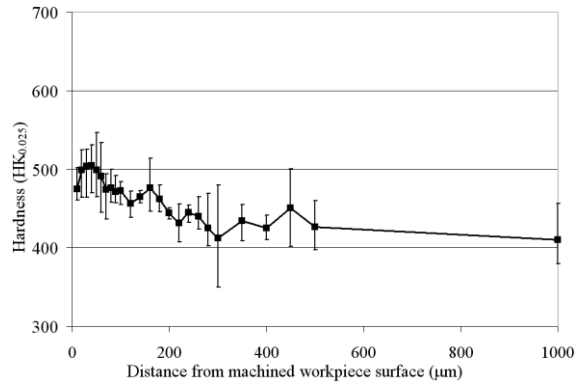
Figure C46: Graph showing cutting forces and maximum flank wear against distance machined for Test 3

Table C5 shows ANOVA table for workpiece surface roughness Ra

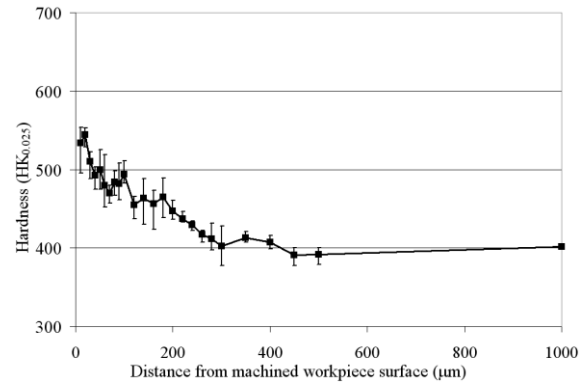
Source	S.S.	D.O.F.	M.S.S.	F _{calc}	PCR%
Workpiece material	0.036817	1	0.036817	-	-
Cutting speed	0.467158	2	0.233579	-	-
Flank wear	0.443367	3	0.147789	-	-
Workpiece material/cutting speed interaction	0.025008	2	0.012504	-	-
Cutting speed/flank wear interaction	0.003350	3	0.001117	-	-
Workpiece material/flank wear interaction	0.254708	6	0.042451	-	-
Workpiece material/cutting speed/flank wear interaction	0.067325	6	0.011221	-	-
Error	-	0	-	-	-
Total	1.297733	23	-	-	-

Table C5: ANOVA table for workpiece surface roughness Ra (Phase 1B)

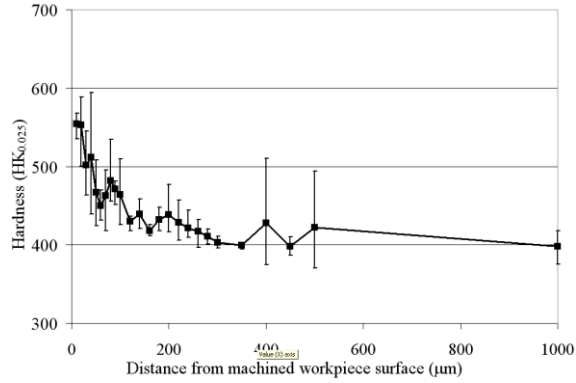
Figures C47 to C50 show individual microhardness profiles for all tests.



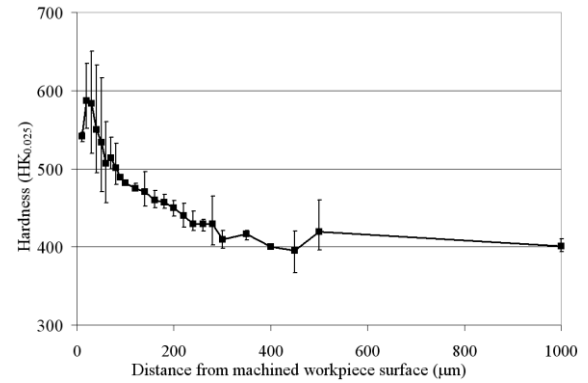
(a) Test 1: Ti-45Al-8Nb-0.2C, $v=160\text{m/min}$, $\text{VBmax}=0\mu\text{m}$



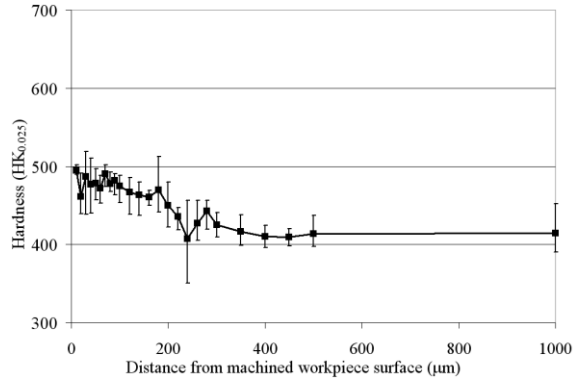
(b) Test 1: Ti-45Al-8Nb-0.2C, $v=160\text{m/min}$, $\text{VBmax}=100\mu\text{m}$



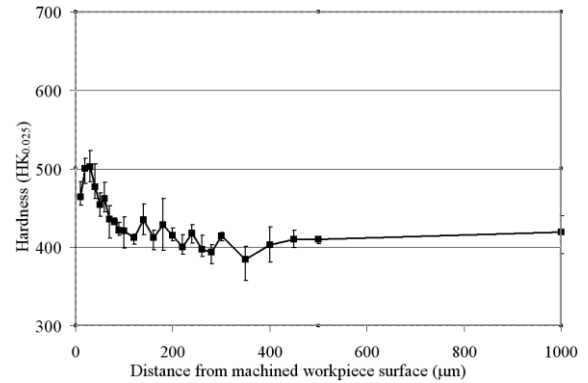
(c) Test 1: Ti-45Al-8Nb-0.2C, $v=160\text{m/min}$, $\text{VBmax}=200\mu\text{m}$



(d) Test 1: Ti-45Al-8Nb-0.2C, $v=160\text{m/min}$, $\text{VBmax}=300\mu\text{m}$

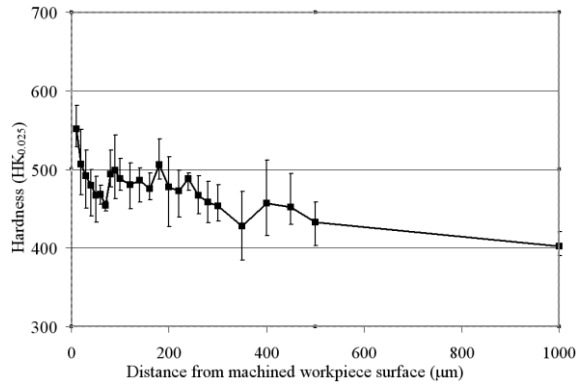


(e) Test 2: Ti-45Al-8Nb-0.2C, $v=250\text{m/min}$, $\text{VBmax}=0\mu\text{m}$

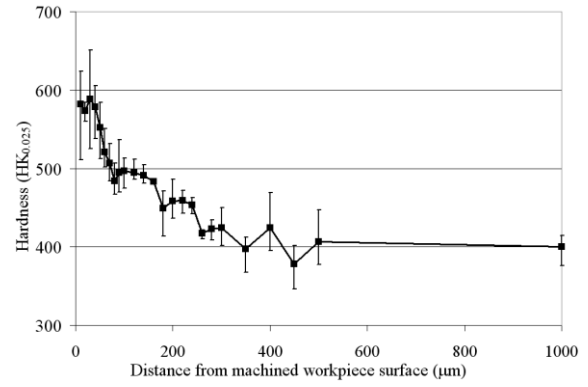


(f) Test 2: Ti-45Al-8Nb-0.2C, $v=250\text{m/min}$, $\text{VBmax}=100\mu\text{m}$

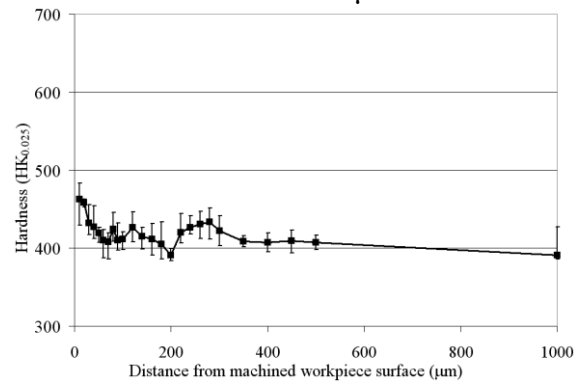
Figure C47: Individual microhardness profiles for Tests 1 and 2 (Phase 1B)



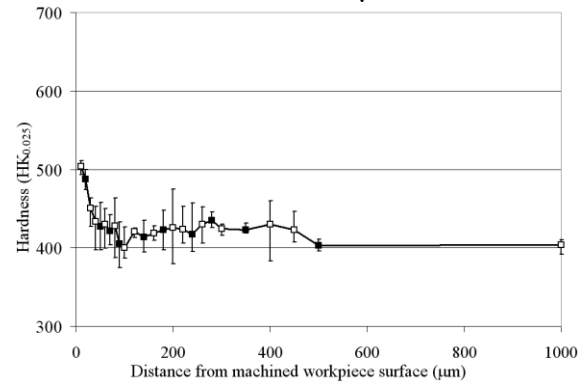
(a) Test 2: Ti-45Al-8Nb-0.2C, $v=250\text{m/min}$, $VB_{\text{max}}=200\mu\text{m}$



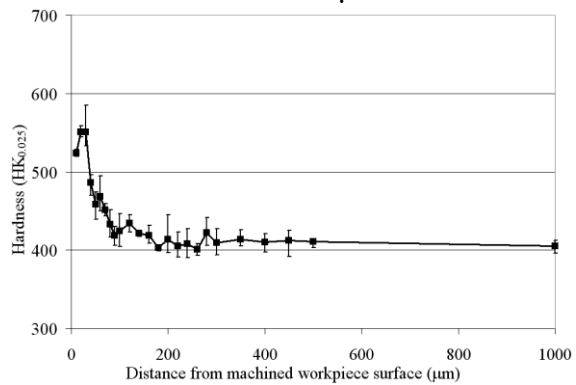
(b) Test 2: Ti-45Al-8Nb-0.2C, $v=250\text{m/min}$, $VB_{\text{max}}=300\mu\text{m}$



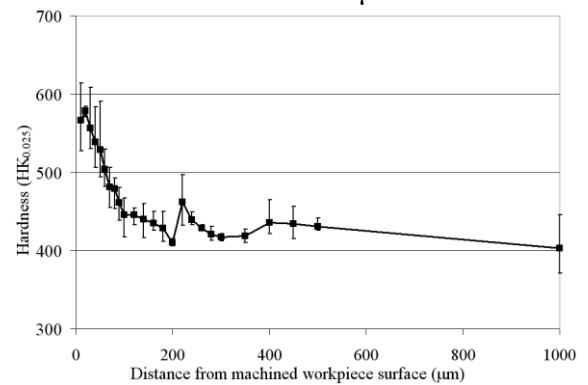
(c) Test 3: Ti-45Al-8Nb-0.2C, $v=340\text{m/min}$, $VB_{\text{max}}=0\mu\text{m}$



(d) Test 3: Ti-45Al-8Nb-0.2C, $v=340\text{m/min}$, $VB_{\text{max}}=100\mu\text{m}$

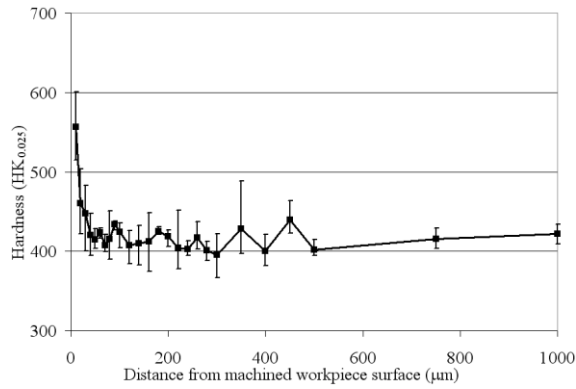


(e) Test 3: Ti-45Al-8Nb-0.2C, $v=340\text{m/min}$, $VB_{\text{max}}=200\mu\text{m}$

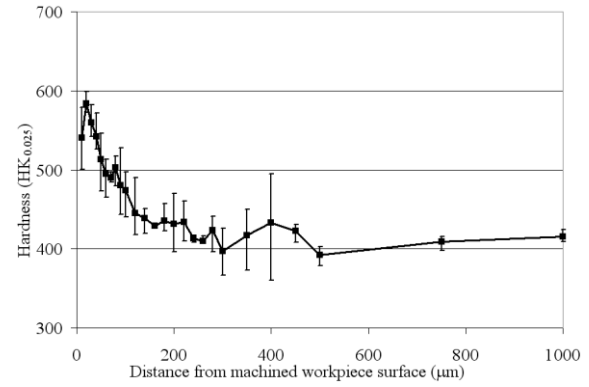


(f) Test 3: Ti-45Al-8Nb-0.2C, $v=340\text{m/min}$, $VB_{\text{max}}=300\mu\text{m}$

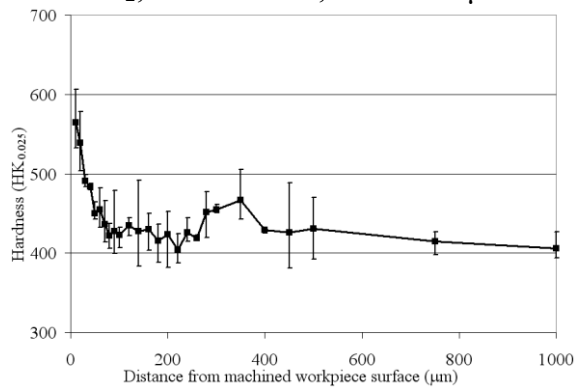
Figure C48: Individual microhardness profiles for Tests 2 and 3 (Phase 1B)



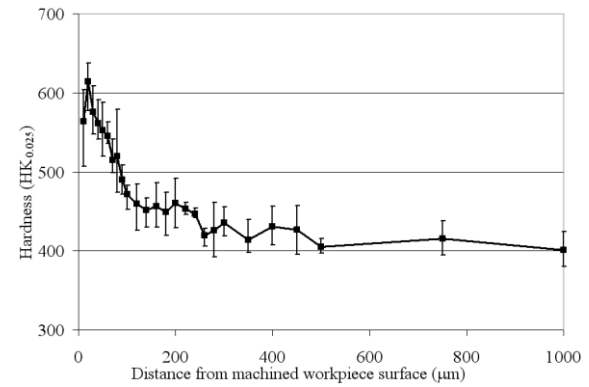
(a) Test 4: Ti-45Al-2Mn-2Nb +0.8%vol. TiB₂, v=160m/min, VBmax=0μm



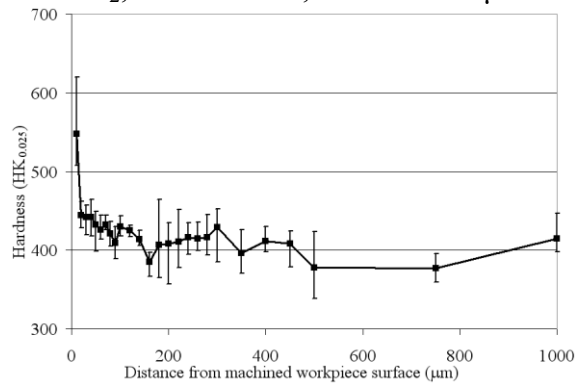
(b) Test 4: Ti-45Al-2Mn-2Nb +0.8%vol. TiB₂, v=160m/min, VBmax=100μm



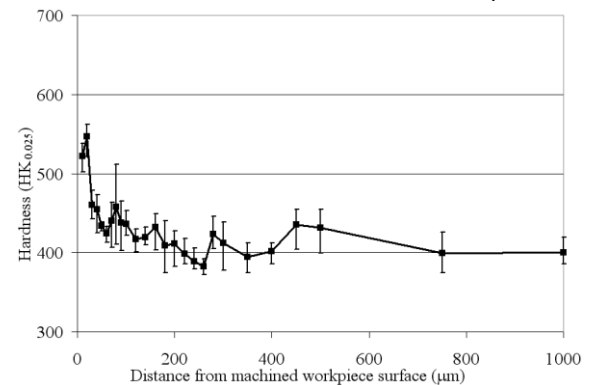
(c) Test 4: Ti-45Al-2Mn-2Nb +0.8%vol. TiB₂, v=160m/min, VBmax=200μm



(d) Test 4: Ti-45Al-2Mn-2Nb +0.8%vol. TiB₂, v=160m/min, VBmax=300μm

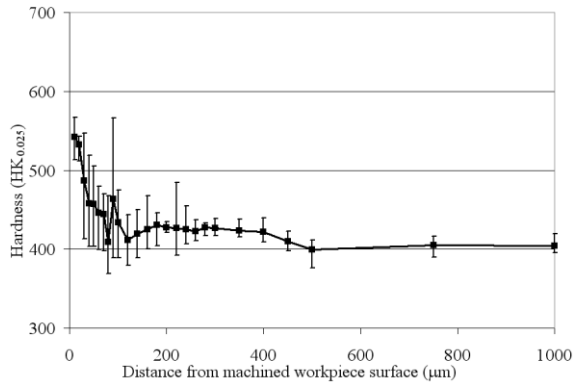


(e) Test 5: Ti-45Al-2Mn-2Nb +0.8%vol. TiB₂, v=250m/min, VBmax=0μm

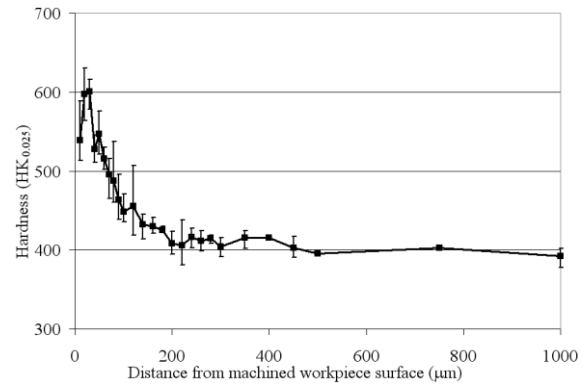


(f) Test 5: Ti-45Al-2Mn-2Nb +0.8%vol. TiB₂, v=250m/min, VBmax=100μm

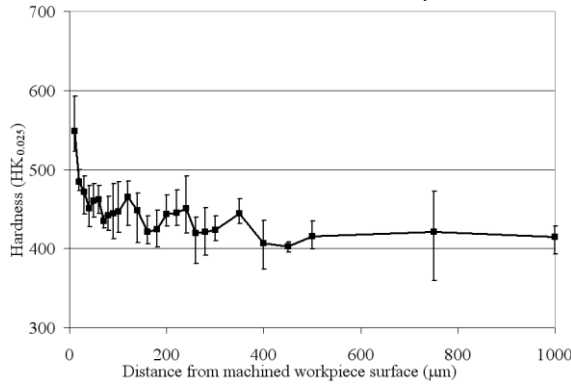
Figure C49: Individual microhardness profiles for Tests 4 and 5 (Phase 1B)



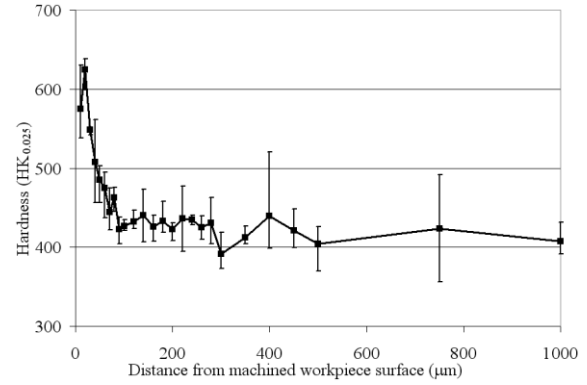
(a) Test 5: Ti-45Al-2Mn-2Nb +0.8%vol. TiB₂, v=250m/min, VBmax=200μm



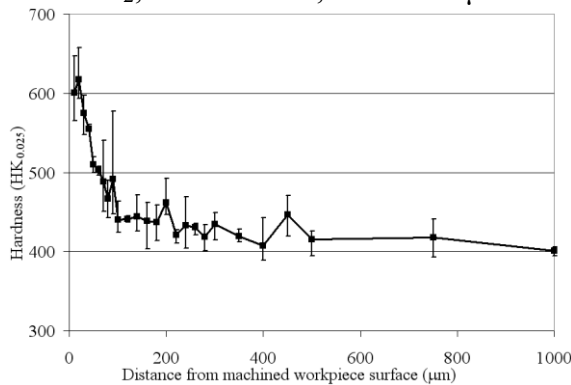
(b) Test 5: Ti-45Al-2Mn-2Nb +0.8%vol. TiB₂, v=250m/min, VBmax=300μm



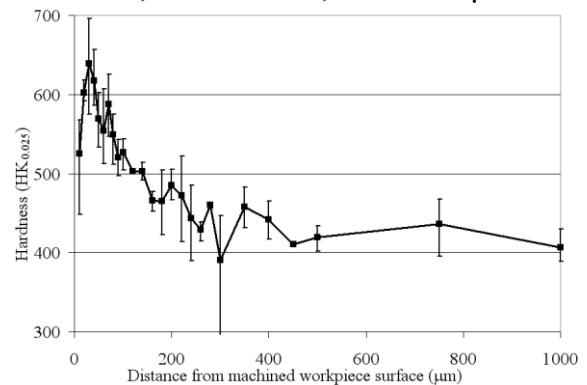
(c) Test 6: Ti-45Al-2Mn-2Nb +0.8%vol. TiB₂, v=340m/min, VBmax=0μm



(d) Test 6: Ti-45Al-2Mn-2Nb +0.8%vol. TiB₂, v=340m/min, VBmax=0μm



(e) Test 6: Ti-45Al-2Mn-2Nb +0.8%vol. TiB₂, v=340m/min, VBmax=0μm



(f) Test 6: Ti-45Al-2Mn-2Nb +0.8%vol. TiB₂, v=340m/min, VBmax=0μm

Figure C50: Individual microhardness profiles for Tests 5 and 6 (Phase 1B)

c) Phase 1C: High speed ball nose end milling of burn resistant titanium alloy (BuRTi)

Tables C6 and C7 show ANOVA tables for material removed and machining time

	S.S.	D.O.F.	M.S.S.	F_{calc}	PCR%
Cutting tool	6828822	1	6828822	0.86	0
Feed rate	1648247	1	1648247	0.21	0
Axial depth of cut	5600786	1	5600786	0.71	0
Radial depth of cut	4505627	1	4505627	0.57	0
Environment	16305619	1	16305619	2.06	17.4
Orientation	5484258	1	5484258	0.69	0
Error	7902797	1	7902797	-	82.6
Total	48276156	7	-	-	-

Table C6: ANOVA table for material removed (Phase 1C)

	S.S.	D.O.F.	M.S.S.	F_{calc}	PCR%
Cutting tool	292.5	1	292.5	1.57	5.9
Feed rate	198.5	1	198.5	1.06	0.7
Axial depth of cut	105.4	1	105.4	0.56	0.0
Radial depth of cut	314.2	1	314.2	1.68	7.1
Environment	497.4	1	497.4	2.66	17.2
Orientation	209.8	1	209.8	1.12	1.3
Error	186.7	1	186.7	-	67.9
Total	1804.5	7	-	-	-

Table C7: ANOVA table for machining time (Phase 1C)

Table C8 shows the ANOVA table for maximum resultant force with a new tool.

	S.S.	D.O.F.	M.S.S.	F_{calc}	PCR%
Cutting tool	150.22	1	150.22	0.02	0.00
Feed rate	8474.48	1	8474.48	1.29	8.40
Axial depth of cut	1055.98	1	1055.98	0.16	0.00
Radial depth of cut	5997.62	1	5997.62	0.91	0.00
Environment	11.48	1	11.48	0.00	0.00
Orientation	337.91	1	337.91	0.05	0.00
Error	6576.25	1	6576.25	-	91.60
Total	22603.93	7	-	-	-

Table C8: ANOVA table for maximum resultant force with a new tool (Phase 1C)

Table C9 shows the ANOVA table for maximum resultant force with a worn tool (VBmax=300μm)

	S.S.	D.O.F.	M.S.S.	F_{calc}	PCR%
Cutting tool	44363.79	1	44363.79	4.02	18.12
Feed rate	4557.92	1	4557.92	0.41	0.00
Axial depth of cut	37641.89	1	37641.89	3.41	14.47
Radial depth of cut	51528.91	1	51528.91	4.67	22.02
Environment	13210.93	1	13210.93	1.20	1.19
Orientation	21656.62	1	21656.62	1.96	5.78
Error	11023.89	1	11023.89	-	38.43
Total	183983.94	7	-	-	-

Table C9: ANOVA table for maximum resultant force with a worn tool (VBmax=300μm) (Phase 1C)

Table C10 shows the ANOVA table for workpiece surface roughness parallel to the feed direction.

	S.S.	D.O.F.	M.S.S.	F_{calc}	PCR%
Cutting tool	0.234	1	0.23	124.61	1.4
Feed rate	14.383	1	14.38	7647.12	88.9
Axial depth of cut	0.027	1	0.03	14.12	0.2
Radial depth of cut	0.138	1	0.14	73.38	0.8
Environment	1.380	1	1.38	733.53	8.5
Orientation	0.013	1	0.01	6.75	0.1
Error	0.002	1	0.00		0.1
Total	16.177	7			

Table C10: ANOVA table for surface roughness Ra parallel to the feed direction (Phase 1C)

C2 Phase 2, creep feed grinding

a) Phase 2Ai: Assessment of significant operating parameters when creep feed grinding

Ti 45Al-8Nb-0.2C using conventional abrasive wheels

Figures C51 and C52 show normal and tangential forces against volume of workpiece material removed for γ -TiAl

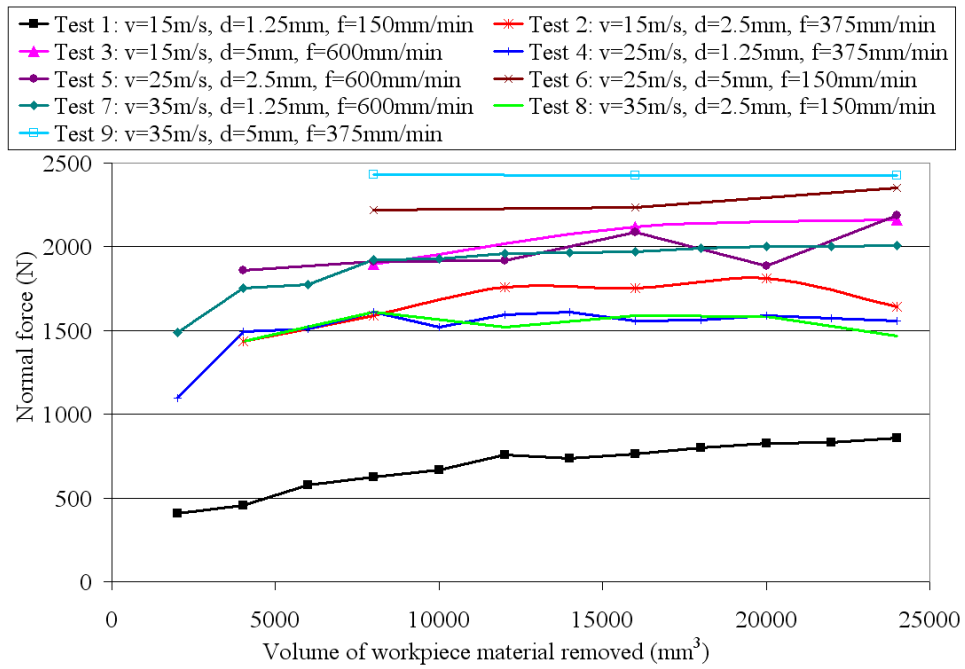


Figure C51: Normal force against volume of workpiece material removed (Phase 2Ai, γ -TiAl)

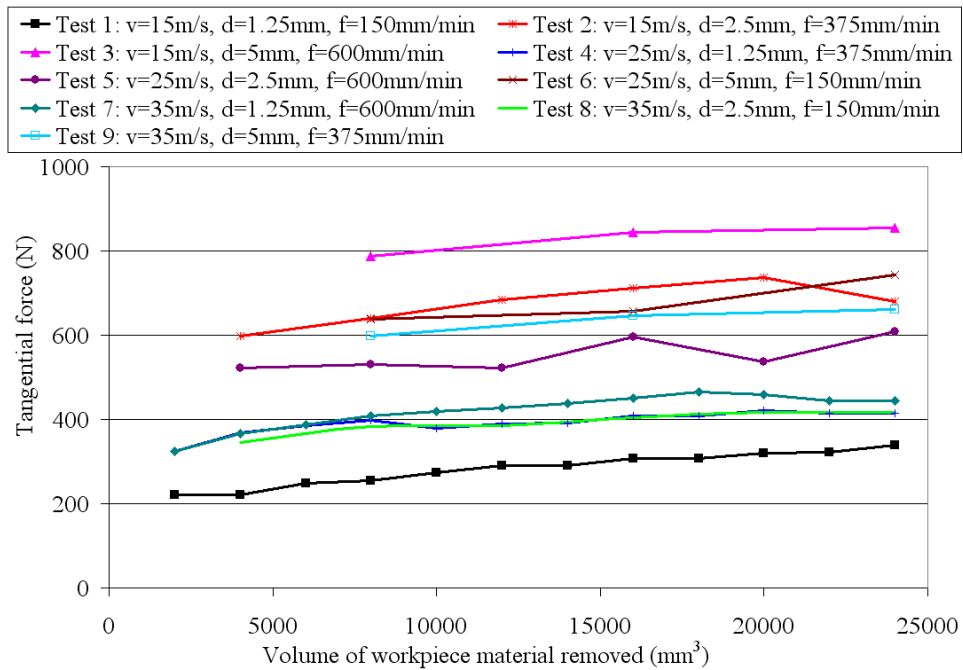


Figure C52: Tangential force against volume of workpiece material removed (Phase 2Ai, γ -TiAl)

Figures C53 and C54 show power and specific energy against volume of workpiece material removed for γ -TiAl.

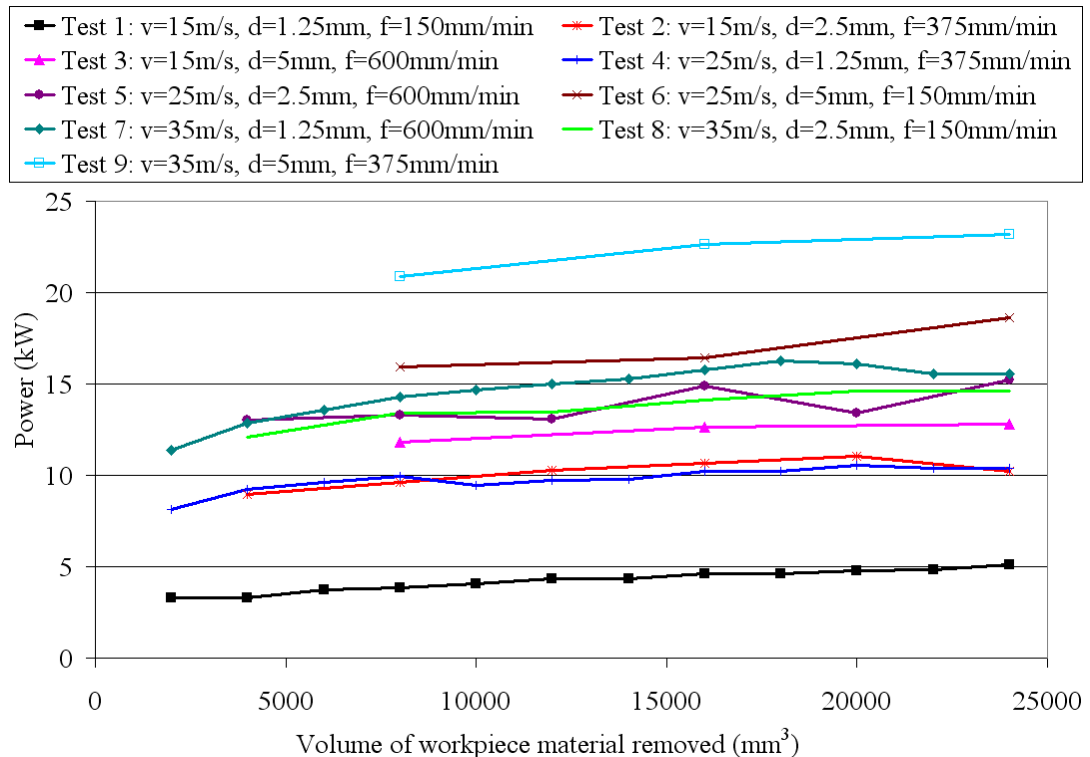


Figure C53: Power against volume of workpiece material removed (Phase 2Ai, γ -TiAl)

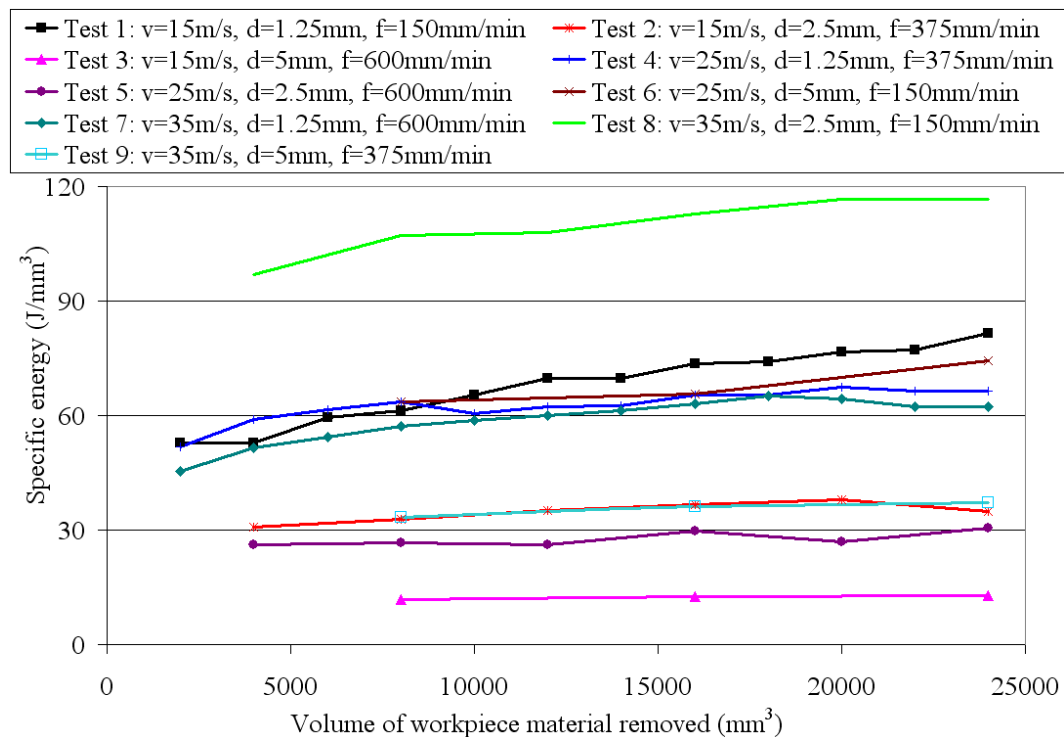


Figure C54: Specific energy against volume of workpiece material removed (Phase 2Ai, γ -TiAl)

Figure C55 shows surface roughness Ra results for γ -TiAl.

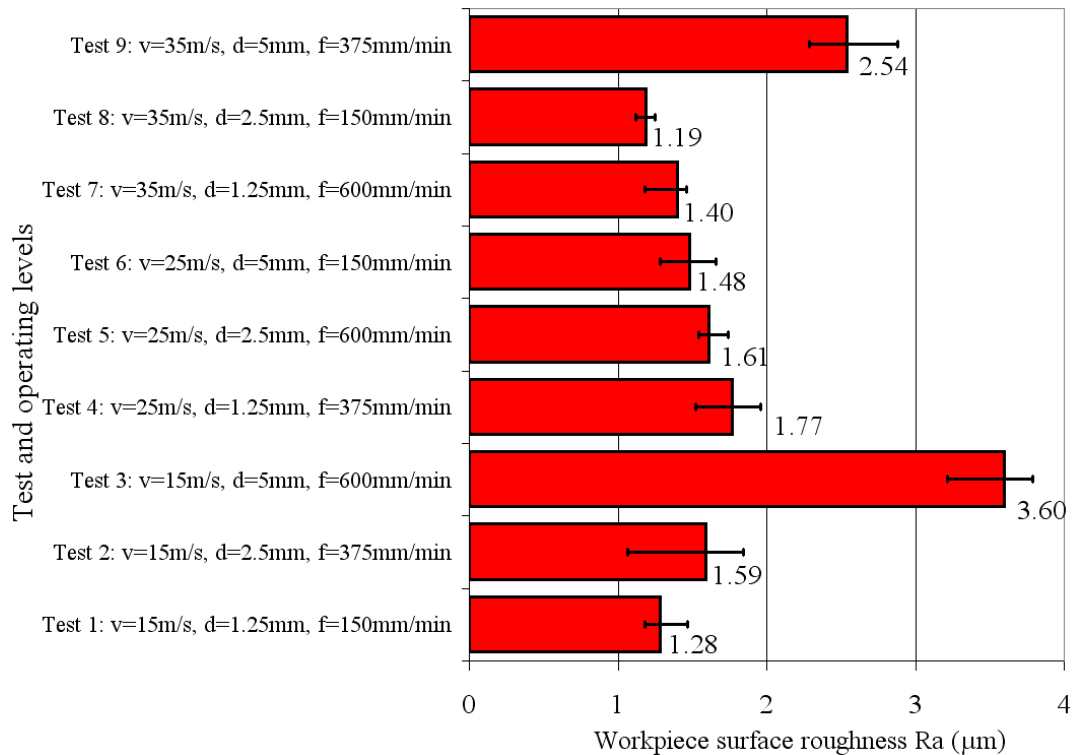


Figure C55: Surface roughness Ra results for γ -TiAl (Phase 2Ai, γ -TiAl)

Figure C56 shows G-ratio against volume of workpiece material removed for BuRTi.

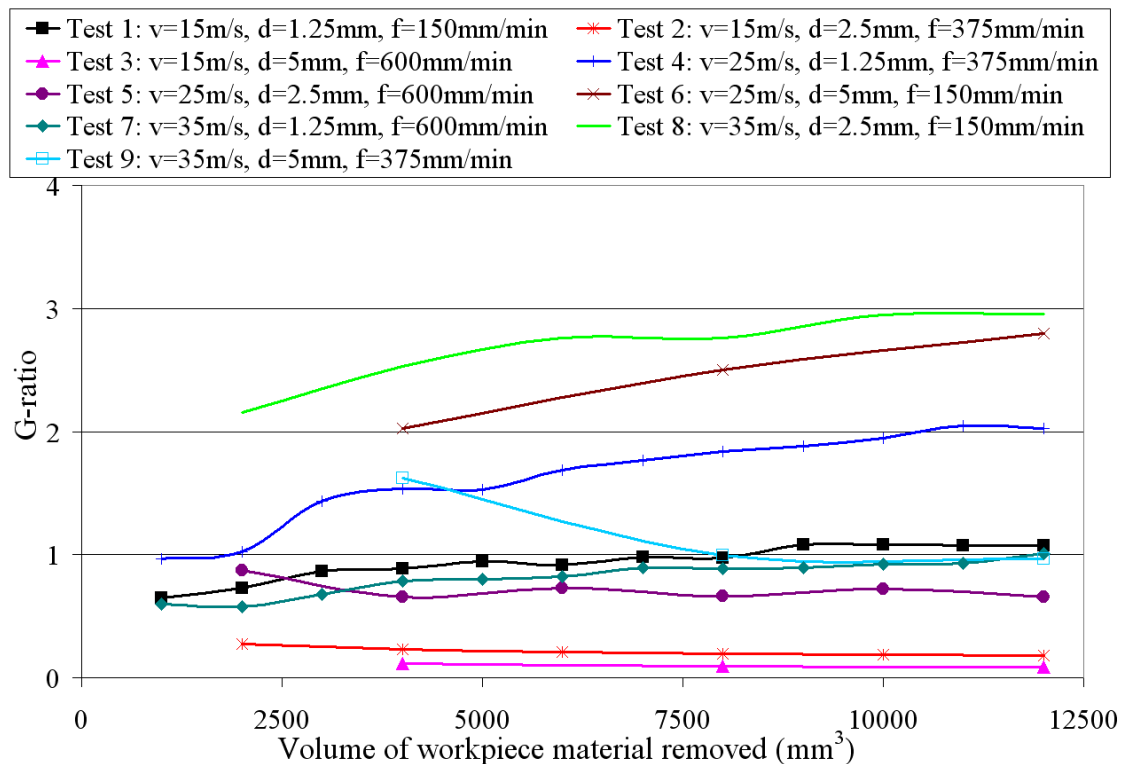


Figure C56: G-ratio against volume of workpiece material removed (Phase 2Ai, BuRTi)

Figures C57 and C58 show normal and tangential forces against volume of workpiece material removed for γ -TiAl

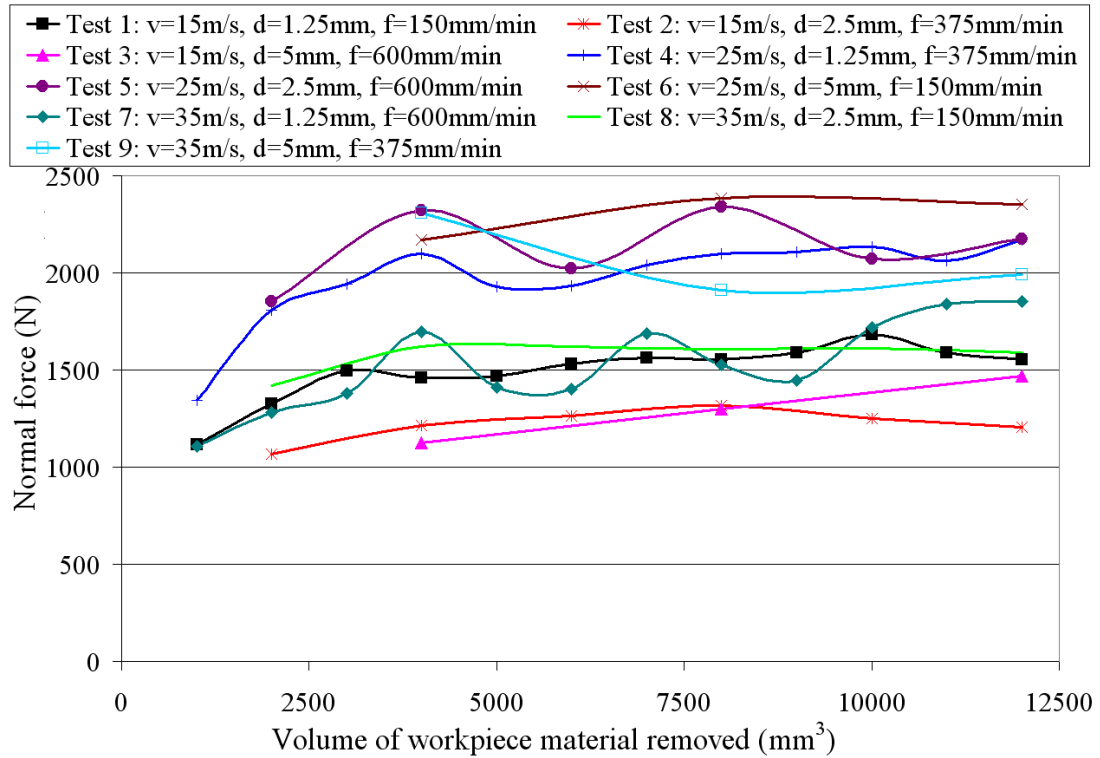


Figure C57: Normal force against volume of workpiece material removed (Phase 2Ai, BuRTi)

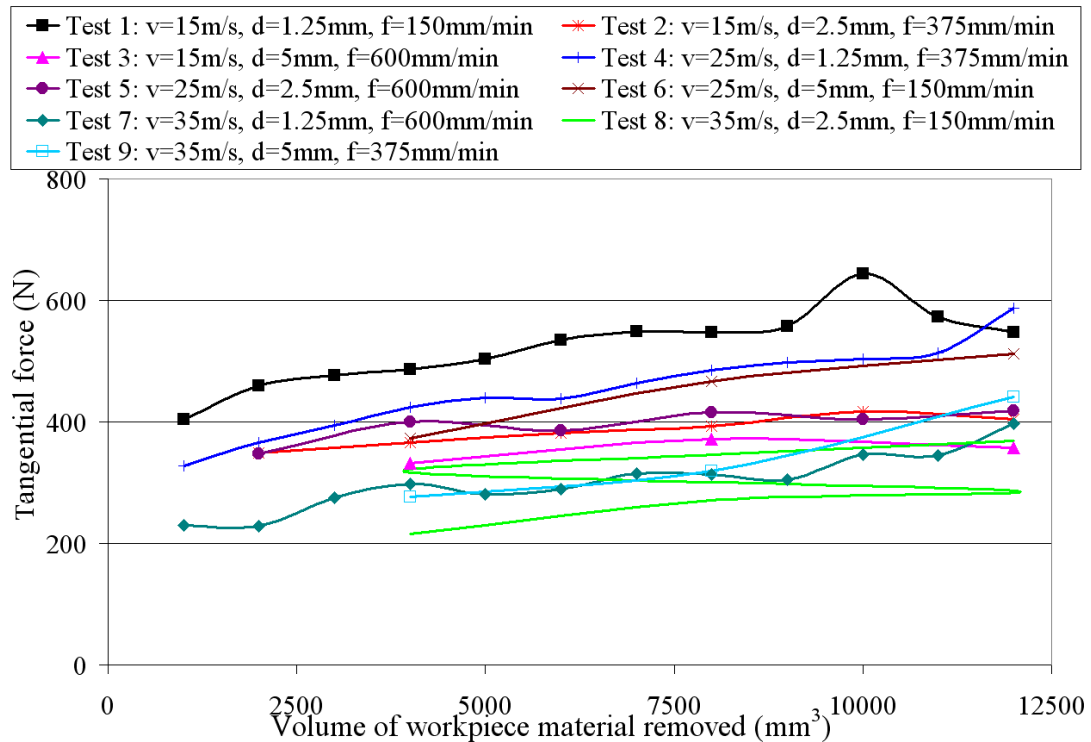


Figure C58: Tangential force against volume of workpiece material removed (Phase 2Ai, BuRTi)

Figures C59 and C60 show power and specific energy against volume of workpiece material removed for BuRTi.

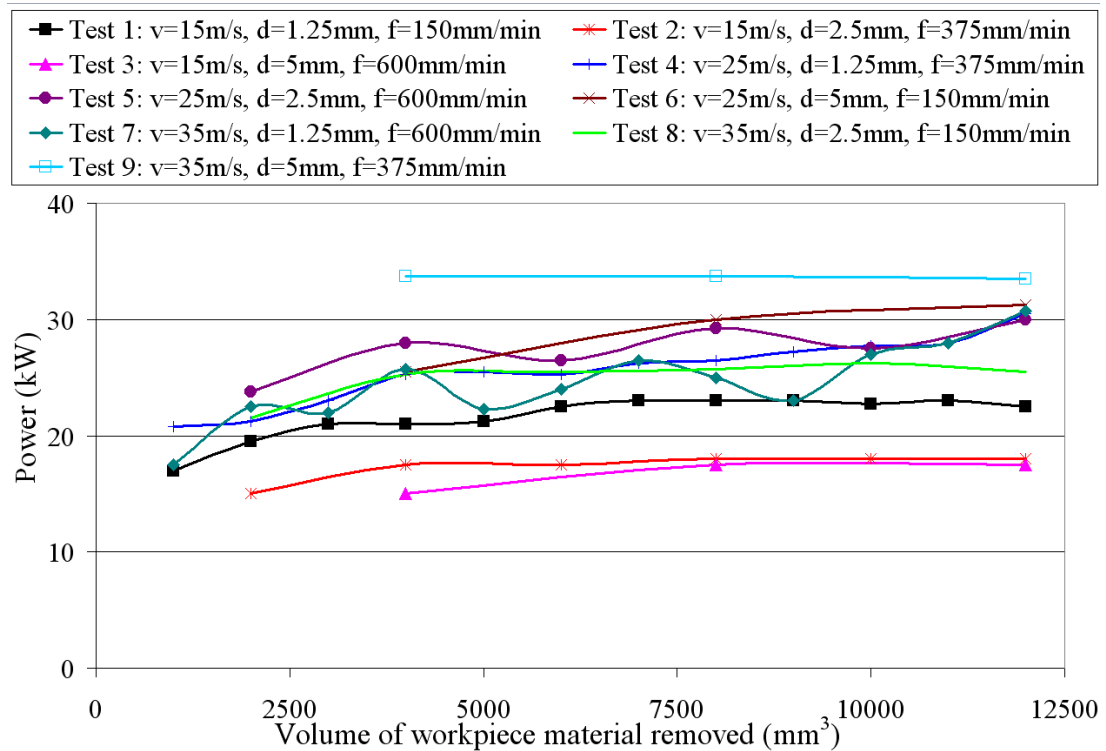


Figure C59: Power against volume of workpiece material removed (Phase 2Ai, BuRTi)

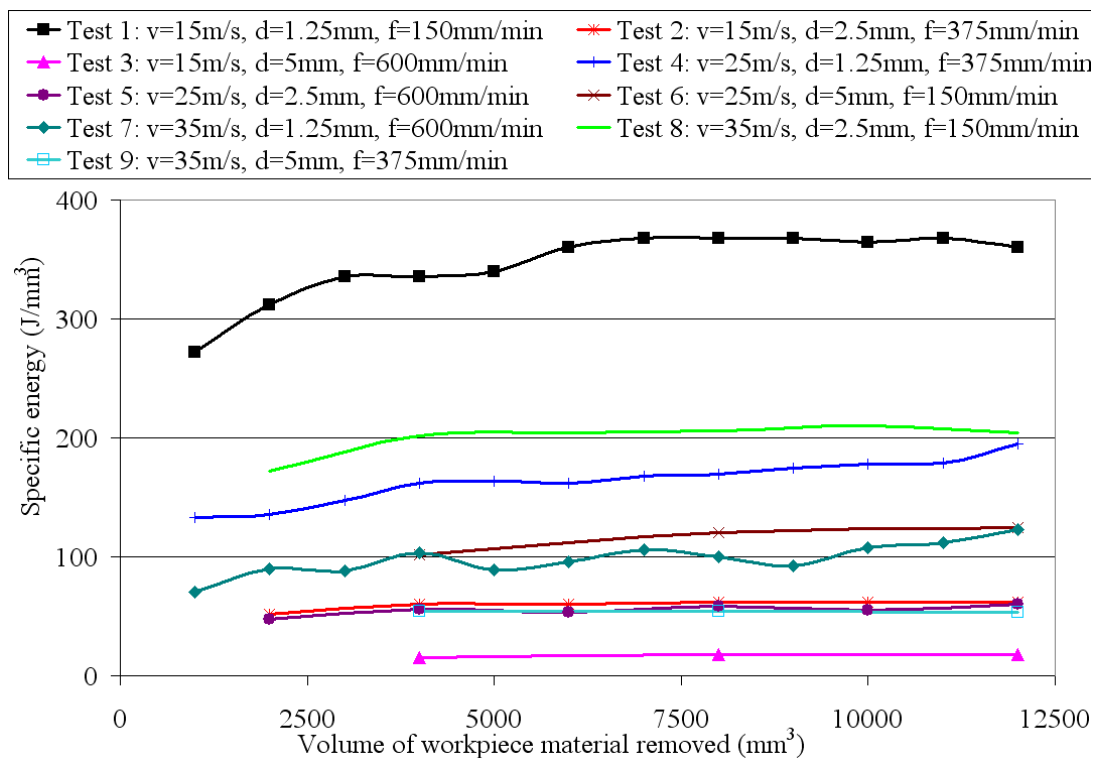


Figure C60: Specific energy against volume of workpiece material removed (Phase 2Ai, BuRTi)

Figure C61 shows surface roughness Ra results for BuRTi.

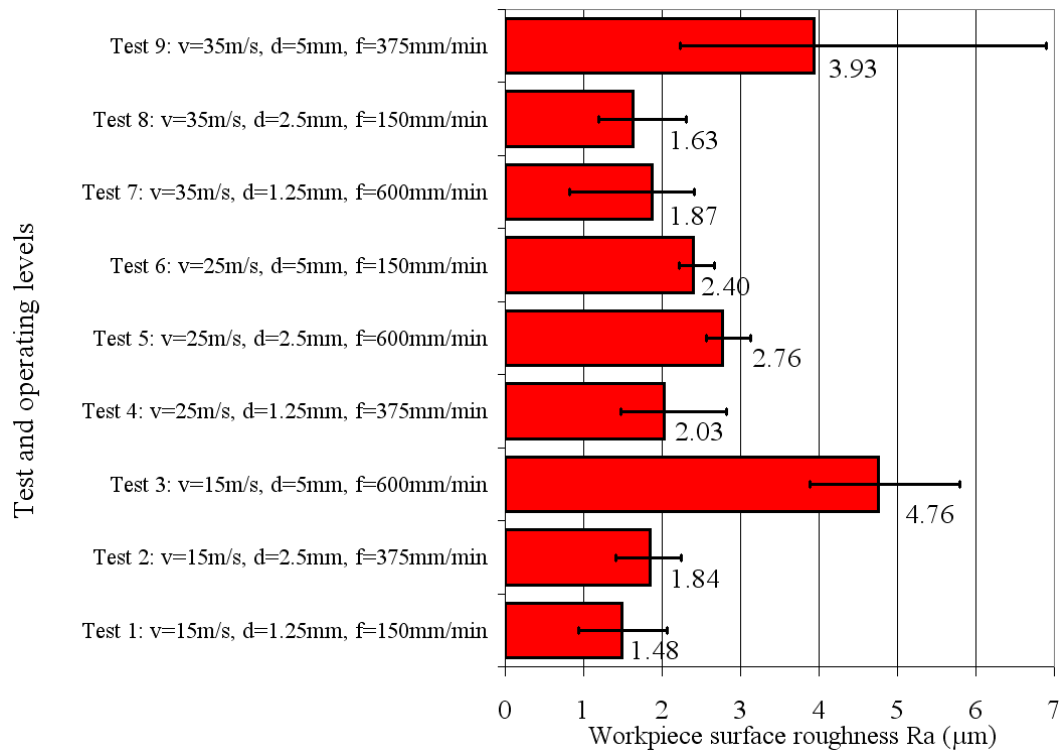


Figure C61: Surface roughness Ra results for BuRTi (Phase 2Ai, BuRTi)

Tables C11 to C15 show ANOVA tables for normal and tangential force, power, specific energy and workpiece surface roughness Ra for γ -TiAl.

Source	SS	DOF	MSS	Fcalc	PCR%
Cutting speed	368859	2	184429	3.07	12.3
Depth of cut	1105891	2	552945	9.20	48.9
Feed rate	420152	2	210076	3.49	14.9
Error	120216	2	60108	-	23.9
Total	2015118	8	-	-	-

Table C11: ANOVA table for normal force (Phase 2Ai, γ -TiAl)

Source	SS	DOF	MSS	Fcalc	PCR%
Cutting speed	21309	2	10655	1.68	3.5
Depth of cut	188542	2	94271	14.89	70.1
Feed rate	26743	2	13372	2.11	5.6
Error	12664	2	6332	-	20.8
Total	249259	8	-	-	-

Table C12: ANOVA table for tangential force (Phase 2Ai, γ -TiAl)

Source	SS	DOF	MSS	Fcalc	PCR%
Cutting speed	107.93	2	53.97	13.20	46.0
Depth of cut	94.90	2	47.50	11.60	40.0
Feed rate	6.07	2	3.04	0.74	0.0
Error	8.18	2	4.09	-	14.0
Total	217.08	8	-	-	-

Table C13: ANOVA table for power for (Phase 2Ai, γ -TiAl)

Source	SS	DOF	MSS	Fcalc	PCR%
Cutting speed	1261.0	2	630.5	2.78	9.8
Depth of cut	1376.1	2	688.1	3.04	11.2
Feed rate	5181.3	2	2590.6	11.43	57.1
Error	453.2	2	226.6	-	21.9
Total	8271.6	8	-	-	-

Table C14: ANOVA table for specific energy (Phase 2Ai, γ -TiAl)

Source	SS	DOF	MSS	Fcalc	PCR%
Cutting speed	0.502	2	0.251	0.69	0.0
Depth of cut	2.283	2	1.141	3.15	32.6
Feed rate	1.265	2	0.633	1.74	11.3
Error	0.726	2	0.363	-	56.1
Total	4.776	8	-	-	-

Table C15: ANOVA table for workpiece surface roughness Ra (Phase 2Ai, γ -TiAl)

Tables C16 to C21 show ANOVA tables for G-ratio, normal and tangential force, power, specific energy and workpiece surface roughness Ra for BuRTi

Source	SS	DOF	MSS	Fcalc	PCR%
Cutting speed	3.3727	2	1.6863	3.59	27.3
Depth of cut	0.0197	2	0.0098	0.02	0
Feed rate	4.5649	2	2.2825	4.85	40.7
Error	0.9407	2	0.4703	-	32.0
Total	8.8979	8	-	-	-

Table C16: ANOVA table for G-ratio (Phase 2Ai, BuRTi)

Source	SS	DOF	MSS	Fcalc	PCR%
Cutting speed	1013545	2	506772	24.82	82.1
Depth of cut	127385	2	63693	3.12	7.3
Feed rate	3451	2	1726	0.08	0.0
Error	40836	2	20418	-	11.6
Total	1185216	8	-	-	-

Table C17: ANOVA table for normal force (Phase 2Ai, BuRTi)

Source	SS	DOF	MSS	Fcalc	PCR%
Cutting speed	16600	2	8300.0	8.39	27.6
Depth of cut	19721.6	2	9860.8	9.97	33.5
Feed rate	14713.1	2	7356.5	7.44	24.0
Error	1978.8	2	989.4	-	14.9
Total	53013.5	8	-	-	-

Table C18: ANOVA table for tangential force (Phase 2Ai, BuRTi)

Source	SS	DOF	MSS	Fcalc	PCR%
Cutting speed	239.01	2	119.51	9.17	73.9
Depth of cut	20.43	2	10.22	0.78	0
Feed rate	2.51	2	1.26	0.10	0
Error	26.06	2	13.03	-	26.1
Total	288.01	8	-	-	-

Table C19: ANOVA table for power (Phase 2Ai, BuRTi)

Source	SS	DOF	MSS	Fcalc	PCR%
Cutting speed	769	2	384	0.17	0
Depth of cut	41496	2	20748	8.99	40.7
Feed rate	43776	2	21888	9.48	43.2
Error	4616	2	2308	-	16.1
Total	90657	8	-	-	-

Table C20: ANOVA table for specific energy (Phase 2Ai, BuRTi)

Source	SS	DOF	MSS	Fcalc	PCR%
Cutting speed	0.1430	2	0.0715	0.13	0
Depth of cut	6.305	2	3.1526	5.86	52.0
Feed rate	2.5381	2	1.2690	2.36	14.5
Error	1.0754	2	0.5377	-	33.5
Total	10.0616	8	-	-	-

Table C21: ANOVA table for workpiece surface roughness Ra (Phase 2Ai, BuRTi)

Figure C62 shows the interactions plot for G-ratio

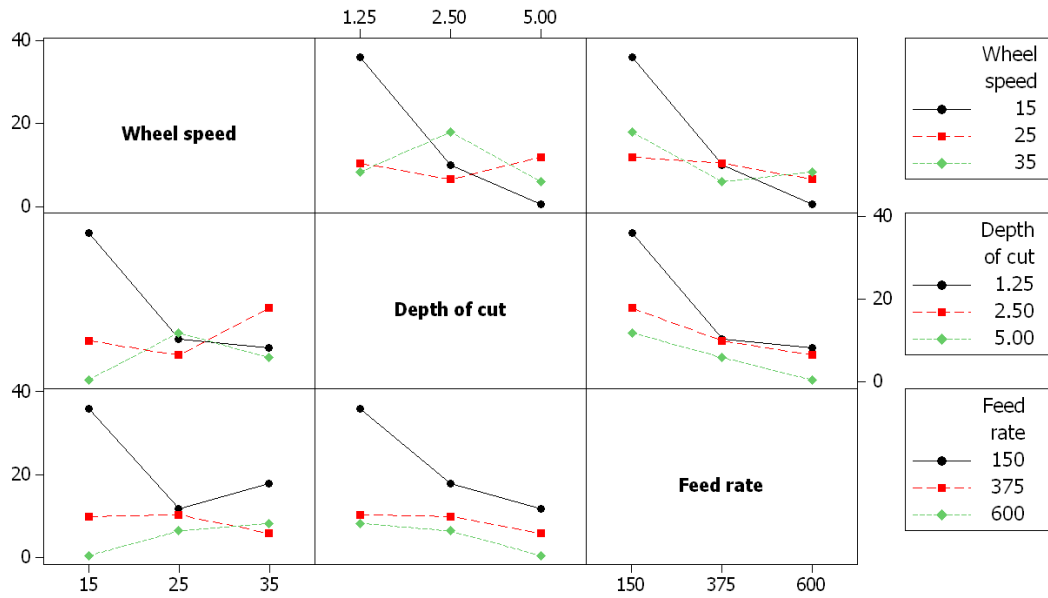
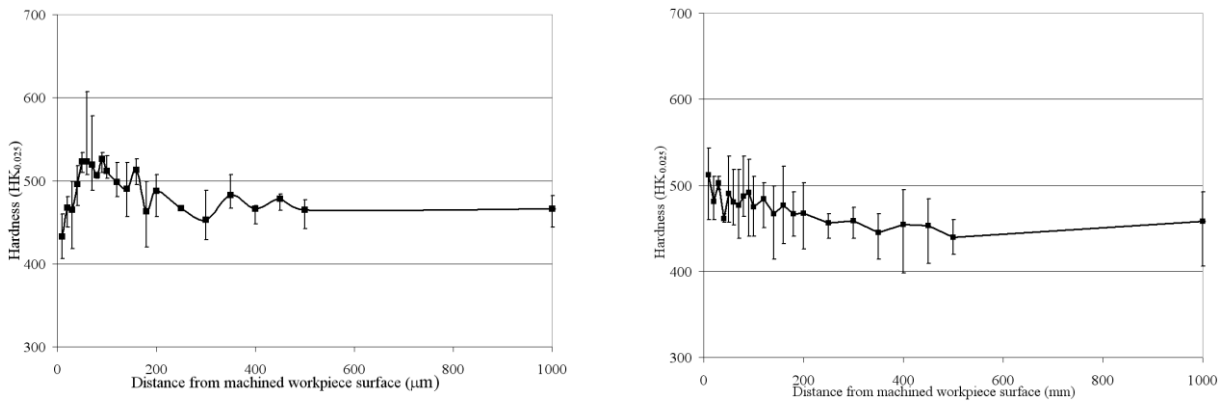


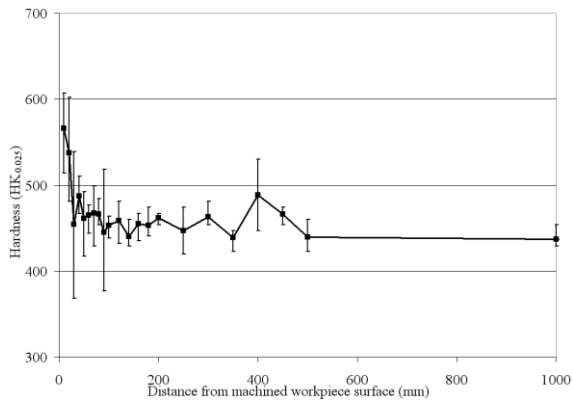
Figure C62: Interactions plot for G-ratio (Phase 2Ai, γ -TiAl)

Figures C63 and C64 show individual microhardness depth profiles for Phase 2Ai.

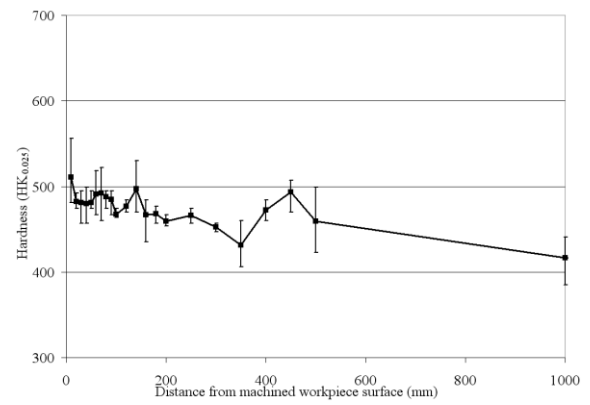


(a) Test 1: v=15m/s, d=1.25mm, f=150mm/min (b) Test 2: v=15m/s, d=2.5mm, f=375mm/min

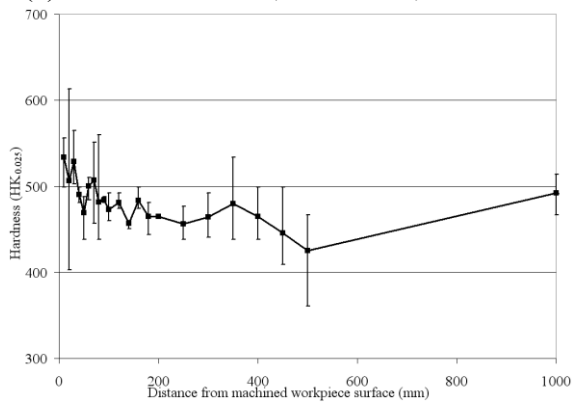
Figure C63: Individual microhardness depth profiles for Tests 1 and 2 (Phase 2Ai)



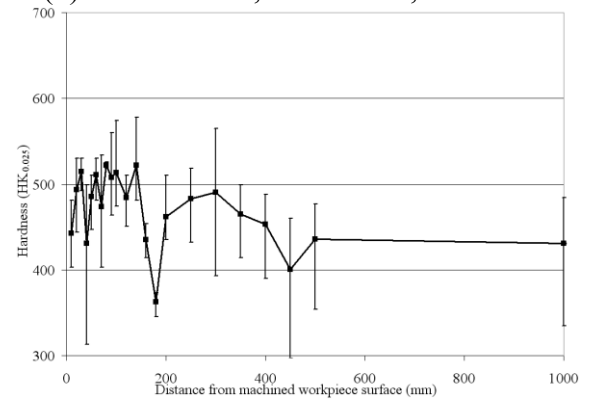
(a) Test 3: $v=15\text{m/s}$, $d=5.0\text{mm}$, $f=600\text{mm/min}$



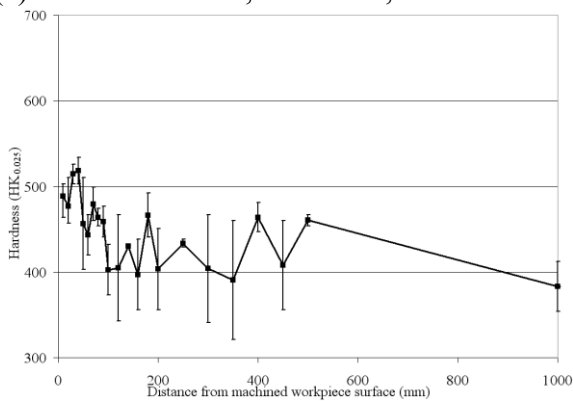
(b) Test 4 $v=25\text{s}$, $d=1.25\text{mm}$, $f=375\text{mm/min}$



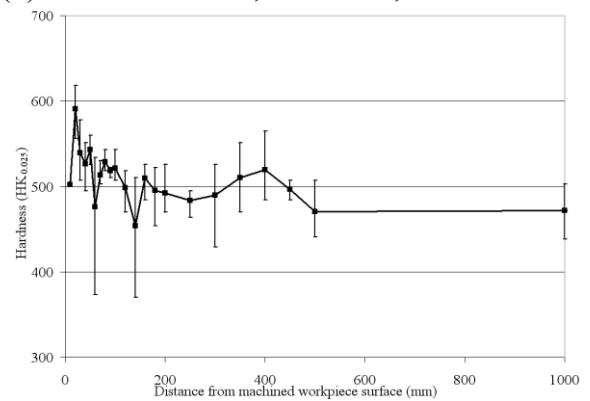
(c) Test 5: $v=15\text{m/s}$, $d=2.5\text{mm}$, $f=600\text{mm/min}$



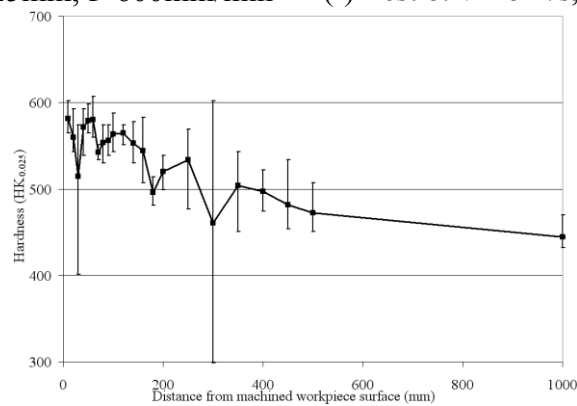
(d) Test 6: $v=15\text{m/s}$, $d=5.0\text{mm}$, $f=150\text{mm/min}$



(e) Test 7: $v=15\text{m/s}$, $d=1.25\text{mm}$, $f=600\text{mm/min}$



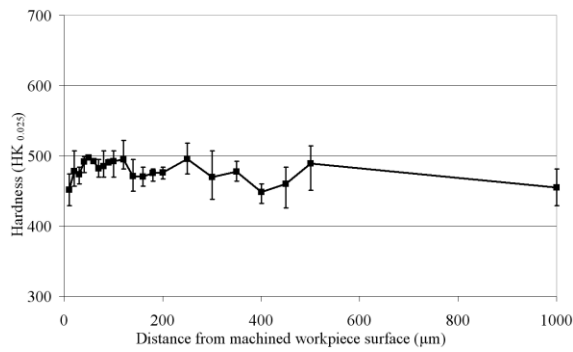
(f) Test 8: $v=15\text{m/s}$, $d=2.5\text{mm}$, $f=150\text{mm/min}$



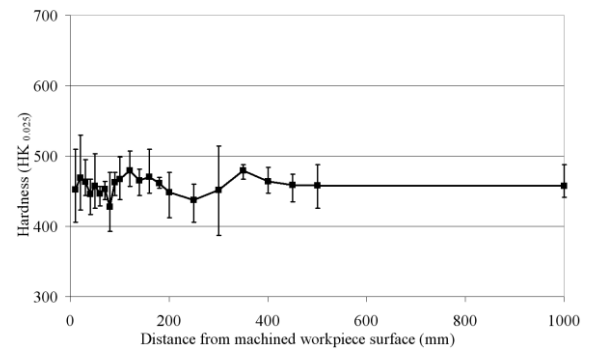
(g) Test 9: $v=15\text{m/s}$, $d=5.0\text{mm}$, $f=375\text{mm/min}$

Figure C64: Individual microhardness depth profiles for Tests 3 to 9 (Phase 2Ai)

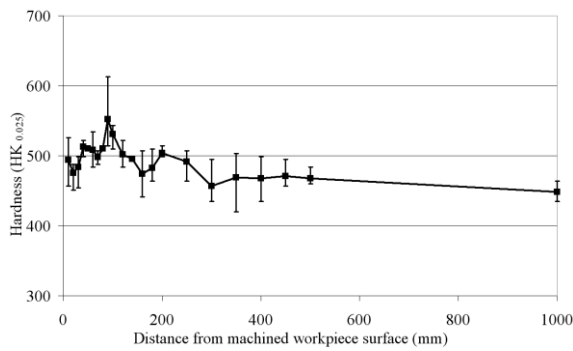
Figure C65 shows individual microhardness profiles for all tests.



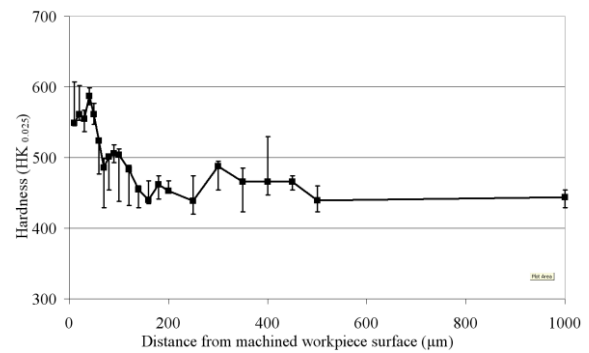
(a) Test 1: $d=1.25\text{mm}$, $f=150\text{mm/min}$



(b) Test 2: $d=1.25\text{mm}$, $f=600\text{mm/min}$



(c) Test 3: $d=5.0\text{mm}$, $f=150\text{mm/min}$



(d) Test 4: $d=5.0\text{mm}$, $f=600\text{mm/min}$

Figure C65: Individual microhardness depth profiles (Phase 2Aiii)

c) Phase 2Aii: Assessment of significant operating parameters when creep feed grinding Ti 45Al-8Nb-0.2C using superabrasive wheels

Figure C66 shows individual microhardness profiles for all tests.

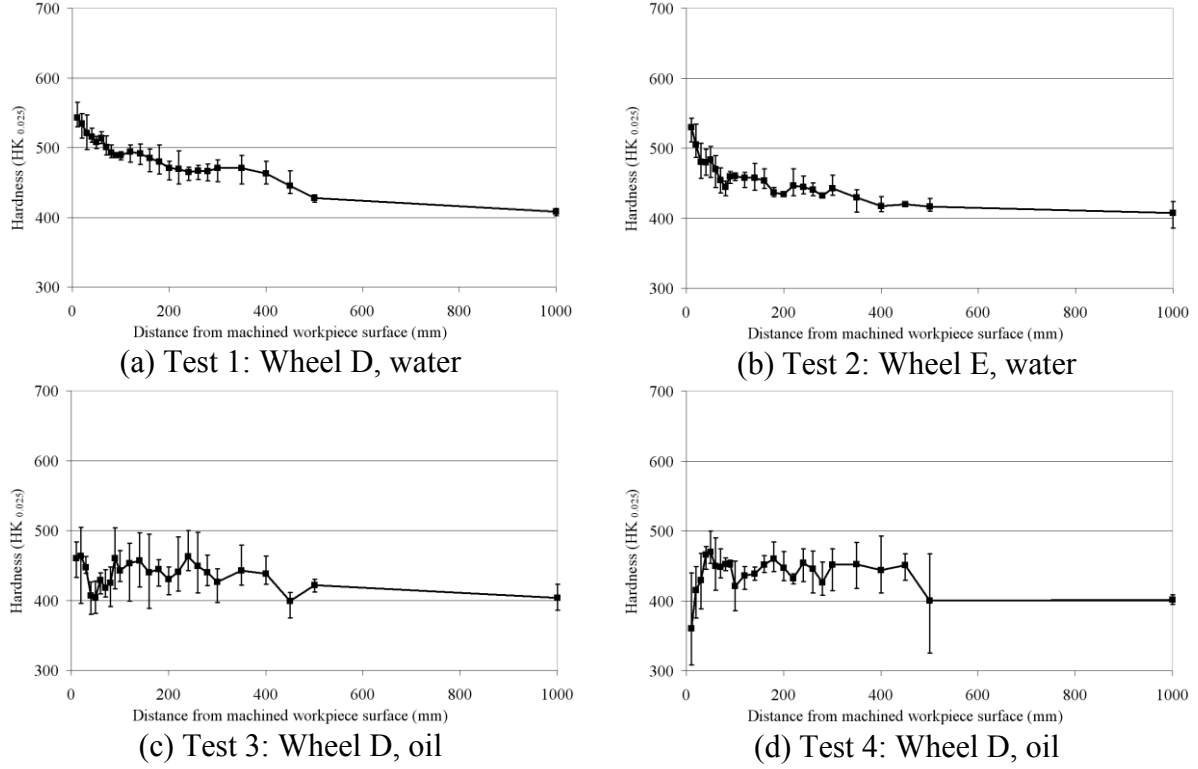


Figure C66: Individual microhardness depth profiles (Phase 2Aiii)

Figures C67 and C68 show normal and tangential forces against volume of workpiece material removed for γ -TiAl

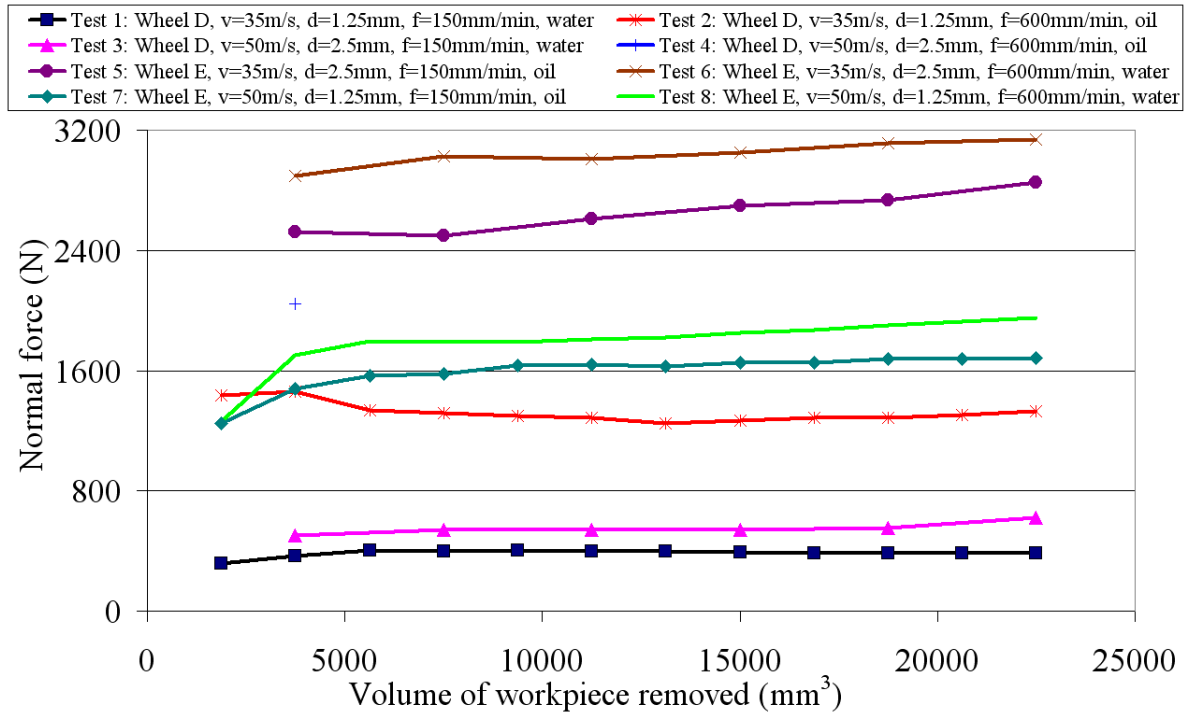


Figure C67: Normal force against volume of workpiece material removed (Phase 2Aiii, γ -TiAl)

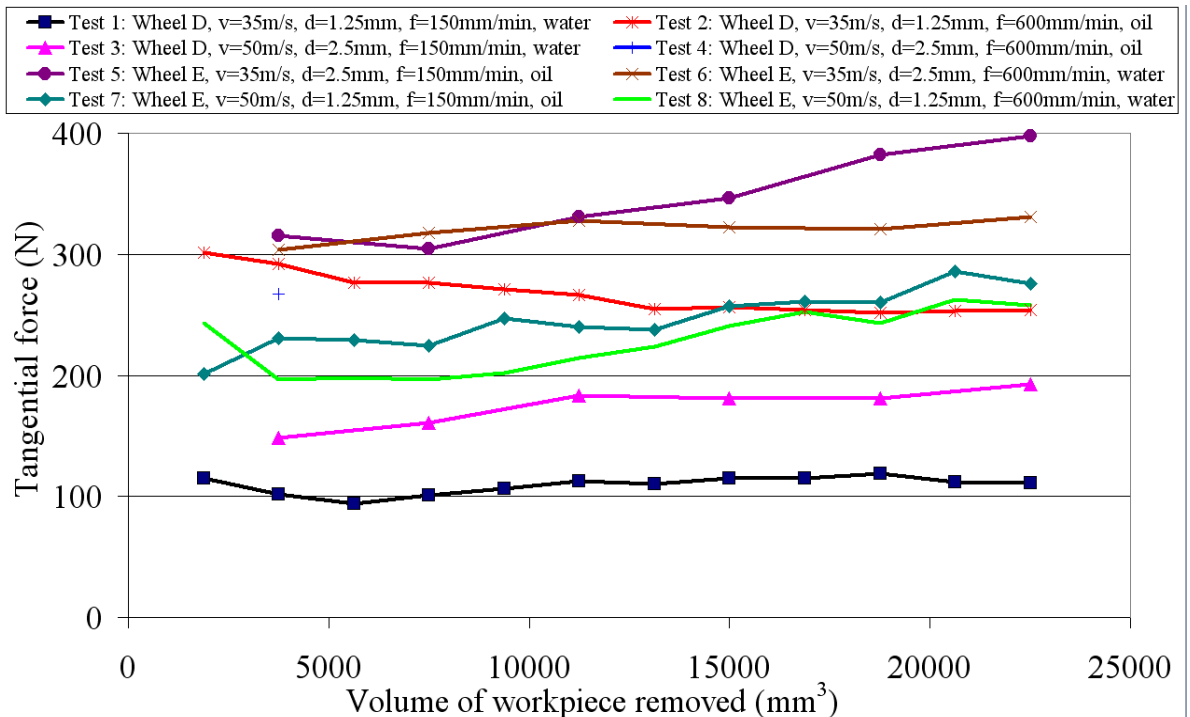


Figure C68: Tangential force against volume of workpiece material removed (Phase 2Aiii, γ -TiAl)

Figures C69 and C70 show power and specific energy against volume of workpiece material removed for γ -TiAl.

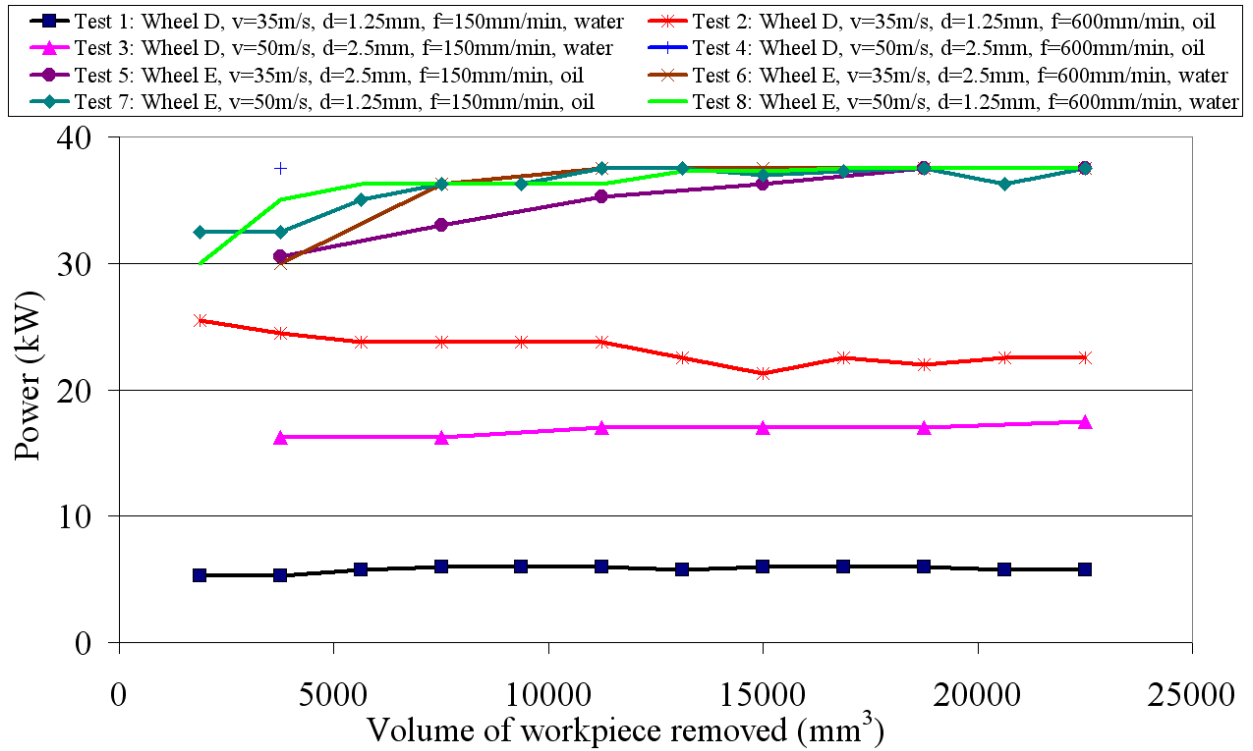


Figure C69: Power against volume of workpiece material removed (Phase 2Bii, γ -TiAl)

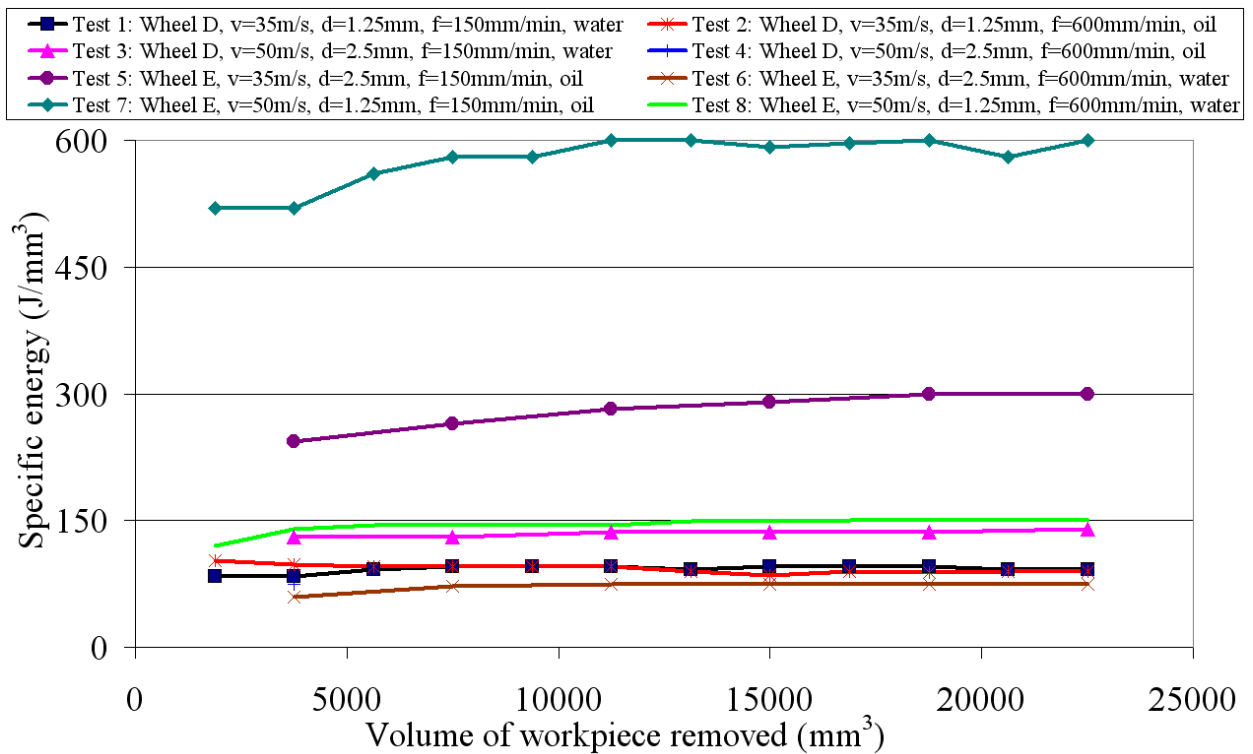


Figure C70: Specific energy against volume of workpiece material removed (Phase 2Bii, γ -TiAl)

Figure C71 shows surface roughness Ra results for γ -TiAl.

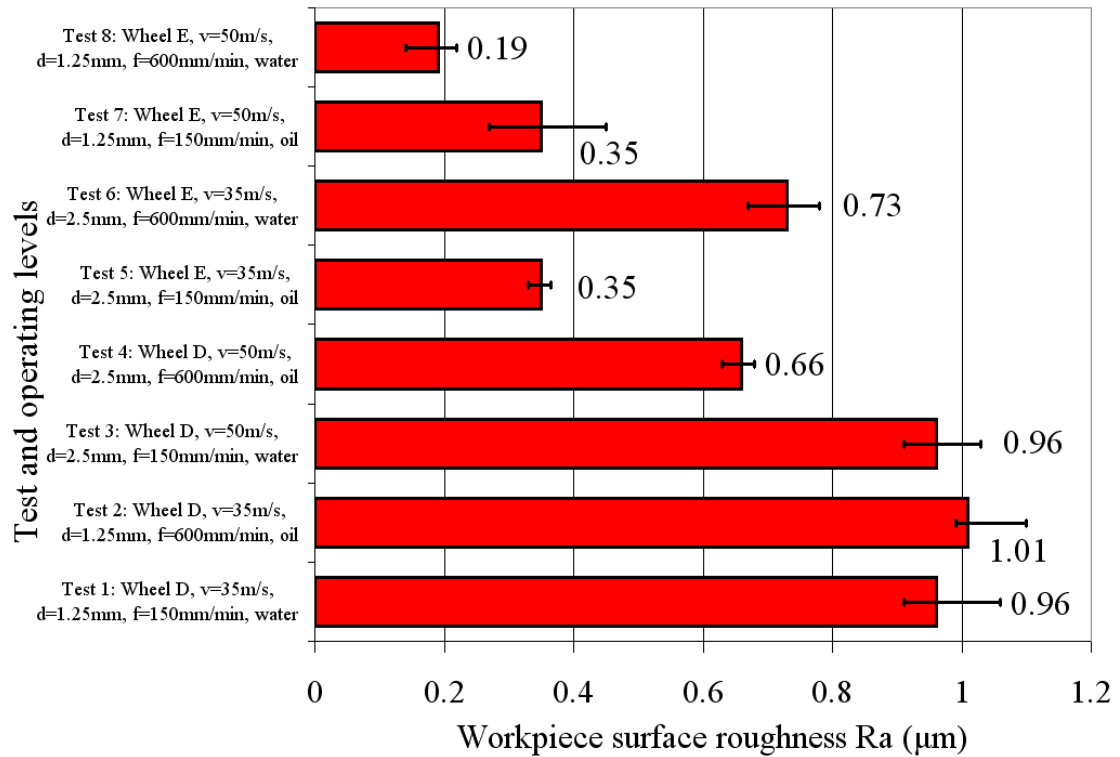


Figure C71: Surface roughness Ra results for γ -TiAl (Phase 2Bii, γ -TiAl)

Figure C72 shows G-ratio against volume of workpiece material removed for BuRTi.

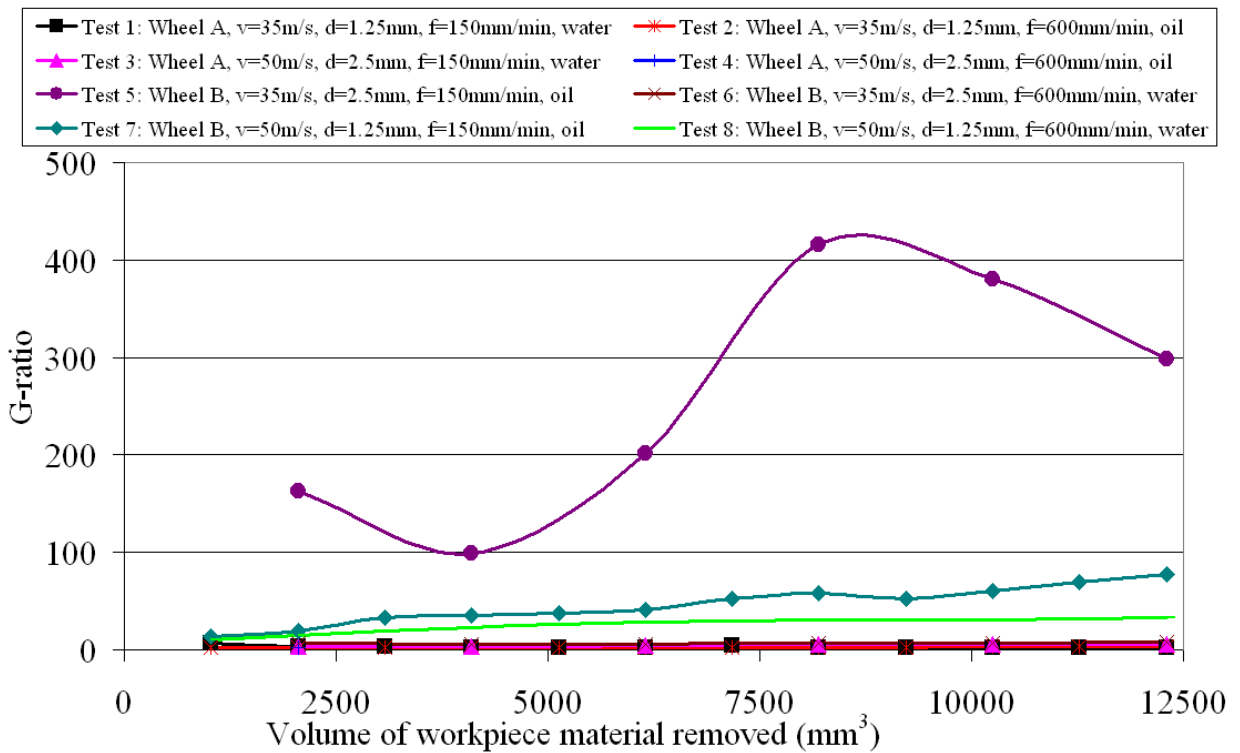


Figure C72: G-ratio against volume of workpiece material removed (Phase 2Bii, BuRTi)

Figures C73 and C74 show normal and tangential forces against volume of workpiece material removed for γ -TiAl

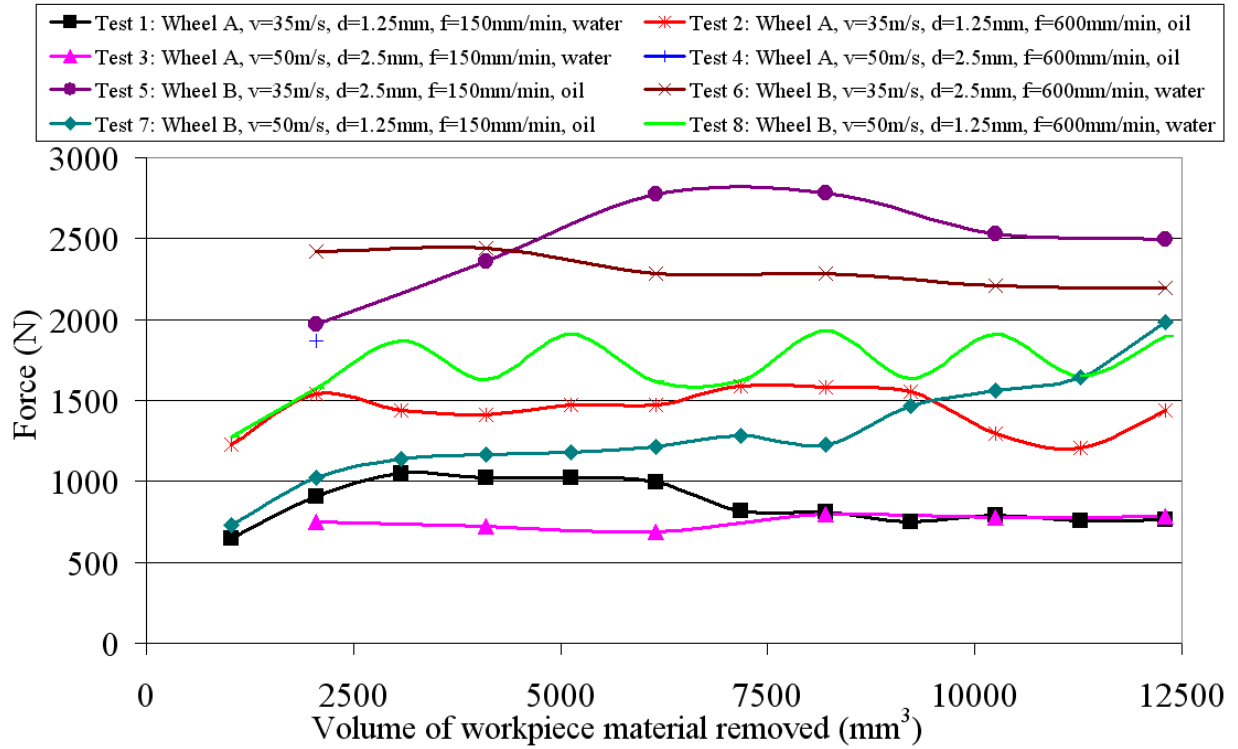


Figure C73: Normal force against volume of workpiece material removed (Phase 2Bii, BuRTi)

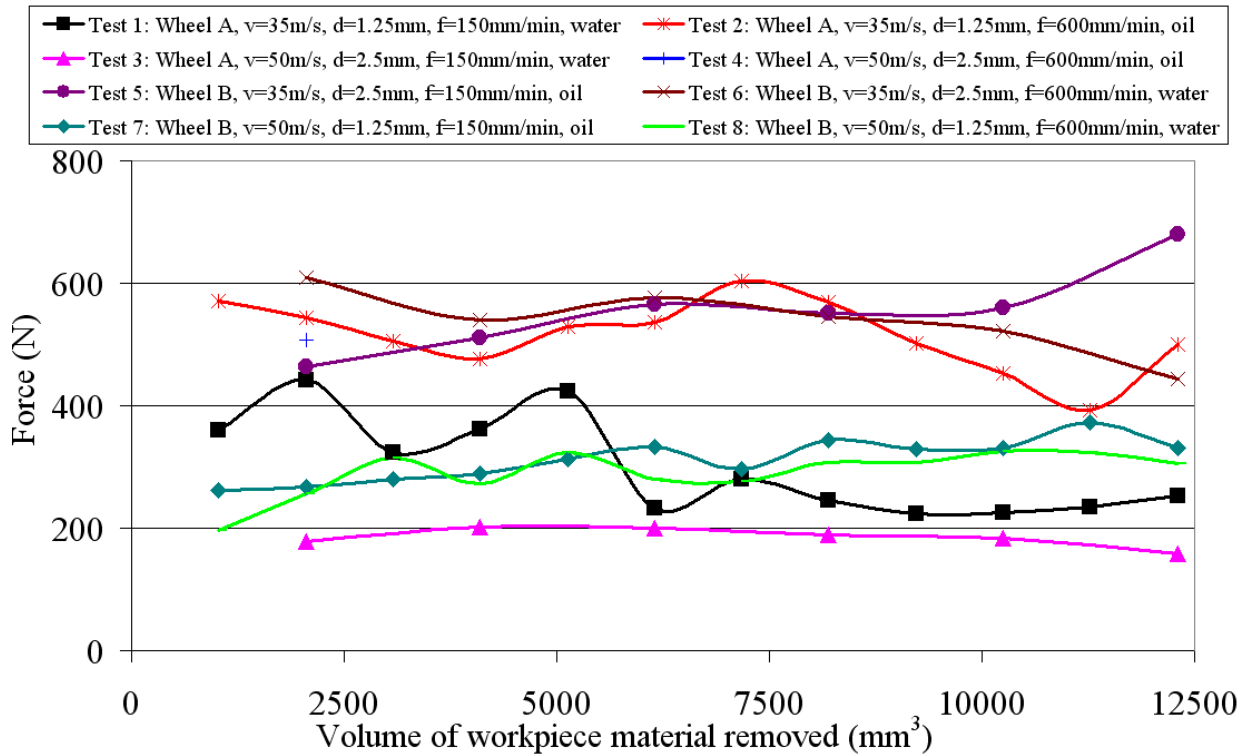


Figure C74: Tangential force against volume of workpiece material removed (Phase 2Bii, BuRTi)

Figures C75 and C76 show power and specific energy against volume of workpiece material removed for BuRTi.

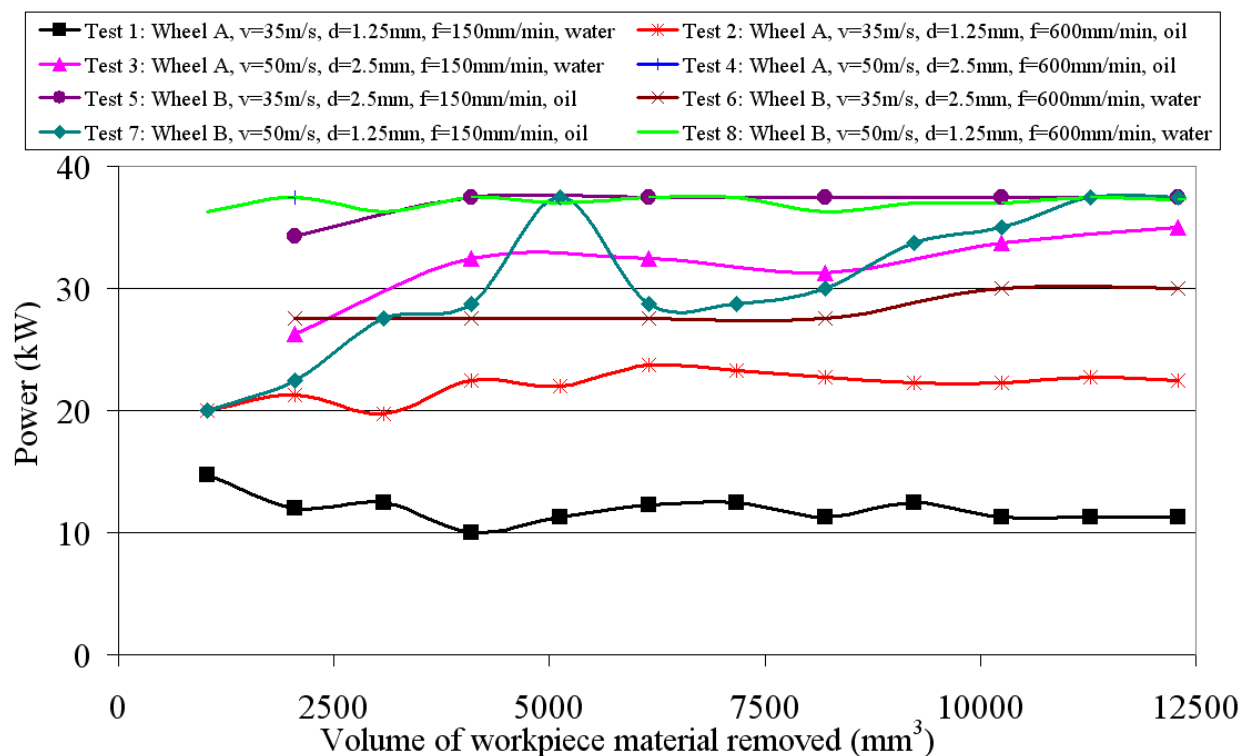


Figure C75: Power against volume of workpiece material removed (Phase 2Bii, BuRTi)

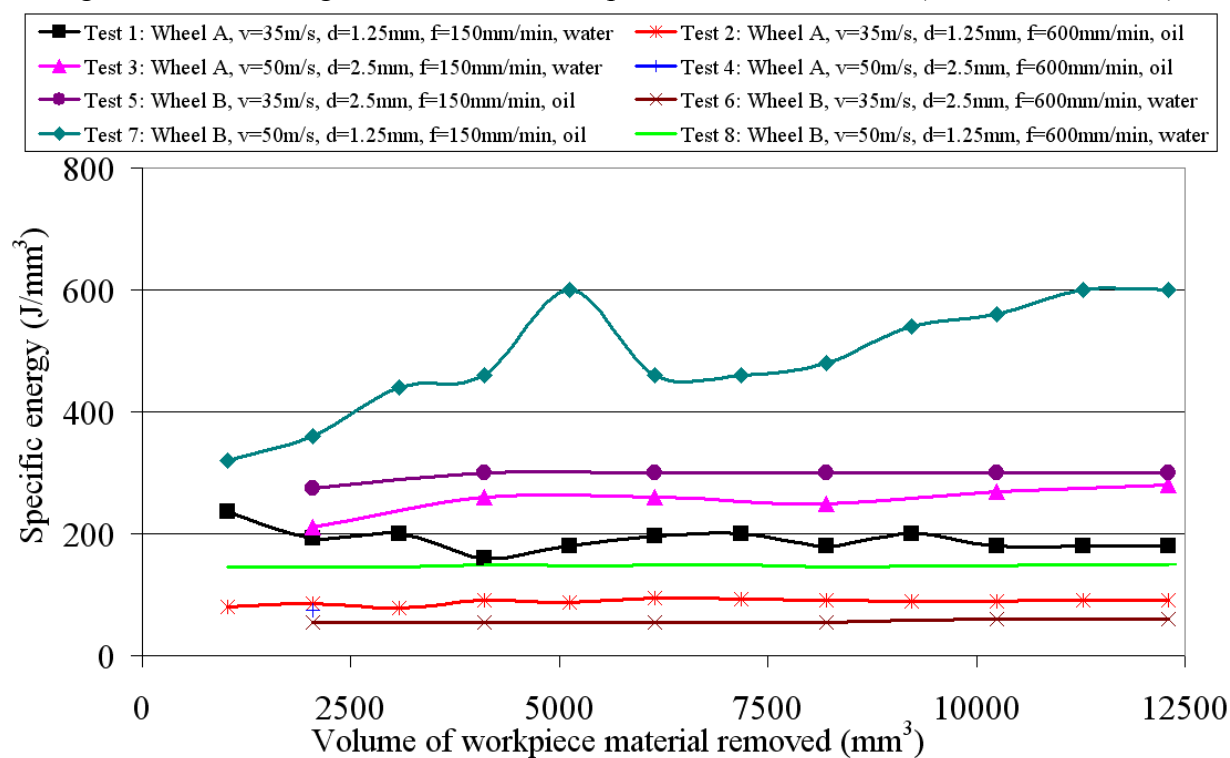


Figure C76: Specific energy against volume of workpiece material removed (Phase 2Bii, BuRTi)

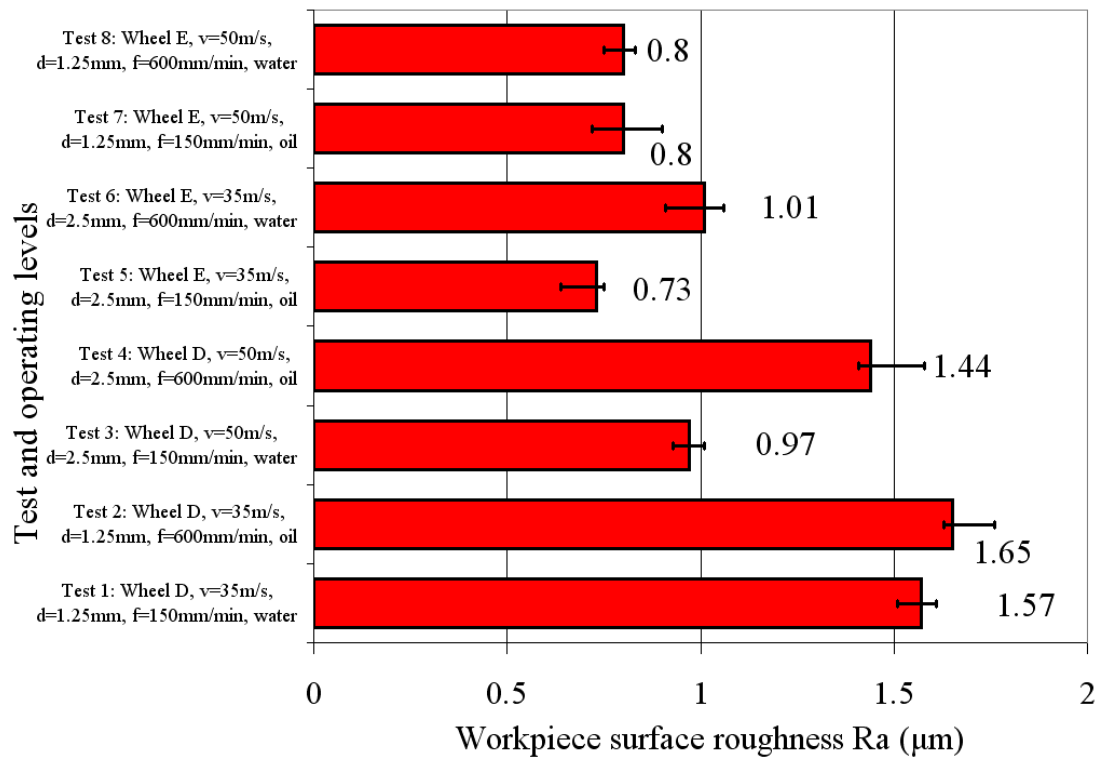


Figure C77: Surface roughness Ra results for BuRTi (Phase 2Bii, BuRTi)

Tables C23 to C27 show ANOVA tables for normal and tangential force, power, specific energy and workpiece surface roughness Ra for γ -TiAl.

Source	S.S	D.F.	M.S.S.	Fcalc	PCR%
Wheel type	1301288	1	1301288	38.86	39.1
Wheel speed	318	1	318	0.93	0.0
Depth of cut	299174	1	299174	8.93	8.2
Feed rate	1046065	1	1046065	31.24	31.2
Fluid type	530234	1	530234	15.83	15.3
Error	66970	2	33485	-	6.2
Total	3244049	7	-	-	-

Table C22: ANOVA table for normal force (Phase 2Bii, γ -TiAl)

Source	S.S.	D.F.	M.S.S.	Fcalc	PCR%
Wheel type	10546	1	10546	5.22	20.4
Wheel speed	3355	1	3355	1.66	3.2
Depth of cut	7398	1	7398	3.66	12.8
Feed rate	9353	1	9353	4.63	17.5
Fluid type	7199	1	7199	3.56	12.4
Error	4039	2	2019	-	33.7
Total	41890	7	-	-	-

Table C23: ANOVA table for tangential force (Phase 2Bii, γ -TiAl)

Source	S.S	D.F	M.S.S.	Fcalc	PCR%
Wheel type	504.03	1	504.03	16129	48.83
Wheel speed	69.03	1	69.03	2209	6.68
Depth of cut	69.03	1	69.03	2209	6.68
Feed rate	195.03	1	195.03	6241	18.89
Fluid type	195.03	1	195.03	6241	18.89
Error	0.06	2	0.03	-	0.02
Total	1032.2	7	-	-	-

Table C24: ANOVA table for power (Phase 2Bii, γ -TiAl)

Source	S.S.	D.F.	M.S.S.	Fcalc	PCR%
Wheel type	63368	1	63368	9.11	24.8
Wheel speed	19208	1	19208	2.76	5.4
Depth of cut	16021	1	16021	2.30	4.0
Feed rate	67344	1	67344	9.68	26.6
Fluid type	47432	1	47432	6.82	17.8
Error	13916	2	6958	-	21.4
Total	227289	7	-	-	-

Table C25: ANOVA table for specific energy (Phase 2Bii, γ -TiAl)

Source	S.S	D.F.	M.S.S.	Fcalc	PCR%
Wheel type	0.48511	1	0.48511	9.37	60.2
Wheel speed	0.09901	1	0.09901	1.91	6.6
Depth of cut	0.00451	1	0.00451	0.09	0
Feed rate	0.00011	1	0.00011	0.00	0
Fluid type	0.02761	1	0.02761	0.53	0
Error	0.10352	2	0.05176	-	33.2
Total	0.71989	7	-	-	-

Table C26: ANOVA table for workpiece surface roughness (Phase 2Bii, γ -TiAl)

Tables C27 to C32 show ANOVA tables for G-ratio, normal and tangential force, power, specific energy and workpiece surface roughness Ra for BuRTi.

Source	S.S	D.F.	M.S.S.	Fcalc	PCR%
Wheel type	20158	1	20158	2.66	17.2
Wheel speed	4603	1	4603	0.61	0
Depth of cut	4978	1	4978	0.66	0
Feed rate	14206	1	14206	1.87	9.1
Fluid type	13823	1	13823	1.82	8.5
Error	15180	2	7590	-	65.2
Total	72948	7	-	-	-

Table C27: ANOVA table for G-ratio (Phase 2Bii, BuRTi)

Source	S.S	D.F.	M.S.S.	Fcalc	PCR%
Wheel type	1730786	1	1730786	66.91	60.7
Wheel speed	15904	1	15904	0.61	0
Depth of cut	197368	1	197368	7.63	6.1
Feed rate	233443	1	233443	9.02	7.3
Fluid type	578307	1	578307	22.36	19.7
Error	51738	2	25869	-	6.2
Total	2807546	7	-	-	-

Table C28: ANOVA table for normal force (Phase 2Bii, BuRTi)

Source	S.S.	D.F.	M.S.S.	Fcalc	PCR%
Wheel type	14628	1	14628	2.16	4.0
Wheel speed	41670	1	41670	6.14	17.8
Depth of cut	20007	1	20007	2.95	6.8
Feed rate	13915	1	13915	2.05	3.6
Fluid type	91911	1	91911	13.55	43.5
Error	13567	2	6783		24.3
Total	195698	7			

Table C29: ANOVA table for tangential (Phase 2Bii, BuRTi)

Source	S.S	D.F	M.S.S.	Fcalc	PCR%
Wheel type	162	1	162	10.04	22.6
Wheel speed	264.5	1	264.5	16.39	38.5
Depth of cut	124.03	1	124.03	7.68	16.7
Feed rate	4.5	1	4.5	0.28	0
Fluid type	57.78	1	57.78	3.58	6.5
Error	32.28	2	16.14	-	15.7
Total	645.09	7	-	-	-

Table C30: ANOVA table for power (Phase 2Bii, BuRTi)

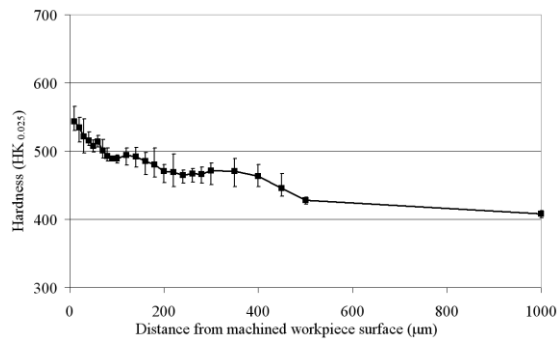
Source	S.S.	D.F.	M.S.S.	Fcalc	PCR%
Wheel type	29282	1	29282	4.06	9.8
Wheel speed	28084	1	28084	3.89	9.3
Depth of cut	11552	1	11552	1.60	1.9
Feed rate	121524	1	121524	16.84	50.9
Fluid type	19602	1	19602	2.72	5.5
Error	14437	2	7218	-	22.6
Total	224481	7	-	-	-

Table C31: ANOVA table for specific energy (Phase 2Bii, BuRTi)

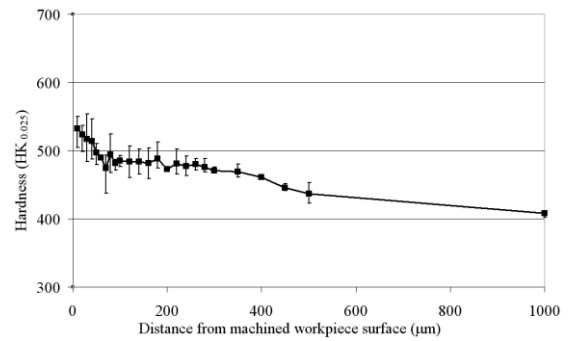
Source	S.S	D.F.	M.S.S.	Fcalc	PCR%
Wheel type	0.65551	1	0.65551	22.75	64.1
Wheel speed	0.11281	1	0.11281	3.92	8.6
Depth of cut	0.05611	1	0.05611	1.95	2.8
Feed rate	0.08611	1	0.08611	2.99	5.9
Fluid type	0.00911	1	0.00911	0.32	0.0
Error	0.05763	2	0.02881	-	18.4
Total	0.97729	7	-	-	-

Table C32: ANOVA table for workpiece surface roughness Ra (Phase 2Bii, BuRTi)

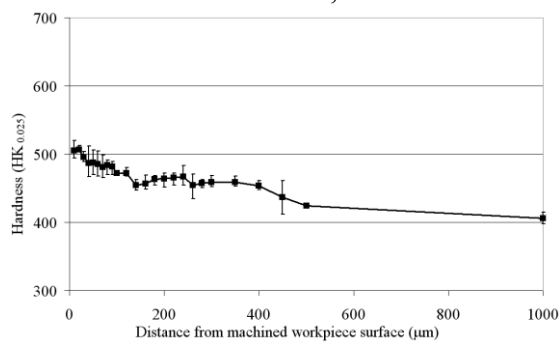
Figure C78 shows individual microhardness depth profiles for Phase 2Bii.



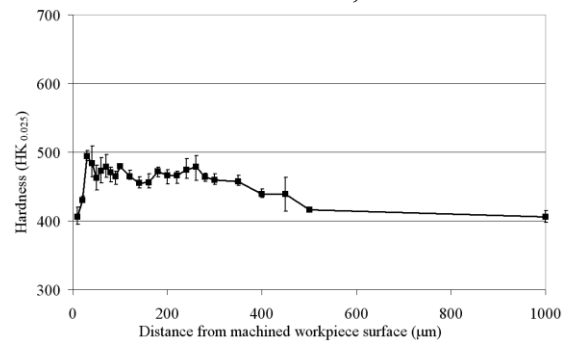
(a) Test 1: Wheel D, $v=35\text{m/s}$, $d=1.25\text{mm}$, $f=150\text{mm/min}$, water.



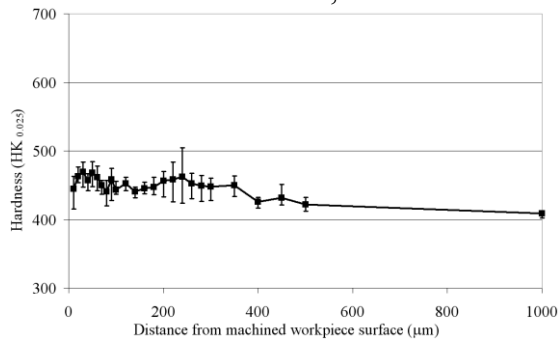
(b) Test 2: Wheel D, $v=35\text{m/s}$, $d=1.25\text{mm}$, $f=600\text{mm/min}$, oil.



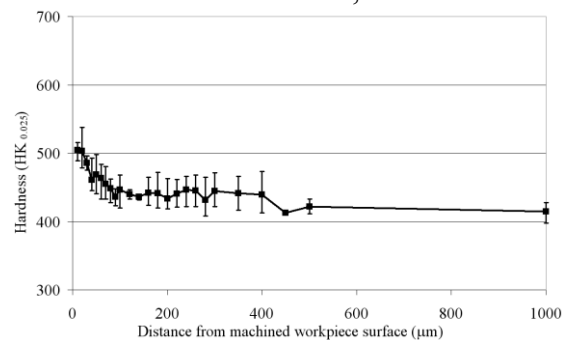
(c) Test 3: Wheel D, $v=50\text{m/s}$, $d=2.5\text{mm}$, $f=150\text{mm/min}$, water.



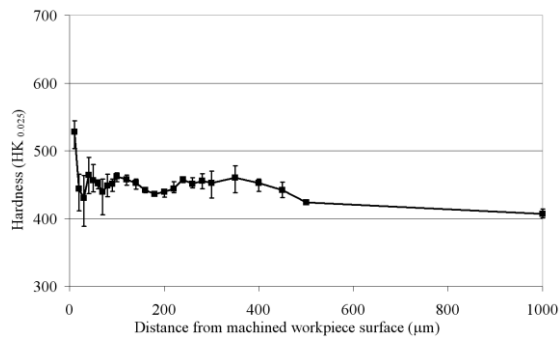
(d) Test 4: Wheel D, $v=50\text{m/s}$, $d=2.5\text{mm}$, $f=600\text{mm/min}$, oil.



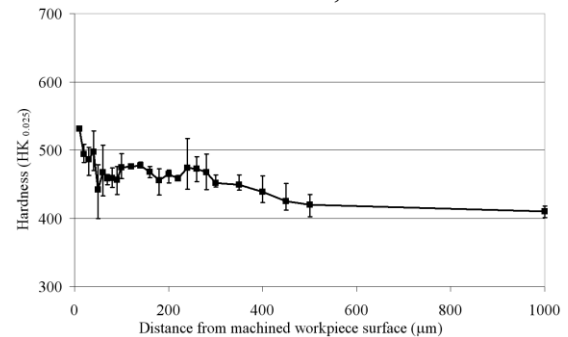
(e) Test 5: Wheel E, $v=35\text{m/s}$, $d=2.5\text{mm}$, $f=150\text{mm/min}$, oil.



(f) Test 6: Wheel E, $v=35\text{m/s}$, $d=2.5\text{mm}$, $f=600\text{mm/min}$, water.



(g) Test 7: Wheel E, $v=50\text{m/s}$, $d=1.25\text{mm}$, $f=150\text{mm/min}$, oil.



(h) Test 8: Wheel E, $v=50\text{m/s}$, $d=1.25\text{mm}$, $f=600\text{mm/min}$, water.

Figure C78: Individual microhardness depth profiles (Phase 2Bii)

Figures C79 and C80 show graphs of normal force and tangential force against volume of workpiece material removed for Phase 2Biii.

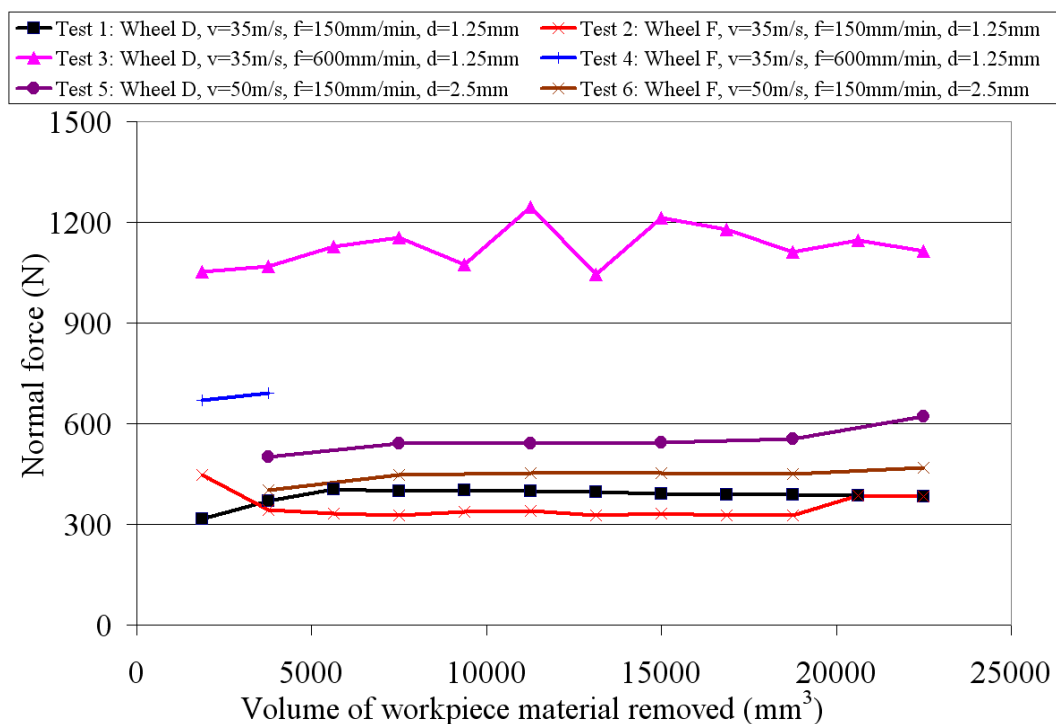


Figure C79: Tangential force against volume of workpiece material removed (Phase 2Biii)

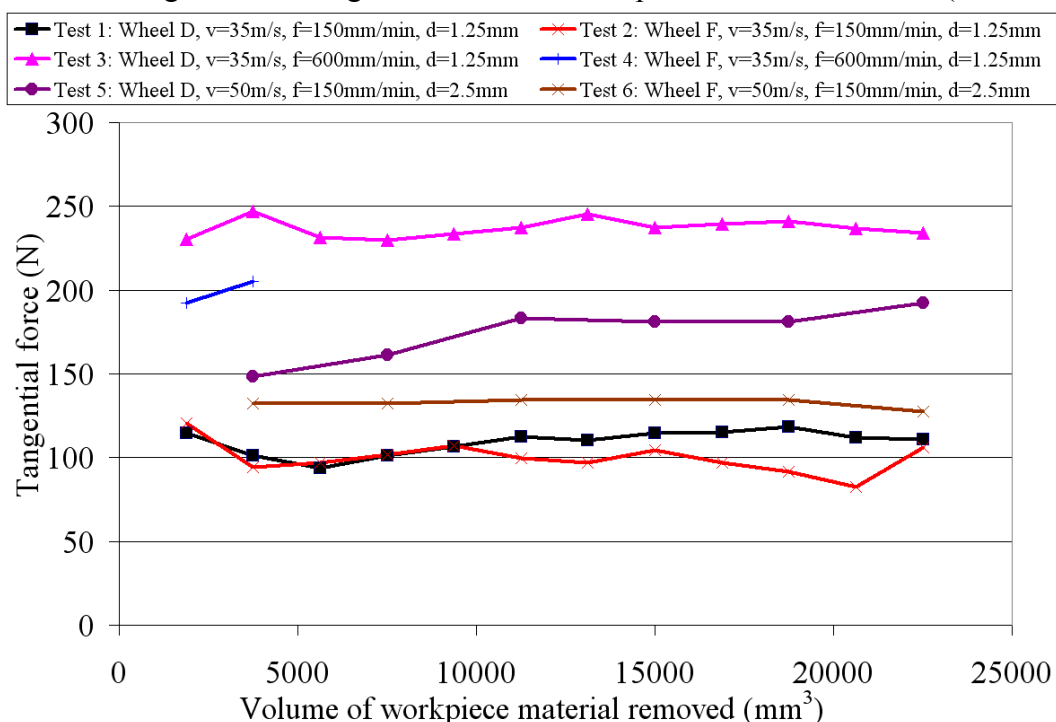


Figure C80: Tangential force against volume of workpiece material removed (Phase 2Biii)

Figures C81 and C82 show power and specific energy against volume of workpiece material removed for Phase 2Biii.

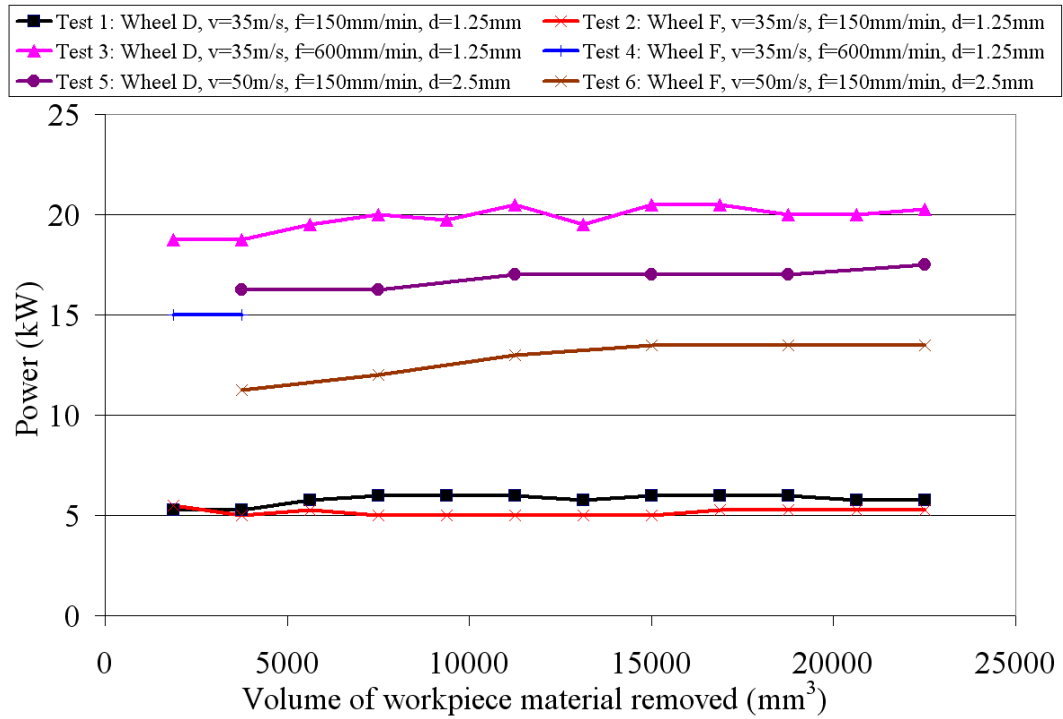


Figure C81: Tangential force against volume of workpiece material removed (Phase 2Biii)

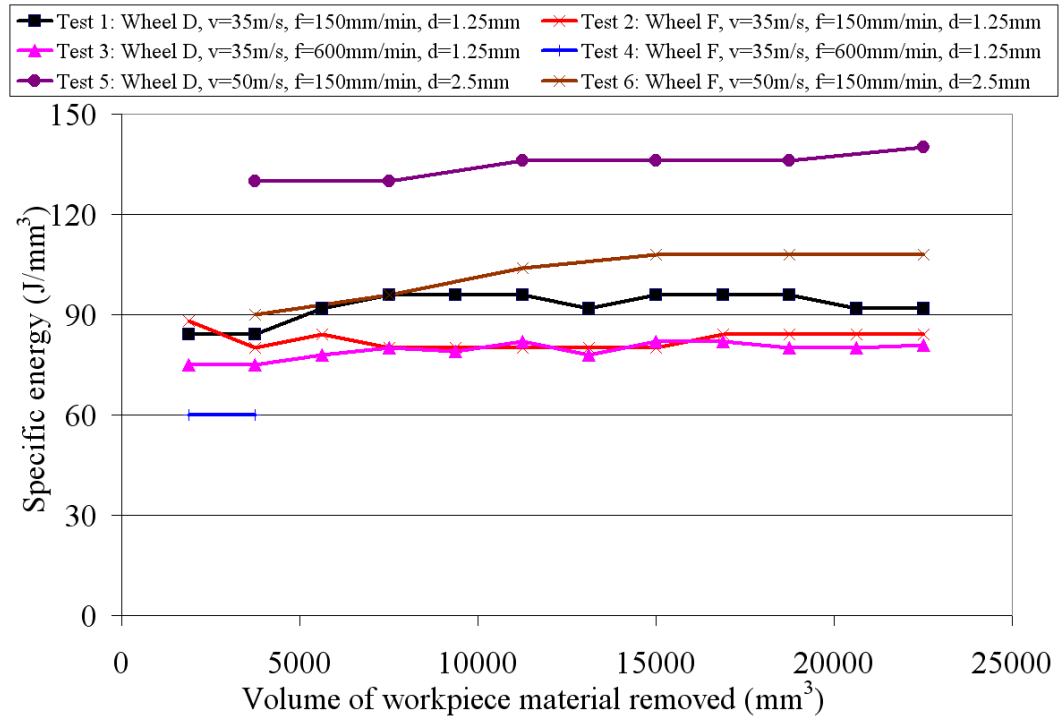


Figure C82: Tangential force against volume of workpiece material removed (Phase 2Biii)

APPENDIX D: List of Publications

Papers published:

- [1] R.Hood, D.K.Aspinwall and W.Voice, (2005), A Review of the Machinability of Gamma Titanium Aluminide Intermetallic Alloys, Proceedings of the 22nd International Manufacturing Conference (IMC22), Pages: 315-323, ISBN: 0-9551218-0-9.
- [2] R.Hood, F.Lechner, D.K.Aspinwall and W.Voice, (2006), Creep Feed Grinding of Gamma Titanium Aluminide and Burn Resistant Titanium Alloys Using SiC Abrasive, Proceedings of the 2nd CIRP High Performance Cutting Conference (CD ROM), Vancouver, Canada.
- [3] R. Hood, D.K. Aspinwall and W. Voice, (2006), Creep Feed Grinding of a Gamma Titanium Aluminide Intermetallic Alloy Using SiC Abrasives, Proceedings of the Advances in Materials and Processing Technologies (AMPT) (CD ROM), July 30th-August 3rd 2006, Las Vegas, Nevada, USA.
- [4] R.Hood, D.K.Aspinwall and W.Voice, Creep Feed Grinding of Gamma Titanium Aluminide and Burn Resistant Titanium Alloys Using SiC Abrasive, International Journal of Machine Tools and Manufacture, Volume 47, Issue 9, July 2007, Pages 1486-1492, ISSN: 0890-6955.
- [5] R. Hood, D.K. Aspinwall and W. Voice, Creep Feed Grinding of a Gamma Titanium Aluminide Intermetallic Alloy using SiC abrasives, Journal of Materials Processing Technology, Volume 191, Issues 1-3, 1 August 2007, Pages 210-214, ISSN: 0924-0136.
- [6] R.Hood, D.K.Aspinwall, W.Voice, P.Dando and K.Tuffy, (2007), Creep Feed Grinding of γ -TiAl Using Superabrasive Wheels, Advances in Abrasive Technology X, Proceedings of the ISAAT 2007 Conference, September 25-29th 2007, Detroit, USA, Pages: 397-403, ISBN: 087263853-7.

Papers submitted:

- [1] S.L.Soo, R.Hood, M.Lannette, D.K. Aspinwall and W.Voice, Creep Feed Grinding of Burn Resistant Titanium (BuRTi) using Superabrasive Grinding Wheels, The International Journal of Advanced Manufacturing Technology, Submitted: March 2010.

Papers under preparation:

- 1] R.Hood, C.M.Johnson, S.L. Soo and D.K. Aspinwall, High Speed Ball Nose End Milling of Burn Resistant Titanium (BuRTi).
- [2] R.Hood and D.K. Aspinwall, High speed milling of a Gamma Titanium Aluminide Intermetallic Alloy.